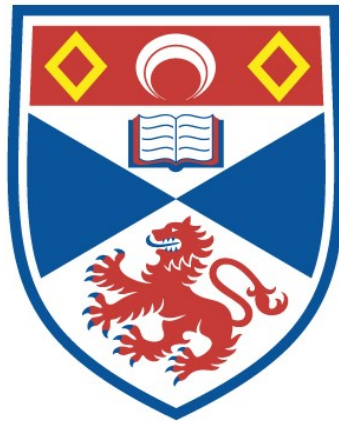


SEDIMENTOLOGY AND PETROLOGY OF THE  
CARBONIFEROUS ROCKS OF ST MONANCE, FIFE,  
SCOTLAND

Mohammed A. Al-Rubaii

A Thesis Submitted for the Degree of PhD  
at the  
University of St Andrews



1986

Full metadata for this item is available in  
St Andrews Research Repository  
at:  
<http://research-repository.st-andrews.ac.uk/>

Please use this identifier to cite or link to this item:  
<http://hdl.handle.net/10023/15469>

This item is protected by original copyright

SEDIMENTOLOGY AND PETROLOGY  
OF THE  
CARBONIFEROUS ROCKS  
OF  
ST MONANCE - FIFE - SCOTLAND

Thesis presented for the degree of Doctor of Philosophy in the  
Faculty of Science, University of St Andrews.

by

MOHAMMED A AL-RUBAI

1986



ProQuest Number: 10170839

All rights reserved

INFORMATION TO ALL USERS

The quality of this reproduction is dependent upon the quality of the copy submitted.

In the unlikely event that the author did not send a complete manuscript and there are missing pages, these will be noted. Also, if material had to be removed, a note will indicate the deletion.



ProQuest 10170839

Published by ProQuest LLC (2017). Copyright of the Dissertation is held by the Author.

All rights reserved.

This work is protected against unauthorized copying under Title 17, United States Code  
Microform Edition © ProQuest LLC.

ProQuest LLC.  
789 East Eisenhower Parkway  
P.O. Box 1346  
Ann Arbor, MI 48106 – 1346

TK A 425

*This thesis is dedicated to*

*My mother*

*and*

*To my wife, my daughters, Likaa and Zahaa  
and to my brother, Fadhil A Al-Rubaii*

ACKNOWLEDGEMENTS

I take this opportunity to express my gratefulness to Professor E K Walton, my supervisor for suggesting the project and for his kind advice, stimulating discussions and encouragement throughout my study period.

It is my pleasure to record sincere appreciation and gratefulness to my wife, Layla for her patience and encouragement throughout this study. Not forgetting my mother and other family members for their constant encouragement over the course of the project.

Thanks are also due to the technical staff at St Andrews University, particularly Jim Allan, Andy Mackie, Sandy Edwards, Richard Batchelor, Alistair Reid, Donald Herd, Angus Calder and Judy Kinnaird for their efforts over the last years. I am also thankful to Mrs J Galloway and Mr S Bateman for their general help. Many thanks to Kit Finlay for typing the manuscript.

Sincere thanks are due for the help given by Dr W E Stephens for computing work, Dr A R MacGregor for the identification of some fossil fragments, and to every member of this department for their help and co-operation.

I am also thankful to Mr Andrew Tweedie of the Petroleum Engineering Department, Heriot Watt University and the technical staff particularly Mr Colin McPhee, for porosity/permeability measurements, and Dr P J Hill of the Grant Institute of Geology, Edinburgh, for electron microprobe analyses.

I owe a special thanks to the Iraqi Government for the permission to continue my study.

ABSTRACT

1 The rocks of the study area belong to the upper part of the Calciferous Sandstone Series, and the Lower Limestone Group of the St Monance syncline. The succession consists of alternating limestones, shales, siltstones, and sandstones with occasional coals. Six sedimentary cycles were examined, and the boundaries to cycles were taken at those points where a carbonate lithology occurs.

2 Sedimentary structures include rib-and-furrow structures, large-scale, mainly trough cross-lamination, hummocky cross-stratification, and deformation structures including pseudonodules. Lenticular, wavy and flaser bedding are common. The main palaeocurrent directions are towards the south-west.

3 Sediment distribution, structures, and grain size studies lead to the depositional model of deltaic sediments prograding from NE to SW.

4 Petrological studies by optical microscope, SEM, and X-ray diffraction have been carried out especially on the sandstones. The rocks classify as orthoquartzites. The provenance suggested is principally one of low-grade metamorphic rocks.

5 Studies of diagenesis show cements of carbonates, quartz and iron-oxides. Authigenic clay minerals are mainly kaolinite with smaller amounts of illite, chlorite and smectite.

6 The amount of original pore space has been reduced by precipitation of cement and clays. Before the reduction the porosity value may have reached 40%. Two methods were used to get the actual amount of porosity, core sample and thin-section, and they gave values of 30-60% and 25% respectively. The sandstones are mostly permeable, and the pore types associated are intergranular, either formed through dissolution of carbonate cement or other unstable materials. If there has been little or no dissolution, and/or if a high amount of clay is present, microporosity is developed and thirteen types have been recognized. Microporosity may reach up to 89% of the total porosity as determined by mercury injection.



In submitting this thesis to the University of St Andrews I understand that I am giving permission for it to be made available for use in accordance with the regulations of the University Library for the time being in force, subject to any copyright vested in the work not being affected thereby. I also understand that the title and abstract will be published, and that a copy of the work may be made and supplied to any bona fide library or research worker.

<u>CONTENTS</u>	<u>PAGE NO</u>
ACKNOWLEDGEMENTS .. .. .	I
CERTIFICATE .. .. .	II
ABSTRACT .. .. .	III
COPYRIGHT .. .. .	V
CONTENTS .. .. .	VI
LIST OF ILLUSTRATIONS .. .. .	XI
LIST OF TABLES .. .. .	XLIV
LIST OF APPENDICES .. .. .	XLV
<u>CHAPTER 1 INTRODUCTION</u> .. .. .	1
1.1 Location of the area .. .. .	1
1.2 History of previous research .. .. .	1
1.3 Cyclicity .. .. .	5
1.4 Aims of the study .. .. .	7
<u>CHAPTER 2 THE SUCCESSION</u> .. .. .	9
2.1 Choice of cycle boundaries and succession .. .. .	9
2.2 Facies cycle W .. .. .	9
2.2a Description .. .. .	9
2.2b Interpretation .. .. .	10
2.3 Facies cycle L .. .. .	12
2.3a Description .. .. .	12
2.3b Interpretation .. .. .	13
2.4 Facies cycle B .. .. .	16

	<u>PAGE NO</u>
2.4a Description .. .. .	16
2.4b Interpretation .. .. .	20
2.5 Facies cycle T .. .. .	24
2.5a Description .. .. .	24
2.5b Interpretation .. .. .	28
2.6 Facies cycle F .. .. .	30
2.6a Description .. .. .	30
2.6b Interpretation .. .. .	37
2.7 Facies cycle S .. .. .	40
2.7a Description .. .. .	40
2.7b Interpretation .. .. .	52
2.8 Tectonic activity .. .. .	52
2.9 Depositional environment .. .. .	56
2.10 Depositional modal .. .. .	57
2.11 Summary and conclusion .. .. .	60
<u>CHAPTER 3 TRACE FOSSILS</u> .. .. .	62
3.1 Introduction .. .. .	62
3.2 Teichichnid Units .. .. .	62
3.3 Units T2 and T3 .. .. .	67
3.4a Unit F2 .. .. .	70
3.4b Units F3 and F4 .. .. .	72
3.5a Unit S1 Mill Hill Marine Band .. .. .	76
3.5b Units S3 and S5 .. .. .	81
3.5c Unit S8 .. .. .	84
3.5d Unit S12 to S17 .. .. .	84
3.5e Unit S24 .. .. .	86
3.6 Discussion .. .. .	86

	<u>PAGE NO</u>
<u>CHAPTER 4 INORGANIC SEDIMENTARY STRUCTURE</u> .. .. .	89
4.1 Sedimentary structure and geometry of sandstone .. ..	89
4.2 Palaeocurrent analysis .. .. .	89
4.2.1 Cycle L .. .. .	90
4.2.1a Ripple bedding unit (L3*) .. .. .	90
4.2.2 Cycle B .. .. .	92
4.2.a Ripple and trough cross- stratification unit (B7B) .. .. .	92 92
4.2.3 Cycle T .. .. .	92
4.2.3a Units T2 and T3 .. .. .	98
4.2.4 Cycle F .. .. .	98
4.2.4a Units F1 - F4 .. .. .	98
4.2.4b Unit F5 .. .. .	105
4.2.5 Cycle S .. .. .	115
4.2.5a Units S2 and S3 .. .. .	115
4.2.5b Units S12 - S20 .. .. .	117
4.3 Secondary deformation structures .. .. .	122
4.3.1 Distorted lamination unit (B7) .. .. .	124
4.3.2 Pseudonodules unit (F3) .. .. .	124
4.3.3 Deformed sandstone unit (S21) .. .. .	125
4.4 Conclusion .. .. .	131
 <u>CHAPTER 5 PETROGRAPHY</u> .. .. .	 133
5.1 Petrography .. .. .	133
5.2 Quartz .. .. .	135
5.2.1 Polycrystalline grains .. .. .	139
5.2.1a Number of crystal units .. .. .	142

5.2.1b Kind of intercrystalline boundaries	..	..	142
5.2.2 Monocrystalline	..	..	142
5.2.2a Non-undulatory quartz	..	..	146
5.2.2b Undulatory quartz	..	..	146
5.2.3 Discussion	..	..	150
5.3 Feldspar	..	..	150
5.4 Rock fragments	..	..	152
5.5 Heavy minerals	..	..	155
5.6 Cement	..	..	155
5.6.1 Carbonate cement	..	..	155
5.6.2 Silica overgrowth	..	..	157
5.6.3 Iron-oxide	..	..	162
5.6.4 Cement relationships	..	..	168
5.6.5 Conclusions	..	..	173
5.7 Micras and clay minerals	..	..	174
5.7.1 Large detrital grains	..	..	174
5.7.2 Fine grained clay	..	..	175
5.7.3 Characteristics of the common forms of clay	..	..	183
5.7.3a Kaolinite	..	..	183
5.7.3b Illite	..	..	183
5.7.3c Chlorite	..	..	187
5.7.3d Smectite	..	..	187
5.8 Overall Conclusion	..	..	187
<u>CHAPTER 6 POROSITY PERMEABILITY AND PORE GEOMETRY</u>	..	..	194
6.1 Introduction	..	..	194
6.2 Porosity	..	..	194
6.3 Mechanisms of porosity reduction	..	..	199



LIST OF ILLUSTRATIONS

Text Figure No

- 1.1 Geological sketch-map of the coast of St Monance.
- 1.2 Vertical section of Carboniferous Measures in the St Monance area (after Forsyth et al, 1968).
- 1.3 Comparison of different methods of placing cyclothem boundaries (after Belt, 1975).
- 2.1 Generalised succession of cycles (W) and (L) on both sides of the St Monance syncline.
- 2.2 Calcareous shales crowded with brachiopods especially Rhynchonellid. Unit (W1) - West side.
- 2.3 Slab of fossiliferous brachiopod shale. Unit (W2) - West side.
- 2.4 Slab of sandstone with parallel and micro-cross-lamination. Unit (L2) - West side.
- 2.5 Upper part of Unit (L3), showing the deformed bed and contains burrows. West side.
- 2.6 Herringbone structure in contact with the deformed bed

	above it. Unit (L3) - West side.	15
2.7	Generalised succession of cycle (B) on both sides of the St Monance syncline.	17
2.8	General view of the channel sandstone (B7), showing the erosional contact between Units (B7a, B7b) - West side.	19
2.9	Photograph showing the upper surface of Unit (B7B) covered by ripples. West side.	19
2.10	General view of the channel sandstone (B7) showing the sandstones with mud chips lying at the base of Unit (B7N) - West side.	21
2.11	Deformation sandstone (water escape). Unit (B7N). - West side.	21
2.12	The upper part of Unit (T1) and lower part of Unit (T2) showing the predominance of shale with streaks of siltstone. East side.	22
2.13	Slab showing the wave ripple. Unit (T2) - East side.	22
2.14	Sketch illustrating the gradual increase in thickness and in grain size of Units T1 to T3 - East side.	23
2.15	Sketch showing the morphological of lateral variation in	



	lithofacies of Units T4 to T15, and especially the position of bed containing herringbone structure Unit (T8) - East side.	23
2.16	General view showing the lithofacies from units (T2 to T3), and especially the sharp contact between Units T2 and T13 - East side.	26
2.17	Stigmaria roots on the upper surface of the massive sandstone Unit (T15) - East side.	26
2.18	Sketch showing the lateral variation in the second coarsening upward sequence - West side.	27
2.19	Generalised succession of cycle (T) on both sides of the St Monance syncline.	29
2.20	Slab showing the core of the septarian nodules.	33
2.21A	Photograph showing the facies of Unit (F4) - East side.	33
2.21B	Photograph showing the starved ripples in the mudstone facies of Unit (F4), which are sometimes connected together. East side.	33
2.22	Photograph showing the erosional base of the channel (F5), (F5), cut through the Unit below (F4). East side.	34
2.23	Photograph showing superimposed fine-grained sandstone in	

	first member (F5a), with micro-trough cross-lamination. East side.	34
2.24	General view of the channel body sandstone, showing that the first member (F5a) is thinning towards the West. East side.	35
2.25	General view of the first unit of second member (F5b), with low angle planar cross-bedding. East side.	35
2.26	Photograph showing the micro-cross-lamination and flaser bedding in the second unit of the second member (F5b) - East side.	35
2.27	General view of the second and third member of the channel body (F5b and F5c) - East side.	36
2.28A	Slab contains plant fragment from the upper part of the channel unit. East side.	36
2.28B	Photograph showing rib-and-furrow, and coalified coal stem oriented in the same direction as the ripple-forming current. Lower surface of linguoid ripple beds of (F5c) - East side.	36
2.29	Generalised succession of cycle (F). East side.	39
2.30	General view showing the upper part of the channel Unit (S15) and the coarsening upwards Units (S16, S17), truncated by an erosion surface below Unit (S18) which	

	contains large scale cross-stratification. East side.	45
2.31	Photograph showing Unit (S16) with trace fossils and the interbedded sandstone of Unit (S17) which is formed of ripples and small scale trough cross-stratification. East side.	45
2.32	General view of deformation sandstone Unit (S21c). East side.	47
2.33	Sketch showing the vertical succession and lateral variation of Unit (S24). East side.	48
2.34A	General view of interbedded sandstone and siltstone, showing the smooth contact between them. Unit (S24) - East side.	50
2.34B	Interbedded sandstone or silty shale with irregular contact. Ripples and small scale trough cross-stratification. Unit (S24) - East side.	50
2.35	Photograph showing the large channel of Unit (S24) contains planar cross-stratification. East side.	51
2.36	Upper surface of seat-earth sandstone contains plant fragment and stigmara root. East side.	51
2.37	Generalised succession of cycle (S) - East side of the St Monance syncline.	53

2.38	The thickness and arrangement of cyclothems.	54
2.39	Schematic reconstruction of sediments in St Monance area.	59
3.1	General view of teichichnids and planolites in the lower surface of bioturbation bed (W4) - East side.	65
3.2	Vertical sand-plugged teichichnid found in contact between Unit (T14) and Unit (T15) - East side.	65
3.3	<u>Teichichnus</u> ; Unit F2, laminae are horizontal and concave upwards. East side.	66
3.4	Sand-plugged teichichnid in bioturbation bed. Unit (S14) - East side.	66
3.5	Example of <u>Teichichnus</u> in the lower surface of limestone. Unit (F) - East side.	68
3.6	Cross-section of the <u>Teichichnus</u> in figure above. Also showing <u>Zoophycus</u> and other fossil fauna crinoid and brachiopods.	68
3.7	Example of <u>Scolicia</u> , Unit (T2) - East side.	69
3.8	Example of <u>Aulichnites</u> , Unit (T2) - East side.	69

	<u>Page No</u>
3.9	Example of <u>Pelecypodichnus</u> , Unit (T2) - East side. 71
3.10	Example of <u>Conichnus</u> , Unit (T3) - East side. 71
3.11	Example of <u>Chondrites</u> , Unit (F2) - East side. 73
3.12A	Linear footprints, trace fossils, Unit (F3) - East side. 73
3.12B	Sketch showing the size, distance of the large footprint in Figure 3.12A. 73
3.13A	Three sets of parallel lines of depressions produced by crabs on recent sediment. 74
3.13B	Close up of figure 3.13A. 74
3.14	Two types of trace fossils <u>Scolicia</u> and <u>Monocraterion</u> . Unit (F3) - East side. 75
3.15	Trace fossils tube with laminae as <u>Teichichnus</u> . Unit (F3) - East side. 75
3.16	Trace fossil on the upper surface of linguoid ripples. Unit (F4) - East side. 77
3.17A, B	Similar trace as above formed on recent sediment by gastropods. 77
3.18	Example of <u>Diplocraterion</u> as U-shaped. Lower part of

		<u>Page No</u>
	Unit (S2) - East side.	78
3.19	Example of <u>Diplocraterion</u> , not complete U-shape. Unit (S2) - East side.	78
3.20A	Example of <u>Palaeophycus</u> on the surface of nodules band. Unit (S2) - East side.	79
3.20B	Example of <u>Palaeophycus</u> showing the dimension. Unit (S2) - East side.	79
3.21	Example of <u>Eione</u> , showing the radiating, branching and segmentation. Unit (S2) - East side.	80
3.22	Example of <u>Palaeophycus</u> in transitional zone.	80
3.23	Cross-section showing <u>Planolites</u> in different orientation and locally disturbing the cross- stratification.	82
3.24	Escape structure and <u>Lockcia</u> . Unit (S3a) - East side.	82
3.25	Cross-section showing <u>Planolites</u> . Unit (S5) - East side.	83
3.26	Example of <u>Chondrites</u> showing the dendritic shapes of small cylindrical. Unit (S8) - East side.	83
3.27	Example of <u>Teichichnus</u> as simple U-shaped. Unit (S11) -	

	East side.	85
3.28	Example of <u>Rhysonetron</u> . Unit (S17) - East side.	85
3.29	Cross-section showing circular to oval in shape of <u>Laevicyclus</u>	87
3.30	Example of <u>Monocraterion</u> showing the series of rings. Unit (S24) - East side.	87
4.1	Photograph showing different orientation of ripple marks. Unit (L3) - West side.	91
4.2	Rose diagrams showing the palaeocurrent direction of Unit (L3) - West side. a Palaeocurrent direction of the entire foresets structure. b Ripples and the divergence in directions.	91
4.3	Photograph showing the orientation of ripple marks and Rose diagrams showing the palaeocurrent direction as towards SE. Unit (B7B) - West side.	93
4.4	Slab showing the entire sedimentary structure of Unit (B7B) - West side.	93
4.5	Photograph showing the predominance trough cross-bedding above Unit (B7B) - West side.	93

- 4.6 Palaeocurrent patterns of individual cross-beds, showing the slight variation from one bed to another. Unit (B7) - West side. 94
- 4.7 Histogram of cross-bed dips of trough cross-beds. Unit (B7) - West side. 95
- 4.8 Photograph showing parallel lamination, wavy lenticular together with wave ripples with bipolar foresets. Unit (T2) - East side. 97
- 4.9 Photograph showing the sand content increasing upwards. Unit (T2) - East side. 97
- 4.10 Sketch showing the location of plant fragment samples. 99
- 4.11 Rose diagrams showing the orientation of plant fragment and the palaeocurrent direction of cross-lamination. Unit (T2) - East side. 100
- 4.12 Slab showing parallel lamination of siltstone and silty shale with mudstone. The boundary is usually sharp, but gradational is also present. Unit (F2) - East side. 101
- 4.13 Slab showing the association of large ripple form sets, gradually change into parallel lamination, then into small form sets. Rose diagram showing the different direction of these form sets. 102



		<u>Page</u> <u>No</u>
4.14	Slab showing the rich array of cross-lamination in sandstone. The direction of cross-lamination frequently reverses NNW and SSE.	102
4.15	Slab showing bidirectional cross-lamination typical of wave ripples.	102
4.16	Slab showing different shape of bidirectional cross-lamination, boundaries are curved and diffuse. Wave direction predominant towards NNE.	103
4.17	Slab showing vertical change into bidirectional cross-lamination with sign of bioturbation.	103
4.18A	Photograph showing lenticular and sometimes streaks in the highest lithotype Unit (F3).	104
4.18B	Sketch showing the main sedimentary structure found in the highest lithotype Unit (F3).	104
4.19	Photograph showing the flute crust and their orientation. Unit (F4) - East side.	106
4.20	Linguoid ripples and their palaeocurrent direction of Unit (F4) - East side.	106

4.21	Photograph showing the first unit of the first member (F5a), and their vertical and lateral variation. Palaeocurrent direction towards the W.	108
4.22	Photograph showing the medium scale trough cross-bedding in (F5a) and their palaeocurrent direction as towards SW.	108
4.23	Slabs within scour and fill unit in (F5a) showing their ripple set. Palaeocurrent direction towards SW.	110
4.24	Photograph showing the lamination sandstone with primary current lamination, second member (F5b) - East side.	111
4.25	Photograph showing parallel trough cross-lamination separated by cusp-like ridge. Palaeocurrent direction is towards SE. Second member (F5b) - East side.	111
4.26	Slab of rippled sandstone showing the climbing sets of lee side laminae. Second member (F5b) - East side.	111
4.27	Photograph showing the large scale trough cross-stratification with erosional base of the first unit in the third member (F5c). Palaeocurrent direction is towards SSE - East side.	113
4.28	Photograph showing the rib-and-furrow in the lower surface of linguoid ripple, their palaeocurrent direction is $200^{\circ}$ towards SW.	113

4.29	Rose diagram of linguoid ripples in third member (F5c). East side.	114
4.30	Rose diagram of the internal structure of the last unit in the third member (F5c). East side.	114
4.31	Hummocky cross-stratified sandstone and their palaeocurrent direction. Unit (S2) - East side.	116
4.32	Photograph showing the scour surface within the hummocky cross- stratification. Unit (S2) - East side.	116
4.33	Slab showing sharp contact between the trough cross-lamination and the horizontal laminae. Palaeocurrent direction is towards NW.	118
4.34	Slab showing the planar cross-lamination of fine grained sandstone.	118
4.35	Section showing vertical section and lateral variation in Units S12-S20 at St Monance Bathing Pool. (modified after Chisholm 1971).	119
4.36	Slab showing wavy, flaser and the trough cross-lamination. Unit (S13) - East side.	121
4.37	Rose diagram of the large scale trough cross-stratification. Unit (S13) - East side.	121

	<u>Page No</u>
4.38	Rose diagram of the large scale trough cross-stratification. Unit (S14) - East side. 121
4.39	Slab showing the internal structure of the first bed in Unit (S17), and their palaeocurrent direction as towards WNW - East side. 123
4.40	Isolated set of cross-strata below the ripple marks, and their palaeocurrent direction as towards the W. Unit (S17) - East side. 123
4.41	Large scale trough cross-stratification of Unit (S18), and their palaeocurrent direction towards WSW. 123
4.42A	Photograph showing the distorted lamination. Unit (B7) - West side. 127
4.42B	Sketch showing the development of the distorted lamination. 127
4.43	Photograph showing the pseudonodules deformation structure. Unit (F3) - East side. 128
4.44	Illustration from Kuenen's paper (1965). 128
4.45	Sketch showing the sequence of events leading to the development of the pseudonodules deformation structures. 129

4.46A	Sketch showing the horizons and the subhorizons of the deformation structure. Unit (S21) - East side.	130
4.46B	Photograph showing the typical deformation structure. Unit (S21) - East side.	130
5.1	Petrographic analysis of St Monance syncline.	134
5.2	Classification of sandstone (after McBride 1963).	136
5.3A	Photomicrograph showing detrital quartz grain with abundant acicular shaped rutile inclusions. Ordinary light, x 500.	137
5.3B	Photomicrograph showing globular liquid/gas (biphase) and monophasic inclusions in quartz grain. Ordinary light, x 1000.	137
5.3C	Photomicrograph showing regular tiny inclusions in quartz grain. Ordinary light, x 1000.	138
5.3D	Photomicrograph showing mono and biphase of regular inclusions in quartz grain. Ordinary light, x 1000.	138
5.4	The relationship between the percentage of polycrystalline in total quartz and the modal sand size.	140
5.5	The relationship between polycrystalline and carbonate cement.	141
5.6	Four parameters of detrital quartz to identify source rock	

	<u>Page No</u>
of the quartz (after Basu <u>et al</u> 1975).	143
5.7A Photomicrograph of polycrystalline quartz grain showing both straight and sutured intercrystalline boundaries. Crossed polars, x 100.	144
5.7B Photomicrograph of polycrystalline quartz grain showing the sutured intercrystalline boundaries, and bimodal size distribution. Crossed polars, x 250.	144
5.8 Photomicrograph of polycrystalline quartz, showing sutured intercrystalline boundaries and elongated crystal. Crossed polars, x 50.	144
5.9 Photomicrograph of polycrystalline quartz-grain, with sutured intercrystalline boundaries, and extremely elongated crystal. Crossed polars, x 125.	145
5.10 Photomicrograph showing polycrystalline quartz-grain, formed of two crystals, with curved to straight intercrystalline boundaries. Crossed polars, x 100.	145
5.11 Photomicrograph showing polycrystalline quartz-grain, seems to represent an arrested stage. Crossed polars, x 100.	145
5.12 The relationship between percent of non-undulatory quartz and modal sand size.	147

5.13A	The relationship between quartz in sand-sized grains and non-undulatory quartz in non-polycrystalline quartz. (after Blatt and Christie 1963).	148
5.13B	Histogram of the quartz grain types.	148
5.14	The relationship between percentage of undulatory and polycrystalline in total quartz.	149
5.15	Undulatory quartz fraction of sandstone plotted against soft material (clay, iron-oxide, and carbonate).	151
5.16	SEM photograph showing block feldspar, fractured and altered to clay material.	153
5.17	Photomicrograph showing feldspar with typical plagioclase twinning, and has been partly replaced by carbonate cement. Crossed polars, x 200.	153
5.18	Photomicrograph showing plagioclase feldspar with overgrowth. Crossed polars, x 200.	154
5.19	Photomicrograph showing microcline feldspar with overgrowth. Crossed polars, x 100.	154
5.20	The relationship between the percentage of clay and carbonate.	156
5.21	SEM photograph showing carbonate cement enclosing and	

	corroding the quartz grain overgrowth.	158
5.22	SEM photograph showing two types of carbonate, calcite and dolomite.	158
5.23A, B	SEM photograph showing poikilitic calcite cement, with more than one set of cleavages.	159
5.24	Photomicrograph showing groups of grains with overgrowth, pressolving leads to dissolving some silica overgrowth. Crossed polars, x 250.	160
5.25	Photomicrograph showing polycrystalline quartz grain with overgrowth. Crossed polars, x 125.	160
5.26	Photomicrograph showing normal overgrowth with triple junction. Crossed polars, x 200.	160
5.27A	Photomicrograph showing uneven quartz overgrowth. Crossed polars, x 100.	161
5.27B	Photomicrograph showing uneven quartz overgrowth due to pressolving after silica overgrowth formed. Crossed polars, x 250.	161
5.28	Photomicrograph showing double quartz overgrowth. Crossed polars, x 200.	161



5.29	SEM photograph showing quartz grain not well developed overgrowth.	163
5.30	SEM photograph showing well-developed but incomplete crystal faces.	163
5.31	SEM photograph showing multiple overgrowth.	164
5.32	SEM photograph showing the fourth stage of formation of euhedral quartz crystal.	164
5.33	SEM photograph showing quartz overgrowth as complete layers.	165
5.34	Photomicrograph showing thick reddish-brown material surrounding the original quartz grain. Ordinary light, x 500.	166
5.35A	SEM photograph showing rounded flakes of iron oxide.	166
5.35B	SEM photograph and EDS analysis showing the authigenic hematite crystals and their major element.	167
5.36	Photomicrograph showing order of precipitation of cement. Crossed polars, x 250.	170
5.37	The relationship between carbonate cement and silica overgrowth.	172
5.38A	XRD scans of clay function showing the effects of various treatments.	176

		<u>Page No</u>
5.38B	XRF scans of standard kaolinite sample and the percentages of kaolinite in 23 samples.	178
5.39A	Standard curve of different percentages of kaolinite clay supplied by china clays.	179
5.39B	Comparison between the percentage of kaolinite estimated by XRD and the percentage of clay from point counting.	179
5.40	Plot kaolinite against mica.	181
5.41	Plot of feldspar (from thin section) against kaolinite (XRD).	181
5.42	The relationship between stratigraphic level and percentages of kaolinite (XRD).	182
5.43	SEM photograph showing quartz grain overgrowth coated by authigenic kaolinite.	184
5.44A	SEM photograph showing authigenic kaolinite arranged in 'book' as filling large pore between quartz overgrowths.	184
5.44B	SEM photograph showing alignment of authigenic kaolinite as pore lining.	185
5.45	SEM photograph showing typical vermicular authigenic kaolinite.	185

5.46	SEM photograph showing typical bent 'accordion' of authigenic kaolinite.	186
5.47	SEM photograph showing authigenic kaolinite as simultaneously with silica overgrowth, or even before.	186
5.48A	SEM photograph showing illite occurring as irregular flakes.	188
5.48B	SEM photograph showing illite irregular flakes beside the chlorite honeycomb.	188
5.49A	SEM photograph showing chlorite 'rosettes' filling the pore.	189
5.49B	SEM photograph showing chlorite 'cabbagehead' structure.	189
5.49C	SEM photograph showing chlorite 'honeycomb' growth form.	190
6.1A	Chart showing the relationship between depth and porosity, and the difference between the percentages of porosities from thin section and routine core samples.	197
6.1B	Chart showing the relationship between depth and porosity (routine core sample) and the difference between the percentage of porosity from samples parallel and normal to the bedding plane.	198
6.2	Effect of burial depth on the types of grain-to-grain contact.	200

	<u>Page No</u>
6.3	Photomicrograph showing the silica overgrowth filling the spaces and enlargin the quartz grains leads to different types of contact. Crossed polars, x 500. 202
6.4	Photomicrograph showing pressure solution between two quartz grains. 202
6.5	SEM photograph showing quartz overgrowth forming micro-porosity. 203
6.6	SEM photograph showing mica bent and fractured. 203
6.7	Photomicrograph of microcline grain fracture and associated with clay matrix. 204
6.8	Permeability reduction. 206
6.9A	Chart showing porosity-permeability relationship. 207
6.9B	Chart showing cement-permeability relationship. 208
6.10	Plot showing the effect of clay + carbonate on porosity. 209
6.11	Variation of porosity with clay. 210
6.12	Mercury-injection pressure, pore diameter, and cumulative percent of different samples. 212

		<u>Page No</u>
6.13	A relationship between cumulative percent and pore size.	213
6.14	Relation between grain size and microporosity.	214
6.15A	SEM photograph showing pores and not completely filled by clay.	216
6.15B	SEM photograph showing the "oversized pore" larger than the surrounding grains.	216
6.16	The relationship between clay + carbonate and microporosity.	217
6.17	Mercury-injection curve and photomicrograph of medium grains. Unit (S27a) - East side.	220
6.18	SEM photograph showing the rock has obvious pores despite a lot of quartz overgrowth.	221
6.19A	Photomicrograph showing feldspar grain nearly completely dissolved. Ordinary light, x 500.	222
6.19B	Photomicrograph showing two grains of feldspar nearly completely dissolved. Ordinary light, x 250.	222
6.19C	Three grains of feldspar effected by dissolution, and good interconnection between inter, and intragranular pores. Ordinary light, x 50.	223

		<u>Page No</u>
6.20	Photomicrograph of partial dissolution of feldspar grain. Ordinary light, x 50.	223
6.21	Mercury-injection curve and photomicrograph. Unit (S26) - East side.	224
6.22A	Photomicrograph showing vugs, good interconnection with intergranular pores. Ordinary light, x 25.	225
6.22B	Photomicrograph showing the oversized pore. Ordinary light, x 125.	225
6.23	Mercury-injection curve and photomicrograph. Unit (S3a) - East side.	227
6.24	Mercury-injection curve and photomicrograph. Unit (T7c) - West side.	228
6.25	Mercury injection curve and photomicrograph. Unit (F5b) - East side.	229
6.26	Example of porosity after dissolution of cement. Ordinary light, x 125.	231
6.27	Secondary porosity resulting from dissolution of cement after replacing the feldspar grain and margin of quartz. Ordinary light, x 500.	231

	<u>Page No</u>
6.28 Diagenetic history of secondary porosity of St Monance sandstones.	235
6.29 Photomicrograph of open grain fracture. Ordinary light, x 125.	237
6.30 Photomicrograph showing carbonate cement deposited after the silica overgrowth. Crossed polars, x 500.	237
7.1 Diagram showing the solubility of silica, aluminium, and the effect of mixing silica and alumina (after Millot 1970).	239
7.2 SEM photograph showing pits formed on the surface of quartz overgrowth due to a chemical solution.	241
7.3 SEM photograph showing the formation of sub-parallel ridges due to a chemical solution.	241
7.4 SEM photograph showing the effect of chemical weathering and etched areas are common.	242
7.5 SEM photograph showing euhedral overgrowth and the chemical corrosion of quartz.	242
7.6 Photomicrograph of feldspar overgrowth and quartz overgrowth associated with clay material. Crossed polars, x 500.	245

7.7	SEM photograph showing carbonate cement replacing the feldspar, while kaolinite is associated with feldspar alteration.	245
7.8	SEM photograph and the EDX analysis showing that authigenic kaolinite formed directly from feldspar grain.	248
7.9	SEM photograph showing that three kinds of clay minerals are arranged sequentially in pore.	252
7.10	Photomicrograph showing detrital mica passing into illite, and then to kaolinite, crossed polars, x 100.	252
7.11A	Plot $K_2O$ Vs $Al_2O_3$ .	254
7.11B	Plot $K_2O$ Vs $TiO_2$ .	254
7.11C	Plot $TiO_2$ Vs $Al_2O_3$ .	254
7.12	Photomicrograph showing the difference between carbonate cement filling and replacing. Crossed polars, x 200.	256
7.13	SEM photograph and EDX analysis showing carbonate cement replacing the kaolinite.	258
7.14	Scheme showing the variation of MgO and FeO wt %.	260
7.15	Plot of CaO and $SiO_2$ wt %.	261



7.16	Time-related environment zonation.	265
8.1	Vertical section of Carboniferous Measures, Facies Variation, of the St Monance syncline.	270

Appendix Figure No

6.1	Microporosity in St Monance Sandstones.	310
6.2	SEM photograph showing the smooth contact between quartz grain and carbonate cement.	311
6.3	SEM photograph showing irregular contact of carbonate cement with quartz grain.	311
6.4	SEM photograph showing the irregular pore formed by replacement, the edge of the quartz by carbonate and then dissolution of some of the carbonate.	312
6.5	SEM photograph showing lamella microporosity along cleavage plane of carbonate crystal.	312
6.6	SEM photograph showing micropores formed from the fracture of calcite crystal followed by dissolution.	314
6.7	SEM photograph showing three different directions of cracks	

	through calcite crystal and formation of micropores.	314
6.8	SEM photograph showing pitted or corroded detrital quartz grain by carbonate which was then dissolved to leave the micropores.	315
6.9	SEM photograph showing corrosion of two quartz grains overgrowth, and formation of micropores.	315
6.10	SEM photograph showing feldspar grain corroded to form micropores.	316
6.11	SEM photograph showing micropores formed by interconnection of more than two basic types and formed as channel micropore.	316
6.12	SEM photograph showing mica, fractured and bent and micropore in between.	318
6.13	SEM photograph showing mica grain splitting and alteration along the cleavage lead to form micropore.	318
6.14	SEM photograph showing lamella microporosity between two quartz grains with overgrowth.	319
6.15	SEM photograph showing micropores along the cleavage by splitting, alteration and pitting of feldspar grain.	319

6.16	SEM photograph showing network pattern of micropores in between clay materials.	320
6.17A	SEM photograph showing micropores between kaolinite particles.	321
6.17B	SEM photograph showing micropores within and in between the particles of varmicular authigenic kaolinite.	321
6.18	SEM photographs showing micropores formed in between polycrystalline grain as lamella and triangular shape.	323
6.19	Genetic classes of secondary sandstone porosity (modified after Schmidt and McDonald 1979b).	326
6.20	Example of secondary porosity resulting from partial dissolution of intergranular cement. Ordinary light, x 125.	327
6.21	Example of porosity created after replacement. Ordinary light, x 250.	327
6.22	Photomicrograph showing secondary porosity resulting from dissolution of carbonate cement filling the fracture of feldspar grain. Ordinary light, x 500.	328
6.23	Photomicrograph showing secondary porosity created by dissolution of sedimentary material as dolomite. Ordinary light, x 125.	328

6.24	Example of porosity resulting from shrinkage of feldspar grain. Ordinary light, x 125.	329
6.25	Example of hybrid porosity. Ordinary light, x 125.	329
6.26	Types of secondary porosity texture (modified after Schmidt and McDonald, 1979b).	331
6.27	Intergranular texture of secondary porosity.	332
6.28	Example of regular intergranular pores resulting from partial dissolution of carbonate cement. Ordinary light, x 125.	334
6.29	Example of regular intergranular pores resulting from nearly complete dissolution of intergranular cement. Ordinary light, x 125.	334
6.30	Example of intergranular pores which were reduced by carbonate cement nearly completely filling the spaces. Ordinary light, x 125.	335
6.31	Photomicrograph showing silica cement reducing the intergranular pores. Crossed polars, x 500.	335
6.32	Photomicrograph of clay matrix filling the pores and reducing the intergranular pore spaces. Crossed polars, x 125.	336

	<u>Page No</u>
6.33      Photomicrograph of intergranular pores reduced by hematite. Ordinary light, x 125.	336
6.34      Photomicrograph of fringing cementation around quartz grain leads to reduction of the intergranular pore. Crossed polars, x 250.	337
6.35      Photomicrograph of enlarged intergranular texture. Ordinary light, x 125.	337
6.36      Photomicrograph of enlarged intergranular texture. Ordinary light, x 125.	339
6.37      Photomicrograph of oversized texture. Ordinary light, x 125.	339
6.38      Photomicrograph of sub-moldic texture. Hand shape, sub- moldic pore. Ordinary light, x 250.	340
6.39      Photomicrograph of sub-moldic texture. Ordinary light, x 250.	340
6.40      Photomicrograph of intragranular pore texture. Crossed polars, x 250.	342
6.41      Photomicrograph of intragranular pore in quartz grain. Ordinary light, x 250.	342

6.42	Photomicrograph of carbonate cement that incompletely replaced a feldspar grain and formed intragranular pores. Ordinary light, x 250.	343
6.43	Photomicrograph of intra-matrix pore texture. Ordinary light, x 250.	343
6.44	Photomicrograph of intra-cement pore texture. Ordinary light, x 500.	345
6.45	Photomicrograph of intra-cement pore texture. Ordinary light, x 125.	345
6.46	Photomicrograph of intra-replacement pore texture. Ordinary light, x 125.	346
6.47	Photomicrograph of intra-replacement pore texture. Crossed polars, x 250.	346
6.48	Photomicrograph of intra-replacement pore texture. Ordinary light, x 125.	347
6.49	Photomicrograph of open rock fracture. Ordinary light, x 25.	347
6.50	Photomicrograph of open grain fracture. Ordinary light, x 250.	350

	<u>Page No</u>
6.51A Photomicrograph of open grain fracture. Ordinary light, x 250.	350
6.51B SEM photograph showing detrital feldspar grain fracture forming branching pore fracture.	351
6.52A SEM photograph of open intragranular fracture.	351
6.52B SEM photograph of open intragranular fracture.	352
6.53A SEM photograph of intergranular sub-isolated pore texture.	352
6.53B SEM photograph of intra-cement sub-isolated pore texture.	353
6.53C SEM photograph of sub-isolated pores created from incomple filling of the intergranular pore by clay matrix.	353
6.53D SEM photograph of intra-granular sub-isolated pore texture.	354
6.53E SEM photograph of intra-granular sub-isolated pore texture.	354

List of Tables

<u>Table No</u>		<u>Page No</u>
2.1	Coal horizons and weight sediment relationship.	55
2.2	Characteristics of sediment of St Monance syncline.	58
3.1	Distribution of trace fossils at St Monance.	64
5.1	Comparison of kaolinite estimated by XRD and clay amount by point counting.	180
6.1	Variation of porosity.	195
7.1	Microprobe analysis of K-feldspar.	246
7.2	Microprobe analysis of mica-illite-kaolinite alteration.	251
7.3	Chemical analysis.	262
7.4	Possible diagenetic reactions.	267



List of Appendices

<u>Appendix No</u>		<u>Page No</u>
5.1	Clastic sediment composition of St Monance sandstones.	296
5.2	Modal composition of sandstones.	297
5.3	Number of units and types of contacts in polycrystalline grains (followed Basu, <u>et al</u> , 1975).	298
5.4	Details of quartz and other components of petrographic analysis.	299
5.5	Separation of clay fraction from the whole rock.	300
5.6	Instrumental condition of XRD for clay mineral determination.	301
6.1	Textural parameters.	302
6.2	Calculation of original porosity (after Rittenhouse 1971).	303
6.3	Values of grain-to-grain contact.	304
6.4	Variation. of reservoir qualities and cementation.	305

	<u>Page No</u>
6.5 Correlation between the cumulative percent pore space with ideal pore diameter in ( $\mu\text{m}$ ).	306
6.6 Comparison between microporosity percentages and the main petrographic variables.	307
6.7 Summary of two highest percent microporosity samples contain.	308
6.8 Classification of microporosity in St Monance sandstones.	309
6.9 Secondary porosity - classification.	324
6.10 Texture of secondary porosity.	330
7.1 Microprobe analysis of carbonate cement.	355
7.2 Precision of electron microprobe data.	356
7.3 Precision of XRF analysis.	357
7.4 Wet chemical techniques.	358

## CHAPTER 1

### 1 INTRODUCTION

#### 1.1 Location of the Area

The present study is mainly concerned with the clastic sedimentary rocks comprising the uppermost Calciferous Sandstone Measures, and the Lower Carboniferous Limestone Group, both of Visean (Currie, 1954; Neves et al., 1973) or Late Mississippian age. George, et al., (1977); considered that the age of the Lower Limestone Group is Brigantian. The rocks occupying the area between Pathhead in the East and St Monance to the West (Fig 1.1, 1.2).

Six sedimentary cycles were examined as exposed on the eastern limb of the St Monance syncline. Whilst four of them are exposed in the western side, the rest are removed through St Monance harbour. The syncline is asymmetrical and plunges  $18^{\circ}$  to  $032^{\circ}$  NE. The boundary for each cycle was taken at a limestone bed. The succession examined was from St Monance White Limestone to the Hosie Limestone.

#### 1.2 History of Previous Research

Previous studies of the Carboniferous Measures in this area have been mainly stratigraphical and have been carried out mostly by officers of the Geological Survey. Investigations on the geology at East Fife prior to 1902 have been summarized by Geikie (1902). Subsequently, little work has been published but it includes Crampton (1905), Macnair (1917), Macgregor (1930), Plemister (1956), Mitchell (1956), Goodlet (1957, 1959), Francis (1965) and Selim et al., (1974). Other workers have been concerned with correlation with other regions,

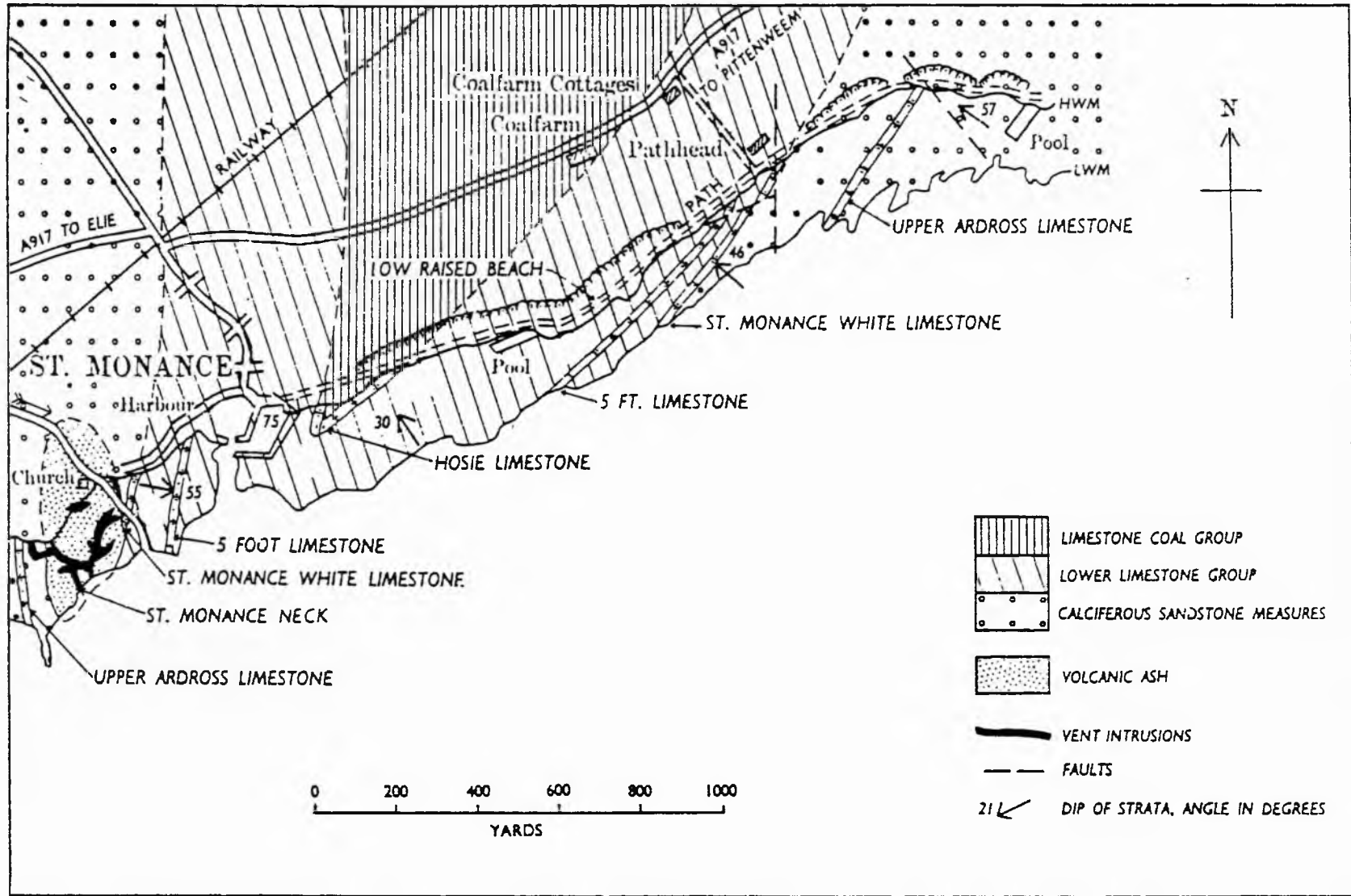


Fig 1.1 Geological sketch-map of the coast of St. Monance  
(after MacGregor, 1968)

eg Wilson (1966), Neves et al., (1973); the paleoecology of invertebrates, (Bennison, 1960, 1961, 1962, Ferguson, 1962, 1963), stratigraphic mapping and correlation of borehole data, (Forsyth and Chisholm, 1968), trace fossil paleoecology, (Chisholm, 1968, 1970a, b), sedimentology, (Greensmith, 1961, 1965, 1966, Belt, 1975, Wilson, 1978), and regional geology (MacGregor, 1968).

Generally, it has been recognized that the St Monance sequence consists of repeated sedimentary cycles of carbonate units which alternate with shales, siltstones, sandstones, shales with clay-band ironstones or nodules and occasional coals. Kirkby (in Geikie, 1902) described four major limestone bands of about 30 ft in total thickness in addition to a minor pseudo-brecciated calcareous band of about 6.5 ft in thickness (Fig 1.2), this latter band has been considered as a major band by Forsyth and Chisholm (1968), Crampton (1905), and others, because it has been taken as equivalent to the Hurlet Limestone of West Scotland which is the base of the Lower Limestone Group.

Goodlet (1957, 1959) studied the lithological variations in the Lower Limestone Group by isopach, isolith, and ratio maps which show relative properties of the shale, limestone and sandstone rock-types, and concluded that the sediments of the Lower Limestone Group were laid down by the delta of a large river which debouched from the North. Although the regional sedimentational setting for the east end of the Midland Valley was established by his pioneering work it was primarily concerned with the Late Visean and Namurian; the framework was similar during the early Visean time (Greensmith, 1962, 1968). Belt (1975, p 446) suggested a destructive, wave dominated delta as the environment of deposition for the sediments of the Lower Limestone

# ST. MONANCE COAST SECTION

(after Forsyth et al, 1968)

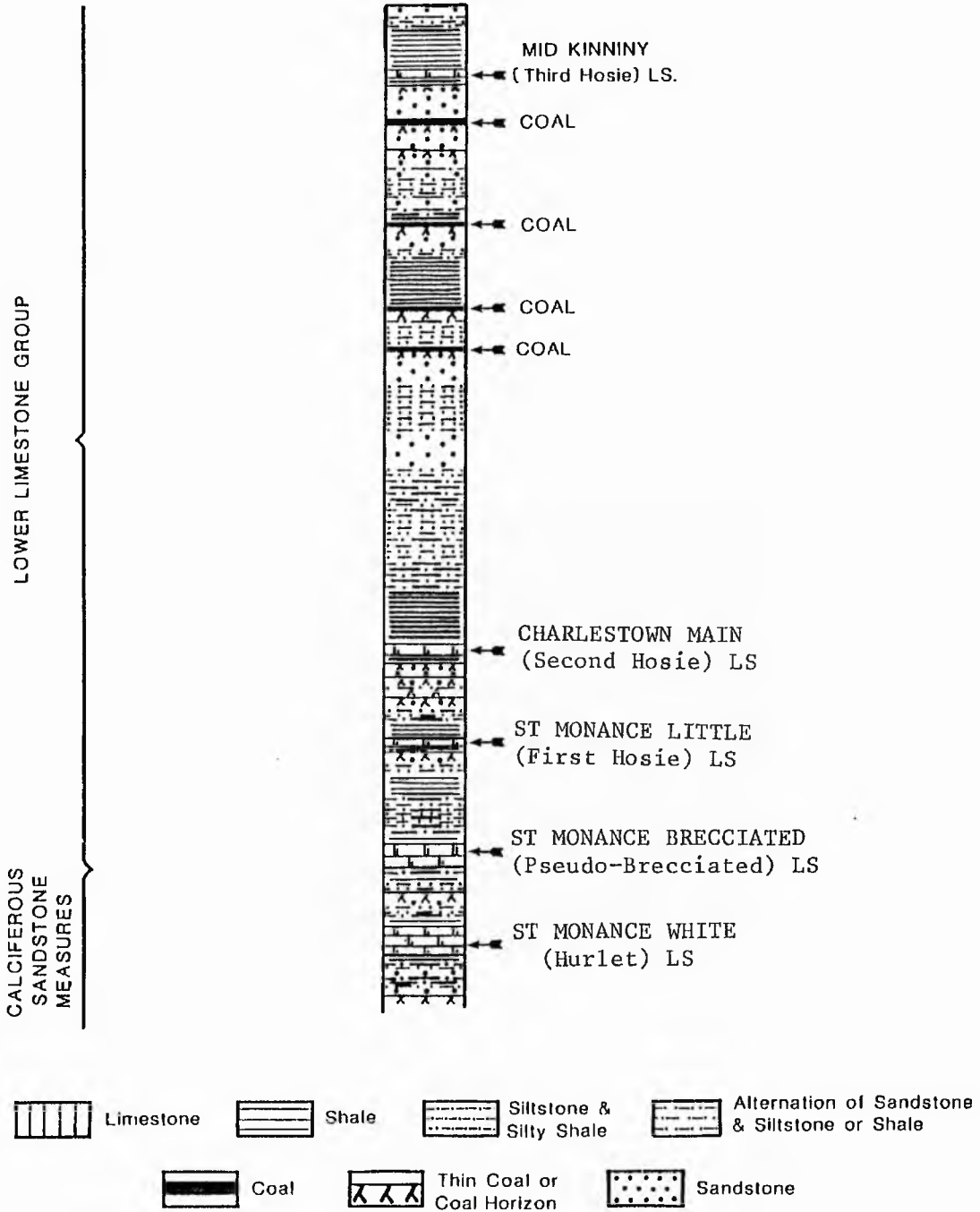


Fig 1.2 Vertical section of Carboniferous Measures in the St. Monance area

Group in this area.

There has been no specific and detailed work on coarse clastic sediment of the Lower Limestone Group sediments in the studied area. The main conclusion based on previous work is that non-carbonate sediments were deposited on the delta, and the carbonate units were deposited in a relatively shallow marine environment.

This study has been based on the stratigraphic section because the exposure is so poor away from the coast, that areal study of the sediments is not possible. The two sections on either side of the syncline allow some limited appreciation of lateral variation.

For the clastic sediments, the study involved the classification of clastic sediments, grain-size analysis, sedimentary structures, trace-fossils, petrology, geochemical analysis, porosity, permeability and diagenetic feature.

### 1.3 Cyclicality

The Lower Limestone Group and the uppermost Calciferous Sandstone Measures consists of cycles, and the investigations of these cycles suggest that they have a deltaic origin. Belt (1975), discussed some Scottish Carboniferous Cyclothem patterns. He divided each cycle into transgressive or destructional, progradational and aggradational, and indicated that there are three schools of thought for the origin of cyclicality. The 'American School', the 'European School' and the 'Deltaic School' (Fig 1.3).

The 'American School' placed the base of the cyclothem below the sandstone which resulted from a fluvial channel that cut down into marine shales; some writers related this down cutting or erosion to eustatic lowering of sea-level which in turn might have been produced

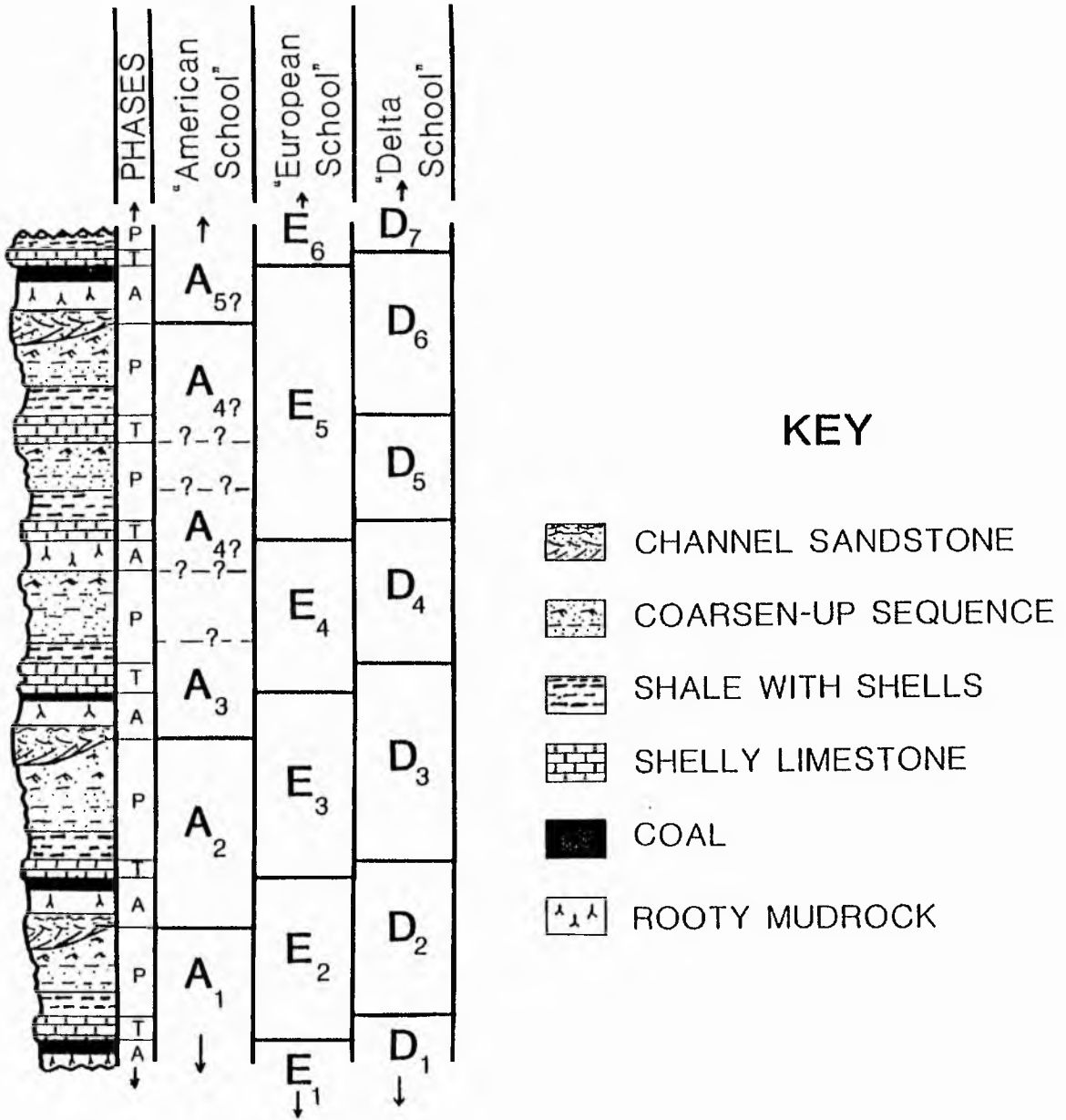


Fig 1.3. Comparison of different methods of placing cyclothem boundaries. The smaller letters, T, P, A refer to transgressive, progradational, and aggradational phases of cycles. This section is hypothetical, although based on the east Fife cycles (after Belt, 1975).



by tectonism or climatic change.

The 'European School' placed the cyclothem boundary between the coal or rooty bed and the overlying marine shale or limestone and related the origin of the cyclicity to tectonism, climate change or change in the pattern of sedimentation.

The 'Deltaic School' placed the boundary of each cycle at the horizon between the marine limestone (transgressive or destructive phase), and the overlying progradational shale or sequence of sandstone and shale as coarsening upward and considered that the cyclicity resulted from repeated delta lobe progradation and abandonment. Belt (175, p 430) concluded that the cycles in the Lower Carboniferous sediments of East Fife were most likely to have resulted from delta progradation and abandonment.

This study has shown that the coal and rooty beds are very common and that some two-thirds of the succession has no cross-bedded or erosive sandstones. The 'European School' (in Belt terms) has been followed in that the cycle boundaries have been taken at the base of the limestone. Other authors in the 'European School' (eg Duff and Walton, 1962) have used the top of the coal or seat-earth as a cycle boundary with or without a limestone.

#### 1.4 Aims of Study

The purpose of this study was to investigate the paleo-environment of sandstones of different sedimentary structures, composition, trace-fossils and other attributes. Petrology, provenance and other features such as porosity, permeability, and pore geometry was applied to understand the diagenesis of the sediments in this area. Various types of techniques used during the present

investigation, include, ordinary optical microscope, SEM, Microprobe, XRD, XRF, Mercury Penetration porosimeter, Helium gas expansion Porosimeter and Permeameter.

## CHAPTER 2

### 2 The SUCCESSION

#### 2.1 Choice of Cycle Boundaries and Succession

Cycle boundaries are the same as those selected by Belt (1975). The boundary is taken at that point in the succession where a carbonate lithology occurs. This area consists of seven carbonate units interbedded with, shales, siltstones, sandstones and occasionally thin seams of coal. Read (1959) pointed out that the Lower limestone Group consists of cycles in which each cycle tends to pass upward from limestone into shales, siltstone, sandstones, and coal.

The cycles coarsen upwards and, delta progradation is suggested as the principal cause of the cyclicity. Six delta advances are recorded in the area studied and their recognition is based on facies association, vertical profiles, and on lateral facies variation within the sediment of each cycle. Each cycle advance was followed by the deposition of a carbonate member formed while the delta lobe was abandoned.

#### 2.2 Facies cycle W

##### 2.2a Description

Facies cycle 'W' begins with the St Monance White Limestone. Immediately above lies a shale with marine fossils, grey in colour, overlain by a thick band of greenish grey shale, richly fossiliferous, a common fossil in it being Rhynchonella pleurodon, (Tait and Wright,

1923, p 168) (Fig 2.1). The seat-earth (W2) above is pale grey, and sedimentary structures are absent. It has irregular concretions (24 - 51 cm) in diameter, which in some places form a band. These are, fine-to very fine-grained, subangular to subrounded in shape. The upper part of the seat-earth (1.35 m thick) becomes darker and harder, with many rootlets below the overlying thin coal (W3). The top unit of the cycle is formed of a bioturbated mudstone with siltstone (W4) and/or very fine grained sandstone, containing brachiopods, shale fragments and pyrite in it; on the lower surface of the bed trace fossils such as Teichichnus were observed.


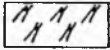

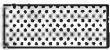




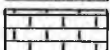
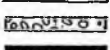
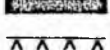
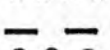
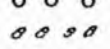


On the West side of the St Monance syncline the cycle is slightly different. The Limestone bed passes upward into calcareous shales crowded with brachiopods, including Rhynchonellids (Fig 2.2). In the middle and upper part of these, there are calcareous nodules, (2.3 - 6.3 cm) in diameter with a brownish weathering surface, some of them contain fossils such as brachiopods and crinoids. Above a non-erosional surface comes a band of shale, grey to dark grey, rich in brachiopods (Fig 2.3). The high proportion of fossils may be due to winnowing of the band.

#### 2.2.b Interpretation







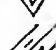
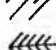


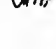
The sequence (Fig 2.1) is interpreted as having accumulated in an interdistributary bay, and formed perhaps by the encroachment of a minor mouth bar. The presence of a marine fauna in the basal shale testifies to the fact that the bay was open to the sea. It was very shallow and only a few metres of clay sedimentation was enough to allow colonisation by plants and the development of a seat-earth to the east. To the west the bay deepened sufficiently to inhibit plant

# EXPLANATION

## LITHOLOGY

	Covered area
	Bioturbation
	Seatearth
	Sandstone medium to fine
	Sandstone fine to very fine
	Alternation of sandstone and siltstone or silty shale
	Siltstone and silty shale
	Shale or Mudstone
	Limestone including Dolomite
	Conglomeritic zone
	Coal
	Rootlet
	Ironstone band
	Ironstone nodules
	Burrow

## STRUCTURE

	Wavy bedding
	Ripples bedding
	Linguoid ripples
	Micro cross lamination
	Starved ripples
	Trough cross stratification
	Planar cross stratification
	Low angle stratification
	Herringbone structure
	Ball & pillow
	Deformation structure

## OTHER SYMBOLS

W	=	ST. MONANCE WHITE LIMESTONE
L	=	LENTICULAR LIMESTONE
B	=	PSEUDO-BRECCIATED LIMESTONE
T	=	ST. MONANCE LITTLE LIMESTONE
F	=	CHARLESTOWN MAIN LIMESTONE
S	=	SANDY LIMESTONE
M	=	MARINE BAND

Key to symbols used in the diagrams of this chapter.

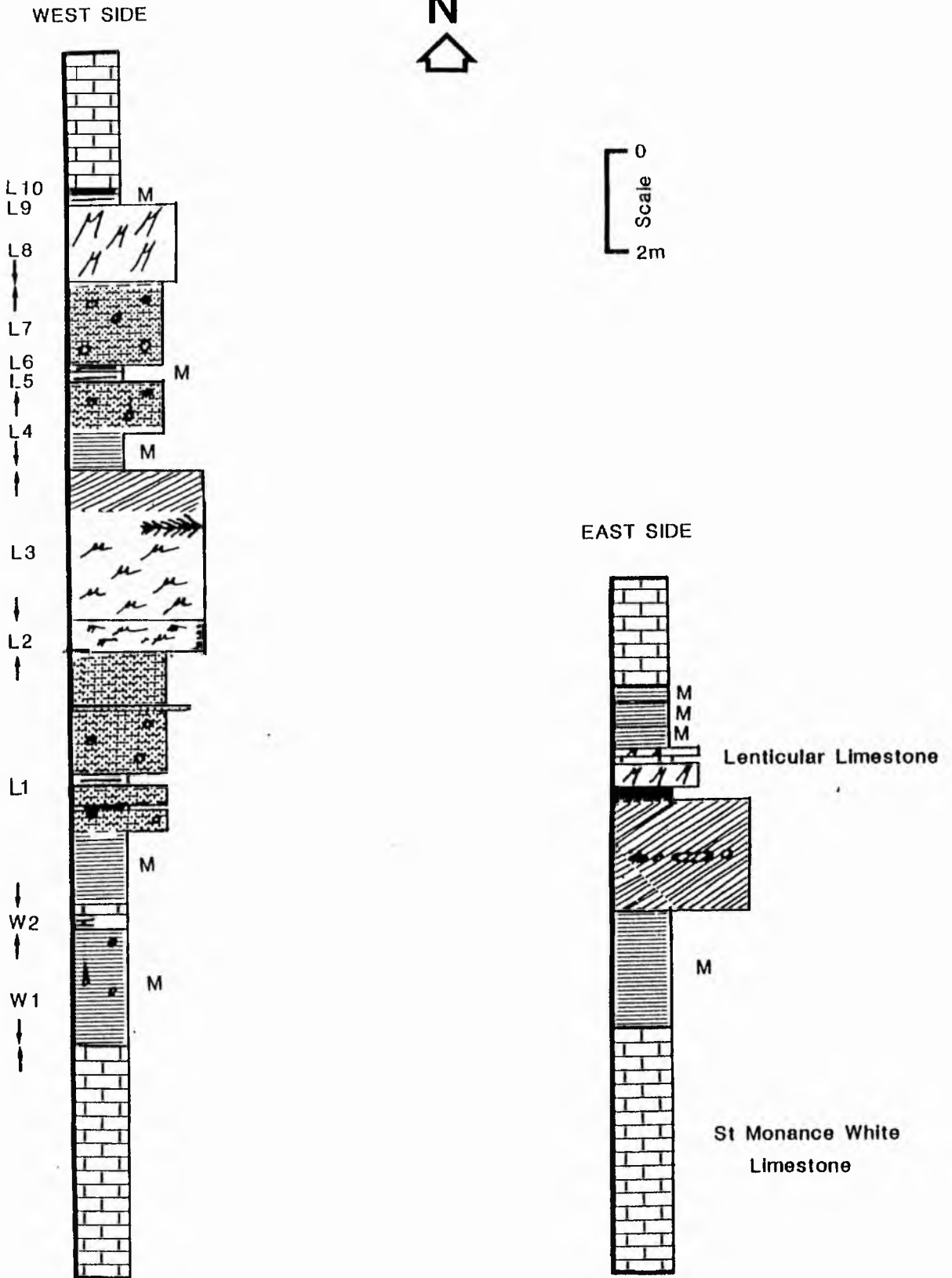


Fig 2.1 Generalised succession of cycles (W) and (L) on both sides of the St Monance syncline.

colonisation.

The presence of the bioturbation unit represents a destructive facies which formed after delta abandonment. Scott and Fisher (1969) noted that in the Mississippi delta, the upper part of the distributary mouth bar (constructive facies) contains concentrations of shells and burrows formed during delta abandonment. Elliott (1976) noted that the presence of a thin horizon of bioturbated siltstone at the top of the cycle represent prolonged periods of non-deposition and biogenic reworking after abandonment.

## 2.3 Facies cycle L

### 2.3a Description

Facies cycle 'L' comprises a band of lenticular limestone, weathering a deep red colour, and varying in thickness from 6 cm to 16 cm. The limestone is overlain by a bioturbated unit (L1) of shale and very fine grained sandstone, with trace fossils. Then come three marine bands of mudstone, a Zoophycus band (L2), black mudstone with trace fossils at the top (L3), and a dark grey crinoidal mudstone (L4).

The facies on the West side are different from the East side. The cycle starts with lenticular limestone in shale, and then a bed of the same type of limestone, 15 cm thick, overlain by a coarsening-upward sequence (L1), 4.58 metres thick. It comprises, fossiliferous shale at the base, becoming more silty upward with nodules, then it passes into interbedded siltstone and sandstone (L2). The sandstone is very fine grained, reddish brown, very compact with parallel lamination, and micro cross-lamination, with some

bioturbation (Fig 2.4). At the top it becomes yellowish grey with small-scale trough cross-stratification, darker and coarser. Above it comes a group of fine grained, well sorted and highly quartzose, white sandstone units (L3) with asymmetrical ripples. They become medium-grained towards the top with plant fragments, rootlets and burrows. The burrows are of two groups, smaller with diameters between 0.5 to 0.7 cm and a larger 4.5 cm to 9.8 cm. The burrows are filled with similar sand to their host unit but are bleached a lighter colour, possible due to a localised reducing environment being established during decay of the organic material lining the burrows. The smaller ones are much more abundant than the larger ones and increase in amount upward (Fig 2.5). In the middle part of this unit there was found a herringbone structure (Fig 2.6).

Passing upward, a band of marine mudstone (L4), contains bivalves especially in the lower 69 cm and becomes more silty upward with nodules in the upper part. L5 is a marine band, of dark grey compact mudstone, highly calcareous and fossiliferous with crinoids. It passes into much more compact (L6), mudstone, greyish-to-dark grey in which fossils are found such as, bivalves; foraminifera; gastropods; ostracods; brachiopods and crinoids. There follows a shale (L7), grey-to-dark grey, containing nodules, overlain by a bioturbation unit (L8). Then follows two marine bands separated by shale (L9) a dark pyritic mudstone while L10, is greenish grey to dark-grey with abundant crinoids.

### 2.3b Interpretation

The transgressive phase responsible for the limestone was followed by minor regression with accumulation of mud in the east,



Fig 2.2 Photograph showing calcareous shales crowded with brachiopods especially Rhynchonellid. Unit (W1) - West side of the St Monance syncline. Camera lens hood is 5 cm in diameter.

Fig 2.3 Slab of fossiliferous brachiopod shale. This abundance of fossils may be due to winnowing of the unit (W2) - West side of the St Monance syncline.

Fig 2.4 Slab of sandstone, very fine grained, compact with parallel and micro-cross-lamination, locally effected by bioturbation (arrow). Unit (L2) - West side of the St Monance syncline.

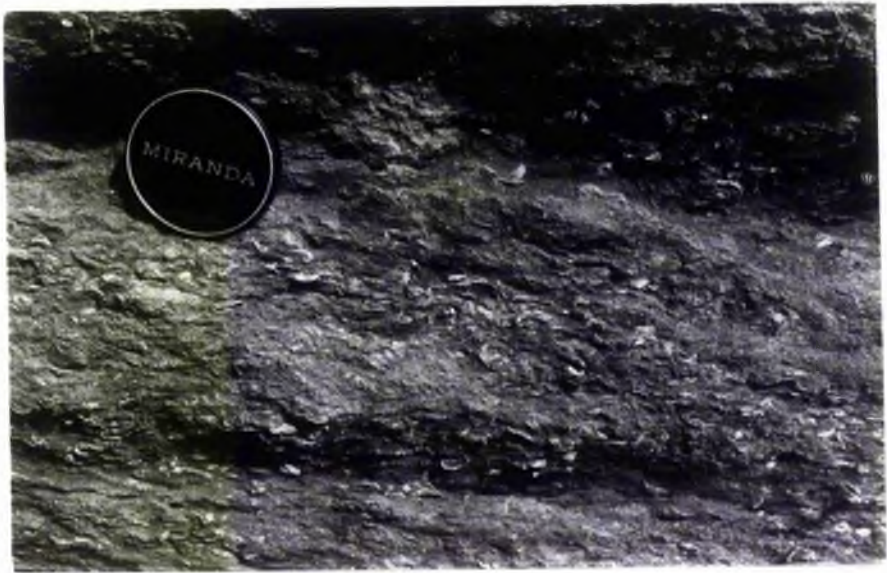


Fig 2.5 Photograph of the upper part of the unit (L3) as seat-earth, showing the bed as deformed and contains burrows. Large one as in (a) and the small one which is increasing upward as in (b) plant fragment and roots (c) are also present. Camera lens hood is 5 cm in diameter.

Fig 2.6 Photograph showing the herringbone structure in contact with the deformed bed above it. Unit (L3) - West side of the St Monance syncline. Camera lens hood is 5 cm in diameter.



bioturbated at first followed by the establishment of crinoids. The bay continued open. The deeper area to the west was filled by an encroaching mouth bar giving a coarsening-upward cycle with minimum tidal action. Current and wave activity in the open bay gave rise to trough cross-stratification and some wave rippling. Plants were established for a while but this culmination of a regressive phase was succeeded by abandonment and a return to clay deposition with some bioturbation and a distinctly marine episode leaving a variety of marine fossils and leading to the limestone of the next cycle. (cf. Coleman and Gagliano 1965; Leeder, 1972, 1974; Elliott 1975).

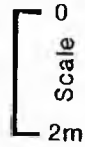
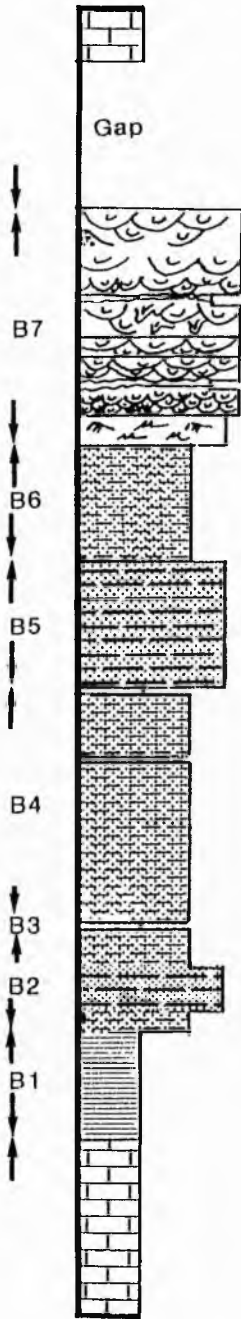
#### 2.4 Facies cycle 'B'

##### 2.4a Description

Facies cycle 'B' on the east side comprises the Pseudo-brecciated Limestone overlain by mudstone which is generally silty but has quite a large suite of fossils mainly brachiopods and crinoids in the lower 40 cm. Then comes silty shale with ironstone as nodules which gradually decrease in size upward. This variation in size may be related to the clay content which becomes less upward. Moore (1966) pointed out that the size of ironstone nodules may be controlled by the proportion of clay in the sediments. In the middle there is a band up to 10 cm thick of very fine-grained laminated, dolomitic sandstone. Above it comes a ripple laminated sandstone interbedded with silty shale. This sandstone (1.12 m thick), is very fine-grained, mean (3.218 $\phi$ ), well-sorted (0.426), with carbonate material occurring in patches of ferroan calcite, while the clay content increases upward. This sandstone is overlain by seat-earth



WEST SIDE



EAST SIDE

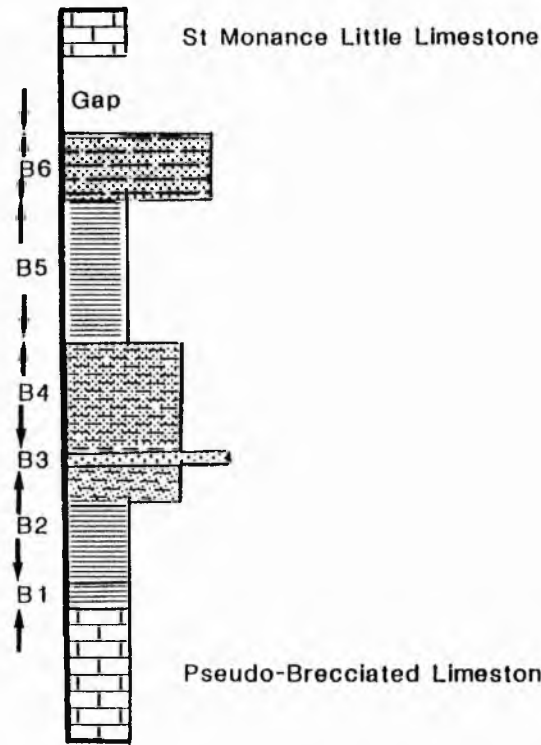


Fig 2.7 Generalised succession of cycle (B) on both sides of the St Monance syncline.

affected by bioturbation, characterised by fine-grained (3.00 $\phi$ ), and well-sorted (0.429) quartz. Kirkby (in Geikie 1962, p 150) pointed out that this seat-earth is covered by a coal seam 60 cm thick, and then a band of siltstone, mudstone and shale below the next limestone bed, but except for a patch of mudstone with plant fragment in the middle of the area this sequence is not exposed.

The succession on the west side comprises the Pseudo-brecciated Limestone followed by marine, poorly fossiliferous, dark grey to black mudstone (B1), then a sequence of alternating shales with nodules (B2) and siltstone (B3) which coarsening-upward into a very fine-grained sandstone (B4). The sequence then reverts to shale, mudstone and siltstone units (B5, B6) (Fig 2.7). Interbedded sandstone and mudstones follow with some laminae of starved ripples (B7a). The sandstone becomes more conspicuous upwards and micro-trough cross-lamination suggests linguoid bed forms.

Above this sequence there is a group of sandstones different in colour, texture, and in sedimentary structures; starting with sandstone (B7b) (Fig 2.8), reddish brown, medium-grained and well sorted. Sedimentary structures include, micro and trough cross-lamination, which are formed from the ripples on the upper surface of the bed (Fig 2.9).

All the succession above unit (B7b) is formed of thinly bedded or laminated, fine-grained sandstone with silty shale. Wavy lamination to parallel lamination is picked out by colour and texture. Fining upward sandstone units have sedimentary structures such as medium to small scale cross-stratification; which might be formed by migration of subaqueous sand dunes. Near the cliff and under the unit (B7N, Fig 2.10), there is a sandstone with mudstone

Fig 2.8 General view of the channel sandstone showing the gradational of the lower part of the sequence (B7a) and with erosional base of unit (B7b) - West side of St Monance syncline.

Fig 2.9 Photograph showing the upper surface of unit (B7b) covered by ripples. West side of the St Monance syncline. Pen is 15 cm long.





chips. A deformation structure, anticlinal in shape and interpreted as a water escape structure is associated with unit (B7N) (Fig 2.11).

All the sequence above is covered up to the St Monance Little Limestone.

#### 2.4b Interpretation

This third cycle accumulated in an interdistributary bay and there is no big difference in the sediment on both sides of St Monance, except for the presence of a channel and a thicker sequence on the west side. Normally, the sediments of the lower part which are represented mainly by siltstone and mudstone have been deposited partly by overbank flooding and partly from crevasse channels in which the facies were carried baywards beyond the coarse sediments of the crevasse splays. Arndorfer (1973) described the discharge pattern in two crevasses of the Mississippi delta and indicated that they built lenticular sedimentary deposits within the interdistributary bay. He added also that maximum discharge was attained in these crevasses during flood tides, when seaward flow is inhibited in the main delta distributaries. The presence of a thin bioturbation unit represents a destructive facies. De Raaf, et al, (1965) in their study of the Lower Westphalian Sediment of North Devon, England, indicated that during delta progradation, a thick sequence of deltaic sediments was deposited representing the constructive facies, whereas thin bioturbation units represent the destructive facies which formed after delta abandonment.

The intermediate parts of these sequences comprise mudstone siltstone background sediment into which coarser siltstone and sandstone beds are repeatedly intercalated. This intercalated

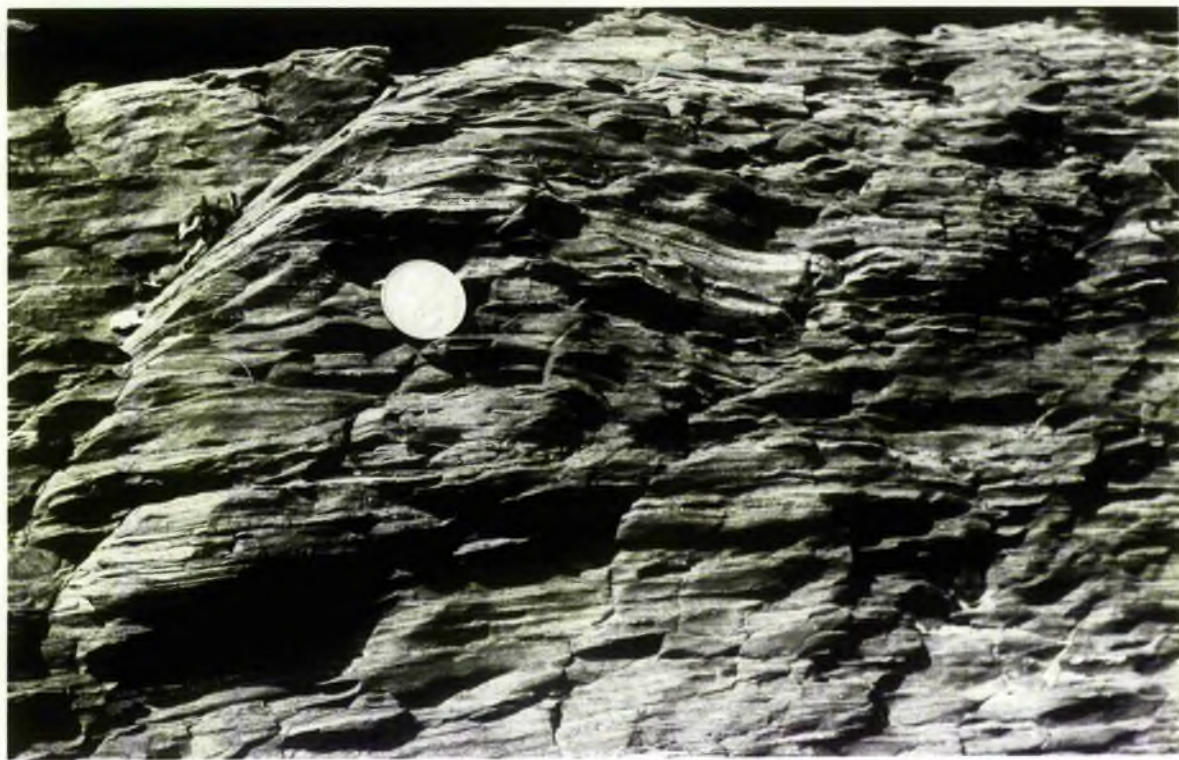
Fig 2.10 General view of the channel sandstone showing the sandstones with mud and chips lying at the base of the Unit (B7N). West side of the St Monance syncline.

Fig 2.11 Deformation structures (water escape) associated with more than one unit in this sandstone. Unit (B7N) - West side of the St Monance syncline. Camera lens hood is 5 cm in diameter.



Fig 2.12 Photograph of the upper part of unit (T1) and lower part of Unit (T2) showing the predominance of shale with streaks of siltstone. East side of the St Monance syncline. Coin is 2.5 cm in diameter.

Fig 2.13 Slab cutting parallel to the strike, showing the wave ripple. Unit (T2) - East side of the St Monance syncline.



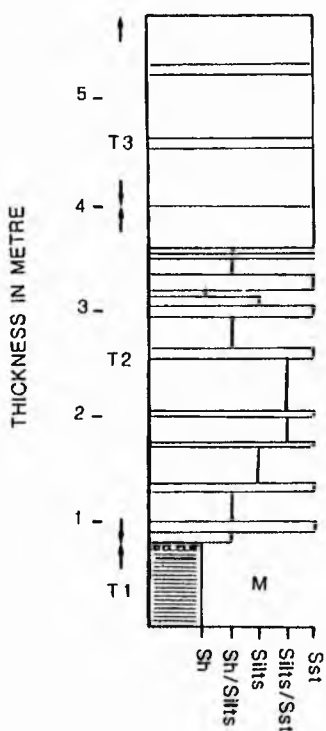


Fig 2.14 Sketch illustrating the gradual increase in thickness and in grain size of Units T1 to T3.

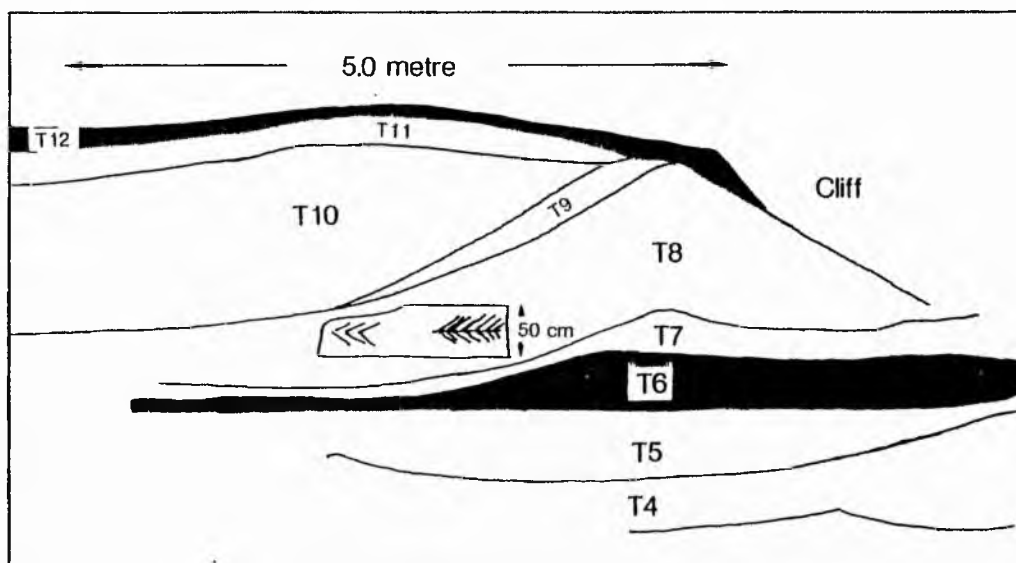


Fig 2.15 Sketch showing the morphological of lateral variation in lithofacies of Units T4 to T15, and especially the position of bed containing herringbone structure Unit (T8). East side of the St Monance syncline.

sequence with a predominance of wave ripples, micro, and trough cross-lamination sets may reflect moderate wave action reworking passing up into a distributary channel.

## 2.5 Facies cycle (T)

### 2.5a Description

Facies cycle (T) (Fig 2.19, p. 29) comprises the St Monance Little Limestone overlain by dark, fossiliferous calc-mudstone (T1) (Fig 2.12). Calcareous nodules are found in the last 10 cm, ranging in size from 1.95 cm-to-3.18 cm, ellipsoidal and irregular, with long axis parallel to the bedding. The sequence passes into (T2) interbedded greyish-green, siltstone-silty shale with lenticular bodies of reddish brown sandstones. Fine-to-very fine grained and, slightly calcareous they increase upwards in grain size, thickness (Fig 2.14). The sedimentary structures include ripples, wavy bedding (Fig 2.23), parallel lamination and micro-cross-lamination. Plant fragments are also present (see Chapter 4). Unit (T3) is of light grey, sandstone, fine-grained (Fig 2.16) with wavy lamination at the base and parallel lamination at the top. Trace fossils are present in both units (T2, T3) (see Chapter 3). With non-erosional surface unit (T3) passes through to a seat-earth facies (T4), in which sedimentary structures are absent. It is rich in ironstone nodules, which coalesce at the top to form an ironstone band, and covered by a grey laminated siltstone (T5) with occasional small plant fragments preserved in pyrite. Finally it is overlain by coal (T6), decreasing in thickness to the west.

With a sharp contact with the unit below (T6), unit (T7) is a



siltstone with fine-grained sandy bands and small plant fragments, and it grades into a band of highly carbonaceous sandstone, with non-erosional base passing into unit, (T8) of sandstone; this has a unit, 50 cm thick containing herringbone planar cross-stratification (Fig 2.15).

Unit (T9) thins out and disappears upward to the east (Fig 2.16). It is formed of fine-grained sandstone with cracks and rootlets from the coal above, and passes through into clay siltstone (T10), with ironstone nodules, a grey siltstone with plant fragment (T11), and is covered by a coal unit (T12).

The fine-grained sandstone unit (T13) grades into mudstone (T14) with large stigmara, which passes into a massive fine-grained sandstone (T15) with plant fragments and stigmara roots (Fig 2.17). It may contain sedimentary structures, which can be seen in X-ray radiographs (c.f. Hamblin, 1965). The carbonaceous shale (T16) comes above, with large plant fragments (10-15 cm) in length. Wilson (1978) pointed out that higher in the shale Lingula squamiformis, appears, along with a brackish water bivalves assemblage, the bivalves are still attached and in the stable position. He added that the Lingula shells are also in a stable position and lie parallel to the bedding. Higher still in the shale a fully marine fauna comes in but plant fragments are still common.

On the west side of the St Monance Syncline, the facies development is similar to the east except for the absence of the coal horizon and a smaller content of plant fragments. There is also considerable lateral variation in lower facies of the second coarsening-upward sequence (Fig 2.18). Overall the succession divides into two coarsening-upwards sequences with fining up sequences

Fig 2.16 General view showing the lithofacies in units from (T2 to T13) and especially the sharp contact between T2 and T3 as different in colour. East side of St Monance syncline. Indicator is 30 cm. This face has now been removed by quarrying.

Fig 2.17 Photograph of the massive sandstone unit (T15) showing stigmara roots on upper surface and lying nearly parallel to inclined to the bedding plane. East side of the St Monance syncline. Camera lens hood is 5 cm in diameter.



N S  
Cliff Sea

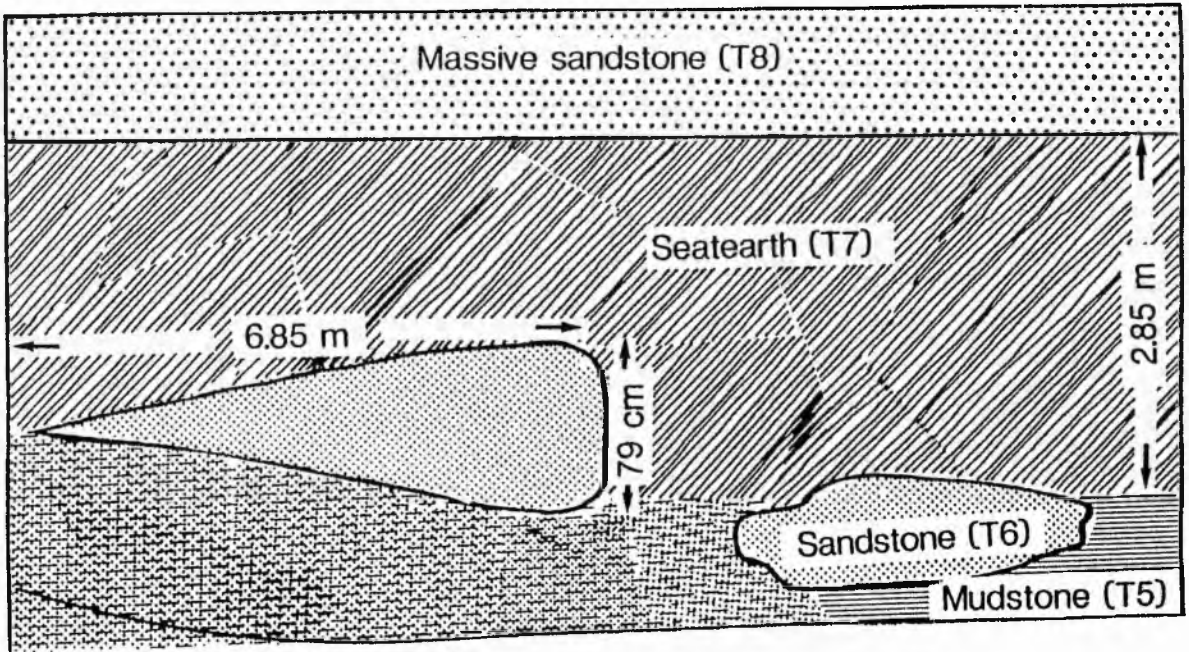


Fig 2.18. Sketch showing the lateral variation in the second coarsening upwards sequence. West side of the St Monance syncline.

intercalated to the east.

### 2.5b Interpretation

This fourth cycle is inferred, from the distribution of sediment (Fig 2.19) as having accumulated in an interdistributary bay which was shallower towards the east, where there are plant fragments.

Two coarsening-upwards sequences are present. The first records a passage from marine limestone into fossiliferous fine-grained prodelta facies upwards into interbedded silty shale, siltstone and the fine-to-very fine grained sandstone with trace fossils. This is the result of progradation of a minor delta front, culminating in the coal.

The second coarsening-upward trend (T13-to-T15) may represent a levee deposit. Fisk (1947) and Allen (1965a) reported that levee sediments generally comprise rapidly alternating coarse and fine beds (centimetre-decimetre scale). Here unit (T15) is up to 2.34 metres thick, this is suggested as due to encroachment of the levee into the bay. Elliott (1974b, p 613) pointed out that encroachment of levee into the bay produces a coarsening-upwards sequence characterized by interbedding and increasing thickness of coarse beds upwards. The presence of a sharp based sandstone in lower facies (west side), (Fig 2.18), within the delta front siltstone suggests that it was possibly produced during storm action or rapid stream flooding episodes. Elliott (1975) considered such deposits to be related to the rapid rise of flow with deposition during the maximum and waning stages.

The fining-upward sequences units (T7-to-T12) probably represent a lenticular shallow crevasse channel in the interdistributary bay. Elliott (in Reading, 1970, p 105) reported that channels and bars are



WEST SIDE

EAST SIDE

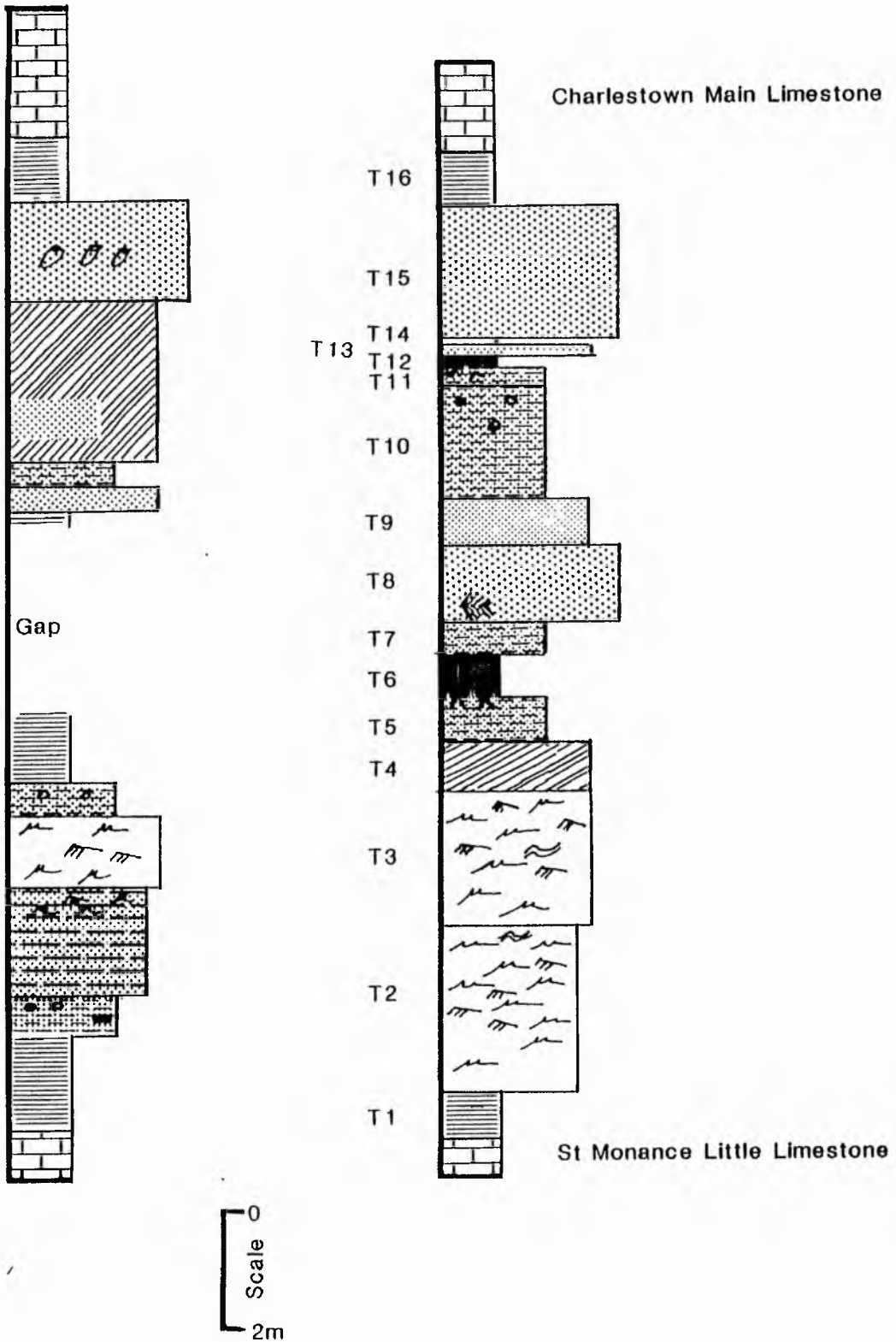


Fig 2.19. Generalised succession of cycle (T) on both sides of the St Monance syncline.

an important feature of interdistributary areas. The presence of herringbone structure in unit (T8) could reflect some tidal action. Coleman et al., (1964, p 252) stated that the interdistributary bays of the Mississippi delta are "... areas of shallow open water which may be completely surrounded by marsh or levee, partially open to the sea, or connected to it by tidal channel". Units T11 and T12 represent marsh and swamp environments respectively.

## 2.6 Facies cycle F

### 2.6a Description

The facies of this cycle is formed of two types, coarsening and fining-upwards sequences. The first part, lying between the roof of the limestone and the base of a channel (F1-F4 Fig 2.29), and the second part, from the base of the channel to the top of the cycle.

In part 1, the facies comprises a fossiliferous marine shale of the Neilson Shell Bed (F1), and has yielded a rich and varied fauna (Wilson, 1966). This passes gradually upward into a limited iron-rich siltstone and grey mudstone with ironstone septarian nodules (F2) (Fig 2.20). The nodules decrease in size upward, they are large when enclosed in the lower part of the fine grained clayey shale and become smaller upwards as the shale becomes coarser (c.f. Moore, 1966).

Thinly bedded, very fine-grained sandstone and silty shale - shales follow; and Wilson (1978) noted that large plant fragments (10-15 cm) are found in the laminated sandstone. These laminated sandstone which coarsening-upward in thickness as well as in grain size, are of two types of sandstones. One is a 'dirty' sandstone, brown-to-reddish brown in colour, fine-grained. Sedimentary

structures are micro-cross-lamination, trough cross-lamination; deformed bedding is also present. The second is 'clean' sandstone, pale grey-to-white, fine-grained, well-sorted, with abundant ripples. There is also a conglomeratic sandstone with plant fragments, up to 22 cm thick and 8 metres long.

When the reddish-brown rocks are broken they reveal a light-grey interior, although sometimes the reddish colour reaches more than 3 cm deep. The presence of the films of iron oxide in between detrital grains and the authigenic rims indicates the primary nature of the iron cement, and the extensive iron staining of most of the interbedded sandstone and the siltstone in this part indicates that the environment was sufficiently oxidising to allow the iron pigment to remain in the ferric state. The grey and white colour of the 'clean' sandstones may be due to the environment being reduced perhaps due to organic material. Different types of trace fossils throughout these units are found (see Chapter 3).

F4 is made up of medium-grained sandstone bands with linguoid-ripples trace fossils (see Chapter 3), and mudstone. Starved sand ripples are sometimes connected together to form a continuous bed (Fig 2.21A, B).

In part 2 of this cycle, the facies (F5) has an erosional base, starting with sandy breccia (often referred to as a melange in Carboniferous channel sandstones) and mudstone; plant fragments are also present (Fig 2.22). The breccia is localized with maximum thickness about 90 cm. The sandstone, buff-coloured, very fine-grained (3.03 $\phi$ ), and well-sorted, has a clay matrix; carbonate cement is also present. This part is divided into many members, as it is composed of a varied group of sandstones.



The first member (F5a) begins with a basal part has two sets of cross-stratified sandstone up to 1 m thick, lenticular bedding and climbing ripples cross-lamination. Scour-and-fill structures (Shrock, 1948), up to 47.5 cms thick and 1.6 m wide are present (Fig 2.23), most being filled with cross-laminated sandstone, but thinly laminated sand is also present. Most of the beds in this member are thinning and dying out towards the west (Fig 2.24).

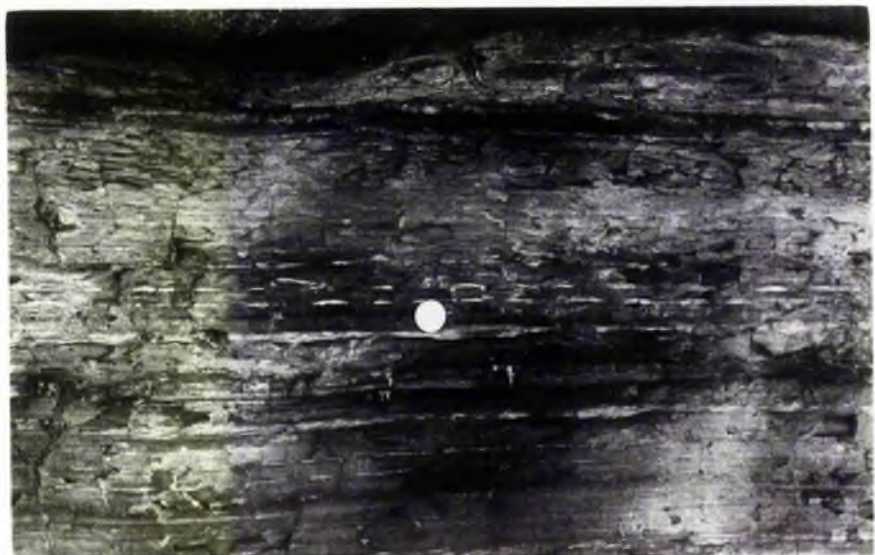
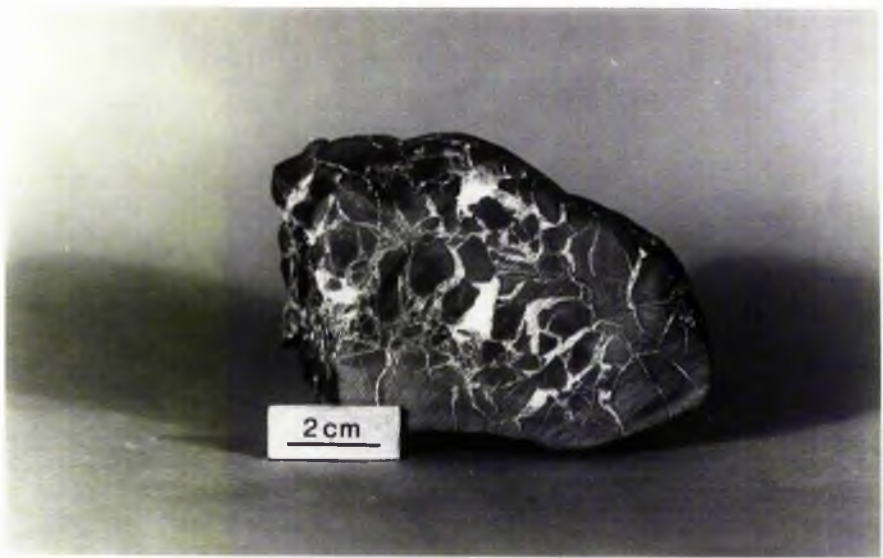
The second member (F5b) starts with an erosional surface, sandy breccia and mudstone up to 70 cms thick. This sandstone is fine-grained and well-sorted, carbonate cement may be up to 40.2 percent and mostly flat-bedded (Fig 2.25), with primary current lineation on the low angle foresets. Although these laminae with current lineation are suggestive of beach under wave action (Thomson, 1937; McKee, 1938; Van Straaten, 1959), Allen (1964) pointed out the combination of lineation and lamination in the Lower Old Red Sandstone, and he suggested that it could represent at least two distinct geographical environments, either a beach subject to repeated exposure, or submerged channel, and the latter is preferred here. Rippled bedded sandstone follows, with micro cross-lamination and flaser bedding (Fig 2.26). Laterally it contains rib-and-furrow structure. Above it comes interbedded silty shale with starved ripples with fine-grained sandstones containing cross-lamination.

The third member (F5C) of sandstone with cross-stratification forms with an erosional base (Fig 2.27). It is covered by linguoid ripples interbedded with silty shale. Rib-and-furrow, plant fragments are also present in the lower surface (Fig 2.28A, B). The coalified plant stem has nearly the same orientation as the rib-and-furrow. Most of these beds are horizontal, the thickness of each is up to 10

Fig 2.20 Slab showing the core of the septarian nodules as brecciation of different pieces of ellipsoidal nodules. The surface of nodules may be smooth, or irregular. Unit (F2) - East side of St Monance syncline.

Fig 2.21A Photograph showing the facies of unit (F4), as sandstone with linguoid ripples interbedded with mudstone, and truncated by erosional base of the channel with sandstone breccia (Middle of the hammer shaft). Hammer is 35 cm long.

Fig 2.21B Photograph showing the mudstone facies of Unit (F4) containing starved ripples, which are sometimes connected together. Coin is 2.8 cm in diameter.



Fog 2.22 Photograph showing the erosional base of the channel cut through the unit below (F4). Brecciated sandstone and mudstone with plant fragment. Fault cut the sandstone later on. Hammer is 35 cm long.

Fig 2.23 Photograph showing superimposed fine-grained sandstone in first member (F5a), with micro-trough cross-lamination perpendicular to the current in section. Coin is 2 cm in diameter.



Fig 2.24 General view of the channel body sandstone, showing that the first member (F5a) is thinning towards the west.

Fig 2.25 General view of the first unit of second member (F5b) with low angle planar cross-bedding. Hammer is 35 cm long.

Fig 2.26 Photograph showing the second unit of the second member (F5b), with micro-cross-lamination and flaser bedding. The current direction is from right to left. Indicator is 3 cm.



Fig 2.27 General view of the second and third member of the channel body (F5b and F5c). The second member (F5b) starts with planar cross-bedding, whilst the third member (F5c) (Hammer indicator) is formed of trough cross-bedding and covered by linguoid ripples. Hammer is 35 cm long.

Fig 2.28A Slab contains plant fragment from the upper part of the channel unit. Camera lens hood is 5 cm in diameter

Fig 2.28B Photograph of the lower surface of linguoid ripple bed of the third member (F5c), showing rib-and-furrow and coalified plant stem oriented in the same direction as the ripple-forming current. Coin is 2.5 cm in diameter.





cms. Above it comes very fine-grained rippled sandstone with micro cross-lamination interbedded with silt-mud intervals. Carbonaceous material is also found in between as streaks.

Through the vertical section, which includes a wide variety of facies there is a systematic decrease in overall size going upwards.

## 2.6b Interpretation

This cycle represents a progradational deltaic lobe which is finally abandoned with probably rapid subsidence to open marine conditions.

The coarsening-upward nature (part 1) (Fig 2.29), the presence of a marine fauna in the shale at the base of the sequence, and the presence of thin fossiliferous siltstone and very fine sandstone indicate that it was deposited by the progradation of deltaic lobes. The presence of the deformed structures (ball and pillow) indicate rapid sedimentation during the deposition on this delta part (Allen, 1963; Walker, 1963; McKee, 1965; Kuenen and Prentice, 1957; Kuenen, 1965). Vos (1977) pointed out that the ball and pillow structures are attributed to deposition of sand over a hydro-plastic muddy layer. Furthermore, the predominance of wave-ripples and wave-formed lamination in this coarsening-upward suggest that wave-action is largely responsible for its formation and the current activity was not continuous.

The presence of a high proportion of suspended sediments, deformation features, wave features, and sheet-like sand bodies with trace fossils such as Teichichnids, suggest sand bodies formed in a delta lobe. The presence of trace fossils as a crawling trace on the upper surface of linguoid ripple sandstone in unit (F4), flaser, and

lenticular bedding, and the interbedding of sand and mud, may indicate some tidal action.

The characteristic upward-coarsening sequences were produced by the development of mouth bars fed by a crevasse channel (part 2) in which the siltstone and sandstone represented a delta front sediments, and the shales represented a prodelta sediment deposited seaward below the wave action. The conglomeratic sandstone found within this coarsening-upwards sequence may represent development of minor channel resulting perhaps from a change in flood events during the coarsening-upwards deposition.

The fining-upward sequence (part 2) (Fig 2.29), with repeated erosional bases, with medium-to-large scale cross-bedding represented by (1st, 2nd and 3rd) members, were evidently deposited by highly erosive, unidirectional partly confined flows with deposition from several flood pulses. Collectively they represent crevasse channels with little depth. The presence of organized as well as disorganized sandstone units indicates rapid and quite persistent long-lived avenues of sediment transport and deposition. Fielding (1984) pointed out that disorganized sandstone unit indicates rapid deposition. Crevasse channels here seem to have been filled by erosively based bodies of sand which generally become thinner, less confined laterally and less erosive as they splay out downcurrent (Fig 2.24), and similar to those described by Arndorfer, 1973; Saxena, 1979; Fielding, 1984 .

The upper part of the third member (F5C) is very fine-grained sands interbedded with silt containing micro cross-lamination and ripples with rootlets and capped by mudstone (F6) suggest a levee deposit. Coleman et al., (1964) pointed out that the levee part of the interdistributary bay sediments of the Mississippi delta is of

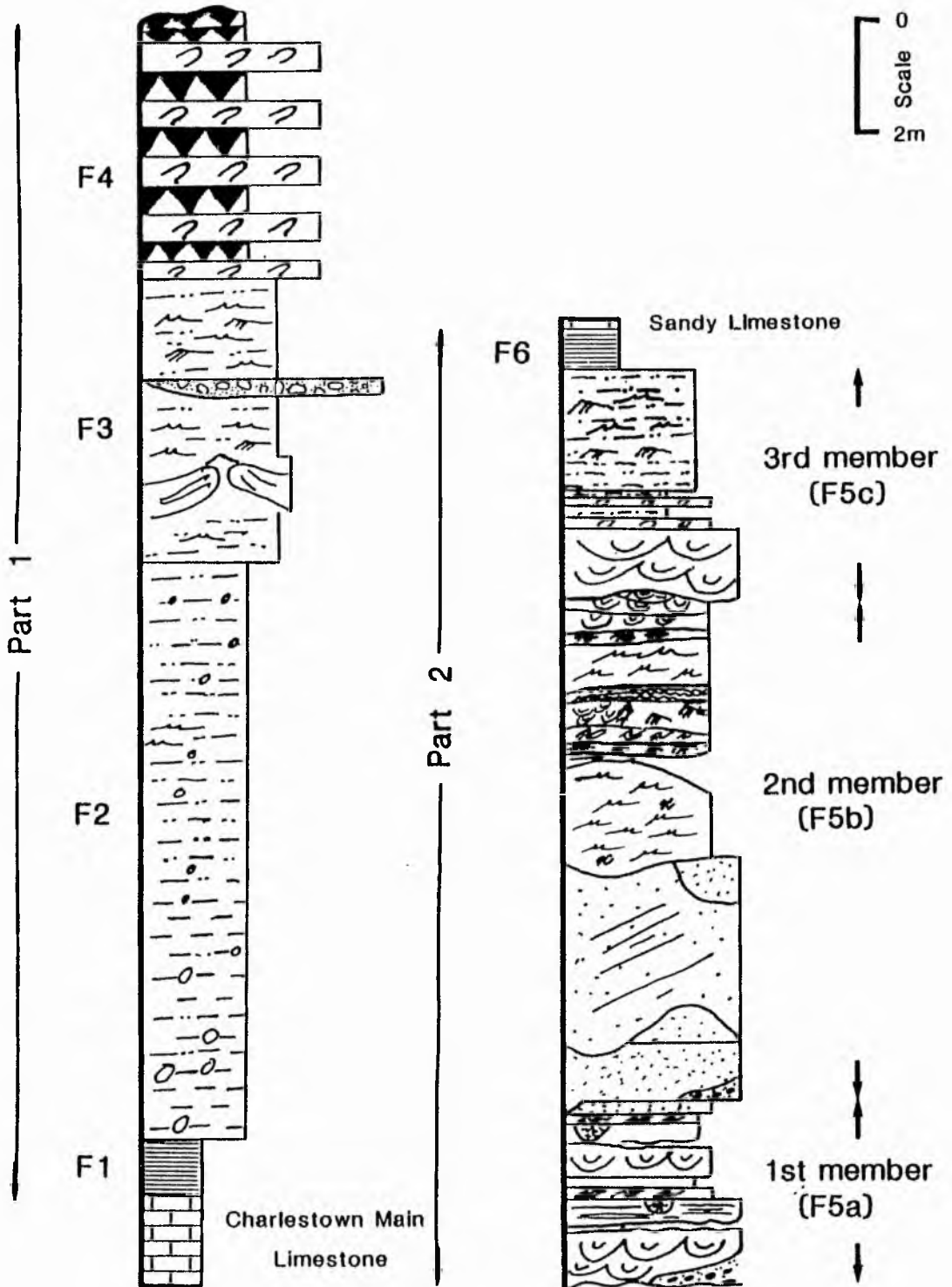


Fig 2.29. Generalised succession of cycle (F). East side of the St Monance syncline.

fine-grained sediments, deposited from suspension by flood water, containing parallel lamination and micro-cross-lamination. Elliott (1974, p 615) reported that the shallow crevasse channels are bounded by levees and characterized by unidirectional current with a maximum during the flood period. The facies of unit (F6) with the unit above (next cycle) could represent a marine transgression probably owing to delta lobe abandonment, hence the sediment influx to the area declined. Assuming that subsidence is operative, the conditions of sedimentation give way to that of an open marine shelf.

Summarizing, these features could reflect that this delta is a highly constructive fluviially influenced elongate type in which the sediment supply was high and exceeded the energy of the coastal process.

## 2.7 Facies cycle S

### 2.7a Description

This cycle is the thickest progradational deltaic sequence, reaching more than 67.0 m and formed of 28 members of different lithologic units (excluding the limestone beds) Fig 2.37. It starts with a sandy limestone which occurs as a lenticular bed of 13 cms, with brachiopods, Spirifer, sp., and large crinoid ossicles. According to thin-section study, it is impure, contains sandstone grains of different shape and size which are floating in carbonate. An overlying black non-fossiliferous sulphurous mudstone (S1), represents the influx of fine clastic material into a stagnant environment.

The Mill Hill Marine Band (S2) was first recognized by Wood

(1887, p 501), who provided a succinct and accurate description, confirmed by Wright (1912). It consists of a strongly bioturbated calcareous sandstone with carbonaceous nodules, it is increasing in thickness towards the west; isolated patches of cross-stratification are also present. The body fossil assemblage is truly marine, with a goniatite fragment identified as Sudeticeras, sp. (Wilson, 1978). Different types of trace-fossils are present (see Chapter 3).

Unit (S3) is a sandstone, very fine-grained, well-sorted, predominantly with carbonate cement. It consists of two different lithologies. The lower (S3a) is very fine-grained with cross-stratification disturbed locally by burrows (see Chapter 3). While the upper part (S3b) is formed of a seat-earth with ironstone nodules, and overlain by a coal (S4).

Above it comes unit (S5) made up of thinly bedded sandstones and micaceous mudstones with some pyrite; burrows are present. Internally they have alternating dark and light laminae which exhibit parallel or micro cross-lamination. Sometimes wavy laminae are present. These micro cross-lamination could be produced by current and wave action. This unit grades up into the Largoward Black Coal (S6).

Collectively this sequence is interpreted as sedimentation in a marine environment followed by filling by a minor distributary mouth bar. A phase of stagnant conditions is represented by the black sulphurous mudstone (S1). Conditions cleared to give the Mill Hill Marine Band with currents strong enough to supply some sand grains. Build-up to swamp conditions was effected by the sand on which vegetation was established. Subsidence caused flooding after peat formation and thin sands and muds as overbank deposits (S5) filled up the flood-basin until swamp conditions were re-established (S6)

The second marine band in this cycle, unit (S7), is gradually developed. It is the Seafield Marine Band (Francis et al, 1961, p 27; Forsyth and Chisholm, 1968, p 71), which contains a rich marine fauna including brachiopods, molluscs, and crinoid ossicles. It is overlain by a well-jointed fine-grained sandstone seat-earth (S8), with trace-fossils. It is covered by a thin coal unit (S9). Unit (S10) is a thin bed of sandstone fine-to-very fine grained with abundant carbonaceous material and a few larger plant fragments. Sedimentary structures are parallel lamination, wavy lamination (few), and micro-cross-lamination. Then the Largo Ward Splint Coal Unit (S11) occurs.

The alternation of shales, coals and sandstones can be interpreted as marine muds alternating with sands formed as reworked sands on a delta platform. Fisk et al, (1954) reported wave reworking of crevasse sands, produced small spits and coarsening-upwards sequences. This could lead to the establishment of swamps for peat formation.

The top of Largo Ward Splint Coal is seen beneath dark grey mudstone of a poorly exposed unit (S12) (see Chapter 3). The succession passes upwards through a zone of interbedded sandstone and mudstone unit (S13), in which the thickness of sandstone beds increases upward (7.5 cms at the base, and 18 cms at the top). The sandstones contain parallel to wavy lamination and micro trough-cross-lamination, and grade into a band of fine-grained sandstone with ripple-lamination and trough-cross-stratification.

In the mudstone a sparse marine fauna consists mainly of the bivalves Sanguinolites, Solenomorpha and Streblopteria with some brachiopods, chiefly productids and Lingula (Chisholm, 1970). A

sparse development of Teichichnids are present in the alternation zone and in the overlying sandstones.

The presence of marine fauna is believed to represent the horizon of the Lower Kinniny Limestone (Forsyth and Chisholm, 1968) and, could reflect pro-delta deposits while the coarsening-upward could indicate a mouth bar, in which the top of this sequence is absent due to erosion by the channel above (S14).

With an erosional base and lenticular shape cut into unit (S13) and reaching the mudstone unit (S12) the sandstone (S14) forms a sequence of fining upward beds. The sandstone, is coarser at the base than at the top; the lowest parts are medium grained and trough cross-stratified. This bed passes upwards into finer-grained ripple-laminated and some small lenticular sets of cross-strata in places, which are extensively reworked by Teichichnids (see Chapter 3). Chisholm (1970) reported that the reworking and sand deposition went on together, or at least in alternating periods through out the formation of this sequence. Above it with non-erosional surface, a dark grey silty mudstone passes into a strongly bioturbated grey silty sandstone bed, both together forming a unit (S15) a seat-earth which varies in thickness between 0.6 and 1.00 m. Trace fossils are present.

All these features indicate that this channel appears to have been extensively reworked by Teichichnids especially in the finer, upper part. Grain size and form suggest a river channel, but the presence of teichichnids in such abundance may indicate the presence of marine or brackish rather than fresh water. In addition, the presence of parallel Rhizocorallium tubes in the mudstone below (S12) give a suggestion of environment as either near-marine or perhaps



tidal. Farrow (1966) interpreted the orientation of parallel Rhizocorallium tubes observed in Jurassic of England as having formed in response to a tidal current.

An upward-coarsening sequence (S16, S17), is truncated by an erosion surface (S18) (Fig 2.30). Unit (S16) is a dark grey silty mudstone which changes in the upper part to more silty and paler coloured. It has a few shells identified by Dr R B Wilson as Streblopteria ornata (Wilson, 1978), marine bivalves, and in the bioturbated upper part, planolites-like tubes and Teichichnids, some of them extend upward into the lower part of the unit (S17) (Chisholm, 1970). Generally, towards the top of this unit (S16) more silty laminae are preserved and the burrowing activity decreases. Unit (S17) is invariably composed of well-sorted, horizontally bedded sand which contains parallel lamination; ripples, and trough cross-lamination (Fig 2.31) intercalated with siltstone and silty shale. An upward increase in grain size, occurs and fauna is absent.

This coarsening-upward trend with marine fauna at the base unit (S16) is similar to the sequences described by Oomkens (1970) as marine regressive sequences in Rhone delta. The top of this sequence was absent due to erosion by the channel unit (S18).

Above an erosional base comes a bed of well sorted, medium-grained sandstone (S18) (Fig 2.30). The common sedimentary structures are Beta-cross-stratification of (Allen, 1963) with set height of 5-10 cm. This large scale cross-stratification results from migration of subaqueous dune bed forms (Harms and Fahnestock, 1965; Allen, 1970). Overlying this is a thin poorly bedded micaceous mudstone, which is riddled with rootlets representing a swamp accumulation unit (S19), and passing into cleated lustrous coal (S20)

Fig 2.30 General view showing the upper part of the channel unit (S15) and the coarsening upward units (S16, S17), truncated by an erosion surface below unit (S18) which contains large scale cross-stratification. Hammer is 35 cm long.

Fig 2.31 Close-up of the east side of section shown in fig (2.30) showing unit (S16) with trace-fossils and the interbedded sandstone of unit (S17) which is formed of ripples and small-scale trough cross-stratification (pen). East side of St Monance syncline. Pen is 15 cm long.



with sandstone nodules derived from the unit above.

This fining upward with an erosional surface cross-stratification at the base could represent a channel fill deposit, while the absence of levee sediment above the channel and the lack of any upward change in sedimentary structure indicates a low sinuosity form.

Above the coal appears a deformed sandstone bed (S21) which is slightly different in grain size through the unit, and the finer the sediment the more complex the deformation (Fig 2.32). The clay content of the sandstone is highest in a much more deformed subunit (about 21.0%). The composition of the sediment and the grain size therefore appears to have played a part in controlling the development of the deformation.

Collectively, this part is fining upward, and the sequence of cross-stratification which is deformed later in unit (S21) as deposited on delta top may be a channel fill, while the seat-earth (S22) represents a swamp accumulation and covered by swamp peat accumulation (S23).

Unit (S24) exposed over a cliff section 150 m long, and 4.54 m thick (Fig 2.33), is a fining-upward channel sandstone. Channels cut through the coal below into the seat-earth, while a large channel is found towards the top. This unit is divided into four groups above the basal scoured surface of 1-2 m long, 10-23 cm deep.

Group A is formed of thinly bedded sandstone, fine-to-very fine grained (3 cm thick) with siltstone and/or mudstone at 9 cm thick, in the form of lenses, which lie on an undulating surface. Flaser bedding is developed locally. There follows group B of siltstone and sandstone lying on another erosion surface; some of the beds are even

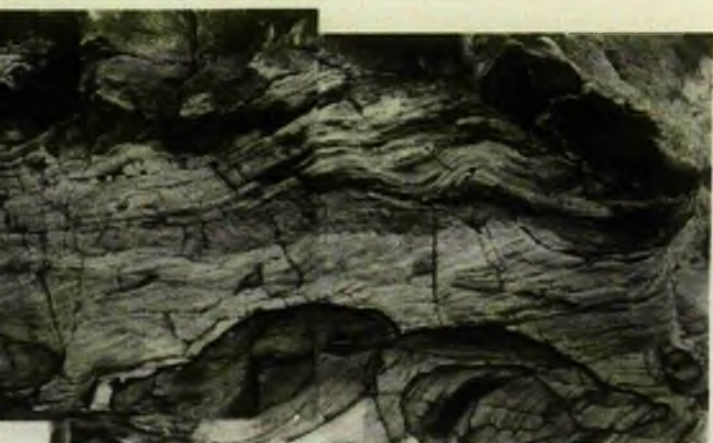
Fig 2.32 General view of deformed sandstone Unit (S21C) - East side of St Monance syncline.

a

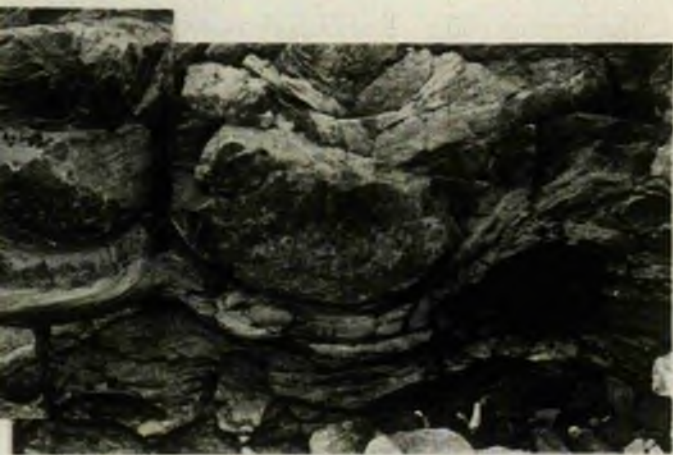


a





10cm



a

a

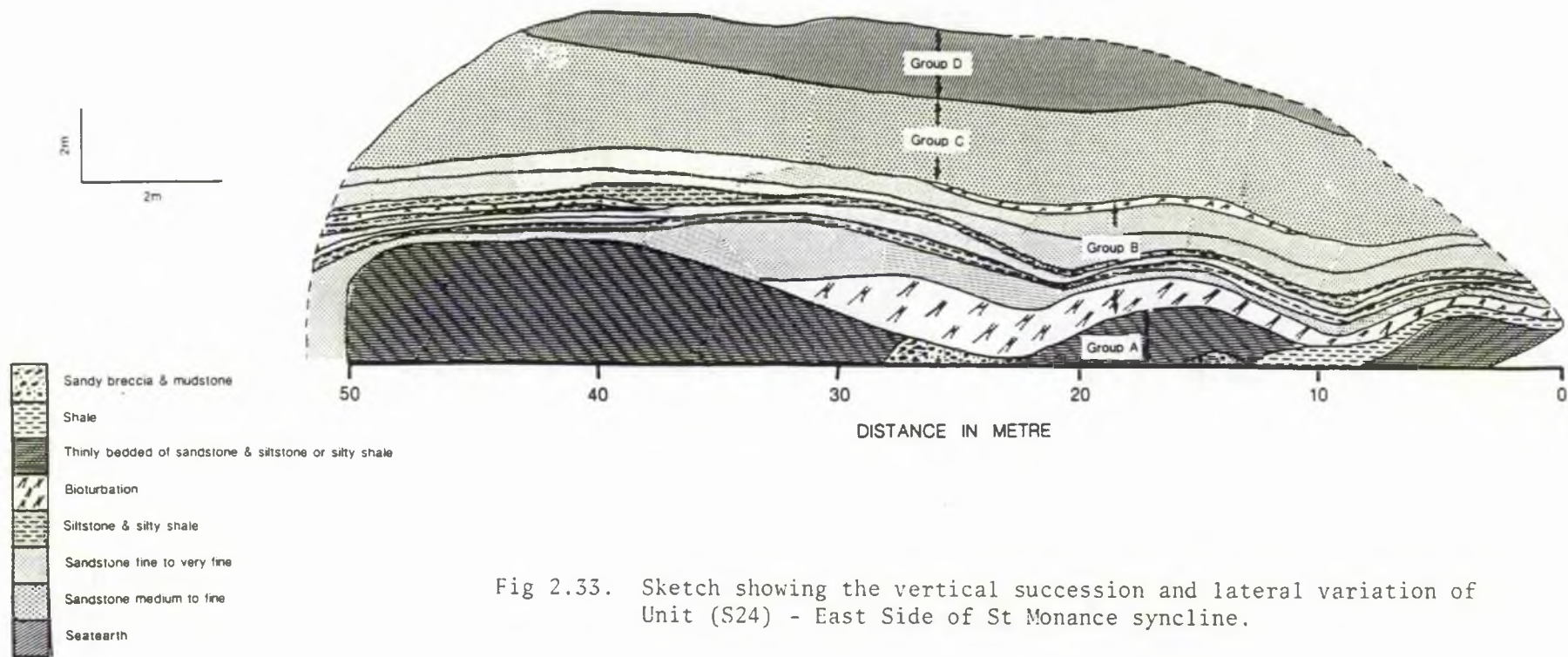


Fig 2.33. Sketch showing the vertical succession and lateral variation of Unit (S24) - East Side of St Monance syncline.



laminated, others are rippled with shaly or silty interbeds (Fig 2.34A). Starved ripples and small linguoid ripples are present, overlain by small scale trough cross-lamination produced by ripple migration (Fig 2.34B). Trace-fossils are found as vertical tubes and Monocraterion (see Chapter 3). Above an erosional surface, group C is formed of alpha cross-stratification (Allen, 1963b). Most sets are planar (McKee and Weir, 1953), and few approach typical trough cross-lamination at the top (Fig 2.35). Straight crested dunes probably generated the planar type (Allen, 1963). Group D fine-grained sandstone contains plant fragments and rootlets coming from the coal above, tree trunks on its top are also found (Fig 2.36) up to 62 cm long and 4 cm maximum diameter with rootlet scars, locally small-scale cross-stratification is also present.

This unit is covered by seat-earth unit (S25) and thin bed of coal unit (S26), and these are overlain by a flat-bedded sandstone, medium-grained, containing large plant fragments and trace-fossils on the upper surface (S27). The last marine transgression in this succession is represented by a grey mudstone unit (S28) with Lingula squamiformis and a brackish bivalve assemblage (Wilson, 1978). It is covered by the Mid Kinniny Limestone.

Summarizing, units S24 represent deposition in a channel with repeated phases of aggradation, and channel scouring. The sequence is regarded as a unity because of uniform palaeocurrents and the relationship of successive facies. A large channel formed towards the top but this was filled, abandoned and succeeded by a fine grained clay deposition which formed eventually a seat-earth. The sandstone (S27) represents a sub-aqueous delta platform deposit overwhelmed by the marine transgression muds gradually giving way to carbonates.

Fig 2.34A General view of interbedded sandstone and siltstone, showing the smooth contact between them. Unit (S24) - East side of St Monance syncline. Camera lens hood is 5 cm in diameter.

Fig 2.34B Photograph of interbedded sandstone and siltstone or silty shale showing irregular contact between them. Ripples and small scale trough cross-lamination are present. Unit (S24) - East side of St Monance syncline. Coin is 2.0 cm in diameter.

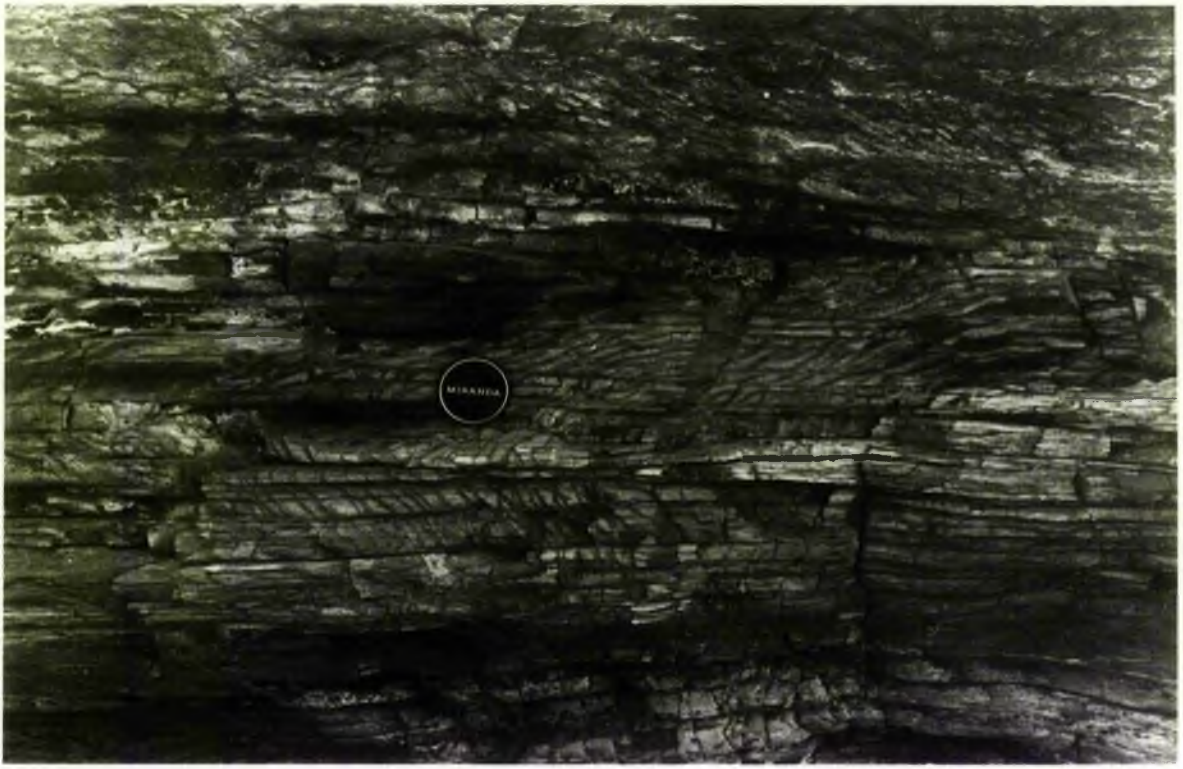


Fig 2.35 Photograph showing the large channel of unit (S24) contains planar cross-stratification and small trough cross-lamination just above the hammer. East side of St Monance syncline. Hammer is 35 cm long.

Fig 2.36 Photograph showing the upper surface of seat-earth sandstone contains plant fragment and stigmaria root of 62 cm long and up to 4 cm in diameter, with rootlet scars - East side of St Monance syncline.



### 2.7b Interpretation

In this cycle Fig (2.37) there are four progradational deltaic sequences; these are from units S to S6, S7 to S11, S12 to S15 and S16 to S26. The upper boundaries are marked by a coal or, if absent, a seat-earth overlain by prodelta facies which indicate rapid subsidence in the area of deposition. The absence of coal seams does not necessarily indicate a high energy wave environment but could be the effect of rapid oxidation on the delta top or a combination of both.

The last three units S27, S28 and the Mid-Kinniny (Hosie) Limestone indicate a marine transgressional sequence and marking an episode of rapid subsidence and delta lobe abandonment.

### 2.8 Tectonic activity

The thickness of the cycles increases upwards except for cycle L (Fig 2.38). There is also a change in thickness from east to west from 40.0 to 60.40 m (measurement for the first four cycles only). This variation could reflect some relation to subsidence, because thickness variation is related to the origin pattern of subsidence. This pattern is thought to be deep-seated in origin and probably related to the Variscan orogeny (Goodlet, 1959).

There are two theories relating to the thickness of cycles, Scottish workers, have generally preferred the theory of intermittent subsidence. A second group, have concluded that the amount of subsidence is directly related to the weight of sediments deposited (Russell and Russell, 1939). In fact there is no correlation between the amount of sediment in a cycle and the subsidence as indicated by the cycle above. As shown in table (2.1), for instance the sediment

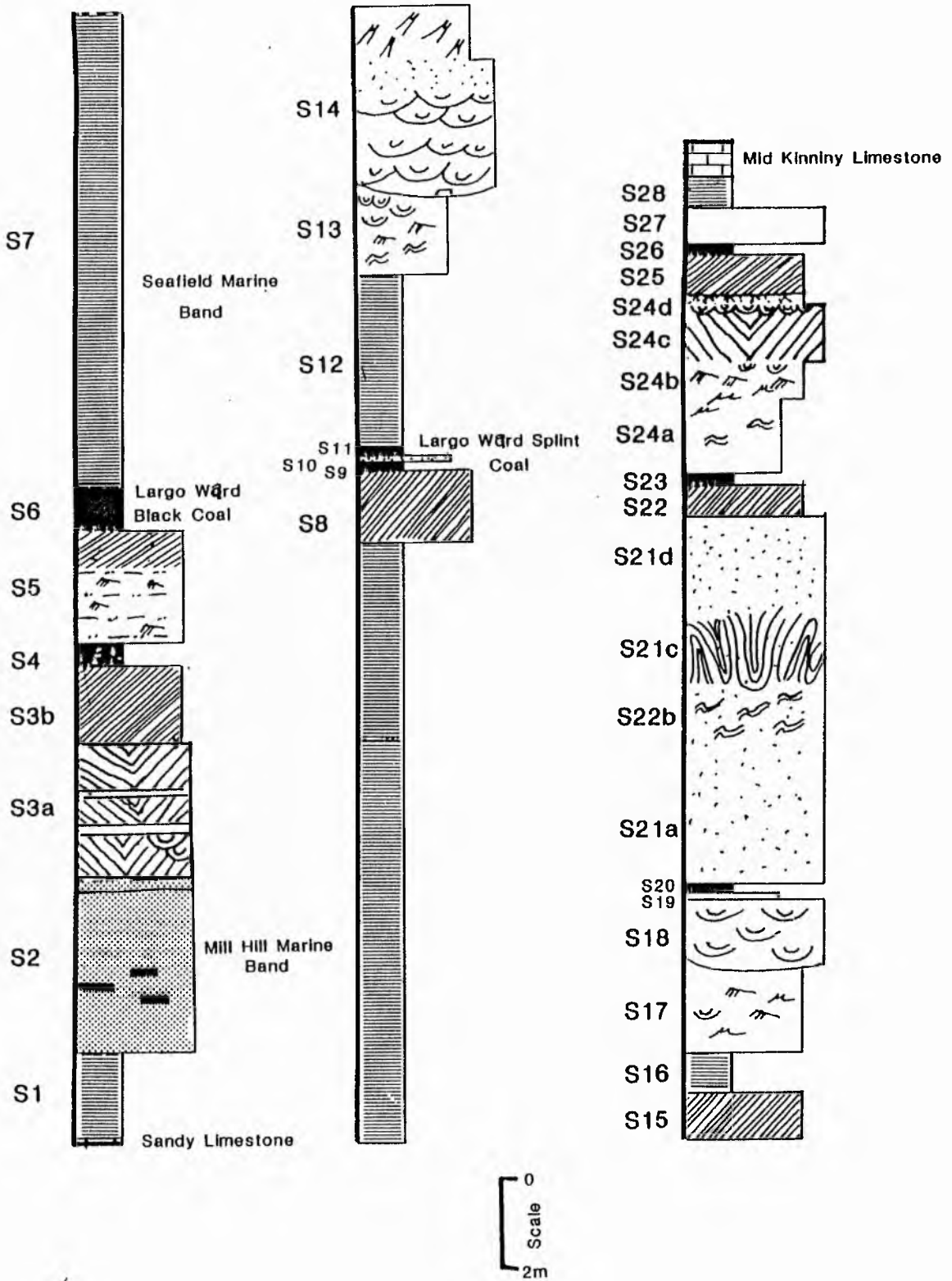


Fig 2.37. Generalised succession of cycle (S) of the St Monance syncline.

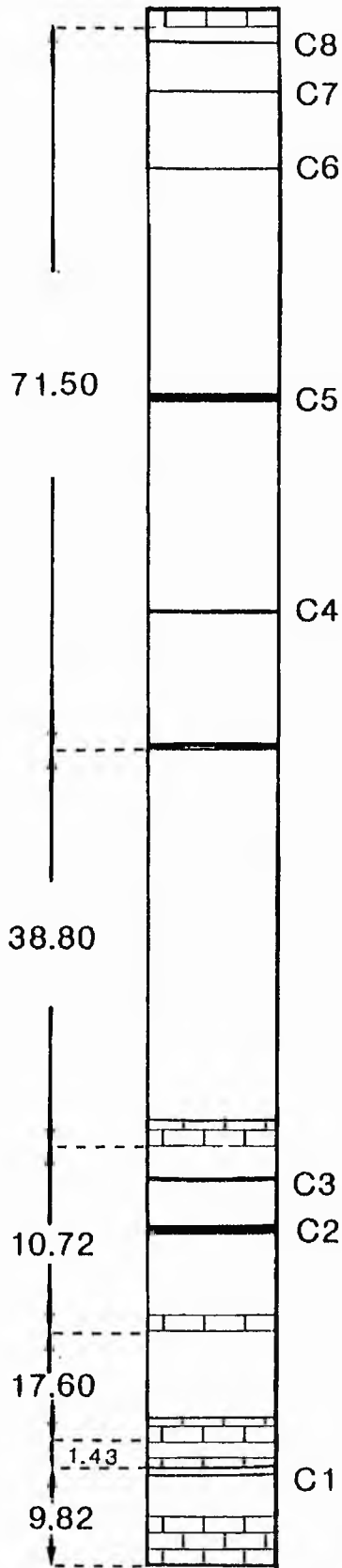


Fig 2.38. The thickness in (m) and arrangement of the cyclothems.  
C<sub>1</sub>, C<sub>2</sub> ..... etc = No of coal horizons.

Scale 1 cm = 6 m.



Table 2.1 Coal horizons and weight sediments relationship

Number of Coal	Coal thickness in cms	Thickness of sediments under the coal in metres	Thickness of sediments above the coal in metres	
8	12	4.30	-	up succession ↑
7	11	8.80	4.30	
6	23	15.20	8.80	
5	20	25.60	15.20	
4	90	45.70	25.60	
3	20	4.90	45.70	
2	60	20.90	4.90	
1	22	-	20.90	

thickness under the coal No 3, is nearly 5 m, which after the subsidence, must have deposited a small amount of sediments according to this view, but the sediment is nearly 45.70 m thick. It may therefore be considered that the variation in thickness in this area is controlled by tectonic subsidence and supply of sediment. The subsidence between coal seams was greater in amount at the later periods. This could be due to constant rate of subsidence allied to slower filling of the basin, or more rapid subsidence and similar rate of supply as time progressed. Goodlet (1959) mentioned that the variation in thickness of mid-Carboniferous strata in the Midland Valley reflects variation in the original pattern of subsidence. Greensmith (1965, p 239) pointed out that the East Fife lithological assemblage gives every indication of having been deposited in a much more unstable part of the basin, because of the closer position to the main axis of the Carboniferous North Sea Basin delta.

It is clear from the difference in the total thickness of the sequence from east to west that overall subsidence was greater in the West. Thickness of individual cycles at different parts in the basin is therefore controlled by the basin configuration.

## 2.9 Depositional Environment

Any classification of deltaic deposits must include criteria for distinguishing between deltas built by young rivers carrying predominantly a bed load of medium-to-coarse grained sand, and those formed by mature rivers carrying predominantly a suspended load of fine sand, silt and clay. In the present study area, the sandstones are predominant fine grained, carried by mature river probably of high sinuosity. This leads the marine processes to be more active than if

the river building up the delta was young. Belt (1975) described the Scottish Carboniferous Cyclothem Patterns and their Palaeoenvironment Significance and interpreted the St Monance section as of a destructive delta facies. The rate of sediment during destruction is dependent on the basinal configuration, marine process and river activity, and the rate of subsidence, and as a consequence units are different in thickness within one cycle. In the St Monance delta system, destruction units consist of very well-sorted fine-grained, sometimes bioturbated, mudstone (either burrowed) or containing a marine fauna, for example units (L1-L4)

The general stratigraphical consideration of all sediments in both sides of the St Monance Syncline, reflect a predominantly coarsening upward sequence. The cycles consist of progradational sequences (pro-delta, mouth bar), (eg T1 and T2-T3) aggradational sequences (fining upwards channel sequences) (eg F5) and sporadically developed abandonment facies (thin bioturbation siltstone eg W4; and coal horizons, eg W3).

#### 2.10 Depositional model

Relationships between the various facies recognized for this area and used to deduce the depositional environments model are summarized in table (2.2). The variety of facies reflect the numerous subenvironments within this area. These have been identified and shown diagrammatically on figure (2.39).

In the proposed delta the sediment was carried into the area by larger channel or channels outside the area, and smaller shallow distributaries led to sedimentation especially during flood. Mouth bar progradation produced coarsening-upward sequences, the lower parts

Table 2.2 Characteristics of Sediments of St Maurice syncline

Environment	Lithology	Sedimentary Structures	Units	Trace Fossils	
Increased river influence	Crevasse splay channel	Channelized, erosively based sandstone	B7N, F5, S14, S18, S21, S24	Teichichnids, Monocraterion, simple vertical tube? (Lacvivacyclus).	
	Levee	Coarsening upward from siltstone into massive sandstone with rootlets	T13 to T15, F5d		
	Crevasse splay	Interbedded sandstone and thinly laminated siltstone with shale 'Coarsening upward'	Ripples and ripples cross-lamination wavy parallel lamination, trough cross-bedding, and trough cross-lamination deformed structure	B7b to B7m, F3	Demconichnus, scolicia, monocraterion simple tube.
	Peat and swamp accumulation	Soft-earth sandstone fine to very fine grained and coal	absent	W2, T4, S3b, S20, S25, W3, T6, T12, S6, S9, S11, S20, S23, S26	-
	Fine and coarse	Interbedded sandstone, siltstone and shales, containing nodules in siltstone sediments	Flat lamination, wave ripples micro and small scale trough cross-lamination	F2, B1, B6, S7, B7a, S5	Chondrites, teichichnids, planolites
Increasing marine influence	Minor mouth bars	Interbedded sandstone, siltstone and silty shale 'Coarsening upward'	symmetrical and asymmetrical ripples parallel lamination, wavy bedding, ripple cross-lamination, micro and trough cross-lamination	L3, T2, T3, S13, S17	Teichichnids, Aulichnites, Pelecypodichnus, Conichnus, Rhysoneuron.
	Distal part	Interbedded very fine grained sandstone and siltstone or silty shale	parallel lamination, micro and small scale trough cross-lamination	L2	
	small scale spit	thin bed of sandstone	parallel lamination, micro cross-lamination	S10	-
	Distributary mouth bar	fine grained sandstone	small to medium scale cross-lamination	S3a	Pelecypodichnus, planolites
	Abandonment	bioturbation sandstone with siltstone or silty shale	absent	W4, L1, S15	Planolites, Teichichnids
	Marine band	fossiliferous mudstone	absent	W1, L2, L3, L4, B1, T1, T16, F1, S2, S7, S12, S28	Diplocraterion, Paleophycus Etone, Teichichnids
Marine shelf sediment	limestone		W, L, B, T, F, L	Teichichnids, Zoophycus	

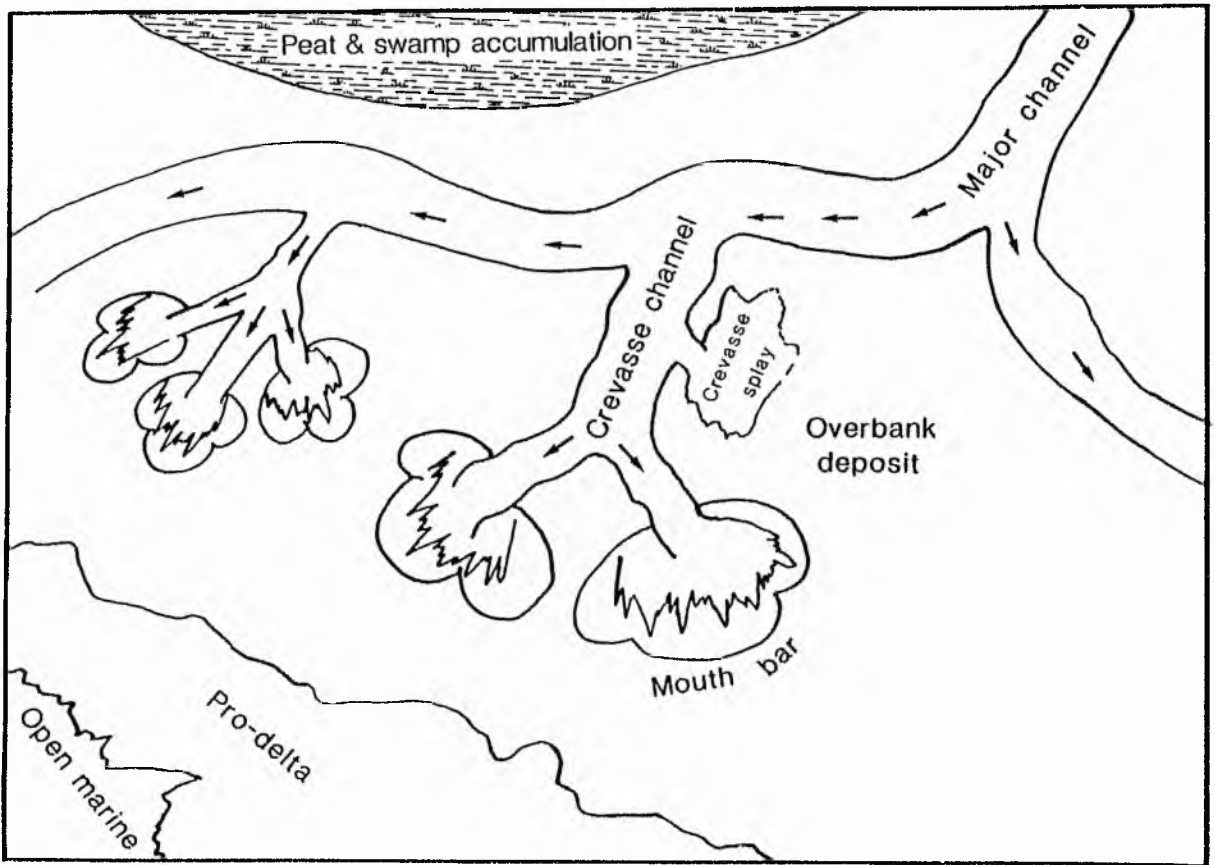


Fig 2.59. Schematic reconstruction of sediments in St Monance area.

of the mouth bar representing distal parts. Furthermore, channels were eroded in the upper part of the mouth bar sequences as progradation continued (eg cycle S units S16-S17). In this progradational phase, the siltstone and sandstone represented delta front sediment and the shale represented a prodelta sediment deposited seaward below the wave action and leading into the marine shelf deposits.

Simultaneously, during the channel flood periods, overbank and levee sediments were formed. The predominance of wave reworking of the overbank deposit led to the formation of sand spits. Levee sediment sometimes without rootlets suggests a subaqueous deposit. Peat and swamp accumulation became established followed by abandonment deposits.

## 2.11 Summary and Conclusion

The sedimentary succession of this study area is predominantly deltaic in origin and includes, delta top, delta-front, and prodelta sediments separated by marine horizons. At intervals the deltaic facies were partially or nearly completely inundated by marine water advancing from the south. The sediment laid down on these occasions consisted of marine limestone and fossiliferous mudstones.

The change from Calciferous Sandstone conditions began with general subsidence at the time of the Lower Ardross Limestone, when marine influences, became much stronger than previously. The majority of sedimentary sequences are small, and large scale coarsening-upward representing infilling of bays. The presence of wave-dominated coarsening-upward sequences and marine horizons suggested that the interdistributary bay was open.

The descriptive model devised for the deposition of the sediments is that of a destructive delta.

## CHAPTER 3

### 3 TRACE FOSSILS

#### 3.1 INTRODUCTION

Trace fossils are abundant in this area and were encountered in many horizons of the field exposure. The most abundant are present in sequences of interlaminated sandstone, siltstone and shale. They are also present in shales, sandstones and even in limestone beds. During the examination of the exposures it became apparent that many of trace fossils were of types previously recorded and described from the Carboniferous of east Fife (Forsyth and Chisholm 1968; Chisholm 1968, 1970), but that new forms were also present. A detailed account of trace fossils found which shows their distribution, kind of activity, lithofacies, and fossils associates (Table 3.1). The most abundant type, mostly present in very fine grained materials, is Teichichnus but its abundant patterned feeding structure is nowhere well developed. In the following, a description is given of each trace fossil in each unit and in each cycle.

#### 3.2 Teichichnid units

This type is found in varying sizes and in different orientations, mostly in very fine materials, as tubes up to 2.5 cm width, and up to 10 cm length. The tubes are generally filled with material slightly coarser than the surrounding sediment. The group of trace fossils described as Teichichnids (Chisholm, 1970) consist of a number of forms, most of which are similar to the present type. As a group these trace fossils are characteristically found in poorly



sorted, bioturbated (units W4, L1, S5, S15; Fig 3.4), argillaceous sediments (units L3, T14, F2, S12, S13, S14, S16; Fig 3.3) and carbonate rock (unit F, Fig 3.5). (Table 3.1).

The sand-plugged burrows are orientated oblique or parallel to bedding (Fig 3.1), and sometimes even vertical dependent on the energy of the environments. Chisholm (1970) described each burrow as consisting of an L-shaped tube, vertical and unbranched with a sinuous horizontal limb containing a small septum. Most of these trace fossils according to Chisholm's description are incomplete either vertical tubes (Fig 3.2) as simple and filled with fine-to-very fine grained sand derived from the overlying sandstone, with no sign of any lamination in the sand plugging, and the burrow walls show no sign of any multilayered structure; only a very thin skin of disturbed mudstone can be detected around them. In some a horizontal limb is present in which generally the laminae are horizontal and concave upwards. The laminae consist of pale coloured fine-and-very fine-grained sand with some laminae in between consisting of argillaceous material, in the upper part carbonaceous material is present. The width is about 2.5 cm; and the length is about three times the width (Fig 3.3).

Teichichnids are mostly associated with marine fauna. It is suggested as they formed in a marine environment. This is confirmed by those found in a fully marine unit F (Charlestown Main Limestone) as a colony on the lower surface of the bedding plane (Fig 3.5; width up to 17 mm, length variable). In cross-section there is no sign of any lamination; they look like tubes filled with materials similar to that of the surrounding sediment. Zoophycus trace fossils are also present, as well as a fully marine fauna such as crinoids and

Table 3.1 Distribution of trace-fossils at St Monance,  
 Note:- Excluding trace-fossils identified by Chisholm (1970)

Unit Type	Kind of activity	Brief description	Lithology	Associated body fossils
W4 Planolites Teichichnids?	infilled burrow feeding structure	Tubes different in length, generally oblique orientation to the bedding plane, and slightly curved, some of them contain laminae and might be Teichichnids trace-fossils (?)	Lower part of bio- turbated mudstone, siltstone and/or very fine grained sandstone	Associated W1 brachiopods and overlying by fully marine horizon (L)
L1 Teichichnids	feeding structure	different orientation of incomplete trace fossils, with laminae, and different size.	upper of bioturbated horizon	associated with a fully marine horizon below and marine mudstone above
L3 "	" "	rounded in shape, rough surface or pitted, 1.13 cm in diameter suggest as sand-plugged.	Mudstone, dark in colour	fully marine Crinoid above it.
T2 Aulichnites Pelecypodichnus or Lockcia Scolicia or Olivellites	grazing trials major crawling trials resting traces trials	it consists of 2-convex ridge, separated by deep median groove straight to gently curved, non-branching, more or less horizontal or oblique to the bedding plane, almond shape meandering-crawling with traverse paching and median furrow	reddish brown sandstone very fine grained, interbedded with silt- stone or silty shale. All of them are observed in lower surface of the bedding plane	marine mudstone below this unit
T3 Conichnus Pelecypodichnus	dewlling burrow or resting trial resting traces	Conical tube with circular cross-section, filling with the same material in which they lie straight, non-branching, oblique or horizontal to the bedding plane	Light grey laminated sandstone, very fine grained.	None
T8 Diplocraterion	feeding structure	U-shape, retrusive (see Wilson, 1978)	flat-bedded, fine to medium grained sst, buff in colour	None
T14 Teichichnids	feeding structure	vertical tube, filled with sandstone, slightly curved, lower part wider than the upper part, (3.5-4 cm) length 7 mm in diameter.	mudstone dark in colour	None
F Teichichnids Zoophycus	feeding structure " "	inside the section, it is Gauda-galli related to genus Zoophycus.	Lower surface of Carbonate rock (Lst) Upper surface of 1st	fully marine horizon
F2 Chondrites Teichichnids	feeding structure " "	tube filling, branching, more concentric. vertical tube, length 3.64 x the width, laminated horizontal and concave upward	surface of the nodules silty shale or siltstone	fully marine horizon below it (Neilson shell bed)
F3 Beaconichnus	crawling and walk- ing trials	Series of parallel lines of footprints, distance between two depression of row = 12 mm	interbedded of siltstone and sandstone very fine- grained	None
F3 Scolicia Monocraterion Simple tube	trials dewlling burrow feeding burrow	slightly curved to horizontal tube, mostly parallel or inclined to the bedding trumpet shape, penetrates into the sediment curved in shape, 1.01 cm width with laminae, filling with sst.		
F4 Unknown		Traces as a result of animal activity as crawling, suggest- ing as formed by gastropod	upper surface of linguoid ripples	None
S2 Diplocraterion Paleophycus Elone = Taenidium	feeding structure " " " "	Complete, U-shape, vertical to the bedding, limbs are , bottom is semicircular Cylindrical burrows, sinuous, unbranched, some are inter- secting Radiating, branching, segmentation.	Mill Hill marine band	fully marine band
S3a Pelecypodichnus Planolites	resting traces infilling structure	A series of solitary resting traces results from animal moving through the sediment and burrow formed below tubular in shape, rounded at lower end, circular to oval in cross-section, 4 to 10 mm in diameter, 40 to 16 mm long	Sandstone, very fine- grained with x-strati- fication	fully marine band below
S5 Planolites	infilling structure		interbedded of sand- stone very fine grained W1 siltstone of siltyshale	fully marine (seafield)
S8 Chondrites Paleophycus	feeding structure feeding burrow	dendritic shapes, small cylindrical, 0.66 mm in diameter cylindrical, crowded, sinosity, more or less obliquely to the bedding	well-jointed sandstone	fully marine band below
S11 Teichichnids?	feeding structure?	simple U-shape, oblique to parallel bedding, tube less than 1 mm in diameter and 2.5 cm long, tubes parallel to each other	upper surface of siderite nodules	associated with fully marine horizon
S17 Rhysonetron	Unknown	cylindrical curved, wide up to 7 mm, one cuts the other	preserved in sandstone troughs of ripple marks	scarce marine bivalves
S24 Laevicyclus Monocraterion	feeding burrow dewlling burrow	cylindrical tube at right to the bedding, crowded, variable in diameter regular concentric circular-to-oval in shape funnel structure, penetrated perpendicular to the bedding, formed of a series of rings.	lower part of fining up- ward sandstone	None
S27 Monocraterion	" "	as above but much more crowded	sandstone fine-to-medium grained	fully marine horizon above it

Fig 3.1 General view of teichichnids (a) and planolites (b) trace-fossil in the lower surface of bioturbation bed (W4), and overlying the coal bed (W3), showing oblique to horizontal orientation of trace-fossil to the bedding plane. East side of the St Monance syncline. Coin is 2.8 cm in diameter.

Fig 3.2 Example of vertical sand-plugged teichichnid found in contact between the mudstone unit (T14) and the massive sandstone unit (T15). East side of the St Monance syncline.



Fig 3.3 Teichichnus; unit F2, length 3.64 x the width, laminae are generally horizontal and concave upwards, material very fine grained sand with argillaceous materials. Carbonaceous materials are present in the upper part. St Monance, East side, Unit (F2). Coin is 2.8 cm in diameter.

Fig 3.4 General view of sand-plugged teichichnid in bioturbation of the upper part of unit (S14). East side of the St Monance syncline. Coin is 2.5 cm in diameter.



brachiopods (Fig 3.6).

Planolites trace fossils are generally associated with teichichnids (units W4, S5, and S16; Fig 3.1). Chisholm (1970, p 31) pointed out that Planolites are associated with fauna ranging from fully marine to non-marine. Therefore, it is suggested that the Planolites found at these horizons formed in a marine environment, as well as the Phycodes - like trace fossils which are found in unit (S15) and associated with Teichichnus.

### 3.3 Units T2 and T3

In these two units four types of trace-fossils are present. In the very fine-grained reddish-brown sandstone interbedded with siltstone and/or shale (Unit T2), three types of trace fossil are found, all of them in the lower surface of the bedding plane. The first is a meandering crawling trace, has a median furrow with elevated medial ridge, and perhaps represents creeping or feeding trails made by burrowing gastropods; it compares with Scolicia (Olivellites) (Fig 3.7). The second, Aulichnites has two-convex ridges separated by a deep median furrow [interpreted by Fenton and Fenton (in Hantzschel, 1975) as a crawling and/or grazing trail most probably made by gastropod] (Fig 3.8). The third type which is found associated with Aulichnites is small almond shaped with a smooth surface, varies in length, is straight to gently curved, and non-branching, and more or less horizontal or oblique to the bedding plane. It is considered to be resting trails of small burrowing Pelecypods. It is Pelecypodichnus (Lockeia) (Fig 3.9), and is also found in Unit T3, along with a vertical conical tube with circular cross-section filled with the same material in which it lies (Fig

Fig 3.5 Example of Teichichnus in unit (F) showing a colony of tubes on the lower surface of the bedding plane. Width up to 17 mm, length variable, non-branching, some of them cut across one another. Lower surface of Charlestown Main Limestone - St Monance, East side.

Fig 3.6 Cross-section showing there is no sign of any lamination structure, material inside the tube similar to the surrounding sediments. Zoophycus (a) and fossil fauna crinoid and brachiopods are also present (arrows).





Fig 3.7 Example of Scolicia == Olivellites.

Trace-fossil as meandering, crawling, and median furrow, shows elevated mesial ridge in the middle formed by grazing gastropod. St Monance, East Side, Unit (F2). Coin is 2.8 cm in diameter.

Fig 3.8 Example of Aulichnites.

It is different from Scolicia in having 2-convex ridge separated by a deep median furrow and associated with Lockcia (left side), formed by gastropod. St Monance, East Side, Unit (T2). Coin is 2.8 cm in diameter.



3.10); it compares with Conichnus, [interpreted by Myannil (in Hantzschel, 1975) as dwelling burrow or resting trails produced by a Cerianthid sea anemone].

These trace-fossils Scolicia, Aulichnites, Pelecypodichnus are associated with an underlying marine horizon suggesting that a marine environment was favoured by the animals responsible for these trace fossils. Chisholm (1968, p 117) also pointed out that Scolicia traces are found only in fully marine strata.

#### 3.4a Unit F2

This unit is a shale containing nodules. In some of the nodules both surfaces are flattened, the lower surface is irregularly flattened around a convex centre point, while the other surface is convex. The nodules have trace-fossils shaped in a dendritic pattern of small cylindrical branches, up to 0.6 cm in diameter, lying parallel to the bedding plane, and more or less radiating (Fig 3.11). The nodules are roughly ellipsoidal in shape, up to about 7 cm in diameter, and up to 2 cm thick. Simpson (1957) suggested that the laminated internal structure of the traces was formed by a process of back-filling with faecal or other displaced material, but this is not a feature of Chondrites (as feeding burrows). Chisholm (1970, p 29) pointed out that for convenience, the nodules themselves are referred to as 'burrowed iron nodules'. They are associated with teichichnid trace-fossils (Fig 3.3) and the unit below was formed in a fully marine environment (Neilson Shell bed, F1) but the marine fossils become smaller and fewer into the shales suggesting the environment was becoming less fully marine in character.

Fig 3.9 Example of Pelecypodichnus Lockeia. These resting traces, formed by pelecypod, are almond-shape, straight to gently curved, non-branching, more or less oblique to the bedding plane, observed in the lower surface, Unit (T2). St Monance, East Side. Coin is 2.8 cm in diameter.

Fig 3.10 Example of Conichnus. This dwelling burrow, shows conical tubes with circular cross-section, filled with the same as the surrounding material. Observed in Unit (T3) at 43 cm above the contact with Unit (T2). St Monance, East Side. Coin is 2.8 cm in diameter.



### 3.4b Units F3 and F4

In F3, and below the conglomerate bed, (Fig 3.12A) is a series of parallel lines of footprints, the distance between the two rows of depressions is about 12 mm. The author has found that crawling crabs also form these parallel lines (Fig 3.13A, 13B). If this comparison can be accepted, it can be suggested that the direction of the animals' movement (Fig 3.13A) was inclined to the pen, in Fig 3.12A. Another group of footprints (Fig 3.12A) (Fig 3.12B) is formed of 12 depressions, 6 posterior, and 6 anterior, the size of each footprint is about 20 mm and perpendicular to the first group. In the latter case, the crawling tracks might have been formed by larger crustaceans.

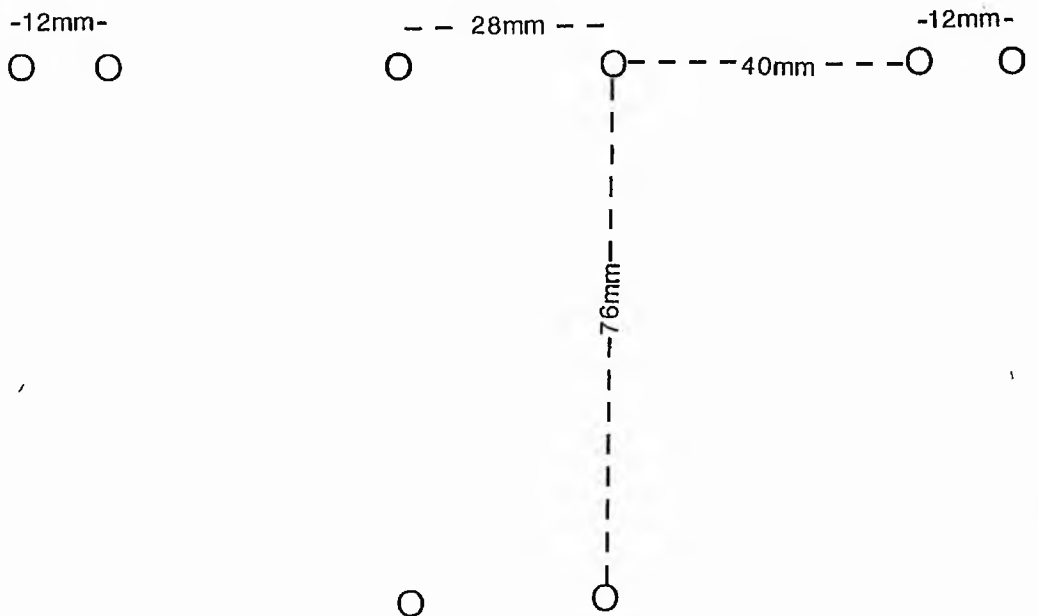
The second type of trace-fossil (Fig 3.14) is Scolicia. Another type Monocraterion is also present with a trumpet shape, penetrating into the sediment and containing concentric lamination varying in diameter. While about 1.70 m above the conglomerate bed and there is a tube burrow with laminae (Unit F3) width 1.01 cm where curved shape is probably not the original shape but was deformed during burial (Fig 3.15). There is no sign of branching, and this would seem to eliminate Phycodes; nor is there any sign of U-shaped burrow, so that Diplocraterion is also excluded. The form does, however, show all the features which is thought to have been provided by an organism similar to that responsible for Teichichnus and will be referred to that genus.

In unit F4, only one trace-fossil is present on the upper surface of the linguoid ripples (Fig 3.16) as a crawling trace. The width is about 1.5 to 5 mm, with a ridge in the centre, and the structure is comparable with one formed on the recent sediment by

Fig 3.11 Example of ? Chondrites. Flattened nodules showing burrows in a dendritic pattern of small branching cylinders filling nearly parallel to the bedding plane. Unit (F2). St Monance, East side.

Fig 3.12A In Unit (F3) they look like rain pits, but they are not, because of linear pattern suggesting that they are trace fossils, formed by crustaceans. They are observed on the upper surface; 40 cm below the conglomerate bed Unit F3. St Monance, East Side. Pen is 17 cm long.

Fig 3.12B Sketch, size, distance of the larger footprints.





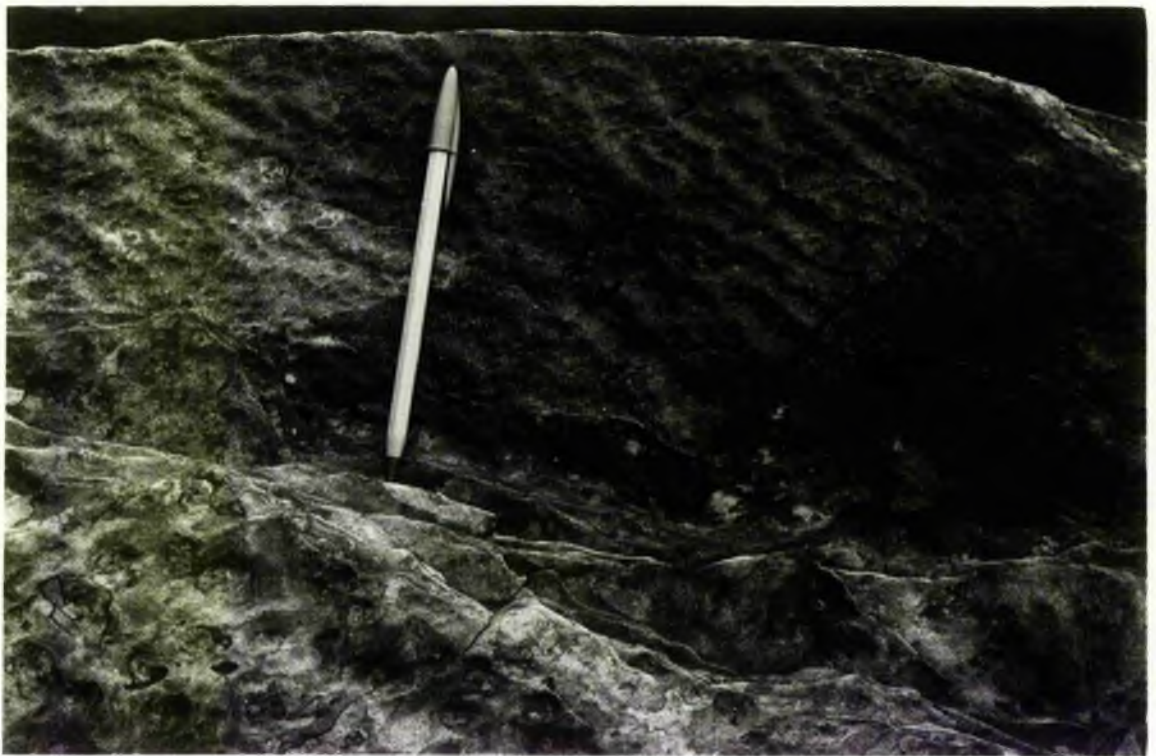


Fig 3.13A Three sets of parallel lines of depressions produced by crabs on recent sediment. The direction of movement from left to right.

Fig 3.13B Close up of figure 3.13A.



Fig 3.14 Two types of trace fossil; group (a) are slightly curved to horizontal tubes, mostly parallel-to-inclined to the bedding suggested as Scolicia; group (b) are trumpet shaped penetrating into the sediment, - Monocraterion.  
Unit (F3). Photograph of upper surface of the bed, 50 cm below the conglomerate bed. St Monance, East Side, camera lens hood is 5.0 cm in diameter.

Fig 3.15 Trace fossil tube with laminae (width 1.01 cm) curved shaped could not be the original. Suggest as Teichichnus.  
Unit (F3), 1.30 m above the Conglomeratic bed.  
St Monance, East side. Coin is 2.5 cm in diameter.



moving gastropods (Fig 3.17A, 17B).

The trace-fossils which are present in these two units may be found in part associated with Scolicia, and in part with Monocraterion often found in nearly fresh water. It seems likely, therefore, that a marine to brackish rather than fully marine environment was favoured by this particular variety of trace-fossils.

### 3.5a Unit S2 Mill Hill Marine Band

The Mill Hill marine band is a carbonaceous nodular calcareous sandstone which is strongly bioturbated. The body fossil assemblage is truly marine. Trace fossils in this unit are present between 0.50 to 1.00 m above the base, as Diplocraterion, a complete U-shape burrow (Fig 3.18). The tube is funnel shaped, vertical to the bedding plane and both limbs are parallel, while the bottom is semicircular; some are truncated due to erosion (Fig 3.19). Palaeophycus is found on the bedding surface as cylindrical burrows, sinuous, unbranched, up to 0.6 cm in diameter, and up to 6.0 cm in length; some of them intersect one another (Figs 3.20A, 3.20B). It is present in the transition zone between this unit and the unit above (S3) (Fig 3.22). The other type of trace fossil is shown in (Fig 3.21), as radiating, branching and segmentation and is possibly Taenidium (Heer, 1877) Eione (Tate, 1859) It is similar to Keckia with segmentation on the out side, but commonly smaller (Hantzschel, 1975). It was originally interpreted as an alga (Liburnau, 1900), but originates in feeding burrows by periodic filling of the funnel in a backward direction, and occurs in a wide range of environments (Hantzschel, 1975).

It is clear from the above that these trace-fossils have lived in a fully marine environment, and were able to withstand the movement

Fig 3.16 and 3.17A, B: On the upper surface of linguoid ripples  
Unit (F4), traces as a result of animal activity as crawling  
on the sediment. Width 1.5-5 mm, with ridge in the centre.  
Similar traces (Figs 3.17A, 17B) are formed on recent  
sediment by gastropods.





Fig 3.18 Example of Diplocraterion. U-shaped, vertical to the bedding plane. Lower part of Unit (S2). East side of the St Monance syncline. Coin is 2.5 cm in diameter.

Fig 3.19 Example of Diplocraterion. Unit (S2), one limb is present (a) or half of the trace (b) due to erosion. St Monance syncline, East Side. Coin is 2.5 cm in diameter.

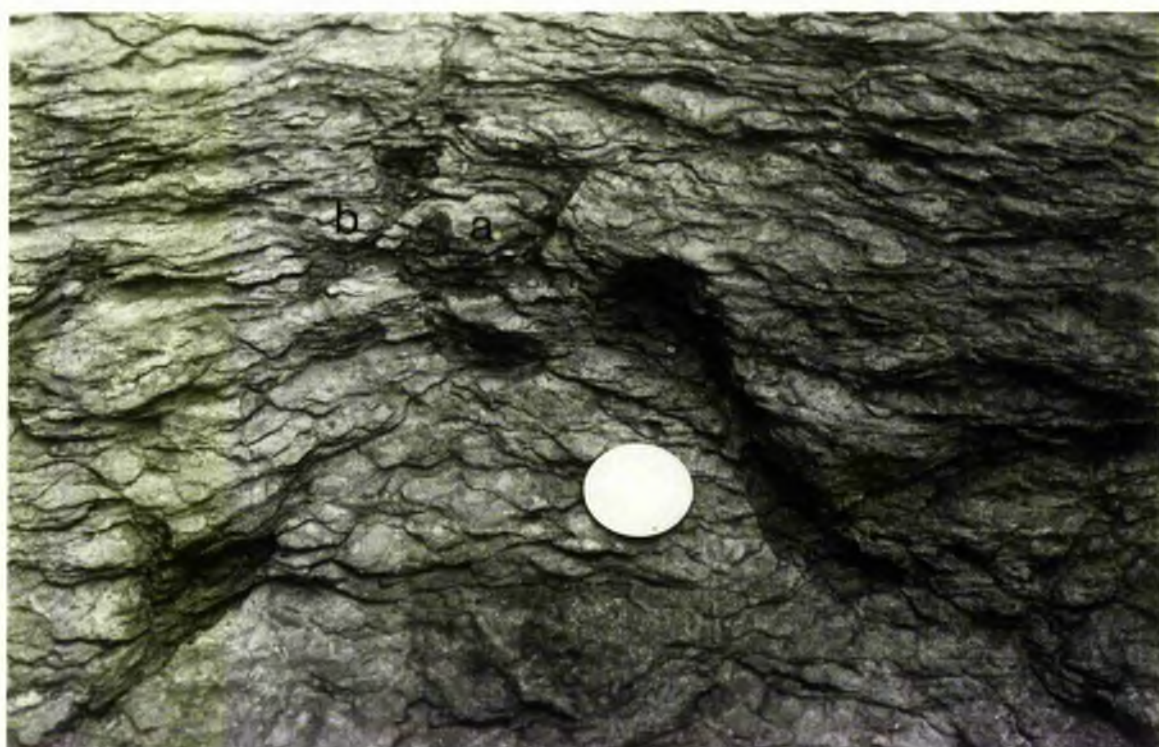


Fig 3.20A Example of Palaeophycus in Unit (S2). On the surface of nodules band as cylindrical, unbanded, some of them cut across one another. East side of the St Monance syncline. Coin is 2.5 cm in diameter.

Fig 3.20B Example of Palaeophycus, showing the longest one up to 6.0 cm, and 0.6 cm in diameter. St Monance, East side, Unit (S2).



Fig 3.21 Example of Eione trace fossil Unit (S2). Showing the radiating (arrows), branching (b) and segmentation (a). St Monance, East Side. Camera lens hood is 5 cm in diameter.

Fig 3.22 Palaeophycus in transitional zone between Unit (S2) and (S3), showing these burrows are more crossed and sinuous than in Unit (S2) and smaller in size. St Monance, East Side.



of sediment that prevailed during deposition.

### 3.5b Units S3 and S5

Unit (S3) in overlying the Mill Hill marine band consists of two lithologies. The lower part (S3a) is very fine-grained with cross-stratification, while the upper part (S3b) is formed of seat-earth with ironstone nodules. The subunit (S3a) has burrows running in all directions, but the majority are orientated roughly parallel to the bedding and locally disturbing the cross-stratification. The tubes, rounded at the lower end, are circular to oval in cross-section, with a diameter of 4 to 10 mm, and up to 16 mm long, filled with sediment similar to that of the surrounding rock, and in some examples a faint lamination can be seen. As trace-fossils they compare with Planolites (Fig 3.23). The other type of trace-fossils show a Pelecypodichnus escape structure, resulting from the moving of the animal through the sediments, and burrows formed below (Fig 3.24).

Unit (S5) is very fine-grained sandstones interbedded with micaceous mudstone in the lower part and seat-earth with plant fragment coming from the coal above in the upper part. One type of trace-fossil present is regarded as Planolites, up to 4 mm in diameter, and the burrow is surrounded by carbonaceous and micaceous material (Fig 3.25).

From that described above, it can be concluded that the Planolites trace-fossil lived in different environments. In unit (S3a) which is associated with a fully marine band below it seems likely that a marine or quasi-marine environment was favoured while the Planolites in unit (S5) existed in a non-marine environment.

Fig 3.23 Example of Planolites cross-section showing different orientation of tubes and locally disturbing cross-stratification (arrow), and they are found in clean well-sorted sandstone with diameter up to 10 mm.

Fig 3.24 Escape structure, (right side), resulting from the moving of the animal through the sediment, and burrow formed below equal to the animal width. Left side (arrow) shows the trace fossils, almond shape, smooth surface as resting trace compared with Lockeia (Pelecypodichnus). St Monance, East side, Unit (S3a). Coin is 2.8 cm in diameter.



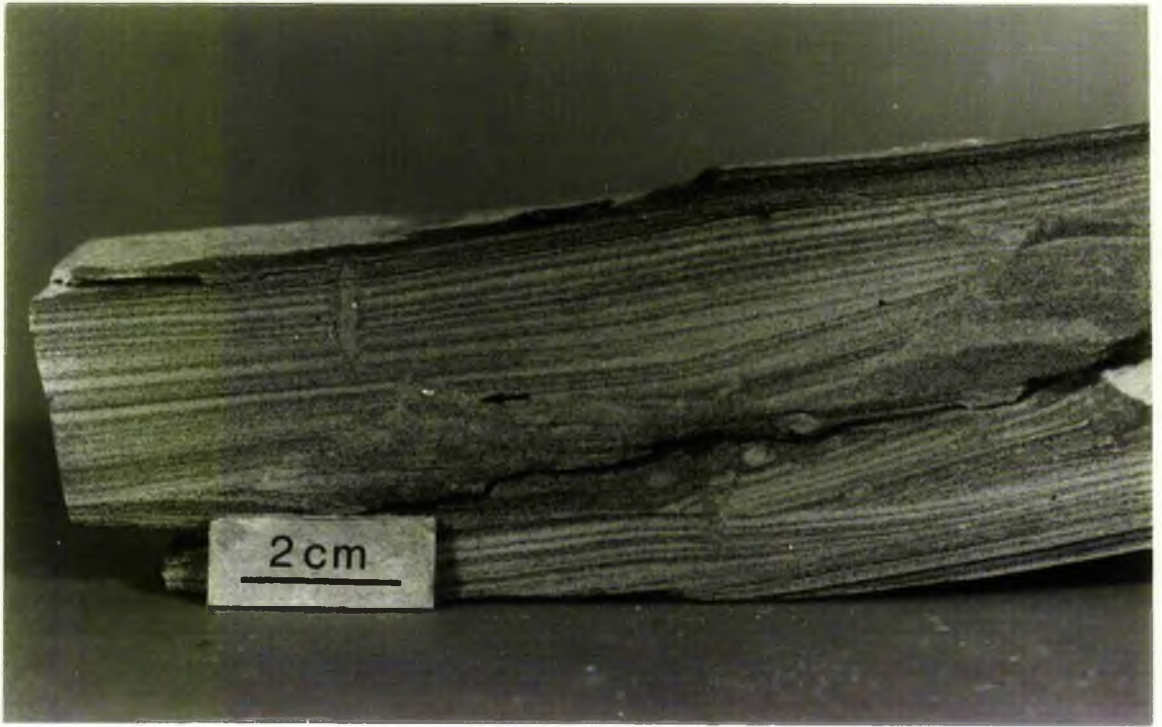


Fig 3.25 Example of Planolites. Section cut perpendicular to bedding, showing mainly horizontal tubes, concentrated in lower part of the slab, and up to 4 mm in diameter. St Monance, East side, Unit (S5).

Fig 3.26 Example of Chondrites showing the dendritic shapes of small cylindrical trace. Diameter is about 0.66 mm of feeding burrow organism. Upper surface of Unit (S8). St Monance swimming pool Eastern side. Coin is 2 cm in diameter.



Chisholm (1970, p 31) also pointed out that Planolites can be associated with faunas ranging from fully marine to non-marine.

### 3.5c Unit S8

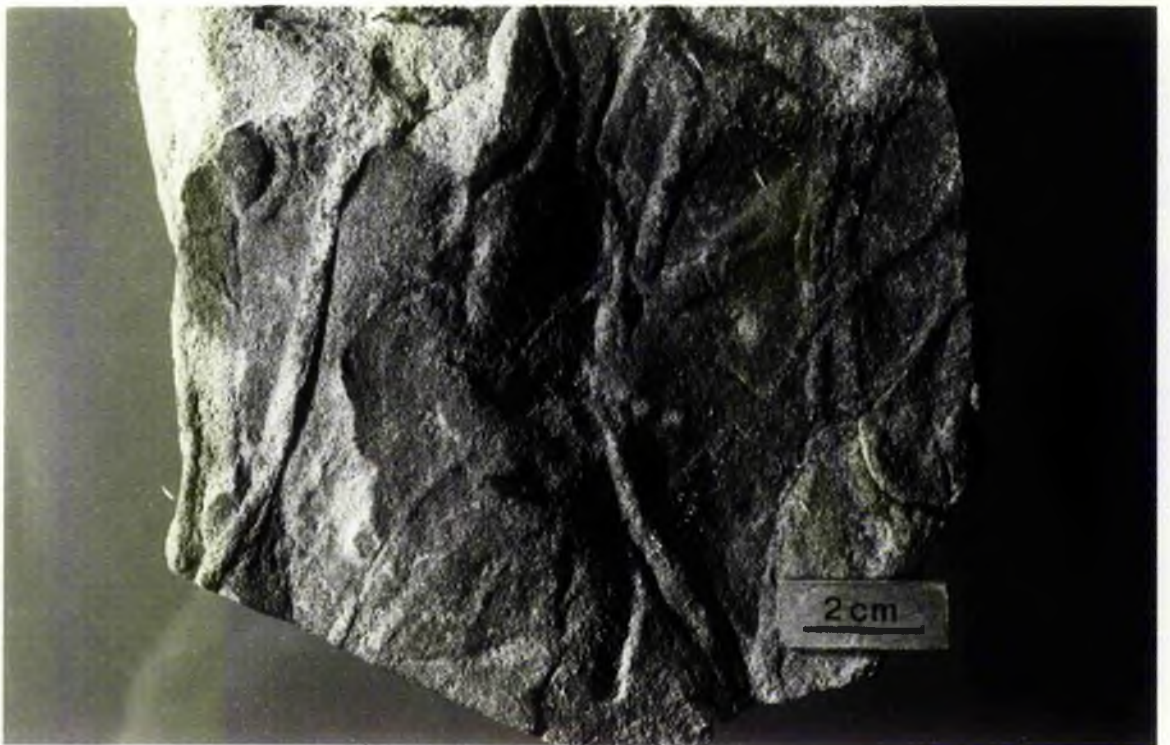
This is a well jointed fine-grained sandstone associated with an underlying fully marine horizon the Seafield Marine Band (Francis and others, 1961, p 27; Forsyth and Chisholm, 1968, p 71). Two types of trace-fossil have been observed in this unit (S8). In the eastern side of the swimming pool, the trace fossil is present on the upper surface of the bed, as plant-like dendritic pattern of small cylinders (Fig 3.26) 0.66 mm in diameter. It is to be regarded as a feeding structure of sediment-eating animals, and comparable with Chondrites feeding burrows, belonging to the Fodinichnia (Richter, 1927a, 1928, 1931). The second type has been found on the western side of the St Monance pool as Palaeophycus.

### 3.5d Units (S12 to S17)

The trace fossils in these units are described in detail by Chisholm (1970, p 21-51). In addition to Rhizocorallium, Teichichnus, Phycodes and Planolites, another two types of trace fossils have been observed. One on the upper surface of a siderite band (S12), is a simple U-shaped tube, oblique to parallel to bedding, tube less than 1 mm wide, and 20 mm long, and it bends downwards (Fig 3.27). It is not Rhizocorallium, but might be a U-shaped teichichnid trace. Chisholm (1970, p 46) suggested that the existence of depositional slopes may have been responsible for a characteristic feature of the orientated U-shape forms of Teichichnus. The second type has been observed on the upper surface of unit (S17), as cylindrical, curved, width up to 7

Fig 3.27 Example of (?) Teichichnus. This trace fossil observed on the upper part of siderite nodules as simple -U- shape oblique or parallel to bedding, tube less than 1 mm in diameter, and 25 mm long, parallel to each other. St Monance, East side. Unit (S12).

Fig 3.28 Example of Rhysonetron cylindrical curved, preserved in sandstone troughs of ripples marks, up to 7 mm wide, in branching, sometimes one cuts the other. St Monance, East side. Unit (S17).



mm, intersecting and, preserved in the sandstone troughs of ripple marks (Fig 3.28). It compares with tubes of modern annelids, and is interpreted by Donaldson (1967), and explained by Hofman (1971) as a diagenetic structure resulting from shrinkage-crack filling modified by composition and injection processes followed by impressing into substrate and superstrate, and then to the final Rhysonetron stage.

### 3.5d Unit S24

This is a unit of fining upward channel sandstones. There are two types of trace-fossil observed in this unit. The first one is a cylindrical tube formed at right angles to the bedding plane. The diameter is variable up to 7 mm, and 16 mm long. On the bedding plane it appears as nearly regular concentric circular to oval in shape, of 2 to 5 layers. Carbonaceous material is often concentrated in a thin skin around the circles, comparable with Laevicyclus (?) feeding burrow (Fig 3.29). The other type is a funnel structure, a slightly curved plugged tube perpendicular to the bedding (diameter up to 2.43 cm), formed of a series of rings (Fig 3.30) comparable with Monocraterion.

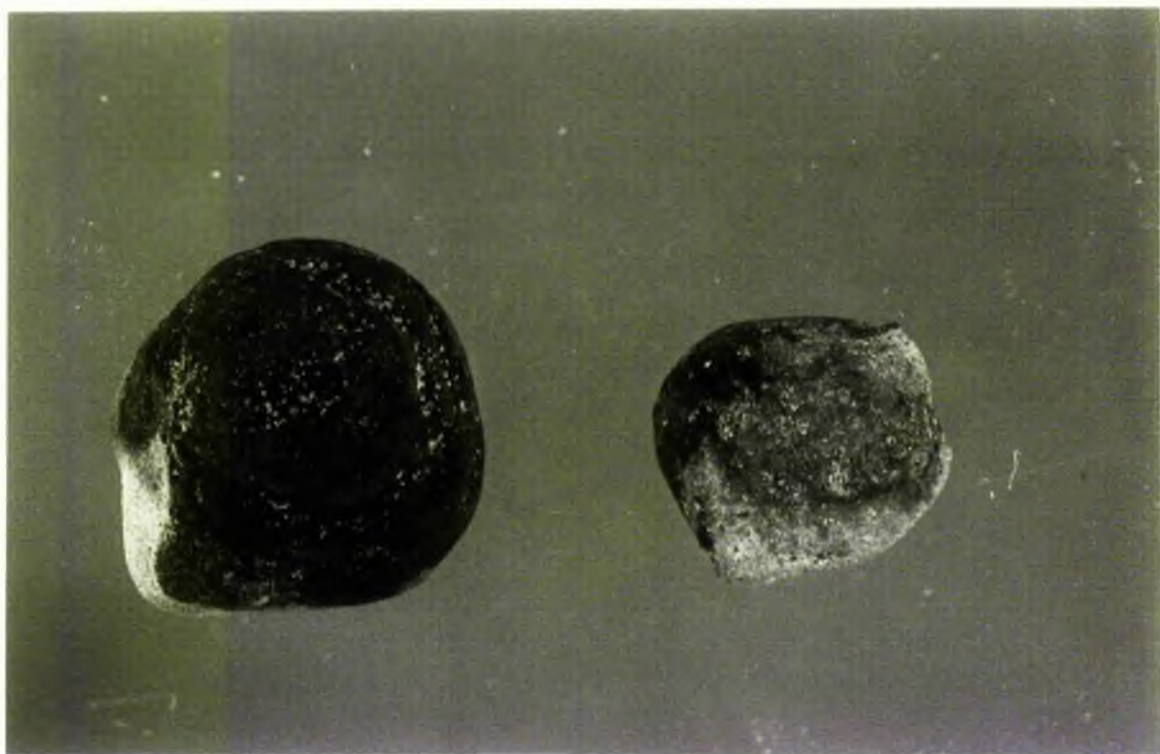
### 3.6 DISCUSSION

Abundant trace-fossils are found at several horizons and occur in different environments, with fully marine to non-marine. Six pattern types of animal activity are counted (Table 3.1). Chisholm as (1968) pointed out that only two types of animal activity (feeding and grazing burrow) are present, and he pointed out that the trace-fossils observed are probably all burrow rather than surface trails or resting marks.

Fig 3.29 Example of (?) Laevicyclus. Cross-section parallel to the bedding plane showing circular -to- oval shape, formed of 2 to 5 circles, and variable in size up to 7 mm in diameter, 16 mm long. St Monance, East Side. Unit (S24).

Fig 3.30 Example of Monocraterion showing the lower part of the structure, and the series of rings in the left sample which increase in diameter upward, up to 2.43 cm. St Monance, East side. Unit (S24).





The dominant trace-fossil assemblages with their type of activity are feeding structures such as Teichichnus; Palaeophycus; Zoophycus; Chondrites; Diplocraterion; and Eione. They are found in a fully marine or associated with marine strata, and in different lithofacies from carbonate (Unit F) up to sandstone (Unit S8). Zoophycus, Eione and Diplocraterion, occur in a fully marine environment. Other traces of this type of activity tend to occur in different types of sedimentary sequences and with different types of fauna, either in or associated with a fully marine band. Some of these forms would probably have required tranquil conditions with little or no erosion of sediment. This condition probably existed more often at the beginning of a cycle than during later stages when the silts and sands deposition was taking place. Diplocraterion is an example of this type.

The dwelling, crawling burrows and resting trails include Aulichnites; Pelecypodichnus; Conichnus; and Monocraterion. The first three types are related to quasi-marine environments, although they are associated with Scolicia as in units (T2 and T3), but even Scolicia, may be quasi-marine as well as fully marine as suggested by (Chisholm, 1968). Monocraterion, although it is commonly found associated with non-marine sediment as in unit (S24), may also be present in quasi-marine environment as in Unit (F3) and associated with Scolicia.

The infilled Planolites is found in different environments and in different lithofacies, as marine associated with Teichichnus (Unit W4), to quasi-marine Unit S3), and in a non-marine environment unit (S5) thus confirming Chisholm's (1970 p 31) findings.

## CHAPTER 4

### 4. Inorganic Sedimentary Structures and Palaeocurrents

#### 4.1 Sedimentary Structure and Geometry of Sandstones

Inorganic sedimentary structures will be discussed in the order that they were studied, namely, L, B. T ... etc as cycles and, L3, B7 ... etc as a unit in each cycle, and the asterisk indicates locality on the west side of the syncline.

The structures involved are ripple marks and associated cross lamination including rib-and-furrow structure; large-scale mainly trough cross lamination, hummocky cross stratification and deformation structures including pseudonodules. Lenticular, wavy and flaser bedding are common.

#### 4.2 Palaeocurrent Analyses

Measurements were made on thirty-eight beds throughout the sequence and a minimum of twelve readings were taken from each horizon. At each locality readings were taken over an area of the bed in the order of tens of square metres. To analyse the palaeocurrents many categories of sedimentary structures were considered. Some of them were examined in the field (such as ripples, lineation, flute casts ..... etc), by measuring the angle of pitch and noting whether the angle opens clockwise or anticlockwise relative to the strike and the sense of direction of flow if possible. In the case of cross-lamination, orientated samples were taken to ascertain the dip direction of the foreset laminae, the observed direction being marked and the azimuths measured. In order to bring the measured current

directions into their original positions, corrections were made first for the plunge and then for the dip. From dip readings the plunge was estimated at  $18^{\circ}$  to  $032^{\circ}$ .

Ramsay (1961, Fig 2) has shown that there is no need to correct linear structures of low dipping strata such as bedding plane lineation is altered less than  $3^{\circ}$  in beds tilted up to  $25^{\circ}$ . More than nineteen hundred readings were measured and corrected because the dip of strata is generally more than  $25^{\circ}$ .

#### 4.2.1 Cycle L#

##### 4.2.1a Ripple bedding Unit (L3\*)

This unit is characterized by wave ripple marks on the upper surface of each bed. Small scale cross-lamination in the entire unit was observed, formed by migrating ripples marks. These ripples are characterized as follows.

Types: slightly asymmetrical, (Fig 4.1)

Wave length: 3 cm - 5.33 cm

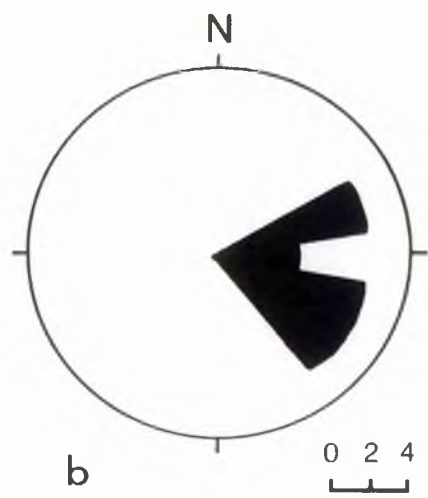
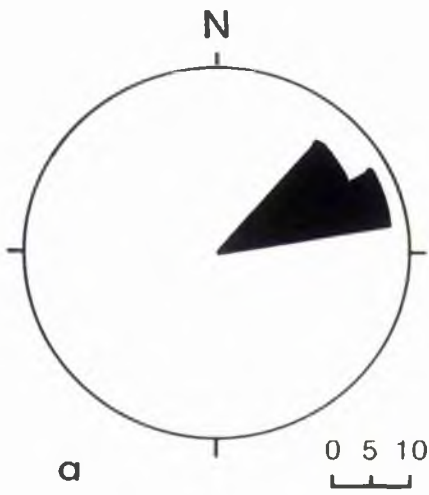
Amplitude: 0.2 cm - 1.1 cm

$$R.I: \quad = \frac{4.17}{0.65} = 6.4$$

The rippled sand is overlain by beds with marine fauna at the base through interbedded of siltstone with silty shale, and above it is succeeded by seat-earth. The main directional structures include wave ripples and cross-lamination (Fig 4.2). Ripple direction

Fig 4.1 Photograph showing different orientation of ripple marks. The divergence is nearly about  $60^{\circ}$ . Unit (L3) - West side of St Monance syncline. Pen is 14.5 cm in length.

Fig 4.2 Rose diagrams showing the palaeocurrent direction of unit (L3) - West side, (a) showing the palaeocurrent direction of the entire foresets structure, while (b) shows the ripple and the divergence in direction.



reflects two modes, one running towards ESE with lesser mode at ENE (Fig 4.2b). The foreset current direction towards ENE (Fig 4.2a). Collectively, the palaeocurrent direction was mainly from the south west with occasional swing to the north west. Such a variation in direction is not unusual with ripples.

The unit as a whole is interpreted as having formed in a minor mouth bar (see Chapter 2).

#### 4.2.2 Cycle B\*

##### 4.2.2a Ripple and trough cross-stratification Unit (B7B\*)

In this unit, asymmetrical wave ripples occur. (wavelength 5.5 cm; height 0.8-1.4 cm; ripple index 3.93-6.9; Fig. 4.3), with wave cross-lamination (Fig. 4.4). They are overlain by sandstone with medium to large-scale trough cross-lamination (Fig 4.5).

Currents forming the ripples were predominantly from  $110^{\circ}$ . Individual cross-sets (Fig 4.6) show current mainly from the south-west with occasional swings to the north-west and the south. Since the sets are probably the results of migrating linguoid dunes such a variation in direction might be expected. A histogram of the attitude of the foreset laminae (Fig 4.7) shows a mode at  $25^{\circ}$  with some higher readings suggesting some deformation in some sets.

The unit as a whole is interpreted as having formed in a channel (See Chapter 2, p 20).

#### 4.2.3 CYCLE T

##### 4.2.3a Units T2 and T3

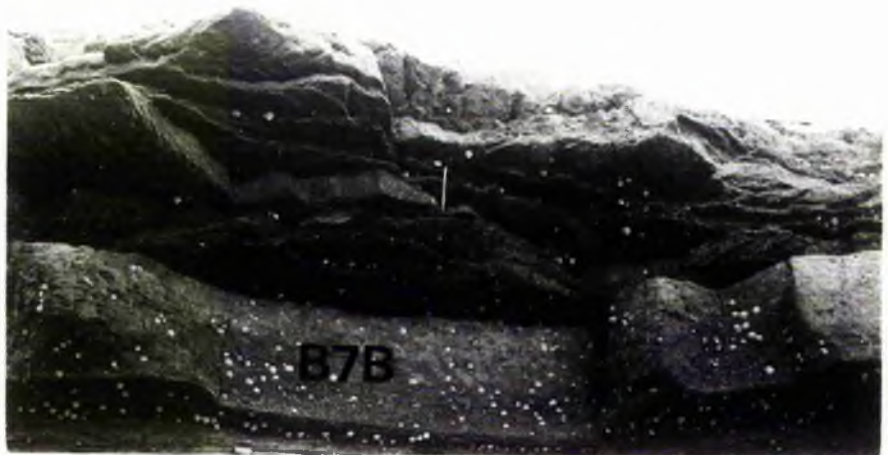
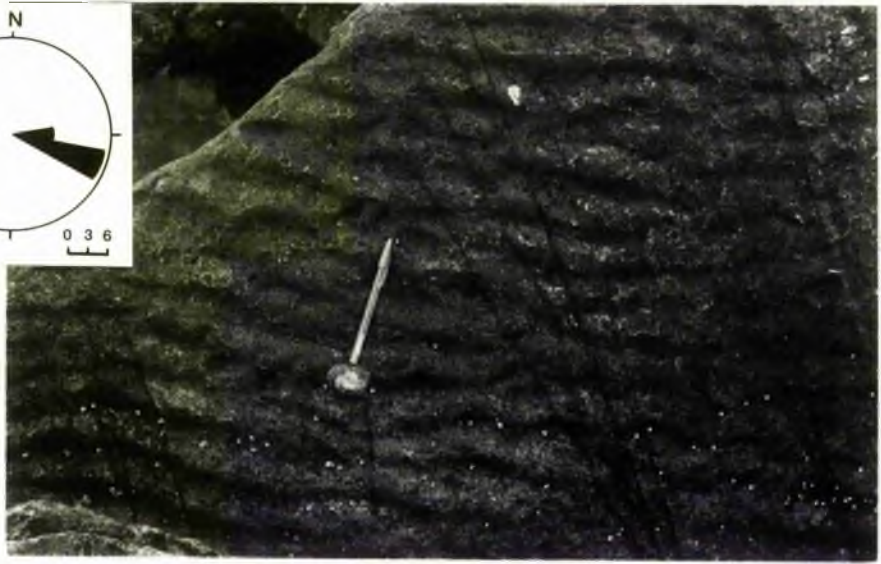
The facies of these two units consists mainly of interbedded

Fig 4.3 Photograph showing the orientation of ripple marks. Rose diagram showing the palaeocurrent direction towards the south east. Unit (B7B) - West side of St Monance syncline. Pen is 15 cm in length.

Fig 4.4 Slab cut parallel to the strike showing the entire sedimentary structure of unit (B7B). West side of St Monance syncline.

Fig 4.5 Photograph showing the predominant trough cross-bedding above unit (B7B). West side of St Monance syncline. Pen is 15 cm in length.





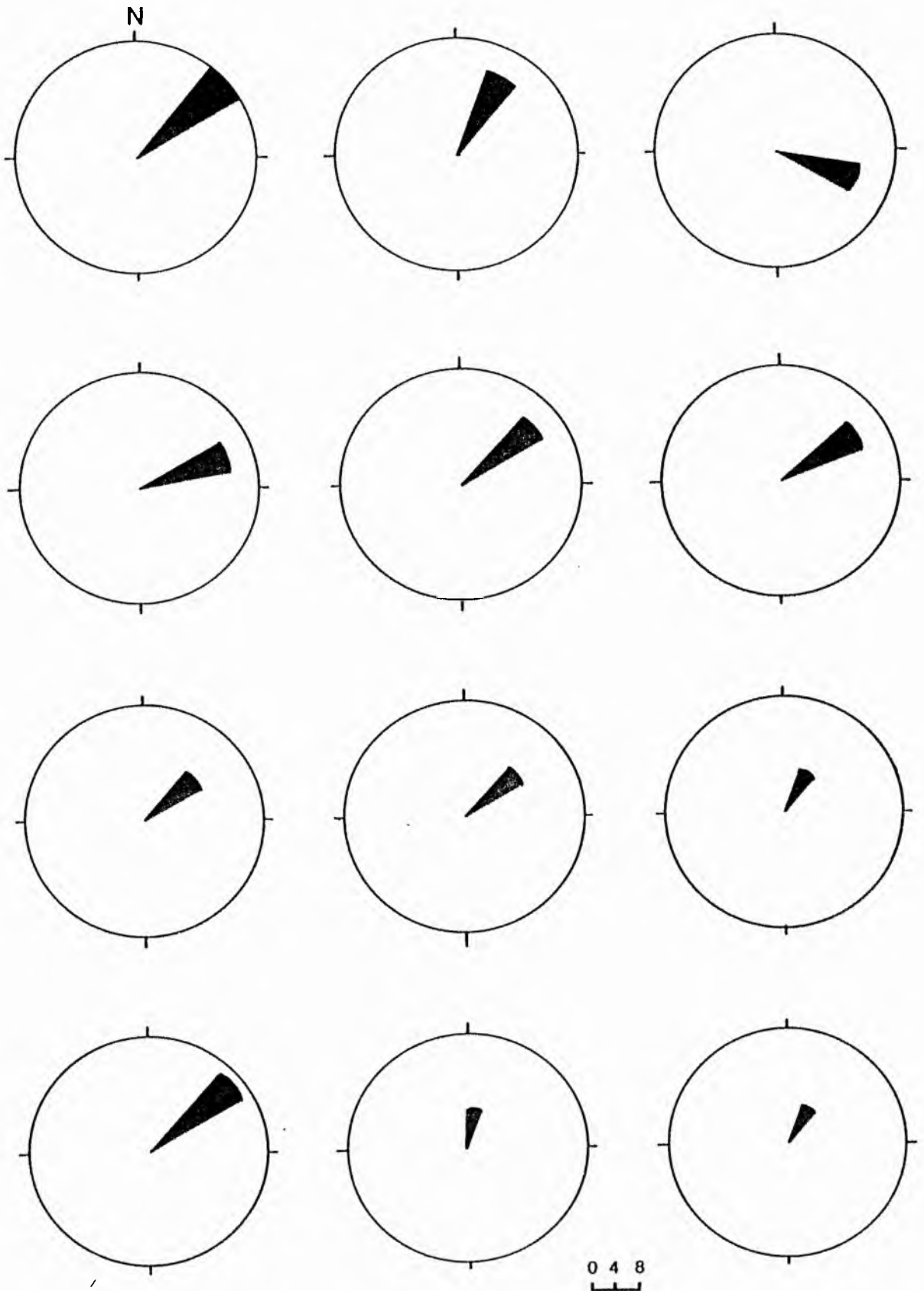


Fig 4.6. Palaeocurrent patterns of individual cross-beds showing the slight variation from one bed to another. Unit (B7). West side of St Monance syncline.

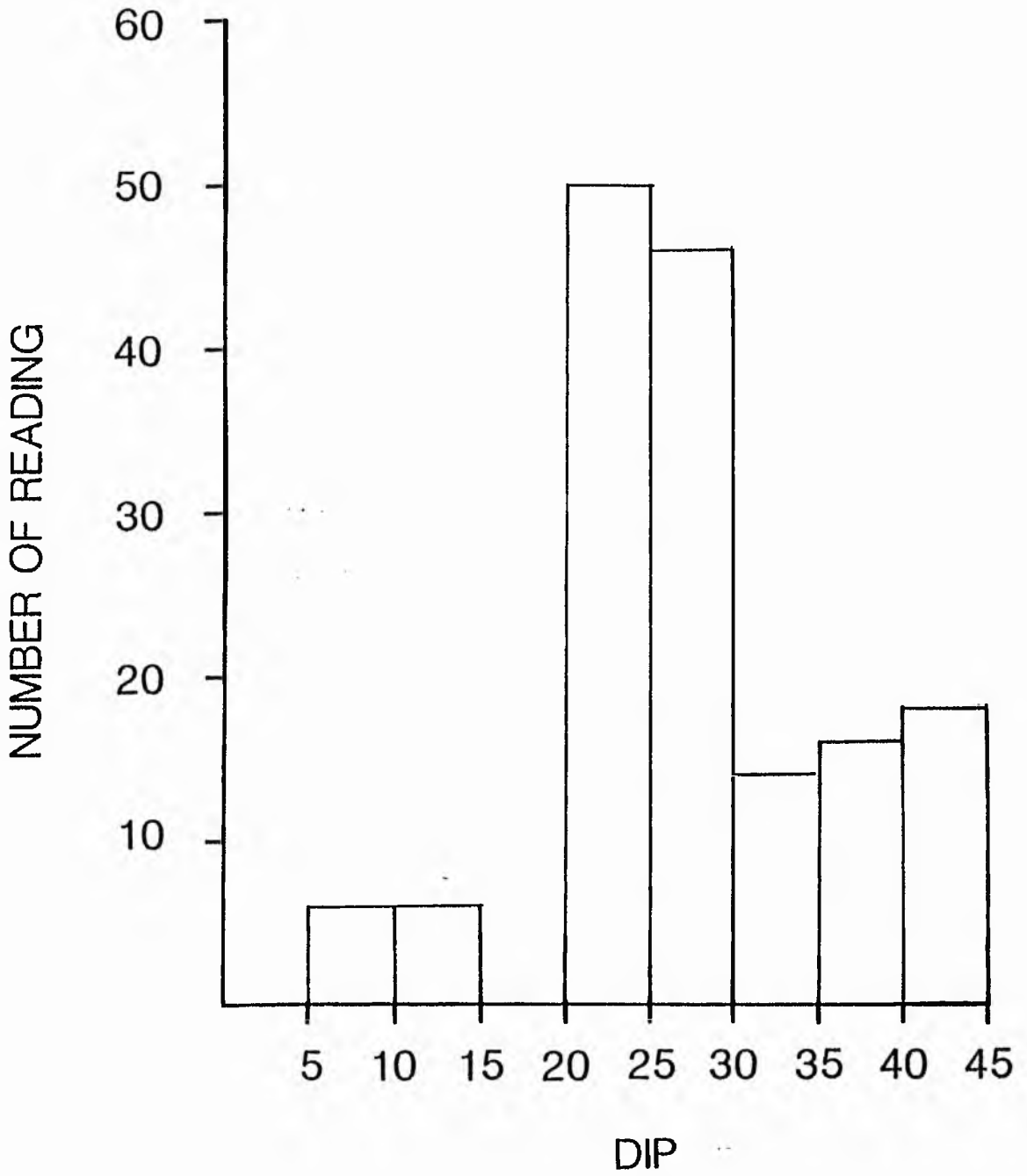


Fig 4.7. Histogram of cross bed dips of trough cross beds unit after correction.

fine-grained sandstone and green siltstone or silty shale. Sandstone beds become more abundant upward through the sequence. Siltstone and silty shale are generally thinner upward above a non-erosional base with marine shale at the base. Trace fossils are found in the sandstone mostly in the lower surface (see Chapter 3). The coarsening-upward sequence is interpreted (see Chapter 2 p 28 ) as having formed as a minor mouth-bar.

The main sedimentary structure throughout the facies are ripples (symmetrical and asymmetrical), lenticular, wavy, and flaser bedding, parallel lamination and cross-lamination, which increase in abundance as the sandcontent increases (Fig 4.8). The lower part of this sequence is characterized by mm-cm thick silty and sandy intercalations in mud which are predominantly parallel laminated. They increase upward to form local swellings with weak cross-lamination which gives an undulatory form. It is suggested a postdepositional reworking took place of the sandy streaks by wave action. As the silt and sand particles settled down from suspension wave oscillations could reach the bed thus modifying the lamination into a weak cross-lamination (see de Raaf et al, 1977).

Above as the sand content increases, lenticular, wavy and flaser bedding increase (Fig 4.9). The lenticular beds are composed mainly of symmetrical ripples. The internal structure is mostly unidirectional but there are some opposed cross-laminae, wave generated. Raaf et al, (1977) mentioned that wave ripples often have more or less symmetrical outlines, continuous, parallel crests, although the outward form may be discordant with the internal structure. The facies were generated under condition of wave flow which gradually increased in energy upward.

Fig 4.8 Photograph showing the parallel lamination in (a) and grading upwards into sandstone and siltstone, silty shale. Wavy bedding, lenticular bedding are seen together with wave ripples and bipolar foresets (arrow). Unit (T2) - East side.

Fig 4.9 Photograph showing the sandcontent increasing upwards (a) represents a predominant silty shale, (b) increase of sandcontent, (c) predominant sandstone. Coin is 2.5 cm in diameter. Unit (T2) - East side.



Unit T2 contains abundant pencil-shaped plant fragments which show strong orientation. 773 plant fragment orientations were taken from 6 orientated sandstone slabs, collected from different beds (Fig 4.10). The samples on which the plant fragments are found mostly are cross-laminated. Analysis of cross-lamination in the ripples and ripple crests suggests a current movement predominantly from the east (Fig 4.11). The plant fragments show some spread in orientation but tend to lie at right angles to the predominant current.

#### 4.2.4 CYCLE F

##### 4.2.4a Units F1-F4

The vertical sequence of these units is characterized by coarsening-upwards, while nodules are found throughout as well as different types of trace fossils (see Chapter 3).

The lowest beds are of shale, silt and fine-grained sand in parallel laminae (Fig 4.12). The lower contact of silt or sand with shale is usually sharp whereas above it tends to be gradational. In these, lowest energy lithotypes deposition was from suspension with variation in supply causing sharp lower contacts and grading above.

Beds above show increasing current activity, in the greater abundance of sandstone and the development of ripples with micro-cross-lamination. The rich development of structures is interpreted as the effect of wave movements producing ripples, continued sedimentation and the superimposition of sets above one another (Figs 4.13, 4.14, 4.15, 4.16, 4.17 and 4.18). The variety of features characteristic of wave ripples (de Raaf et al., 1977) can be seen in these units eg.

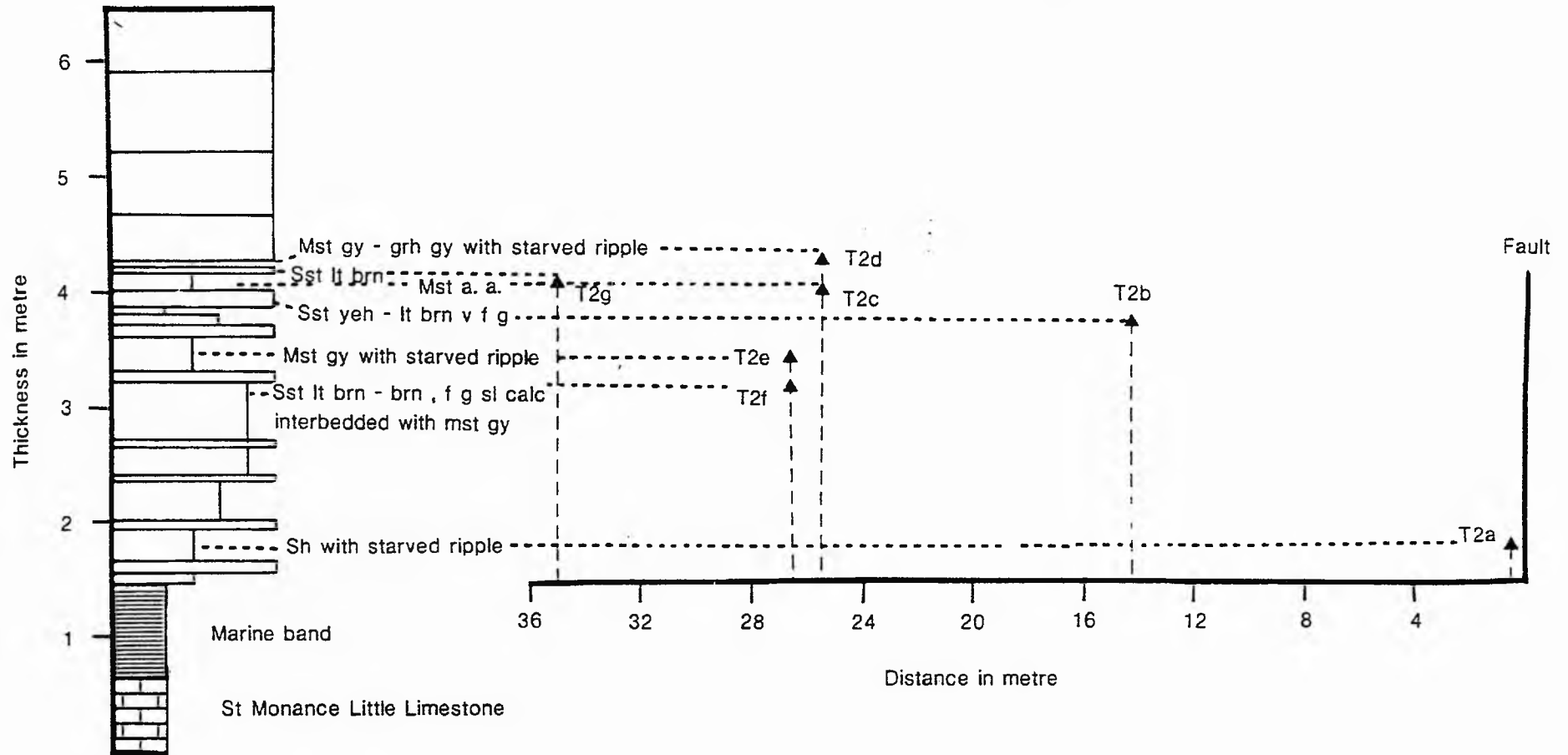


Fig 4.10. Sketch showing the location of plant fragment samples.



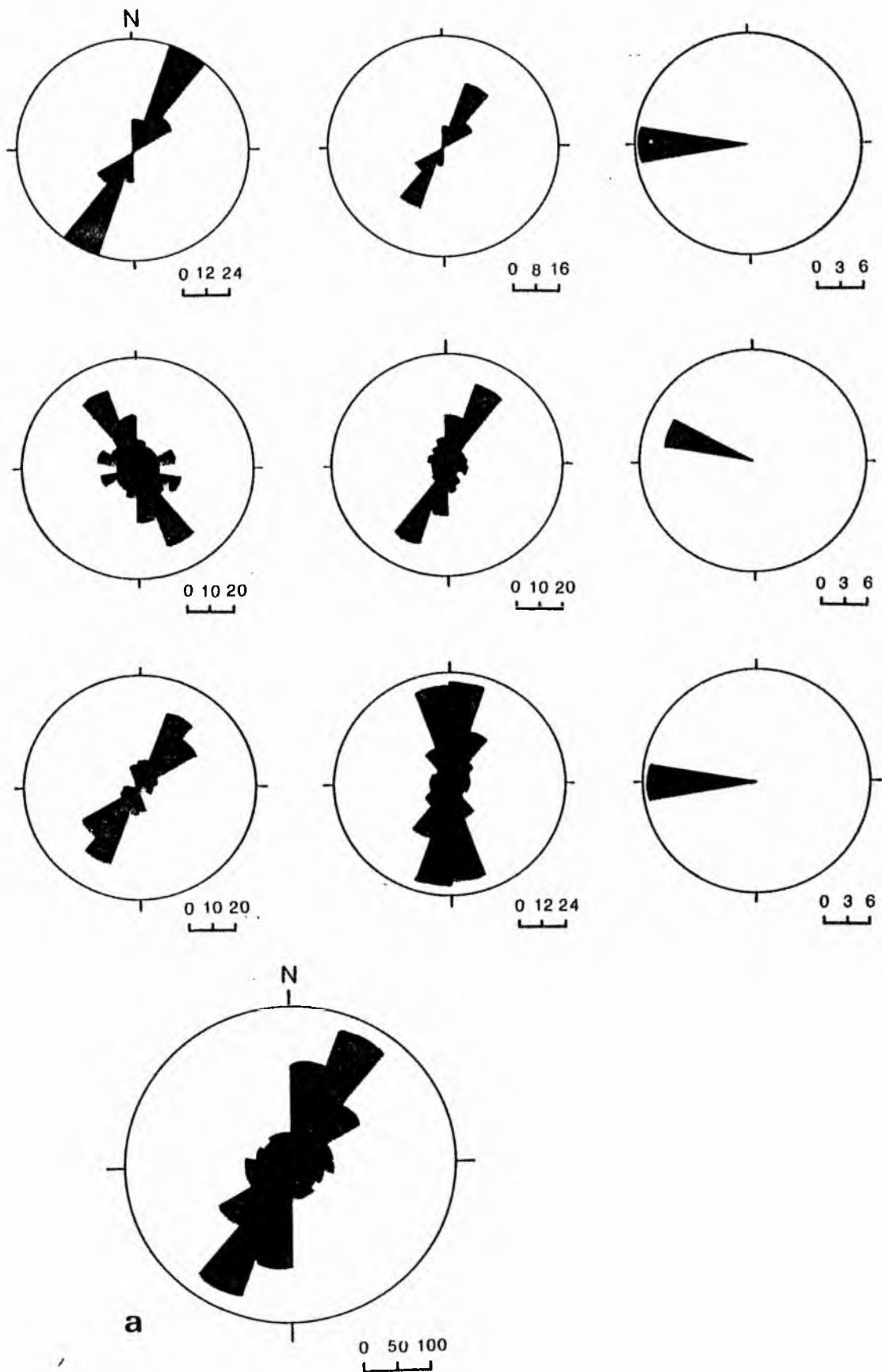


Fig 4.11. Rose diagrams showing the orientation of plant fragments and the palaeocurrent direction of cross-lamination. Note: (a) total reading of plant fragments only.

Fig 4.12 Slab cut parallel to the strike, showing parallel lamination of siltstone and silty shale with mudstone, their lower boundary is usually sharp, whereas above it tends to gradational. Unit (F2) - East side.

Fig 4.13 Slab cut perpendicular to the strike, showing the association of large ripple form sets (at A), gradually change into parallel lamination with low angle of inclination (at B), containing set of cross lamination (arrow), then into small form sets (at C). Rose diagram showing the different directions of both units (A, C) as trough cross-lamination, from Unit B as low angle cross-lamination. Unit (F3) - East Side.

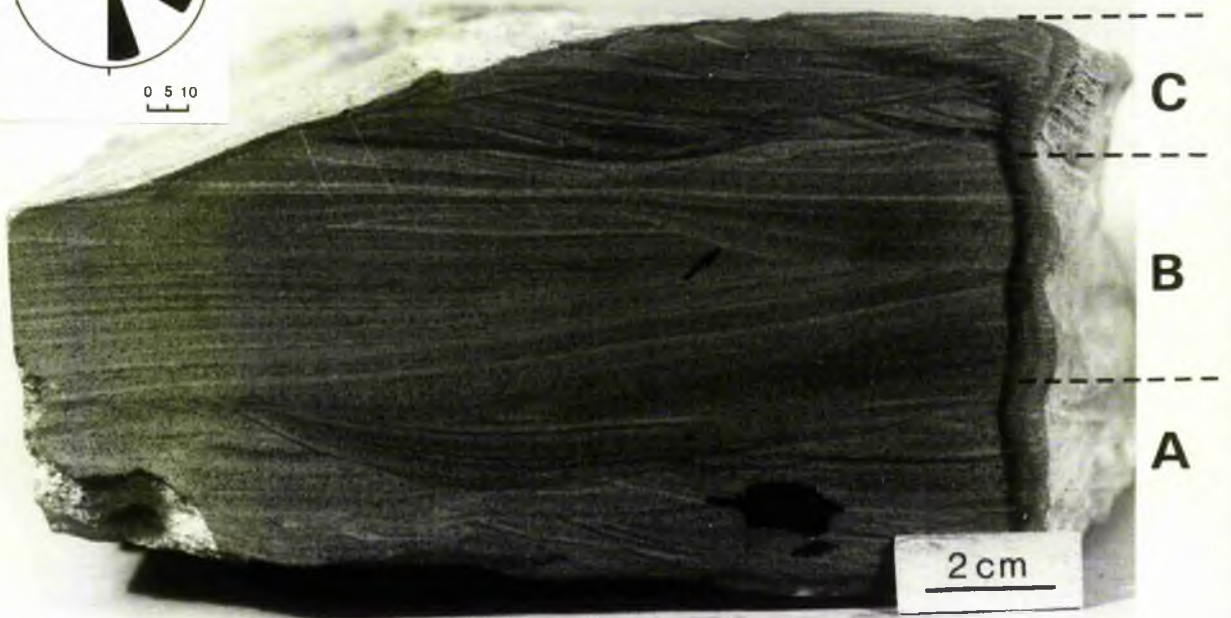
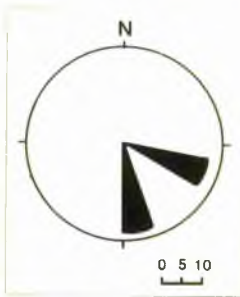


Fig 4.14 Rich array of cross-lamination in sandstone. Most of the individual sets are rather short and swollen with curved boundaries conforming to the external shape. The direction of cross-lamination frequently reverses NNW and SSE.  
Unit (F3) - East side.

Fig 4.15 Slab cut parallel to the strike, showing bidirectional cross-lamination typical of wave ripples. Unit (F3) - East side.

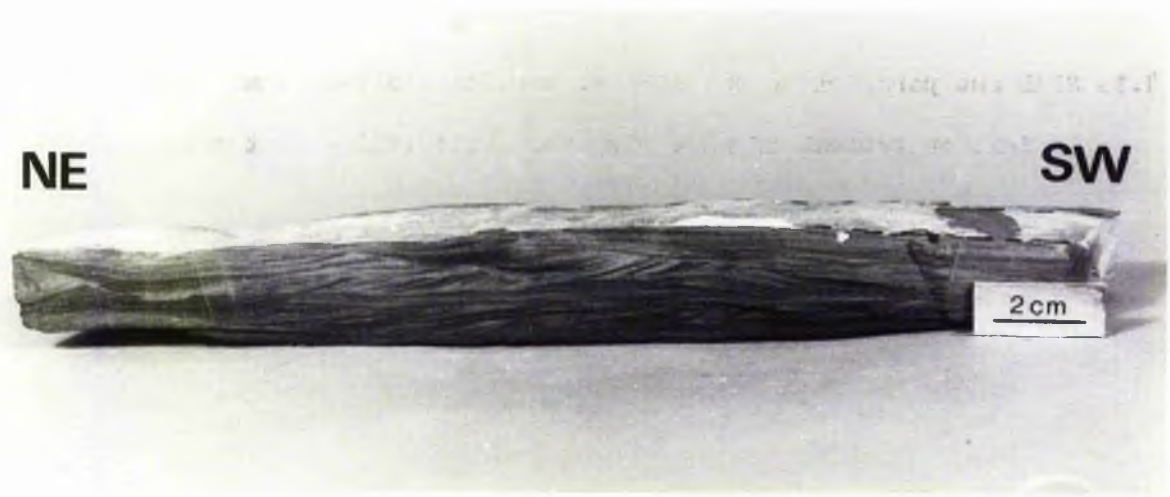
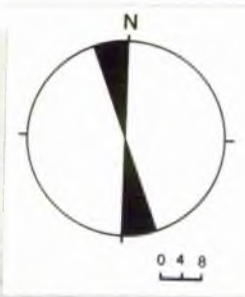


Fig 4.16 Slab out parallel to the strike showing different shape of bidirectional cross-lamination, while the set boundaries are curved and diffuse. Bidirectional cross-lamination and different size, they seem to be complex, and the complexity increases with shortening of the wave. Where they become longer, the cross-lamination merges into horizontal lamination (right side of the photograph). Wave direction predominate towards NNE and local variation towards SSW. Unit (F3) - East side.

Fig 4.17 Slab out perpendicular to the strike showing vertical change into bidirectional cross-lamination with sign of bioturbation. Unit (F3) - East side.



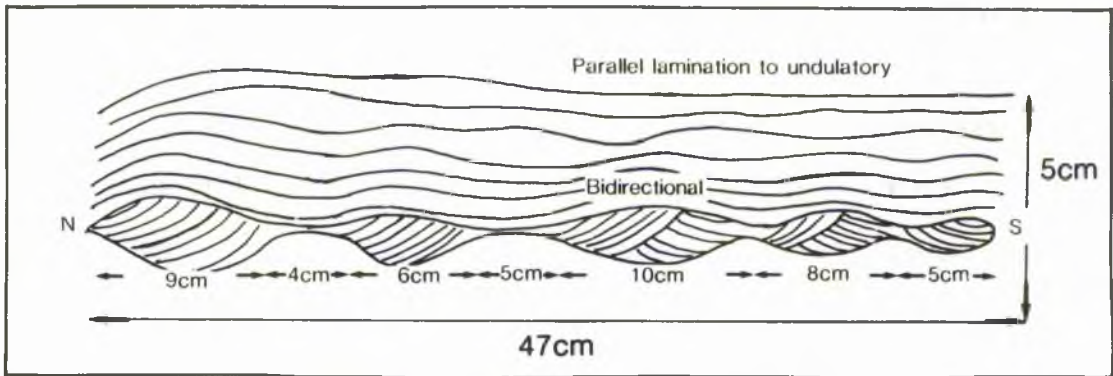
SE

NW



Fig 4.18A Photograph showing lenticular and sometimes streaks of sandstones, in the highest lithotype of unit (F3) - East side. Coin is 2.0 cm in diameter. Sketch of sedimentary structure associated with this lithotype are present (Fig 2.18B).





- 1 Bi-directional cross-lamination.
- 2 Swollen ripples, convex down as well as up.
- 3 Internal and external structure not always concordant.
- 4 Erosional sets on curved and undulating surfaces.
- 5 Ripples indices (height/length) generally less than 10.

The uppermost part of this sequence is made up of sandstone beds with lenticular beds and ripples. This top of the coarsening-upwards sequence is separated from the channel sandstone above by a number of sandstone beds (F4), sometimes only a set of starved ripples but increasing in thickness upwards to beds of 10-30 cm. These are unique in the sequence in having sole markings on the base (Fig 4.19) and linguoid ripples on top surfaces (Fig 4.20).

Trends of ripple crests are variable but are mostly NNE-SSW with foresets dipping in both directions at right-angles to this. Swings in wave movement took place from northerly to around almost eastward, a variation which might be expected controlled as it would be by variable wind directions and basin geometry.

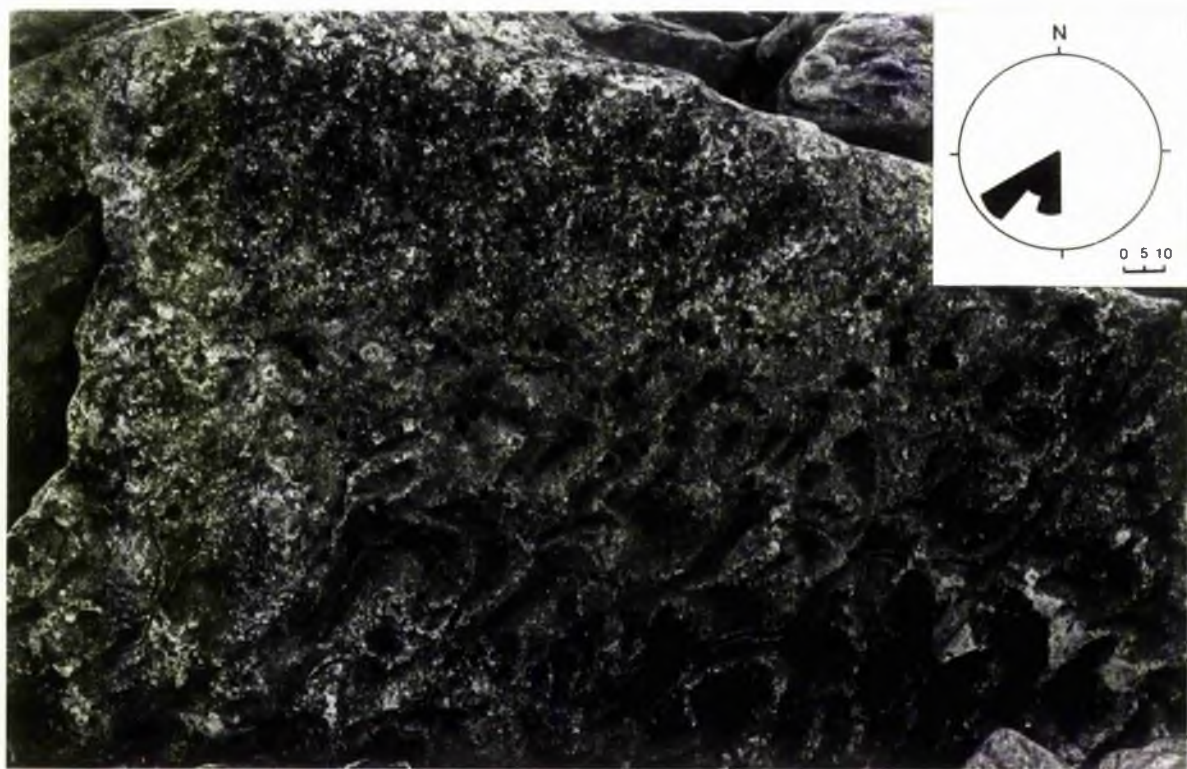
By contrast the linguoid ripples, produced by crevassing show distinct current movement towards the south-west.

#### 4.2.4b Unit F5

This part 2, the sequence most commonly consists of a lower medium-to coarse-grained and thick-bedded facies that is gradationally or abruptly overlain by finer grained and thinner bedded facies deposited either during or shortly after channel abandonment. Most of the channel lenses sequence display a distinct fining - and

Fig 4.19 Photograph showing the flute cast and their orientation as arrow direction. Unit (F4) - East side. Pen is 15 cm in length.

Fig 4.20 Photograph showing the linguoid-rippled sandstone surface and the trace-fossil, and palaeocurrent direction of 52 field measurements is towards the SW. Unit (F4) - East side.



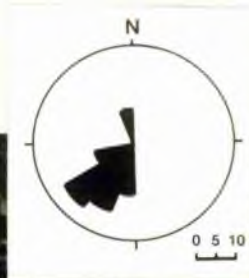
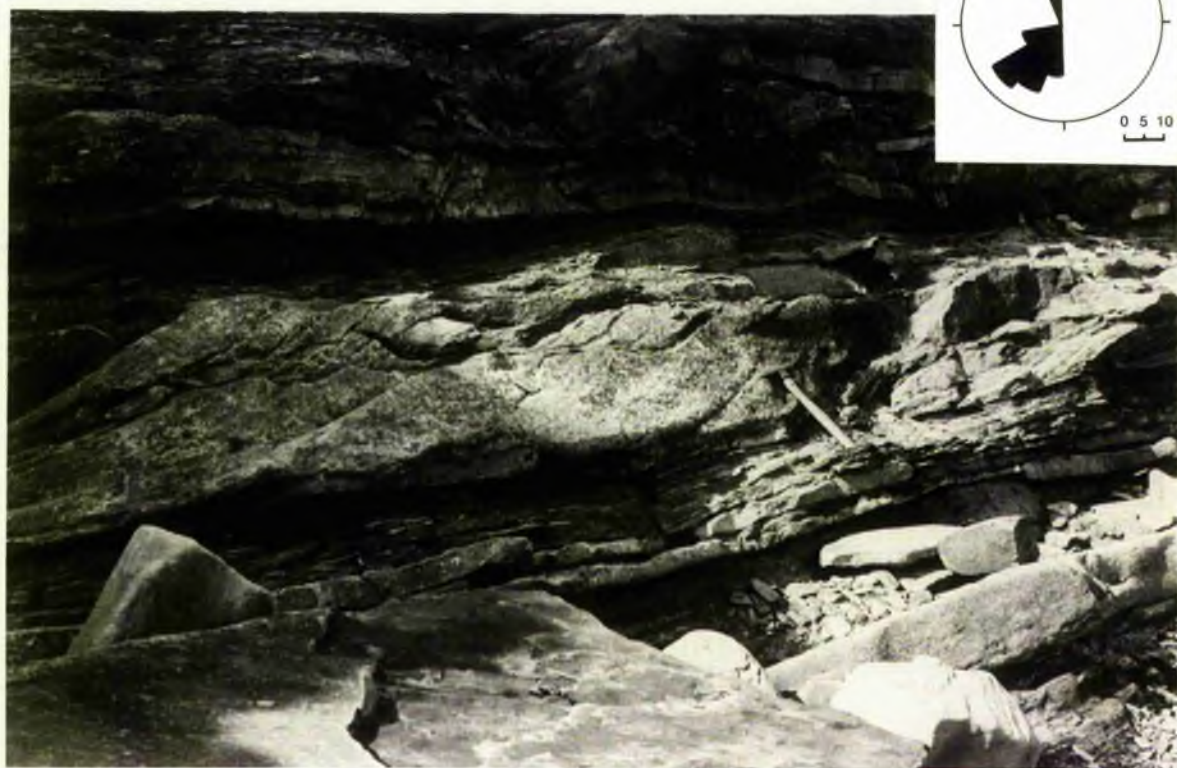
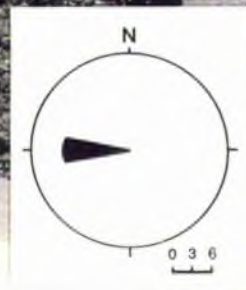
thinning-upward character.

This part of the succession is divided into many members, as it is composed of a group of cross-stratified sandstones and beds with other sedimentary features. A large number of primary sedimentary structures of varied scale and geometry are recognized.

The main sedimentary structure in the first members begins at the basal part of the outcrop and has large scale cross-stratification with thickness more than 1 metre. This Pi-cross-stratification (Allen, 1963b), have sharp boundaries with palaeocurrent direction towards the west (Fig 4.21). Laterally and vertically thin bedded sandstones show lenticular bedding and wavy bedding. Inside thinly bedded sandstone, ripple drift-lamination is observed and characterized by the presence of clay or mica. Individual laminae of ripples often continue from one ripple to the other and can occasionally be traced for over 30 cm. This type of lamination is variously termed a ripple drift-lamination by Walker (1963); climbing ripple by Coleman et al (1964); or steeply climbing small scale stratification sets by Allen (1968). It is formed by rapid net sedimentation accompanying rippling in a sandy bed-load (Allen, 1968). The medium scale trough cross-stratification varies in thickness between 37-60 cm. Each trough set consists of an elongate erosional scour infilled with laminae (Fig 4.22). The infilling laminae of the trough sets have dips that average  $28^{\circ}$  and range from  $12^{\circ}$  to  $35^{\circ}$ . The palaeocurrent directions are towards SW with local variation (Fig 4.22). Scour-and-fill structures (Shrock, 1948) up to 47.5 cm thick and 1.6 m width are present, most being filled with cross-lamination, but thinly laminated sand also occurs. The curved infilling laminae are in most cases symmetrical. Asymmetrical

Fig 4.21 Photograph showing the first unit of the first member (F5a) and the erosional contact with the lower facies (arrow). Also showing the lateral and vertical variation as generally thin towards the east side, lenticular and wavy bedding is also present. Palaeocurrent direction towards the West. Hammer is 35 cm long.

Fig 4.22 Photograph showing the medium scale trough cross-bedding in the first member of different dip. Palaeocurrent direction predominantly towards south west. Hammer is 35 cm long.



infilling is also observed (Fig 4.23A). They are filled with different type of sediment (high carbonate cement content) into which they have been cut, and most of them contain a complex internal structure of sets composed of numerous thin sets (Fig 4.23B), suggesting that cutting and subsequent infilling were independent events and are the result from the channel sinous by powerful current that flows out of the main channel. Scours are elongated parallel to the flow direction and plunge in a down current direction. The palaeocurrent direction from the analysis of internal structures which are predominant as small-scale trough-stratification, micro-trough and micro cross-lamination is towards SW (Fig 4.23C).

The second member (up to 70 cm thick) starts with an erosional surface and clasts. The main sedimentary structure is primary current lineation on the bedding planes of the sandstone (Fig 4.24), which are mostly flat-bedded low-angle sandstone sets. Primary current lineations can be formed by wave action on beach that borders either a river or the sea (Allen, 1964, p 101). Allen (1964, p 107) pointed out the combination of lineation and lamination of the Lower Old Red Sandstone, and he suggested that this could represent a submerged channel. Rippled bedded sandstone with cross-lamination follows (Fig 4.26), composed of climbing sets of lee side laminae, with complete preservation of stoss side laminae. Laminae are not continuous from one ripple to the next. Fine sand is restricted to the stoss side and crest, and grades laterally within individual laminae into clay material in the ripple troughs. Laterally, this member contains parallel troughs separated by cusp-like ridge (Fig 4.25). This pattern is due to migrating linguoid ripples. The palaeocurrent direction from field measurements is towards SW (Fig 4.25). Above



Fig 4.23 Slabs within scour and fill unit in the first member (F5a) showing their ripple set. Palaeocurrent direction generally towards SW (C).

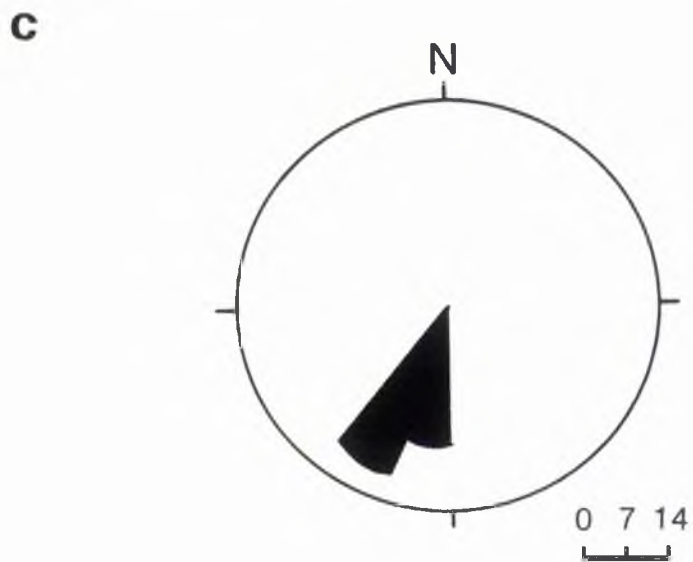
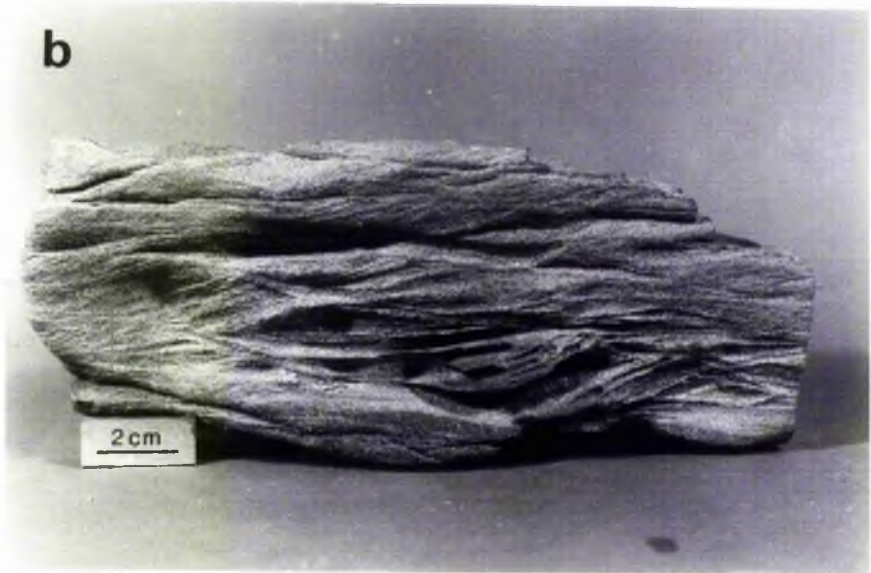
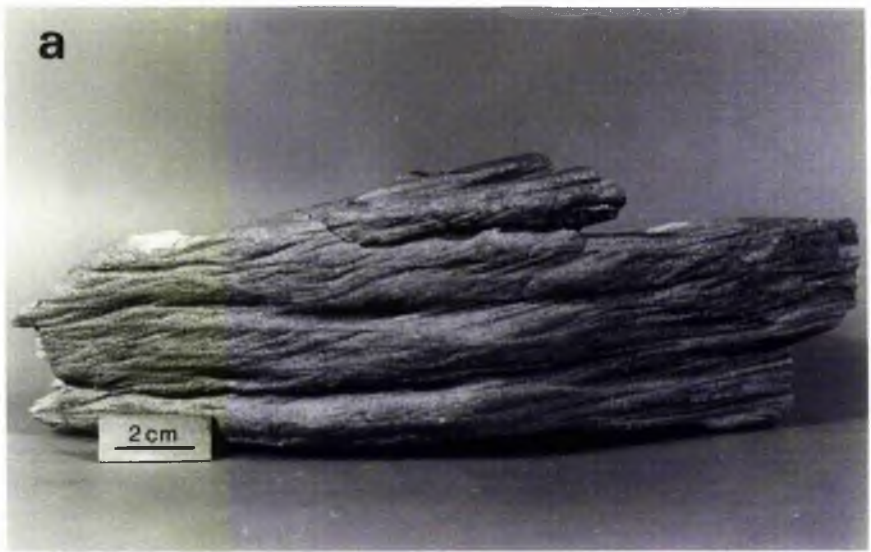
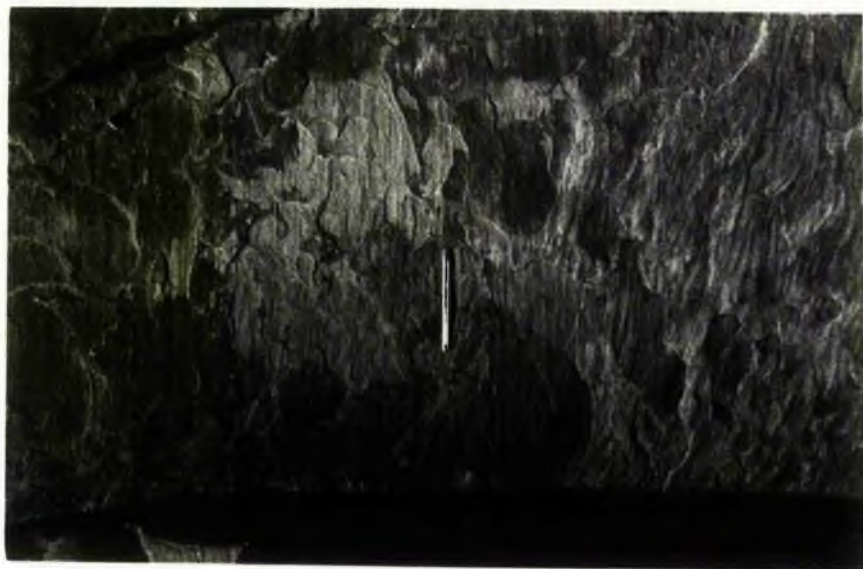


Fig 4.24 Photograph showing laminated sandstone with primary current lineation in the second member (F5b). Pen is 14 cm long.

Fig 4.25 Photograph showing parallel trough cross-lamination separated by cusp-like ridge. Deformed laminae also present (arrow). Palaeocurrent direction is towards south west. Also showing above the horizontal interbedded small scale linguoid rippled sandstone and siltstone or silty shale containing starved ripples. Hammer is 35 cm long.

Fig 4.26 Slab from the second member (F5b) of rippled sandstone as composed of climbing sets of lee side laminae. Laminae are not continuous. Clay material is present in the ripple troughs, palaeocurrent direction from left to right.



comes a linguoid rippled sandstone and siltstone or silty shale containing starved ripple. The thickness of each bed is up to 12 cm. Small scale cross-stratification and, scours filled with trough cross-lamination, up to 18 cm thick are also present.

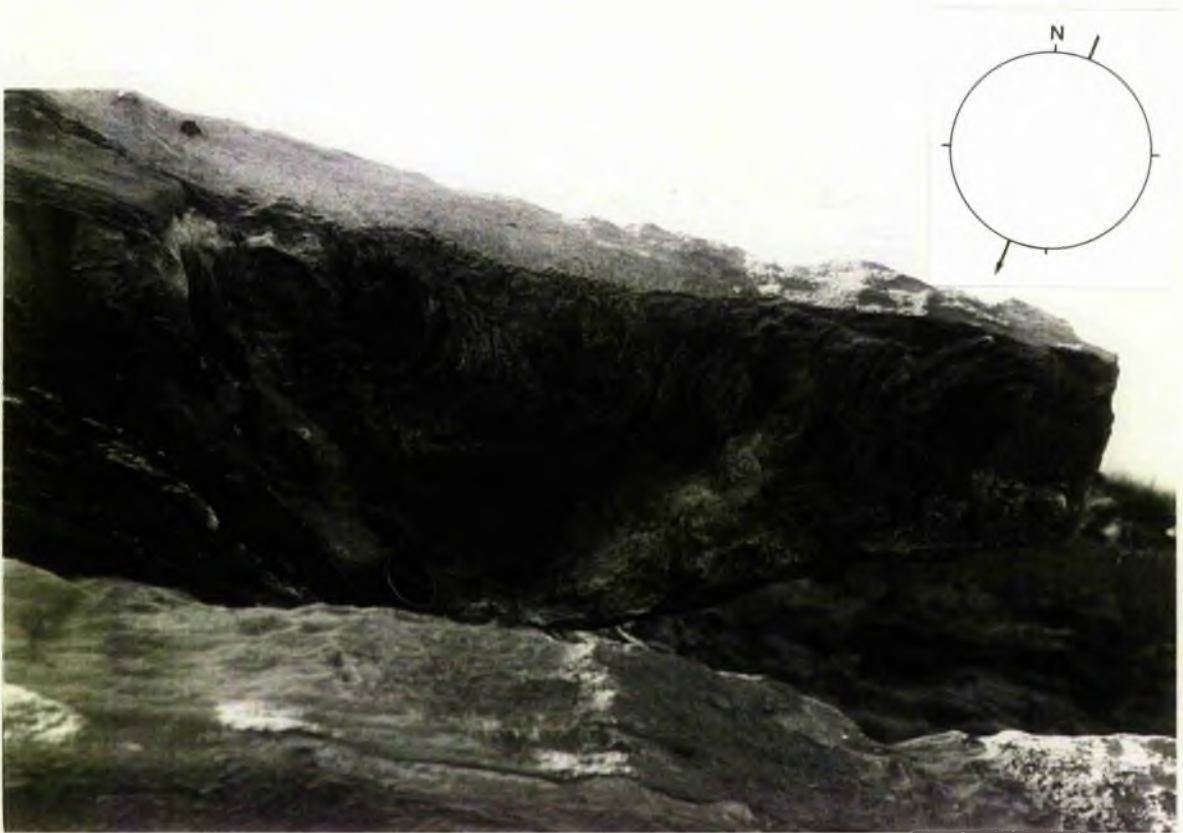
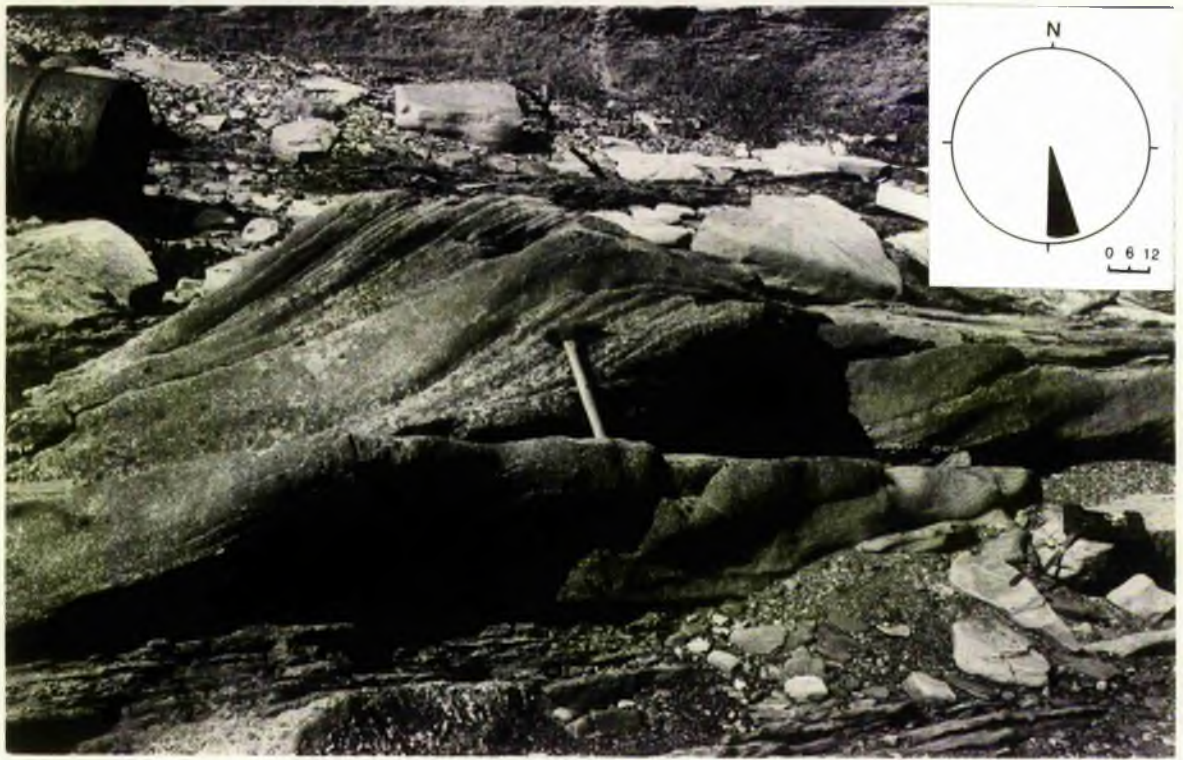
The third member has an erosional base and large-scale trough cross-stratification, and is the thickest bed in the lower part of this member (Fig 4.27). The filling laminae of the trough sets have dips that average  $42^{\circ}$  and range from  $37^{\circ}$  to  $48^{\circ}$ . The palaeocurrent direction from the field measurement is toward the SSE (Fig 4.27). It is covered by linguoid ripple beds and contains rib-and-furrow in the lower surface directed  $200^{\circ}$  towards SW (Fig 4.28). The internal structures are micro-cross-lamination and small scale trough cross-lamination. Palaeocurrent direction of the linguoid ripples is towards SSE (Fig 4.29).

The upper most part is formed of interbedded very fine-grained rippled sandstone and silty shale or siltstone. The thickness of each bed is up to 10 cm. The palaeocurrent direction of micro trough cross-lamination is towards SSW (Fig 4.30).

Although many different beds are present in this unit representing variable conditions there is an essential unity indicated by the predominant palaeocurrent direction towards the SW. In brief the sequence is interpreted as the distal portion of a crevasse channel affected by a number of different flow conditions (see Chapter 2).

Fig 4.27 Photograph showing the first unit of the third member (F5c) as formed of large scale trough cross-stratification with erosional base. Troughs are mostly asymmetrical and plunging in a down-current direction. Palaeocurrent direction from the field measurement are towards SSE. Hammer is 35 cm in long.

Fig 4.28 Photograph showing the rib-and-furrow in the lower surface of linguoid ripples, their palaeocurrent direction is  $200^{\circ}$  towards SW. Camera lens hood is 5 cm in diameter.



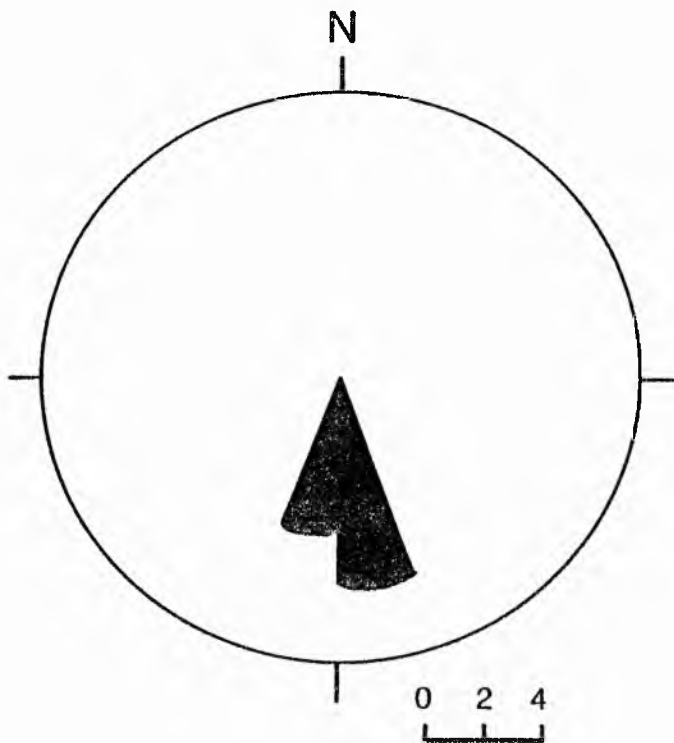


Fig 4.29 Rose diagram of linguoid ripples in third member (F5c), showing the palaeocurrent direction as towards  $170^{\circ}$ .

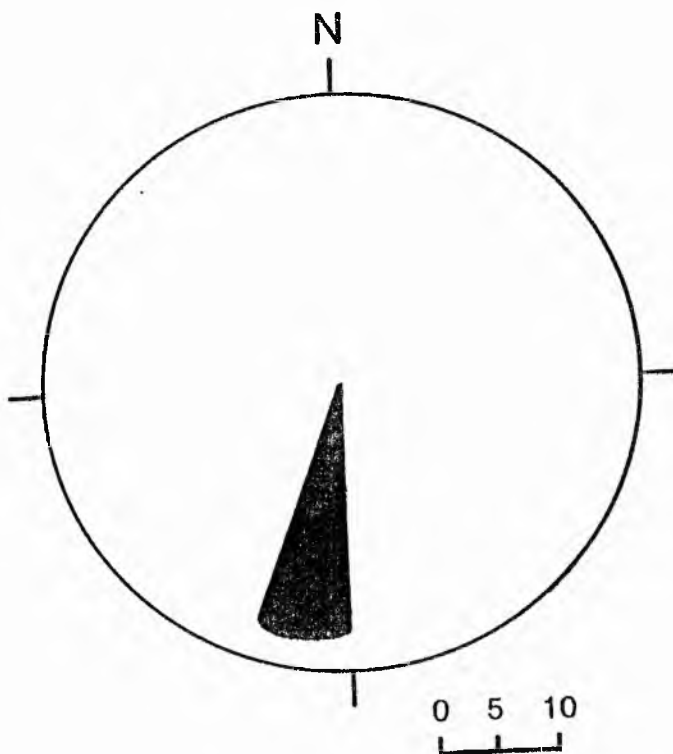


Fig 4.30 Rose diagram of the last unit of the third member showing the palaeocurrent direction of the internal structure as towards  $190^{\circ}$ .



#### 4.2.5 CYCLE S

##### 4.2.5a Units S2 and S3

This unit of shallow marine sandstone is characterized of storm layers with hummocky cross-stratification and non-storm layers. The lower part consists of strongly bioturbated calcareous sandstone with carbonaceous nodules and fully marine strata. Goniatite fragments have been noted, and different types of trace fossils were found (see Chapter 3). Hummocky cross-stratification (HCS) occurs above and is overlain by planar-stratification with local trough cross-stratification (Unit S3a).

##### Hummocky cross-stratification sandstone

The base of this sandstone is a well-defined erosional surface (Fig 4.31). The upper contact, in contrast, is nearly horizontal and may be either sharp or gradational into the overlying sandstone Unit S3. The hummocky cross-stratified sandstone consists of well-sorted fine-grained sand, lamination ranges from well defined to fairly indistinct, picked out by alternations of light coloured, relatively well-sorted sand and darker sand containing a higher proportion of organic detritus and mica.

Internal erosional surfaces are common in the hummocky cross-stratified sandstone. Most can be traced laterally but they merge into sequences of parallel laminae. Also some cut entirely through a hummocky unit (Fig 4.32). The surfaces are rounded and tend to be broadly irregular cross-stratified sandstone. Lamination in the fill approximately conforms to the scoured surface, and many laminae

Fig 4.31 Hummocky cross-stratified sandstone overlying bioturbated sandstone, with broadly irregular erosional contact. On left side of chisel showing domal or the swaley cross-laminae. Arrow indicate an erosion surface cutting through the hummocky cross-stratification and merging into parallel laminae. Palaeocurrent direction from field measurement are towards NW. Unit (S2) - East Side of the St Monance syncline.

Fig 4.32 Scour surface (marked by arrows) within the hummocky cross-stratification. Note also the tendency of the cross-stratification to become progressively flatter upward. Unit (S2) - East side of the St Monance syncline. Camera lens hood is 5 cm in diameter.



can be traced from the scours onto and over adjacent hummocks and they trend to flatten progressively towards the top (Fig 4.31, 4.32).

The hummocky cross-stratification represents a variation from an ideal one in the presence of convex-upward laminae although this is not common (Fig 4.31). Hunter and Clifton (1982) described it as domal structure in the (HCS), while Leckie and Walker (1982) suggested that such stratification be called swaley cross-stratification. The palaeocurrent directions from the field measurements analysis appear to be towards NW (Fig 4.31).

In Unit S3a two types of cross-lamination are observed. Trough cross-lamination is found in fine-to-medium grained sandstone. palaeocurrent directions are predominantly towards the NW (Fig 4.33). The second type is planar cross-laminated sandstone (Fig 4.34). It consists of fine-grained, slightly finer than the trough cross-laminated sandstone, and it is defined by thin alterations of relatively well-sorted light-coloured sand and darker sand containing abundant mica flakes. Locally it is cut by burrows in different orientations, escape burrow as chevron structure are also represent (see Chapter 3, see also Chapter 2 for environmental interpretation).

#### 2.4.5b Units S12-S20

##### Description

Nine units here represent two coarsening-upwards (12-13 and 16-17), and two fining upward sequences with erosional base units (14-15 and 18-20) in between (Fig 4.35). The sequences consist of assemblages of sedimentary structures and palaeocurrent patterns. Each facies is the product of alternate phases of sedimentation during relatively high-and low energy periods.

Fig 4.33 Slab showing sharp contact between the trough cross-lamination and the horizontal (dotted line). The Rose diagram showing the palaeocurrent direction of the trough cross-lamination are towards the NW.

Fig 4.34 Slab showing the planar cross-lamination of fine-grained sandstone. Many of the laminae are graded from light-coloured sand to darker sand.

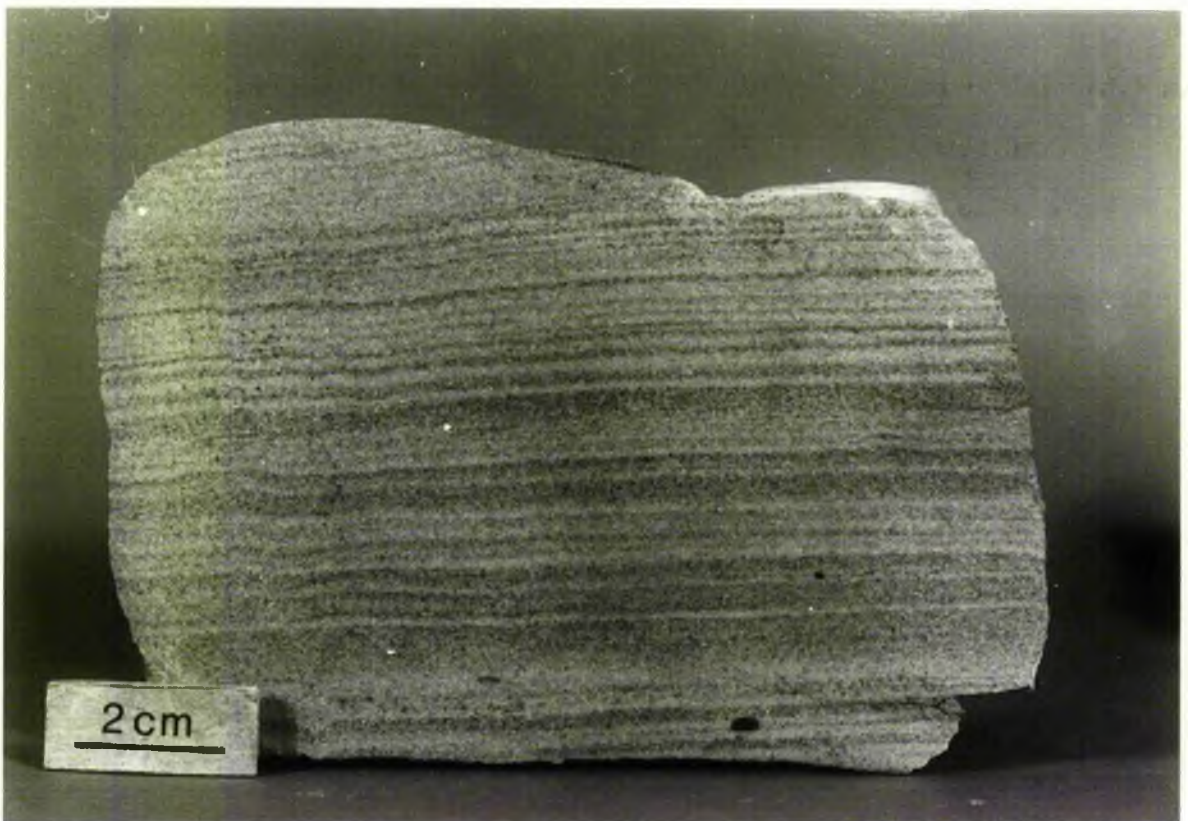
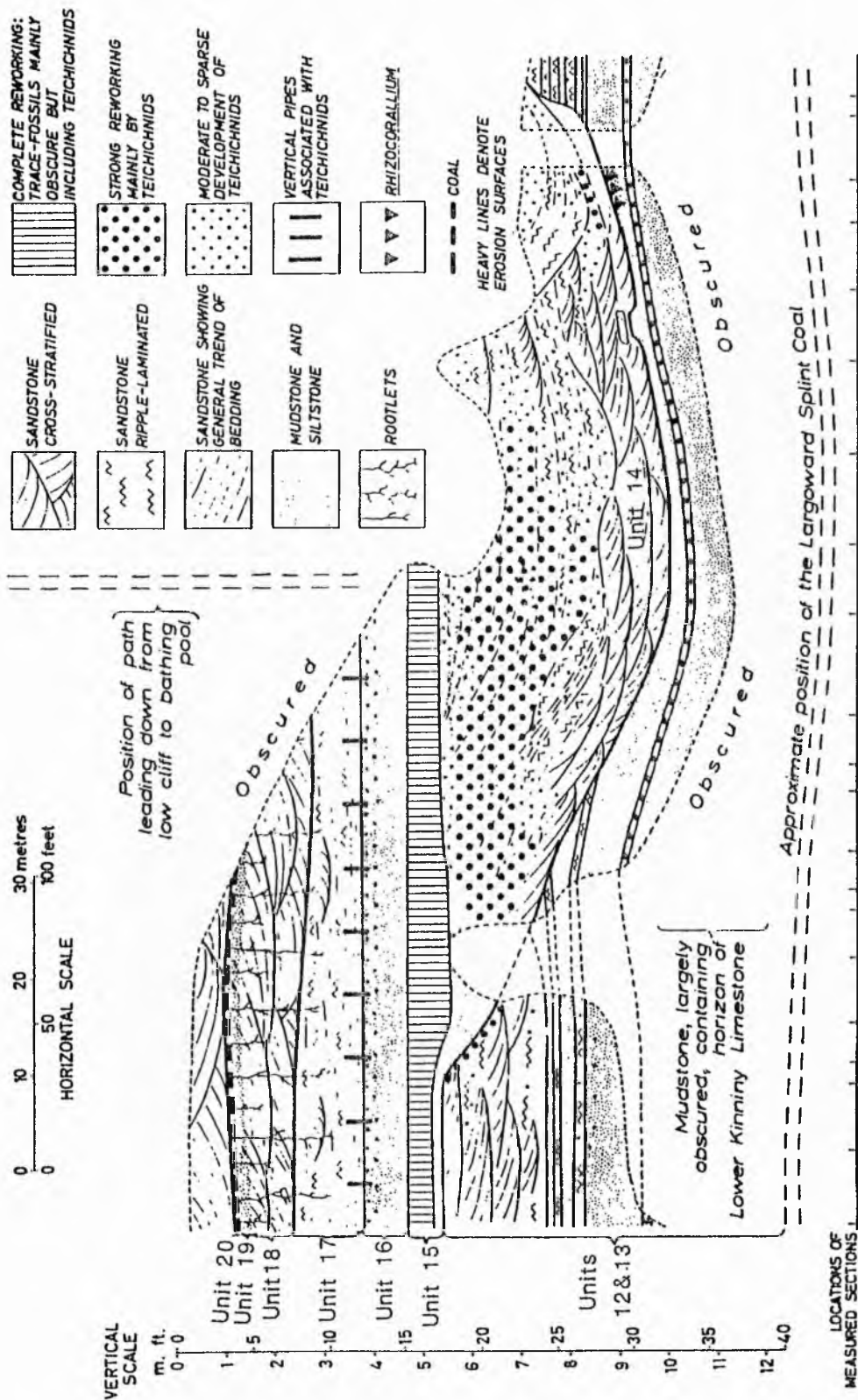


Fig 4.35 Scheme showing the vertical succession of Units (S12 to S20) and Teichichnus and related trace fossils. (after Chisholm, 1970)



Units S12-S13 consist of marine mudstone at the base, believed to lie at the horizon of the Lower Kinniny Limestone (Forsyth and Chisholm 1968). This grades upward into interbedded of siltstone-silty shale and sandstone beds, where the latter increasing in thickness upwards. The internal structure (Fig 4.36) shows wavy, flaser and trough cross lamination increasing in frequency upward. At the top of this sequence large scale trough cross-stratification is observed, formed of lenticular to wedge-shaped sets up to 22 cm thick and about 1.20 m wide. Palaeocurrent direction of the trough cross- stratification is generally towards the E (Fig 4.37).

Units S14-S15 These two units represent a fining upwards sequences. The base is sharp and erosional; lenticular sandstones are medium grained and trough cross-stratification is large scale; the cross-strata in each set are formed with an erosional base and they are homogeneous and classify as pl-cross-stratification (Allen, 1963b). The sequence passes upwards into finer grained ripple-laminated sandstones with small lenticular sets of cross-strata in places. The finer beds are extensively turbated by trace-fossils (see Chapter 3). The palaeocurrent direction of large scale trough-cross-stratification is towards the ESE (Fig 4.38).

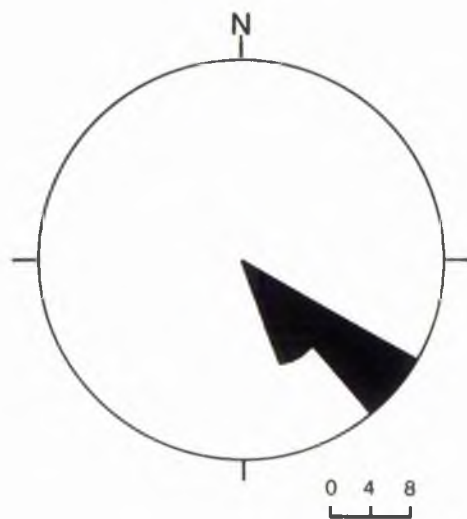
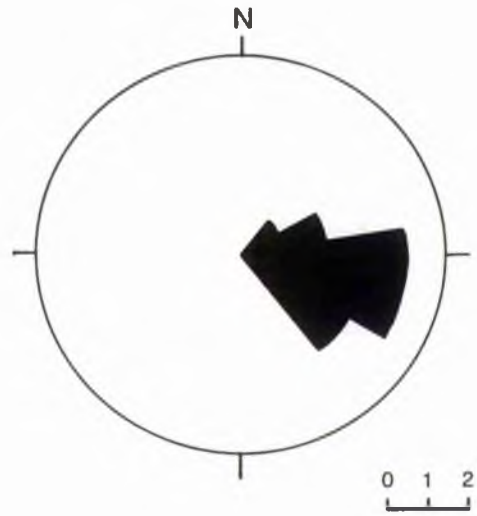
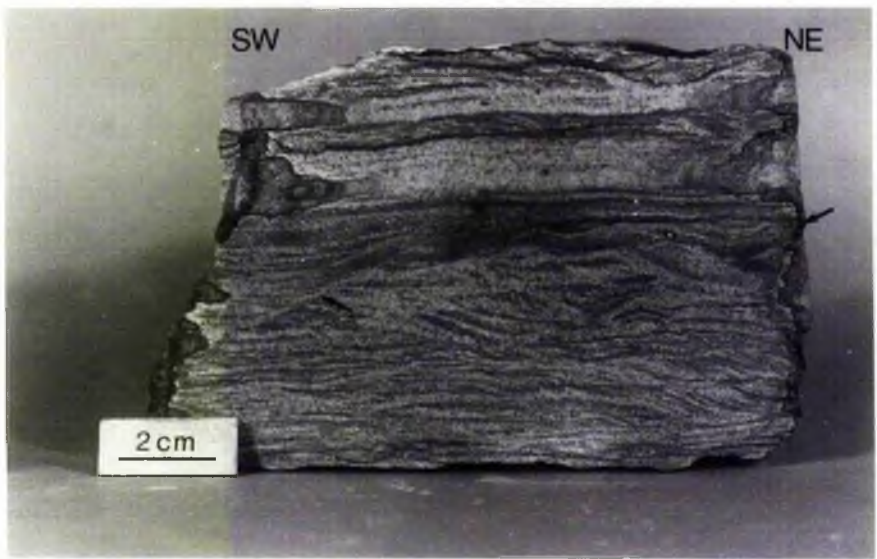
Units S16-S17 These units comprise the second coarsening-upward sequence and start with a dark grey silt mudstone (S16); marine bivalves and trace-fossils are present (Chisholm, 1968, and see Chapter 3). S17 forms thinly bedded sandstones up to 85 cm thick. The first bed is formed of flat bedded, fine-grained well sorted



Fig 4.36 Slab showing wavy, flaser and trough cross-lamination (arrow).  
interbedded siltstone, silty shale and sandstone - Unit (S13) -  
East side of St Monance syncline.

Fig 4.37 Rose diagram of the large scale trough cross-stratification  
of the upper part of Unit (S13). Palaeocurrent direction  
predominantly towards ESE.

Fig 4.38 Rose diagram of the large scale trough cross-stratification of  
Unit (S14), showing the palaeocurrent direction towards SE.



sandstone, up to 18 cm with a few isolated sets of cross-strata (Fig 4.39, 4.40). The second bed is formed of sandstone, fine to medium grained, well sorted, up to 8 cm thick with generally slightly asymmetrical ripples whose crests vary from slightly sinuous to irregular linguoid. The ripples are up to 1.2 cm in height and up to 8.2 cm in wave length. The palaeocurrent movement produced these ripples are nearly towards the W (Fig 4.40).

Units S18-S20 These units start with an erosional surface and are formed of a 98 cm to 110 cm thick bed with large scale trough-cross-stratification (Fig 4.41). Palaeocurrent direction runs towards the WSW (Fig 4.41). The sandstone is overlain by a thin non-fossiliferous micaceous mudstone, of 11 cm thick, riddled with rootlets and followed by thin coal. These facies are regarded as an upward-fining sequence.

The gradational contacts and sedimentary structures indicates that coarsening-upward sequences (S12-S13) (S16-S17), were deposited in minor mouth bar environments, whilst Units (S14-S15) (S18-S20) as fining-upwards sequences were deposited crevasse channels. The dissimilarity of the palaeocurrent direction of the two channel-fill might be due to the nature of the stream-diversion process during abandonment.

#### 4.3 Secondary Deformation Structures

Deformation structures differ in their morphology, occurrence, and scale, and clearly indicate that a variety of processes are responsible for their formation.

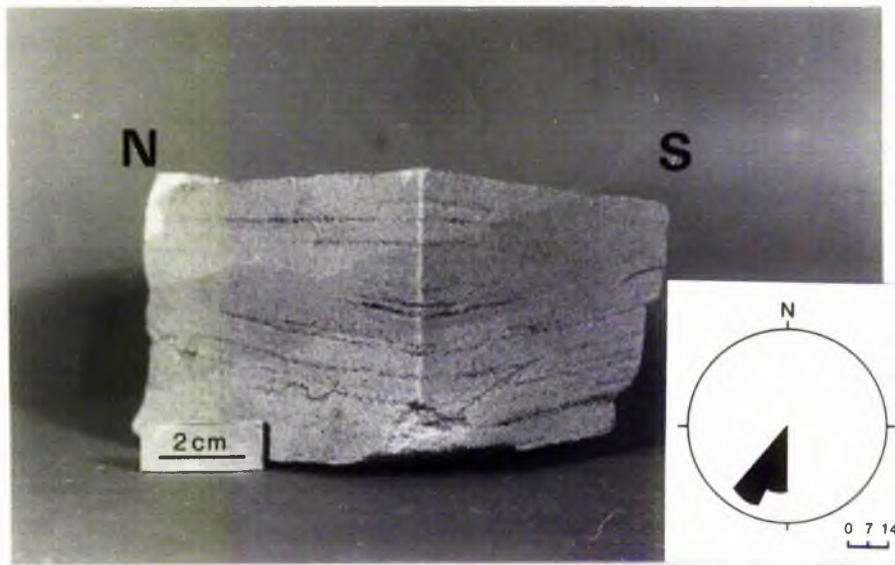
Fig 4.39 Slab of the first bed in Unit (S17) showing the internal structure as cross-stratification. The rose diagram (right side) showing the palaeocurrent direction as towards WNW.

Unit (S17) - East side of the St Monance syncline.

Fig 4.40 Photograph (S17) showing the isolated set of cross-strata below the ripple marks. Palaeocurrent direction from right to left (ie towards west). Pen is 15 cm height. Rose diagram (left side) showing the orientation of the ripple marks as a result of 39 field measurements as EW. Unit (S17) - East side of the St Monance syncline.

Fig 4.41 Photograph showing the large scale trough cross-stratification of Unit (S18). Hammer 30 cm in height. Rose diagram (left side) showing the palaeocurrent direction towards WSW.

Unit (S18) - East side of the St Monance syncline.



#### 4.3.1 Distorted Lamination Unit (B7\*)

The channel sandstone of (B7\*) is fine-grained and well sorted. It lies between undisturbed thinly laminated silty shale and/siltstone (Fig 4.42A). It contains a series of broad synclines with narrow anticlinal crests. It is characterized by the accumulation of fine clay material in the central part of the structure (Fig 4.42B). It is capped by parallel lamination of silty shale indicating that the deformation happened before the deposition of the overlying sediment.

The structure has some similarity with flame structures reported from turbidite sequences but is regarded as a response to some differential loading of the underlying shale accompanied by dewatering (Fig 4.42B). This moves some clay upwards and deforms laminae in the sandstone.

#### 4.3.2 Pseudonodules Unit (F3)

This kind of deformation structure is present in Unit (F3) as siltstone/silty shale interbedded with fine-grained sandstone. Trace fossils are found in this unit (see Chapter 3). The observed deformation structure is kidney-shaped, ranging from (18-52 cm) in size, and the bed involved is about one metre thick, where the lower and upper part are undisturbed; the base is undulatory and the top flat. Most of the underlying facies is squeezed in between and around them (Fig 4.43). They are often elongated parallel to the bedding.

This non-tectonic structure bears a resemblance to similar features previously reported in the literature. Detailed discussion and summaries of previous studies on these deformation structures have been given by Potter and Pettijohn (1963, Chapter 6). Laboratory studies of the formation of each structure have been carried out by

Kuener (1965), Dzulyński and Walton (1963).

Following Kuener's experimental study the structures results (Fig 4.44), when "A sand substratum supported by thixotropic bed of clay, was subjected to mild vibrations simulation an earthquake." A similar process is thought to be responsible for the formation of this deformed sandstone (Fig 4.45) as due to in place sinking of a sandstone bed into the underlying shale silt. The more homogenous sand maintained its coherence, whereas the finer grained unit into which it subsided could not maintain its continuity and hence was squeezed outward and flowed upward as a viscous fluid.

#### 4.3.3 Deformed Sandstone Unit (S21)

This 8.12 m thick sandstone is fining-upwards and the finer the sediment, the more complex the deformation. The beds on either side have been eroded away.

The description of the unit uses the following terminology. Horizon A refers to the base of the unit, horizons B relate to the sediment underlying the disturbed horizon, horizon C to the deformed unit, which is subdivided into subhorizons; and horizon D to the sediment overlying the disturbed horizon.

The Lower part (horizon A), formed of flat bed of 3 m thick medium-grained sandstone, passes gradually upwards into horizon B, (1.5 m thick fine-to-medium grained) with parallel to wavy lamination. It is truncated above by erosional surface by deformed bed (horizon C 1.62 m thick) divided into three parts depending on the shape and degree of deformation (Fig 4.46A, B). In horizon, C1 the laminae form sharp anticlines as an enechelon structure, and broad synclines on both sides. The crests are seen to be narrower than

troughs, and the crests are often tilted in the down-current direction. Horizon C2 is considerably disturbed with a trough cross-stratified unit. The highest part of this horizon is provided by overturned laminae in folds. The upper part of the horizon C3 was removed by erosion before deposition of the next horizon occurred. The common direction of over-turning is towards the east. These are truncated sharply and overlain by horizontal laminated sediment of horizon D.

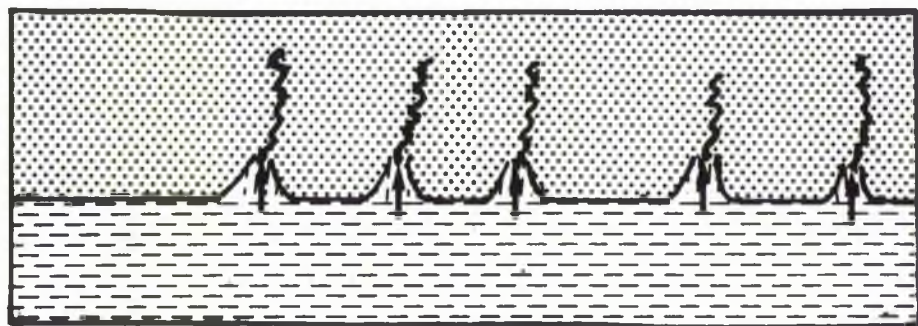
Modal analysis by point counting were carried out, based on 500 counts/section. The results showing a slight fining in grain size upwards, and in the percentage of clay which is highest in the deformed sandstone horizon C (21.0%). Davies (1965) mentioned that during deformation, the increase in the plastic properties of sediment is due mainly to the presence of clay minerals. Several authors mentioned that deformation becomes more complex with a decrease in grain size. The composition of the sediment, and the grain size appears to have played a part in controlling the development of structures.

Greensmith (1965, p 230) reported deformed laminae in the Calciferos Sandstone Series and considered them to result from earth tremors which repacked the sandstones causing a migrating of pore-water upward with the result that the layer becomes more mobile and susceptible to gravitational slip. Lowe (1975) pointed out that water-escaped structures can be expected to form most commonly in fine-to-medium grained sands deposited by aqueous current of declining velocity. He added that during the final waning stage of the current activity the cohesive and less permeable sediment accumulate both because the sediments are finer grained and better packed as a result

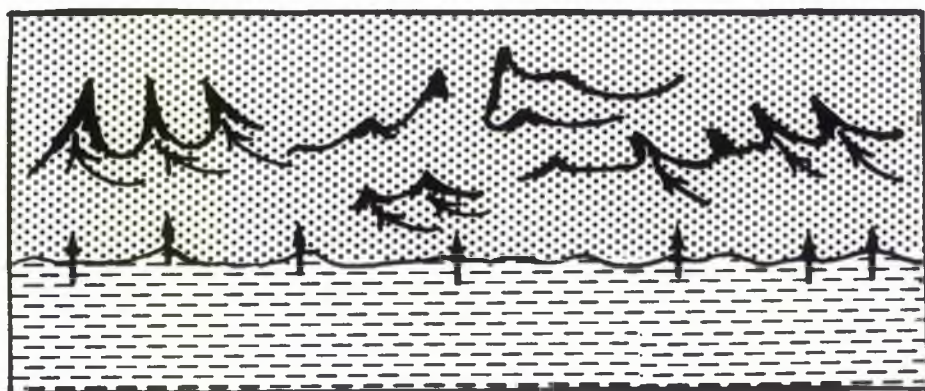


Fig 4.42A Photograph showing a series of broad synclines with narrow anticlinal crest as a result of water escape. Some material of fine clays are present inside the structure as coming up from the underlying sediment with the water movement. The unit above as parallel lamination of silty shale is undisturbed. Unit (B7) - West side of the St Monance syncline. Camera lens hood is 5 cm in diameter.

Fig 4.42B (i) At the points of maximum flow (arrows), and due to differential loading, allow some material of the underlying sediment passing through as the fluids pass and deposited in the central part of the structure when the velocity of fluids decrease and formed the final structure Figure (ii).



(i)



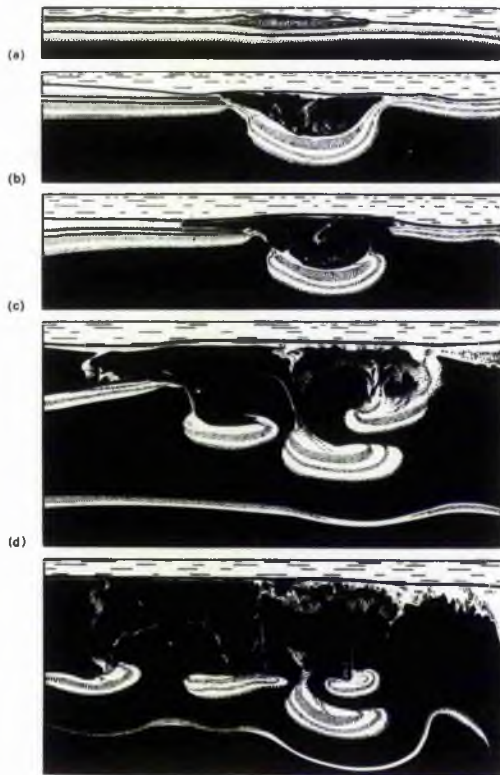
(ii)

Fig 4.43 Photograph showing the different size of the deformed structure and most of the laminae are curving around the margins of this kidney-shape. The strata above this zone appear as flat and undisturbed whilst the lower contact are nearly wavy. Unit (F3) - East side of the St Monance syncline. Camera lens hood is 5 cm in diameter.

Fig 4.44 Drawing from Kuenen's Paper "Value of Experiments in Geology" (1965), illustrating his results from a laboratory study. In this experiment a sand layer overlying a clay substrate foundered and broke into pillow shaped structures when the aquarium was mildly vibrated to simulate an earthquake.



0 5 10 cm



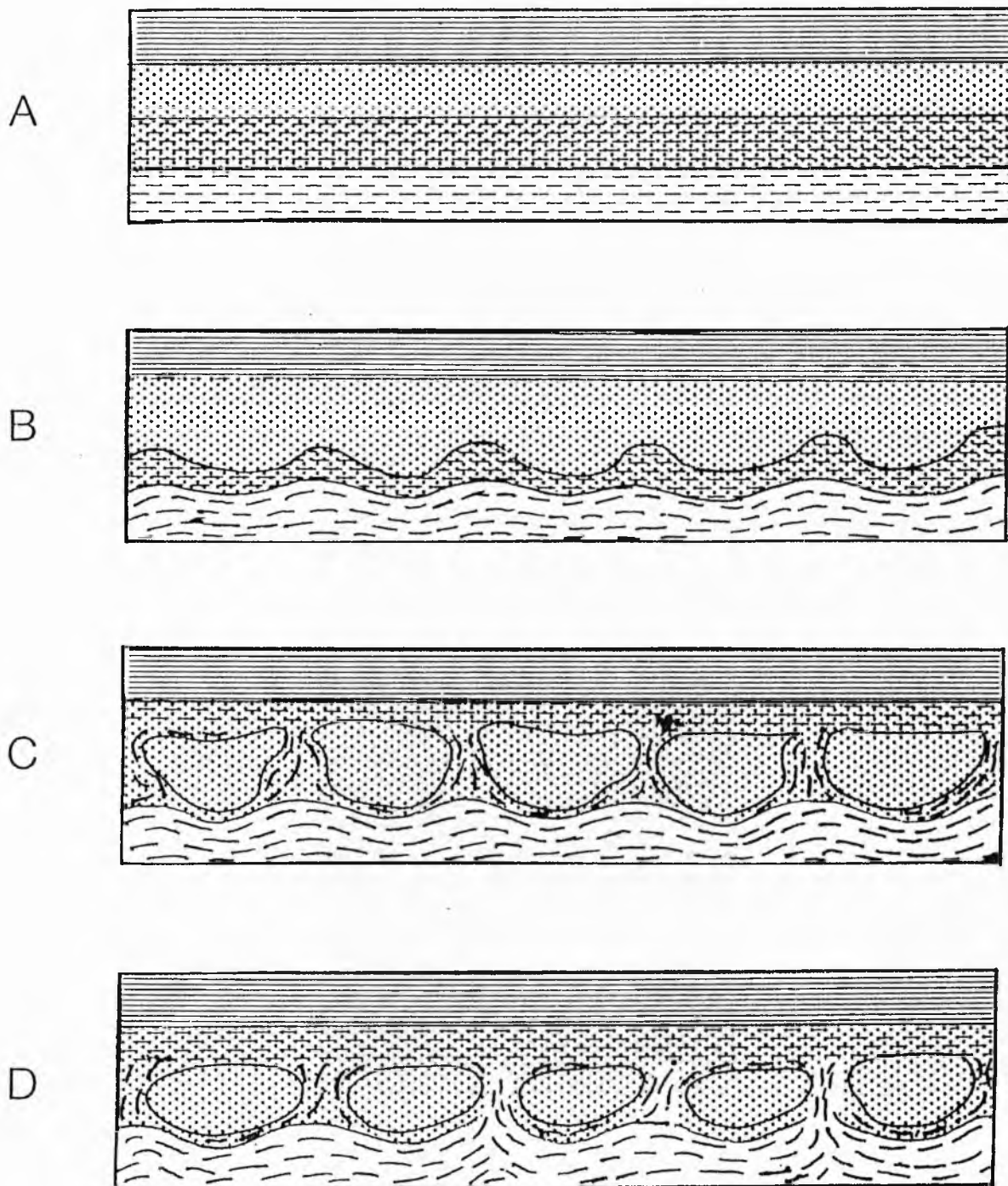
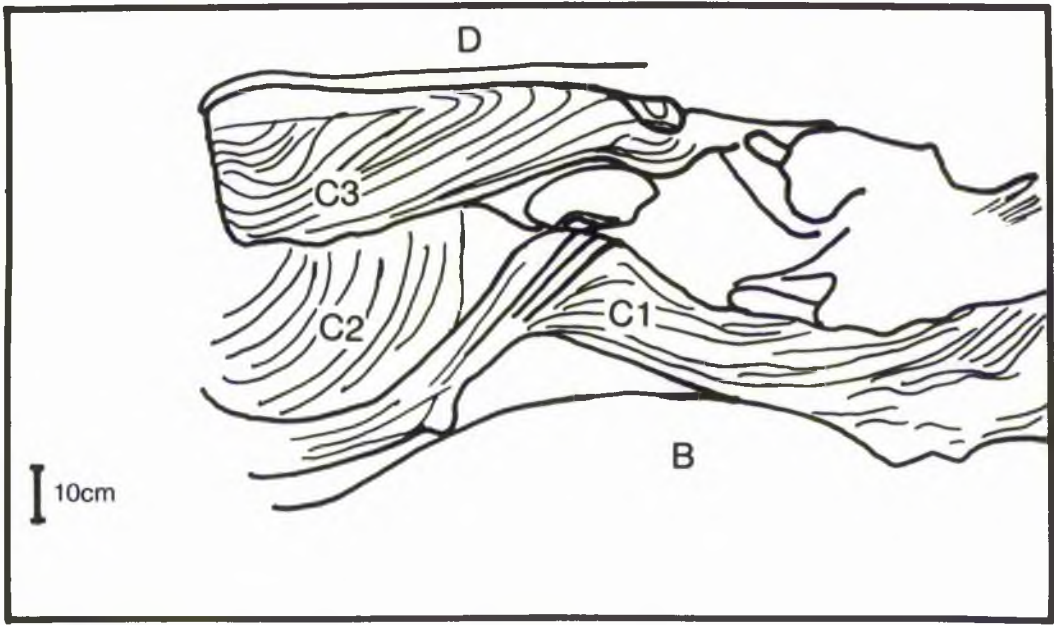


Fig 4.45. Sketch showing the sequence of events leading to the development of the kidney-shaped deformation structures (pseudonodules) based on the nature and composition of outcrop and on laboratory experiments reported by Kuenen (1958, 1965), Dzulynski and Walton (1963), and by Dzulynski (1966).

Fig 4.46A Sketch showing the horizons B, C, and D. Also the subhorizons C1, C2 and C3 which have different types of deformation.

Fig 4.46B Photograph showing the typical deformation structure. Sandstone Unit (S21) - East side of the St Monance syncline.



of the reducing rate of sedimentation.

The author considers that the origin of the observed deformation is syn- or early postdepositional not tectonic, because it has upper and lower sandstone horizons that are almost undisturbed. A triggering mechanism such as an earthquake, caused liquification, the upward movement of pore water caused part to reach overlying sediment which would tend to sink downwards due to differential loading. The synclines in (C1) seems to have been formed by the subsidence of an upper sandstone horizon (C2) into a lower one (C1) which was in a liquified condition due to a high amount of clay and water coming from below.

#### 4.4 Conclusion

The study of the inorganic sedimentary structures and Palaeocurrents throughout the sequence indicates that they consist mainly of ripple marks, and associated cross-lamination including rib-and-furrow structures; large scale mainly trough cross-lamination, hummocky cross-stratification, and deformation structures including pseudonodules. Lenticular, wavy and flaser bedding are common. In order to bring the measured current directions into their original positions, two corrections were made first for the plunge, and then for the dip. Moreover, from the dip readings the plunge was estimated at  $18^{\circ}$  to  $032^{\circ}$ .

Most of these sedimentary structures are found to be in either fining-upward sequences (channel), or coarsening-upward, mouth bar sequences. Palaeocurrent analysis shows that major currents in channels were generally directed to the south-west with brief variation towards ESE or W. This dissimilarity of the palaeocurrent



direction might be due to stream-diversion processes. Many of the ripple marks are wave-generated with a variety of current directions. Analysis of cross-lamination in the ripples and ripples crest suggests a current movement predominantly unidirectional, but there are some opposed cross-lamination. The main characteristic features of these wave ripples are:-

- 1 Bi-directional cross-lamination.
- 2 Swollen ripples, convex down as well as up.
- 3 Internal and external structure not always concordant.
- 4 Erosional sets on curved and undulating surfaces.
- 5 Ripple indices (height/length) generally less than 10.

Rare herringbone cross-beds indicative of tidal action were found in a few units leading to the suggestion that there was perhaps some tidal action.

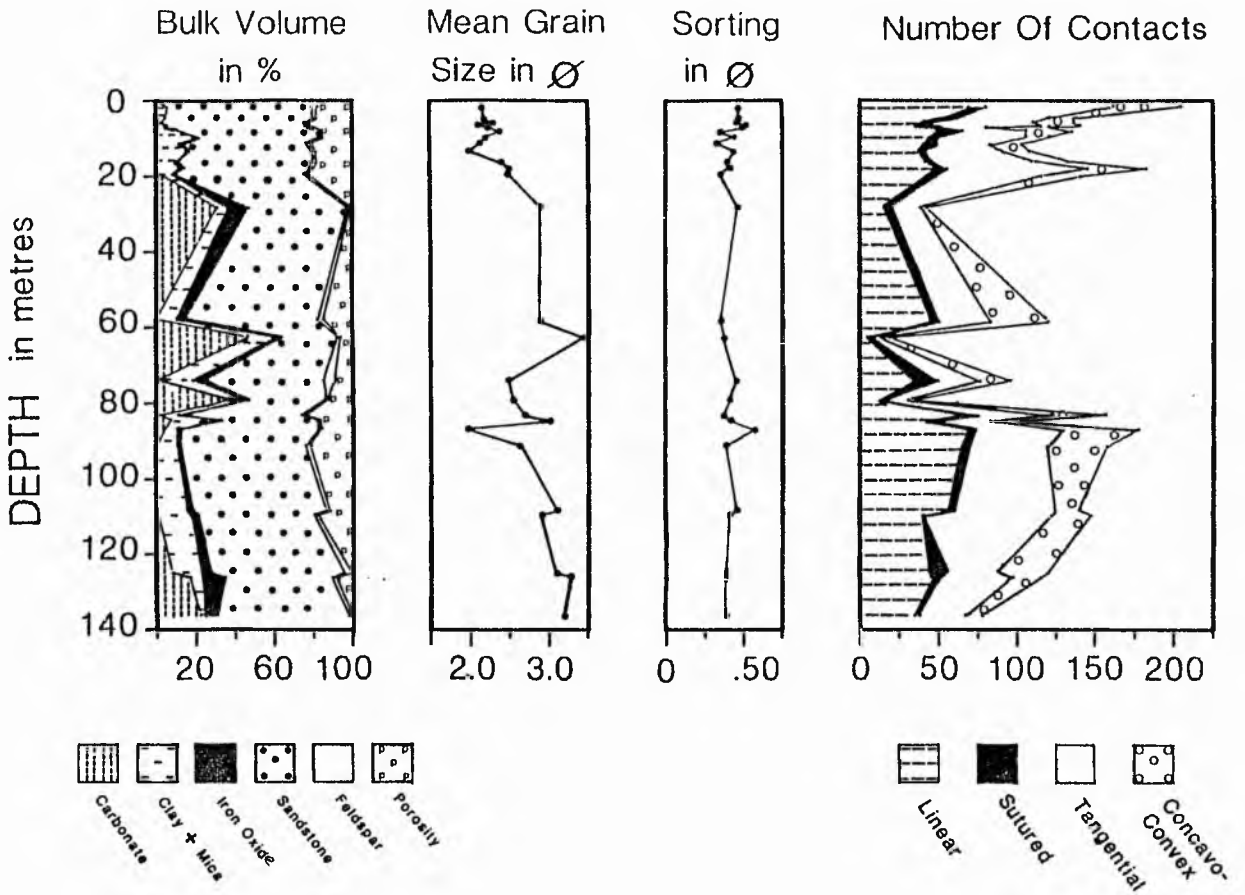
Deformation structures differ in their morphology, occurrence, and scale, and clearly indicate that a variety of processes are responsible for their formation such as differential loading, dewatering, and earthquake shocks, but overall the composition of the sediments, and their grain size seems to have played a major part in controlling the development of these structures.

## CHAPTER 5

### 5.1 PETROGRAPHY

Thin-sections of the sandstones were made after thorough impregnation with coloured epoxy resin. This bound the grains together, prevented damage to the pores and made them easily seen under the microscope by their blue colour. Each thin-section was analysed by counting 500 points at intervals of 0.3 mm using a Swift Automatic point counter. The varieties of rock fragments, feldspar, mica, heavy minerals, porosity, matrix, and cement were counted separately. Quartz grains were separated into monocrystalline and polycrystalline types. In addition, the relative amounts of undulatory and non-undulatory grains of quartz were determined using the technique of Blatt and Christie (1963, p 564) (Appendix 5.1).

Grain-size was estimated by measurement of 122-385 grains per thin-section. The sandstones are very fine-to-medium grained, with a mean grain size ranging from 3.560 to 1.880 and very well to moderately sorted, with graphic standard deviation ranging from 0.324 $\phi$  to 0.635 $\phi$  (Folk, 1968). Figure 5.1 shows results of point-counting analysis. Sorting of medium-grained sandstones appears poorer than the very fine grained sandstones. Detrital grains are generally rounded in medium grained but are angular-to-sub-angular in very fine-grained sandstones. Porosity values of the sandstone units range from a few percent to as high as 25.0 percent, and there is in general a trend of increasing porosity upward through the sequences.



Petrographic Analysis Of St. Monance Syncline  
Data From Point-Counting Analysis.

Fig 5.1 Petrographic Analysis of St Monance Syncline. Data from point-counting analysis.

The sandstones consist predominantly of quartz and classify as orthoquartzite on McBride's (1963) scheme (Appendix 5.2, Fig 5.2).

## 5.2 Quartz

Quartz forms 64.3% on average (standard deviation 10.1%) of the grains of the sandstones. Occasionally acicular inclusions of other minerals such as rutile and zircon were observed within the grains (Fig 5.3a). Globular, regular, and irregular inclusions (Fig 5.3B, C, and D; Mackie, 1896; Keller and Littlefield, 1950) are also found in quartz clasts. They are primary, very rich in gas, and have high content (>60%) and homogenise at temperatures above 300 °C. Some of the inclusions burst open at around 260 °C. The iron cement obscures detail and it is not possible to observe precise temperatures. Collectively, palaeotemperature and the types of fluid inclusions suggest that metamorphic quartz dominates with some igneous quartz. However, secondary inclusions are also common within the syntaxial overgrowths. Some inclusions are pure gas but most contain a watery fluid only. Homogenisation temperature for inclusions trapped in overgrowths are around 70 °C. Some inclusions in healed fractures homogenise at 160 °C. The 90 °C difference in temperature perhaps being due to fractures formed and healed during magmatic activity which pre-dated the overgrowths.

Following Blatt and Christie (1963) and Conolly (1965) the quartz grains were divided into:-

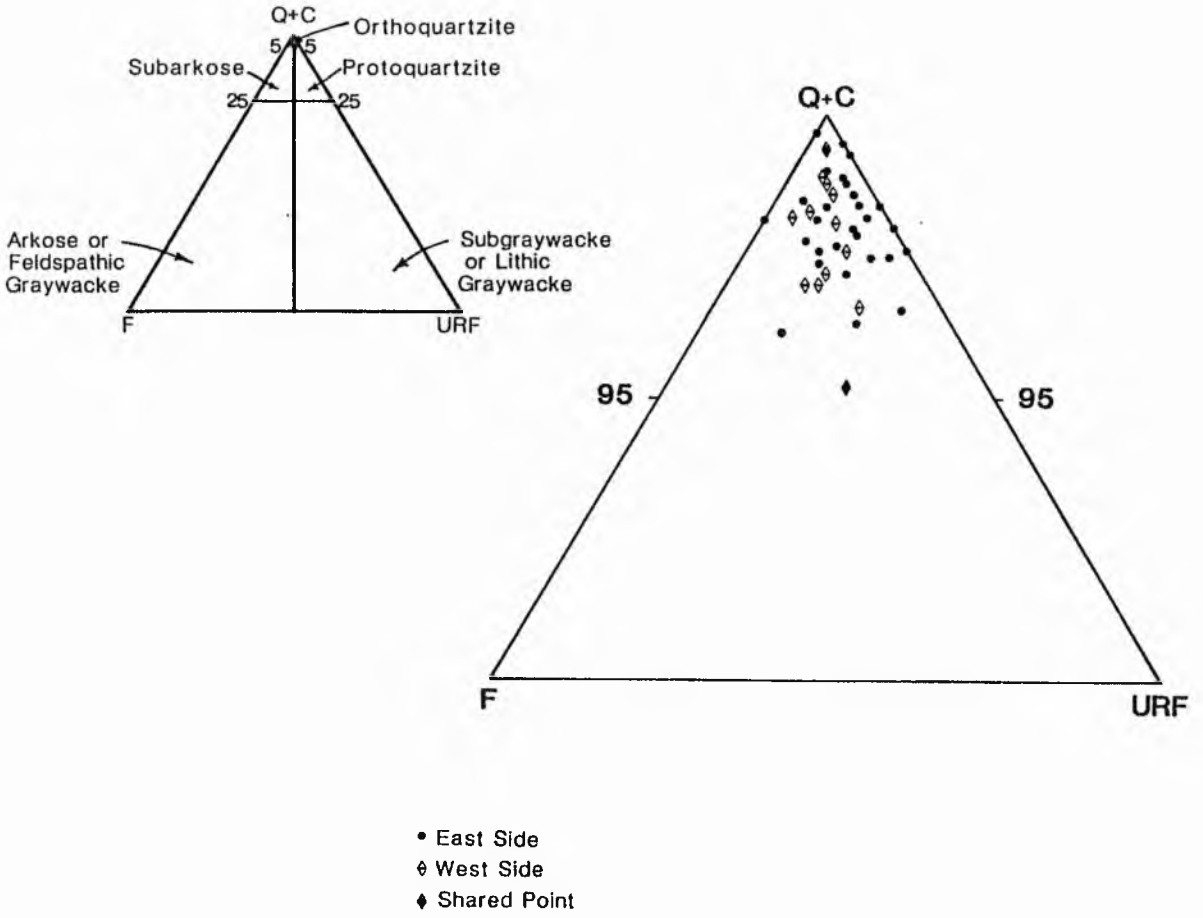


Fig 5.2 Classification of sandstones (after McBride, 1963).

Fig 5.3A Photomicrograph showing detrital quartz grain with abundant acicular shaped rutile inclusions. The quartz grain has some overgrowths which are poorer in inclusions, lower part partially replaced by carbonate cement. Lower part of Sandstone Unit (B7) - West side. Ordinary light, x 500.

Fig 5.3B Photomicrograph showing globular liquid/gas (biphase) and monophasic inclusions in quartz grain and inside the silica overgrowth. Sandstone Unit (S21b) - East side. Ordinary light, x 1000.

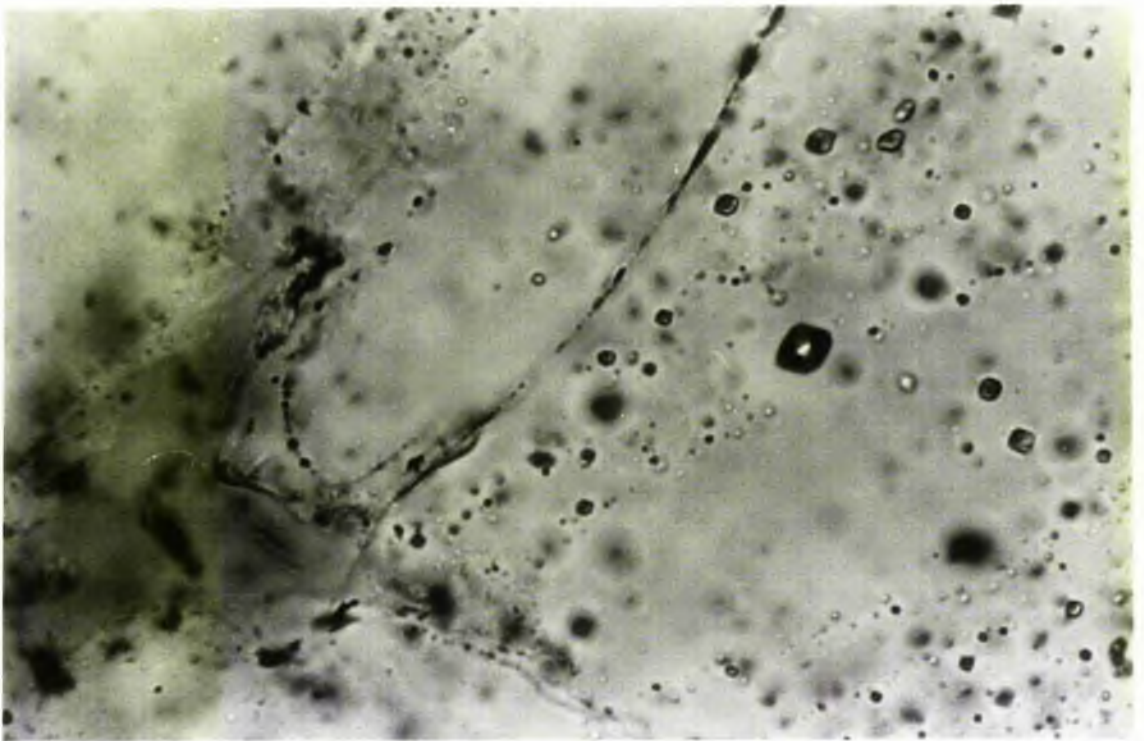
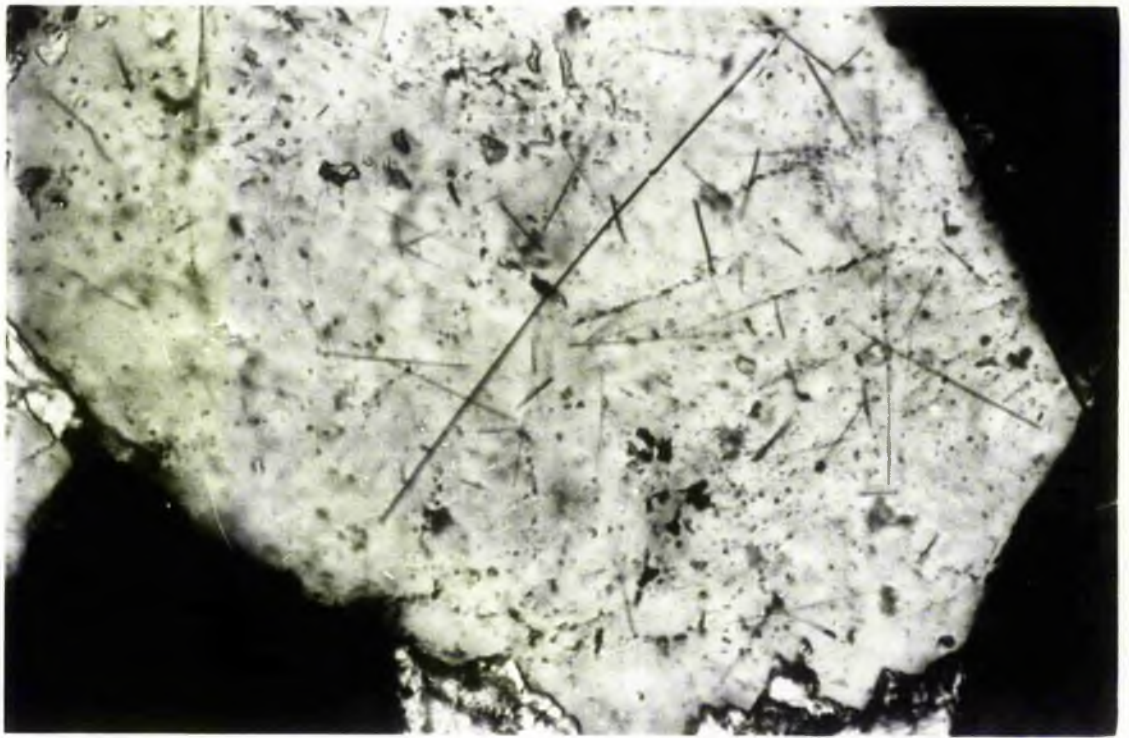
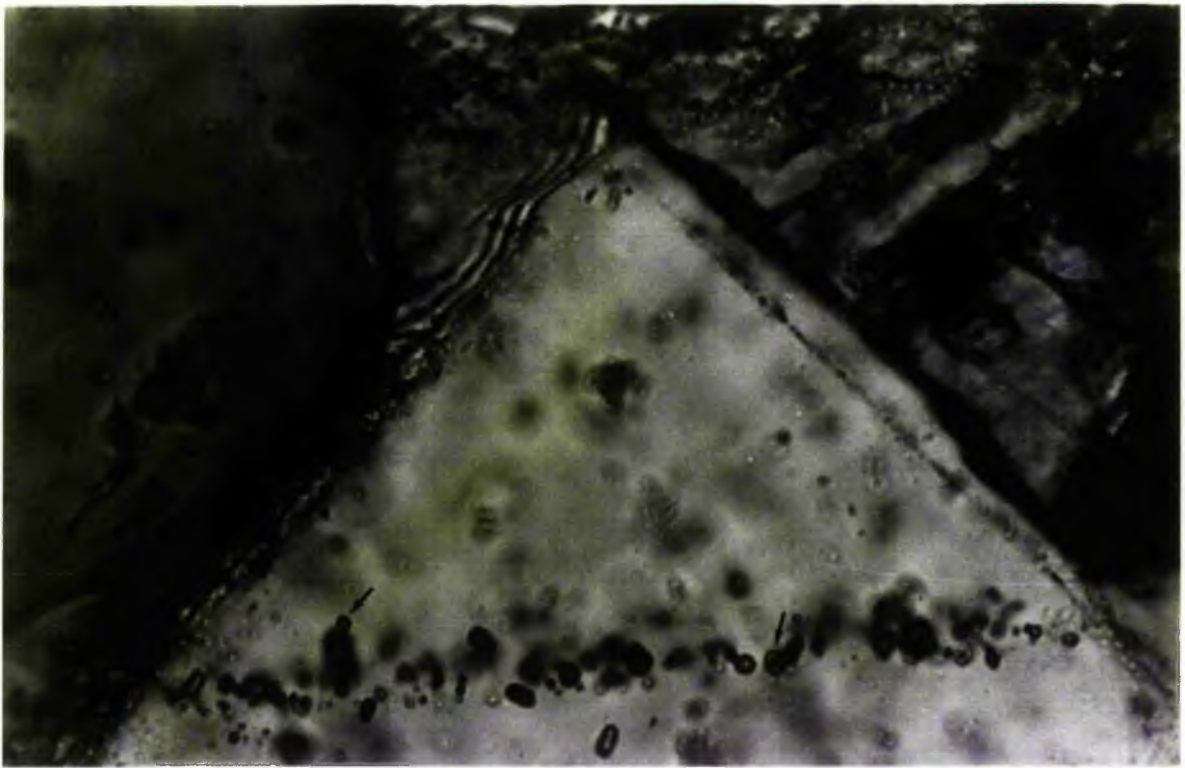
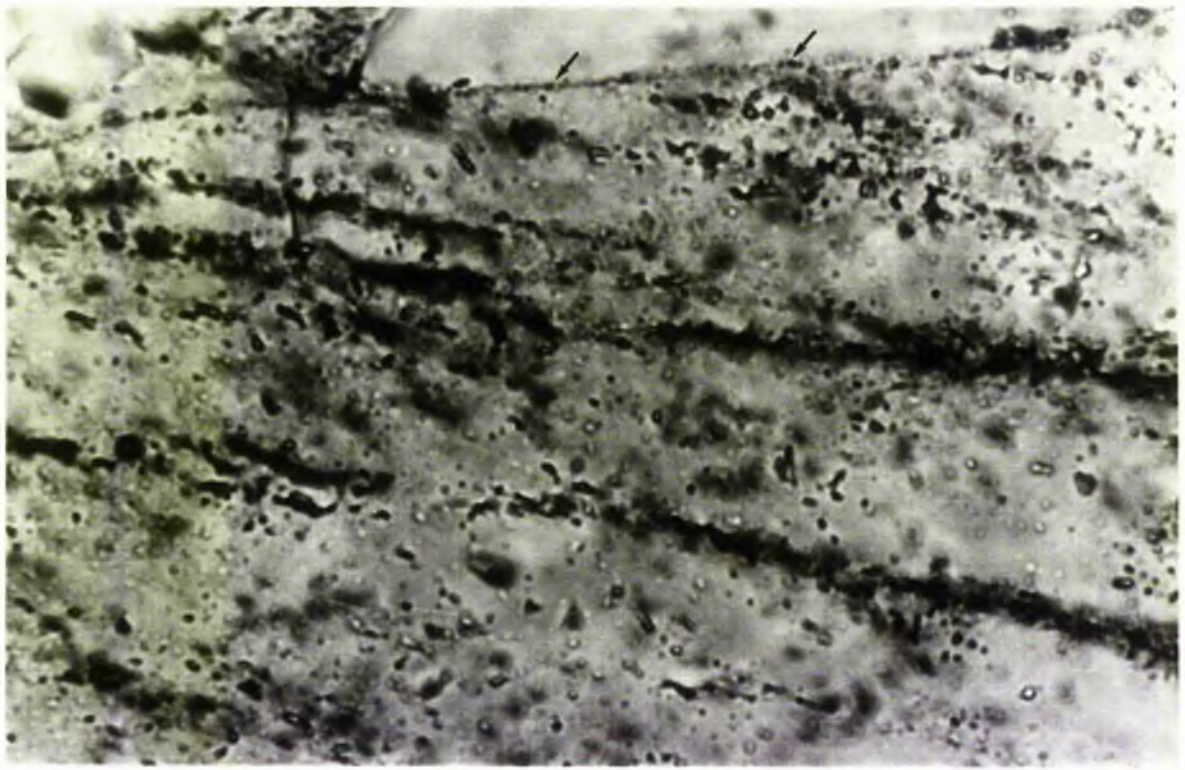


Fig 5.3C Photomicrograph showing regular tiny inclusion in quartz grain as well as associated with the silica overgrowth (arrow). Sandstone Unit (S17). East Side. Ordinary Light, x 1000.

Fig 5.3D Photomicrograph showing mono and biphasic (arrows) of regular inclusion in quartz grain. Sandstone Unit (T8D). West Side. Ordinary light, x 1000.





### 5.2.1 Polycrystalline grains

Polycrystalline grains are those which are made up of two or more interlocking crystals of quartz in different optical orientation. The proportion of polycrystalline grains varies directly with the mean size (Fig 5.4); the amount varies from 2.86% to 15.18% with an average of 7.92% (standard deviation 3.12%). This dependence on grain-size is to be expected because as the grains break down, they tend to form single monocrystalline grains.

In addition, to the effect of grain-size the proportion of polycrystalline grains seems to be affected by the presence or absence of a carbonate cement (Fig 5.5). Sandstones with less carbonate cement have a high proportion of polycrystalline grains, while those with a high amount of carbonate are uniformly low in polycrystalline grains. It might be that the development of carbonate cement was accompanied by some corrosion of the quartz grains. Blatt, et al, (1972, p 291) pointed out that polycrystalline grains are more readily attacked during weathering, transportation, and diagenesis because of the relative weakness of intercrystalline boundaries. During carbonation it is probable that some of the polycrystalline grains were preferentially attacked and either replaced, or more likely, reduced to individual grains.

It has been suggested that the number of crystals and the kind of intercrystalline boundaries making up the polycrystalline grains can give an indication of provenance (Blatt, 1967, Krynine 1940 in Folk 1974, and Basu, et al, 1975).

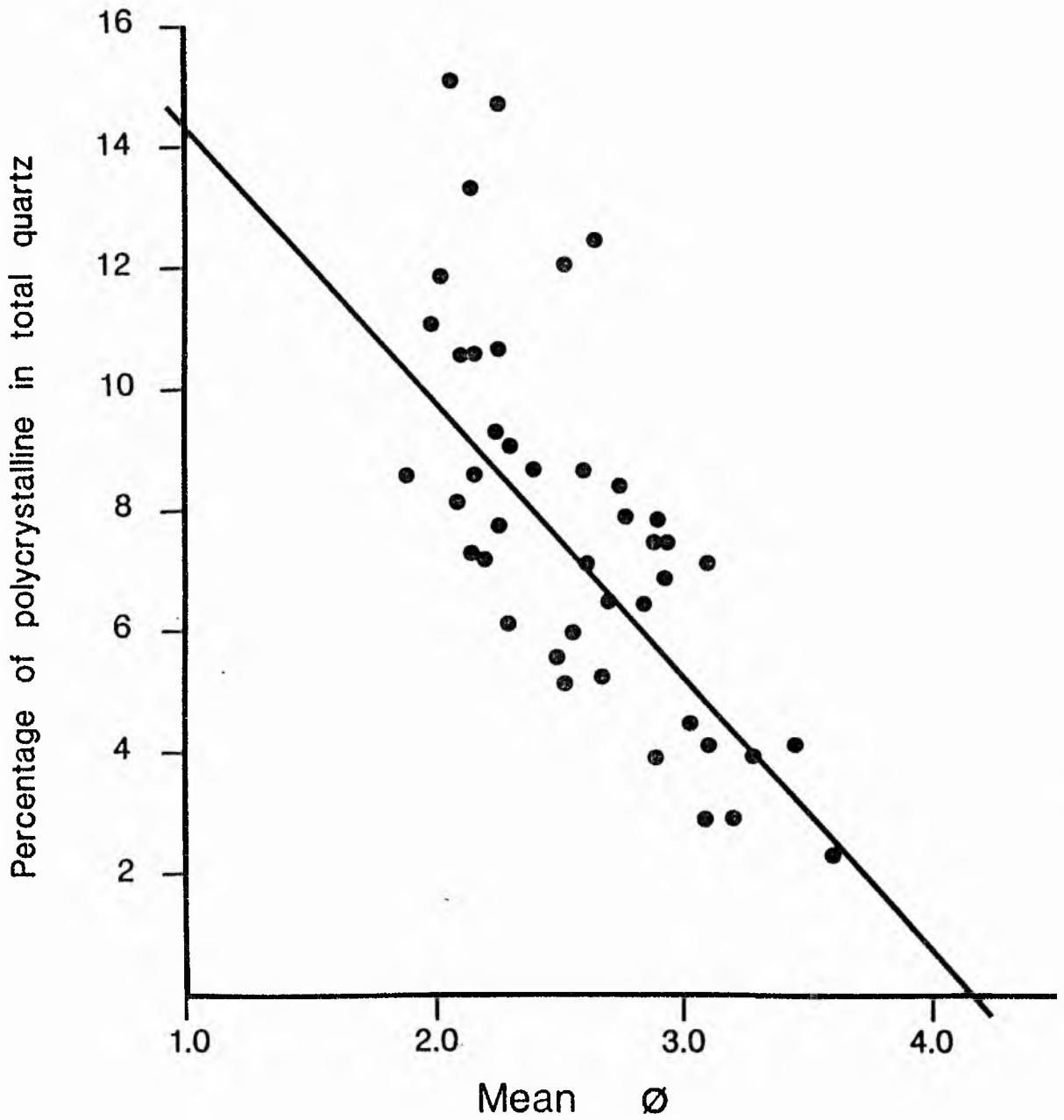


Fig 5.4 The proportion of polycrystalline quartz percent in 43 thin-sections of St Monance orthoquartzite sandstones plotted against modal sand size. The percentage of polycrystalline quartz increases with increase in modal sand-size. Correlation coefficient  $r$  for all data  $r = -0.739$ .

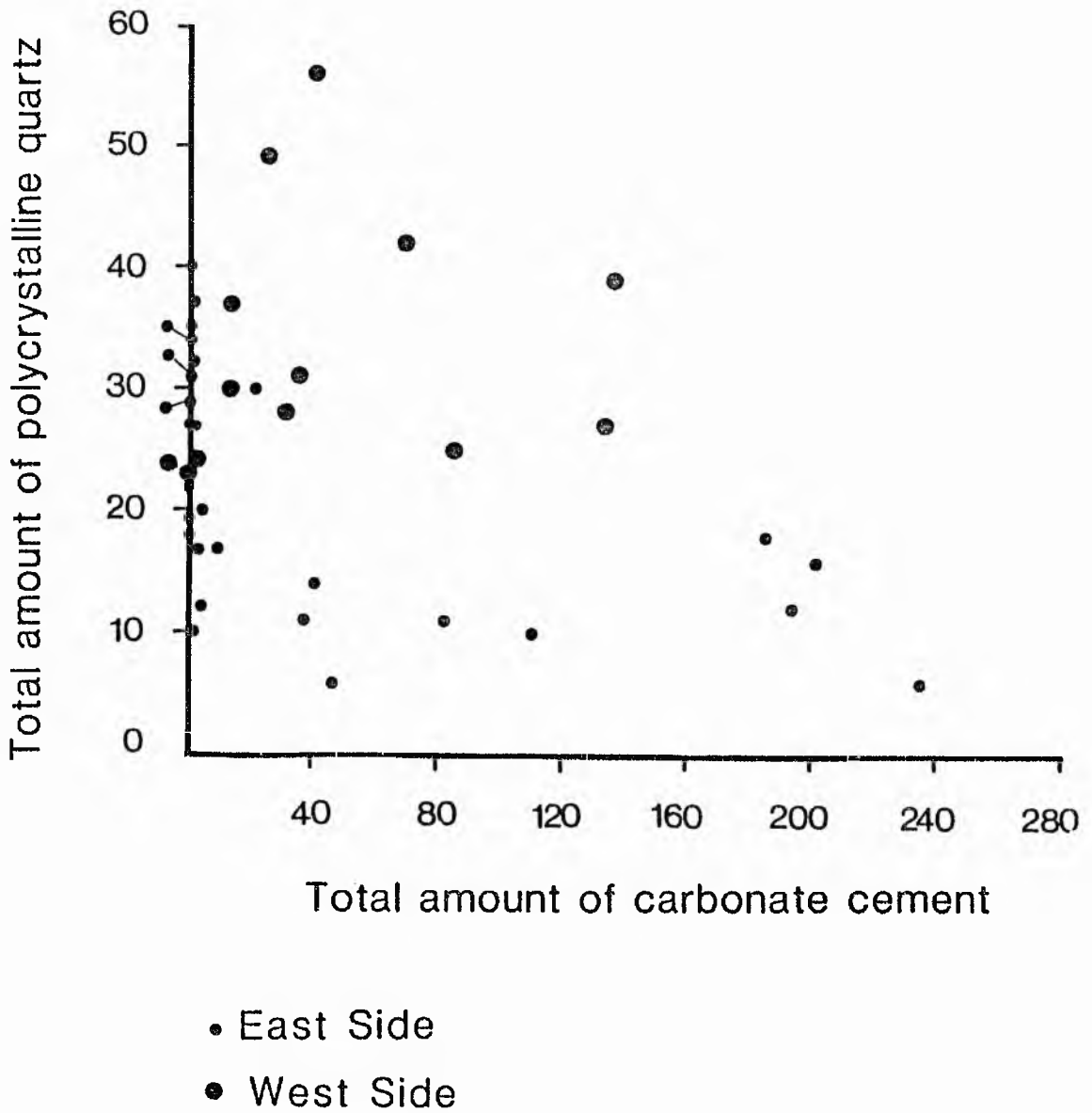


Fig 5.5. Correlation between amount of polycrystalline quartz and carbonate cement, showing the development of the carbonate cement leads to decrease the polycrystalline amount.

### 5.2.1a Number of crystal units

The undulatory extinction of polycrystalline crystals varies with the size of polycrystalline grains and the number of crystals per polycrystalline grain. Fine-to-medium grains with few crystals (2-3), generally have slightly undulose extinction, while the coarse polycrystalline grains with more than (3) crystals have strong extinction. The number of units in the polycrystalline grains of the St Monance sandstones tend to be predominantly more than 3 (Fig 5.7, 5.8 and 5.9) which indicates a provenance of Low-rank metamorphic rocks (Fig 5.6, Appendix 5.3). This is supported by the fact that the quartz crystals often have a bimodal size distribution (Figs 5.7A, 5.7B), and are elongated to extremely elongated (Figs 5.8-5.9). Sometimes the crystals are of two different sizes (Fig 5.11), this seems to be an example of arrested recrystallisation in a quartz aggregate, the smaller crystals being newly developed ones. Such grains are frequently observed in metamorphic detritus (Blatt 1967, p 420).

### 5.2.1b Kind of intercrystalline boundaries

The majority of the contacts between the crystal units are sutured or straight-to-sutured rather than simply straight. (Figs 5.7B-5.8).

### 5.2.2 Monocrystalline

Monocrystalline grains are defined as any which consist of unitary quartz. They form from 28.4%-to-69.4% of the total rock (Appendix 5.1). There is a stratigraphic variation in that the proportion increases up the succession. They vary in size and

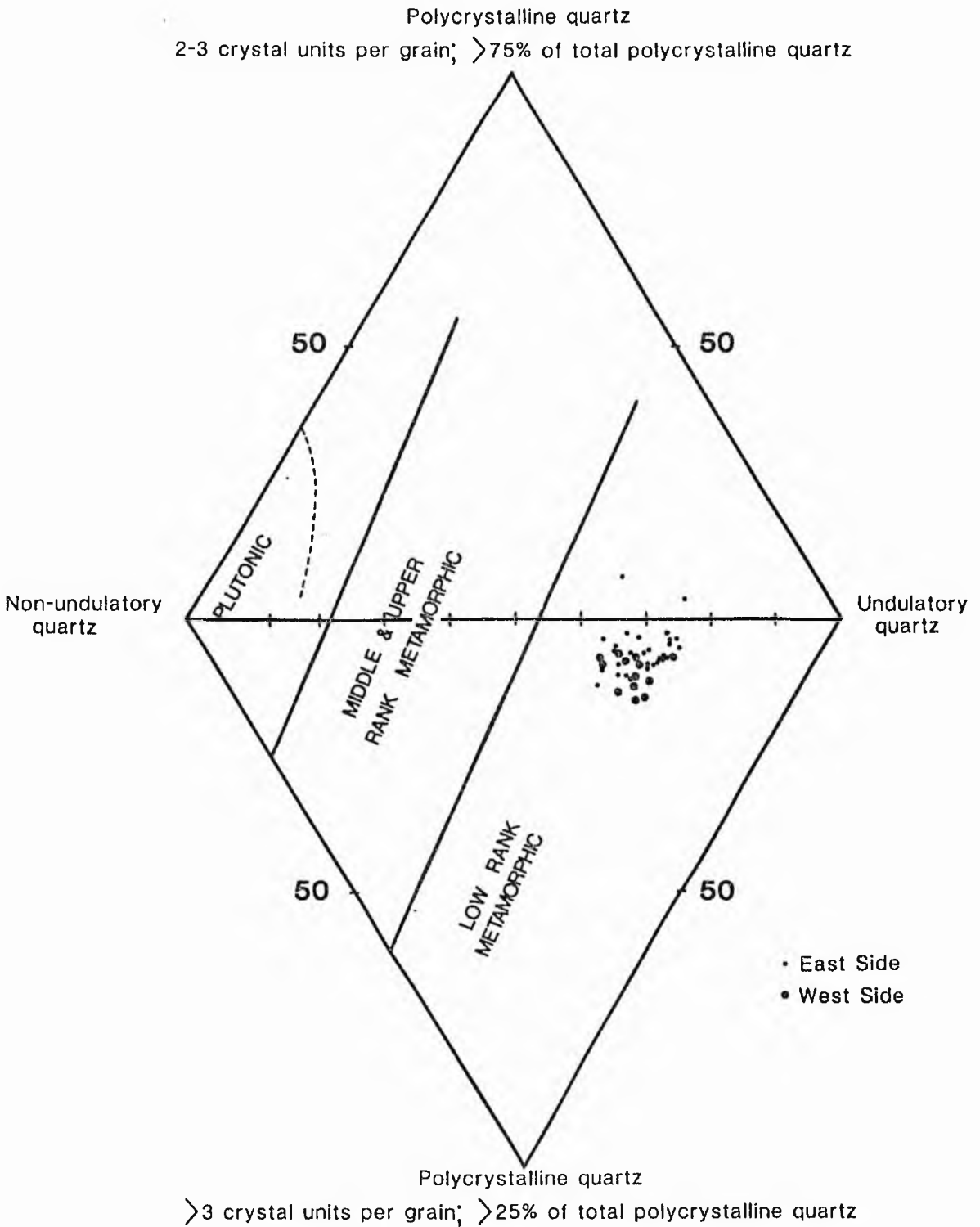


Fig 5.6 Four parameters of detrital quartz to identify source rock of the quartz  
After BASU. et. al. (1975)

Fig 5.7A Photomicrograph of polycrystalline quartz grain, medium-to-coarse sand fraction, showing both straight and sutured intercrystalline boundaries, and formed of more than 5 crystals. Sandstone Unit (S24) - East side. Crossed polars, x 100.

Fig 5.7B Photomicrograph showing polycrystalline quartz grain, medium sand fraction, with sutured intercrystalline boundaries, formed of more than 3 crystals, and bimodal size distribution of contained quartz crystals. Sandstone Unit (S24) - East side. Crossed polar, x 250.

Fig 5.8 Photomicrograph of polycrystalline quartz grain, medium-to-coarse sand fraction, showing sutured intercrystalline boundaries, elongated crystal, formed of more than 3 crystals. Sandstone Unit (S24) - East side. Crossed polars, x 50.

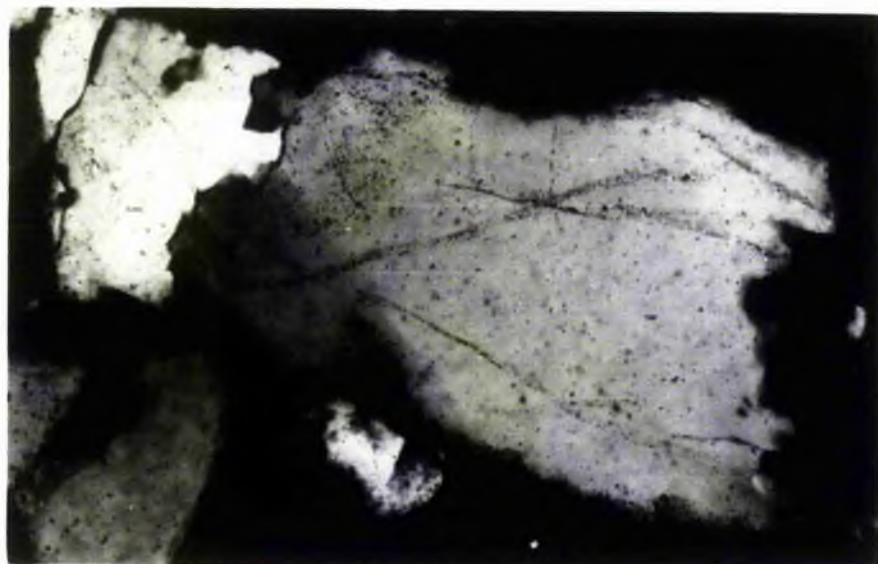
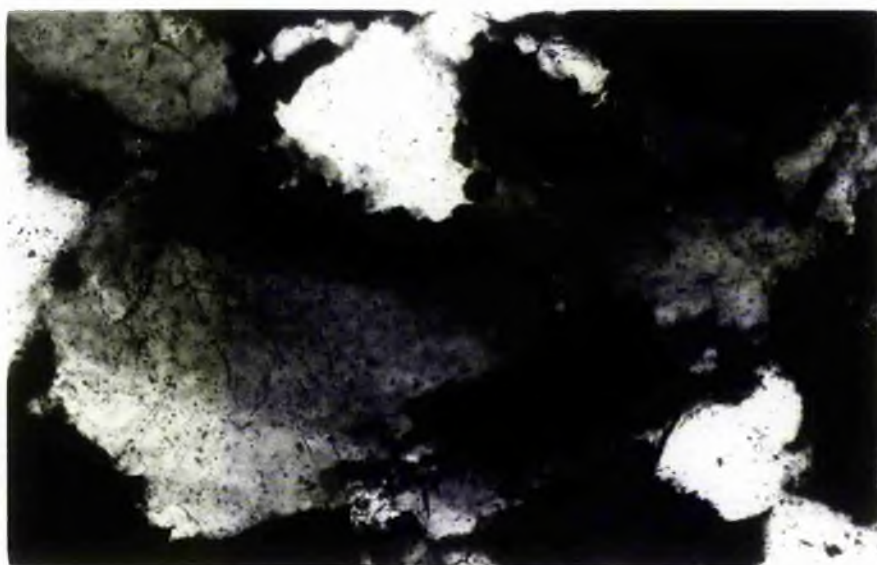
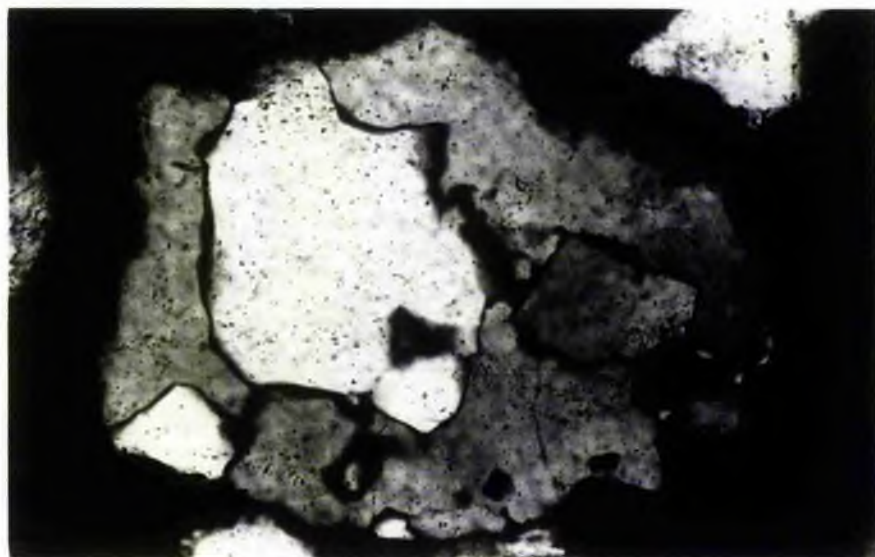
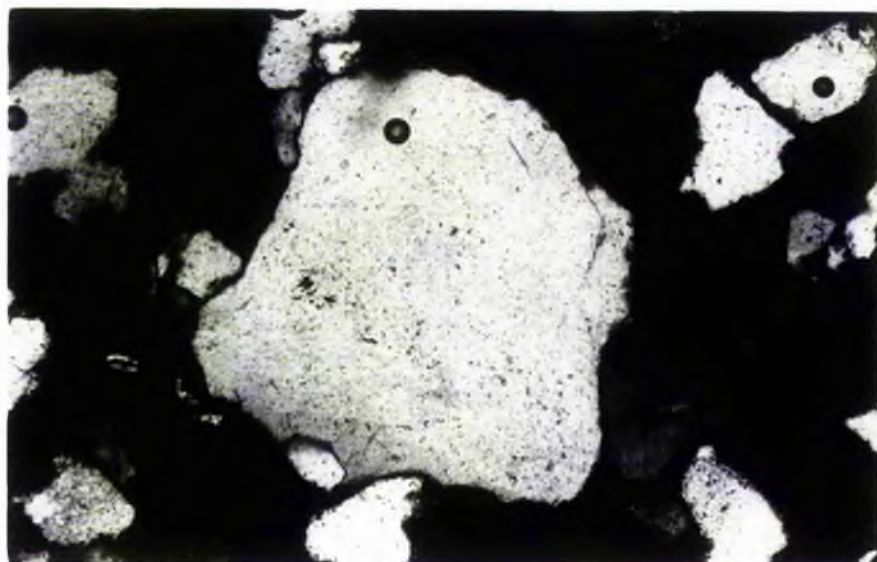
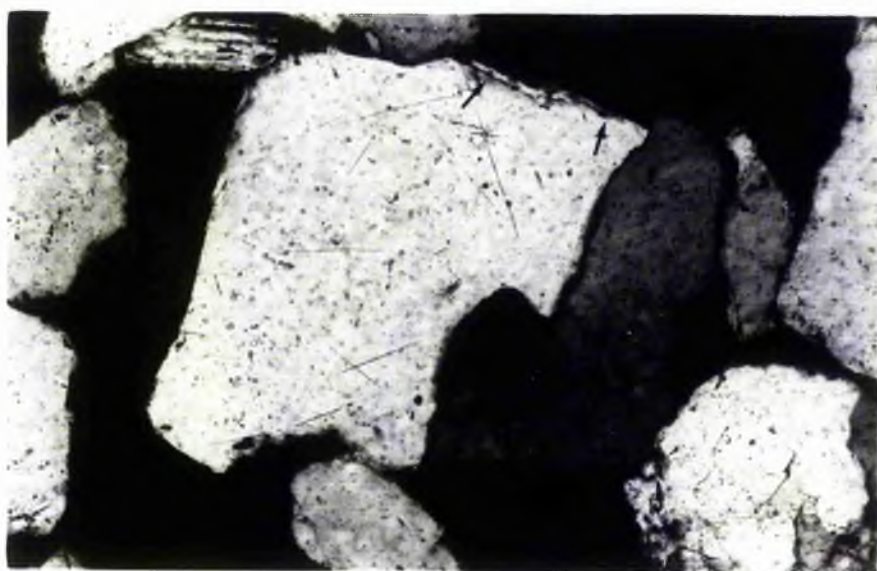
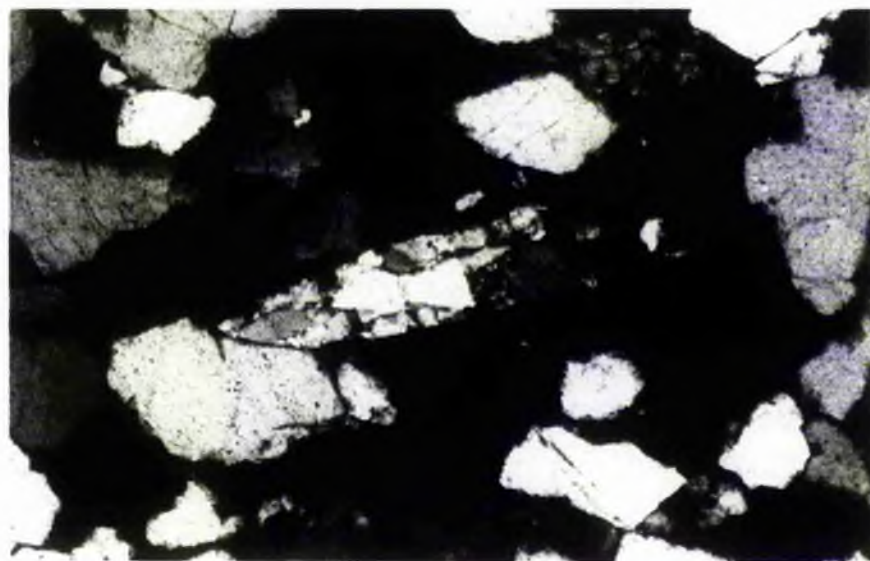




Fig 5.9 Photomicrograph showing polycrystalline quartz grain, fine-to-medium sand fraction, sutured intercrystalline boundaries, and extremely elongated crystal. Sandstone Unit (S24) - East side. Crossed polars, x 125.

Fig 5.10 Photomicrograph showing polycrystalline quartz grain, medium sand fraction, formed of only two crystals, intercrystalline boundaries are curved to straight. Note the presence of overgrowth (arrows), and acicular (rutile) inclusions. Sandstone Unit (S24) - East side. Crossed polars, x 100.

Fig 5.11 Photomicrograph showing polycrystalline quartz grain, seems to represent an arrested stage. The smaller one being the newly developed one. Sandstone Unit (S24) - East side. Crossed polars, x 100.



are generally angular-to-subrounded although some are well rounded. Both undulatory and non-undulatory grains are present.

#### 5.2.2a Non-undulatory quartz

Non-undulatory grains are defined as those which are completely extinguished through a very slight (less than one degree) rotation of the flat microscope stage (Blatt and Christie 1963, p 546; Conolly 1965). The proportion of non-undulatory grains in relation to total monocrystalline quartz varies between 23% and 36% and shows no correlation with grain size (Fig 5.12), although Blatt (1962) and Conolly (1965) suggested that undulatory grains tend to be more unstable and break down most easily to form smaller grains. The relationship between non-undulatory quartz to the total quartz in sand-sized grains of orthoquartzites is illustrated in Fig 5.13 A. The average amount of non-undulatory quartz (Fig 5.13B; Appendix, 5.4), 27.29% (standard deviation 3.43%) is low (see discussion p 5). Some of the grains have been replaced in part by carbonate cement. This has provided irregular margins and may have been responsible for totally replacing some grains.

#### 5.2.2b Undulatory quartz

This category includes those grains which do not extinguish in one position of the stage; in some extreme cases extinction may take place through rotation of more than 25 degrees. It is the most abundant type, forming about two-thirds or more of the total quartz irrespective of grain-size. The relation between undulatory and polycrystalline grains (Appendix 5.4, Fig 5.14)

Percent of non-undulatory in monocrystalline quartz

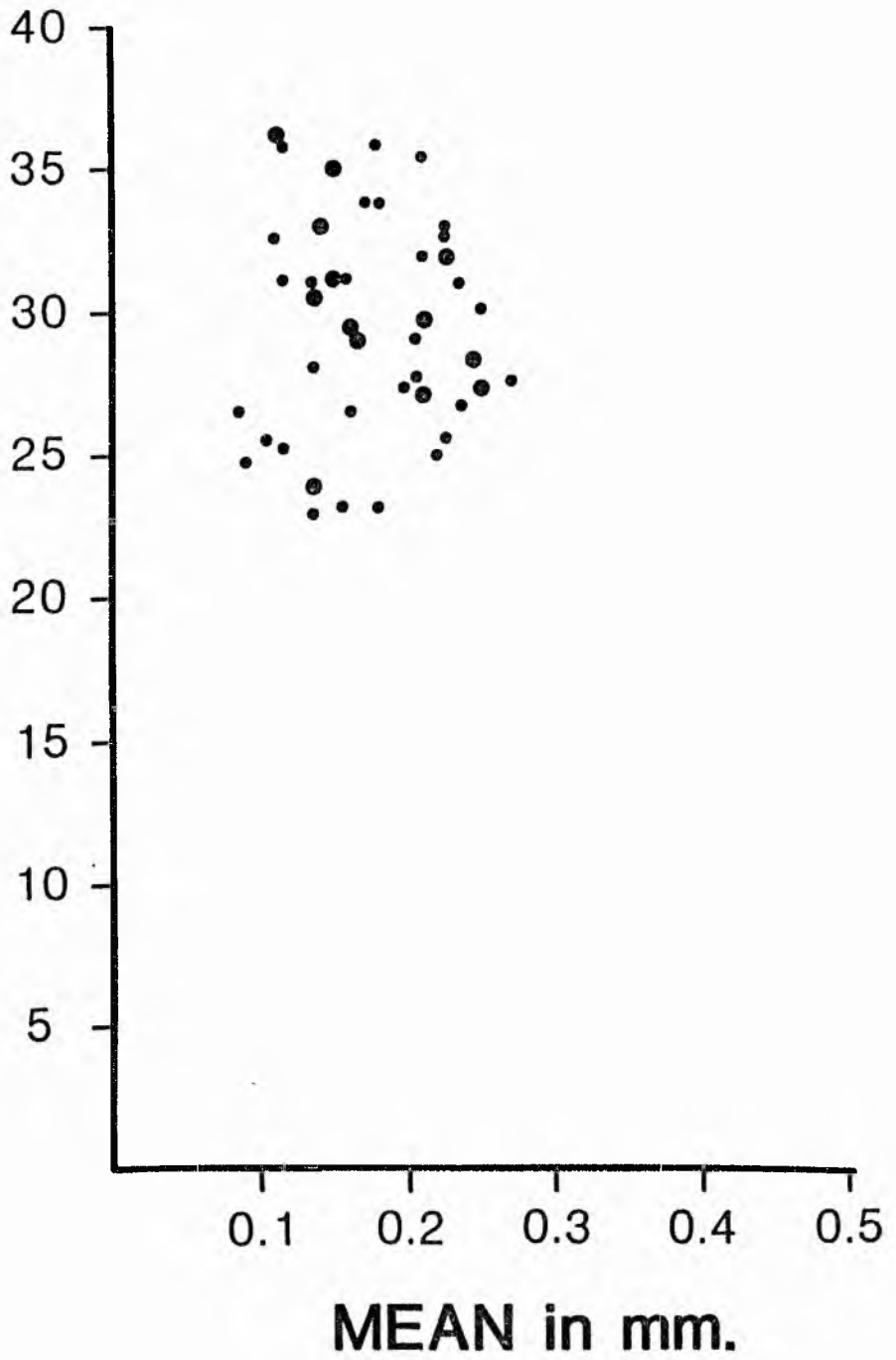


Fig 5.12 Percent of non-undulatory quartz in the monocrystalline quartz fraction of 43 thin-sections of St Monance orthoquartzite sandstone plotted against modal sand-size.

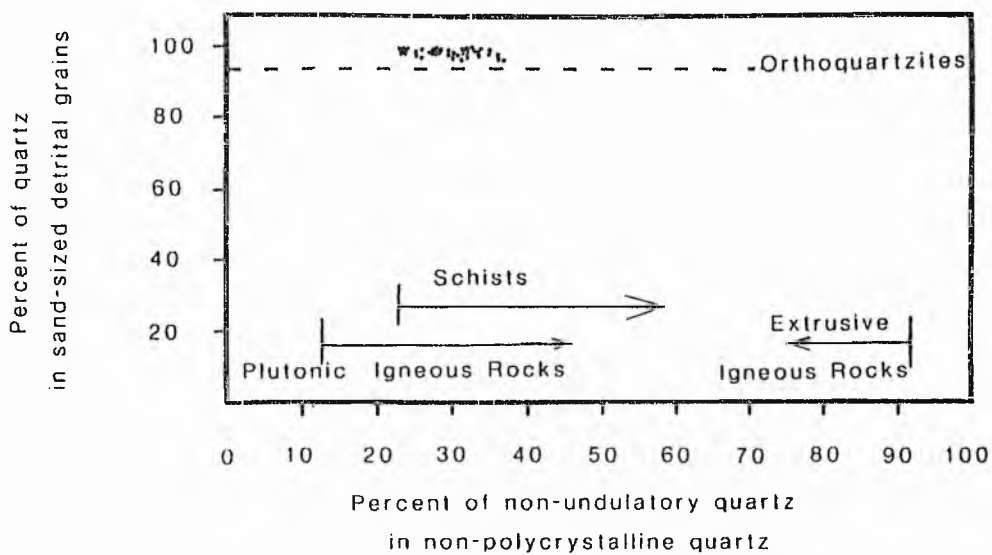


Fig 5.13A. The relationship between quartz in sand-sized grains and non-undulatory quartz in non-polycrystalline quartz fraction of 43 sandstones examined (Blatt and Christie, 1963).

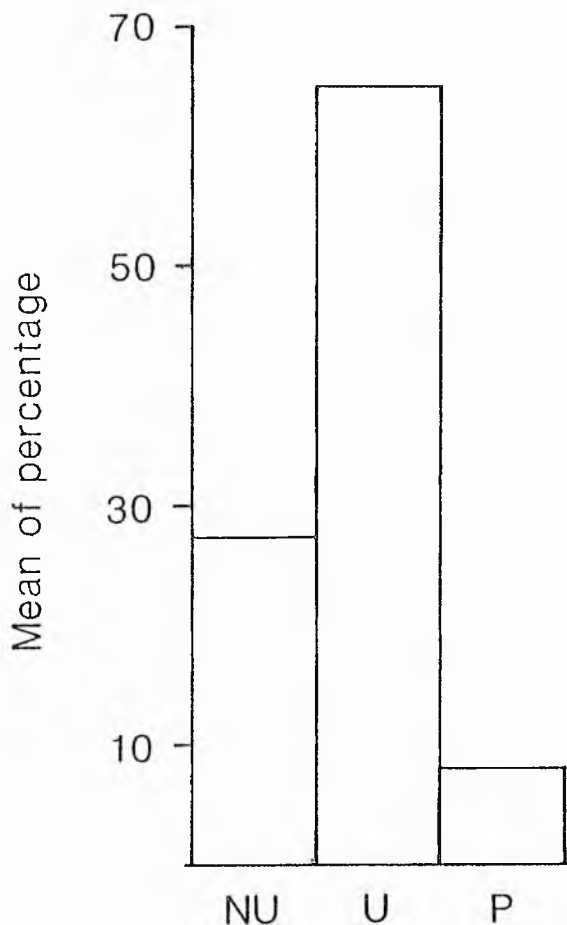


Fig 5.13B. Histogram of the quartz grain types.  
N-U = Non-undulatory; U = Undulatory; P = Polycrystalline.

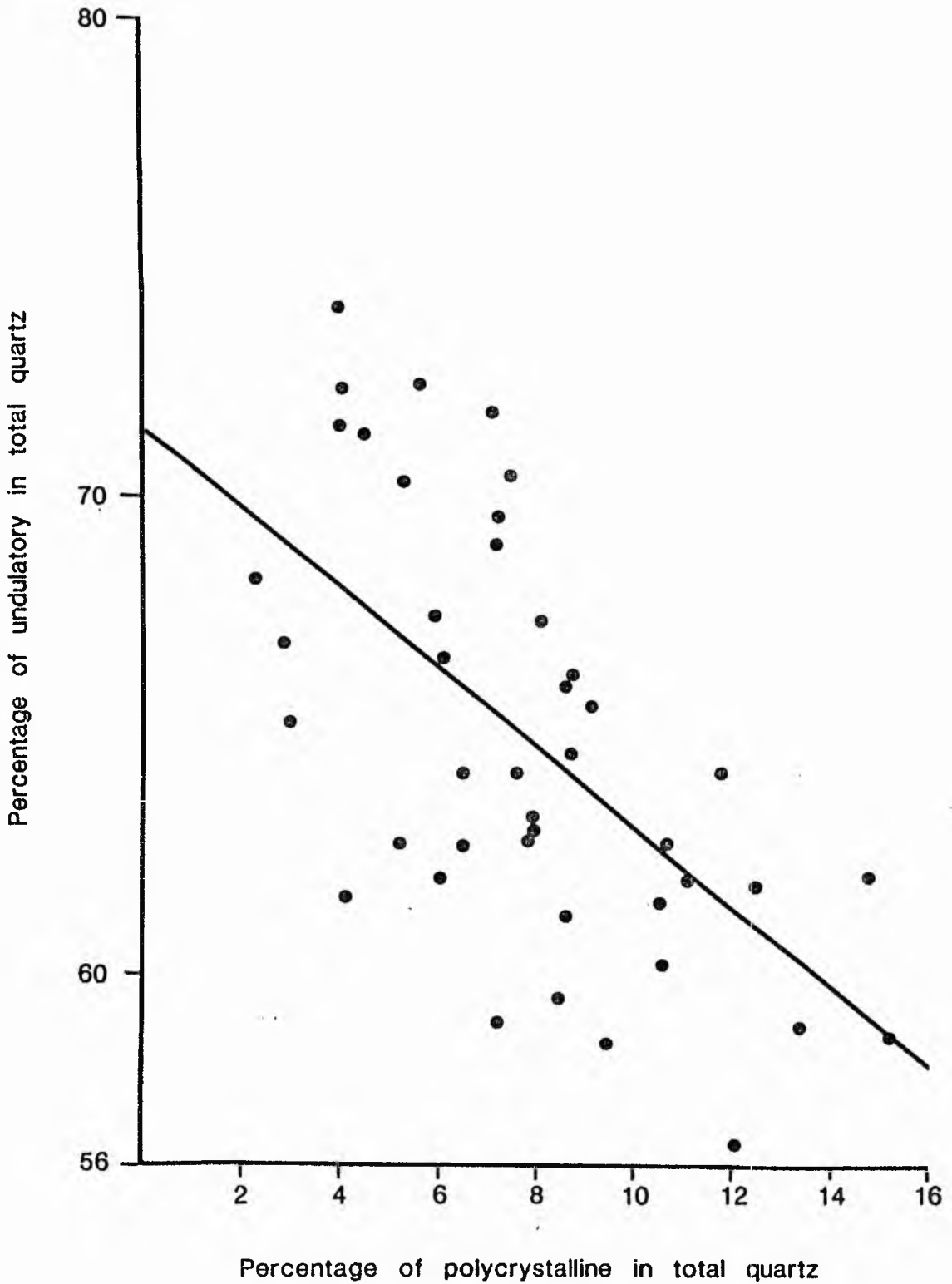


Fig 5.14 The percentage of undulatory quartz in the total quartz of sandstones plotted against percent of polycrystalline quartz for 43 sandstones. Sandstones have high percentages of undulatory (>50%) and have a wide range of polycrystalline quartz percentage. Correlation coefficient  $r$  for all data  $r = -0.598$ .

shows that when undulatory grains are increased the percentage of polycrystalline grain decreases. Plutonic and metamorphic rocks probably supply large amounts of polycrystalline grains to sediments. This low proportion of polycrystalline grains is ascribed to the relative ease with which they break down to monocrystalline grains each of which is undulose. There is no correlation between amount of undulatory grains and clay, carbonate cement, and iron oxide (Fig 5.15).

### 5.2.3 Discussion

The analysis of polycrystalline grains points to a source in low-rank metamorphic rocks.

This does not rule out contribution from plutonic rocks and the few acicular inclusions point to this source. Moreover, the possibility of recycling from older sedimentary rocks has always to be borne in mind. The undulatory quartz is the most abundant type, although, Blatt and Christie suggest that this was probably less stable, and might not be so common in mature sandstones like orthoquartzites. Its presence here may be due to breaking down of polycrystalline grains, and perhaps emphasises the predominance of metamorphic source rocks. The low proportion of non-undulatory quartz is not surprising when it is recognised (Conolly, 1965) that such grains are uncommon not only in metamorphic but also in plutonic rocks.

### 5.3 Feldspar

The percentage of feldspar grains ranges from 0 to 1.8%, with an average of 0.81% (standard deviation 0.43%). In the

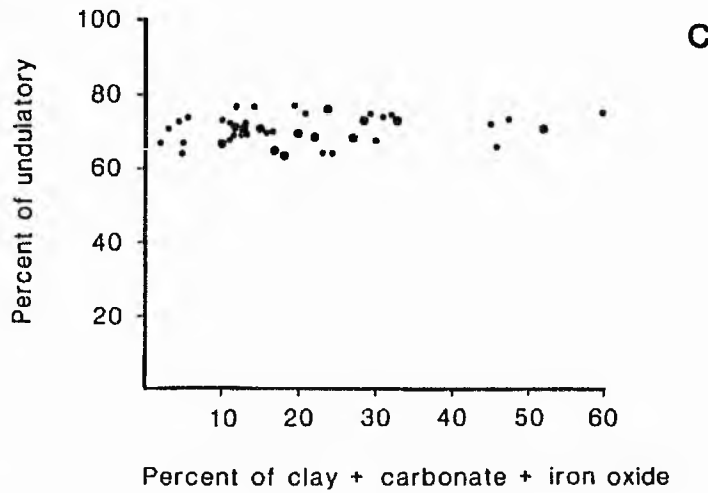
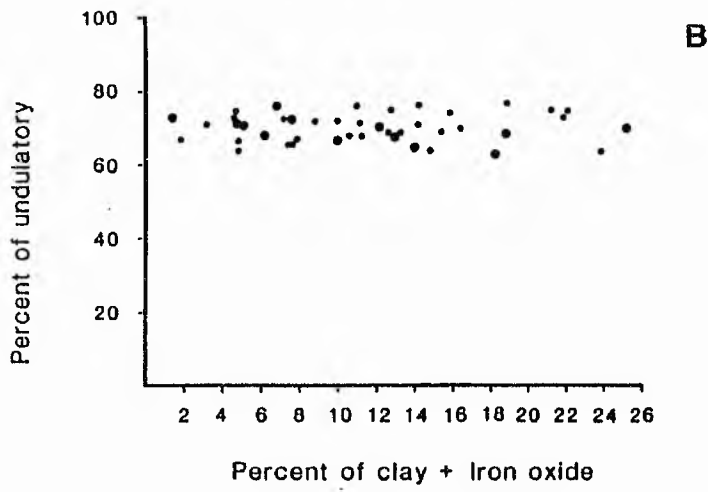
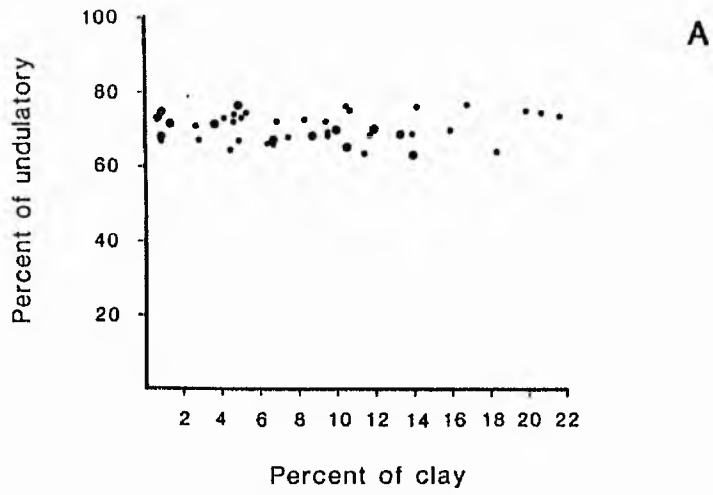


Fig 5.15 Undulatory quartz fraction of sandstone plotted against soft material (clay, iron-oxide, and carbonate).



studied sandstones, plagioclase is the dominant variety in most samples. The average composition of plagioclase is  $An_{35}$  and all the grains range between  $An_{14}$  to  $An_{56}$ , oligoclase to labrodorite. This perhaps suggests that most of the plagioclase occurring as individual grains was derived from metamorphic or plutonic igneous rocks rather than volcanic rocks. Pettijohn (1973, p 37) pointed out that microcline is widely distributed in metamorphic and plutonic igneous rocks. In 1975 (p 203) he mentioned that feldspar of plutonic rocks is more apt to be microcline or orthoclase. The low percentage of feldspar is not original because there are indications that most of the feldspar grains have been destroyed or altered and often show nearly complete or partial dissolution forming pores as irregular pits or elongated tiny pores along cleavage planes (Fig 5.16). The silica released from feldspar may aid euhedral growth of quartz, and the  $K^+$  released from the feldspar goes towards the formation of authigenic kaolinite. Also overgrowths occur in a few feldspar grains and they are found on microcline or on plagioclase (Figs 5.18-5.19).

Carbonate cement may surround and even corrode the overgrowth and the grain (Figs 5.17-5.18) indicating that feldspar overgrowth was formed before carbonate material. Also it was observed that feldspar (plagioclase) may be fractured in the middle and it appears that pyrite was deposited later.

#### 5.4 Rock fragments

Rock fragments are present only as a minor constituent in the rocks and usually never account for more than 1.4% of the

Fig 5.16 SEM photograph showing blocky feldspar, fractured and altered to clay material. Partial dissolution and elongated tiny pores along cleavage planes. Sandstone Unit (S17) - East Side. Scale bar is equal 10  $\mu$ .

Fig 5.17 Photomicrograph showing feldspar with typical plagioclase twinning; quartz overgrowth are present (a). The feldspar has been partly replaced by carbonate cement. Sandstone Unit (T8d) - West side. Crossed polar, x 200.

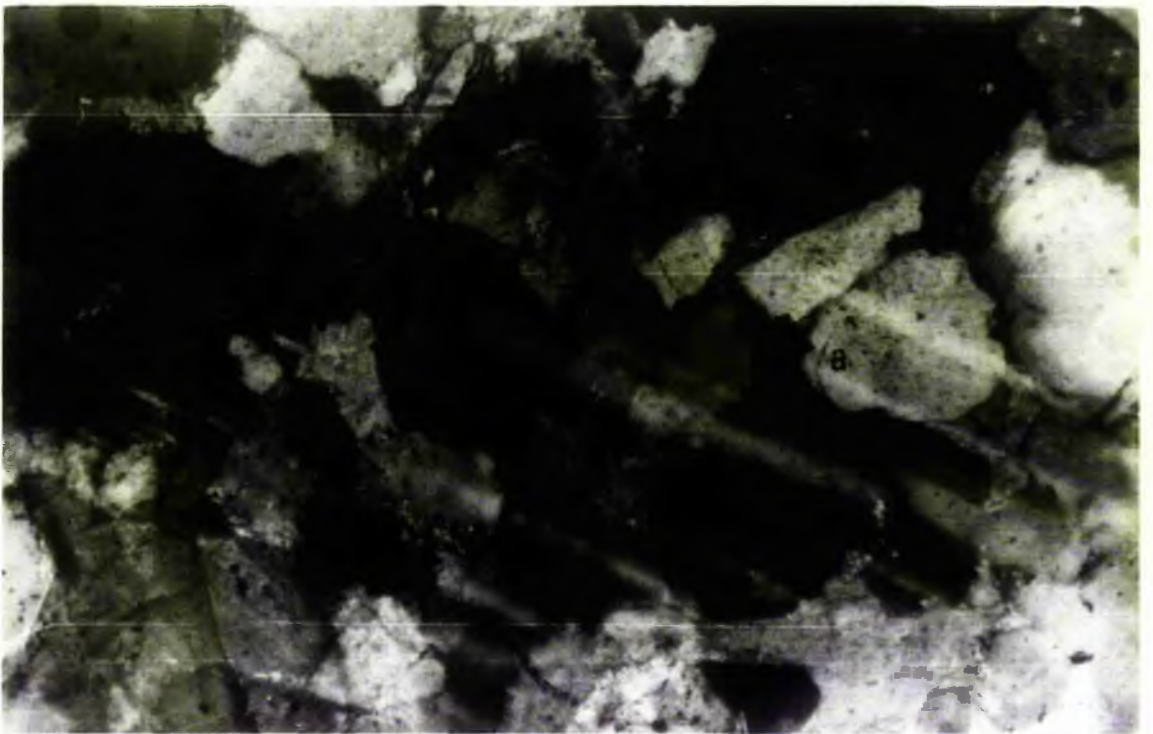
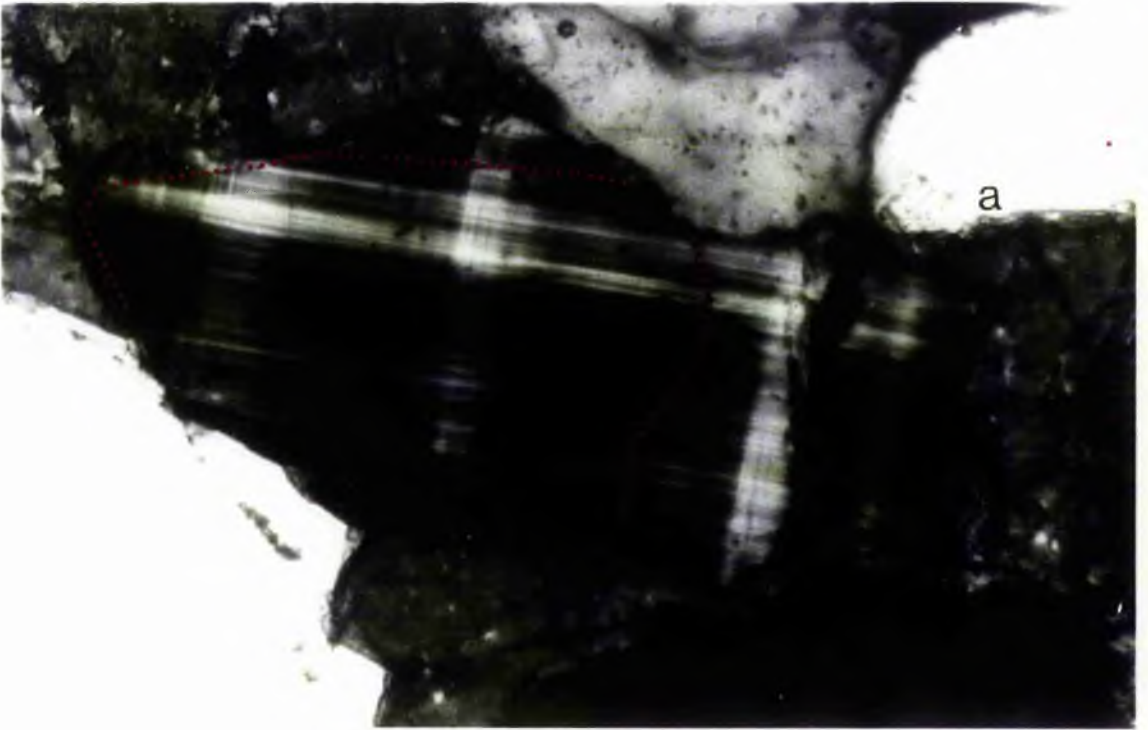


Fig 5.18 Photomicrograph showing plagioclase feldspar with overgrowth (dotted line). Carbonate cement partially replaced the margin of the grain. Sandstone Unit (T8d) - West side. Crossed polar, x 200.

Fig 5.19 Photomicrograph showing feldspar grain (microcline) with overgrowth (dotted line to clarify the original grain). Carbonate cement replaced some of the feldspar grain as well as other detrital grain (quartz) (a). Middle part of Sandstone Unit (E7). West side. Crossed polar, x 100.



whole rock, except one sample in which it is 2.6%. They are igneous rock fragments, rounded-to-subrounded in shape. They are difficult to identify because their minerals are altered, and intergrown. But generally, they are very fine-grained, contain some pale green chlorite, and some other brownish material. They are regarded as rhyolitic in composition.

### 5.5 Heavy minerals

The heavy minerals never account for more than 1% except 2 samples of 1.6% and 3%. Mostly they are rounded-to-well rounded, colourless to purple zircon, and pale green-to-yellowish green tourmaline, in addition, to a few dark brown-to-reddish brown rutiles and apatite. According to Basi (1978 p 163) the rutile indicates a metamorphic origin, and the green variety of tourmaline indicates granite or pegmatite. It is suggested that the source area was metamorphic rocks which also included granite or pegmatite.

### 5.6 Cement

All the sandstones studied in this area contain cement material as iron oxide and/or silica and/or carbonate. The cement varies in amount and there is inverse relation between the amount of cement (carbonate cement) and the amount of clay (Fig 5.20).

#### 5.6.1 Carbonate cement

The amount of carbonate cement varies through the succession. It forms about 47% in one part while in another is

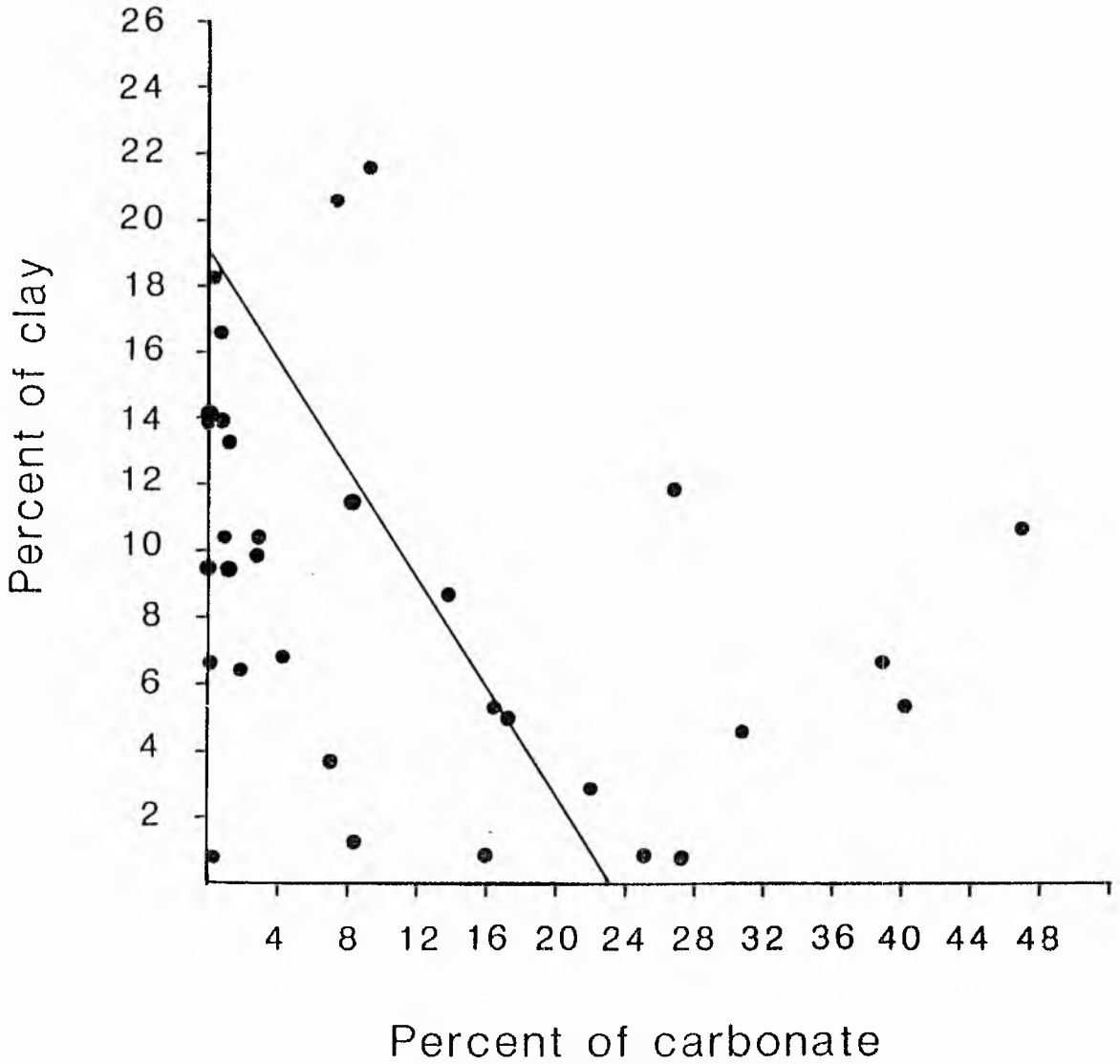


Fig 5.20. Relationship between clay and carbonate. Correlation coefficient  $\gamma$  for all data = -0.352. Reduced major axis regression equation shown:  $y = -0.83X + 19.06$ .

insignificant. Differentiation between the minerals of the carbonate cement was carried out by using the staining method of Dickson (1965), and microprobe analysis. The carbonates are in the form of calcite, dolomite and ankerite, usually ferroan in composition. The most common carbonate is calcite which occurs mostly as a large crystal (Poikilitic texture) filling, enclosing and corroding detrital grains or enveloping quartz overgrowths (Figs 5.21, 5.22). Carbonate may be recognized under SEM by its rhombohedral cleavages. One set of cleavages is seen or more (Figs 5.23A, B).

#### 5.6.2 Silica overgrowth

These sandstones always contain at least a small amount of secondary silica occurring as overgrowth. This can often be recognized in thin-section by a thin dust line in both mono- and -polycrystalline quartz (Figs 5.24 A, 5.25). There are 3 types of overgrowth, normal, uneven, and double overgrowth.

Uneven overgrowths are less common than normal overgrowths. It is suggested that the normal overgrowth formed first, due to the highest porosity and the lowest degree of compaction, and hence the overgrowth had sufficient space in which to develop normal forms, the overgrowths of adjacent grains meeting along the face contact (Fig 5.27A) and due to pressure solution (pressolving) uneven overgrowth formed later (Fig 5.26, 5.27B). Sometimes overgrowth has formed in two stages (Fig 5.28), each stage defined by dust line. Sanderson (1984) pointed out that multiple overgrowths may be the result of two (or more) generations of cement growth separated in time by episodes of



Fig 5.21 SEM photograph showing carbonate cement (c) enclosing and corroding the quartz grain overgrowth (a). Middle part of Sandstone Unit (E7) - West side. Scale bar is equal 40  $\mu$ .

Fig 5.22 SEM photograph showing quartz overgrowth (a) corroded and enclosed by carbonate cement. Two types of carbonate: calcite (c) and dolomite (d). Sandstone Unit (T3). West side. Scale bar is equal 20  $\mu$ .

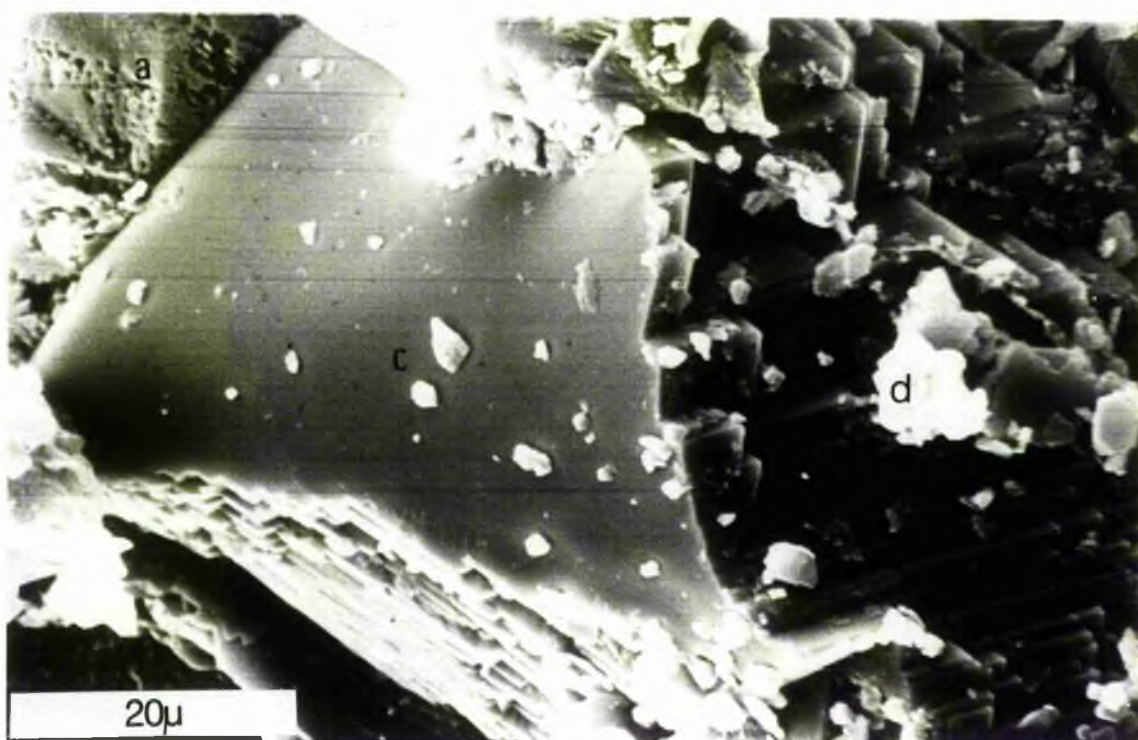
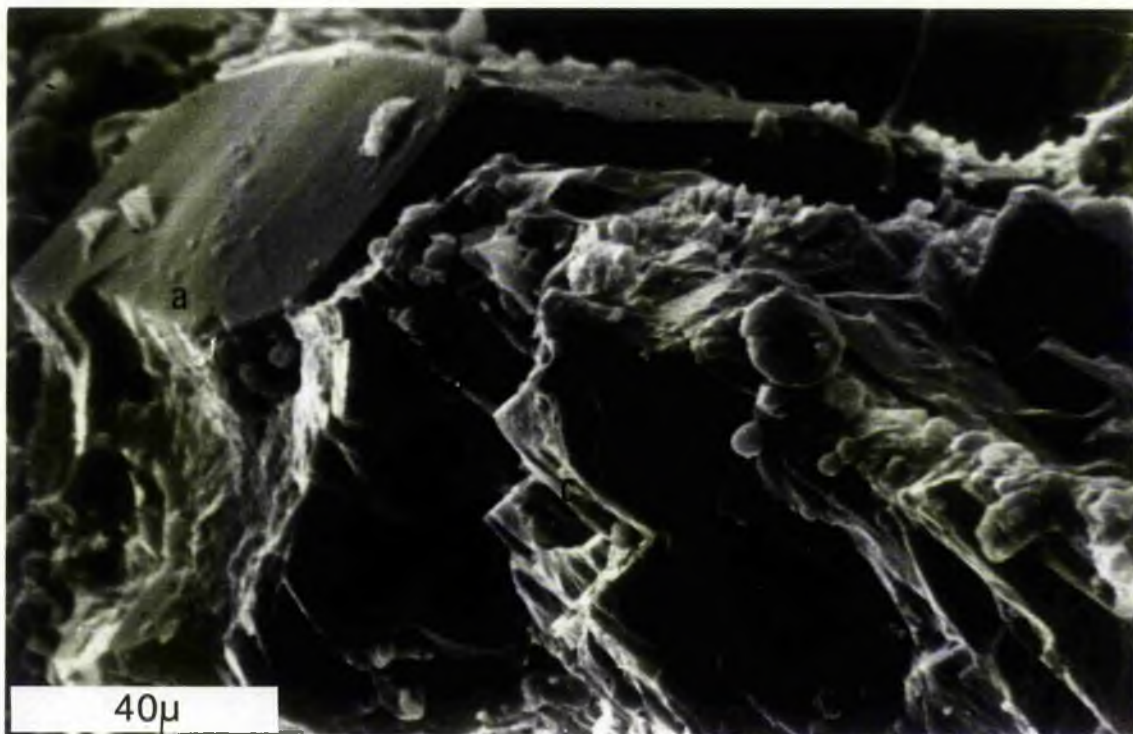
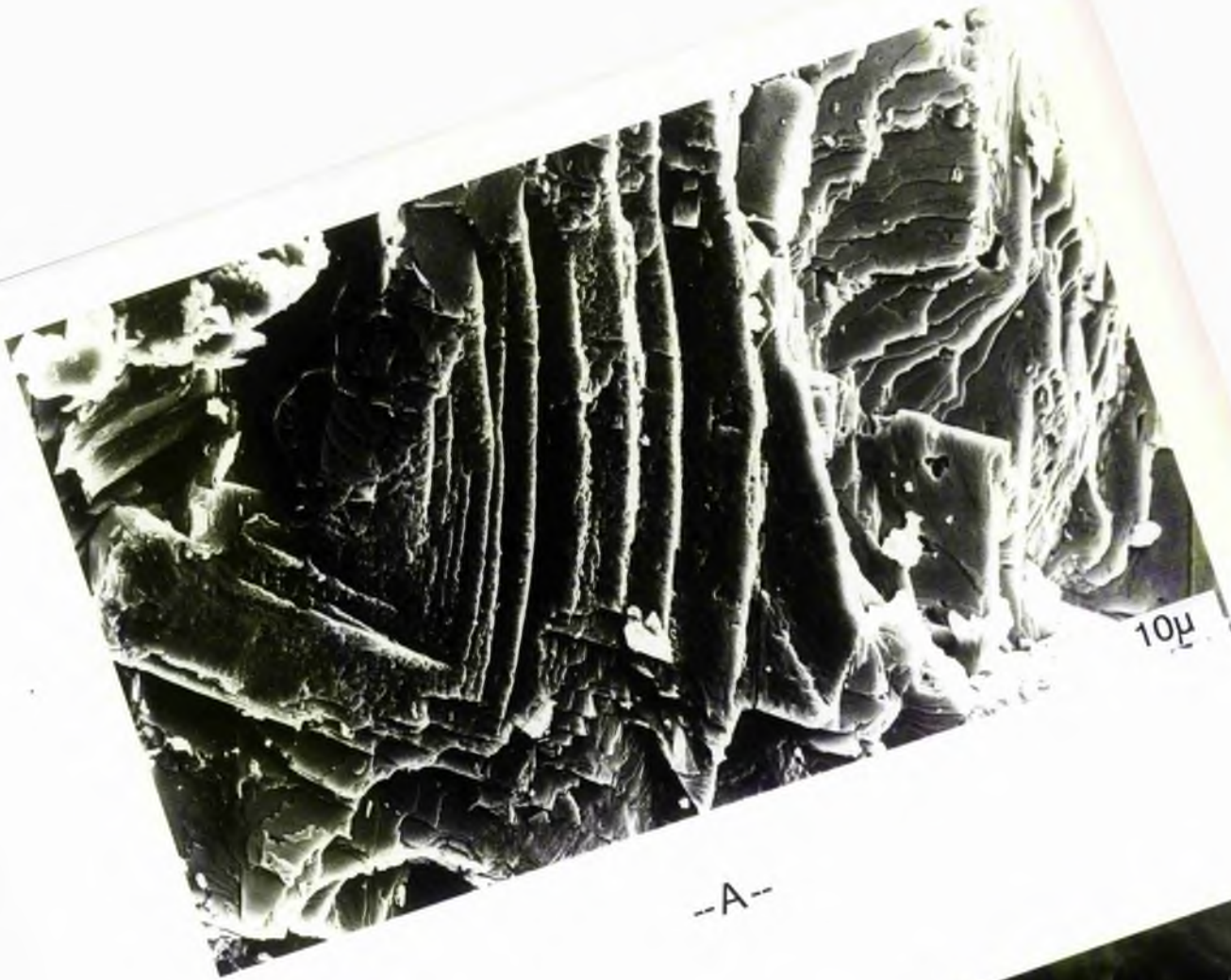
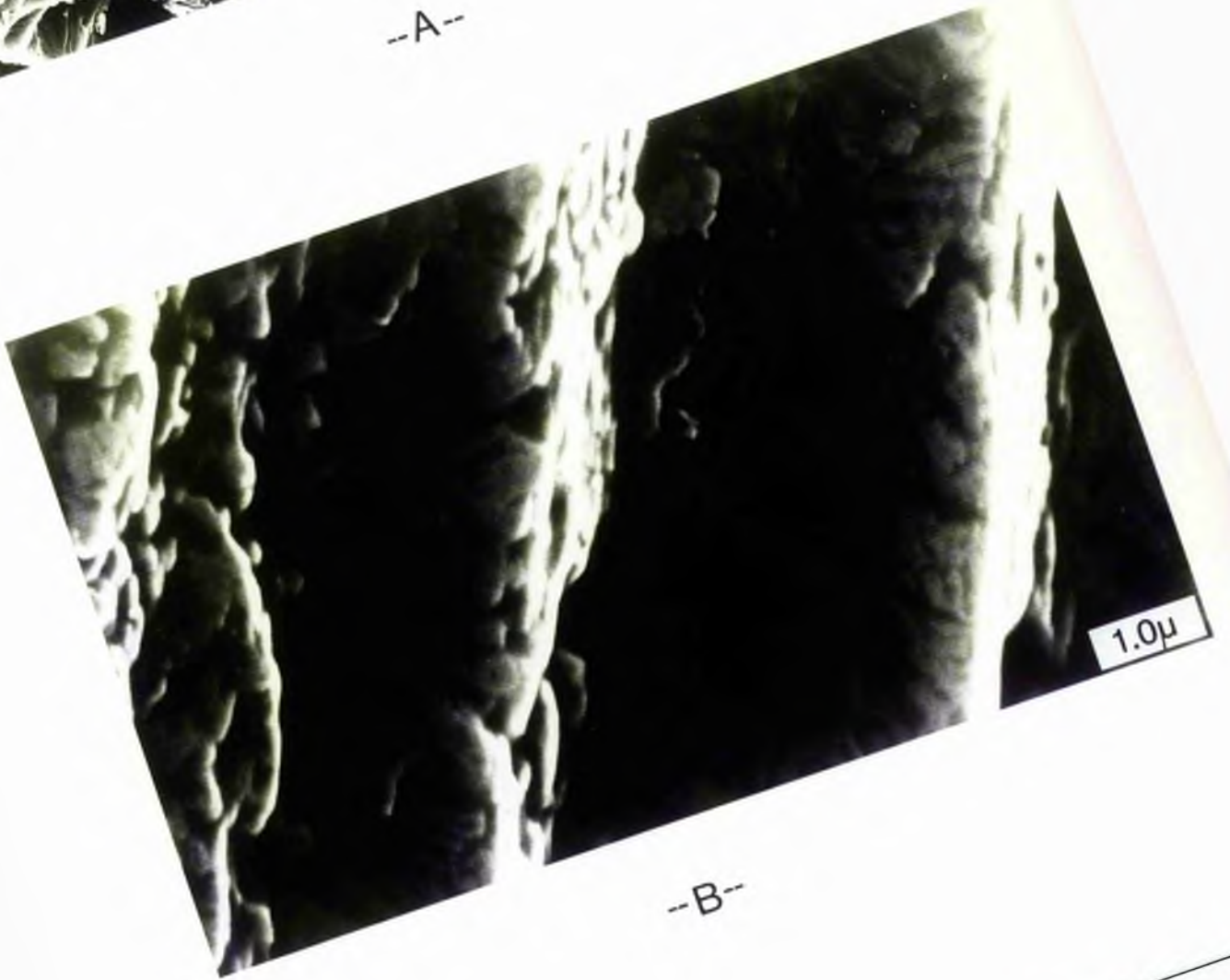


Fig 5.23A, B. SEM photograph showing poikilotopic calcite cement, with more than one set of cleavages. In (B) high magnification view of part (A) showing microcrystals. Sandstone Unit (F5b). East side. Scale bar is equal 10  $\mu$  and 1.0  $\mu$  respectively.



--A--



--B--

Fig 5.24 Photomicrograph showing groups of quartz grains with overgrowth, pressolving has been formed later and lead to dissolve some part of silica overgrowth. Sandstone Unit (B7) - West side. Crossed polar, x 250.

Fig 5.25 Photomicrograph showing polycrystalline quartz grain, bimodal size distribution, with overgrowth. Carbonate cement replacement formed later. Sandstone Unit (B7). West side. Crossed polar, x 125.

Fig 5.26 Photomicrograph showing normal overgrowths formed on 4 quartz grains and coalescing to form triple junctions. Sandstone Unit (T6a) - West side. Crossed polars, x 200.

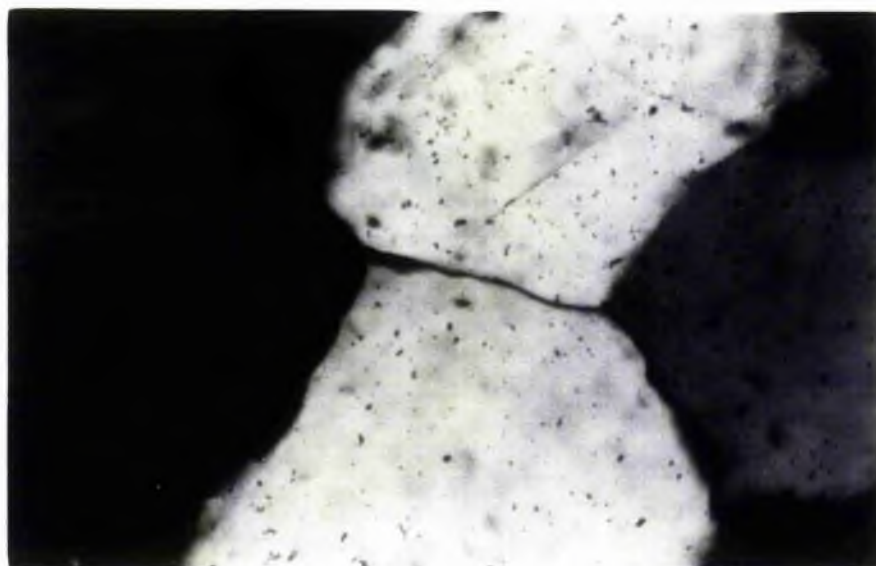
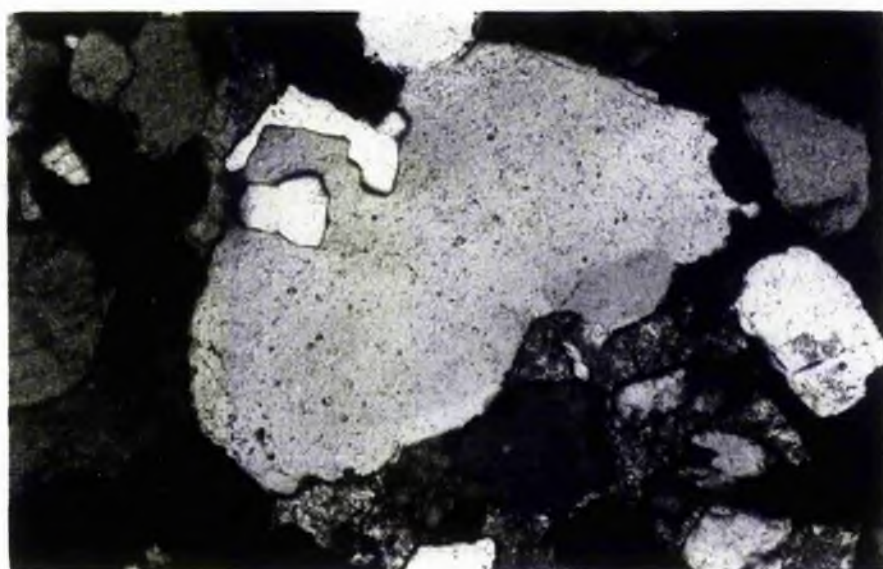
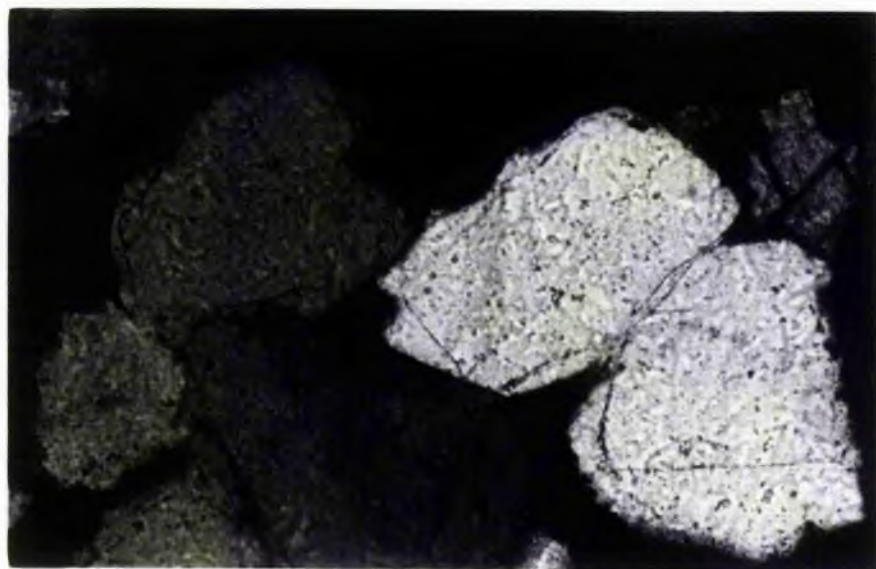
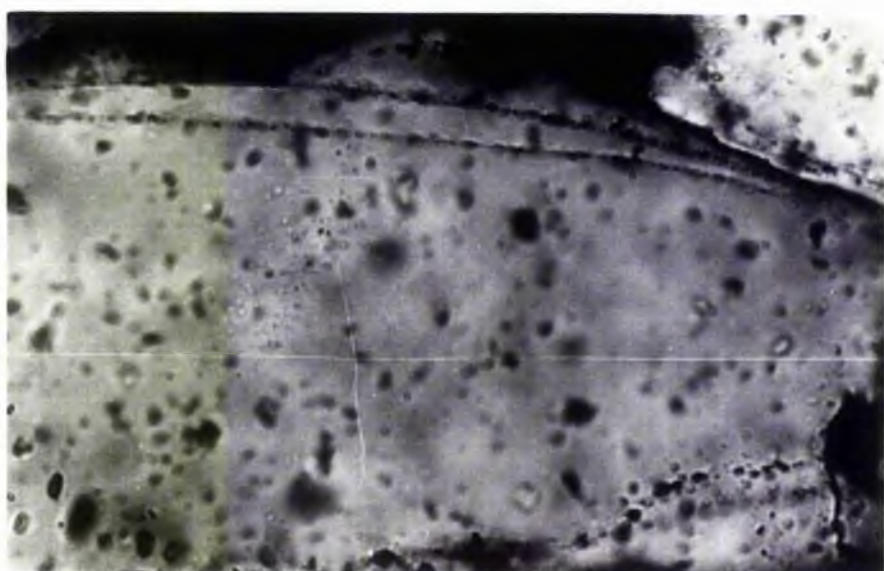
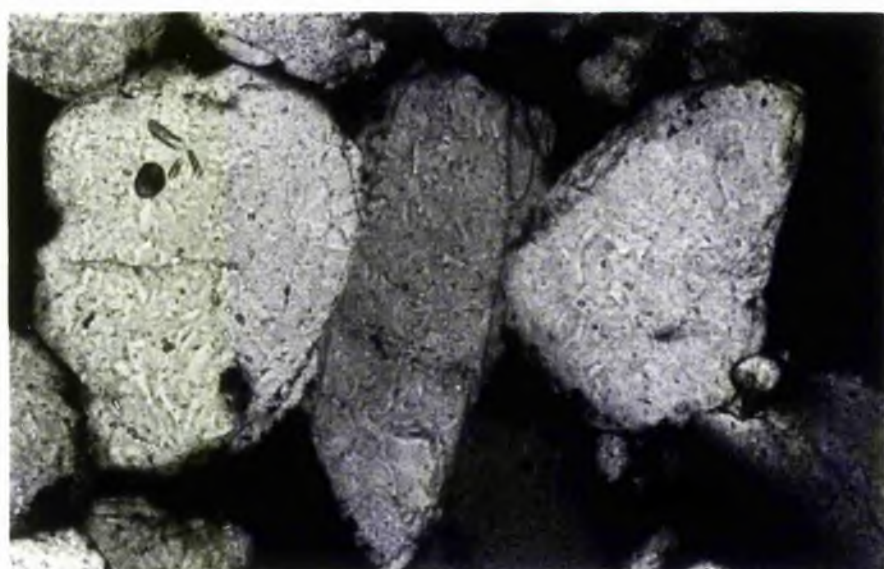
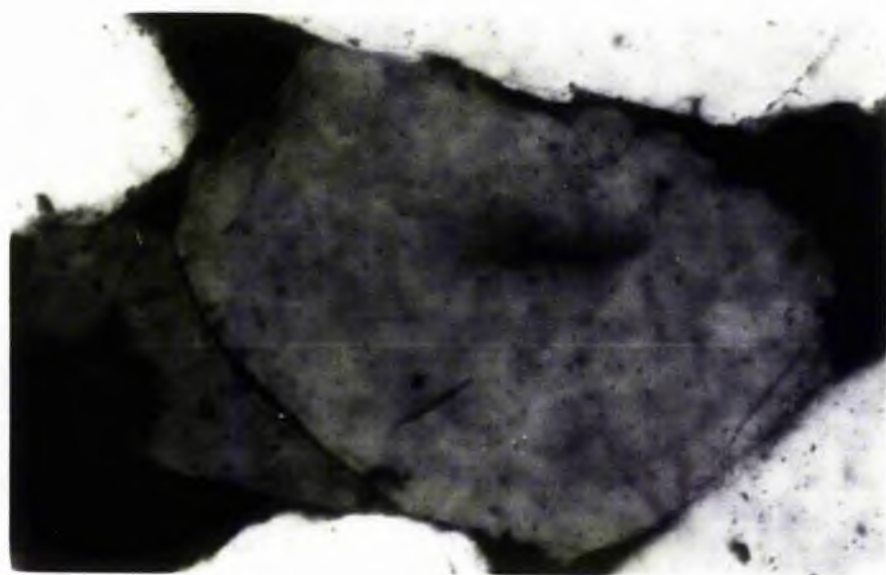


Fig 5.27A Photomicrograph showing uneven quartz overgrowth. The silica cement in (a) more than other parts as adjacent to the grains. This is either due to pressolving or the space in (a) was more than other parts around the grain. Sandstone Unit (S24) - East side. Crossed polars, x 100.

Fig 5.27B Photomicrograph showing uneven quartz overgrowth due to pressolving after silica overgrowth formed. Sandstone Unit (B7) - West side. Crossed polars, x 250.

Fig 5.28 Photomicrograph showing quartz grain with double overgrowth define by dust line. Fluid inclusion also present. Middle part of Sandstone Unit (B7) - West side. Crossed polars, x 200.





detrital abrasion.

The morphological features of silica overgrowths appear very well under the SEM as prism or pyramidal faces. The process leading to the formation of overgrowth started with early overgrowth of isolated, not very well defined crystal and developed in the following stages:-

- a) Isolated incipient not well developed overgrowth (Fig 5.29).
- b) Well developed crystals with cavities (Fig 5.30).
- c) Merging and overlap leading to the formation of larger area of prism face (Fig 5.31).
- d) Formation of euhedral quartz crystal comprising hexagonal prisms (Fig 5.32).
- e) Complete layers; the development of this stage depends on the availability of adequate pore space to form a shells of quartz (Fig 5.33).

### 5.6.3 Iron-oxide

This reddish-brown material was observed in thin-section surrounding the quartz grain before overgrowth (Fig 5.34) as well as in and around the carbonate cement. SEM examination indicates that the particles appear as rounded packets of flakes or as crystals of hematite (Fig 5.35A, 5.35B).

Fig 5.29 SEM photograph showing that quartz grain not well developed overgrowth, as in (a). Authigenic kaolinite (Kao) seems to be formed simultaneously with overgrowth. Sandstone Unit (S21b) - East side. Scale bar is equal 20  $\mu$ .

Fig 5.30 SEM photograph showing well-developed but incomplete crystal faces representing the second stage in overgrowth development. Sandstone Unit (F5b) - East side. Scale bar is equal 10  $\mu$ .

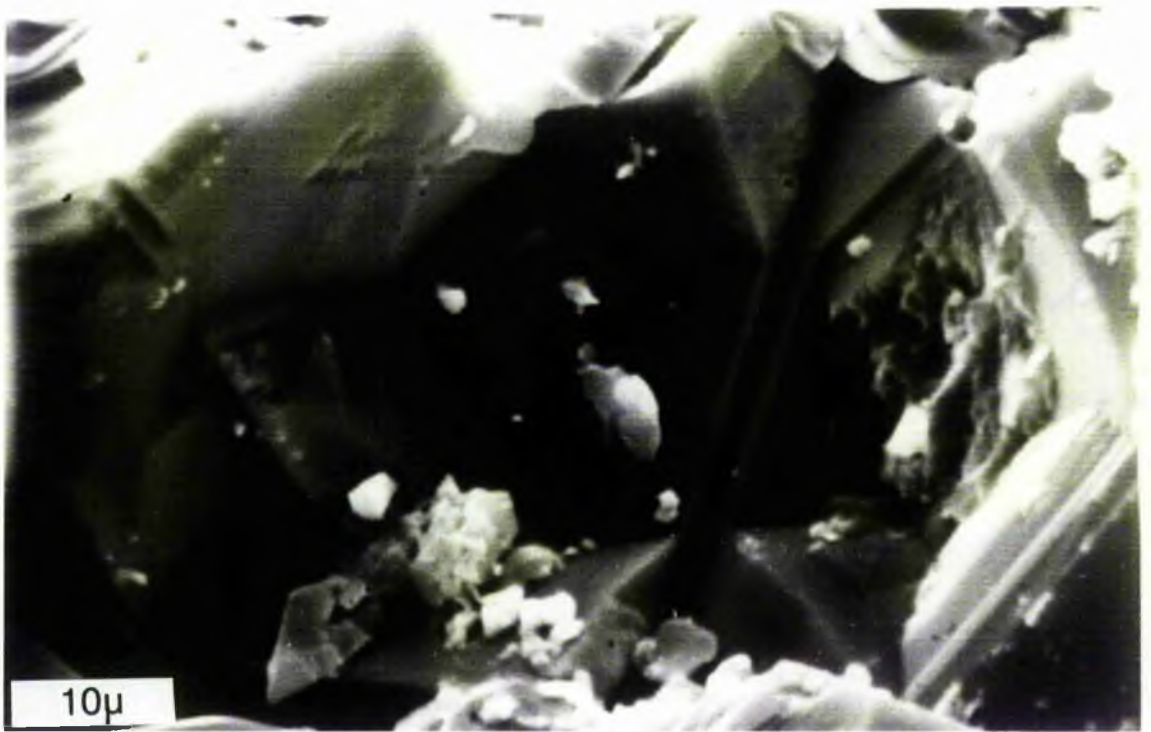


Fig 5.31 SEM photograph showing multiple overgrowth leading to the formation of larger area of prism crystal faces (Third stage).  
Upper part of Unit (B7) - West side. Scale bar is equal  
20  $\mu$ .

Fig 5.32 SEM photograph showing the fourth stage  
of formation of euhedral quartz crystals, comprising a  
hexagonal prism and pyramid faces. Middle part of Sandstone  
Unit (B7) - West side. Scale bar is equal 20  $\mu$ .

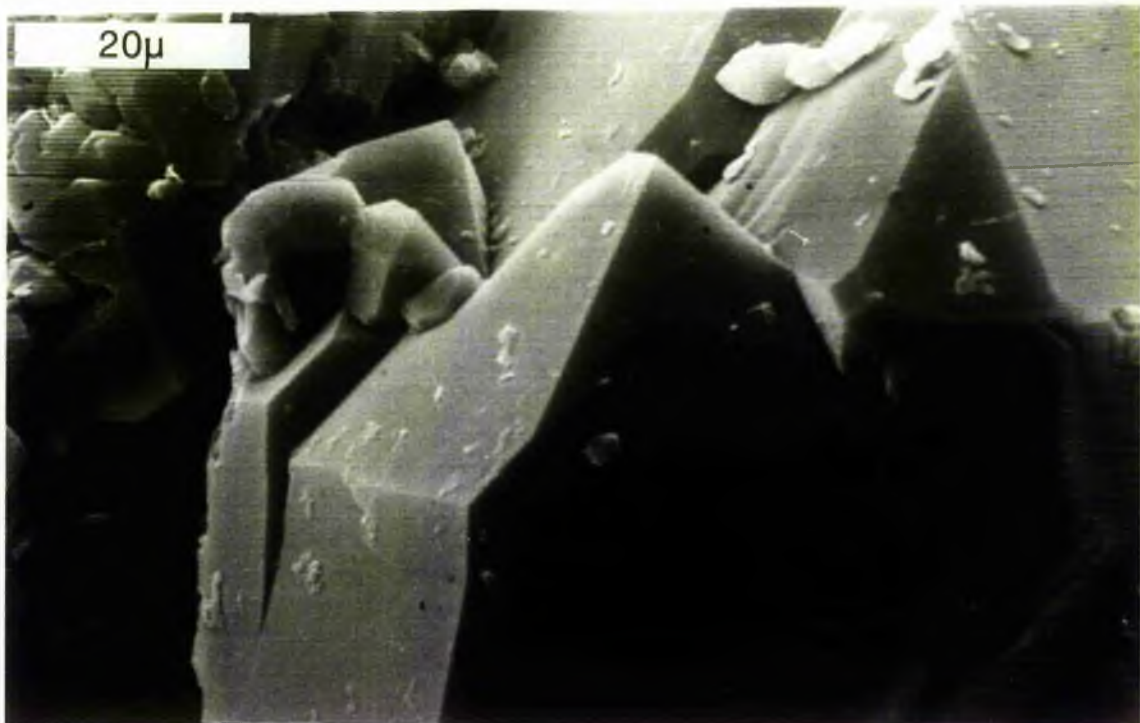
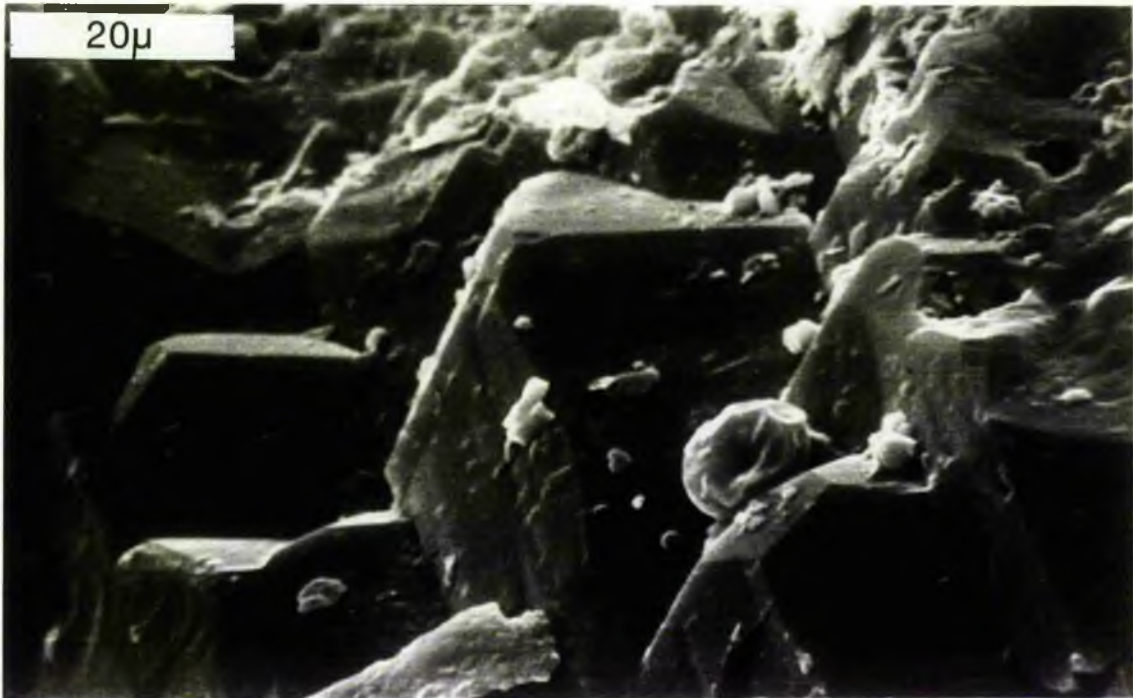


Fig 5.33 SEM photograph photomicrograph showing quartz overgrowth as complete layers. The last stage. Sandstone Unit (S21d) - East side. Scale bar is equal 10  $\mu$ .

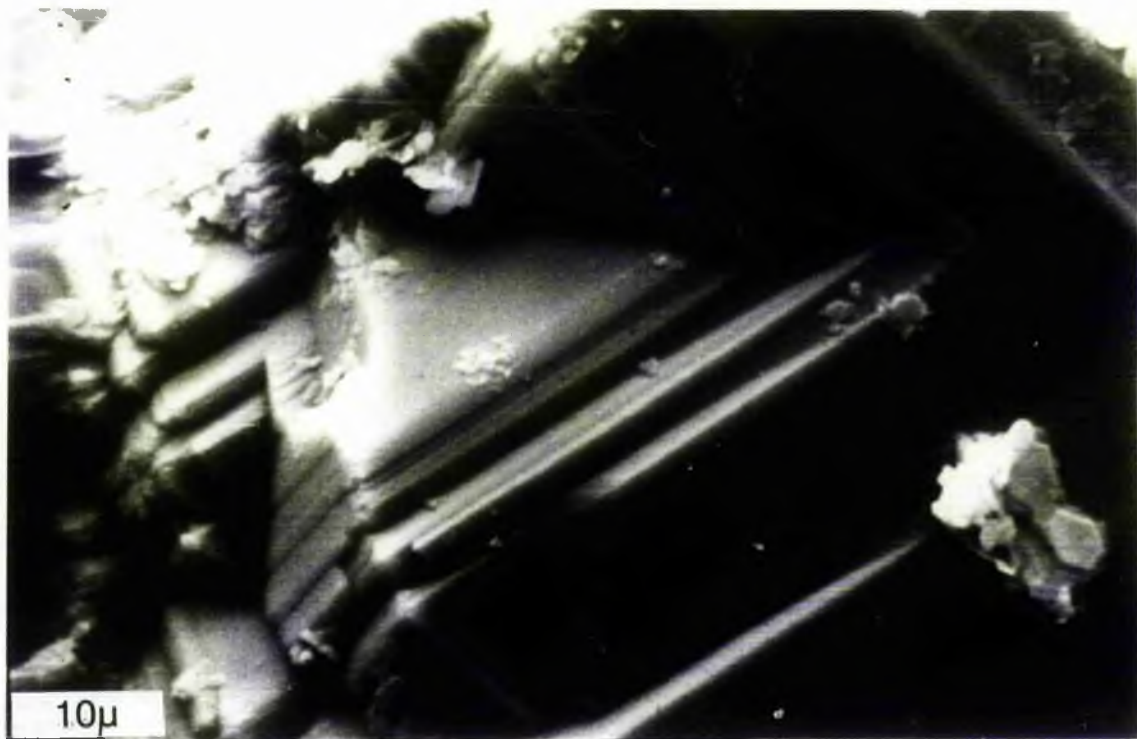


Fig 5.34 Photomicrograph showing thick reddish-brown material surrounding the original quartz grain and silica cement formed later. Sandstone Unit (B7) - West side. Ordinary light, x 500.

Fig 5.35A SEM photograph showing rounded flakes of iron oxide. Sandstone Unit (T7c) - West side. Scale bar is equal 10  $\mu$ .



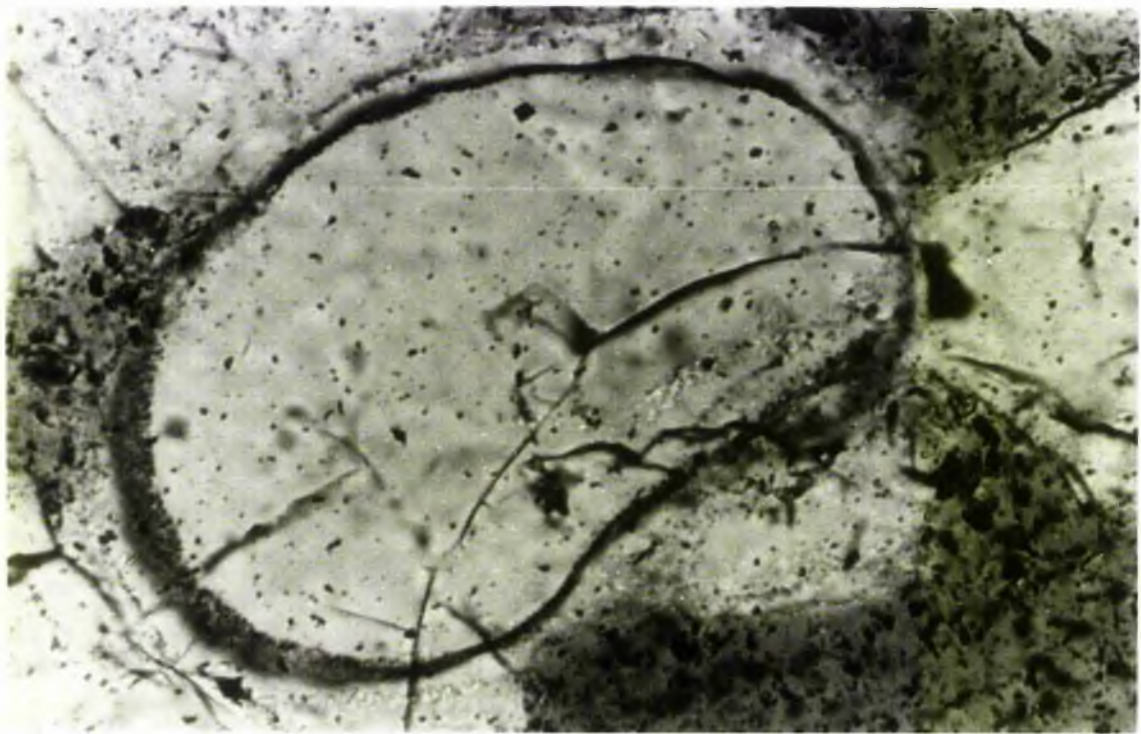
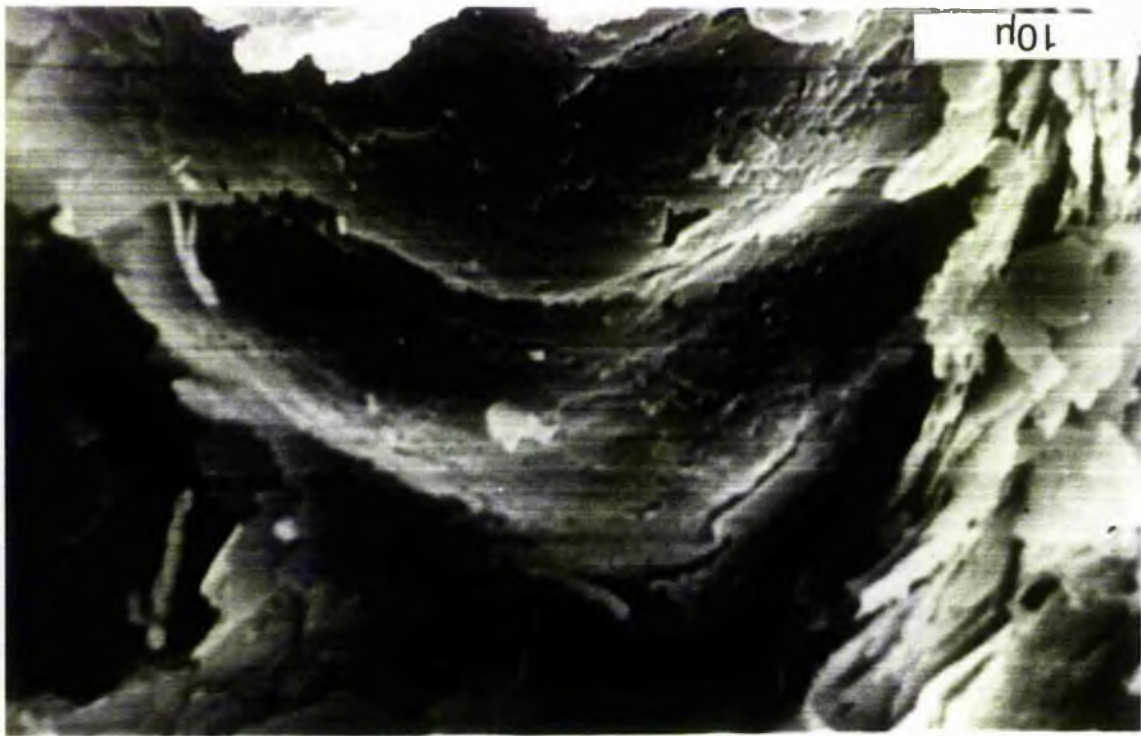
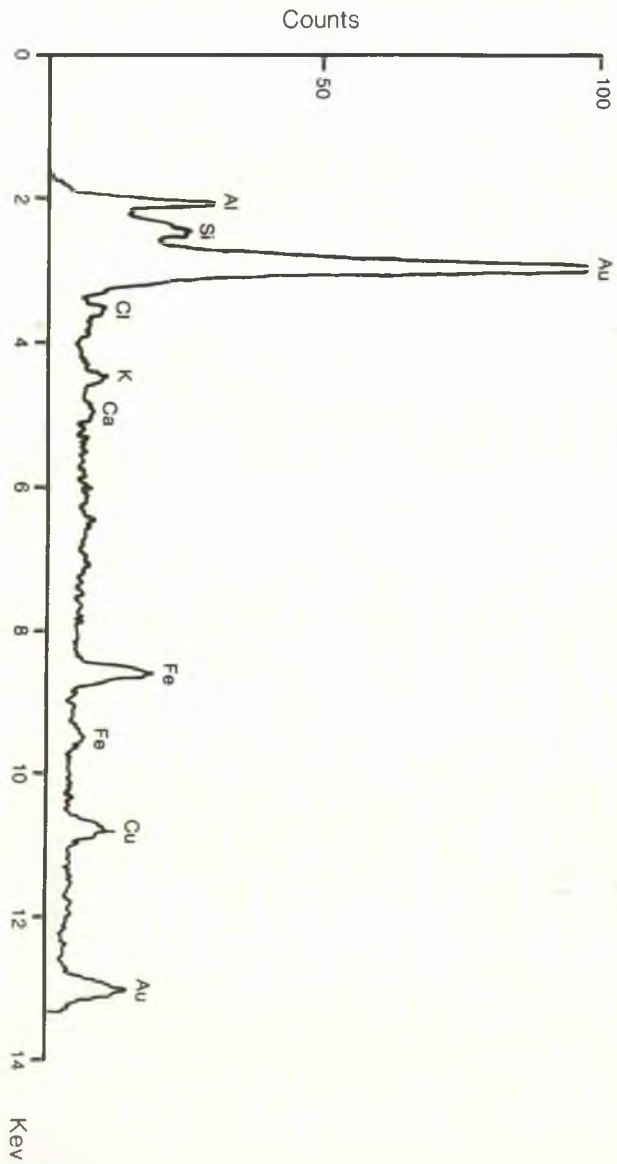


Fig 5.35B SEM photograph showing authigenic hematite crystals.

EDX analysis shows the major element is Fe, but other elements here are not constituents of the hematite, and are contaminants from either underlying or adjacent minerals.

Sandstone Unit (L3) - West side. Scale bar is equal 1.0  $\mu$ .





#### 5.6.4 Cement relationships

Petrographic study of many thin-sections of sandstones reveals cements of carbonate, silica, and iron-oxide. Their relations indicate:-

a) Sometimes the iron-oxide defines the original grains below the overgrowths of silica, which indicates that iron-oxide formed before the silica overgrowth.

b) Quartz grains with overgrowth are embedded in the carbonate cement. It may be suggested that the grains have been secondarily enlarged, before the formation of the carbonate cement.

c) Corrosion of the margins of quartz overgrowths and etching of feldspar grains by carbonate cement. Some carbonate occurs as tongues into quartz overgrowth, indicating replacement of quartz overgrowth by carbonate.

d) Patches and spots of iron-oxide inside and around the carbonate cement indicating that this iron-oxide formed later.

The sequence generally of the sediments changes upward from black shale (with organic content) above limestone beds, to grey siltstone then to sandstones, in other words the colour is dark to grey in fine sediment, and yellowish-brown in coarse sediments. It is suggested that in fine sediments the water circulation is limited. The disintegration of organic material probably consumed the oxygen and a reducing environment was produced. This is supported by the presence of pyrite in the shale and even in some sandstones. In coarse sediments and at a

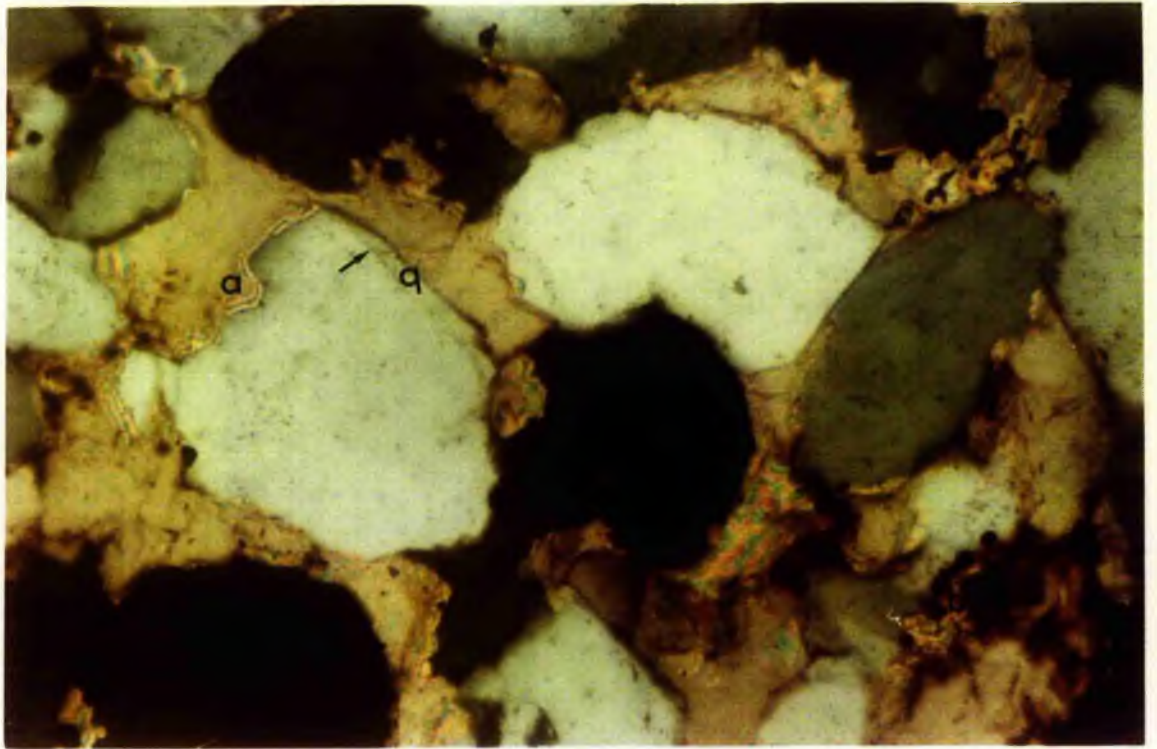
shallow depth below the sediment/water interface there was enough water circulation for oxidising condition to exist. It is suggested also that the pore water was originally rich in ferrous iron (probably migrated from the underlying shales), or iron was released by diagenetic alteration of iron-oxides. Therefore, the iron might have been deposited as ferric oxides in the sandstones. Deegan (1970) indicated that iron was precipitated from solution in oxidizing conditions forming a primary diagenetic iron oxide cement in the lower Carboniferous rocks, Kirkcudbrightshire, Scotland (see also Walker 1967, McBride 1974).

The silica cement is represented by quartz overgrowths on quartz grains and is often defined by dust or iron-oxides. It is best developed in coarse-grained sandstones. Aalto (1972) indicated that the quartz forming overgrowths in orthoquartzite sequences (Devonian-Tertiary), Columbia, may have been derived from solution of fine quartz; such an origin may be applicable to the Lower Limestone Group Sandstones. Under the microscope detrital quartz is seen to have been completely replaced by carbonate as shown in (Fig 5.36). Such large-scale replacement material may be the major source of the silica in the subsurface.

The solubility and precipitation of minerals is a function of various factors (pH, temperature, pressure, and permeability) but the precise controls are still a matter of debate (Correns 1950, Alexander et al, 1954, Krauskopf, 1956, Okamoto et al, 1957, and and Sharma, 1965). At shallow depth in which the pore fluids were slightly acid ( $\text{CO}_2$  formed by bacterial decomposition

Fig 5.36 Photomicrograph showing order of precipitation of cement.

The formation of dust line (arrow) followed by quartz overgrowth (q), then carbonate cement filling pores and replacing the detrital grains (a), later iron oxide as spots inside carbonate cement (b) formed. Sandstone Unit (T8d) - West side. Crossed polars, x 250.





of organic matter), the silica is precipitated as overgrowth (Sharma, 1965). As  $\text{CO}_2$  was depleted at greater depths and higher temperatures, pH rose encouraging carbonate to be precipitated. In some samples the carbonate material cement forms patches through the rock.

Twelve thin-sections of sandstones were selected for point counting to study the relations of calcium carbonate and overgrowths. Samples were chosen from different locations and different environments. There is no correlation between the percentage of carbonate and the percentage of quartz with overgrowths (Fig 5.37).

Sometimes the calcite is surrounded by an iron oxide. The analysis shows that within a single patch of calcite cement surrounded by iron oxide, the part of calcite adjacent to the iron oxide is ferroan. Neal (1969) pointed out that the brownish weathering surface of limestones is the result of iron oxide produced by destruction of ferroan calcite in the Blackjack Creek Formation (Pennsylvanian). Al-hashimi, et al, (1973) indicated that the existence of iron hydroxide together with rhombohedral calcite in the rusty crusts and the absence of both in the unweathered part of dolostone suggested that the iron oxide/hydroxide was formed by the oxidation and hydration of the ferrous iron in the dolomite. They added that this process takes place when the carbonate units are in contact with the present day sea water, as is indicated by the predominance of rusty crust in the coastal exposure compared with inland exposures. They indicated that oxidation of ferrous iron and its hydration to form limonite with consequent gradual breakdown of the dolomite

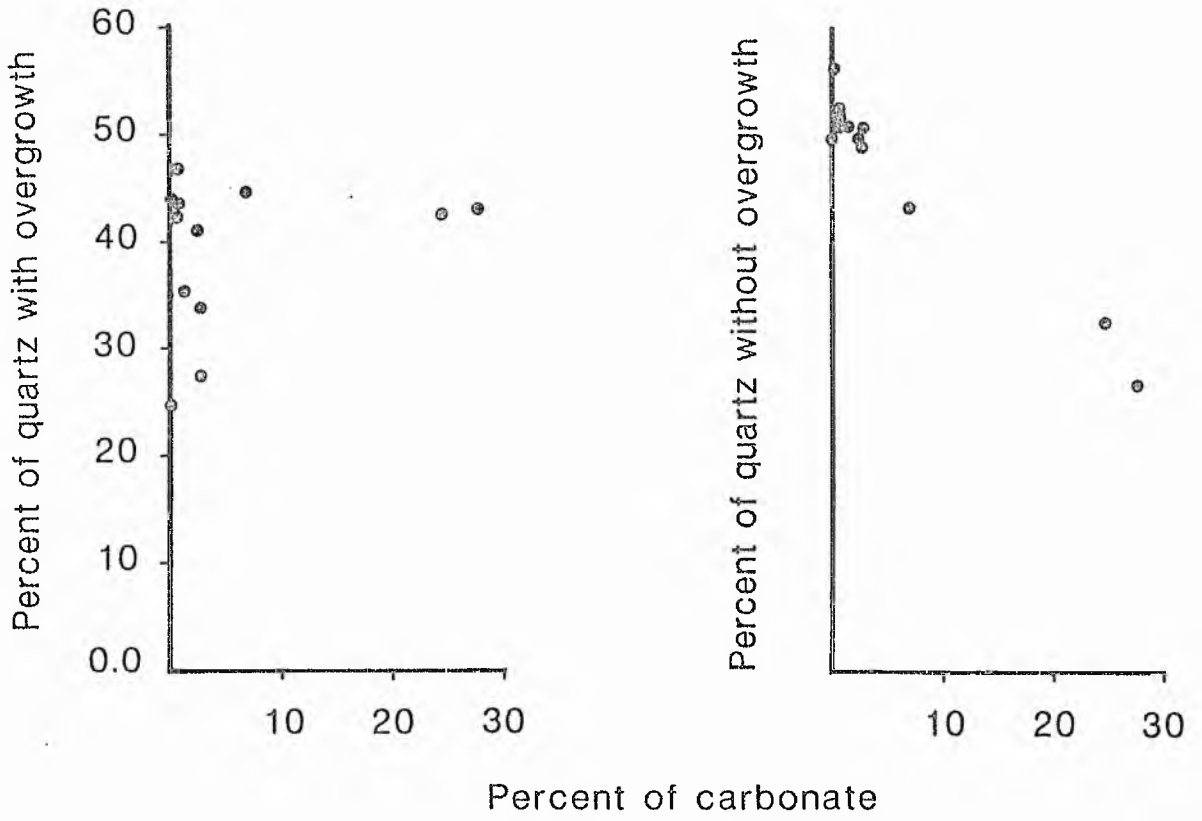


Fig 5.37. Chart showing the relationship between carbonate and quartz grain with and without overgrowth.

crystals can be produced by fresh water (ground water circulation) and the reaction is faster with sea water. Probably the ferroan calcite cement undergoes a similar type of destruction to the ferroan dolomite, the leached ferroan calcite iron being oxidized to iron oxides by reaction with sea water and by the oxygenated ground water.

#### 5.6.5 Conclusions

1) Three types of mineral cements are recognized including carbonate cement (calcite, dolomite and ankerite, often ferroan) silica as secondary overgrowth, and iron oxide. The diagenetic sequence of cement is:-

- (a) Iron oxide
- (b) Quartz overgrowth
- (c) Carbonate cement
- (d) Iron oxide

2) Some iron oxide might have been deposited from solution as ferric oxides in the sandstones under oxidizing condition soon after deposition.

3) Quartz overgrowths were formed when the pore fluids were slightly acidic, and are normally defined by dust or iron oxide and embedded in the carbonate cement.

4) The edge of quartz grains are often corroded where in contact with carbonate cement many grains have been nearly completely or even completely replaced by carbonate and only ghost sandstones with the carbonate testify to their former presence.

5) The destruction of ferroan calcite cement results in the

formation of the late iron oxide cement as spots in and around the carbonate cement.

### 5.7 Micas and Clay minerals

These can be considered together, because they are all closely related in chemical composition. It is frequently impossible to note any discontinuity in size between large flakes, which are easily identifiable as detrital micas, and the very fine grained interstitial clay characteristic of many sandstones. Indeed examples of large detrital micas may be found altering to clay minerals. Nevertheless, there does seem to be some virtue in considering separately the two end members, the large detrital grains, and the fine grained clays.

#### 5.7.1 Large detrital grains

The most common of large detrital grains in the studied sandstones is muscovite, either fresh or altered. Biotite is less common. The percentage of micas is limited between 0.2% to 4.2%, that means in most of the sandstones they are a minor constituent. The proportion increases in amount in calcareous sandstone and in very fine sandstone (shaly sandstone). The higher amount of muscovite than biotite may be because the muscovite is much more resistant to chemical weathering than biotite, and the biotite may be altered to chlorite.

Most of muscovite grains, identified under the microscope especially in calcareous sandstones are bent, deformed and even fractured due to compaction (see Chapter 6). Davies (1967) mentioned remarkably straight micas unaffected by carbonate. He

added that this is in direct contrast to mica flakes in the sand interbeds (friable sandstones), which are bent and sometimes even fractured. But this author has found that the large detrital grains are bent and deformed in both kinds of sandstones, and rather more in calcareous sandstones. This may be due to the fact that the calcareous sandstones are lower in the succession and have suffered deeper burial.

#### 5.7.2 Fine grained clay

The much finer grained flakes found in sandstones as an essential constituent of the matrix are clay minerals. The major clay minerals are, Kaolinite, Illite, Chlorite and Smectite. The major component is kaolinite while smectite is present in only very minor amount. Differentiation between kaolinite and chlorite was based on X-ray diffraction analysis. Sample was reacted with 18% v/v concentrated acid and heated to 80 °C for 8 hours to destroy the chlorite and then analysed. The difference between this and the overlap in the untreated sample gave the percentage of chlorite. Moreover, the samples were treated with ethylene glycol for one hour, and heated up to 600 °C for one hour confirming the presence of predominant kaolinite (Fig 5.38A).

X-ray diffraction powder patterns of oriented bulk clay mounts have proved to be of considerable value in confirming the nature of the authigenic clays in these sandstones. The samples are prepared from crushed sandstones in the usual manner and glycolated for X-ray identification then compared with standard samples prepared in the laboratory from different percent

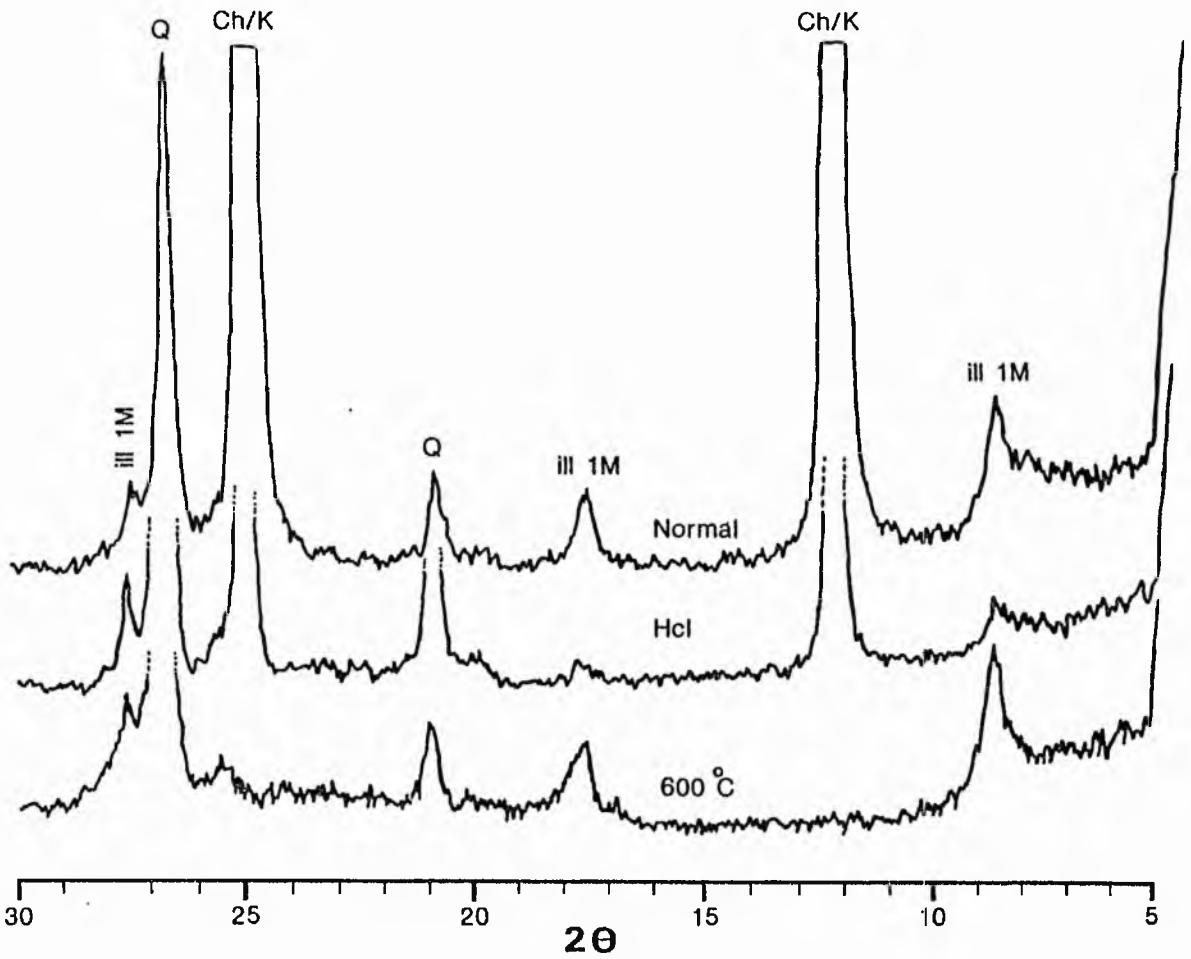


Fig 5.38A XRD scans of clay fraction showing the effects of different treatments on clay minerals, and the quantity of each type.

(between 0 to 50%) of kaolinite clay supplied by china clays (Fig 5.38B, 5.39A).

Unfortunately, with this method there is always doubt in these results when compared with the distribution and relative abundances of corresponding clay minerals as observed in thin-section (Table 5.1, Fig 5.39B). In a few samples the results of kaolinite percentage estimated by X-ray diffraction equalled the percentage of clay estimated by point-counting, but most of these results are 2 to 5 times greater than the percentage of clay estimated by point counter. It is suggested that the difference is either due to micaceous and chloritic rock fragments which are invariably crushed and mixed with clay constituents or due to the orientation of the samples. Comparison between percentage of mica (thin-section) with the percentage of kaolinite (X-ray diffraction) (Fig 5.40), indicated that as the amount of mica increases, the amount of kaolinite increases. There is a minor correlation between kaolinite and feldspar is not statistically significant (Fig 5.41).

Sand intervals consistently have a higher relative kaolinite content than do associated shales, the latter contain high amounts of illite and kaolinite. Kaolinite percentages are unequally distributed through the succession (Fig 5.42), such unequal kaolinite distribution is attributed to variable sand permeability. Thin-sections, X-ray diffraction and SEM observation support this idea. Optically, kaolinite is always in pore spaces, and commonly attacked adjacent quartz, mica, and feldspar. Under SEM it appears more prevalent than has been previously suspected and occurs as coating on sand grains, and in

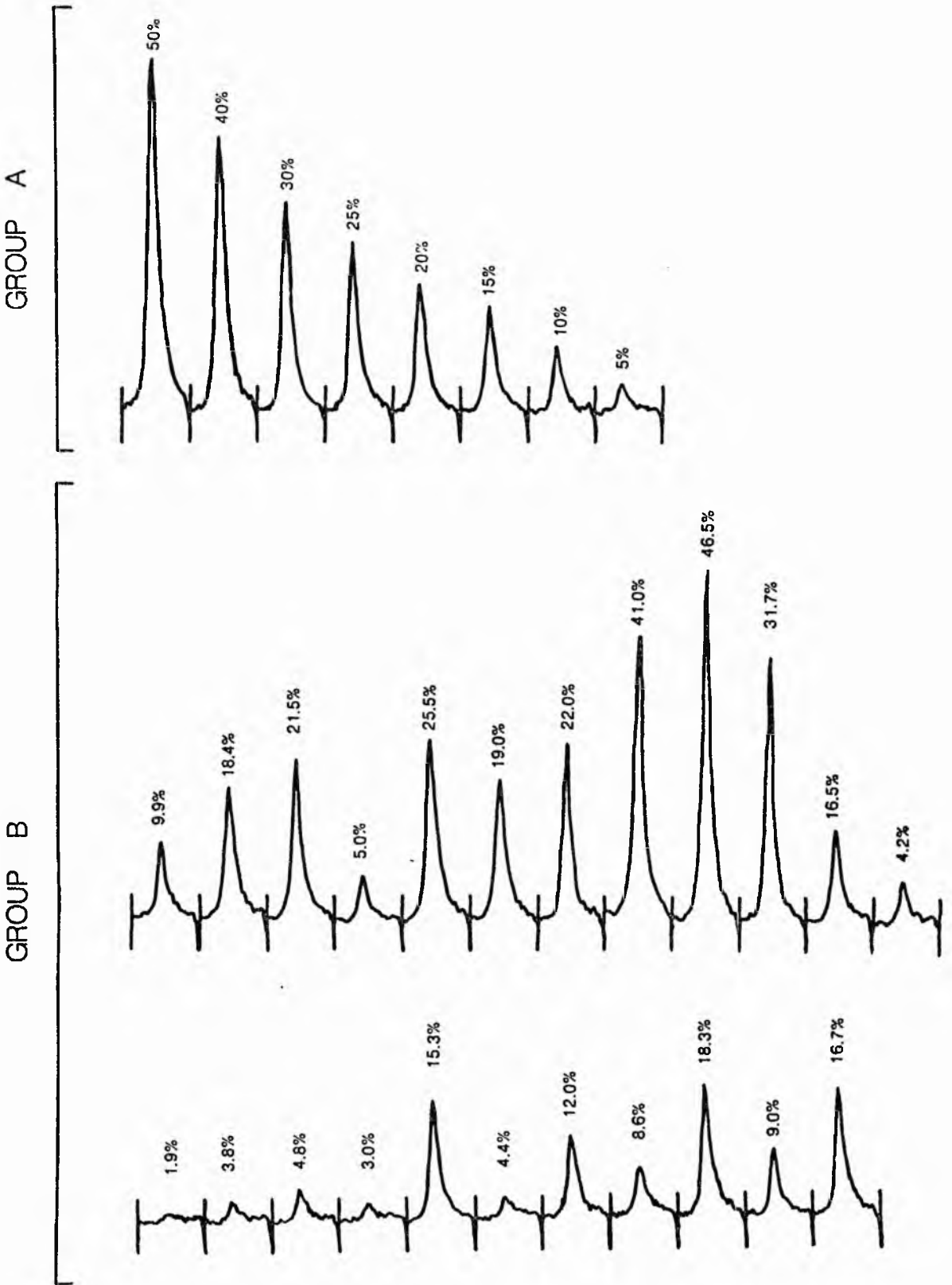


Fig 5.38B XRD scans of standard kaolinite sample (Group A) and the percentages of kaolinite in 23 samples (Group B).



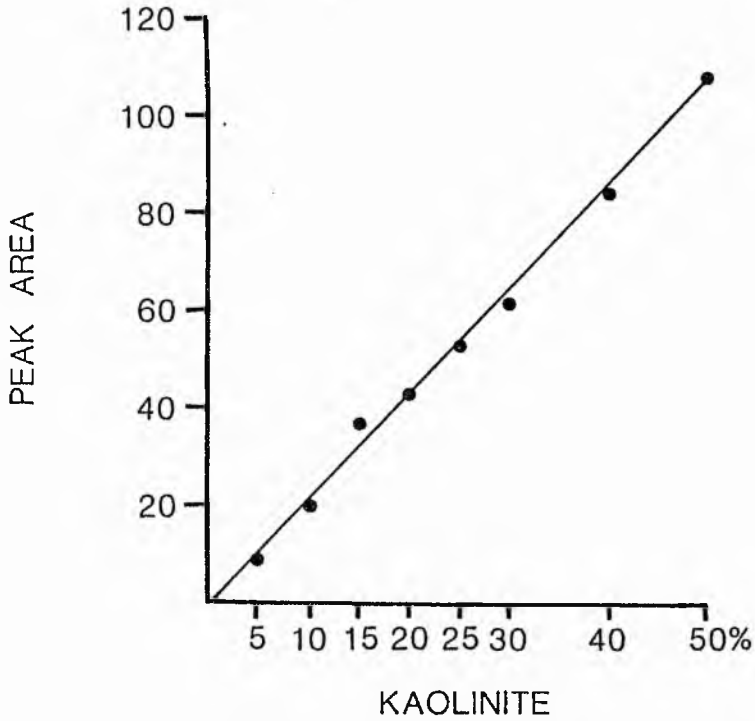


Fig 5.39A Standard curve, resulting from standard samples of different percentages of kaolinite clay supplied by china clays. Correlation coefficient  $r$  for all data  $r = 1.0$ .

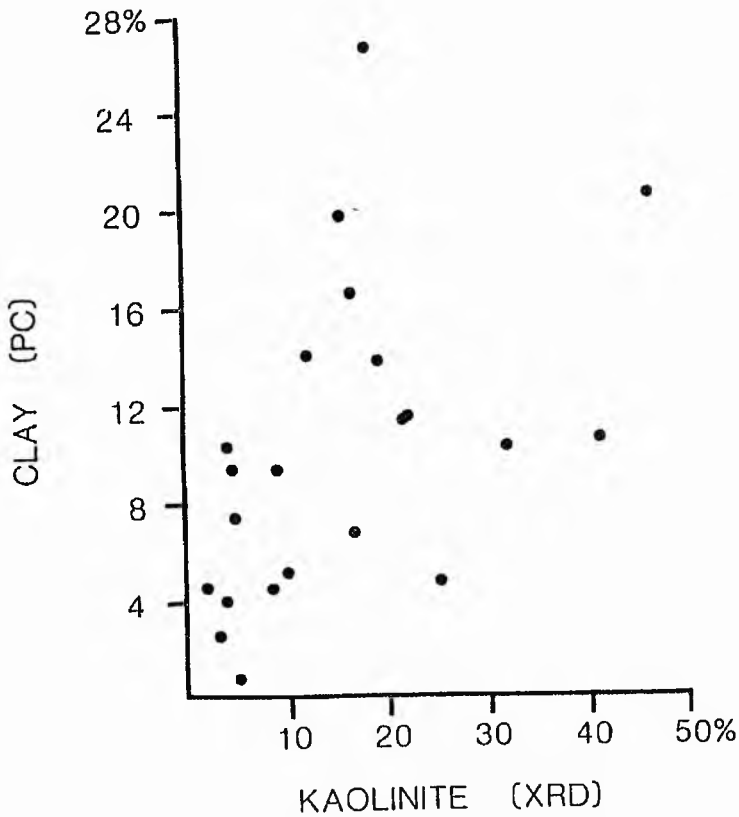


Fig 5.39B Comparison between the percentage of kaolinite estimated by X-ray diffraction and the percentage of clay from point-counting.

Table 5.1 Comparison of Kaolinite estimated by X-ray diffraction and clay amount by point counting.

% of Kaolinite standard samples	Peak Area	No of samples	Peak Area	% of Kaolinite	% of clay by Point Counting	Depth in metres from Hosie Limestone
5	8.5	S27	3.3	1.9	4.6	1.70
10	19.2	S24	7.4	3.8	4.0	4.97
15	36.8	S24	10.2	4.8	7.4	5.91
20	42.8	S24	6.0	3.0	2.6	6.51
25	52.4	S21c	32.4	15.3	19.8	9.84
30	61.2	S21b	47.1	22.0	11.6	11.4
40	84.0	S18	9.0	4.4	9.4	16.59
50	108.1	S17	25.7	12.0	14.0	17.79
		S8	18.3	8.6	4.5	28.58
		S3a	88.7	41.0	10.6	62.5
		F5a	19.1	9.0	9.4	83.46
		F5a	100.5	46.5	20.6	84.2
		F4	35.8	16.7	6.8	86.57
		F3	68.6	31.7	10.4	91.32
		T15a	35.1	16.5	16.6	109.35
		B6b	46.0	21.5	11.4	124.97
		B6a	20.8	9.9	5.2	125.12
		W4	40.0	18.5	26.68	136.19
		T8a*	8.5	4.2	10.4	110.76
		B7*	10.3	5.0	0.8	126.78
		L3*	55.0	25.5	4.8	150.58
		L3*	40.8	19.0	13.8	150.71

Note \* = West-side samples

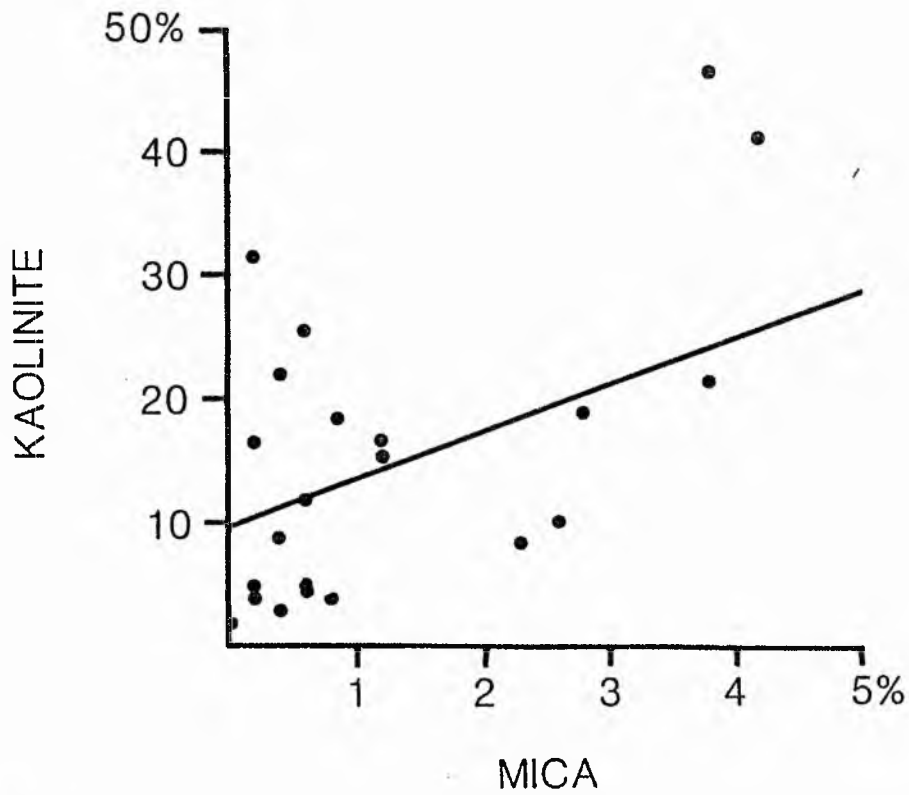


Fig 5.40 Plot kaolinite against mica. Correction coefficient  $r$  for all data  $r = 0.63$

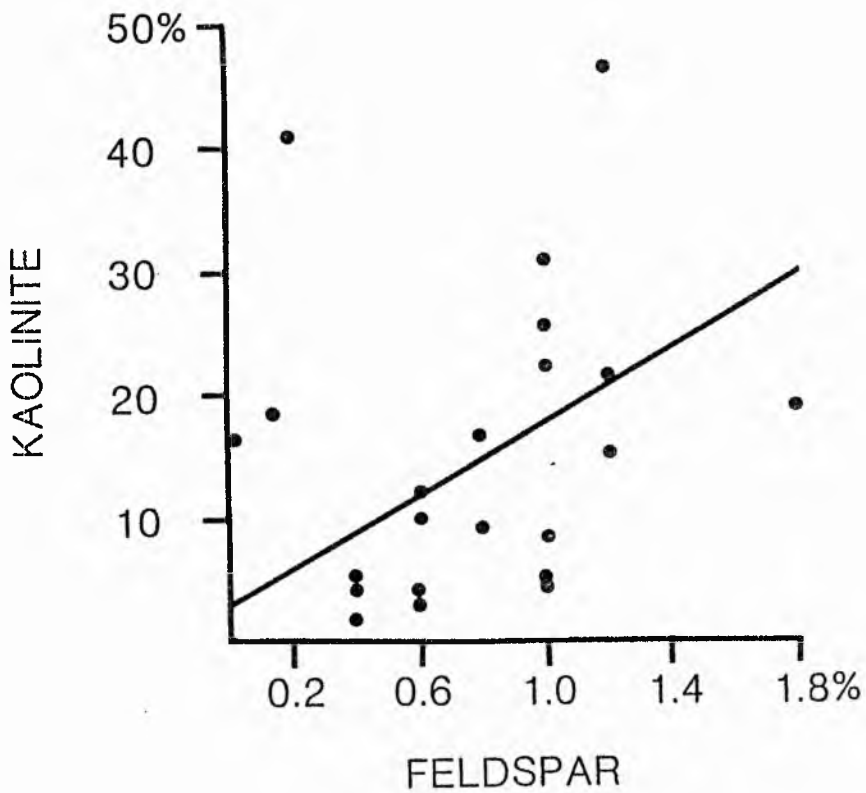


Fig 5.41 Plot of feldspar (from thin section) against kaolinite (XRD). Correlation coefficient  $r$  for all data  $r = 0.45$ .

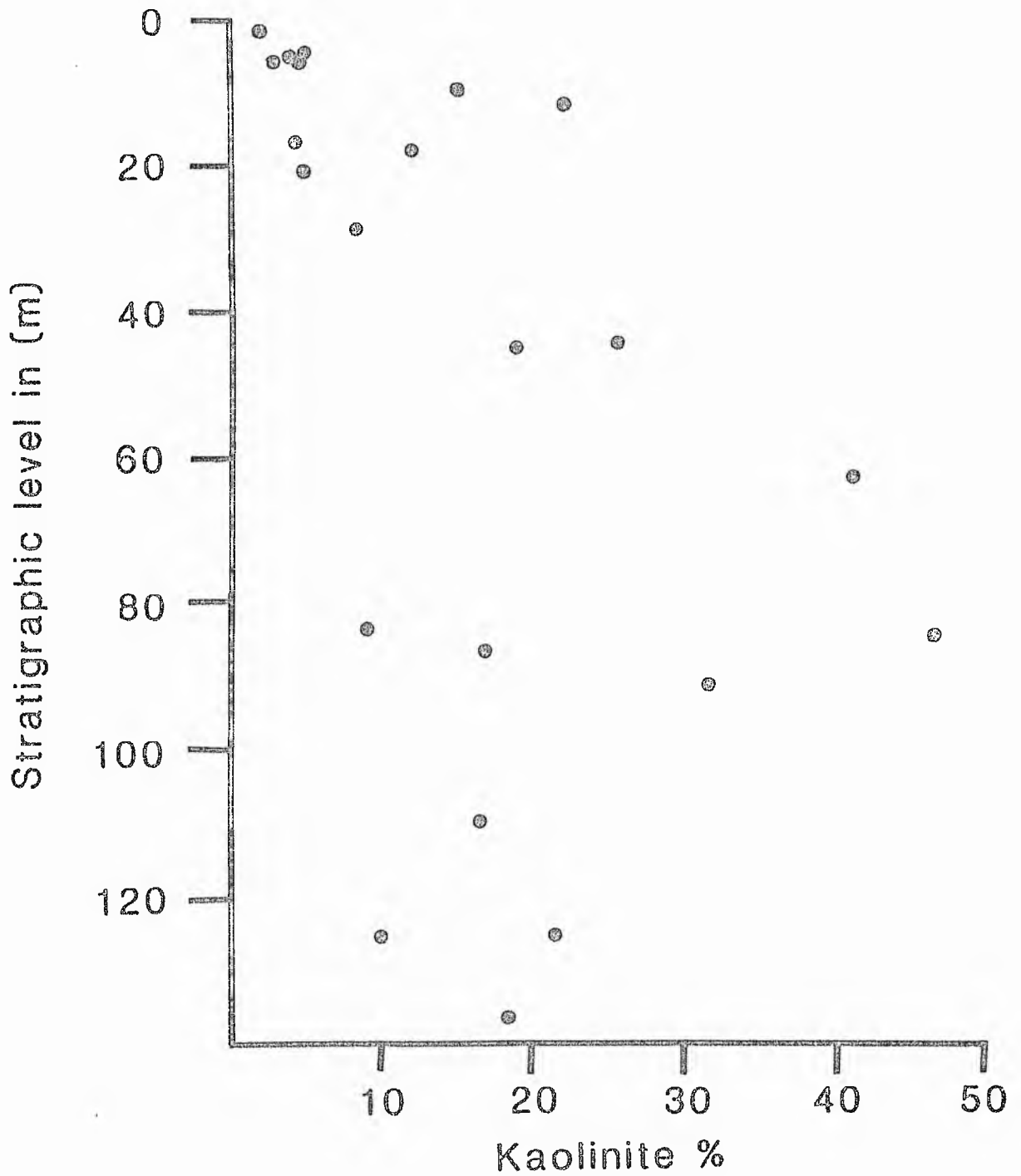


Fig 5.42 Relationship between stratigraphic level (0 = Mid-Kinniny Limestone) in metres and percentages of kaolinite (x-ray diffraction).

pores between sand grains (Fig 5.43). Moreover, X-ray diffraction analysis recorded is sharp peaks. Bucke, et al, (1971) pointed out that kaolinite with sharp X-ray diffraction pattern is highly crystalline; this strongly suggests that kaolinite is an authigenic growth.

### 5.7.3 Characteristics Of The Common Forms Of Clay

#### 5.7.3a Kaolinite

Kaolinite is the most commonly recognized authigenic clay in sandstones, because it is usually coarse enough to be readily visible. It occurs as pore filling, and as pore lining (Figs 5.44 A, B). Vermicular forms are less common (Fig 5.45). The kaolinite filling pores are composed of numerous booklets, which are formed as (books), bent (accordions) (Fig 5.46), and vermicular growth.

In some other sandstones, authigenic kaolinite is formed during and before the complete quartz overgrowth. Figure 5.47 shows that the overgrowth was incomplete, because the overgrowth partially envelopes kaolinite crystals. The kaolinite is authigenic, because the individual booklets are too large to pass through pore-throats as detrital particles. The kaolinite may arise from alteration of feldspar (Fig 5.16) and can be observed developing along the cleavage in partially leached feldspar, as well as from transformation of mica.

#### 5.7.3b Illite

The second most abundant clay mineral in the studied

Fig 5.43 SEM photograph showing quartz grain overgrowth (Q) coated by authigenic kaolinite, and kaolinite filling a large pore. Sandstone Unit (S21a) - East side. Scale bar is equal 10  $\mu$ .

Fig 5.44A SEM photograph showing authigenic kaolinite arranged in 'books' as filling large pore between quartz grain overgrowths. Micropores still remain in between authigenic kaolinite. Sandstone Unit (B7) - West side. Scale bar is equal 40  $\mu$ .



Fig 5.44B SEM photograph showing alignment of authigenic kaolinite as pore lining. The alignment on quartz grain suggesting development outward into the pores during diagenesis. Note the lack of any indication of deformation of authigenic kaolinite adjacent to grain contacts. Sandstone Unit (B7) - West side. Scale bar is equal 10  $\mu$ .

Fig 5.45 SEM photograph showing typical vermicular authigenic kaolinite forming crystals aggregates that make up a spiral in shape formed by free growth in pore. Sandstone Unit (S17) - East side. Scale bar is equal 10  $\mu$ .



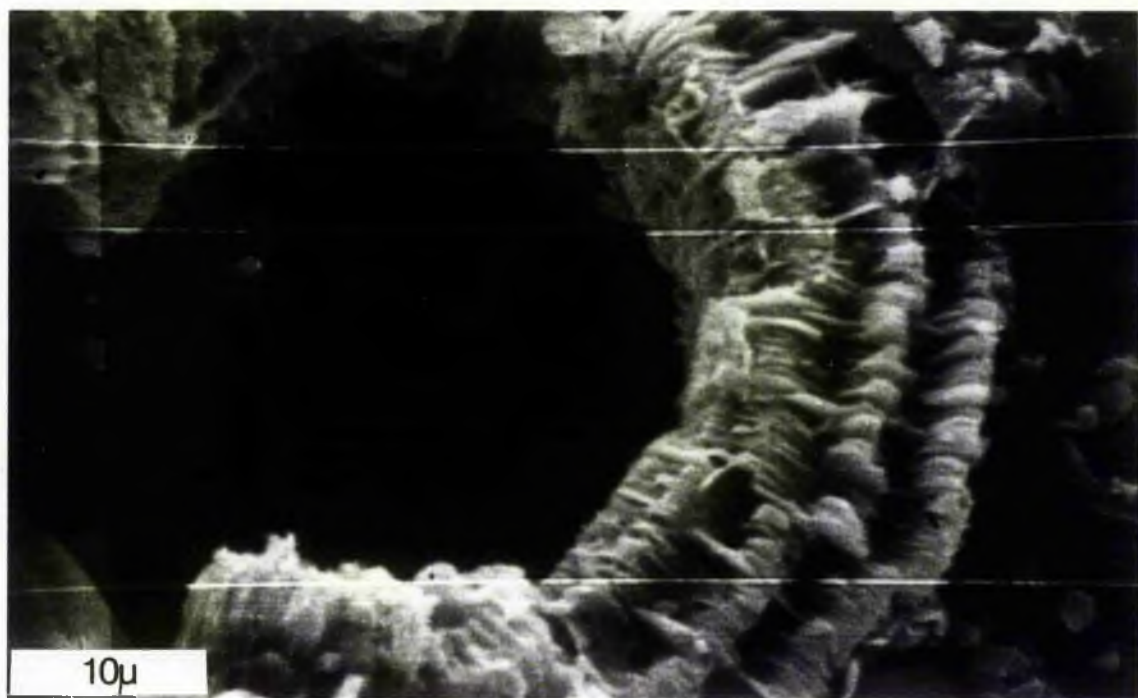
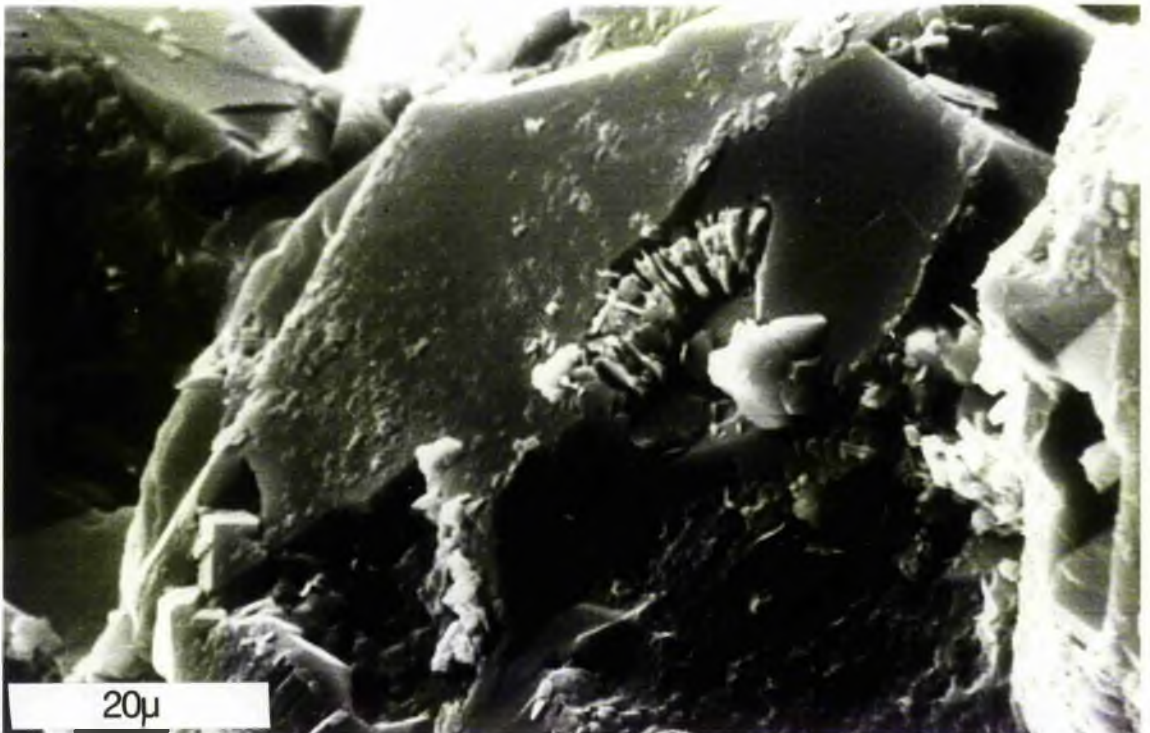
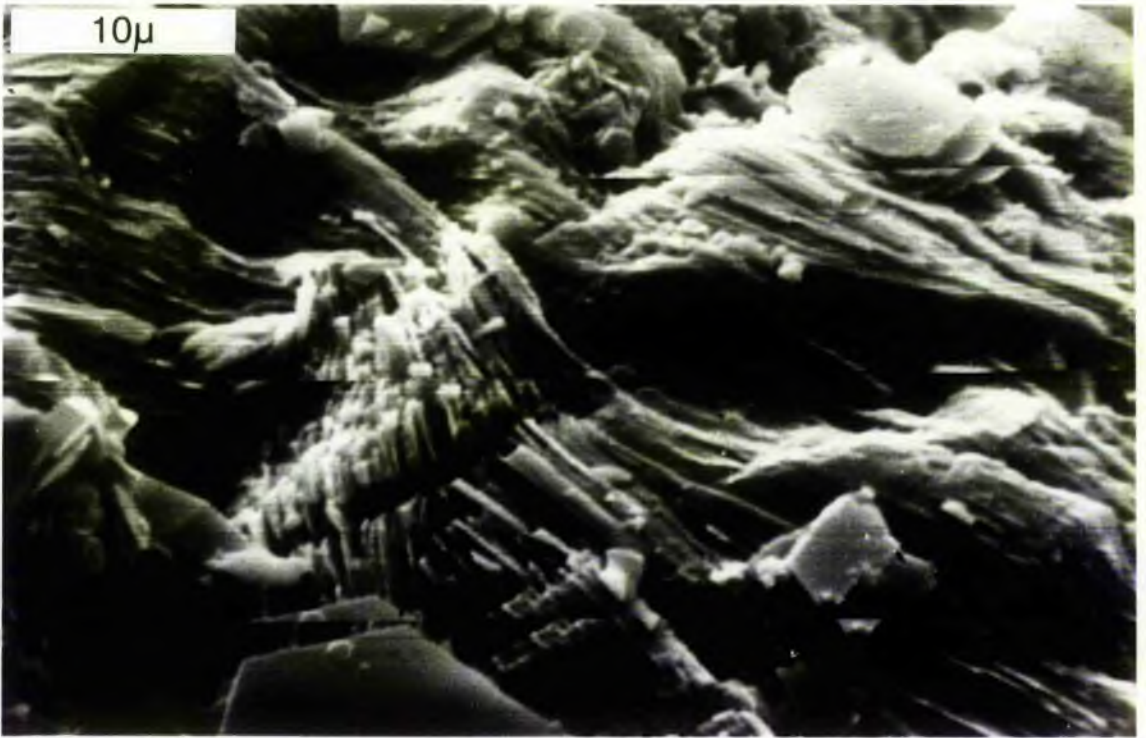


Fig 5.46 SEM photograph showing typical bent 'accordion' form of authigenic kaolinite. The squeezing is more around the quartz overgrowth (left hand corner), suggesting development due to compaction during diagenesis.

Sandstone Unit (T3) - West side. Scale bar is equal 10  $\mu$ .

Fig 5.47 SEM photograph showing authigenic kaolinite as simultaneously with silica overgrowth, or even before the silica cement complete as indicated by presence of cryptocrystalline of silica which have been deposited on the surface of overgrowth. The contact between silica and authigenic kaolinite nearly at right angle as well as corrosion related to growth of kaolinite. Sandstone Unit (T3) - West side.

Scale bar is equal to 20  $\mu$ .



sandstones is illite, while it dominates in shale. In thin-section, it is not easy to differentiate between illite and kaolinite, but sometimes illite can be detected by the birefringence. Under SEM generally it occurs as irregular flakes (Figs 5.48A, B).

#### 5.7.3c Chlorite

This mineral is one of the most variable in form among the authigenic clays. It has been reported as occurring in rosettes, honeycombs (Fig 5.49C); or cabbagehead like growths. Rosette shapes occur as pore filling (Fig 5.49A), beside quartz overgrowth. Cabbagehead habit of authigenic chlorite is usually attached to sand-sized grains (Fig 5.49B).

#### 5.7.3d Smectite

Smectite is present as a minor constituent as reflected by X-ray diffraction analysis.

#### 5.8 Overall conclusions:-

The study of the petrology of the clastic coarse sediments, which are mainly of fine to medium grained sand; and very well to moderately sorted, indicates that they consist mainly of stable light minerals; especially quartz. Minor quantities of feldspar, mica, heavy minerals and rock fragments are found. Matrix and cement (clay, carbonate, iron-oxide and silica) were identified in most thin-sections. Three types of quartz were recognized, undulatory, non-undulatory and polycrystalline. The undulatory type is the predominant variety.

Fig 5.48A SEM photograph showing illite occurring as irregular flakes. Middle part of sandstone Unit (B7) - West side. Scale bar is equal 20  $\mu$ .

Fig 5.48B SEM photograph showing illite (ill) irregular flakes beside the chlorite honeycomb (chl). Sandstone Unit (T7c) - West side. Scale bar is equal 10  $\mu$ .

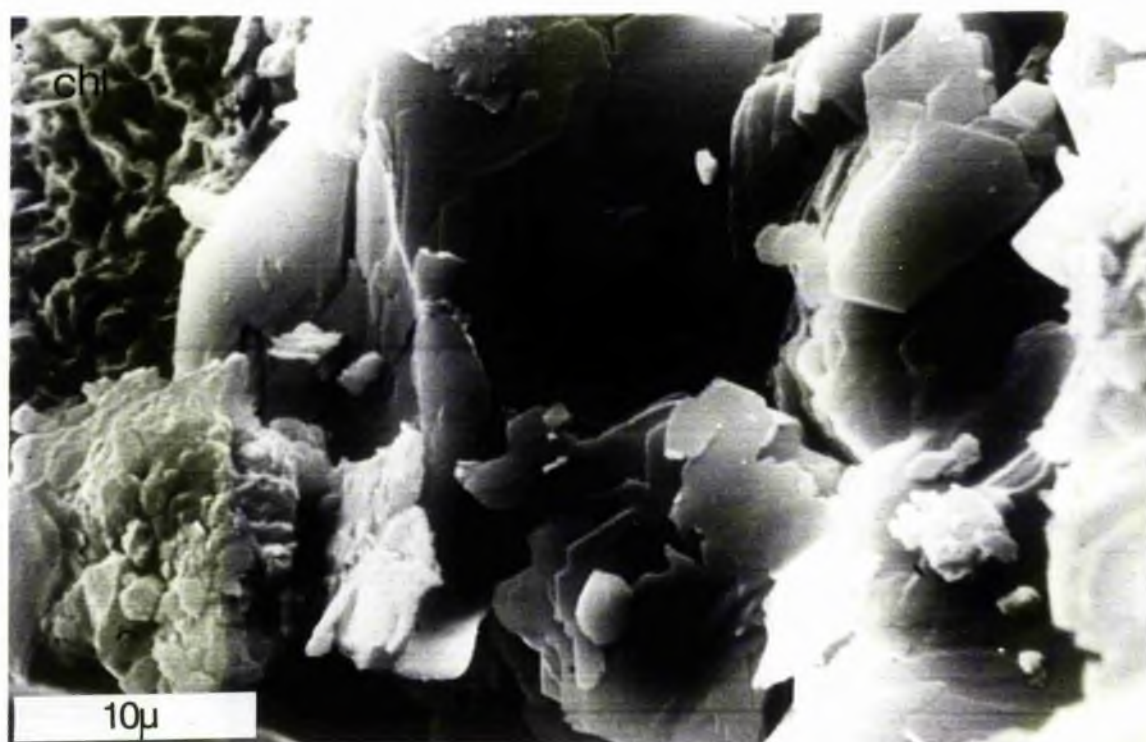


Fig 5.49A SEM photograph showing chlorite 'rosettes' filling the pore beside quartz grain overgrowths. Authigenic kaolinite filling the incomplete quartz overgrowth and minor amounts of cryptocrystalline silica have been formed on the overgrowth surface. Sandstone Unit (T7C) - West side. Scale bar is equal to 20  $\mu$ .

Fig 5.49B SEM photograph showing chlorite "cabbagehead" structure attached to sands-sized detrital grain. Sandstone Unit (T8b) - West side. Scale bar is equal 4  $\mu$ .

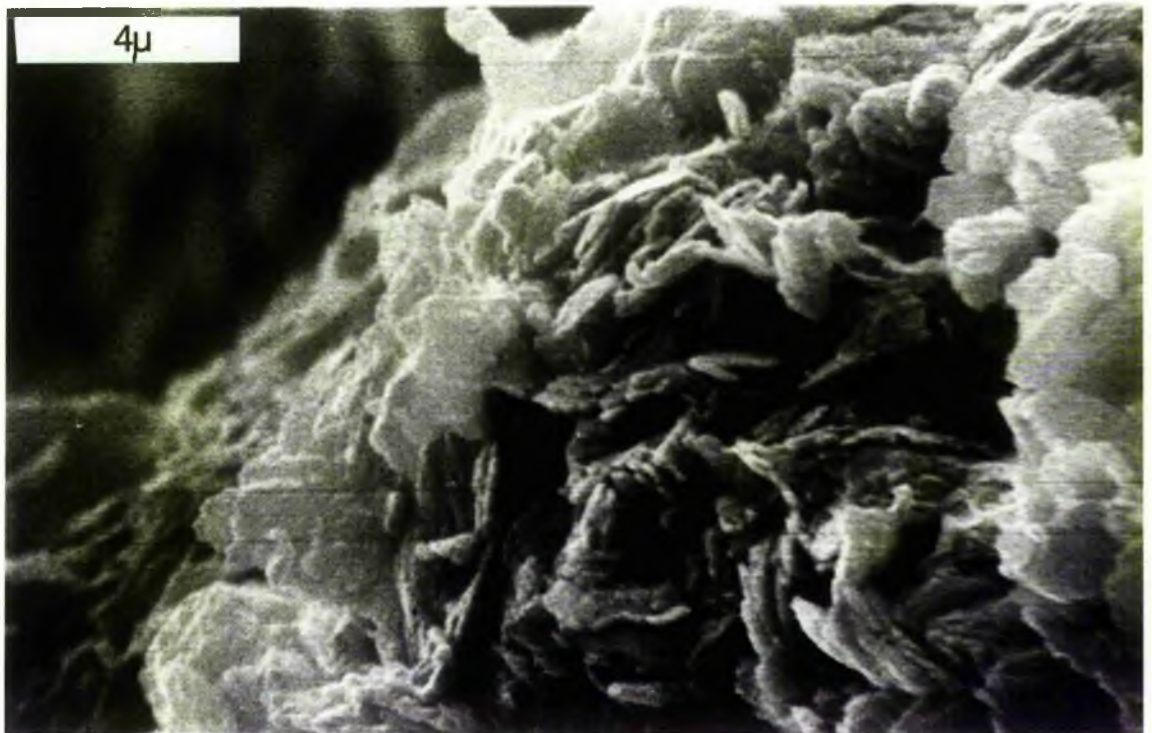
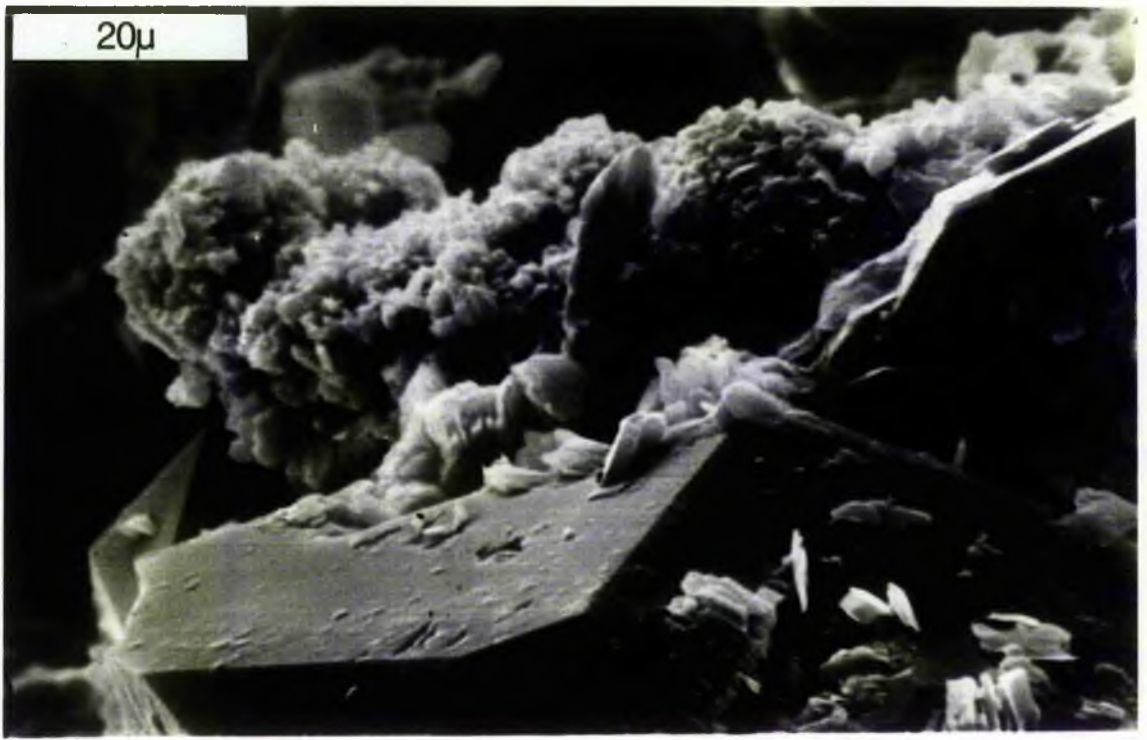
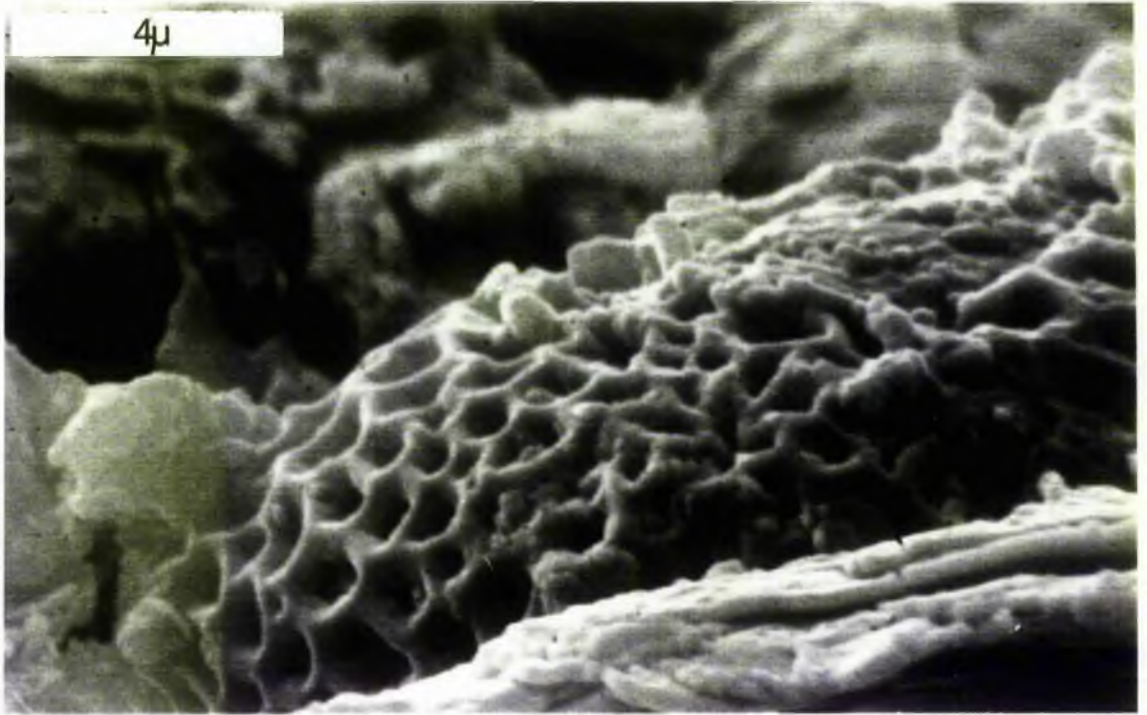




Fig 5.49B SEM photograph showing chlorite "cabbagehead" structure attached to sand-sized detrital grain. Sandstone Unit (T8b) - West side. Scale bar is equal 4  $\mu$ .



From the study of the grain size; shape of the quartz grain; number of the crystal units per grain; and finally the intercrystalline boundaries between the crystals it is concluded that the St Monance quartz grains fall in the field of low-rank metamorphic source rocks (Figs 5.6). But the number of units in polycrystalline grains tends to mixed of both low and high, and this at first sight, may suggest a contribution from plutonic or metamorphic rocks. The grains are often small, and this taken together with the bimodal size of the crystals and elongated grain shape is consistent with a source in low-grade metamorphic rocks. The few acicular inclusions are a reminder of contributions from a plutonic rock sources. The heavy minerals also reveal that the source was in metamorphic rocks with some plutonics as pegmatite or granites.

Three types of cement were observed; iron oxide, silica and carbonate. The iron oxide cement is probably early diagenetic formed soon after deposition, as indicated by the petrographic relationships. Then silica, carbonate, and iron oxide are probably late diagenetic. Authigenic silica cement, usually occurring as rims in optical continuity with detrital quartz grains was noted in most of the samples. Three types of overgrowths were recognized, normal; uneven and double overgrowths. The uneven was suggested to have formed from the normal overgrowth after presolving.

In samples of sandstones containing small amounts of carbonate it can be seen that the carbonate has formed after the crystallisation of the secondary silica since the carbonate occupies the centres of pore spaces which are outlined by the

silica overgrowth from the adjacent detrital grains. Further examination shows there are differences between carbonate filling and carbonate replacing the quartz grains, while in other thin-sections it is clear that carbonate has replaced silica along grain boundaries and along boundaries between grains and rims, thus beginning the process of isolating the detrital grains within the carbonate cement. In other sandstones this process has frequently reached an advanced stage and detritals are floating in the carbonate. Many grains have been nearly completely replaced by carbonate and only ghost structures within the carbonate testify to their former presence. Finally, some of the carbonate in this sandstone has been slightly stained and in part replaced by brownish red to black iron oxide. This iron oxide is thus regarded as the latest mineral phase present.

The major clay minerals were identified are kaolinite, illite and chlorite, with minor amounts of smectite. The main one is kaolinite as authigenic, commonly occurring as pseudo-hexagonal plates and vermicular, which affected porosity. Some kaolinite has been formed during and before the complete silica overgrowth (Figs 5.47A, B and 5.49A). Illite was observed as irregular flakes reducing porosity too. When the illite was fibres which in presence of vermicular kaolinite tended to join across gaps forming a complex pattern of 'bridge', this severely reduced permeability (Whitaker 1978, p 373). Chlorite was identified in variable form. It reflects the appearance of alkaline conditions, and may be expected to develop with deeper burial associated with compaction and dewatering of shales (Muller, 1967). Most of these chlorites are authigenic and may

be formed from biotite as indicated by the less amount of biotite.

In considering these results it has to be remembered that the samples are from surface exposures which have suffered ground water seepage as well as tidal and wave action. It is to be expected that water circulation has increases the kaolinite proportion at the exposure of feldspars and reduced the carbonate content.

## CHAPTER 6

### 6 Porosity, Permeability, and Pore Geometry

#### 6.1 Introduction

This study focuses on the textural and compositional character of surface samples of the Carboniferous St Monance Sandstones. My purpose is to describe the Porosity in terms of origin, amount, pore-size distribution, pore shape, and attendant permeability, and to highlight the principal diagenetic alterations.

#### 6.2 Porosity

In many sandstones, the amount of original pore space has been reduced by precipitation of cements and matrix. But before the processes of porosity reduction can be properly evaluated, it is necessary to estimate the initial porosity of the St Monance Sandstones. The author has followed Rittenhouse (1971) and others who found that the orthorhombic packing best represents the natural situation. This gives a porosity value of 39.54%, (Table 6.1) calculated for slightly compacted, well-sorted, well-rounded, fine-to-medium sand size sediment.

Two methods were used to get the actual amount of porosity. One, from thin-section, was on the basis of impregnation with coloured epoxy resin. Five-hundred point were counted at intervals of 0.3 mm using a Swift Automatic Point Counter. In the second, plugs from outcrop samples were analysed for

TABLE 6.1 Variation of Porosity

Samples number	Radius of grain	% of original porosity	% of porosity from thin-section	% of porosity from core sample		Average porosity percentage	Original porosity percentage (core analysis)	Depth in metre from the top of Hosie Limestone
T15a	1.55	39.54	17.4	22.05	PB	22.05	17.49	109.35
F4	0.94	39.54	15.6	23.3	PB	24.295	14.28	86.57
				25.26	NB			
F5a'	1.35	39.54	25.0	23.5	PB	25.0	13.04	83.46
				26.5	NB			
FSb	1.31	39.54	3.8	8.12	PB	6.97	32.57	79.04
				5.82	NB			
S3a	1.78	39.54	6.4	8.58	NB	8.58	30.96	62.5
S8	1.47	39.54	0.0	3.86	PB	4.62	34.92	28.58
				5.38	NB			
S18	1.15	39.54	18.0	27.21	PB	27.605	11.54	16.59
				28.00	NB			
S21c	1.09	39.54	14.4	25.57	PB	21.985	13.97	9.84
				18.40	NB			
S24	1.12	39.54	19.8	27.06	PB	26.775	12.48	6.51
				26.49	NB			
S24	1.15	39.54	23.3	24.48	PB	25.165	13.69	4.91
				25.85	NB			
S27	1.08	39.54	21.4	28.06	PB	29.33	8.94	1.70
				30.60	NB			
F7	1.46	39.54	10.4	21.57	NB	21.57	17.97	

Note PB = Parallel to bedding

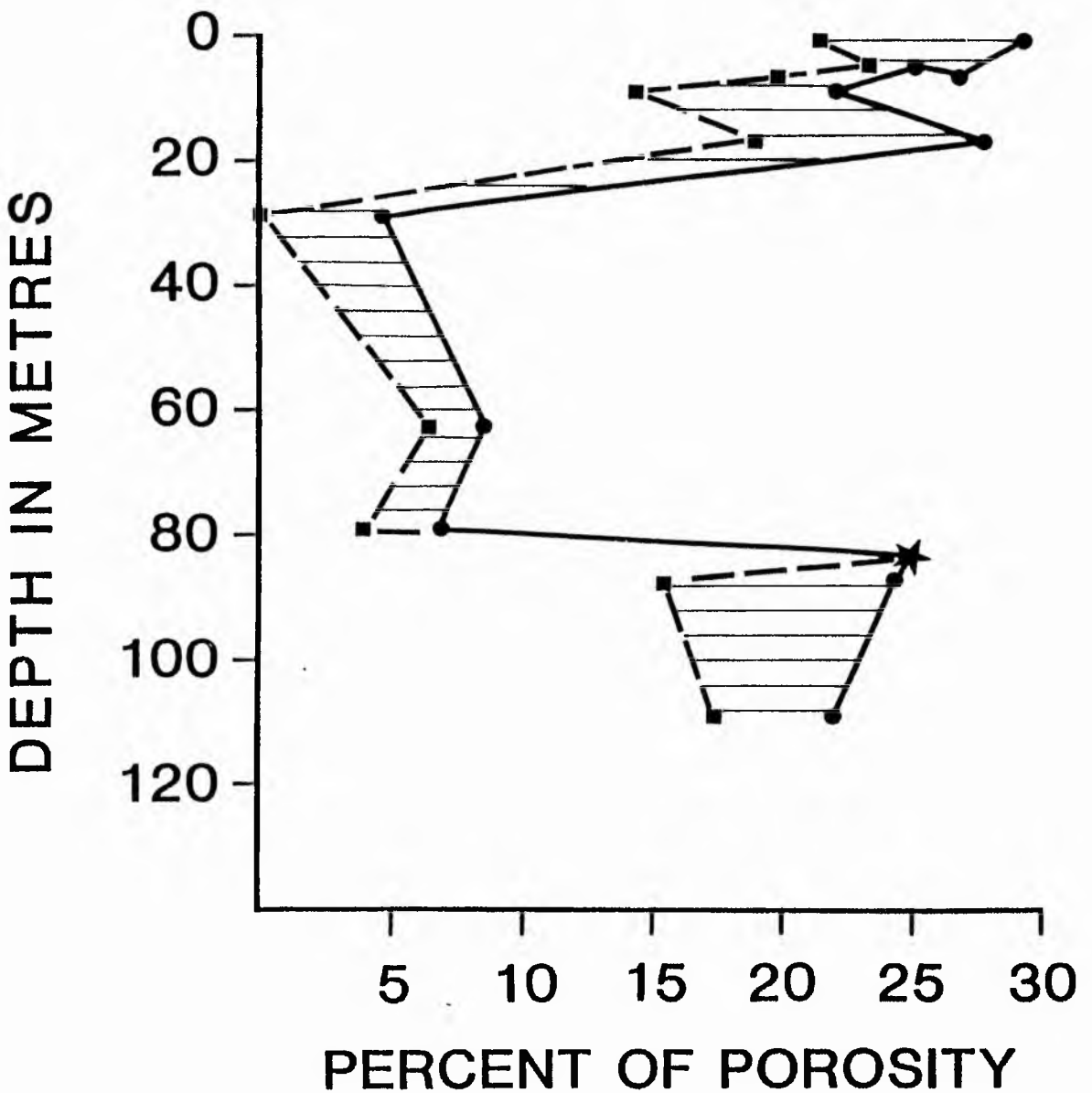
NB = Normal to bedding

effective porosity, and permeability using helium as the saturating fluid. One plug was taken parallel to the bedding, the other perpendicular to the bedding, so that two porosity and permeability values were obtained for each sample.

Most of the sandstones are characterized by porosity developed through solution processes. Most of these sandstones are permeable, and the pore types associated are intergranular, either formed through dissolution of carbonate cement or removal of other unstable materials such as feldspars and rock fragments. The intergranular porosity amount is higher in the presence of a high degree of dissolution, and was determined in thin-section to range from 0-to-25 percent, while in samples it reached 30.60 percent (Table 6.1). If there has been little or no dissolution and or if a high amount of clay is present, microporosity is developed as a function of carbonate and clay material. These type of pores with pore-aperture radii less than  $0.5 \mu\text{m}$ , and determined from core sample by mercury injection may reach up to 89% of the total porosity.

Comparison between porosity estimated from thin-sections and those derived from routine core analysis showed some discrepancies. Between those derived from core analysis which are parallel and perpendicular to the bedding there are also differences (Table 6.1, Figs 6.1 A, B). The relationship between stratigraphic position and porosity might be expected in the simplest of cases to be a linear relationship. In this area there is not a good correlation (Fig 6.1 A), due to the differences in mineralogy and texture and the restricted thickness of succession.





- Thin-section results
- Routine core analysis results (as average)
- ★ Shared point

Fig 6.1A Chart showing the relationship between depth of burial (as indicated by stratigraphic position 0 = Mid-Kinniny Limestone) and porosity, and the difference between the percentage of porosities from thin-section and routine core samples.

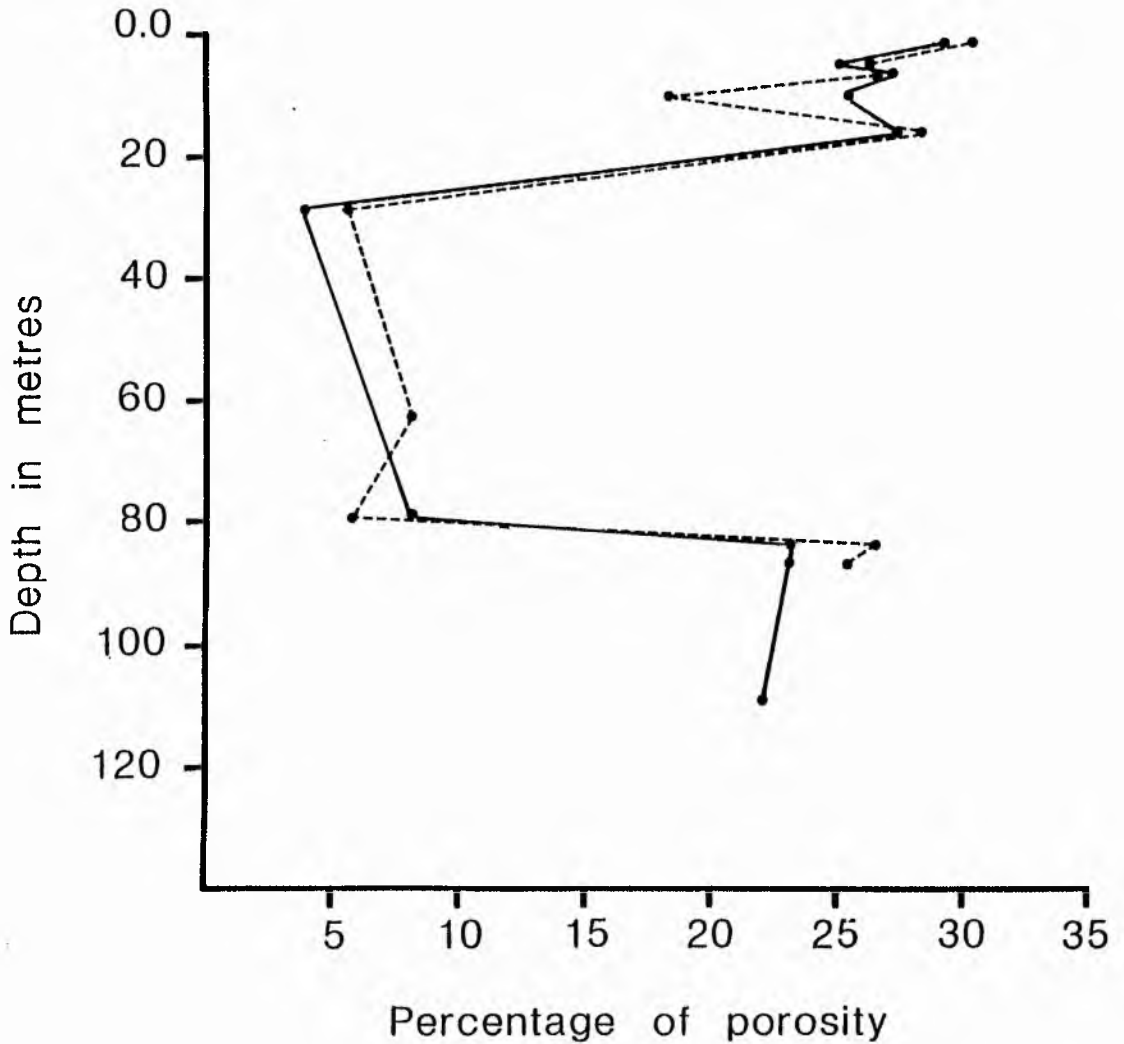


Fig 6.1B Chart showing the relationship between depth of burial and porosity (routine core sample only) and the difference between the percentage of porosities from samples parallel and normal to the bedding plane.

———— parallel to the bedding plane  
- - - - normal to the bedding plane

The porosity values estimated from core sample tests were up to 1.5 times those from thin-section. These results may be due to the difficulty of estimating the percentage of microporosities in thin-section. Other factors influencing the results are the orientation of thin-section (Table 6.1), and the presence of fractures (Appendix 6.9).

Core sample analysis gives more accurate results than thin-section analysis on porosity. On the other hand, evidence of diagenetic events is usually seen better in thin-sections, so that it is necessary to make some synthesis of the two sets of information.

### 6.3 Mechanisms of Porosity reduction

Of the three major processes, which may alter porosity of a pure quartz sand after deposition (Sibley et al 1976). Compaction and cementation were observed in this study; the third, pressure is of little or no importance.

#### 6.3a Compaction

Forty-three samples of St Monance Sandstone were chosen for point counting to study the types of grain-to-grain contacts in thin-section as described by Taylor (1950). The observations demonstrate that tangential contacts decrease in abundance with depth, long contacts increase rapidly with depth at first, then change very little, concavo-convex decrease at first then increase. Sutured contacts generally are very small in amount (Fig 6.2). The observed changes might be related to other factors. Blatt (1979, p 146) pointed out that sands containing

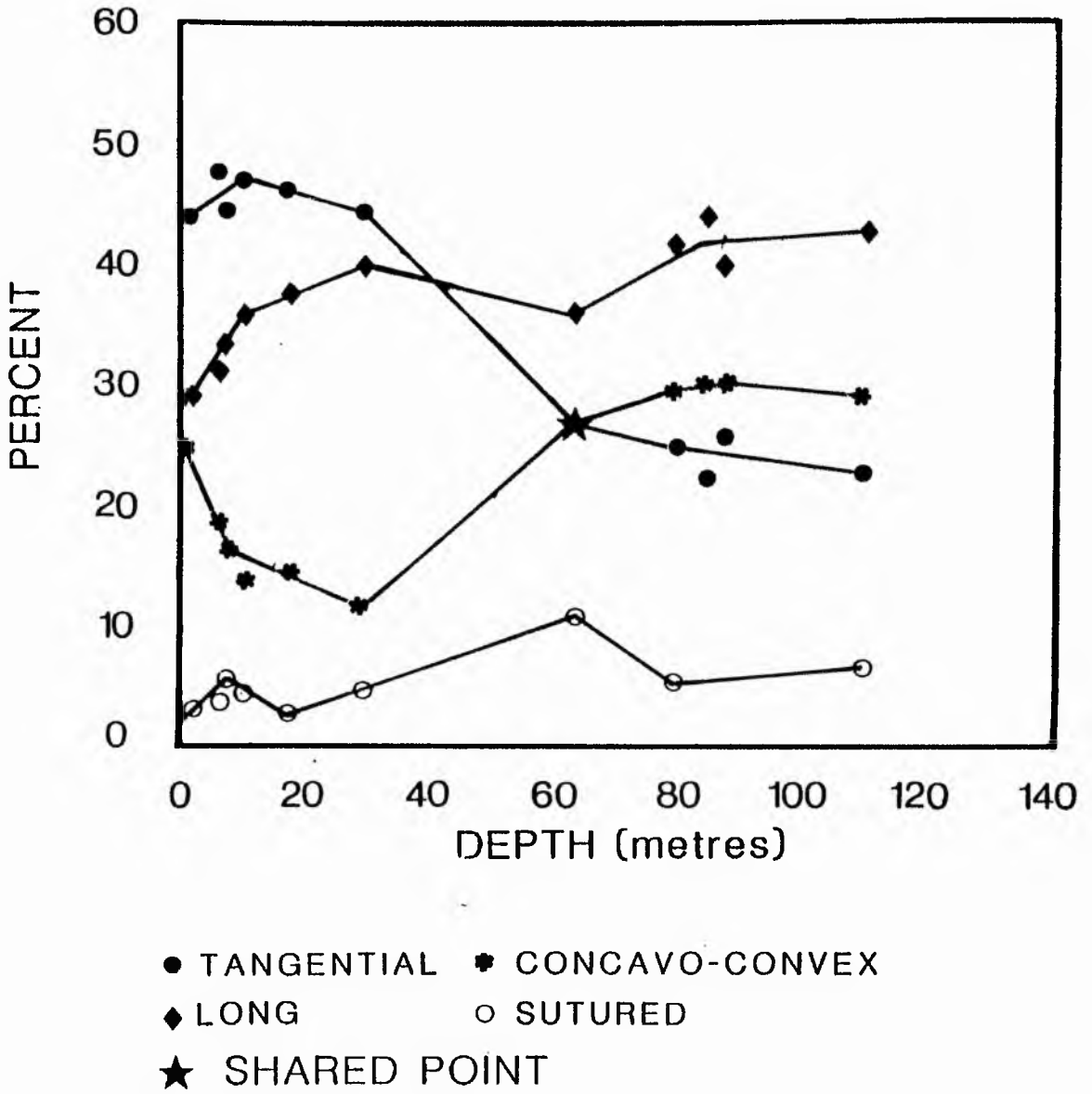


Fig 6.2 Effect on burial depth on the types of grain-to-grain contact.

only unyielding grains such as quartz and feldspar do not compact as much as sands containing appreciable amounts of clay. He added that the latter sands are commonly lithified by compaction alone without noticeable introduction of chemical precipitation such as calcite or quartz. This is right if clay was deposited or precipitated before the silica but in these rocks overgrowth was usually precipitated before clay matrix (Fig 6.5). The silica cement precipitated from solution decreases the spaces between the quartz grains and increases the length of contacts between them; (Fig 6.3) shows that contacts are between the silica overgrowths rather than between the original quartz grains. Therefore, the increase in long contacts for example, instead of being due to compaction is largely due to overgrowths. Occasionally, however there is evidence of pressure solution as well as overgrowth (Fig 6.4) and a small amount of compaction is indicated by the presence of bent and fractured micas and feldspars (Figs 6.6-6.7).

### 6.3b Cementation

Porosity reduction is mainly due to cementation as carbonate cement in pore spaces, and silica cement as overgrowths. For sandstones with or without significant amount of carbonate cements, the porosity and permeability are up to 29.33%, and several hundred millidarcies respectively. For sandstone units which are lightly cemented by calcite and/or silica overgrowth, porosities are only slightly reduced, but the permeabilities are greatly reduced. For instance, sample F4 (Appendix 6.4), has 24.3% porosity and 4.2% cement (carbonate

Fig 6.3 Photomicrograph showing the silica cement overgrowth (arrows) filling the spaces and enlarging the quartz grains leads to different type of contacts. Base of the sandstone unit (B7) - West side. Crossed polars, x 500.

Fig 6.4 Photomicrograph showing pressure solution between two quartz grains, and silica overgrowth reducing the porosity and changing the type of the grain contact (arrow). Carbonate (a) fills the pore and replaced some of quartz overgrowth (b). Middle part of sandstone unit (B7) - West side. Crossed polars, x 250.



Fig 6.5 SEM photograph showing quartz overgrowth forming microporosity.

Clay (kaolinite) tends to fill the remaining pore.

MP = microporosity; Q = quartz grain overgrowth; CL = clay  
(kaolinite). Sandstone Unit (F5b) - East side.

Scale bar equals 20  $\mu$ .

Fig 6.6 SEM photograph showing mica bent (a) and fractured (arrow),  
coating quartz grain (Q). Pores (P) created along the  
cleavage and fracture. Middle part of sandstone unit  
(B7) - West Side. Scale bar equals 20  $\mu$ .



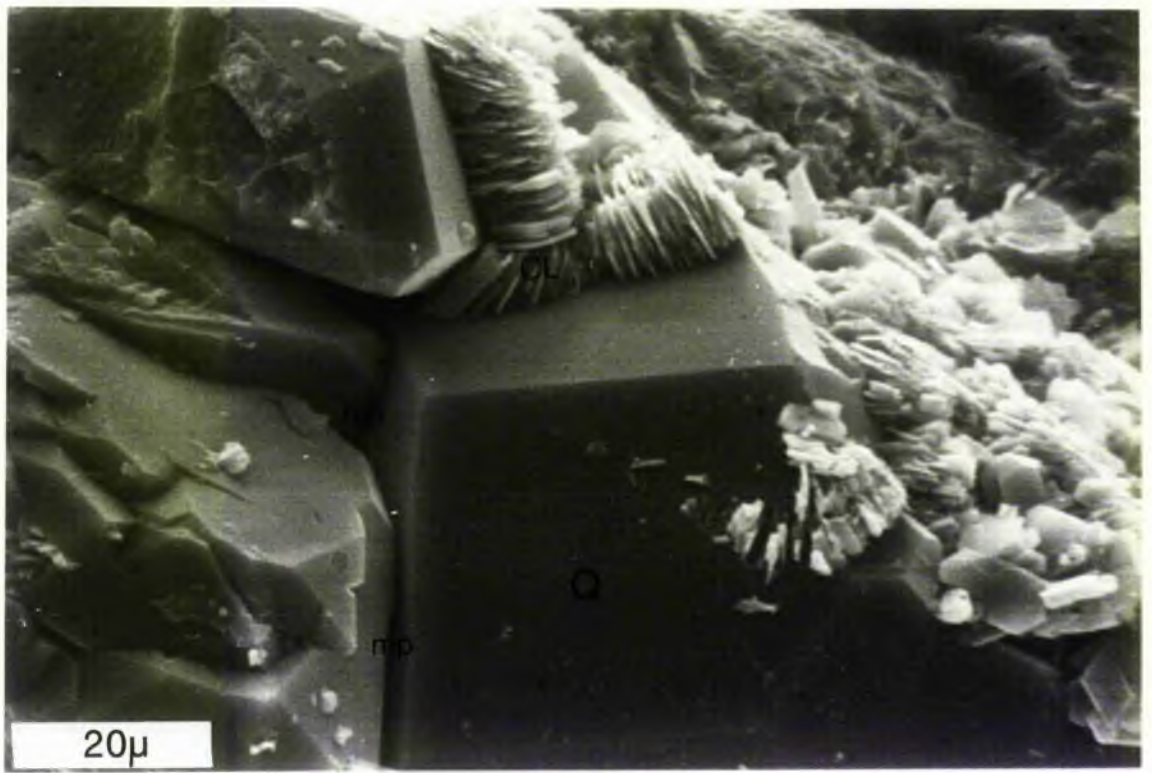
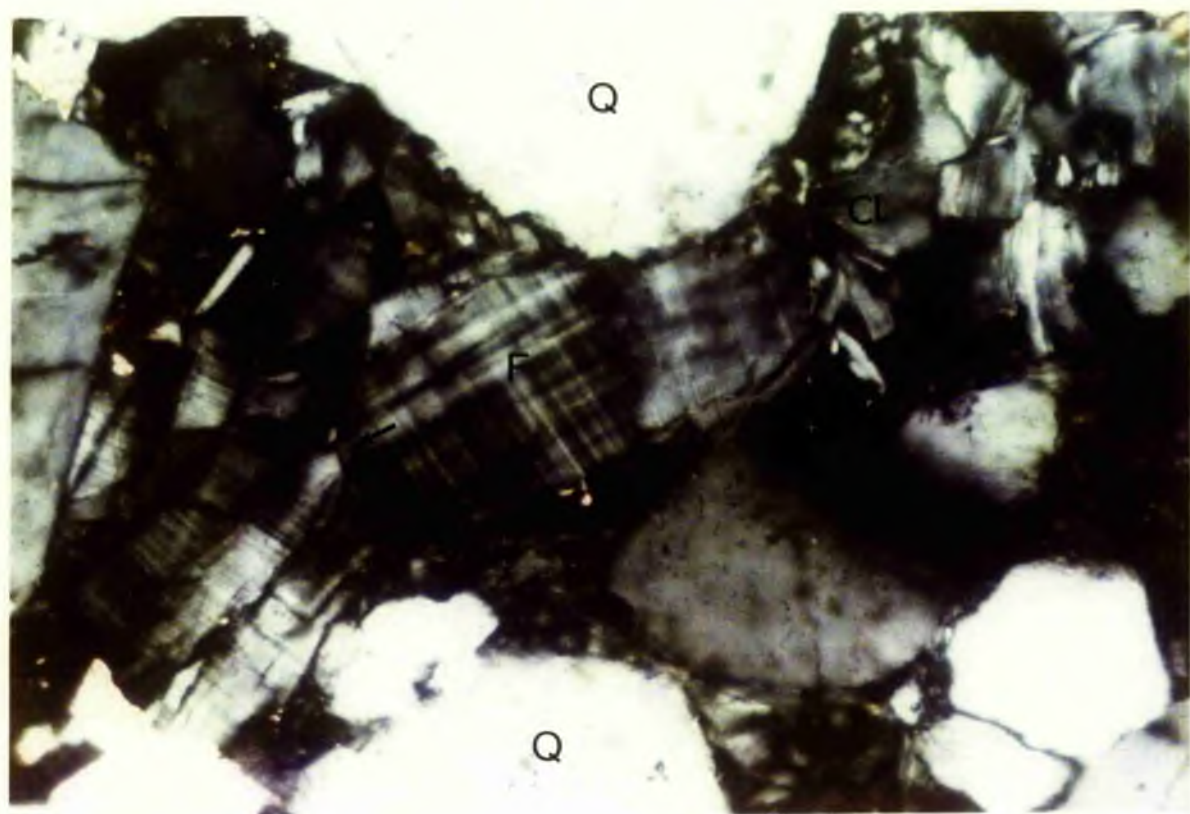


Fig 6.7 Photomicrograph of microcline grain fracture (arrow) and associate with clay matrix. Middle part of sandstone unit (B7) - West side. F = feldspar microcline grain fracture. Q = quartz grains; CL = clay matrix. Crossed polar, x 50.

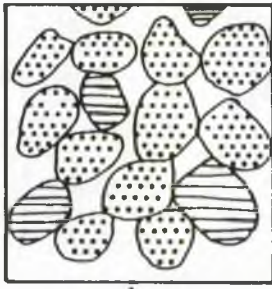


only), but the permeability is only 72.30 millidarcies. When sandstone units are more heavily cemented, permeabilities are further reduced (Fig 6.8). It is not surprising to find a heavily cemented sandstone unit with 4.62% porosity, has only 0.5 millidarcy permeability. Schmidt and McDonald (1980) pointed out that permeability in sandstones is affected by the amount of cement filling the spaces and separating the pores into isolated pores or with only a small pore throat for connection between. SEM study indicates that many of the pore spaces exist as very tiny intercrystalline micropores within the carbonate cement. Such tiny pore throats will not allow fluids to pass through them very easily, and for this reason can be considered as being ineffective porosity.

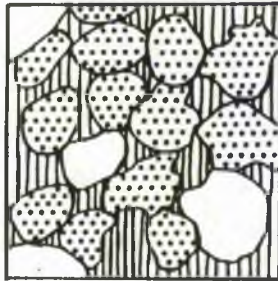
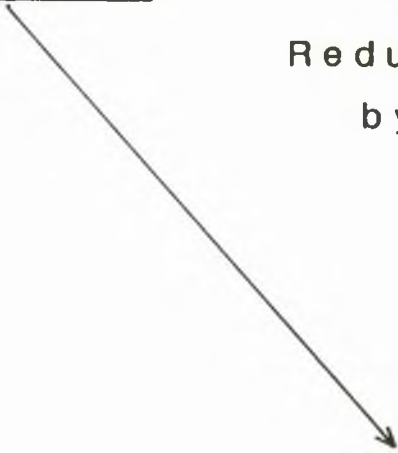
Good correlation exists between reservoir qualities (porosity and permeability) (Figs 6.9 A, B). The correlation between porosities and permeabilities is not a reliable, especially for those high permeability samples, because of drying and wetting at the present exposure level leads to increasing the permeability.

#### 6.4 Pore Size distribution

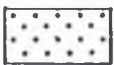
Carbonate cement and clay matrix increase the percentage of microporosity and decrease the size of pores. A close relationship exists between the porosity (estimated from thin-section) and these materials especially clay (Figs 6.10-6.11). There is an overall decrease in porosity with increase in clay although some points lie outside the main field (Fig 6.11). This is due to carbonate cement which is present in



Reduced permeability  
by clay material



Reduced permeability  
by carbonate cement



Quartz grains



Clay material



Feldspar grains



Carbonate cement



Porosity

Fig 6.8 Permeability reduction

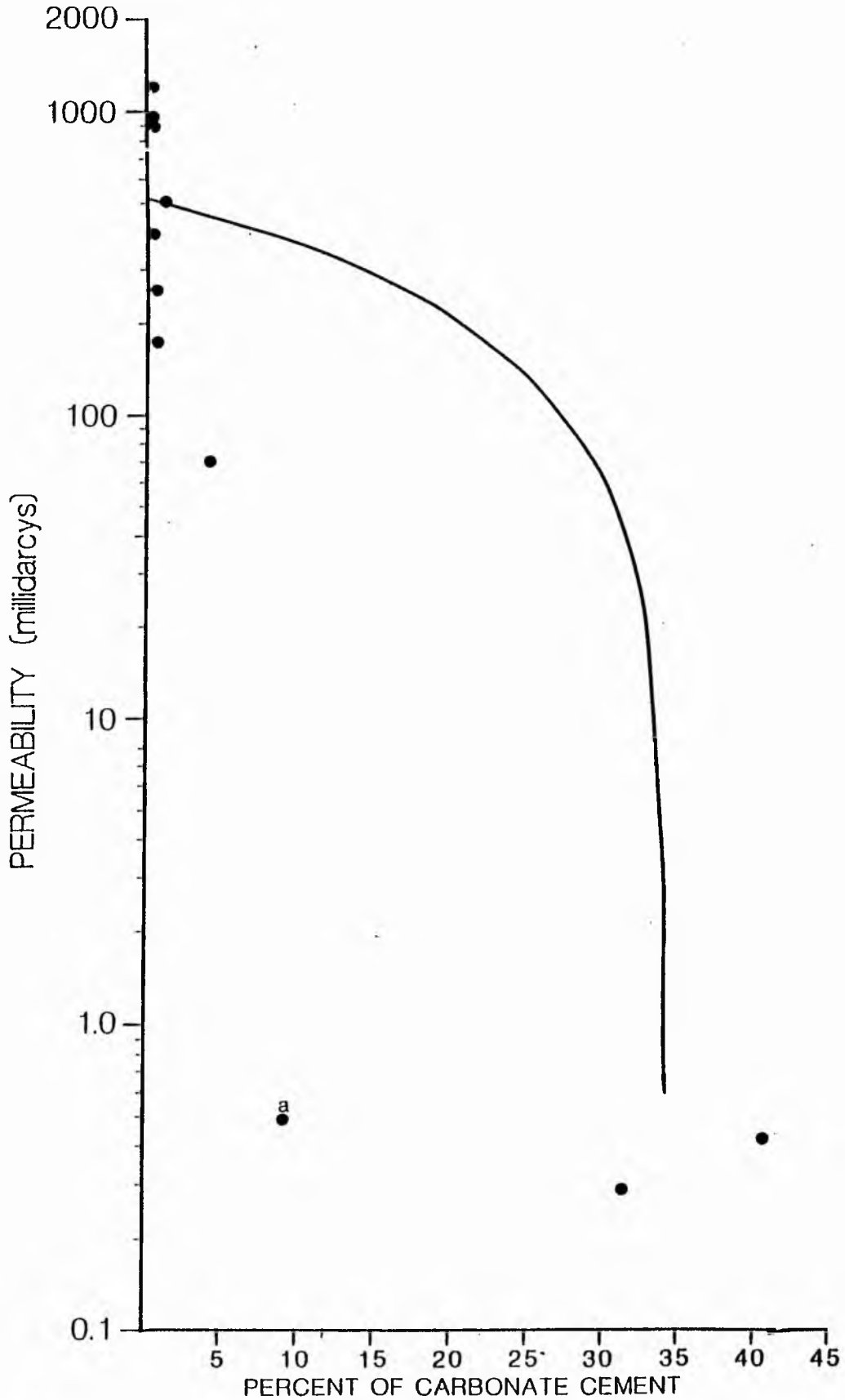


Fig 6.9A Chart showing the cement-permeability relationship. Point (a) has predominant clay material and was omitted from calculation of reduced major axis regression equation,  $y = -14.98 + 510.60x$ . Correlation coefficient  $\gamma$  for all data excluded point (a) = -0.492.

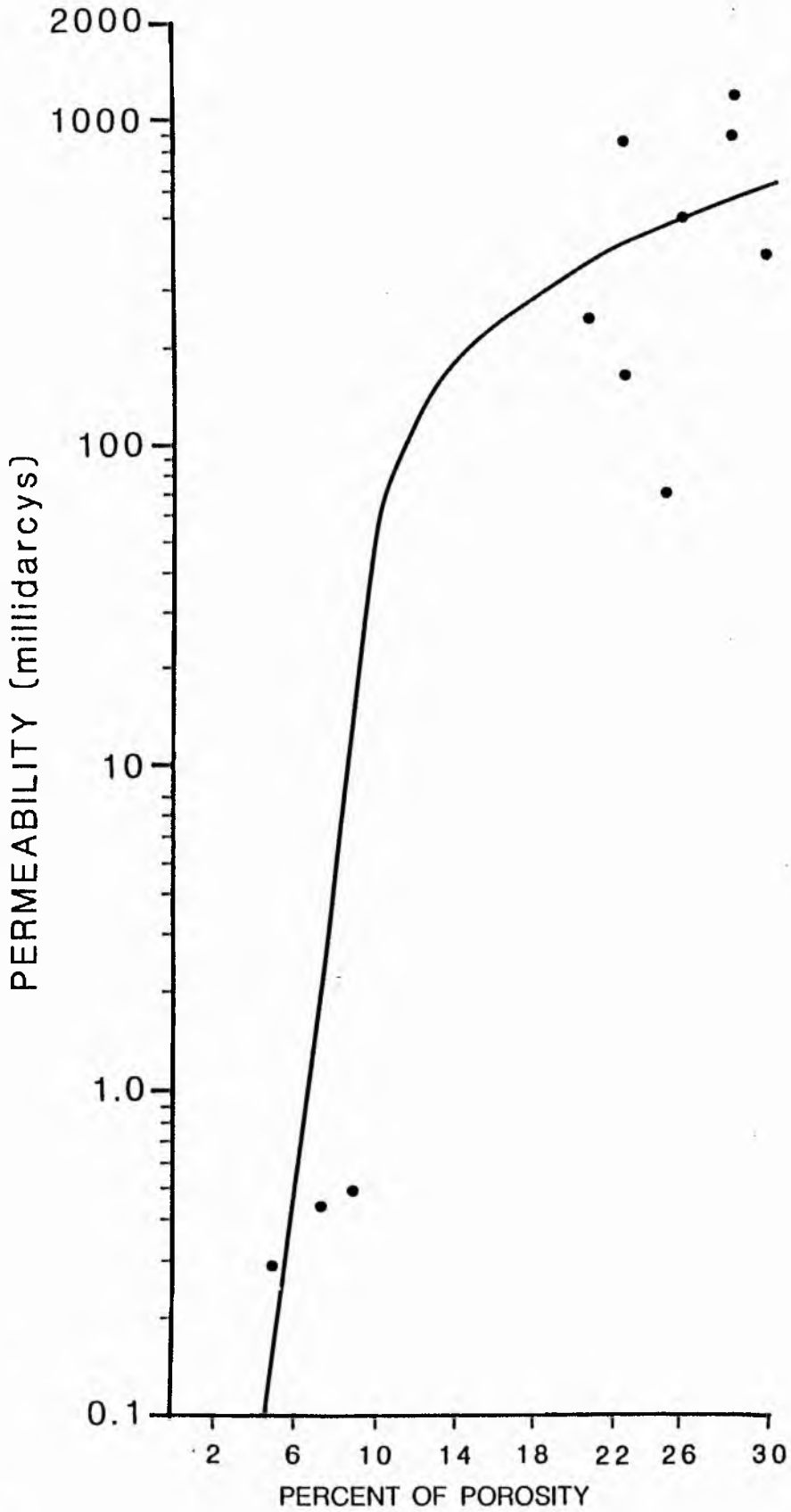


Fig 6.9B Chart showing porosity-permeability relationship. Correlation Coefficient  $\gamma$  for all data = 0.59. Reduced major axis regression equation,  $y = 29.63X - 231.44$ .

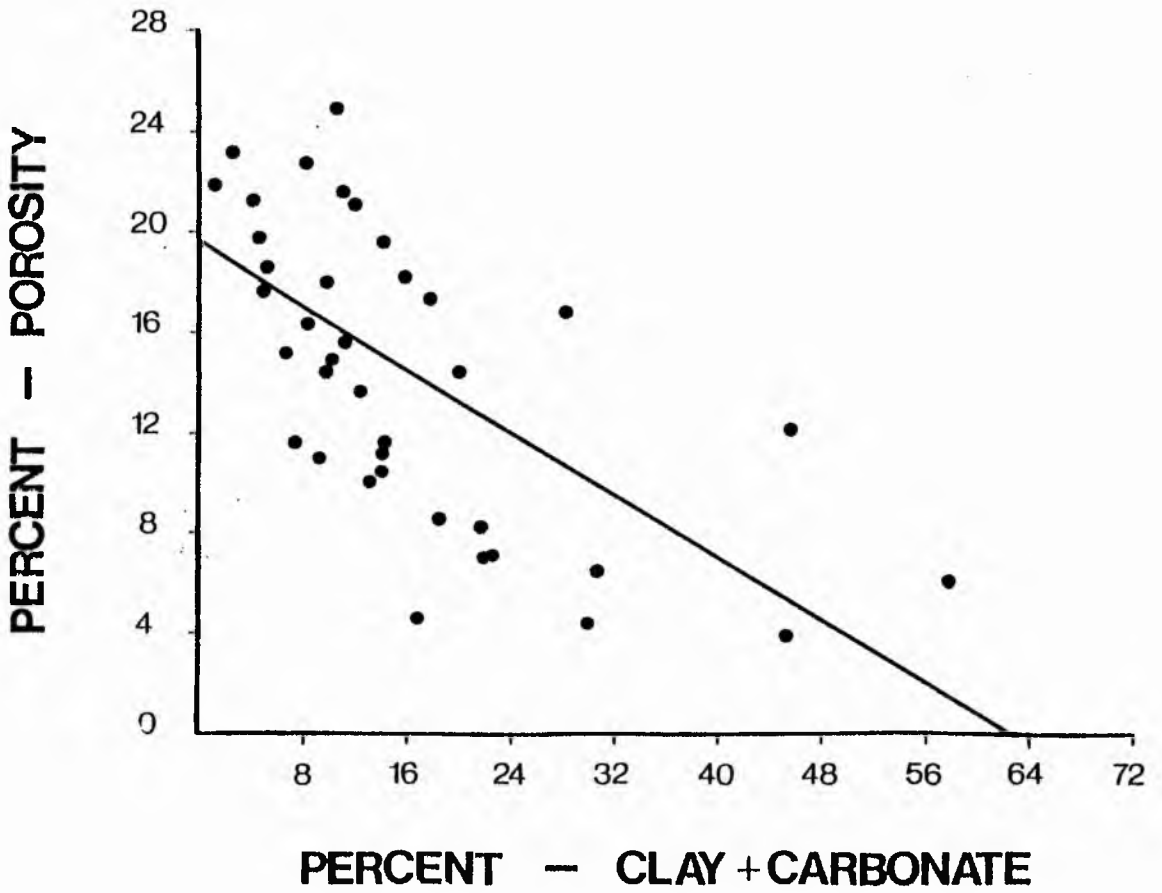


Fig 6.10 Plot showing the effect of clay + carbonate on porosity.

Correlation coefficient  $\gamma$  for all data = -0.633. Reduced major axis regression equation  $y = -0.30X + 19.09$ .



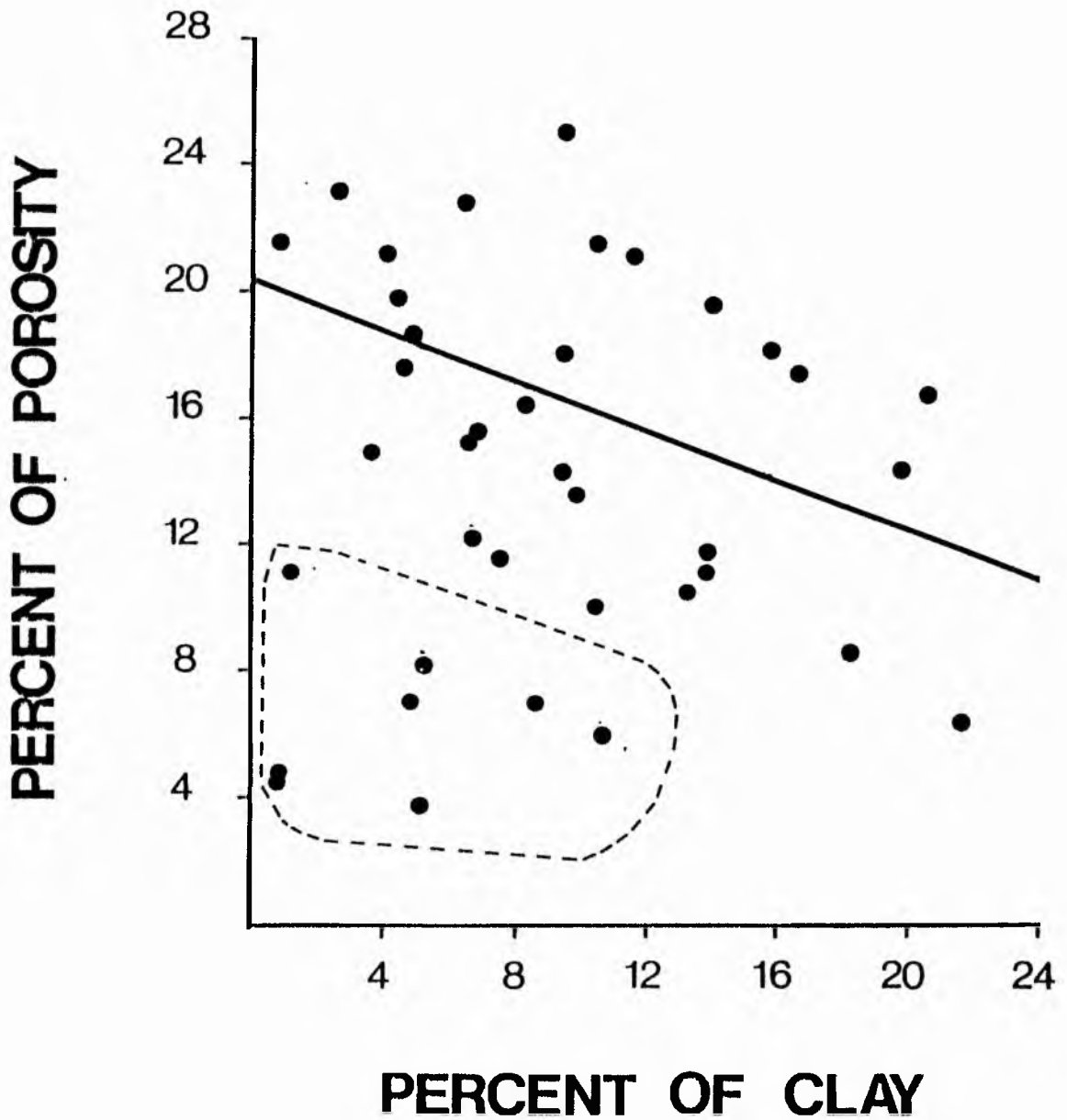


Fig 6.11 Variation of porosity with clay. Correlation coefficient  $\gamma$  for all data =  $-0.015$  - (The lower field within dotted lines, is rejected because of the high content of carbonate cement, up to 47%). A significant correlation ( $\gamma = -0.472$ ) exists for the upper part clay - porosity samples. Reduced major axis regression equation shown for the upper part:  $y = -0.40X + 20.34$ .

large amounts in the samples which plot in the lower field.

Microporosity is the result of a number of different processes acting through time producing a variety of shapes and amounts. The processes include precipitation of different minerals, filling of pores, dissolution and fracture. Pores may be primary or secondary. All the pores are less than 1  $\mu\text{m}$  in diameter and the proportion of micro to macroporosity varies up to 89% (Fig 6.12). These elements have been taken into consideration and produce a classification of thirteen types (Appendix 6.8).

The mercury penetration porosimeter was used to obtain a picture of the pore size distribution of a rock sample (Fig 6.12). The relationship between cumulative percent to the pore size provides three different types (Appendix 6.5 - Fig 6.13). One type (A) contains the highest cumulative percent concentrated in pore size below 1.0  $\mu\text{m}$  (in diameter), type (B) has pore diameter range between (1.0  $\mu\text{m}$  to 15.0  $\mu\text{m}$ ), while type (C) has the highest percent of pores with diameters ranging between (15.0  $\mu\text{m}$ -to-50  $\mu\text{m}$ ).

A number of petrographic characteristics were compared with pore size. The petrographic variables selected include, mean grain size, sorting, percentage of matrix and cement (carbonate only) (Appendix 6.6). The data obtained indicate that inverse relationships exist between mean grain size and microporosity. As the mean grain size decreases, effective microporosity tends to improve (Fig 6.14), but there are other factors which have more affect than the grain size on the microporosity percentage, such as carbonate cement.

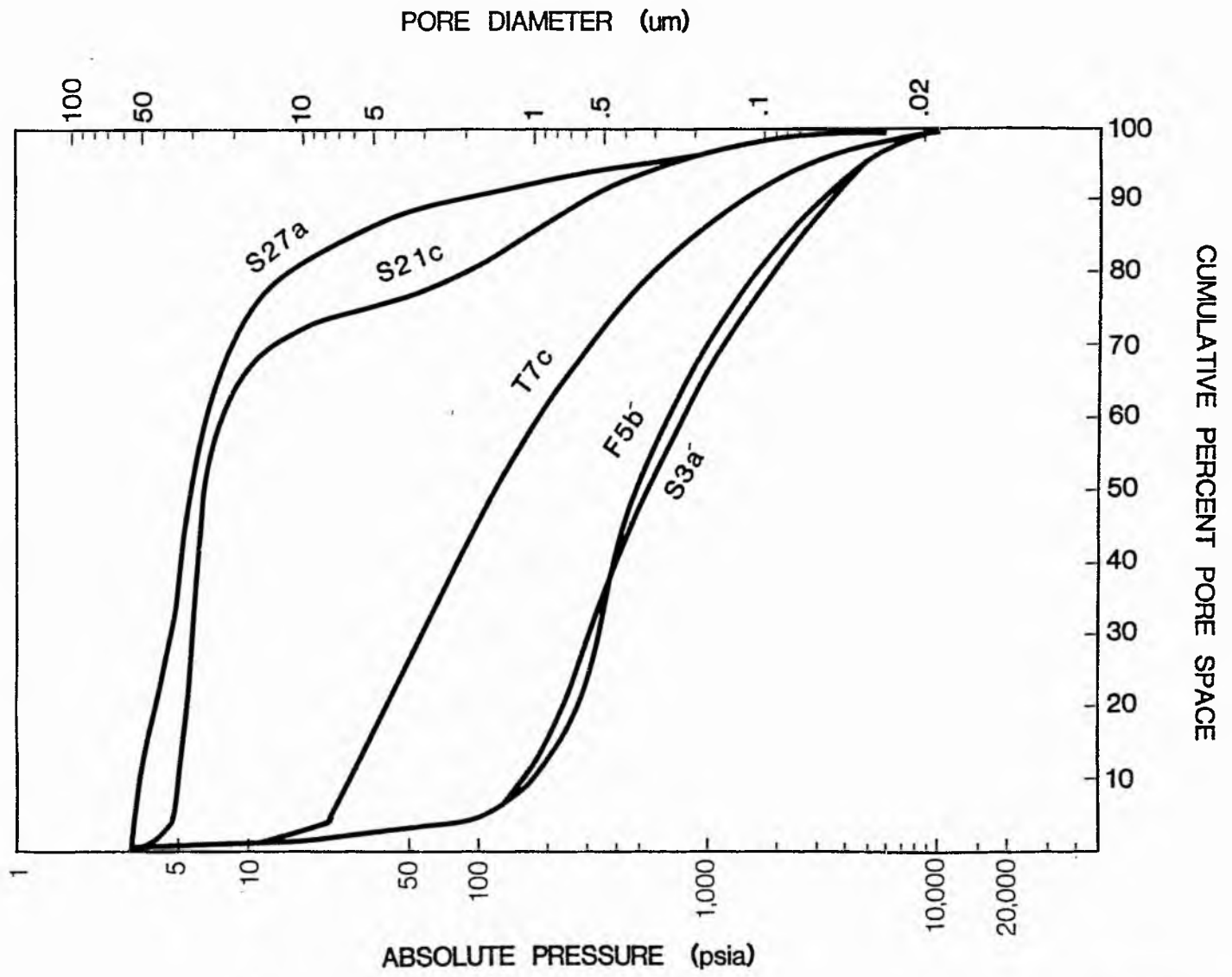


Fig 6.12 Mercury-injection pressure, pore diameter, and cumulative percent of different samples. All samples have different microporosities.

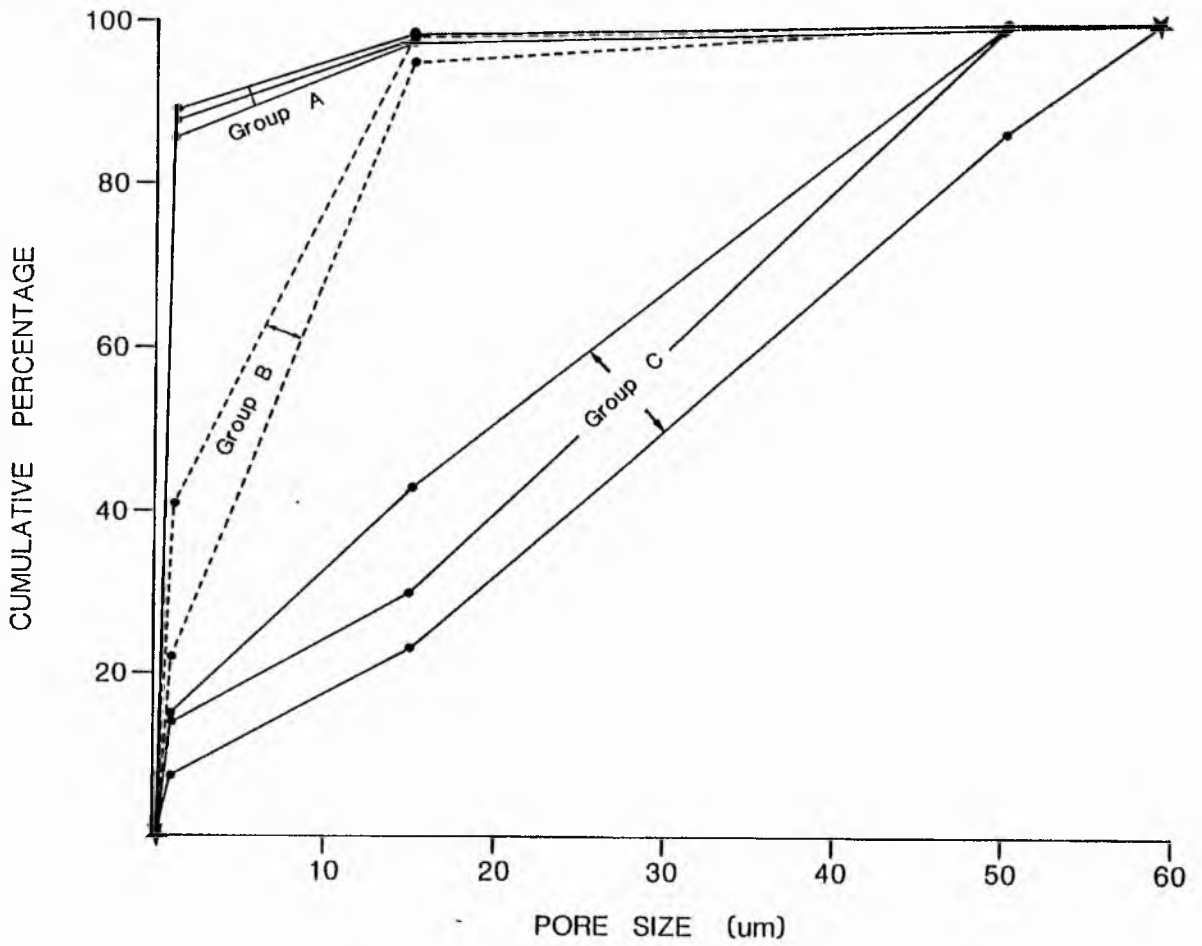


Fig 6,13 A relationship between cumulative percent and pore size.  
This relation provides three groups, A, B and C.

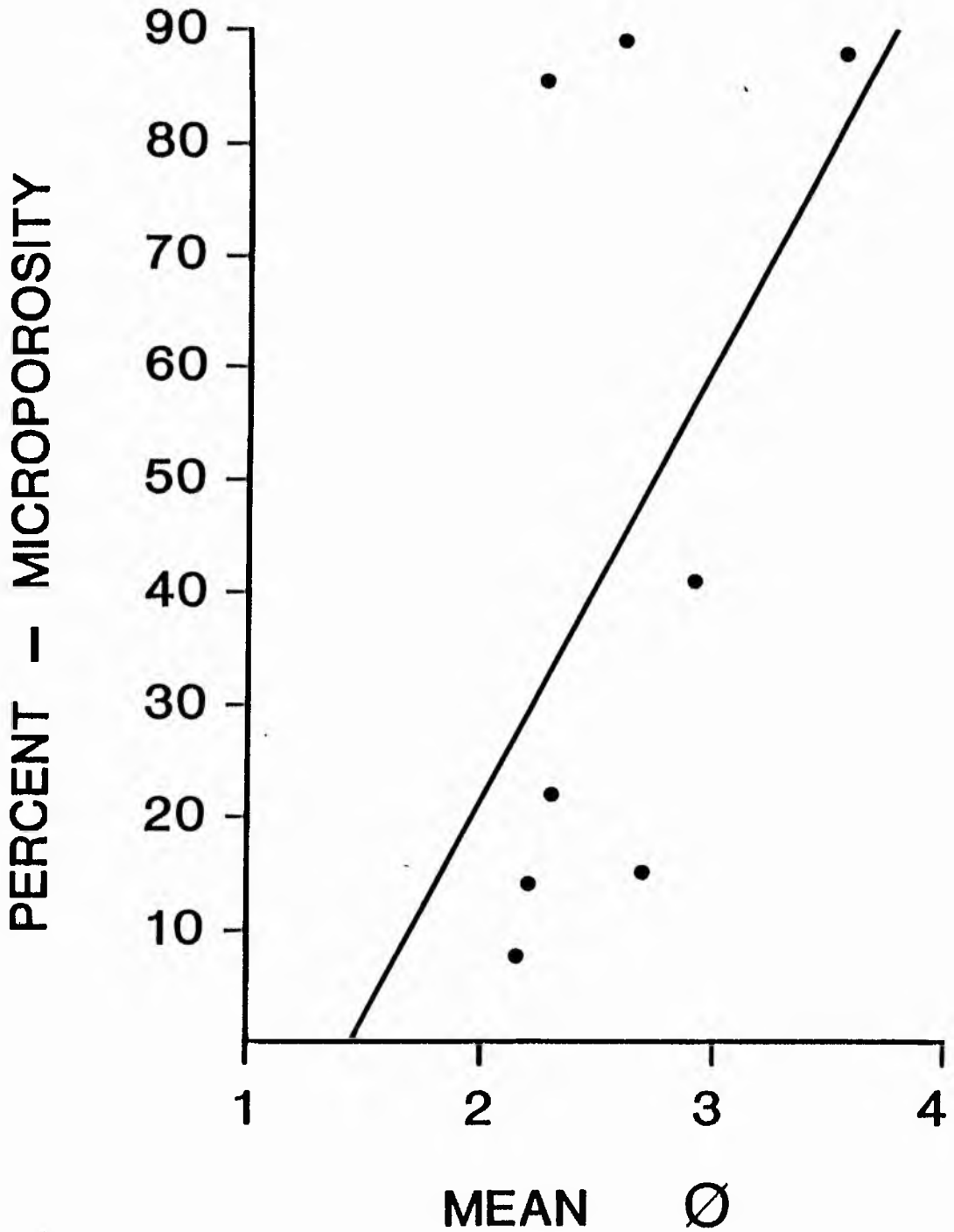


Fig 6.14 Relation between grain size and microporosity. Correlation coefficient  $\gamma$  for all data = 0.50. Reduced major axis regression equation shown:  $y = 38.09X + 53.79$ .

In type (A) microporosity values are associated with the carbonate cement which reaches up to 40.2%. Carbonate cementation decreased the larger pores and increased the microporosity (about 87.5%). Type (B) is formed of fine-to-nearly very fine-grained sand. Sample (T7) has a lot of clay, about 13.2%, which may be responsible for the larger amount of microporosity (41.0%). Sample (S24) has only 22% of microporosity with 2.6% clay. It is clear that not only the clay, but also the silica overgrowth was responsible for producing the microporosity. Type (C) is formed of fine-to-medium grain size. No significant amount of carbonate cement occurs, but clay in one sample reaches 19.8%. In the presence of such amounts of clay, the microporosity is not more than 14%, and the highest amount are found in sizes more than 15  $\mu\text{m}$ . The intergranular pore size sometimes reaches up to that of the containing grains, and the median pore size is about 24.7  $\mu\text{m}$ ; it suggests that the clay was not enough to fill these pores (Figs 6.15 A, B). Generally, the effect of clay material increases as the pore-aperture, and the grain size decreases.

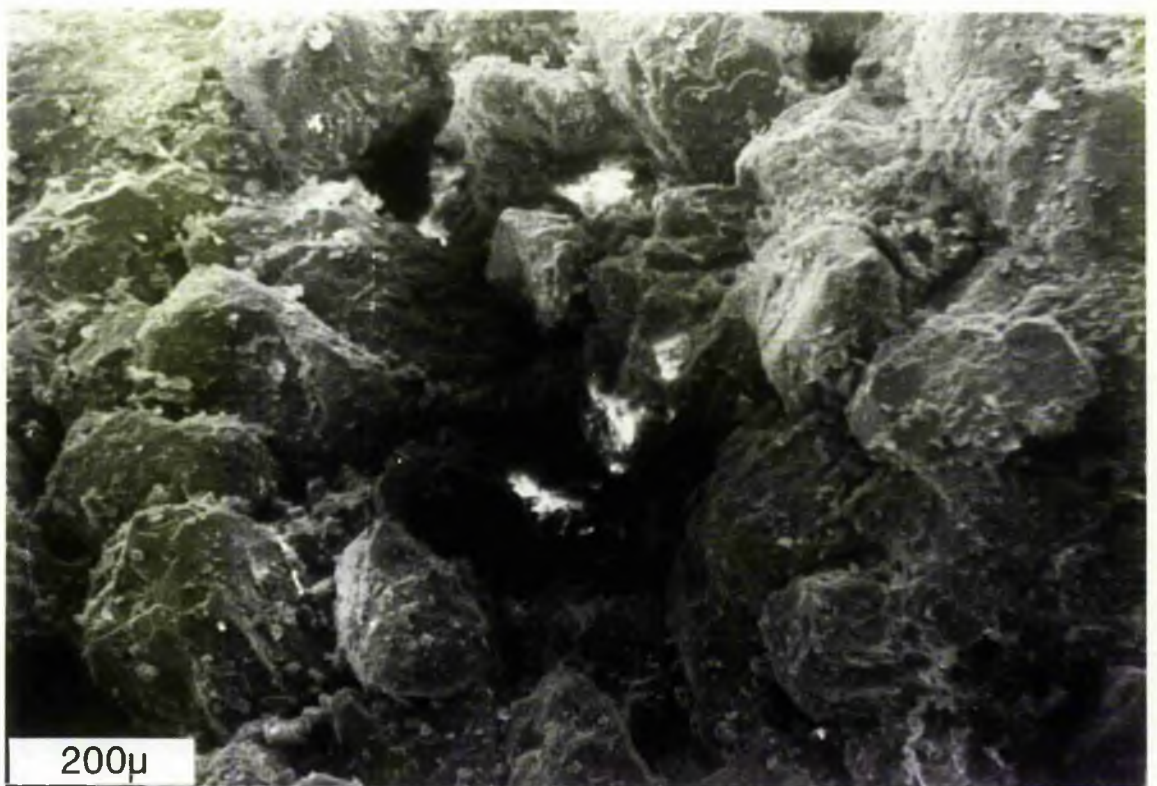
As might be expected from above a positive correlation exists between the percentage of carbonate + clay and microporosity (Fig 6.16).

### 6.5 Mercury injection

Mercury injection capillary-pressure curves provide additional information on the size distribution of pores and micropores, the higher the injection pressure, the smaller the pores, because the mercury cannot penetrate into small pores

Fig 6.15A SEM photograph showing that the pores are not completely filled by clay minerals. Sandstone Unit (S21c) - East side. Scale bar equals 10  $\mu$ .

Fig 6.15B SEM photograph showing the "Oversized pore" larger than the surrounding grains. Sandstone Unit (S21c) - East side. Scale bar equals 200  $\mu$ .





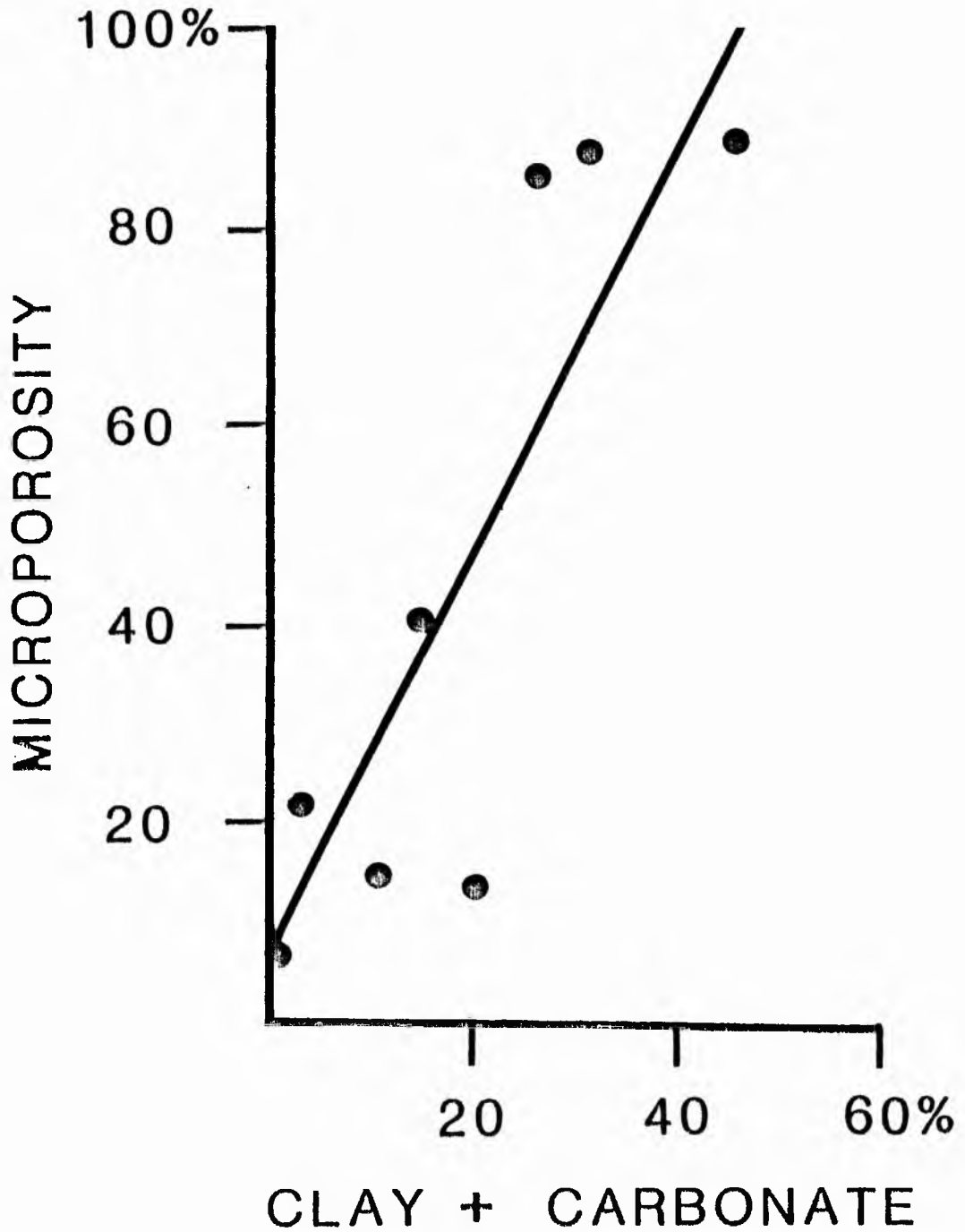


Fig 6.16 The relationship between clay + carbonate and microporosity. Correlation coefficient  $\gamma$  for all data = 0.86. Reduced major axis regression equation shown:  $y = 2.07X + 6.73$ .

until the injection pressure exceeds the capillary pressure. Wardlaw (1976) pointed out that the volume of mercury entering a sample between specific pressure limits is related to the total pore volume connected by pore throats within specific size limits. Thus, a mercury injection pressure curve provides information about the combined volumes of pores and throats.

Fig 6.12 shows the relationships between pore diameter and pressure of five samples containing different percentages of cement and matrix. The samples are different in grain size (increasing from right-to-left). Mercury injection reveals relatively coarse and well sorted pore apertures for samples S27 and S21, indicative of a good reservoir horizon, and the mercury injection break ranging between 38.0  $\mu\text{m}$  to 45.0  $\mu\text{m}$  of pore diameter. The curves for samples F5b and S3a have small pore apertures. The mercury did not break through until about 1.8  $\mu\text{m}$  diameter (0.9  $\mu\text{m}$  radius); those horizons contain a lot of nearly isolated pores with high percentage of interconnected micropores (most of the micropores were identified from these two samples).

On the other hand, the differences in the curve shape may indicate different types of porosity, causing a variable amount of permeability, which is increasing from A (0.5 md) to 4.991 md, in the B, and up to 878.9 md in type C. Pittman (1979) pointed out that sandstones with a significant amount of microporosity and dissolution porosity have lower permeability than sandstones containing predominantly intergranular porosity. In this case, the porosity in C curves is mostly intergranular porosity. This type of porosity decreases to the A curves, while dissolution and microporosity increases.

The orthoquartzite sandstone of sample S27a (Fig 6.17) with predominantly intergranular porosity, has 29.33% as average of porosity, and 393.8 md permeability. A mercury injection curve reveals large, well-sorted apertures (approximately 45  $\mu\text{m}$  breakthrough). A scanning electron micrograph (Fig 6.18) indicate that the rocks have obvious pores despite overgrowths. It is therefore suggested that most of the intergranular porosity has formed by the dissolution of carbonate (Schmidt and McDonald 1979). Plagioclase grains are also almost completely destroyed (Figs 6.19 A to C), while the less abundant microcline grains have suffered partial dissolution (Fig 6.20).

The sandstone illustrated in (Fig 6.21), has 22% porosity, and 879 md permeability. A mercury injection curve reveals large, well-sorted apertures (approximately 38  $\mu\text{m}$  breakthrough). Generally, the sandstone of this sample S21C has intergranular pores and interconnected dissolution pores to provide an effective macropore network. Porosity has been created by fracturing and dissolution of feldspar, polycrystalline, and monocrystalline quartz. It is quite permeable, in spite of the presence of clay minerals (19.8%). Most of the clay is kaolinite (15.3%) (identified by XRD) which has less effect on permeability than other types of clay such as smectite and montmorillonite. Chilingarian and Wolf (1975) pointed out that the sandstones are particularly impermeable in the presence of 6 to 9% montmorillonite, but those containing up to 15% kaolinite can remain quite permeable. SEM and thin section observations (Figs 6.22 A, B - 6.15 A, B), indicate that this horizon contains a lot of vuggy pores, and the clay is not enough to fill these huge

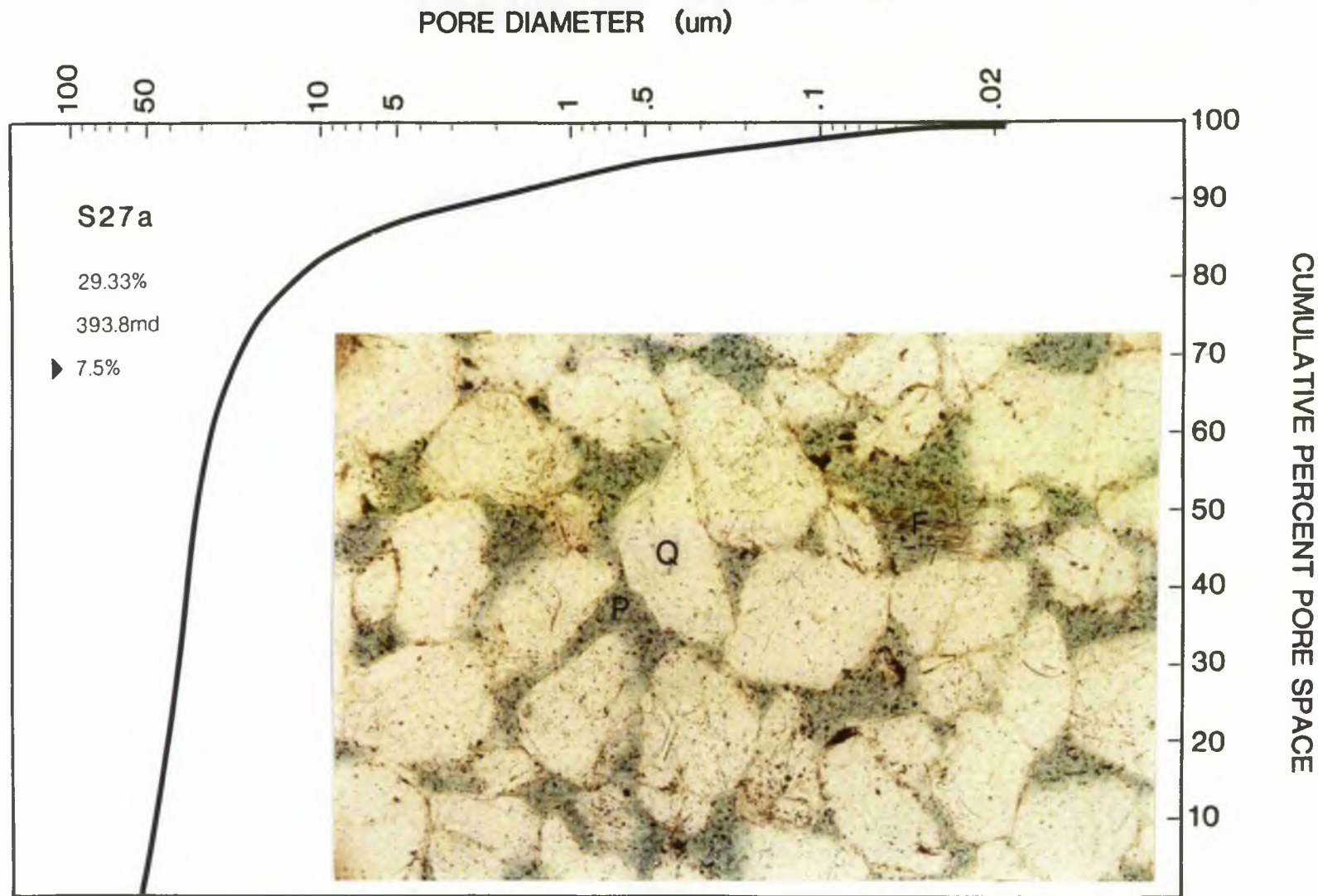


Fig 6.17 Mercury injection curve and photomicrograph of medium grains. Porous sandstones result from nearly complete dissolution of Carbonate Cement and replacement. Grains are cement by quartz overgrowth (Q). Porosity (P), parts of feldspar grain after dissolution of replacive (F). The curve reveals course and well-sorted pore aperture. Ordinary light-x 100. ▶ Percent of microporosity.

Fig 6.18 SEM photograph showing the rock has obvious pores despite a lot of quartz overgrowth. Medium grained sandstone Unit (S27) - East side. Scale bar equals 400  $\mu$ .



Fig 6.19A Photomicrograph showing feldspar grain nearly completely dissolved. Medium grained sandstone Unit (S27) - East side. Ordinary light, x 500.

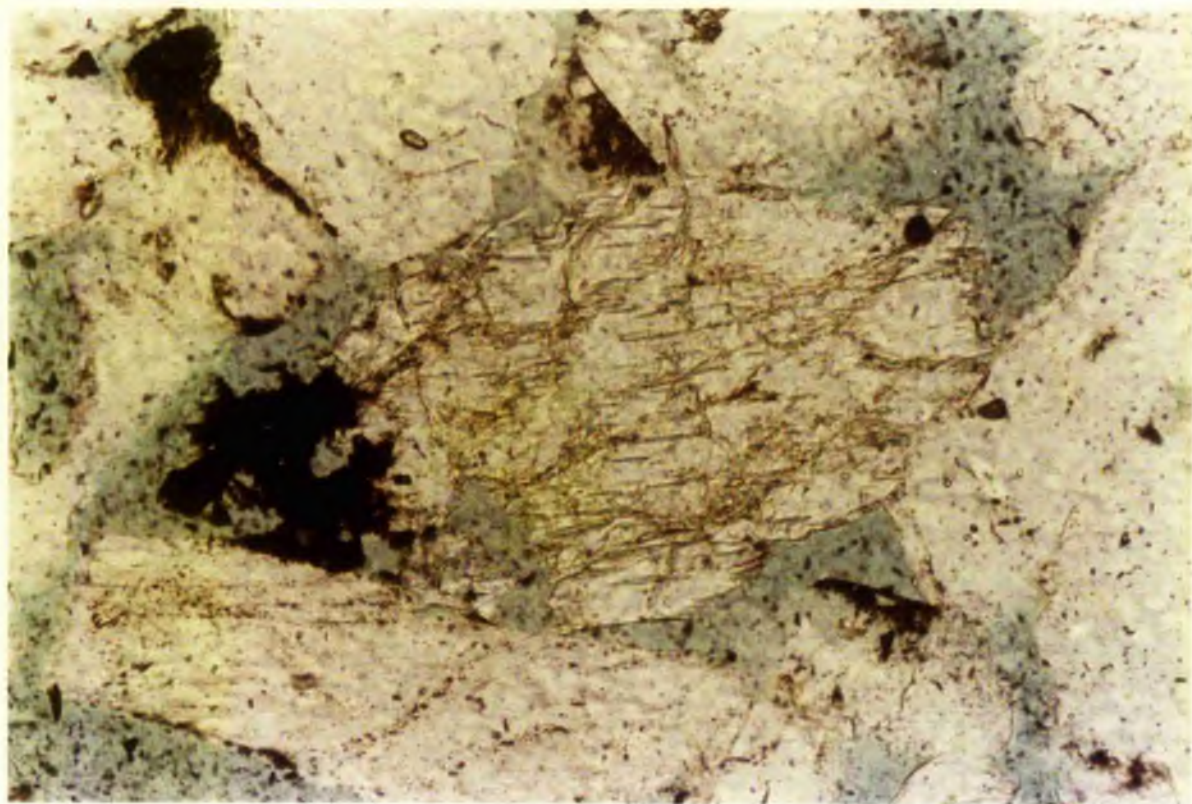
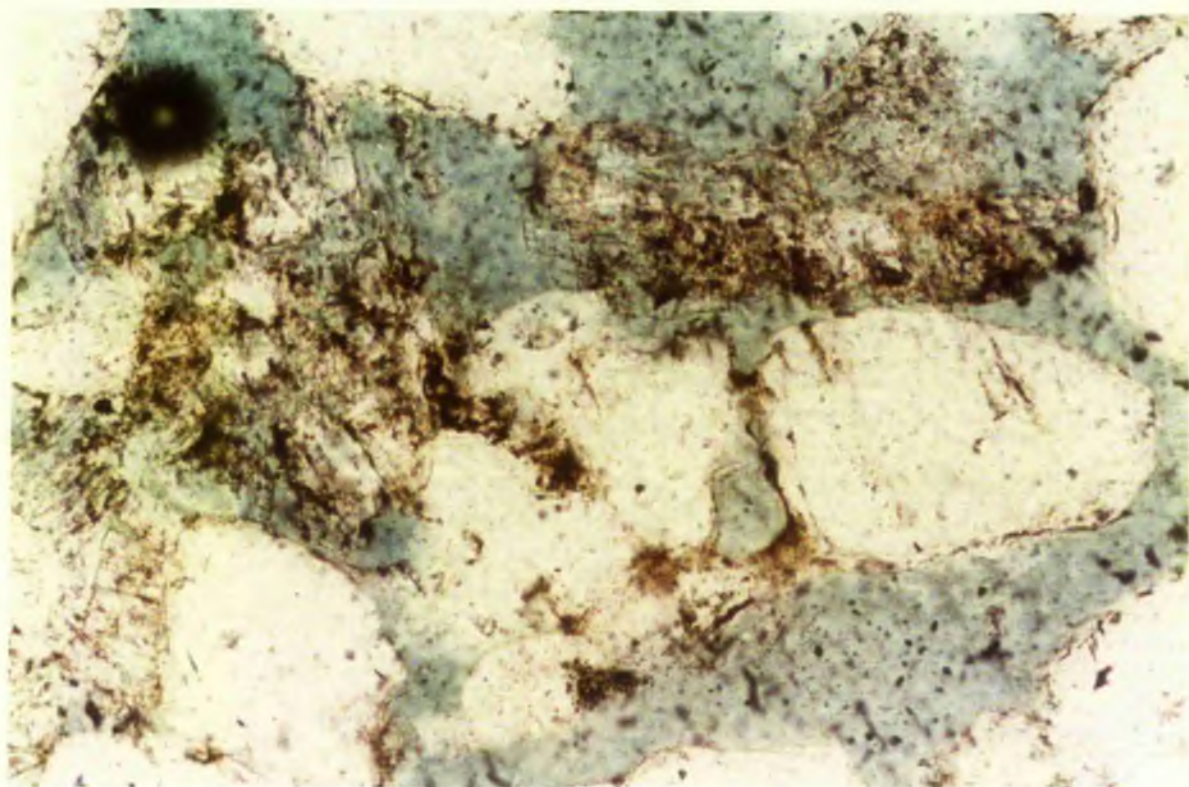
Fig 6.19B Photomicrograph showing two grains of feldspar (F) nearly completely dissolved, only small scraps remain between quartz grains (Q). Medium grained sandstone Unit (S27). Ordinary light, x 250.





Fig 6.19C Photomicrograph showing three grains of feldspar affected by dissolution, and good inter connection between intergranular and intragranular pores. Medium grained sandstone Unit (S27) - East side. Ordinary light, x 50.

Fig 6.20 Photomicrograph showing partial dissolution of feldspar grain. Medium grained sandstone Unit (S27). East side. Ordinary light, x 50.



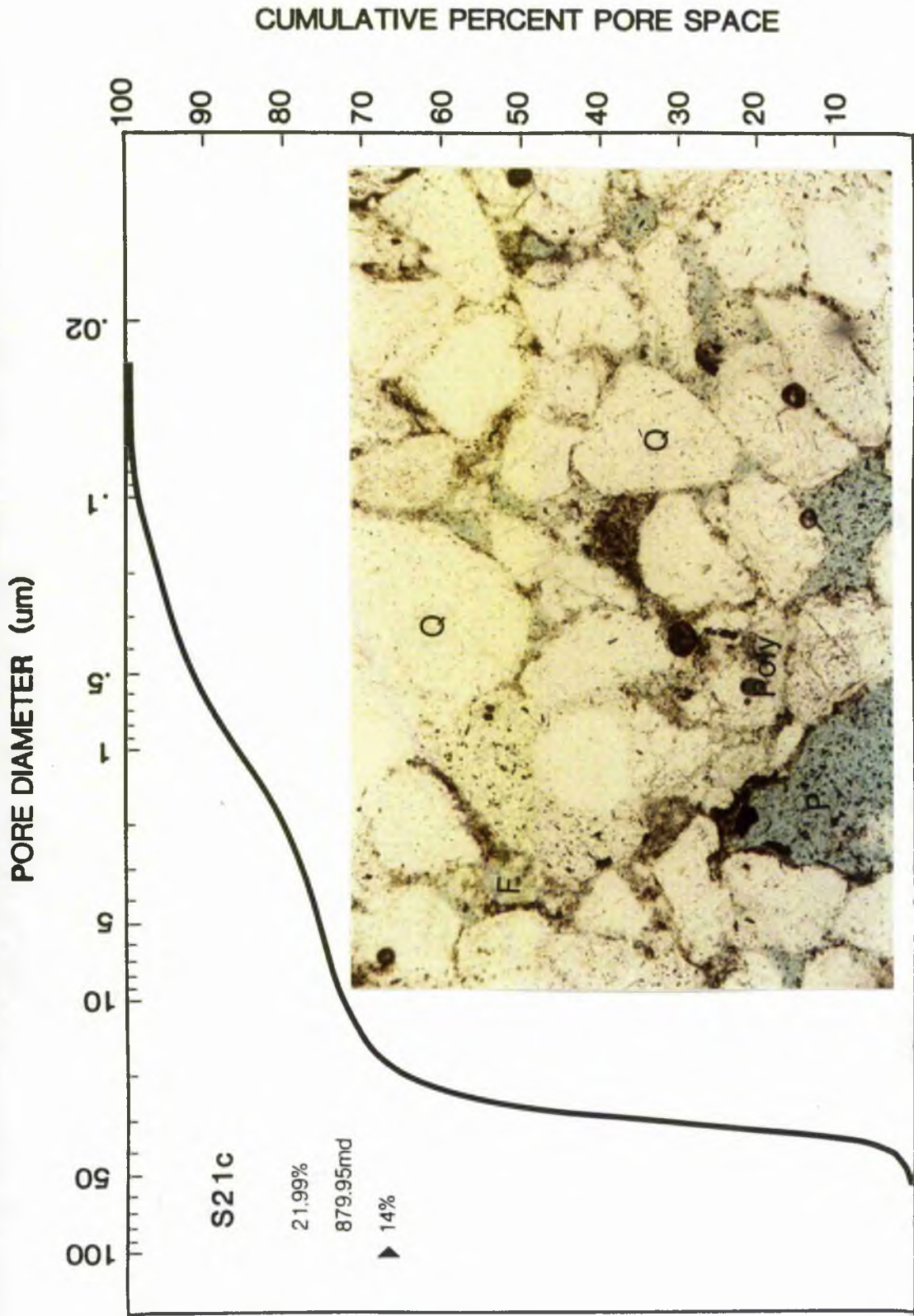
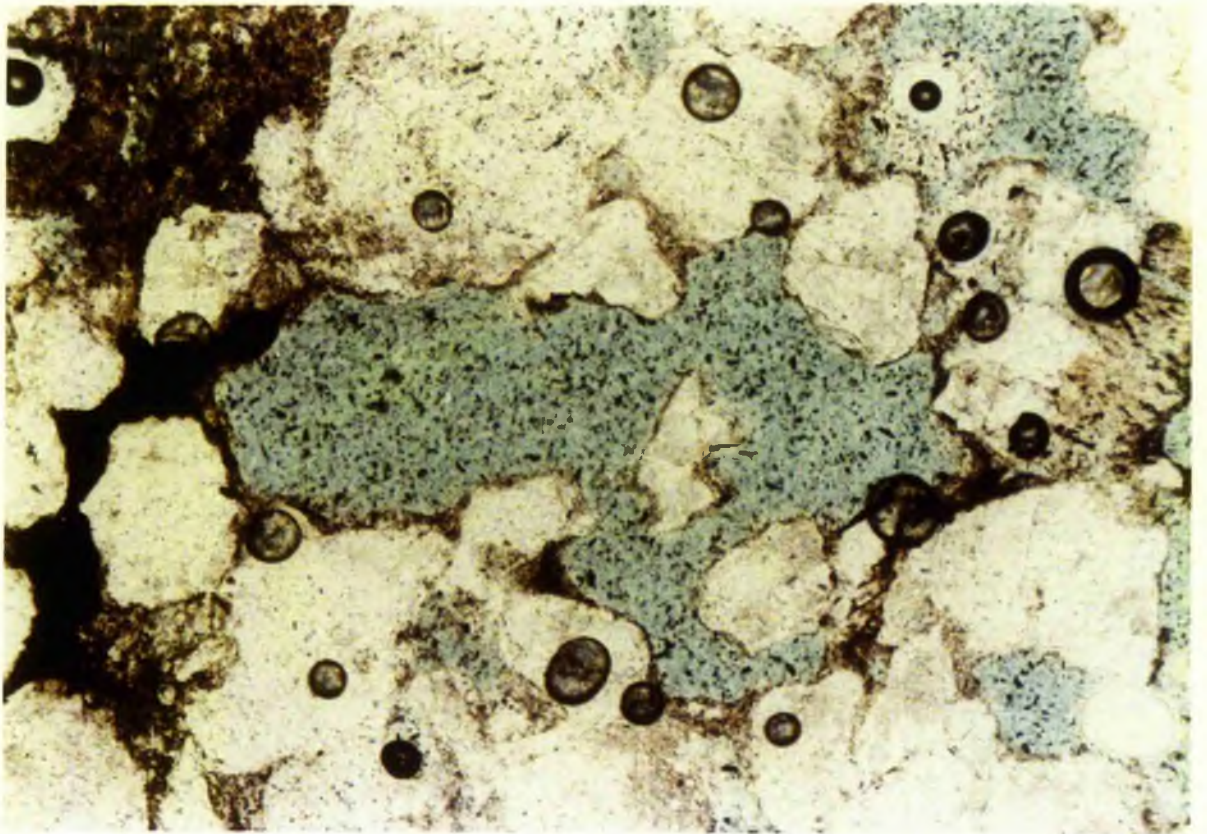


Fig 6.21 Mercury injection curve and photomicrograph. Pores (P), Feldspar (F), Quartz (Q), Polycrystalline (Poly), Quartz with overgrowth (Q). The mercury injection curve indicate the rock has good pore apertures, in spite of the presence of a high amount of clay material. Ordinary light x 100.

▶ Percent of porosity.

Fig 6.22A Photomicrograph showing vugs, good interconnection with intergranular pores. Sandstone Unit (S21c) - East side. Ordinary light, x 25.

Fig 6.22B Photomicrograph showing the oversized pore, and clay filling the pore in the upper light side (CL). Sandstone Unit (S21c) - East side. Ordinary light, x 125.



pores.

The B sample (Fig 6.12) shown in the photomicrograph of figure 6.23, has 21.57% porosity (nearly half of it microporosity), and less than 5 md permeability. In this example (T7), the sandstone has some carbonate material (1.0%), but probably most of it has been dissolved to form secondary porosity, and has small pore apertures in contrast to the previous two samples before (median 3.2  $\mu\text{m}$ ). The very fine grain-size of this horizon (B) and the presence of clay materials 13.2% (thin-section analysis), might be the cause of reduced pore-aperture size and the permeability. A mercury injection curve breakthrough occurs at nearly 8.0  $\mu\text{m}$  of pore diameter. Approximately 50% of the pore apertures in this rock have radii less than 0.5  $\mu\text{m}$ .

The highest percentage of microporosity was found in sandstones of type (A) (Figs 6.24 - 6.25). They have low permeability caused by small pore apertures (median 0.85, 0.9  $\mu\text{m}$  respectively), associated with abundant clay minerals, carbonate cement reaches 21.6% and 40.2%, and fills the intergranular pore spaces. The sandstone of sample S3a (Fig 6.24) has 8.58% porosity and 0.5 md permeability. Eight-eight percent of the pore-aperture diameter are less than 1.0  $\mu\text{m}$  and 66% are less than 0.5  $\mu\text{m}$ . The mercury injection curve reveals small pore throats (breakthrough of mercury at about 1.7  $\mu\text{m}$ ). In the sandstone of sample F5b 89% of the Pore-aperture radii are less than 1.0  $\mu\text{m}$ . This is also created with carbonate cement and 0.5 md permeability. Sand type F5b (Fig 6.25) has less than 7% porosity, most microporosity is found amongst the carbonate

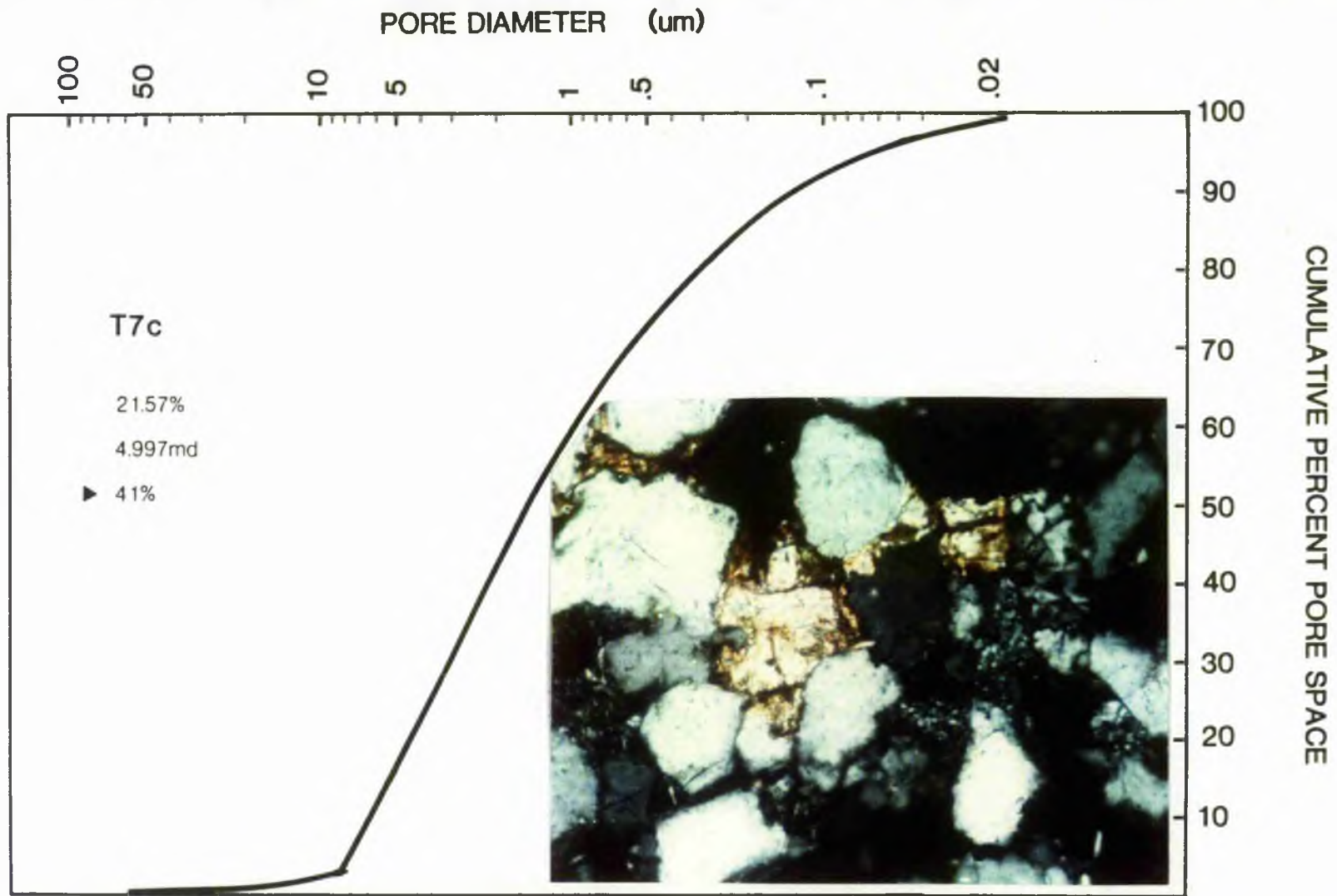


Fig 6.23 Mercury injection curve and photomicrograph reveals that medium size pore aperture with breakthrough at about 8.0  $\mu\text{m}$  (in diameter). The rock has 21.6% porosity, but only 5 md permeability. Porosity created by dissolution of carbonate cement, the lower permeability caused by clay fills the pore. Cross polars x 200. ▶ Percent of microporosity.

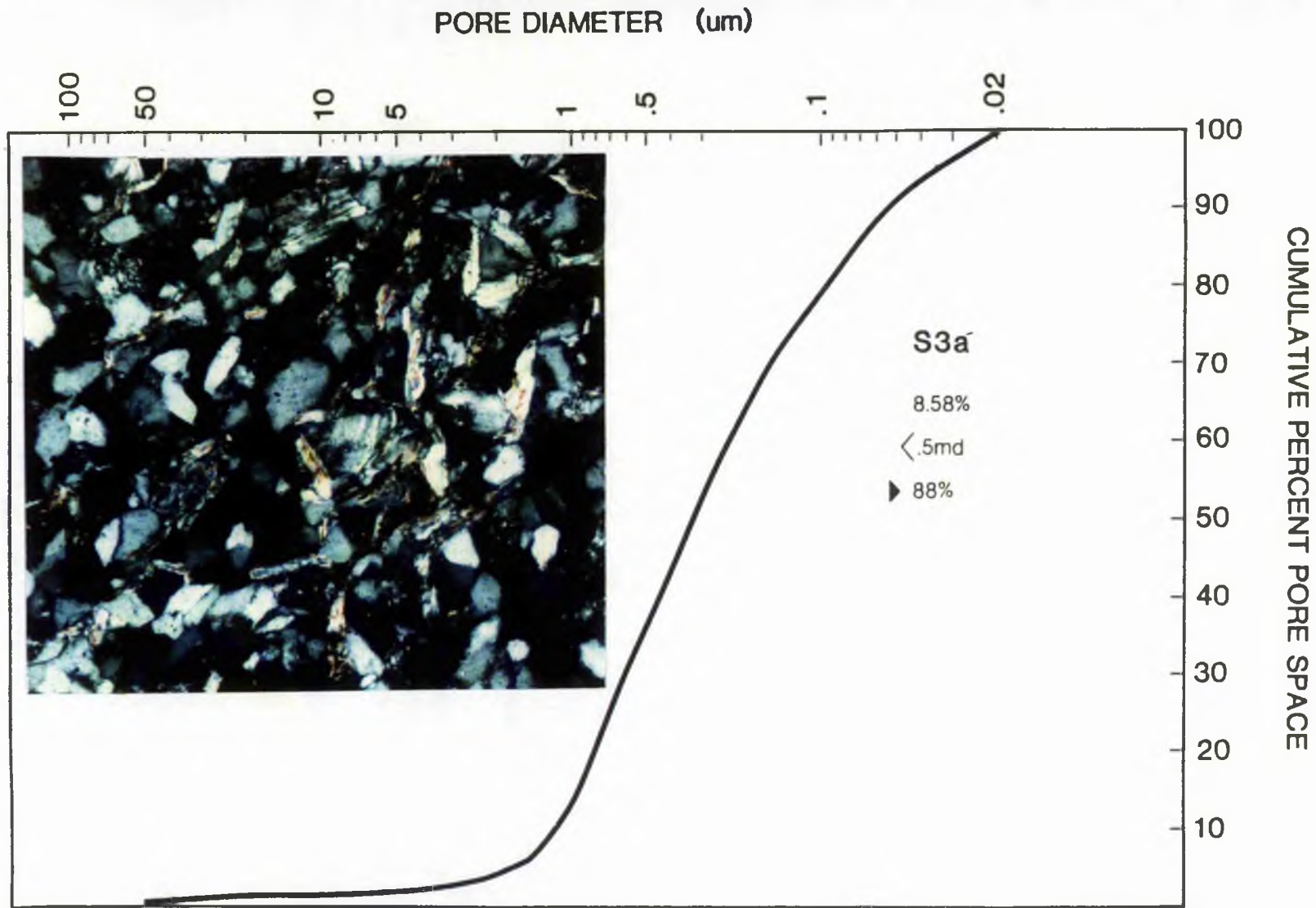


Fig 6.24 Mercury injection curve and photomicrograph, indicate that the intergranular porosity is filled by clay, which has reduced pore aperture. Cross polars x 100. ▶ Percent of microporosity.



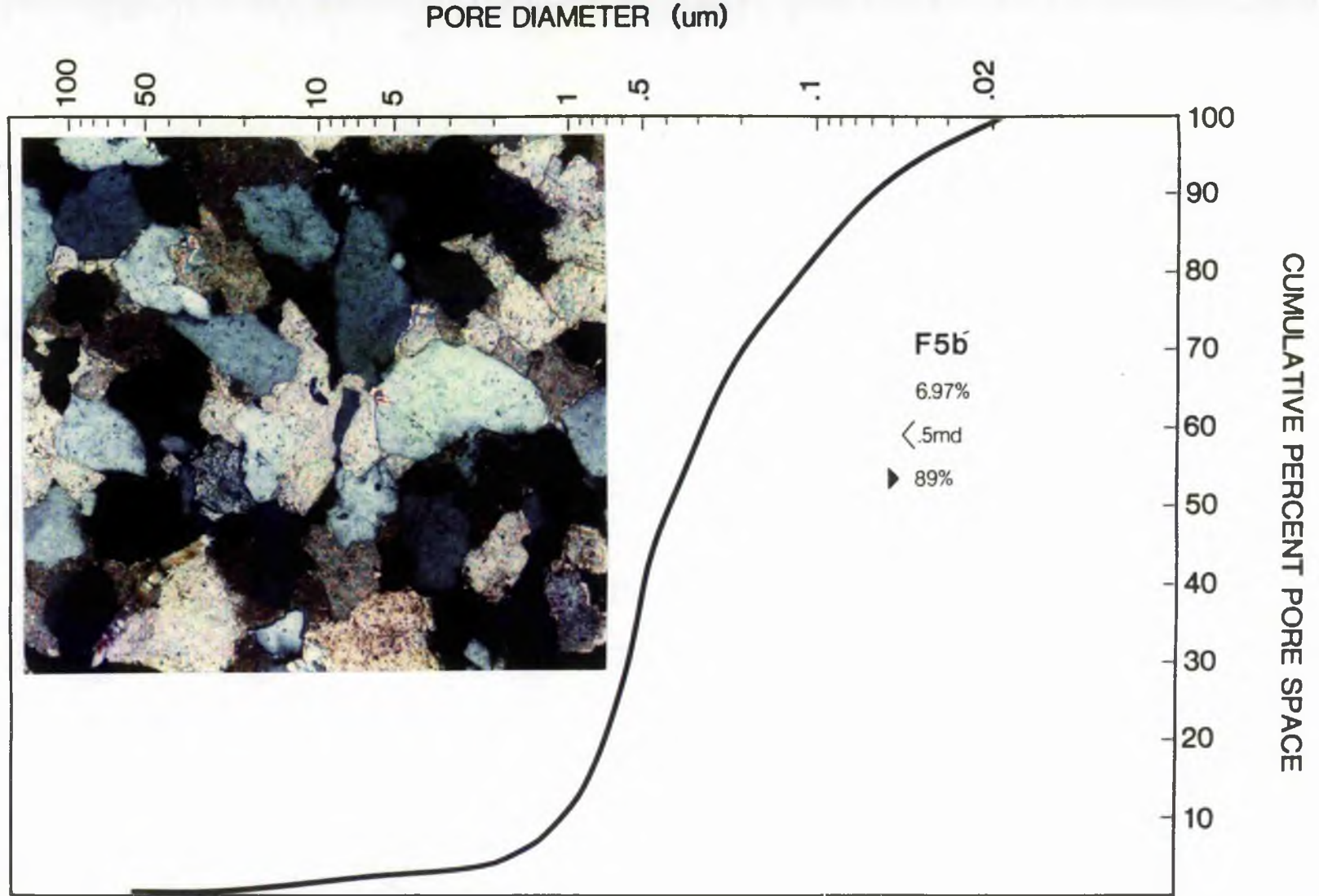


Fig 6.25 Mercury injection curve and photomicrograph, indicate that the pores reduced by carbonate mainly filling the pores and increased the microporosity percent. Cross polars x 100.▶Percent of microporosity.

material. The mercury injection curve indicates that this rock has small pore-aperture which appear to be isolated because mercury did not breakthrough until about 1.8  $\mu\text{m}$  pore diameter. Some of the pores are oversized from dissolution of carbonate cement, but they are isolated from one another and interconnected only by the tiny intercrystalline pores.

### 6.6 Secondary Porosity

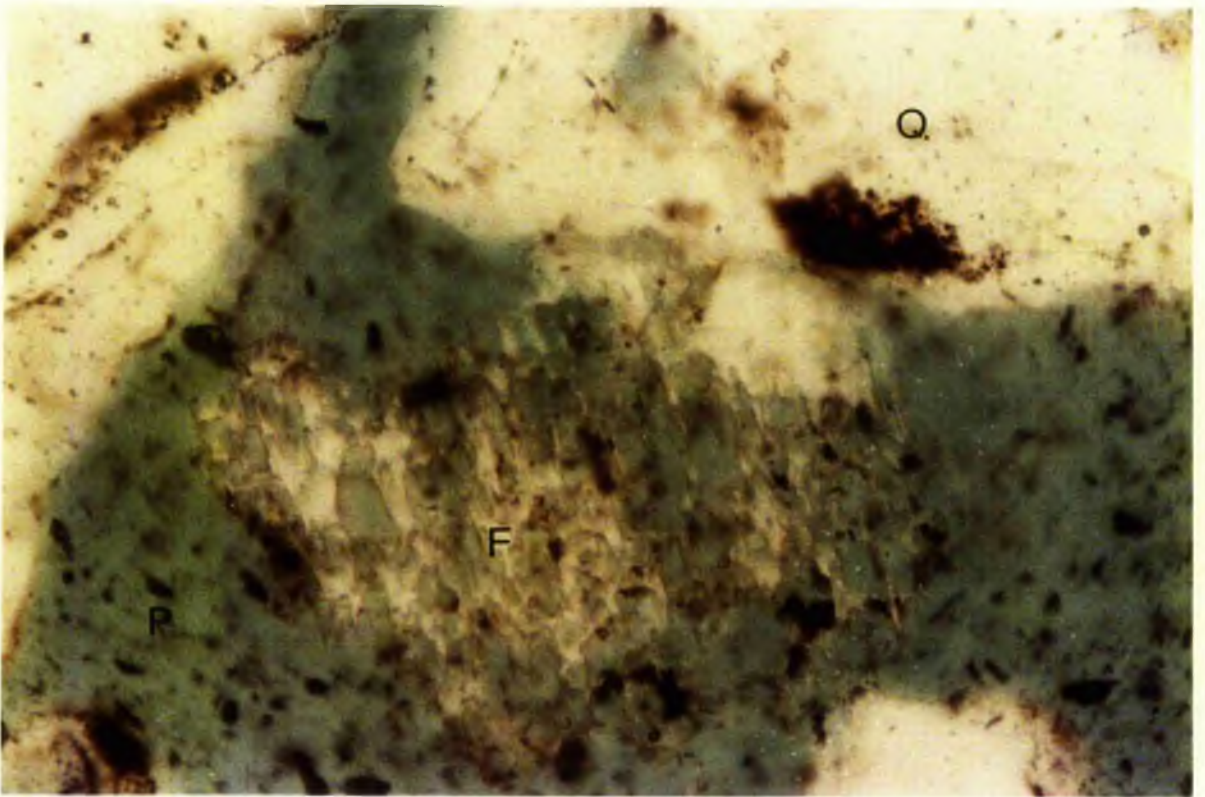
Secondary porosity in St Monance sandstones is mainly the result of dissolution of non-silicate constituents, predominantly carbonate cement. A classification has been developed (modified from Schmidt and McDonald 1979). Of the types in this classification (Appendix 6.9; fig 6.19) the first three types are common and form the bulk of the pores. The first, arising from the dissolution of carbonate cement occurs in pores varying from very small (microporosity) to very large vugs (Figs 6.22 B, 6.26). The second resulted from the dissolution of replaced minerals as calcite dissolved after replacing feldspars or quartz (Fig 6.27), and the third involves pores created by fractures.

Sandstones display a variety of textures (Appendix 6.10). Intergranular texture together with enlarged intergranular texture produced by dissolution of carbonate cement is common and often forms over-sized pores. Moldic pore texture also occurs. I have modified the meaning of this term to include pores which are not entirely isolated but which have micropores present between the surrounding quartz grains.

Other textures included in the classification and commonly found in secondary porosity studies are all represented in the St

Fig 6.26 Example of porosity after dissolution of cement. Secondary porosity resulting from completely dissolution of carbonate cement. Sandstone Unit (B7) - West side. Q = quartz overgrowth prism in shape; P = porosity. Ordinary light, x 125.

Fig 6.27 Secondary porosity resulting from dissolution of cement that nearly completely replaced the feldspar grain and the margin of quartz grain. Sandstone Unit (S27) - East side. P = porosity; F = feldspar; Q = quartz grain. Ordinary light, x 500.



Monance sandstones.

### 6.7 Conclusions

The considerable variation in porosity in these sandstones has been caused by a number of factors. Reduction of pore space is by pore filling by clay, by precipitation of cement and from solution and to a small extent by compaction. Measurement of porosity is affected by the orientation of thin-sections with respect to bedding.

The bulk of porosity estimated from routine core analysis is as good or better than those found by using the thin-section method, but thin-section study of samples often shows fragmentary evidence of past events which cannot be identified from routine core samples.

Early quartz overgrowth is a dominant factor in cementation here; in addition, reduction in porosity is sometimes highest in those sandstones with carbonate cement. Generally, porosity is less than 7% and 0.5 md permeability, where carbonate cement exceeds 20%.

Thirteen basic types of microporosity are recognized. Most of them are associated with carbonate cement. Five factors controlled the abundance of microporosity in these sandstones, as follows:-

- 1 Silica cement overgrowth
- 2 Carbonate cement
- 3 Clay material
- 4 Grain size

and 5 Pore size

Most of the clays in this study area are kaolinite and illite which have less effect on permeability than other types of clay such as smectite and montmorillonite. Smoot (1960) also noted in Chester sandstones a relative increase in permeability with increase in kaolinite. But in considering the correlation between clay and permeability, the grain size of quartz parameter should also be recognized as an important control on permeability reduction. For instance, (Appendix 6.7), the two samples (53a and S21c) which have the highest percentage of clay materials (21.6% and 19.8% respectively), have different grain-size, and the permeability in medium grained rock is much higher than the very fine-grained sandstone. The permeability of very fine-grained sandstone is severely affected by the formation of clay. Galloway (1979) pointed out that coarse sandstones usually experience less serious permeability loss due to development of clay than do fine-grained sandstones.

Most of the secondary porosity results from dissolution of carbonate constituents, mainly cement. It also has formed from the dissolution of replacive material and from fractures. It is suggested that the mesogenetic decarbonatisation created the majority of the secondary pores. This mesogenetic decarbonatisation might be related mainly to the sandstones. The process of decarboxylation leads to the generation of carbon dioxide which in the presence of water produces carbonic acid; such acidic water comes into contact with sandstones and reacts with the carbonate constituents and leads to increased porosity

(Schmidt and McDonald 1979). The oversized pores in particular, must have involved dissolution of unstable rock fragments and feldspars along with carbonate cement.

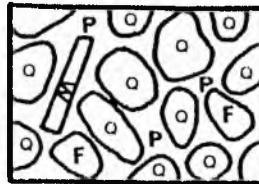
As secondary porosity formation in this area is mainly a function of chemical dissolution, controlled by several factors such as circulation of pore fluids, presence of unstable grains and cement, etc, it is patchy unless there has been extensive dissolution. Overall secondary porosity is higher in coarse grain samples than in fine sediments, and sometimes is as high as 29.33%. It is probably because of more availability of pore spaces in these samples hence, allowing the better circulation of pore solution needed for large scale chemical cementation.

The sequence of diagenetic events concluded from secondary porosity is illustrated in Fig 6.28. It is characterized by a minimal mechanical compaction of clean, uncemented sands. The dissolved material in addition to other sources lead to the development of syntaxial quartz overgrowth which is separated from the original grain often by dust rims. This silica overgrowth has caused partial to complete loss of porosity.

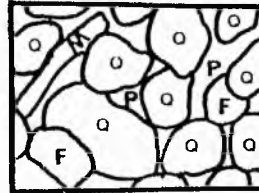
The diagenetic event was followed by the growth of clay material. Kaolinite is more abundant. These clays are believed to have developed at the expense of feldspars, rock fragments, and micas. Changes in the pore fluid chemistry caused feldspars ..... etc; to become unstable in the diagenetic environment and to alter to one of the clay minerals depending upon their composition.

Compaction further reduced the porosity and samples show fracturing of grains, bending of mica, squeezing of clay matrix.

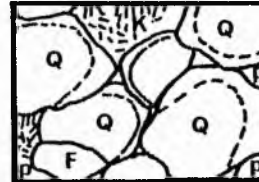
Open-packed clean sandstone



Minimal compaction of uncemented detrital grain



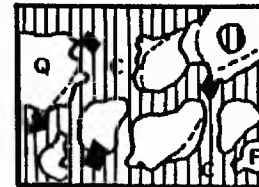
Quartz grow into pore spaces .  
Kaolinite occupies much more space



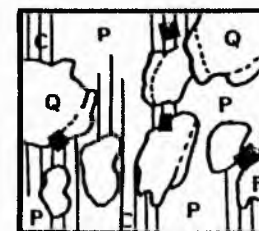
Fracture of detrital grain .  
Muscovite changes to clay



Carbonate cement filling & replacemnt .  
Growth of authigenic iron oxide



Dissolution



KEY:

- |               |                |
|---------------|----------------|
| Q : Quartz    | K : Kaolinite  |
| F : Feldspar  | C : Carbonate  |
| M : Muscovite | I : Iron oxide |
| P : Porosity  |                |

Fig 6.28 Diagenetic history of secondary porosity in St Monance sandstones.

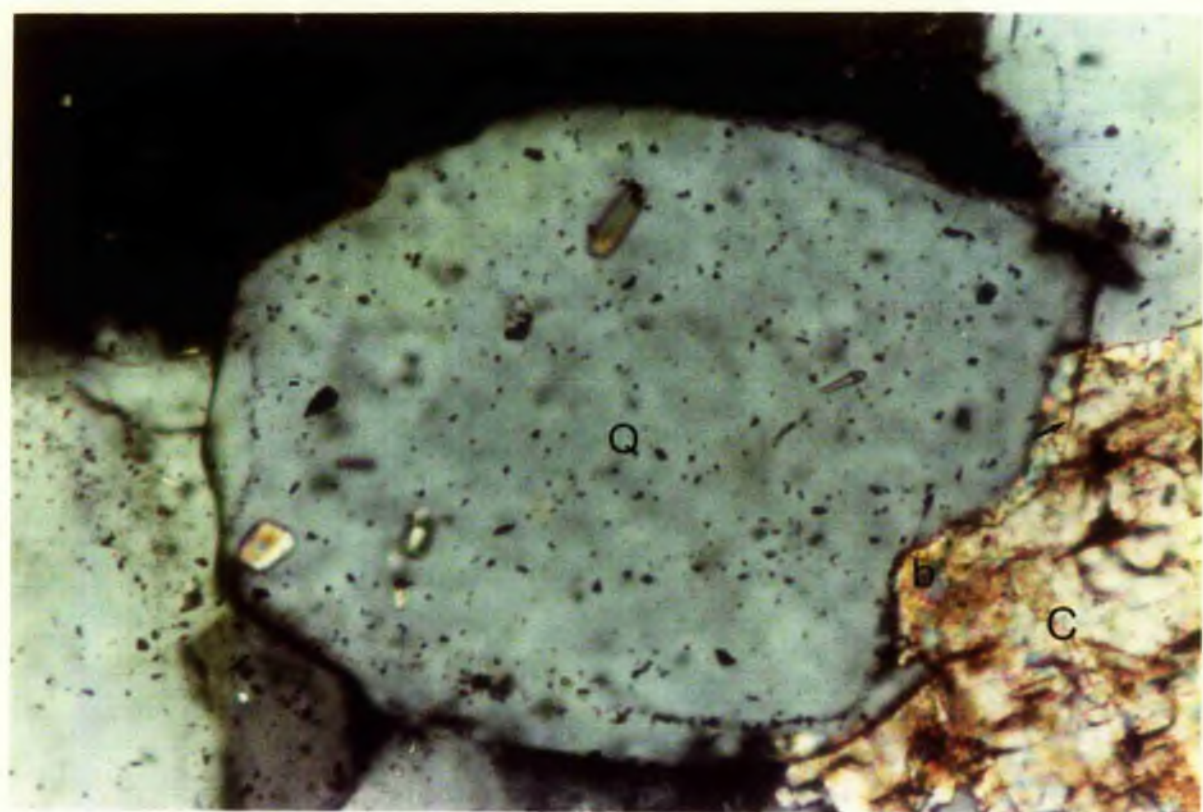
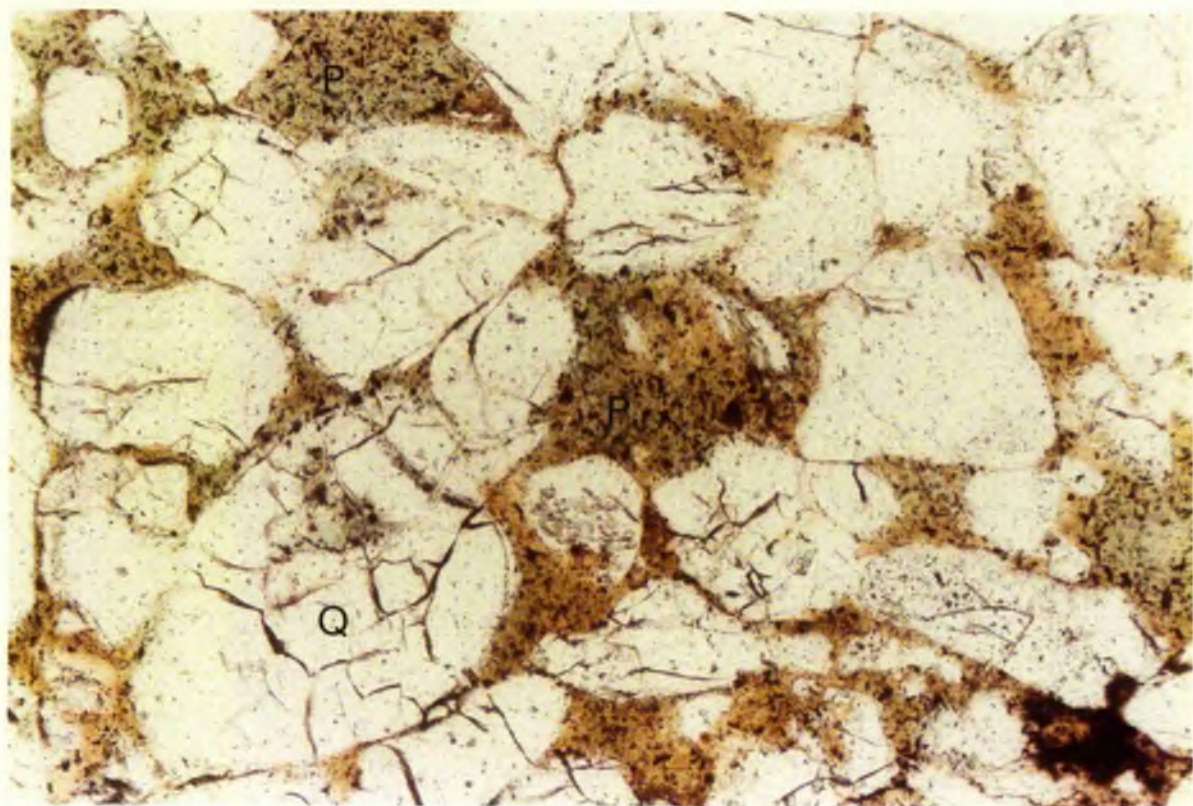


(Figs 6.29 - 6.6, Fig 5.46; Chapter 5).

Carbonatisation occurred when the clay did not develop or as a minor amount, immediately developed after quartz overgrowth, replacing detrital grains (Fig 6.30). Carbonate cement varies in content from traces to nearly 47% and has mainly reduced the primary porosity. Opaque material composed of hematite and pyrite was formed later. No further change occurred until decarbonatisation took place and produced secondary porosities which may be more than those present before the carbonatisation happened.

Fig 6.29 Photomicrograph of open grain fracture. Quartz grains fracture and cut through overgrowth (arrows), created pore grain fracture. Middle of sandstone Unit (B7) - West side. P = porosity; Q = quartz grains. Ordinary light, x 125.

Fig 6.30 Photomicrograph showing carbonate cement deposited after the silica overgrowth, filling the remaining pores and replacing the silica cement (arrow) as well as part of the original grain (b). Q = quartz grain; C = carbonate cement. Middle part of sandstone Unit (B7) - West side. Crossed polars, x 500.



CHAPTER 7

7 DIAGENESIS

A brief examination of almost any thin-section of St Monance sandstone can leave little doubt that the present state of the rock is drastically different from that at the time of deposition. The present texture of the sandstones shows very clearly the effect of diagenesis. Features relating to quartz will be considered first, followed by feldspars, clay and finally carbonate. Illite and chlorite are in trace quantities only.

7.1 Quartz Overgrowth

The silica cement has been previously discussed, therefore, only its position in the diagenetic sequence will be considered here. Most of the evidence suggests that quartz overgrowth is the first diagenetic precipitate and characterizes early burial. This early stage developed in the presence of pore fluids with a high concentration of silicon, potassium and aluminium. Silica cement could begin to precipitate at high pH value and augmented by waters derived from the shallow compaction of the enclosing shales, the original water would become increasingly enriched in silica and alumina. The alumina depresses the solubility of silica. Millot (1970) showed that the mixing of separate silica and alumina rich solutions (Fig 7.1) made the mixtures very insoluble until pH >11. Eventually, dissolved silica would begin to form syntaxial overgrowths on the host quartz grains. Some evidence indicates minimal compaction prior to the present state of overgrowth. Quartz overgrowth in a few samples partly encloses kaolinite (Fig 5.29) and cryptocrystalline

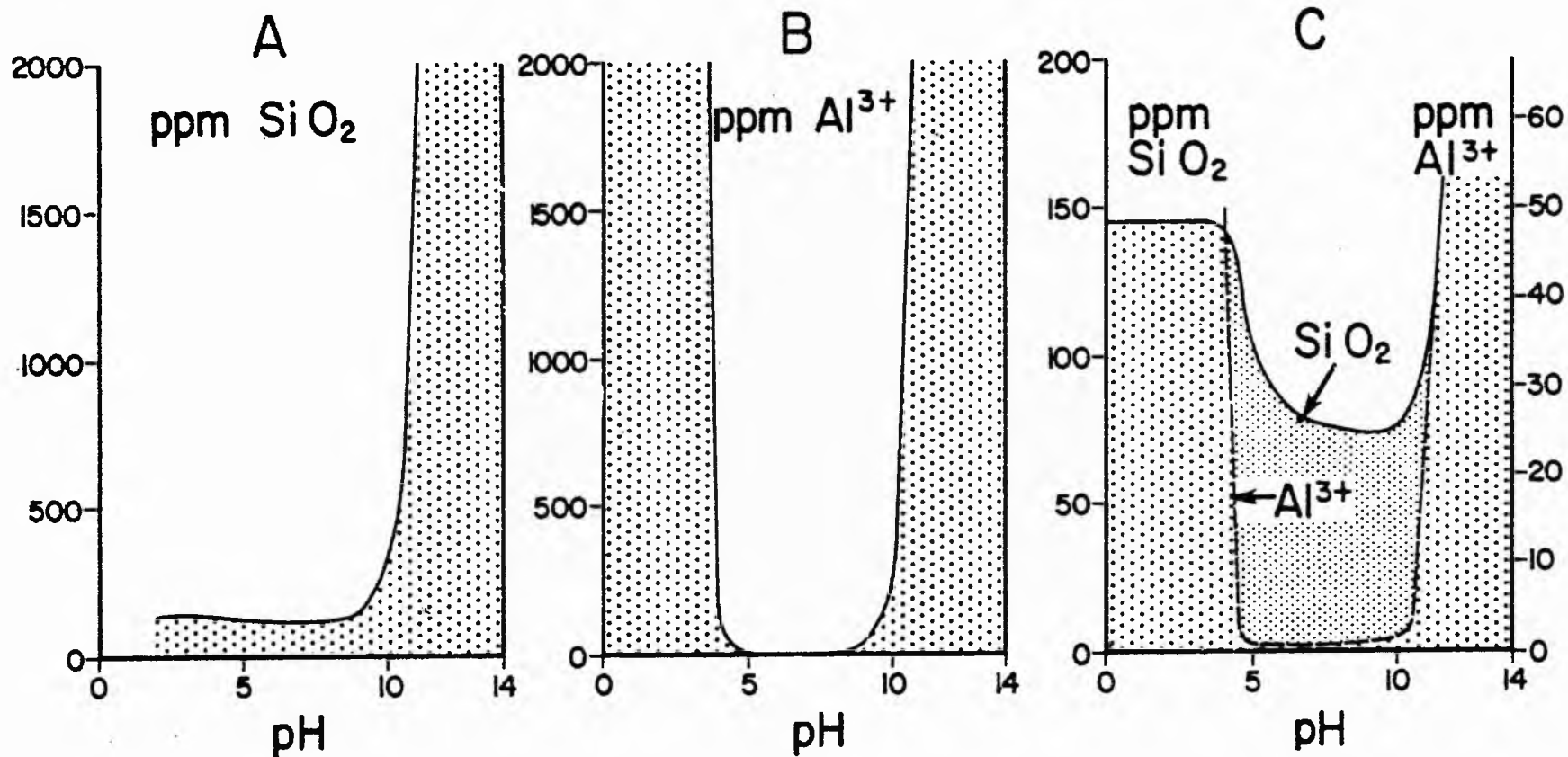


Fig 7.1 Diagram showing the solubility of (A) silica, (B) aluminum, and (C) the effect of mixing silica and alumina solution, all with respect to pH. Note that silica and alumina both become fairly soluble above pH 9-10, but mixtures remain very insoluble until pH >11 the large scale used for (C) shows details of these very low solubilities. After Millot (1970).

silica postdates kaolinite (Fig 5.47). This kind of occurrence could be due to local variation in pH value because kaolinite needs more acid conditions than quartz and the latter must have survived corrosion related to growth of kaolinite. Hoffman and Hower (1979) pointed out that excess silica released from clay alteration may have formed quartz. This probably explains the association of silica cement and clay and suggests that there was concomitant deposition or even that some silica formed later than some clays. The amount of this late quartz cementation varies from minor to enough to form multiple silica overgrowths and occlude most of the pores.

## 7.2 Etch Pits and Dissolution

Oriented pits due to chemical etching along planes of weakness are observed on the grains. Initial pits are small, and as etching proceeds they become larger and coalesce to produce more elongated forms (Figs 7.2 and 7.3). Other grains have suffered more extensive dissolution producing highly etched surfaces (Fig 7.4). Most dissolution features are found on overgrowth surfaces (Fig 7.5), occasionally etching may have been developed on the surface of the original grain. Some of them were probably formed soon after deposition, others were developed later on. It is known that the solubility of quartz increases rapidly above pH 9.0. Etch pits are usually considered to be the result of solution at high pH values, although lower pH values in association with organic matter may produce the same effect (Wilson, 1978). They may have been formed by solutions derived from interbedded peat horizons. Moore and Maynard (1929) pointed out that peat solution is an effective solvent of silica and in their experimental work was found to be the second best

Fig 7.2 SEM photograph showing euhedral crystal growth on the surface of a sandgrain, with little small pits formed due to a chemical solution. Sandstone Unit (L3) - West side. Scale bar equals 10  $\mu$ .

Fig 7.3 SEM photograph showing the effect of chemical alteration which has led to the formation of sub-parallel ridges as elongated forms suggesting etching along oriented lines of weakness. Sandstone Unit (T8b). West side. Scale bar equals 10  $\mu$ .

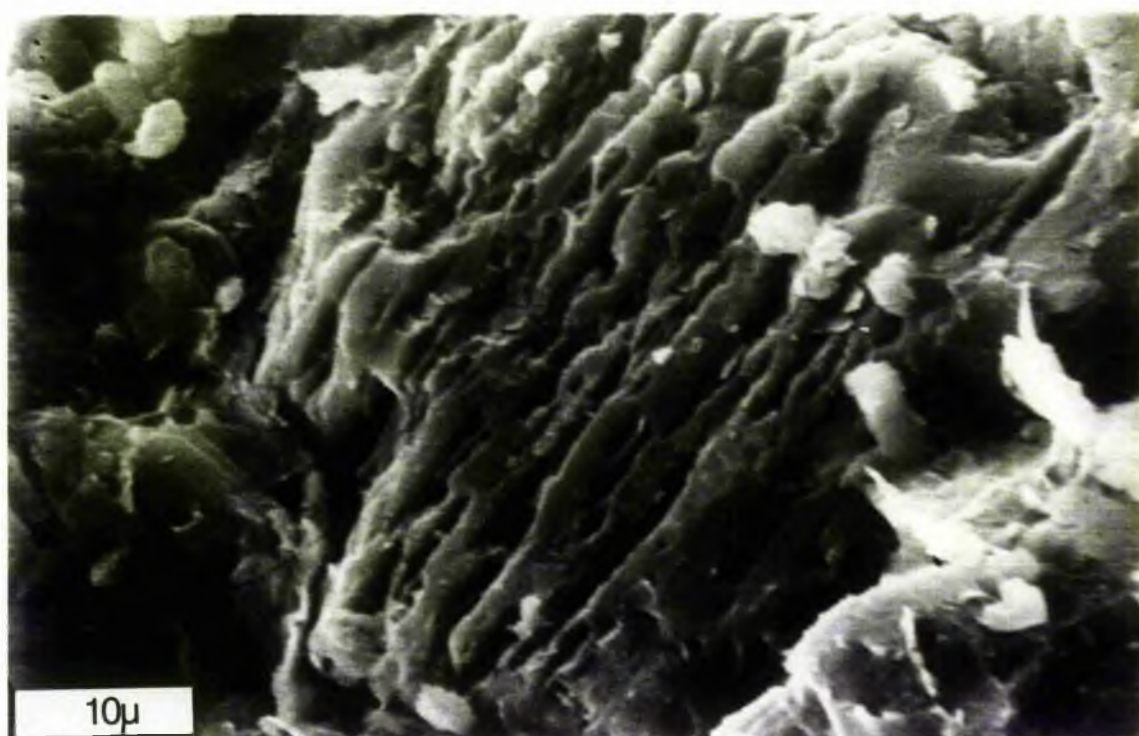
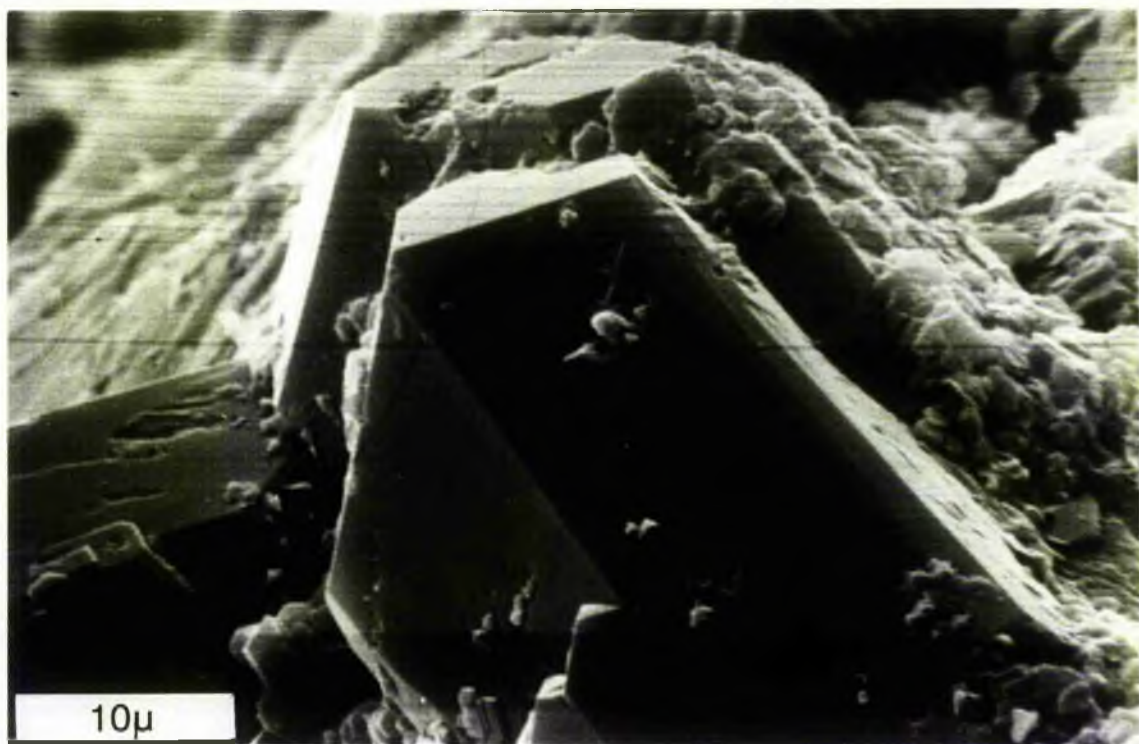
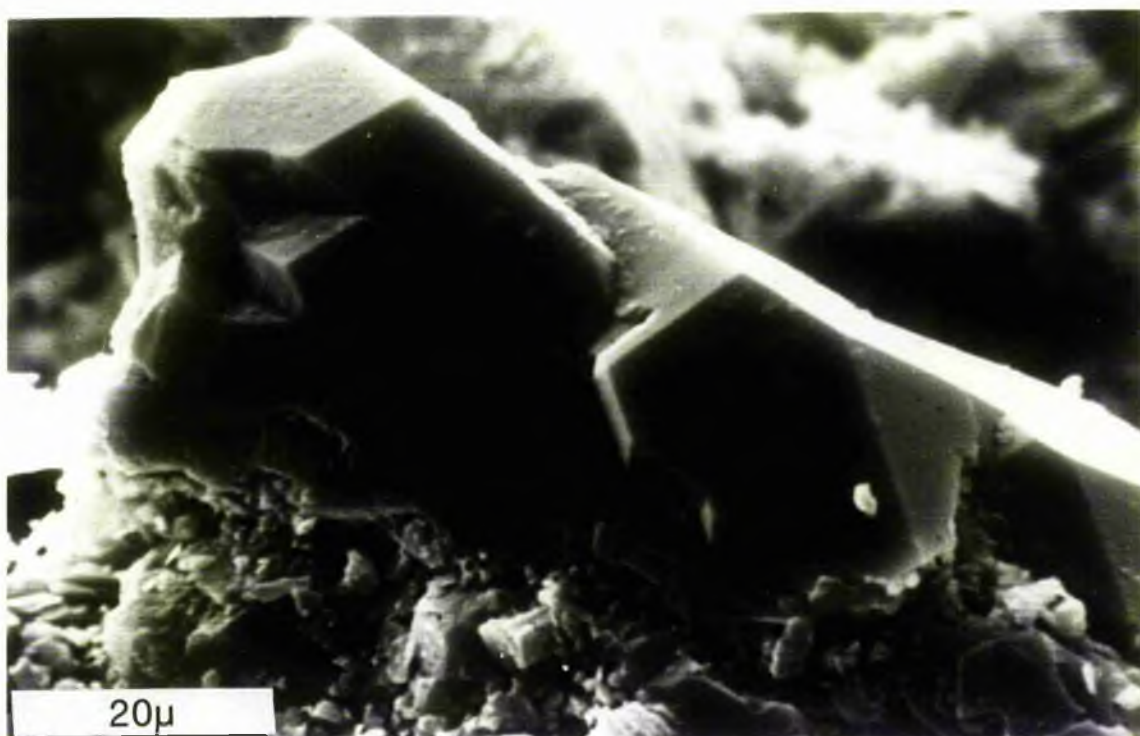
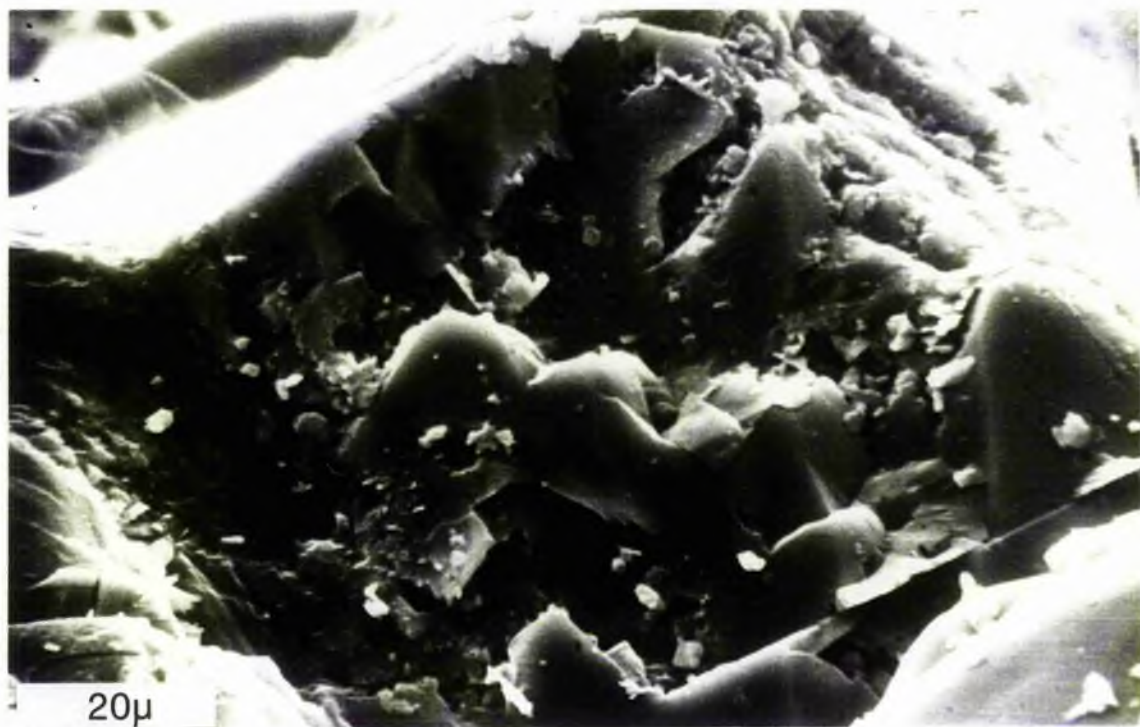




Fig 7.4 SEM photograph showing the effect of chemical weathering and etched areas are common. Middle part of sandstone Unit (B7). West side. Scale bar equals 20  $\mu$ .

Fig 7.5 SEM photograph showing euhedral overgrowth and the chemical corrosion of quartz in the lower part. Middle part of sandstone Unit (B7). West side. Scale bar equals 20  $\mu$ .



solvent of all the solutions used.

### 7.2.1 Origin of the secondary silica

With specific reference to sandstones the most commonly postulated source of secondary quartz is ascribed to the effects of pressure solution. In the St Monance sandstone visible effects of pressure solution are virtually absent or it has had a minimal effect on the sandstone. Therefore; the author believes that most of the silica cement must have been introduced from an outside source, as well as perhaps the direct result of processes active within the environment and penecontemporaneous with sandstone deposition.

In this study area, quartz cement is found in sandstones associated with fresh water deposits as well as in beds associated with marine horizons. Siever et al., (1965) pointed out that diatoms after deposition in marine sediments will make the pore water supersaturated with respect to quartz since the solubility of amorphous silica is 60 ppm at 5 °C in sea water. This equilibrium solubility rises relatively slowly with increasing temperature (Blatt, 1979). The quartz cement indicates a homogenisation temperature for fluid inclusions trapped around 70 °C, and it is presumed that the cementation may have taken place from fluids at this temperature. The figure is high for percolating meteoric water even to some depth in the sediment pile. Perhaps such a temperature might have been achieved even at modest depths, by pore waters, heated by magmatic activity. Francis (1983 p 261), pointed out that the volcanic activity persisted throughout the whole of Lower Limestone Group times.

### 7.3 Feldspar

The second stage of diagenesis involved the formation of authigenic cement and the alteration of feldspar grains. Petrographic studies show that the most common diagenetic features are dissolution and carbonate or clay (kaolinite) replacement (Fig 7.7). It has already been demonstrated earlier (see Chapter 6) that the surface of detrital grains have been deeply affected by the formation of dissolution voids. Overgrowths on detrital feldspar grains occurred early but after silica overgrowth (Fig 7.6). Microprobe analysis of feldspar showed that authigenic cement on detrital feldspar is an extremely pure potash feldspar with a smaller amount of  $\text{Na}_2\text{O}$  than the original grains. It is a clear indication that in early diagenesis of St Monance the pore fluids contained at least a low to moderate amount of K and Al and a large amount of Si. It is believed that silica precipitated with and immediately before K-feldspar. Although the authigenic feldspar development was localized, it is believed that the ions required (potassium, aluminium, and silicon) for the formation of the authigenic alkali-feldspar were supplied by interstitial water; clay minerals; rock fragment; and detrital feldspar. Also it is suggested that during the formation of the authigenic cement, the pore water was richer in  $\text{K}^+$  than  $\text{Na}^+$ . Support for this idea comes from probe analyses of feldspar (Table 7.1) showing the comparison between the composition of detrital and authigenic phases. The results indicate a remarkable uniformity in the composition of  $\text{SiO}_2$ ,  $\text{Al}_2\text{O}_3$  and  $\text{K}_2\text{O}$ , and all grains contained some  $\text{Na}_2\text{O}$  values ranging from 0.3 to 0.62 percent. These analyses indicate that the overgrowth is pure potash feldspar. Later on, some change occurred in the diagenetic environment and they began to alter to one of the clay minerals. The

Fig 7.6 Photomicrograph of feldspar overgrowth and quartz overgrowth associated with clay material probably kaolinite/illite (?); authigenic cement formed before alteration to clay material. F = feldspar, with overgrowth; Q = quartz overgrowth; Cl = clay material. Sandstone Unit (S17). East side. Crossed polars x 500.

Fig 7.7 SEM photograph showing carbonate cement (C) replacing the feldspar grain (F), while kaolinite is associated with feldspar alteration. Sandstone Unit (S17). East side. Scale bar equals 10  $\mu$ .

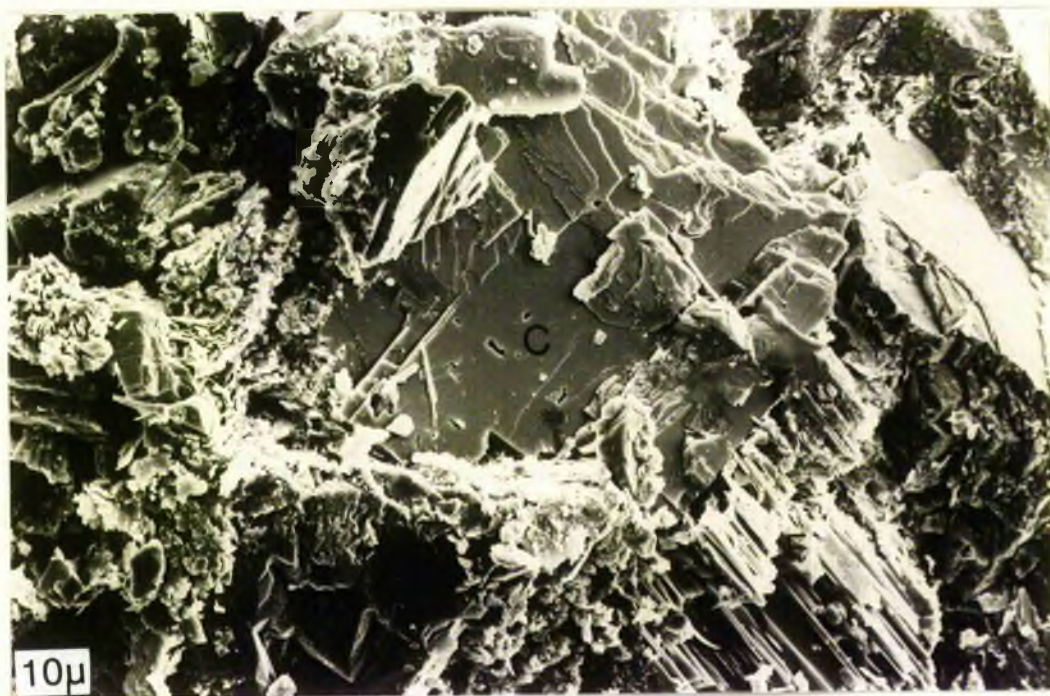
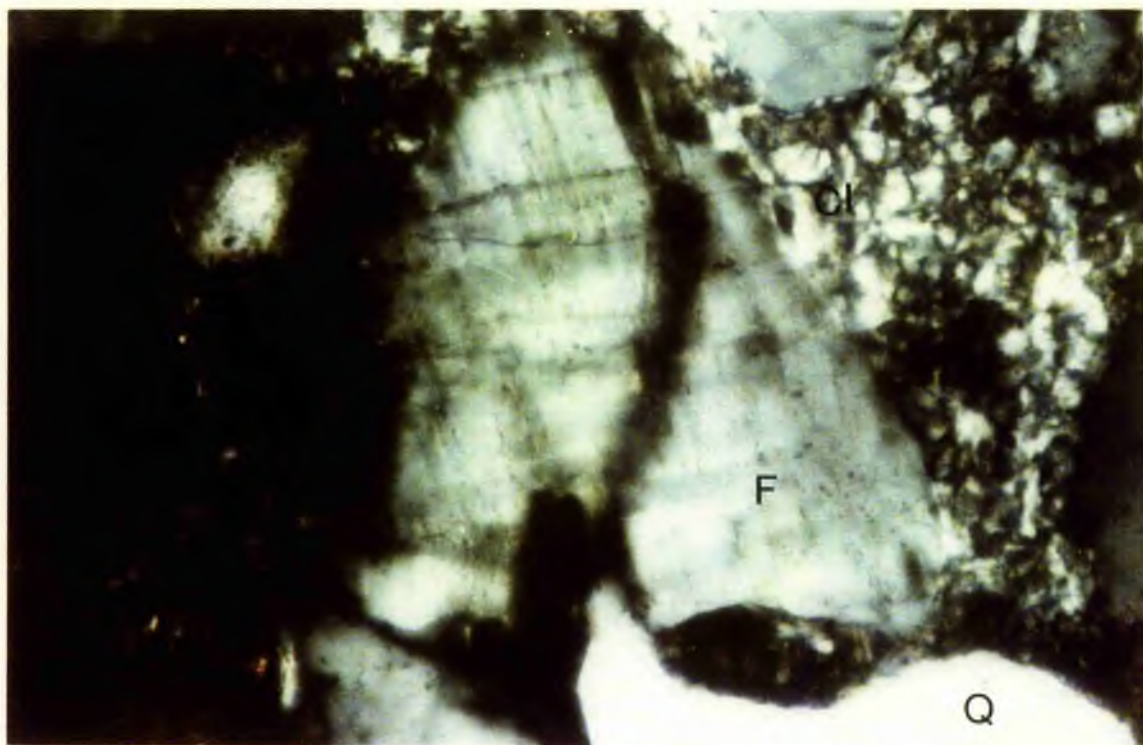


Table:7.1 Microprobe analysis of K-feldspar

	SiO <sub>2</sub>	Al <sub>2</sub> O <sub>3</sub>	K <sub>2</sub> O	Na <sub>2</sub> O	FeO	TiO <sub>2</sub>	P <sub>2</sub> O <sub>5</sub>	MnO	MgO	CaO	SrO	BaO	Total
Detrital grain	63.891	18.566	15.431	0.617	0.024	0.0	0.0	0.091	0.007	0.0	0.103	0.335	99.114
Overgrowth	64.285	18.377	16.469	0.366	0.188	0.0	0.0	0.0	0.016	0.063	0.183	0.345	100.292
Detrital grain	64.359	18.641	15.552	0.45	0.053	0.025	0.073	0.042	0.024	0.05	0.278	0.49	100.057
Overgrowth	63.346	18.400	15.045	0.52	0.035	0.0	0.0	0.00	0.0	0.077	0.088	0.13	97.676
Detrital grain	64.44	18.52	15.95	0.623	0.0	0.0	0.0	0.0	0.0	0.0	0.198	0.408	100.21
Overgrowth	64.79	18.67	16.15	0.594	0.024	0.0	0.0	0.02	0.0	0.02	0.155	0.427	100.86
Detrital grain	64.38	18.36	16.18	0.49	0.024	0.0	0.0	0.0	0.0	0.0	0.105	0.228	99.795
Overgrowth	64.241	18.47	15.89	0.468	0.076	0.025	0.0	0.07	0.0	0.0	0.223	0.17	99.639
Detrital grain	63.867	18.551	15.446	0.537	0.018	0.028	0.0	0.0	0.0	0.002	0.244	0.398	99.108
Overgrowth	64.046	18.702	16.349	0.299	0.04	0.0	0.0	0.021	0.0	0.0	0.119	0.122	99.698
Detrital grain	64.86	18.367	15.229	0.571	0.018	0.0	0.0	0.063	0.0	0.027	0.297	0.073	99.632
Overgrowth	64.69	18.464	16.036	0.456	0.0	0.01	0.066	0.014	0.0	0.0	0.307	0.194	100.237

mineral that developed probably depended upon local variation in the  $\text{Na}^+$  and  $\text{K}^+$  concentration in the pore fluids. Microprobe analysis and SEM observation (Fig 7.8) shows that authigenic kaolinite is generally associated with feldspar probably due to deficiency of K amount in solution which led to more acidic environment, suitable for kaolinite formation.

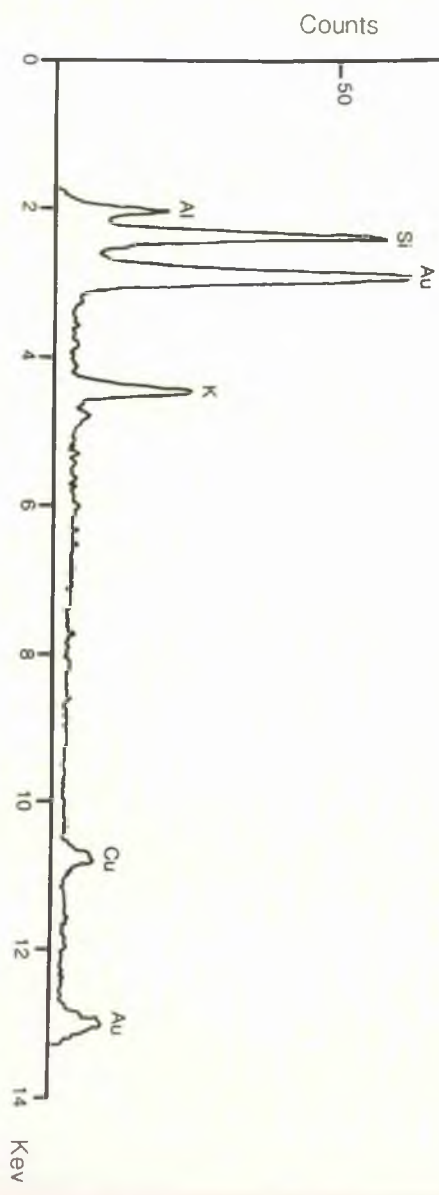
#### 7.4 Growth of diagenetic clays

It is important to recall that the ingredients necessary for the formation of authigenic clay in this area were present as pore filling, and associated with the detrital grains of mica and feldspar.

Because the St Monance sediments were deposited in a variety of depositional environments ranging from marine to non-marine; the composition of the mineral components probably varies among environments. Generally a combination of optical and x-ray diffraction investigations indicates that three types of clay minerals are present. Chlorite as a minor constituent is present only in the lower part, illite and kaolinite occur through the succession. However, the kaolinite is predominant. Normally these clay minerals are authigenic; evidence suggests this as indicated by their well-defined shape and by the presence of alteration mica and feldspar decomposition. Wilson (1971) pointed out that the poorly-shaped clay minerals are of detrital origin. The orientation and arrangement of the kaolinite, illite, and chlorite (Fig 7.9) suggests that these clay minerals are of diagenetic origin, and have formed by precipitation from moving pore-fluids. Almond and Davies (1979) pointed out that without motion and evolution of the pore fluids the authigenic clays



Fig 7.8 SEM photograph and the EDX analysis showing that authigenic kaolinite formed directly from the feldspar grain. EDX analysis shows (black box is the area of analyses) the major elements: Si, Al and K. This is a typical EDX spectrum for K-feldspar. Sandstone Unit (S17) - East side. Scale bar is equal 10  $\mu$ .



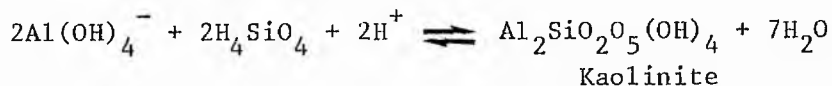


would be randomly, not sequentially arranged in the pores.

One of the most important feature in this section is the abundance of kaolinite, which is characterized and interpreted as follows.

- (i) Unequal distribution of kaolinite is attributed to higher sand permeability, allowing post depositional kaolinite formation.
- (ii) Kaolinite is interpreted as having formed directly from solution and by diagenetic destruction of detrital grains (feldspar and mica).
- (iii) The euhedral shape of kaolinite crystal suggest that they are not detrital
- (iv) Further, the boundaries of kaolinite 'attack' adjacent feldspars and quartz; this strongly suggests authigenic growth.

The precipitation of kaolinite is the first reaction to decrease the pH under slightly acid conditions, probably not less than 5, because the kaolinite crystal often is well-shaped and there is no sign of corrosion. Hurst (1980) pointed out that kaolinite dissolves readily at  $\text{pH} < 5$  or  $\text{pH} > 8$ . Such conditions might exist in ground water or by flushing of sandstone with fresh water as witnessed by the presence of minerals effected by leaching such as feldspars altered to kaolinite; micas too are altered to kaolinite. Quartz grains and particularly their siliceous overgrowths show slightly to deep corrosion features related to the growth of kaolinite. The precipitation of kaolinite would cause a gradual buildup of alumina in solution and the very gradual increase in pH encouraged other authigenic minerals to precipitate. The equilibrium equation for kaolinite can be written (Almond and Davies, 1979).



This is due to the consumption of hydrogen ions during the precipitation of kaolinite. The activity of acid solution is probably responsible for the increase in Fe and Mg ions in solution releasing them by the breakdown of detrital grains such as biotite, and forming either chlorite or Fe, Mg carbonate. Bjorlykke (1979) pointed out that the major source of iron, magnesium and titanium is from the breakdown of biotite.

Microprobe analysis also indicates that kaolinite has formed in some cases from mica, and that most of the clay which fills pores is a mixture of kaolinite and illite. The study of the  $\text{K}_2\text{O}-\text{Al}_2\text{O}_3-\text{SiO}_2-\text{H}_2\text{O}$  system (Hemley and Jones, 1964) showed that a low KCl/HCl mole ratio is necessary for kaolinite to form from K-feldspar; otherwise, the formation of authigenic illite is favoured. In applying this observation to the St Monance kaolinite formation, a mechanism must have been present to keep the level of  $\text{K}^+$  concentration low. The answer lies in the presence of illite which could have acted as acceptor for  $\text{K}^+$  as it was released during feldspar decomposition and muscovite alteration. This idea is supported by muscovite alteration to illite and then to kaolinite after most of  $\text{K}^+$  concentration plays as a main element to form illite (Table 7.2, Fig 7.10). Kaolinite is associated with feldspar decomposition (Fig 7.8) and Bjorlykke *et al* (1979) pointed out that the extensive break down of feldspar and mica to form kaolinite can occur only in pore water with low  $\text{K}^+/\text{H}^+$  ratio.

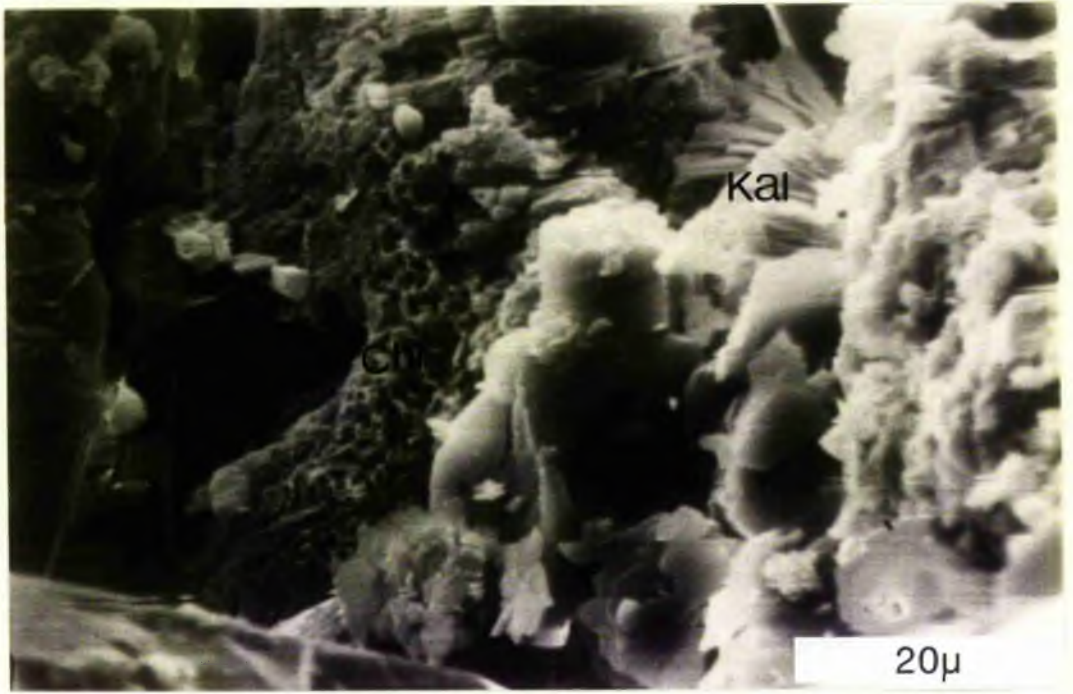
Chemical analyses of seventeen samples by x-ray fluorescence and wet chemical methods included eight samples of sandstones, and nine

Table 7.2: Microprobe analysis of mica-illite-kaolinite alteration

	SiO <sub>2</sub>	Al <sub>2</sub> O <sub>3</sub>	FeO	MgO	CaO	Na <sub>2</sub> O	K <sub>2</sub> O	BaO	Total	-H <sub>2</sub> O
Muscovite unaltered	46.91	36.69	1.16	0.73	0.06	0.56	10.78	0.27	98.92	
Muscovite unaltered	46.43	34.91	3.58	0.89	0.0	1.08	10.11	0.0	98.18	
Muscovite altered/or illite	47.82	38.07	0.46	0.20	0.14	0.12	3.93	0.0	91.29	
Kaolinite	47.6	38.08	0.20	0.06	0.11	0.0	0.58	0.25	86.96	
Kaolinite	46.36	37.25	0.10	0.06	0.03	0.08	0.98	0.17	85.38	
Kaolinite	46.61	37.99	0.0	0.03	0.0	0.02	0.07	0.04	85.34	
Kaolinite	46.07	39.15	0.0	0.02	0.03	0.02	0.21	0.19	86.26	
Kaolinite	46.88	38.28	0.15	0.05	0.14	0.05	0.69	0.0	86.27	
Kaolinite	48.72	37.54	0.71	0.34	0.32	0.09	2.59	0.08	91.17	
Kaolinite	46.68	36.75	0.0	0.26	0.32	0.1	1.77	0.25	87.18	
Illite	48.44	37.22	1.42	0.55	0.03	0.49	7.50	0.0	96.68	
Illite	47.99	36.69	1.57	0.61	0.01	0.5	6.86	0.33	95.27	

Fig 7.9 SEM photograph showing that three kinds of clay minerals are arranged sequentially in pore. From right to left kaolinite (Ka); Illite (ill) and then Chlorite (Chl). Sandstone Unit (T7C - West side. Scale bar is equal 20  $\mu$ .

Fig 7.10 Photomicrograph showing detrital mica (M) passing into (ill) and then to Kaolinite (Ka). While on the other end feldspar grain associated with kaolinite. Identification of these minerals based on microprobe analysis. Polished thin-section. Sandstone Unit (T3) - West side. x 100.





samples from interbedded shales horizons (because monomineralic separation was impossible; analyses were necessarily made of bulk samples).

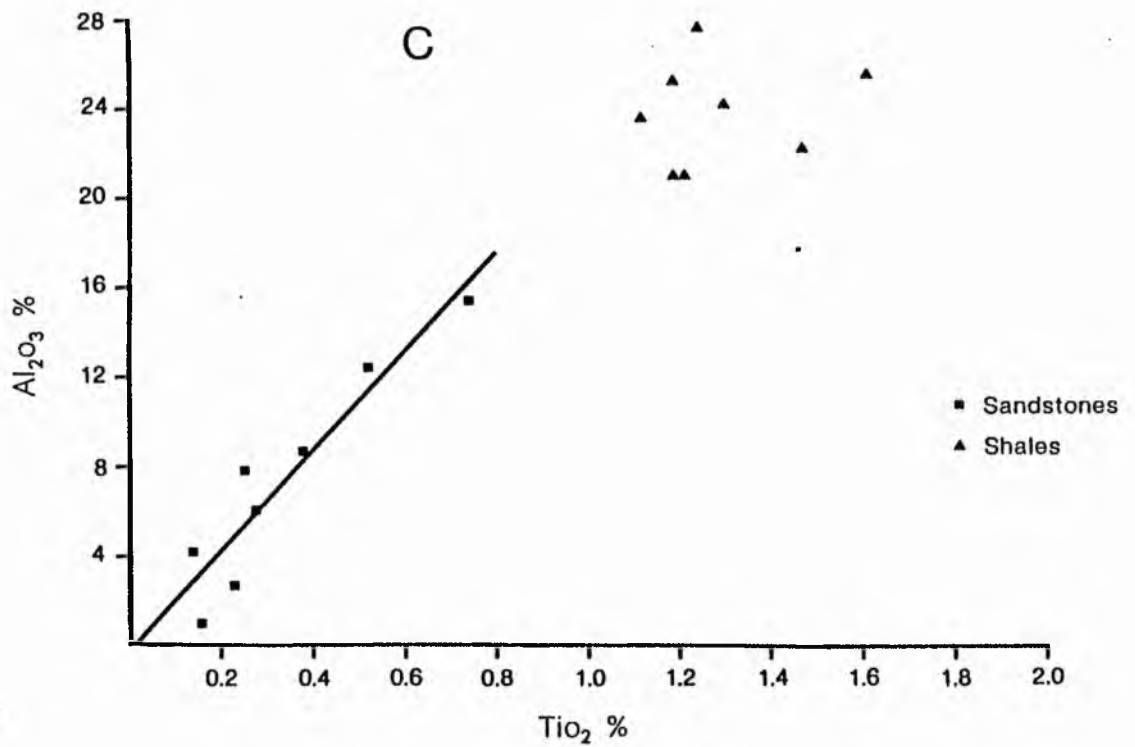
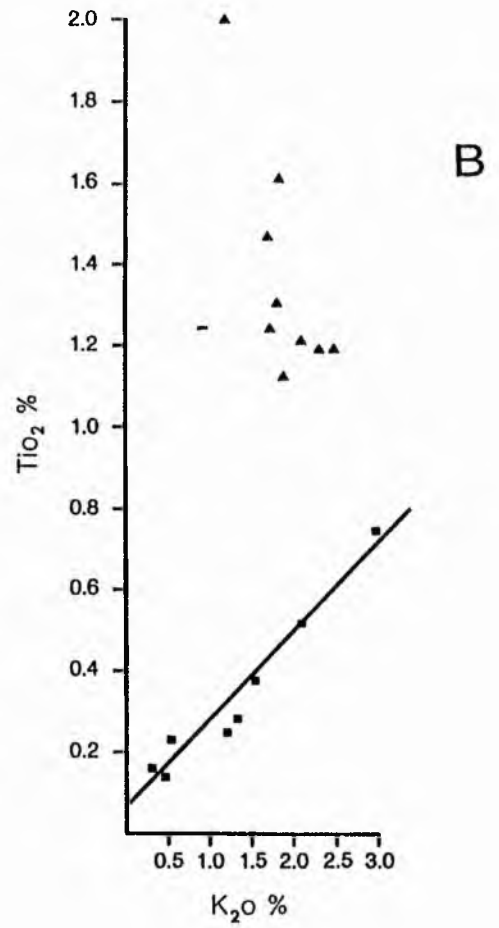
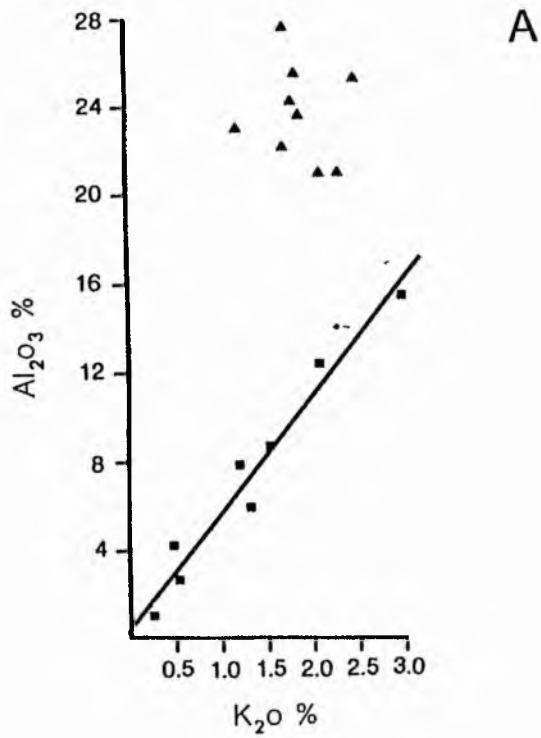
Several items of interest can be derived from a comparison between sandstones and shales. The average  $\text{SiO}_2$  content of the sandstones is higher than that of the shales; 85.16% vs 54.4% and obviously reflects the higher quartz content of the sandstones. Average  $\text{Al}_2\text{O}_3$ ,  $\text{MgO}$ , and  $\text{K}_2\text{O}$  amounts are higher in shales because of more clays especially kaolinite in these samples ( $\text{Al}_2\text{O}_3$ , 23.70% vs 7.29%;  $\text{MgO}$ , 0.83% vs 0.47%;  $\text{K}_2$ , 1.89% vs 1.29%). The presence of increased  $\text{CaO}$ ,  $\text{MgO}$ , and  $\text{FeO}$  in sample (B6a) reflects the predominance of carbonate cement as ferroan calcite and dolomite. Other differences in average composition occur in  $\text{Fe}_2\text{O}_3$  and  $\text{TiO}_2$ , which are more abundant within the shales ( $\text{Fe}_2\text{O}_3$ , 3.80% vs 0.92%;  $\text{TiO}_2$ , 1.37% vs 0.34%). These differences in iron probably reflect a higher percentage of iron rich chlorite in shales. The relative differences of titanium oxide percentage through the sandstone units might be related to mica; for instance sample (S3a) contains a higher percent of mica than other samples. Bjorlykke *et al.*, (1979) pointed out that authigenic titanium oxides might be derived from the breakdown of mica. Also the average  $\text{Na}_2\text{O}$  in shales is higher than that of the sandstones; 1.11% vs 0.33%, probably reflecting larger proportions of feldspar and clay in shales than in sandstones.

Correlation analysis substantiates the above conclusions on the element associations. The plot of  $\text{Al}_2\text{O}_3$  vs  $\text{TiO}_2$  (Fig 7.11C) shows two dominantly clay associated elements. The trends exhibited on (Fig 7.11C) can therefore be attributed to depositional factors. In sandstones, changes in the matrix proportions due to grain size are

Fig 7.11A Plot  $K_2O$  vs  $Al_2O_3$ . Correlation coefficient  $\gamma$  for  
sandstone data alone  $\gamma = 0.978$ ; for shale data  $\gamma = -0.108$ .

Fig 7.11B Plot  $K_2O$  vs  $TiO_2$ . Correlation coefficient  $\gamma$  for  
sandstone data alone  $\gamma = 0.971$ ; for shale data  $\gamma = -0.763$ .

Fig 7.11C Plot  $TiO_2$  vs  $Al_2O_3$ . Correlation coefficient  $\gamma$   
for sandstone data alone  $\gamma = 0.939$ ; for shale data  $\gamma = -0.007$ .



responsible for a linear relationship between  $TiO_2$  and  $Al_2O_3$ . The shales, however, plot above the line, indicating a different matrix. The  $Al_2O_3/TiO_2$  ratio is lower in shales (17.299) than in sandstone matrix (21.44). Spears and Kanaris-sotiriu (1975) pointed out that this ratio decreases as the grain size of the sediment decreases. It may, therefore be suggested that the sandstone matrix contains proportionally less than very fine clay compared shales.

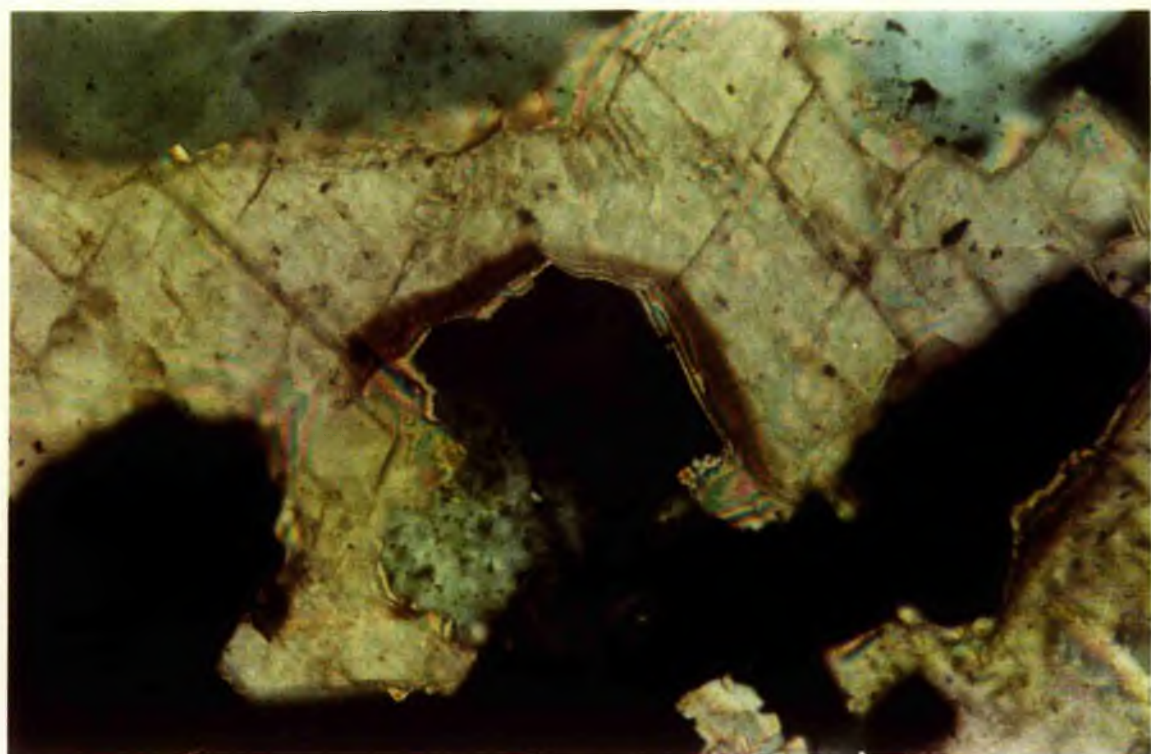
$K_2O$  is plotted against  $Al_2O_3$  in (Fig 7.11A) and  $TiO_2$  in Fig 7.11B. On both figures the sandstone analyses define a linear trend and are comparable in that the shale analyses do not lie on the sandstone trend lines. This adds support to the concept that the shales and the matrix in sandstones are significantly different. The higher mean of  $K_2O$  content of the shales is consistent with observed increase in illite clay relative to kaolinite. This supports the previous conclusions that sandstone contains predominant kaolinite clay minerals.  $Al_2O_3$  is present both in feldspars, and clay minerals, whereas, proportionally more  $K_2O$  is contained by the clay minerals due to the relative less amount of feldspar, therefore suggest that  $K_2O$  content is dominantly clay-associated.

On Figs 7.11A, 11B, and 11C the sandstones plot in a distinctly different field to the shales. The difference between sandstone matrix and shales is consistent with differences in composition and permeability.

### 7.5 Mechanical Compaction

Mechanical compaction which has reduced the porosity, involves penetration of sharp edges formed by early silica overgrowth and produced concave-convex contact, sutured contact, straight contact;

Fig 7.12 Photomicrograph showing the difference between carbonate cement filling and replacement. Also shows a number of replacement phases of detrital grain. Sandstone unit (T6a) - West side. Crossed polars. x 200.



squeezing of clay matrix, fracture of detrital grain, and bent micas, all these are features indicating compaction.

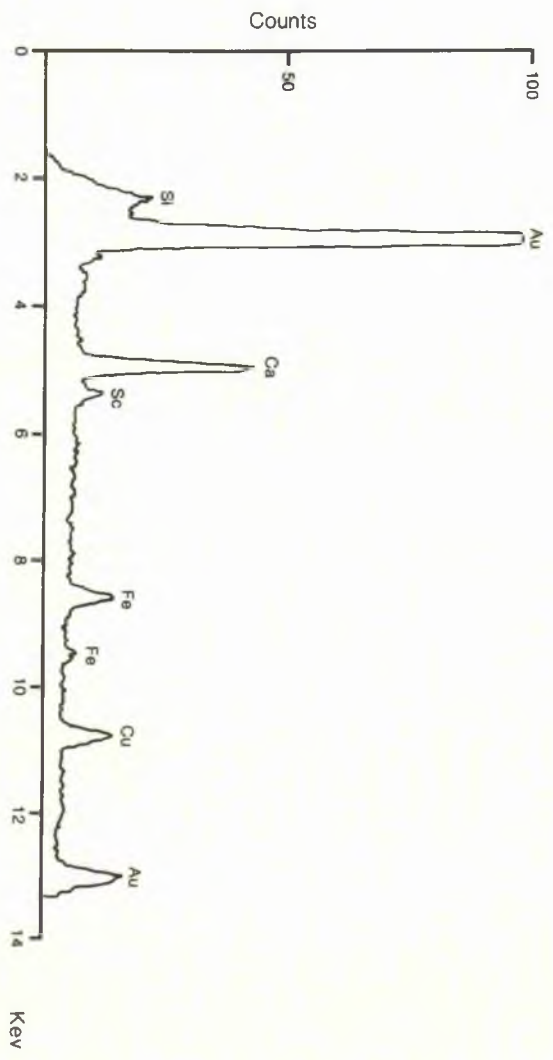
## 7.6 Carbonate Cement

In all instances where paragenesis could be determined, the carbonate cement postdates quartz overgrowth, authigenic feldspar, and authigenic clay. The cement is present as pore filling but rather has partially to completely replaced detrital grains and even the authigenic clay (Kaolinite) (Fig 7.13). Conditions necessary for and mechanisms of precipitation of carbonate cement generally depends upon increasing the  $[Ca^{+2}] [CO_3^{-3}]$  present in solution. A direct way to accelerate the formation is to raise the pH in the environment. Correns (1950) attributed the relationship between carbonate and quartz cement to conditions of varying pH. However, Blatt et al., (1980, p 348) pointed out that quartz solubility is unaffected by pH at values below about 9 and Siever (1962) suggested the temperature increase probably plays a more important role in the precipitation of calcite at the same time causing the dissolution of silica. The St Monance sandstones give an estimate for the quartz overgrowth inclusion as around 70 °C. It is suggested that all the earlier sequence was subject to the same temperature. Then, the concentration of ions in solution and the pH values probably were the main controlling factors in the precipitation of authigenic material. Later on, probably the temperature increase caused by magmatic activity led to an additional factor favouring carbonate formation.

All samples containing carbonate show some differences in composition between cement filling and replacement. The latter, under the ordinary microscope appear to consist of many phases (up to 6)

Fig 7.13 SEM photograph and EDX analysis showing carbonate cement (C) replacing the kaolinite clay minerals (Ka<sup>h</sup>). Also a large amount of microporosity formed inside the carbonate crystal. EDX analysis shows the major elements are Ca, and Fe, and suggest that the mineral is Ferroan calcite. Sandstone Unit (B7). West side. Scale bar is equal 10  $\mu$ .







(Fig 7.12). Microprobe analysis shows a variation in chemical composition along the traverse between the carbonate filling/replacement contact to the rim of the cement replacing the grain (Appendix 7.1). Distinct phases in carbonate cement replacement are revealed by probe analysis, reflecting changes in the chemistry of pore water concomitant with each phase of replacement. The relative changes occur in CaO, FeO, MgO in both phases of cementation (filling and replacement) and they are decreasing generally towards the rim side. Variation in the trends of FeO, MgO, diagrams (Fig 7.14) against a number of analytical points especially through the replacement stages, could reflect the different phases of this replacement (as it is clear from the colour difference, (Fig 7.12). Rim composition could be related to silica contamination in the cement during the replacement, as indicated by probe analysis by increasing in amount from a few hundred moles up to 65600 mole near the rim in contact with the grain (Fig 7.15). Cathodoluminescence failed to reveal the structure of the carbonate cement because manganese is absent (Frank, et al, 1982). The types of carbonate cement indicated by microprobe analyses of these samples are dolomite and ankerite often ferroan. In other thin-sections calcite often ferroan is also present. Curtis (1978) attributed carbonate cement in sandstones as often arising from mudstone and precipitated after compaction. The geochemical analyses of the shales indicate that the elements, MgO, CaO, and FeO in the shales are higher than in sandstones even the unit B6a, (table 7.3) which contains 22% carbonate cement (microscope analysis). Therefore, it is suggested that probably the mudstone was the source of the cement.

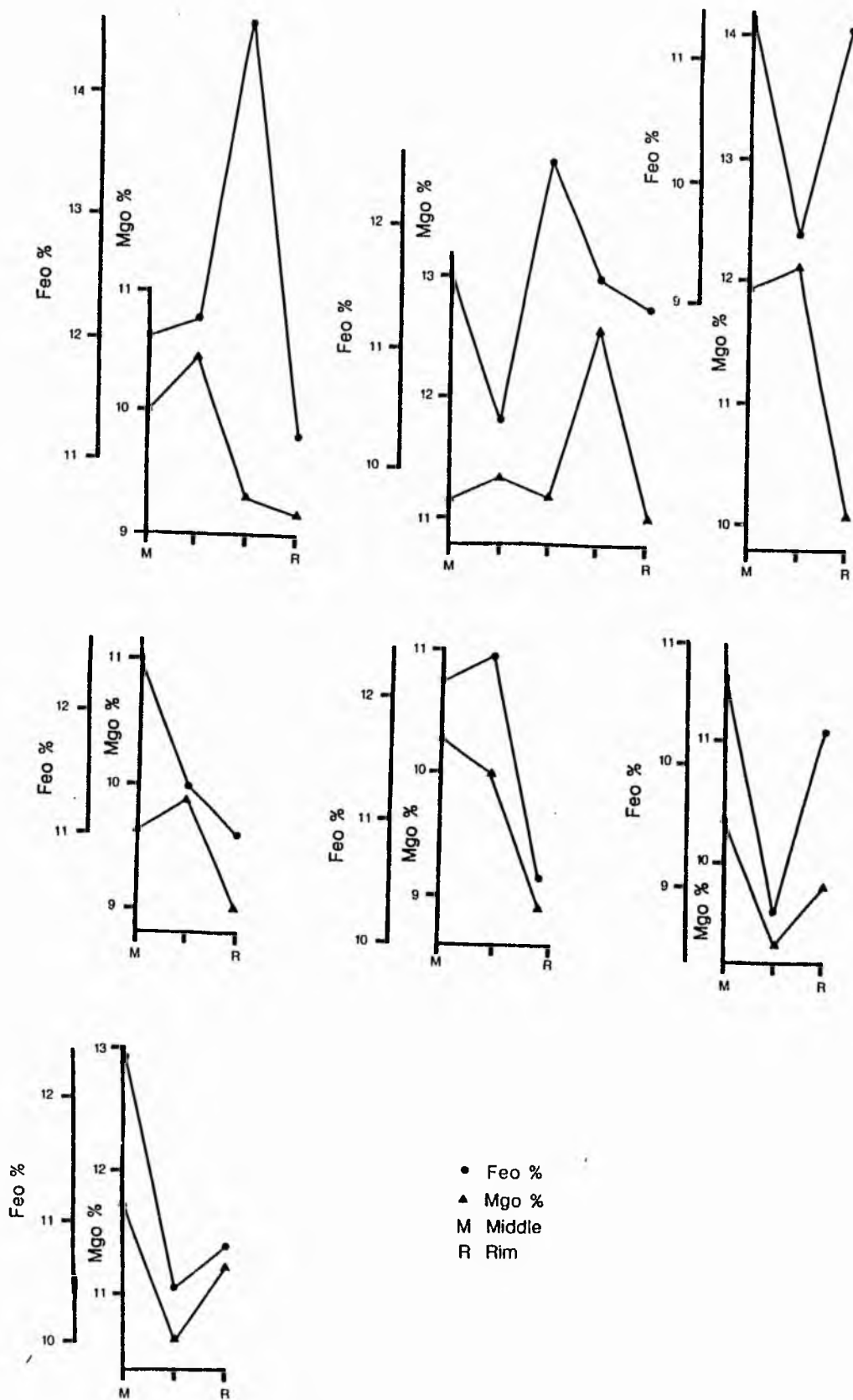


Fig 7.14 Scheme showing the variation of MgO and FeO Wt. % decrease towards the rim, and reflecting the different phases of replacement in the middle.

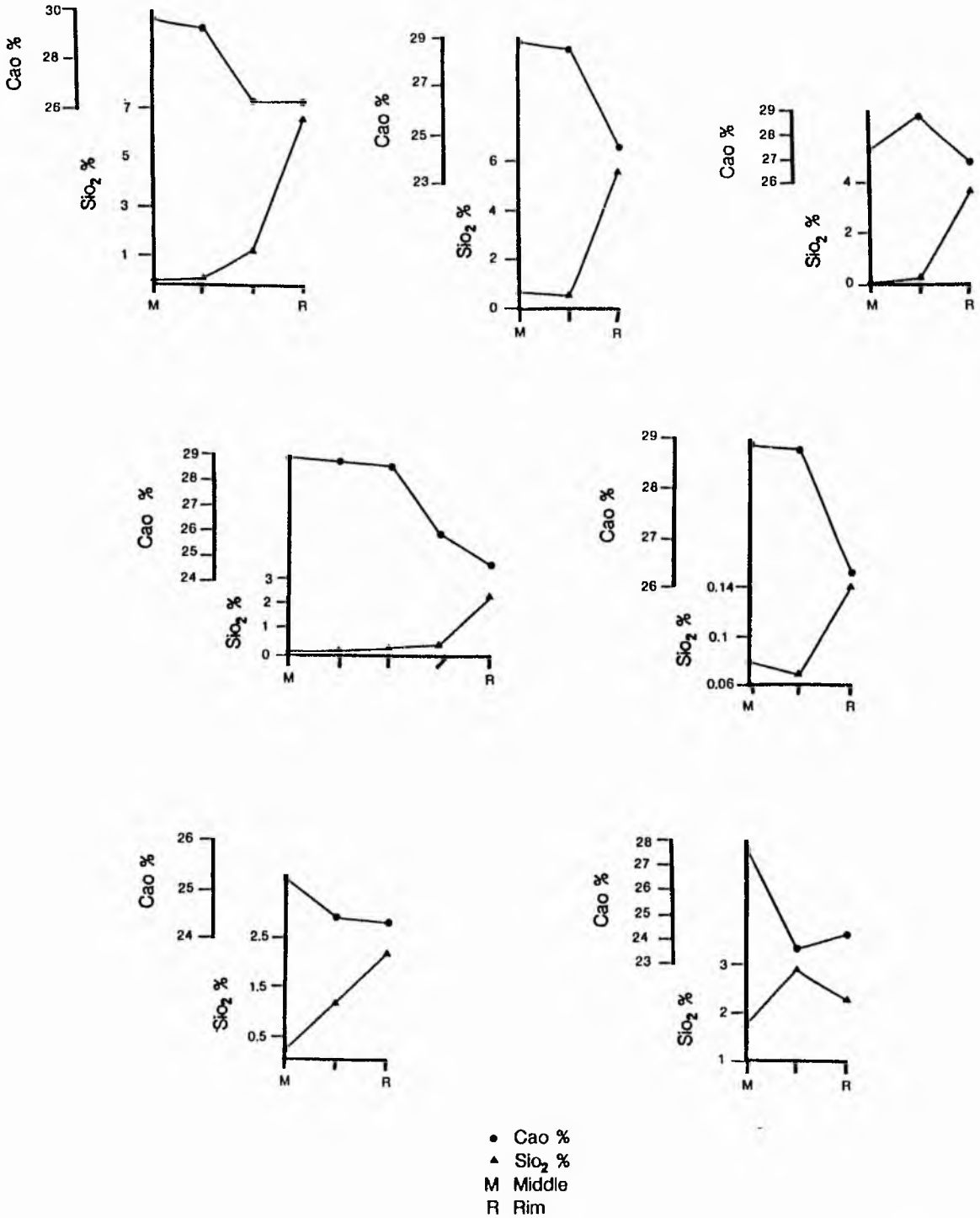


Fig 7.15 The plot of CaO and SiO<sub>2</sub> Wt. % shows that CaO decreases, and SiO<sub>2</sub> increases from the middle towards the rim.

Table 7.3: Chemical analysis

Sandstone samples	SiO <sub>2</sub>	Al <sub>2</sub> O <sub>3</sub>	Fe <sub>2</sub> O <sub>3</sub>	MgO	K <sub>2</sub> O	CaO	P <sub>2</sub> O <sub>5</sub>	Na <sub>2</sub> O	MnO	TiO <sub>2</sub>	Total -H <sub>2</sub> O
B6a	76.35	5.98	2.94	1.63	1.33	4.31	0.11	0.09	0.0	0.28	92.918
B6b	81.16	8.67	1.37	0.67	1.54	1.37	0.04	0.84	0.0	0.38	96.03
F3a	87.45	7.84	0.21	0.08	1.20	0.0	0.03	0.58	0.0	0.25	97.65
F5a	77.44	12.42	1.87	0.4	2.07	0.11	0.06	0.0	0.0	0.52	94.88
S3a'	73.36	15.52	0.94	0.38	2.98	0.21	0.11	0.50	0.0	0.74	94.75
S21a	92.98	4.17	0.0	0.2	0.47	0.0	0.03	0.21	0.13	0.14	98.19
S24	95.33	2.72	0.002	0.3	0.53	0.0	0.01	0.42	0.0	0.23	99.54
S27	97.23	1.02	0.0	0.12	0.26	0.0	0.02	0.0	0.0	0.16	98.8
Mean	85.16	7.29	0.92	0.47	1.29	0.75	0.05	0.33	0.0	0.34	96.595
St deviation	9.32	4.9	1.08	0.5	0.91	1.51	0.04	0.31	0.0	0.20	2.31

Shale Samples	SiO <sub>2</sub>	Al <sub>2</sub> O <sub>3</sub>	Fe <sub>2</sub> O <sub>3</sub>	MgO	K <sub>2</sub> O	CaO	P <sub>2</sub> O <sub>5</sub>	Na <sub>2</sub> O	MnO	TiO <sub>2</sub>	H <sub>2</sub> O	total +H <sub>2</sub> O
W1*	51.5	23.57	4.76	0.85	1.87	6.60	0.16	1.60	0.07	1.12	7.0	99.10
L1*	51.2	25.25	2.47	0.85	2.47	2.64	0.14	2.18	0.05	1.19	7.8	96.24
L3*	63.0	22.15	1.83	0.61	1.70	0.29	0.04	0.07	0.04	1.47	6.4	97.60
L4*	47.0	22.98	7.18	0.61	1.22	0.66	0.28	1.22	0.08	1.98	8.8	92.01
B1*	60.2	21.02	3.02	0.93	2.30	0.44	0.10	1.33	0.03	1.19	6.4	96.96
B1	60.8	21.02	3.37	1.04	2.08	0.74	0.14	0.95	0.07	1.21	6.8	98.22
T7*	54.4	27.65	4.66	0.69	1.73	<0.01	0.05	2.22	0.02	1.24	3.8	96.46
F2a	47.7	24.16	3.96	0.93	1.80	3.38	0.15	0.07	0.04	1.30	1.2	98.69
F2b	53.8	25.54	2.92	0.92	1.84	0.59	0.11	0.32	0.04	1.61	8.0	95.69
Mean	54.4	23.70	3.80	0.83	1.89	1.71	0.13	1.11	0.05	1.37	6.29	96.77
St deviation	5.78	2.21	1.59	0.15	0.36	2.16	0.07	0.83	0.02	0.28	2.36	2.13

\* West side samples

## 7.7 Pyrite

In contrast with the other authigenic minerals in the St Monance sandstones, the major development of pyrite is at a late stage of diagenesis. The formation of this mineral involves early diagenetic formation of hydrotroilite ( $\text{FeS} \cdot n\text{H}_2\text{O}$ ), perhaps concurrent, with deposition. Bacterial decay of organic matter produced sulphur while iron came from detrital minerals. Hydrotroilite remained until alkaline conditions developed favouring formation of pyrite. The associated reddish brown authigenic mineral ilmenite is due to oxidation, this ilmenite being reduced to hematite.

The last stage of diagenesis involved the formation of secondary porosity by dissolution of carbonate cement and other unstable grains.

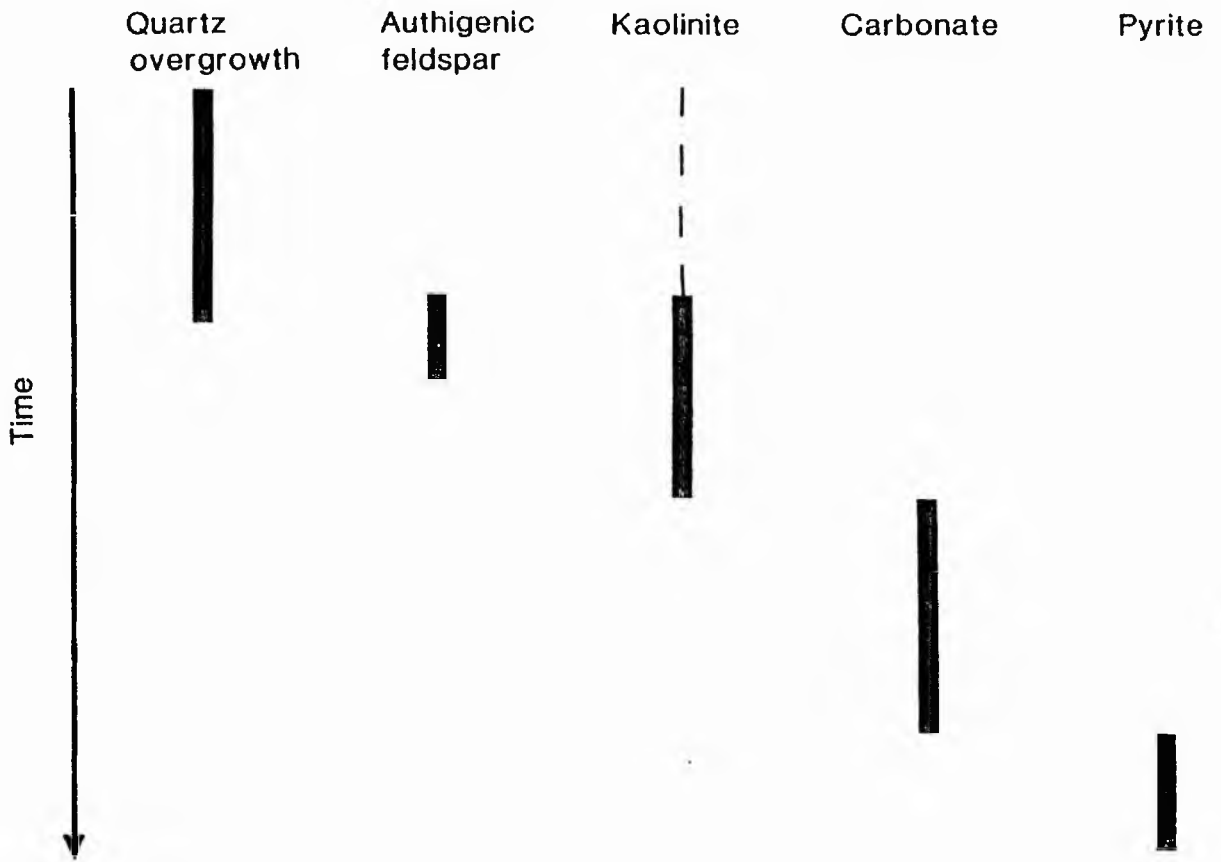
## 7.8 Depth and Temperature of Diagenesis

If it is assumed that the Lower Limestone Group was covered by the subsequent Carboniferous sequence, the depth of burial at the end of that period was <2000 m (Francis, 1983). A definite sequence of early diagenetic events is still observable in the area study (Fig 7.16), the early quartz and feldspar cementation and even the authigenic kaolinite appears to be the initial significant diagenetic event, this probably occurred soon after deposition. Recognition of these early shallow burial or surface diagenetic features raises doubts about the importance of deep burial as a diagenetic agent, and these are confirmed by the presence of minimal pressure solution.

The temperatures during diagenesis were studied by the use of fluid inclusions. Inclusions forming "dust-lines" gave maximum temperatures of 70 °C but a minimum could not be achieved.

Fig 7.16

Time-related environment zonation





Temperatures of inclusions in carbonate lay between 80-140 °C suggesting the effect of contemporaneous igneous activity. Temperatures above this are unlikely ever to have affected the sediment since kaolinite is still present and Keller 1970 pointed out that at temperatures above 150 °C, the kaolinite alters to micaceous minerals.

### 7.9 Summary and Conclusion

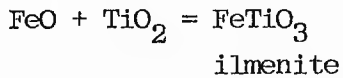
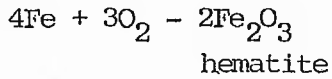
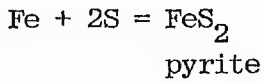
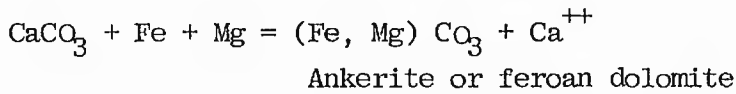
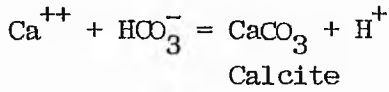
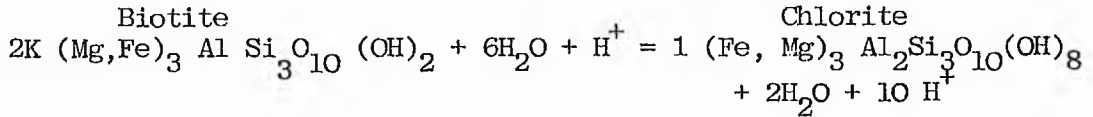
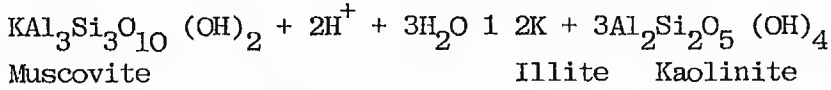
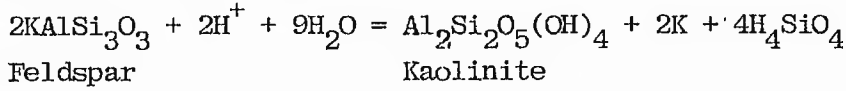
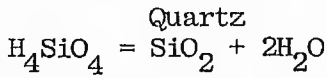
Diagenetic minerals in the St Monance sandstones formed from pore fluids include silica, authigenic feldspar, kaolinite, illite, chlorite, carbonate and pyrite with intergrowth of hematite and ilmenite (Fig 7.16). A significant volume of ions required to form the abundance of authigenic minerals such as silica, must have been supported from an external source.

The arrangement of diagenetic minerals suggested that the moving fluids through the sediments pile may be expected to dissolve the more labile grains and become more enriched in dissolved ionic species. This process will continue until the composition of the fluids becomes supersaturated with a mineral which then begins to precipitate. Ions not involved in the precipitation reaction will continue to increase their concentration in the fluid until the solution is in equilibrium with another which is then precipitated.

The initial K/H ratio was quite high as is evident from the early precipitation of silica overgrowth and K-feldspar which brought the pore fluids into equilibrium with these two minerals. The extensive breakdown of feldspar and mica to form kaolinite only occurred when the pore fluid was low in K/H ratio, as fresh or of low salinity on passing through the sandstones. The equilibrium equations

of such reactions which seem to have taken place shown as in Table 7.4. For St Monance Sandstones the equilibrium and the stability relations appears to agree in the system  $K_2O-Al_2O_3-SiO_2-H_2O$  for quartz, feldspar and kaolinite. The observation gives considerable evidence of such equilibrium. Temperature and depth might have been important as they changed the chemical composition of the pore water during the progressive burial of sediment pile but not the major control. The main control was the primary facies of shales and sandstone units.

Table 7.4 Possible diagenetic reactions.



## CHAPTER 8

### SUMMARY AND CONCLUSION

The broad picture of the upper part of Calciferous Sandstone Series and the Lower Limestone Group (of Visean or late Mississippian age), which emerges from this work is one of deposition on the eastern flanks of a major Carboniferous delta. The investigation of the clastic sediments revealed that they were deposited by a delta prograding from the NE as determined from sedimentary structures within the sandstones. Each delta gradually evolved into a wave-dominated destructive delta.

A variety of facies reflect the numerous subenvironments within this area. These have been identified and shown on (Fig 2.39). In the depositional model of the area study, the major sand bodies are oriented NE-SW. The sediment of this area were derived from an area composed principally of low-rank metamorphic rocks (Chapter 5). These sediments were transported by large channels probably outside the area, and smaller shallow channels led to sedimentation especially during floods. Mouth bar progradation produced coarsening-upwards sequences, while sometimes the upper part of the mouth bar was eroded by the channel as progradation continued (Chapter 2,4). Palaeocurrent analysis shows that the major currents in channels were generally directed to the south-west. Many of the ripple marks are wave-generated with a variety of current directions. Rare herringbone cross-beds as considered to be evidence of tidal action (Ginsburg and Klein, 1973) were found in few units leading to the suggestion that there was little tidal action.

Trace fossils indicate a range from fully marine to non-marine.

Six pattern types of animal activity are counted (Chapter 3, Table 3.1) some of them are found in fully marine or associated with marine strata, and in different lithofacies from carbonate up to sandstone. Consideration of the association of trace fossils and facies has led to tentative conclusions regarding environments, viz.

Marine (Teichichnus; Palaeophycus; Zoophycus;  
Planolites; Scolicia; Chondrites; Diplocraterion;  
and Eione).

Quasi-marine (Aulichnites; Pelecypodichnus; Conichnus;  
Scolicia; and Monocraterion).

Non-marine (Planolites; and Monocraterion)

The two sections on either side of the St Monance syncline (Fig 8.1) reflect variations in thickness of the cycles which was determined by subsidence. The lack of correlation between the amount of sediment in a cycle and subsidence suggests that the latter was tectonically controlled rather than sediment loading.

Petrologic study of the coarse clastic sediments shows them to be mainly of fine to medium grained sand; and very well to moderately sorted. They consist mainly of quartz with minor quantities of feldspar, mica, heavy minerals, and rock fragments. Matrix and cement were found in most thin-sections. Three types of quartz were recognized, undulatory, non-undulatory, and polycrystalline, with undulatory predominant. The study of various factors such as grain

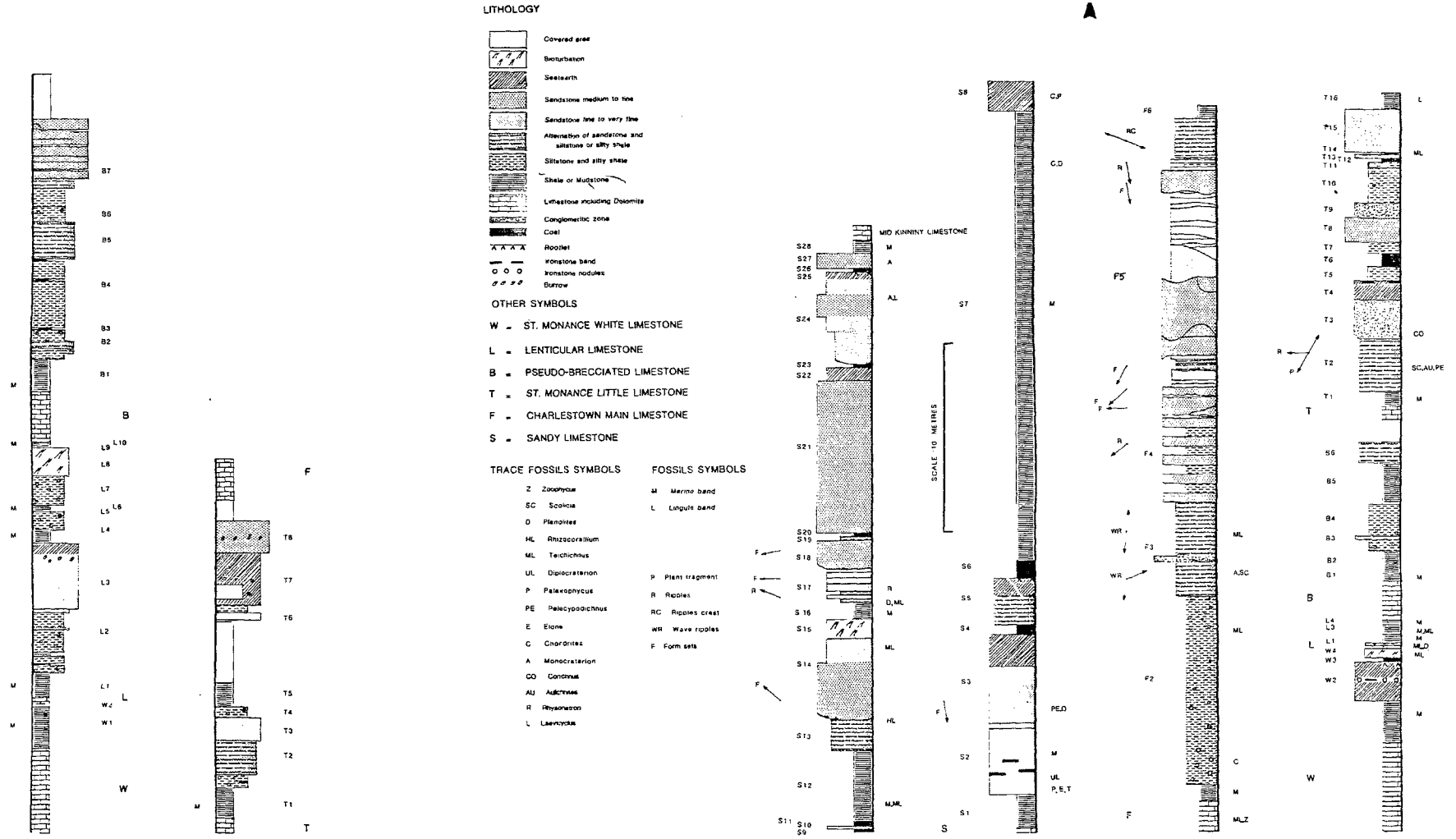


Fig 8.1 VERTICAL SECTION OF CARBONIFEROUS MEASURES, FACIES VARIATION, OF THE ST. MONANCE SYNCLINE

size, shape, number of the crystal units per grains, and finally the intercrystalline boundaries between the crystal, indicates that St Monance grains fall in the field of Low-grade metamorphic source rocks. The number of units in polycrystalline grains may suggest a mixture of both low and high-rank metamorphic or plutonic rocks. The latter probably account for the few acicular inclusions in some quartz grains. But the grains are often small, and this taken together with bimodal size of the crystal, which are elongated to extremely elongated, and the fluid inclusion as small and their temperature of formation about 300 °C, emphasize the contribution of low-rank metamorphic source rocks.

On the basis of petrological and geochemical evidence, including types of porosity and permeability, it is concluded that no one process was responsible for diagenetic events. Temperature and depth of burial exerted some control on processes during burial but primary facies was probably most important. Fluid inclusion studies indicate 70 °C for the temperature during the formation of quartz overgrowths and a maximum of 140 °C for carbonate cement.

The main diagenetic sequence of minerals is dominated by the early formation of quartz, feldspar, and clay minerals mainly kaolinite. These are followed by carbonate and pyrite with ilmenite and hematite.

Three types of silica overgrowths are recognized, normal, uneven, and double overgrowths. The uneven was suggested formed from the normal after pressolving. The silica forms multiple silica overgrowths and caused nearly complete destruction of primary porosity. This significant overgrowth is believed to be due to mixing of fresh waters with marine pore waters as it is found in sandstones

associated with fresh and marine horizons.

Authigenic feldspar is also formed during early diagenesis but after silica overgrowth, and the development was localised. The analyses indicate that it is pure potash feldspar, and it is believed that the ions required (potassium, aluminium and silicon) to form the overgrowth were supplied by interstitial water; clay minerals; rock fragment; and detrital feldspar. Later on, some change occurred in the diagenetic environment and they began to alter to one of the clay minerals. In contrast, authigenic clays found commonly include kaolinite with some illite, chlorite, and smectite. Formation of kaolinite as the predominant clay species suggests relatively acid conditions.

The carbonate cement is present as pore filling but has also partially to completely replaced detrital grains and even the authigenic clay. It has mainly formed of calcite with dolomite, and ankerite usually ferroan in composition, and has reduced the primary porosity, and formed microporosity. Geochemical analyses of the elements in shales and sandstones led to the suggestion that mudstone was the source of the carbonate cement (c.f. Curtis, 1978). All samples containing carbonate show some differences in composition between cement filling and replacement. The latter, under the ordinary microscope appear to consist of a number of phases. Pyrite formed as the products of bacterial metabolism (Curtis *et al*, 1972; Berner, 1970), by the bacterial decay of organic matter produced sulphur, the iron coming from detrital minerals. Oxidation produced ilmenite which partially altered to hematite.

No further change occurred until decarbonisation took place and produced secondary porosities which vary in amount and in size



(Chapter 6). The bulk of porosity estimated from routine core analysis is more reliable than those found by using the thin-section method but thin-section study of samples often shows fragmentary evidence of past diagenetic events. Porosities vary between 3.86% and 30.6% (core analyses). Predominantly they are secondary intergranular amongst primary grains often reduced by silica overgrowth and remnant after carbonate dissolution. Microporosity is often dominant and mostly intercrystalline amongst kaolinite.

REFERENCES

- Aalto, K.R. 1972. Diagenesis of Orthoquartzites near Bogota, Columbia. J. Sediment. Petrol., 42, 330-340.
- Alexander, G.B., Heston, W.M., and Iler, H.K. 1954. The solubility of Amorphous Silica in Water. J. Phys. Chem., 58, 453-455.
- Al-Hashimi, W.S. and Hemingway, J.E. 1973. Recent dedolomitization and the origin of the Rusty Crusts of Northumberland. J. Sediment. Petrol., 43, 82-91.
- Allen, J.R.L. 1963. Deposition Features of Dittonian Rocks: Pembrokeshire compared with the Welsh Borderland. Geol. Mag., 100, No 5, 385-400.
- Allen, J.R.L. 1963a. Asymmetrical ripples marks and the origin of water-laid cosets of cross-strata. Lpool. Manchr. Geol., 3, 187-236.
- Allen, J.R.L. 1963b. The classification of cross-stratified units, with notes on their origin. Sedimentology, 2, 93-114.
- Allen, J.R.L. 1964. Primary current lamination in the Lower Old Red Sandstone, Anglo-Welsh Basin. Sedimentology, 3, 89-108.
- Allen, J.R.L. 1965a. Late Quaternary Niger delta and adjacent areas: Sedimentary environments and lithofacies. Amer. Assoc. Petrol.

Geol. Bull., 49, 457-600.

Allen, J.R.L. 1968. Current ripples. North Holland, Amsterdam,  
The Netherlands. 433 p.

Allen, J.R.L. 1970. Physical Processes of Sedimentation. George Allen  
and Unwin Ltd, London, 248 p.

Almon, W.R. and Davies, D.K. 1979. Regional diagenetic trends in the  
Lower Cretaceous Muddy sandstone, Powder River Basin: In:  
P.A. Scholle and P.R. Schluger (eds.). Aspects of diagenesis-  
symposia. Soc. Econ. Paleontologists and Mineralogists, Spec.  
Publ., 26, 370-400.

Arndorfer, D.J. 1973. Discharge patterns in two crevasses of the Mississippi  
river delta. Mar. Geol., 15, 269-287.

Basi, M.A. 1978. Sedimentary Petrology of the Lower Limestone Group.  
In the Carboniferous Central Basin, Midland Valley of Scotland.  
Unpublished Ph.D. Thesis. University of Strathclyde.

Basu, A., Young, S.W., Suthener, L.J., James, W.C., and Mack, G.H. 1975.  
Re-evaluation of the use of undulatory extinction and polycrystal-  
linity in detrital quartz for provenance interpretation. J. Sediment.  
Petrol., 45, 873-882.

Batchelor, R.A., 1980. Analysis of major, minor and selected trace  
elements in silicate rocks and minerals. Int. Publ., 80/1,

Dept of Geology, University of St Andrews.

- Beerbower, J.R. 1964. Cyclothems and cyclic deposition mechanisms in alluvial plain sedimentation, in Merriam, D.F., ed., Symposium on Cyclic Sedimentation: Kansas Geol. Surv. Bull., 169, 31-42.
- Belt, E.S. 1975. Scottish Carboniferous Cyclothem Patterns and their Paleoenvironmental Significance. In: Broussard, M.L. (ed.), Deltas, Houston. Geol. Soc., 427-499.
- Bennison, G.M. 1960. Lower Carboniferous non-marine Lamellibranchs from East Fife, Scotland. Paleontology, 3, 137-152.
- Bennison, G.M. 1961. Small Naiadites obesus from the Calciferous Sandstones Series. Lower Carboniferous of Fife. Paleontology, 4, 300-311.
- Bennison, G.M. 1962. Palaeontological and physical evidence of the Palaeoecology of some early species of non-marine lamellibranchs. Liverpool and Manchester Geol. J., 3, 41-50.
- Berg, R.R. 1970. Method for determining permeability from reservoir rock properties. Gulf Coast Assoc. Geol. Soc. Trans., 20, 303-317.
- Berner, R.A. 1970. Sedimentary pyrite formation. Am. J. Sci., 268, 1-23.
- Blatt, H. 1962. Selective destruction of undulatory quartz in

Sedimentary-environment. Geol. Soc. Amer. Apec. Paper.,  
73, 118.

Blatt, H. and Christie, J.M. 1963. Undulatory extinction in quartz  
of Igneous and Metamorphic rocks and its significance in  
provenance studies of Sedimentary rocks. J. Sediment. Petrol., 33,  
559-579.

Blatt, H. 1967. Original characteristics of clastic quartz grains.  
J. Sediment. Petrol., 37, No 2, 401-424.

Blatt, H. 1979. Diagenetic processes in sandstone. In: Scholle  
P.A. and Schluger, P.R. (eds.). Aspects of diagenesis-symposia.  
Soc. Econ. Paleo. and Min., Spec. Publ., 26, 141-157.

Blatt, H., Middleton, G. and Murray, R. 1980. Origin of Sedimentary  
rocks. Prentice-Hall, New Jersey, 782 p.

Bjorlykke, K., Malm, O. and Elverhoi, A. 1979. Diagenesis in  
the Mesozoic sandstones from Spitsbergen and the North Sea.  
Geol. Rdsch, 68, 1152-1171.

Bucke, D.P. Jr. and Mankin, C.J. 1971. Clay-mineral diagenesis within inter-  
laminated shales and sandstones. J. Sediment. Petrol., 41, No 4,  
971-981.

Chisholm, J.I, 1968. Trace-fossils from the Geological Survey  
boreholes in East Fife, 1963-4. Geol. Surv. Great Britain,

Bull., 28, 103-119.

Chisholm, J.I. 1970a. Lower Carboniferous trace-fossils in the Lower Carboniferous at St Monance, Scotland. Geol. Surv. Great Britain, Bull., 31, 19-35.

Chisholm, J.I, 1970b. Teichichnus and related trace-fossils in the Lower Carboniferous at St Monance, Scotland. Geol. Surv. Great Britain, Bull., 32, 21-51.

Coleman, J.M., Gagliano, S.M. and Webb, J.E. 1964. Minor sedimentary structures in a prograding distributary. Mar. Geol., 1, 240-258.

Conolly, J.R. 1965. The occurrence of polycrystallinity and undulatory extinction in quartz in sandstones. J. Sediment. Petrol., 35, 116-135.

Correns, C.W. 1950. On the geochemistry of diagenesis, I. The behaviour of  $\text{CaCO}_3$  and  $\text{SiO}_2$ : Geochim. Cosmochim. Acta, 1, 49-54.

Crampton, C.B., 1905. The limestone of Aberlady, Dunbar and St Monance. Trans. Geol. Soc. Edinburgh, 8, 374-378.

Currie, E.D. 1954. Scottish Carboniferous goniatites: Trans. R. Soc. Edinburgh, 62, 527-602.

Curtis, C.D., Petrowski, C., and Oertel, C. 1972. Stable carbon isotope ratio within carbonate concentration: a clue to time and

place of formation. *Nature*, 235, 98-100.

Curtis, C.D. 1978. Possible links between sandstone diagenesis and depth-related geochemical reactions occurring in enclosing mudstones: *J. Geol. Soc. London*, 135, 107-117.

Davie, D.K., 1967. Origin of friable sandstone - Calcareous sandstone rhythms in the Upper Lias of England. *J. Sediment. Petrol.*, 37, 1179-1188.

Davies, H.G., 1965. Convolute lamination and other structures from the Lower Coal Measures of Yorkshire. *Sedimentology*, 5, 305-325.

Deegan, C.E., 1970. The petrology and sedimentology of the Lower Carboniferous rocks between White Port and Kirkbean, Kirkcudbrightshire. Unpublished Ph.D. Thesis. University of Wales.

Deer, W.A., Howie, R.A., and Zussman, J. 1974. An introduction to the rock-forming minerals. Vols. 1-5 (7th ed.). Longmans, London, 528 p.

Dickson, J.A.D. 1965. A modified staining technique for carbonates in thin section. *Nature*, 205, 587.

Donaldson, J.A., 1967. In: Hantzschel, W., (1975). Trace fossils and problematica. *Treatise on Invertebrate Paleontology*, Part W, *Miscellanea*, Suppl. 1, W1-W269.

Duff, P.McL.D. and Walton, E.K. 1962. Statistical basis of cyclothems:

A quantitative study of the Sedimentary succession in the east Pennine Coal-Field. *Sedimentology*, 1, 235-255.

Dzulynski, S. and Walton, E.K. 1963. Experimental production of sole markings. *Trans. Geol. Soc. Edinburgh*, 19, 279-305.

Dzulynski, S., 1966. Sedimentary structures resulting from convection-like pattern of motion. *Rocz. Pol. Tow. Geol. (Ann. Soc. Geol. Pol.)*, 28, 3-21.

Elliott, T. 1974b. Interdistributary bay sequences and their genesis. *Sedimentology*, 21, 611-622.

Elliott, T. 1975. The sedimentary history of a delta lobe from a Yoredale (Carboniferous) Cyclothem. *Proc. Yorks. Geol. Soc.*, 40, 505-536.

Elliott, T. 1979. *Deltas: In: Reading, H.G. (ed) Sedimentary Environments and Facies. Blackwell Scientific Publications, Oxford, London, Edinburgh, Melbourne, 97-142.*

Farrow, G.E. 1966. Bathymetric zonation of Jurassic trace fossils from the coast of Yorkshire, England. *Palaeogeogr., Palaeoclimatol., Palaeoecol.*, 2, 103-151.

Fenton C.L. and Fenton, M.A., 1937b. In: Hantzschel, W., (1975). Trace fossils and problematica. *Treatise on Invertebrate Paleontology, Part W, Miscellanea, Suppl. 1*, W1-W269.



- Ferguson, L. 1962. The paleocology of a Lower Carboniferous marine transgression. *J. Paleont.*, 36, 1090-1107.
- Ferguson, L. 1963. The paleocology of Lingula squamiformis, Phillips during a Scottish Mississippian marine transgression. *J. Paleont.*, 37, 669-681.
- Fielding, C.R., 1984. Upper delta plain lacustrine and fluviolacustrine facies from the Westphalian of the Durham coalfield, NE England. *Sedimentology*, 31, No 4, 547-567.
- Fisk, H.N. 1947. Fine Grained Alluvial Deposits and their Effects on Mississippi River Activity: In: Elliott, T. 1974. Interdistributary bay sequences and their genesis. *Sedimentology*, 21, 611-622.
- Fisk, H.N., Kolb, C.R. and Wilbert, L.J. Jr., 1954. Sedimentary framework of the modern Mississippi delta. *J. Sediment. Petrol.*, 24, No 2, 76-99.
- Folk, R.L. and Ward, W.C. 1957. Brazos river bar, a study in the study in the significance of grain size parameters. *J. Sediment. Petrol.*, 27, 3-27.
- Folk, R.L. 1968. Petrology of Sedimentary rocks. Hemphills, Austin, Texas, 170 p.
- Forsyth, I.H. and Chisholm, J.I. 1968. Geological Survey boreholes

in the Carboniferous of East Fife, (1963-4). Geol. Survey  
Great Britain, Bull., 28, 61-101.

Francis, E.H. 1965. Carboniferous, Midland Valley in the Geology of  
Scotland; Edinburgh. Oliver and Boyd, 309-339.

Francis, E.H. 1983. Carboniferous. In: Craig, G.Y. (ed.) Geol.  
of Scot., Scot. Acad. Press, Edinburgh,, 253-296.

Francis, E.H., Allan, J.K., and Knox, J. 1961. The economic geology of  
the Fife Coalfield, Area II. 2nd edit. Mem. Geo. Surv., 153 p.

Frank, J.R. Carpenter, A.B. and Oglesby, T.W. 1982. Cathodoluminescence  
and composition of calcite cement in the Taum Sauk Limestone  
(Upper Cambrian), Southeast Missouri. J. Sediment. Petrol., 52, No 2,  
631-638.

Friedman, G.M. 1958. Determination of sieve-size distribution from  
thin-section data for sedimentary petrology studies. J. Geol.,  
66, 394-416.

Galloway, W.E. 1979. Diagenetic control of reservoir quality in arc-  
derived sandstones. Implications for petroleum exploration.  
In: Scholle, P.A. and Schluger, P.R. (eds.). Aspects of  
diagenesis-symposia. Soc. Econ. Paleontologists and Mineralogists,  
Spec. Publ., 26, 251-262.

Geikie, A. 1902. The geology of Eastern Fife. Geol. Surv. Scot.

Mem., 385 p.

George, T.N., Johnson, G.A.L., Mitchell, M., Prentice, J.E., Ramsbottom, W.H.C., Sevastopulo, G.D. and Wilson, R.B. 1977. A correlation of Dinantian Rocks in the British Isles. Geol. Soc. Spec. Rept., No. 7, 87 p.

Ginsburg, R.N., and Klein, G. deV., 1973. Tidal deposits: A compilation of examples: Printed notes for a colloquium: Comparative Sedimentology Laboratory. In: Belt, E.S. 1975. Scottish Carboniferous Cyclothem Patterns and their Palaeoenvironmental Significance. In: Broussard, M.L. (ed.), Deltas, Houston. Geol. Soc., 427-499.

Glenn, N. Hower, W.F. and Davies, D.K. 1980. Nature of authigenic illite in sandstone reservoirs. J. Sediment. Petrol., 50, 761-766.

Goodlet, G.A. 1957. Lithological variation in the Lower Limestone Group of the Midland Valley of Scotland. Geol. Surv. Great Britain, Bull., 12, 52-65.

Goodlet, G.A. 1959. Mid-Carboniferous Sedimentation in the Midland Valley of Scotland. Trans. Geol. Soc. Edinburgh, 17, pt. 3. 217-240.

Gray, D.H., and Rex, R.W. 1966. Formation damage in sandstones caused by clay dispersion and migration. Clays and clay minerals, 14, 355-366.

- Greensmith, J.T. 1961. The petrology of the Oil Shale Group Sandstones of West Lothian and Southern Fifeshire. Geol. Assoc. Lond. Proc., 72. 49-71.
- Greensmith, J.T. 1962. Rhythmic deposition in the Carboniferous Oil-Shale Group of Scotland. J. Geol., 70, 355-364.
- Greensmith, J.T. 1965. Calciferous Sandstone Series Sedimentation at the eastern end of the Midland Valley of Scotland. J. Sediment. Petrol., 35, 233-242.
- Greensmith, J.T. 1966. Carboniferous deltaic Sedimentation in eastern Scotland. A review and reappraisal, in Deltas in their Geological Framework: Houston Geol. Soc., p. 189-211.
- Greensmith, J.T. 1968. Paleogeography and rhythmic deposition in the Scottish Oil-Shale Group. UN Symposium on the development and utilization of Oil Shale resources. Tallinn, 1968, Sect. B1, 16 p.
- Hamblin, W.K., 1965. Internal structures of "homogeneous" sandstones. Bull. Kansas Geol. Survey, 175, 569-582.
- Hantzschel, W. 1975. Trace fossils and problematica. Treatise on Invertebrate Paleontology, Part W, Miscellanea, Suppl. 1, W1-W269.
- Harms, J.C. and Fahnestock, R.K. 1965. Stratification, bed forms,

and flow phenomena (with an example from the Rio Grande). In: Middleton G.V. (ed.). Primary Sedimentary Structures and their Hydrodynamic Interpretation. Soc. Econ. Paleontologists and Mineralogists. Spec. Publ. Tulsa, 12, 84-115.

Harvey, P.K., Taylor, D.M., Hendry, R.D., and Bancroft, F. 1973. An accurate fusion method for the analysis of rocks and chemically related materials by X-ray fluorescence spectrometry. X-ray Spectro., 5, 33-44.

Heer, O. 1877. In: Hantzschel, W. 1975. Trace fossils and problematica. Treatise on Invertebrate Paleontology, Part W, Miscellanea, Suppl. 1, W1-W269.

Hembey, J.J., and Jones, W.R. 1964. Chemical aspects of hydrothermal alterations with emphasis on hydrogen metasomatism. Econ. Geol., 59, 538-569.

Hoffman, J. and Hower, J. 1979. Clay mineral assemblages as low grade metamorphic geothermometers. Application to the thrust faulted disturbed belt of Montana, U.S.A. In: Scholle, P.A. and Schluger, P.R. (eds.). Aspects of diagenesis-symposia. Soc. Econ. Paleontologists and Mineralogists, Spec. Publ., 26, 55-79.

Hofmann, H.J. 1971. In: Hantzschel, W. 1975. Trace fossils and problematica. Treatise on Invertebrate Paleontology, Part W, Miscellanea, Suppl. 1, W1-W269.

- Hsu, K.J. 1977(a). Studies of Ventura Field, California, I. Facies geometry and genesis of Lower Pliocene turbidites: Amer. Assoc. Petrol. Geol. Bull., 61, 137-168.
- Hsu, K.J. 1977(b). Studies of Ventura Field. California: II Lithology, Compaction and Permeability of Sands. Amer. Assoc. Petrol. Geol. Bull., 61, 169-191.
- Hunter, R.E. and Clifton, H.E. 1982. Cyclic deposits and hummocky cross-stratification of probable storm origin in Upper Cretaceous rocks of the Cape Sebastian area, Southwestern Oregon. J. Sediment. Petrol., 52, 127-143.
- Hurst, A.R. 1980. Occurrence of corroded authigenic Kaolinite in a diagenetically modified sandstone. Clays and Clay Minerals, 28, No. 5, 393-396.
- Keller, W.D. 1970. Environmental aspects of clay minerals. J. Geol., 40, No. 3, 788-813.
- Keller, W.D. and Littlefield, R.F. 1950. Inclusion in quartz of igneous and metamorphic rocks. J. Sediment. Petrol., 20, 74-84.
- Kirkby, J.W. 1902. In: Geikie, Sir A. The Geology of Eastern Fife, Geol. Surv. Scot. Mem.
- Krauskopf, K.B. 1956. Dissolution and precipitation of silica at low temperatures. Geochim. Cosmochim. Acta, 10, 1-26.

- Krynine, P.D. 1940. Petrology and genesis of the Third Bradford Sand. Penn. State Coll. Min. Indus. Expt. Sta. Bull., 29, 134 p.
- Kuenen, PH.H., 1958. Experiments in geology. Trans. Geol. Soc. Glasgow, 23, 1-28.
- Kuenen, PH.H. 1965. Value of experiments in geology. Geol. en. Mijnb., 44, 22-36.
- Kuenen, P.H.H. and Prentice, J.E. 1957. Flow markings and load-casts. Geol. Mag., 94, 173-174.
- Leckie, D.A. and Walker, R.G. 1982. Storm- and tidal-dominated shorelines in Cretaceous Moosebar-Lower Gates interval-outcrop equivalents of deep-basin gas traps in Western Canada. Amer. Assoc. Petrol. Geol. Bull., 66, 138-157.
- Leeder, M.R. 1972. Upper Old Red Sandstone - Tournaisian sedimentology and the initiation and origin of the Northumberland basin. Unpublished, Ph.D. Thesis, University of Reading.
- Leeder, M.R. 1974. Lower Border Group (Tournaisian) Fluvio-deltaic Sedimentation and Palaeogeography of the Northumberland Basin.
- Lorenz Von Liburnau, J.R. 1900. In: Hantzschel,, W. 1975. Trace fossils and problematica. Treatise on Invertebrate Paleontology,

Part W, Miscellanea, Suppl. 1, W1-W269.

Lowe, D.R. 1975. Water escape structure in coarse-grained sediments.  
Sedimentology, 22, 157-204.

MacGregor, A.R. 1968. Fife and Angus Geology, an excursion guide. Edin.,  
Wm. Blackwood and Sons Ltd., 194-201.

MacGregor, M. 1930. Scottish Carboniferous Stratigraphy. An introduction  
to the study of the Carboniferous rock of Scotland. Trans. Geol. Soc.  
Glasgow, 18, 442-558.

MacKie, W. 1896. The sand and sandstones of east Moray. Trans.  
Geol. Soc. Edinburgh, 7, 148-172.

MacNair, P. 1917. The Hurlet Sequence in East of Scotland and the  
Abden Fauna as an index to the deposition of the Hurlet Limestone.  
Roy. Soc. Edinburgh, 37, 137-209.

McBride, E.F. 1963. A classification of common sandstones. J. Sediment.  
Petrol., 33, 664-669.

McBride, E.F. 1974. Significance of Colour in red, green, purple,  
olive, brown, and grey beds of Difunta Group, Northeastern Mexico.  
J. Sediment. Petrol., 44 760-773.

McKee, E.D. 1938. Original structure in Colorado River flood deposits  
of Grand Canyon. J. Sediment. Petrol., 8, 77-83.



- McKee, E.D. 1965. Experiments on ripple lamination. In: Middleton G.V. (ed.). Primary Sedimentary Structures and their Hydrodynamic Interpretation, Soc. Econ. Paleontologists and Mineralogists, Spec. Publ. Tulsa, 12, 66-83.
- McKee, E.D. and Weir, G.W. 1953. Terminology for stratification and cross-stratification. Geol. Soc. Amer. Bull., 64, 381-390.
- Millot, G. 1970. Geology of clays. Springer-Verlag, Berlin, 429 p.
- Mitchell, R.L. 1956. The Limestones of Scotland. Mem. Geol. Surv. Min. Res., No. 37.
- Moore, E.S. and Maynard, J.E. 1929. Solution, transportation and precipitation of iron and silica. Part 1. Econ. Geol., 24, 272-303.
- Moore, D. 1966. Deltaic Sedimentation. Earth Sci. Rev., 1, 87-104.
- Muller, G. 1967. Diagenesis in argillaceous sediments. In: Diagenesis in sediments, Larsen, G. and Chilinger, G.V. (eds.). New York, Elsevier Pub. Co., 127-178.
- Myannil, R.M. 1966. In: Hantzschel, W., (1975). Trace fossils and problematica. Treatise on Invertebrate Paleontology, Part W, Miscellanea, Suppl. 1, W1-W269.
- Neal, W.J. 1969. Diagenesis and dolomitization of a Limestone (Pennsylvanian

of Missouri) as revealed by staining. *J. Sediment. Petrol.*, 30,  
No. 3, 1040-1045.

Neves, R., Gueinn, K.J., Clayton, G., Ioannides, N.S., Neviue, R.S.W.  
and Kruszezwska, K. 1973. Palynological correlation within the  
Lower Carboniferous of Scotland and northern England. *Trans. Royal. Soc.*  
Edinburgh, 69, 23-70.

Norrish, K., and Chappell, B.W. 1977. pages 201-272 in Ed. Zussman  
'Physical methods in Determinative Mineralogy'. *J. Academic Press.*

Okamoto, G., Ohura, T., and Goto, K. 1957. Properties of silica in water.  
*Geochim. Cosmochim. Acta*, 12, 123-132.

Oomkens, E., 1970. Depositional sequences and sand distribution in the  
post-glacial Rhone delta complex. In: Morgan, J.P. and Shaver,  
R.H. (eds.). *Deltaic Sedimentation Modern and Ancient*; Soc.  
Econ. Paleontologists and Mineralogists, Spec. Publ., Tulsa, 15,  
198-212.

Pettijohn, F.J., Potter, P.E. and Siever, R. 1973. *Sand and sandstone.*  
New York: Springer-Verlag, 618 p.

Pettijohn, F.J. 1975. *Sedimentary rocks.* 3rd Ed.: New York, Harper  
and Bros., 628 p.

Phemister, J. 1956. *The Limestones of Scotland: Mem. Geol. Surv. Min.*  
*Resources*, No. 27.

- Pittman, E.A. 1979. Porosity, diagenesis and productive capability of sandstone reservoirs. In: Scholle, P.A. and Schluger, P.R. (eds.). Aspects of diagenesis-symposia; Soc. Econ. Paleontologists and Mineralogists, Spec. Publ., 26, 159-173.
- Potter, E.D. and Pettijohn, F.J. 1963. Paleocurrent and Basin Analysis. Academic Press, New York, 296 p.
- Raaf, J.F.M. de, Boersma, J.R. and Gelder, A. Van. 1977. Wave-generated structures and sequences from a shallow marine succession, Lower Carboniferous, County Cork, Ireland. *Sedimentology*, 24, 451-483.
- Ramsay, J.G. 1961. The effect of folding upon the orientation of sedimentary structures. *J. Geol.*, 69, 84-100.
- Richter, R. 1927a. In: Hantzschel, W., (1975). Trace fossils and Problematica. *Treatise on Invertebrate Paleontology, Part W, Miscellanea, Suppl. 1, W1-W269.*
- Richter, R. 1928. In: Hantzschel, W. (1975). Trace fossils and Problematica. *Treatise on Invertebrate Paleontology, Part W, Miscellanea, Suppl. 1, W1-W269.*
- Richter, R. 1931. In: Hantzschel, W. (1975). Trace fossils and Problematica. *Treatise on Invertebrate Paleontology, Part W, Miscellanea, Suppl. 1, W1-W269.*

- Rittenhouse, G. 1971. Pore space reduction by Solution and Cementation; Amer. Assoc. Petrol. Geol. Bull., 55, 80-91.
- Robert, B.A., 1971. Principle of chemical sedimentology, McGraw-Hill, New York, 240 p.
- Russell, R.J. and Russell, R.D., 1939. Mississippi River Delta Sedimentation. In: Trask, P.D. (ed.). Recent Marine Sediments Symposium. Amer. Assoc. Petrol. Geol., 153-177.
- Sanderson, I.D. 1984. Recognition and significance of inherited quartz overgrowths in quartz arenites. J. Sediment. Petrol., 54, No. 2, 473-486.
- Saxena, R.S. 1979. Depositional environments and processes on the lower delta plain of the Mississippi River. In: Carboniferous Depositional Environments in the Appalachian Region (Ed. by Fern, J.C. and Horne, J.C.). Carolina Coal Group, Columbia, South Carolina. 305-343.
- Schmidt, V. and McDonald, D.A. 1979(b). Texture and recognition of secondary porosity in sandstones: In: Scholle, P.A. and Schluger, P.R. (eds.). Aspects of diagenesis-symposia. Soc. Econ. Paleontologists and Mineralogists. Spec. Publ., 26, 209-225.
- Schmidt, V. and McDonald, D.A. 1980. Secondary reservoir porosity in the course of sandstone diagenesis. Amer. Assoc. Petrol.

Geol. Series No. 12, 125 p.

Scott, A.J. and Fisher, W.L. 1969. Delta systems and deltaic deposition. In: Delta Systems in the Exploration for Oil and Gas. Bureau - Econ. Geol. Austin, Texas. 10-29.

Selim, A.A. and Duff, P.McL.D. 1974. Carbonate facies in the Lower Carboniferous (Visean) of St Monance, East Fife, Scotland. J. Sediment. Petrol., 44, No. 3, 806-815.

Sharma, G.D. 1965. Formation of silica cement and its replacement by carbonates. J. Sediment. Petrol., 35, 733-745.

Shrock, R.R., 1948. Sequence in layered rocks. McGraw-Hill, New York, N.Y., 507 p.

Siever, R. 1962. Silica solubility, 0-200 °C and the diagenesis of Siliceous Sediments: J. Geol., 70, 55-79.

Siever, R., Beck, K.C. and Berner, R.A. 1965. Composition of interstitial waters of modern sediments. J. Geol., 73, 39-73.

Simpson, S. 1957. On the trace-fossil Chondrites. Quart. J. Geol. Soc. London, 112, 475-96.

Smout, T.W. and Narain, K. 1960. Clay mineralogy of Pre-Pennsylvanian sandstones and shales of the Illinois Basin II: Clay mineral variations between oil-bearing and non-oil-bearing sandstones.

Illinois State Geol. Survey, Circ., 287, 14 p.

- Spears, D.A. and Kanaris-Sotiriou, R. 1975. Titanium in some Carboniferous sediments from Great Britain: *Geochim. Cosmochim. Acta*, 40, 345-351.
- Tate, G. 1859. In: Hantzschel, W., (1975). Trace fossils and problematica. *Treatise on Invertebrate Paleontology, Part W, Miscellanea, Suppl. 1*, W1-W269.
- Taylor, J.M. 1950. Pore-space reduction in sandstones. *Amer. Assoc. Petrol. Geol. Bull.*, 34, 701-716.
- Thompson, W.O., 1937. Original structures of beaches, bars and dunes. *Geol. Soc. Amer. Bull.*, 47, 723-752.
- Van Straaten, L.M.J.U. 1959. Minor structures of some recent littoral neritic sediments. *Geol. Mijnbouw*, 21, 197-216.
- Vos, R.G. 1977. Sedimentology of an upper Paleozoic River, wave and tide influence delta system in Southern Morocco. *J. Sediment. Petrol.*, 47, 1242-1260.
- Walker, R.G. 1963. Distinctive types of ripple drift cross-lamination. *Sedimentology*, 2, 173-188.
- Walker, T.R. 1967. Formation of red beds in modern and ancient deserts: *Geol. Soc. Amer. Bull.*, 78, 353-368.

- Wardlaw, N.C. 1976. Pore geometry of carbonate rocks as revealed by pore casts and capillary pressure. Amer. Assoc. Petrol. Geol. Bull., 60, 245-257.
- Waugh, B. 1979. Petrology, provenance and silica diagenesis of the Penrith Sandstone (Lower Permian) of Northwest England: In: Diagenesis of Sandstones: Cement-Porosity relationship: Compiled by Earle, F. McBride. SEPM. Reprint series No. 9. 139-153.
- Whitaker, J.H.McD. 1978. Diagenesis of the Brent Sand Formation: a scanning electron microscope study, In: Whalley, W.B. (ed.) Scanning electron microscopy in the study of Sediment-A symposium. Geo. Abstracts, Norwich, England. 363-382.
- Wilson, M.J. 1971. Clay mineralogy of the Old Red Sandstones (Devonian) of Scotland. J. Sediment. Petrol., 40, No. 4, 995-1007.
- Wilson, P. 1978. A scanning electron microscope examination of quartz grain surface texture from the weathered Millstone Grit (Carboniferous) of the Southern Pennines, England. In: Scanning electron microscopy in the study of sediments a symposium. Ed. Whalley, W. Brian, by Geo. Abstracts, Norwich, England, 307-318.
- Wilson, R.B. 1966. A study of Nielson Shell bed, a Scottish Lower Carboniferous marine Shale. Geol. Surv. Great Britain, Bull.,

24, 105-130.

Wilson, R.M. 1978. A sedimentology study of 3 sedimentary cycles of the Lower Limestone Group at St Monance, Fife. Honours Thesis. University of St Andrews.

Wood, W. 1887. The East Neuk of Fife, its history and antiquities: Douglas, Edinburgh. Second Edition.

Wright, J. 1912. Addition to the fauna of the Lower Carboniferous Limestones of Leslie and St Monance, Fife. Trans. Geol. Soc. Edinburgh, 10, 131-147.



Samples number	Total point counter	Quartz				Feldspar				Micas			Cement			Mat-rix	Type of contact				Heavy minerals							% of Rock Frag-ment	% of Porosity
		Monocrystalline Quartz (P)	% of undulatory Quartz in (P)	% of Non-Undulatory Quartz in (P)	Polycrystalline Quartz in total Qz	% of Microcline	% of Orthoclase	% of Plagioclase	Total percentage	% of Muscovite	% of Biotite	Total percentage	% of Carbonate	% of Iron Oxide	% of Clay		Linear	Sutured	Tangential	Concave-convex	% of Zircon	% of Tourmaline	% of Rutile	% of Garnet	% of Epidote	Total percentage			
M4	500	65.4	67.28	32.72	2.97	0.0	0.0	0.8	0.8	1.0	0.0	1.0	22.0	5.0	2.8	39.2	1.3	45.6	13.9	0.0	0.0	0.0	0.0	0.0	0.2	1.0	0.0		
B6a	500	53.2	74.44	26.56	3.97	0.0	0.0	0.6	0.6	2.6	0.0	2.6	16.4	10.5	5.2	41.7	2.6	40.0	15.7	0.2	0.0	0.0	0.0	0.0	0.2	0.8	0.0		
B6b	500	66.4	64.16	35.84	4.05	0.0	0.0	1.0	1.2	1.0	0.0	3.8	8.2	3.4	11.4	8.3	27.5	27.5	0.2	0.4	0.0	0.0	0.0	0.2	1.0	0.2	0.0		
B7a	500	58.2	76.99	23.01	3.96	0.0	0.0	0.0	0.0	1.2	0.0	1.2	0.8	0.8	16.6	2.2	55.3	15.6	0.4	0.4	0.0	0.0	0.0	0.2	1.0	0.2	0.0		
B7b	500	68.0	69.18	31.18	2.86	0.0	0.0	0.2	0.2	1.8	0.2	1.8	0.4	0.6	13.8	4.1	44.0	10.6	0.2	0.0	0.0	0.0	0.0	0.2	0.2	0.2	0.0		
B7c	500	68.0	69.18	31.18	2.86	0.0	0.0	0.2	0.2	1.8	0.2	1.8	0.4	0.6	13.8	4.1	44.0	10.6	0.2	0.0	0.0	0.0	0.0	0.2	0.2	0.2	0.0		
B7d	500	68.0	69.18	31.18	2.86	0.0	0.0	0.2	0.2	1.8	0.2	1.8	0.4	0.6	13.8	4.1	44.0	10.6	0.2	0.0	0.0	0.0	0.0	0.2	0.2	0.2	0.0		
B7e	500	68.0	69.18	31.18	2.86	0.0	0.0	0.2	0.2	1.8	0.2	1.8	0.4	0.6	13.8	4.1	44.0	10.6	0.2	0.0	0.0	0.0	0.0	0.2	0.2	0.2	0.0		
B7f	500	68.0	69.18	31.18	2.86	0.0	0.0	0.2	0.2	1.8	0.2	1.8	0.4	0.6	13.8	4.1	44.0	10.6	0.2	0.0	0.0	0.0	0.0	0.2	0.2	0.2	0.0		
B7g	500	68.0	69.18	31.18	2.86	0.0	0.0	0.2	0.2	1.8	0.2	1.8	0.4	0.6	13.8	4.1	44.0	10.6	0.2	0.0	0.0	0.0	0.0	0.2	0.2	0.2	0.0		
B7h	500	68.0	69.18	31.18	2.86	0.0	0.0	0.2	0.2	1.8	0.2	1.8	0.4	0.6	13.8	4.1	44.0	10.6	0.2	0.0	0.0	0.0	0.0	0.2	0.2	0.2	0.0		
B7i	500	68.0	69.18	31.18	2.86	0.0	0.0	0.2	0.2	1.8	0.2	1.8	0.4	0.6	13.8	4.1	44.0	10.6	0.2	0.0	0.0	0.0	0.0	0.2	0.2	0.2	0.0		
B7j	500	68.0	69.18	31.18	2.86	0.0	0.0	0.2	0.2	1.8	0.2	1.8	0.4	0.6	13.8	4.1	44.0	10.6	0.2	0.0	0.0	0.0	0.0	0.2	0.2	0.2	0.0		
B7k	500	68.0	69.18	31.18	2.86	0.0	0.0	0.2	0.2	1.8	0.2	1.8	0.4	0.6	13.8	4.1	44.0	10.6	0.2	0.0	0.0	0.0	0.0	0.2	0.2	0.2	0.0		
B7l	500	68.0	69.18	31.18	2.86	0.0	0.0	0.2	0.2	1.8	0.2	1.8	0.4	0.6	13.8	4.1	44.0	10.6	0.2	0.0	0.0	0.0	0.0	0.2	0.2	0.2	0.0		
B7m	500	68.0	69.18	31.18	2.86	0.0	0.0	0.2	0.2	1.8	0.2	1.8	0.4	0.6	13.8	4.1	44.0	10.6	0.2	0.0	0.0	0.0	0.0	0.2	0.2	0.2	0.0		
B7n	500	68.0	69.18	31.18	2.86	0.0	0.0	0.2	0.2	1.8	0.2	1.8	0.4	0.6	13.8	4.1	44.0	10.6	0.2	0.0	0.0	0.0	0.0	0.2	0.2	0.2	0.0		
B7o	500	68.0	69.18	31.18	2.86	0.0	0.0	0.2	0.2	1.8	0.2	1.8	0.4	0.6	13.8	4.1	44.0	10.6	0.2	0.0	0.0	0.0	0.0	0.2	0.2	0.2	0.0		
B7p	500	68.0	69.18	31.18	2.86	0.0	0.0	0.2	0.2	1.8	0.2	1.8	0.4	0.6	13.8	4.1	44.0	10.6	0.2	0.0	0.0	0.0	0.0	0.2	0.2	0.2	0.0		
B7q	500	68.0	69.18	31.18	2.86	0.0	0.0	0.2	0.2	1.8	0.2	1.8	0.4	0.6	13.8	4.1	44.0	10.6	0.2	0.0	0.0	0.0	0.0	0.2	0.2	0.2	0.0		
B7r	500	68.0	69.18	31.18	2.86	0.0	0.0	0.2	0.2	1.8	0.2	1.8	0.4	0.6	13.8	4.1	44.0	10.6	0.2	0.0	0.0	0.0	0.0	0.2	0.2	0.2	0.0		
B7s	500	68.0	69.18	31.18	2.86	0.0	0.0	0.2	0.2	1.8	0.2	1.8	0.4	0.6	13.8	4.1	44.0	10.6	0.2	0.0	0.0	0.0	0.0	0.2	0.2	0.2	0.0		
B7t	500	68.0	69.18	31.18	2.86	0.0	0.0	0.2	0.2	1.8	0.2	1.8	0.4	0.6	13.8	4.1	44.0	10.6	0.2	0.0	0.0	0.0	0.0	0.2	0.2	0.2	0.0		
B7u	500	68.0	69.18	31.18	2.86	0.0	0.0	0.2	0.2	1.8	0.2	1.8	0.4	0.6	13.8	4.1	44.0	10.6	0.2	0.0	0.0	0.0	0.0	0.2	0.2	0.2	0.0		
B7v	500	68.0	69.18	31.18	2.86	0.0	0.0	0.2	0.2	1.8	0.2	1.8	0.4	0.6	13.8	4.1	44.0	10.6	0.2	0.0	0.0	0.0	0.0	0.2	0.2	0.2	0.0		
B7w	500	68.0	69.18	31.18	2.86	0.0	0.0	0.2	0.2	1.8	0.2	1.8	0.4	0.6	13.8	4.1	44.0	10.6	0.2	0.0	0.0	0.0	0.0	0.2	0.2	0.2	0.0		
B7x	500	68.0	69.18	31.18	2.86	0.0	0.0	0.2	0.2	1.8	0.2	1.8	0.4	0.6	13.8	4.1	44.0	10.6	0.2	0.0	0.0	0.0	0.0	0.2	0.2	0.2	0.0		
B7y	500	68.0	69.18	31.18	2.86	0.0	0.0	0.2	0.2	1.8	0.2	1.8	0.4	0.6	13.8	4.1	44.0	10.6	0.2	0.0	0.0	0.0	0.0	0.2	0.2	0.2	0.0		
B7z	500	68.0	69.18	31.18	2.86	0.0	0.0	0.2	0.2	1.8	0.2	1.8	0.4	0.6	13.8	4.1	44.0	10.6	0.2	0.0	0.0	0.0	0.0	0.2	0.2	0.2	0.0		
B8a	500	65.6	66.97	33.03	6.45	0.4	0.0	0.6	1.0	0.8	0.0	3.4	1.0	3.6	13.2	3.1	31.2	9.6	0.4	0.0	0.0	0.0	0.0	0.6	1.2	15.2	0.0		
B8b	500	58.8	69.19	30.81	7.55	0.2	0.0	0.6	1.0	0.8	0.0	3.4	1.0	3.6	13.2	3.1	31.2	9.6	0.4	0.0	0.0	0.0	0.0	0.6	1.2	15.2	0.0		
B8c	500	58.8	69.19	30.81	7.55	0.2	0.0	0.6	1.0	0.8	0.0	3.4	1.0	3.6	13.2	3.1	31.2	9.6	0.4	0.0	0.0	0.0	0.0	0.6	1.2	15.2	0.0		
B8d	500	58.8	69.19	30.81	7.55	0.2	0.0	0.6	1.0	0.8	0.0	3.4	1.0	3.6	13.2	3.1	31.2	9.6	0.4	0.0	0.0	0.0	0.0	0.6	1.2	15.2	0.0		
B8e	500	58.8	69.19	30.81	7.55	0.2	0.0	0.6	1.0	0.8	0.0	3.4	1.0	3.6	13.2	3.1	31.2	9.6	0.4	0.0	0.0	0.0	0.0	0.6	1.2	15.2	0.0		
B8f	500	58.8	69.19	30.81	7.55	0.2	0.0	0.6	1.0	0.8	0.0	3.4	1.0	3.6	13.2	3.1	31.2	9.6	0.4	0.0	0.0	0.0	0.0	0.6	1.2	15.2	0.0		
B8g	500	58.8	69.19	30.81	7.55	0.2	0.0	0.6	1.0	0.8	0.0	3.4	1.0	3.6	13.2	3.1	31.2	9.6	0.4	0.0	0.0	0.0	0.0	0.6	1.2	15.2	0.0		
B8h	500	58.8	69.19	30.81	7.55	0.2	0.0	0.6	1.0	0.8	0.0	3.4	1.0	3.6	13.2	3.1	31.2	9.6	0.4	0.0	0.0	0.0	0.0	0.6	1.2	15.2	0.0		
B8i	500	58.8	69.19	30.81	7.55	0.2	0.0	0.6	1.0	0.8	0.0	3.4	1.0	3.6	13.2	3.1	31.2	9.6	0.4	0.0	0.0	0.0	0.0	0.6	1.2	15.2	0.0		
B8j	500	58.8	69.19	30.81	7.55	0.2	0.0	0.6	1.0	0.8	0.0	3.4	1.0	3.6	13.2	3.1	31.2	9.6	0.4	0.0	0.0	0.0	0.0	0.6	1.2	15.2	0.0		
B8k	500	58.8	69.19	30.81	7.55	0.2	0.0	0.6	1.0	0.8	0.0	3.4	1.0	3.6	13.2	3.1	31.2	9.6	0.4	0.0	0.0	0.0	0.0	0.6	1.2	15.2	0.0		
B8l	500	58.8	69.19	30.81	7.55	0.2	0.0	0.6	1.0	0.8	0.0	3.4	1.0	3.6	13.2	3.1	31.2	9.6	0.4	0.0	0.0	0.0	0.0	0.6	1.2	15.2	0.0		
B8m	500	58.8	69.19	30.81	7.55	0.2	0.0	0.6	1.0	0.8	0.0	3.4	1.0	3.6	13.2	3.1	31.2	9.6	0.4	0.0	0.0	0.0	0.0	0.6	1.2	15.2	0.0		
B8n	500	58.8	69.19	30.81	7.55	0.2	0.0	0.6	1.0	0.8	0.0	3.4	1.0	3.6	13.2	3.1	31.2	9.6	0.4	0.0	0.0	0.0	0.0	0.6	1.2	15.2	0.0		
B8o	500	58.8	69.19	30.81	7.55	0.2	0.0	0.6	1.0	0.8	0.0	3.4	1.0	3.6	13.2	3.1	31.2	9.6	0.4	0.0	0.0	0.0	0.0	0.6	1.2	15.2	0.0		
B8p	500	58.8	69.19	30.81	7.55	0.2	0.0	0.6	1.0	0.8	0.0	3.4	1.0	3.6	13.2	3.1	31.2	9.6	0.4	0.0	0.0	0.0	0.0	0.6	1.2	15.2	0.0		
B8q	500	58.8	69.19	30.81	7.55	0.2	0.0	0.6	1.0	0.8	0.0	3.4	1.0	3.6	13.2	3.1	31.2	9.6	0.4	0.0	0.0	0.0	0.0	0.6	1.2	15.2	0.0		
B8r	500	58.8	69.19	30.81	7.55	0.2	0.0	0.6	1.0	0.8	0.0	3.4	1.0	3.6	13.2	3.1	31.2	9.6	0.4	0.0	0.0	0.0	0.0	0.6	1.2	15.2	0.0		
B8s	500	58.8	69.19	30.81	7.55	0.2	0.0	0.6	1.0	0.8	0.0	3.4	1.0	3.6	13.2	3.1	31.2	9.6	0.4	0.0	0.0	0.0	0.0	0.6	1.2	15.2	0.0		
B8t	500	58.8	69.19	30.81	7.55	0.2	0.0	0.6	1.0	0.8	0.0	3.4	1.0	3.6	13.2	3.1	31.2	9.6	0.4	0.0	0.0	0.0	0.0	0.6	1.2	15.2	0.0		
B8u	500	58.8	69.19	30.81	7.55	0.2	0.0	0.6	1.0	0.8	0.0	3.4	1.0	3.6	13.2	3.1	31.2	9.6	0.4	0.0	0.0	0.0	0.0	0.6	1.2	15.2	0.0		
B8v	500	58.8	69.19	30.81	7.55	0.2	0.0	0.6	1.0	0.8	0.0	3																	

APPENDIX NO 5.2 Modal composition of sandstones

Samples number	a		b		c		Total sand-sized grains
	% of Quartz		% of Feldspar		% of Rock Fragment		
W4	67.4	97.4	0.8	1.2	1.0	1.4	69.2
B6a	55.4	97.5	0.6	1.1	0.8	1.4	56.8
B6b	69.2	97.2	1.2	1.7	0.8	1.1	71.2
T15A	60.6	99.7	0.0	0.0	0.2	0.3	60.8
T15B	70.0	99.4	0.2	0.3	0.2	0.3	70.4
F3	64.6	98.2	1.0	1.5	0.2	0.3	65.8
F4	70.0	98.6	0.8	1.1	0.2	0.3	71.0
F5a	48.8	97.6	1.2	2.4	0.0	0.0	50.0
F5a	62.0	98.4	0.8	1.3	0.2	0.3	63.0
F5b	40.0	98.04	0.8	1.96	0.0	0.0	40.8
F5b	45.2	96.17	1.2	2.55	0.6	1.28	47.0
F5D	61.4	96.54	1.8	2.83	0.4	0.63	63.6
S3a	29.6	99.3	0.2	0.7	0.0	0.0	29.8
S3a	52.4	98.13	1.0	1.87	0.0	0.0	53.4
S3c	68.2	96.3	1.6	2.3	1.0	1.4	70.8
S8	61.0	98.4	1.0	1.6	0.0	0.0	62.0
S14	66.0	98.8	0.6	0.9	0.2	0.3	66.8
S17	64.4	98.8	0.6	0.9	0.2	0.3	65.2
S18	68.2	98.0	1.0	1.4	0.4	0.6	96.2
S21a	63.2	97.5	1.4	2.2	0.2	0.3	64.8
S21b	64.4	97.9	1.0	1.5	0.4	0.6	65.8
S21c	61.2	97.5	1.2	1.9	0.4	0.6	62.8
S21d	71.2	97.8	0.6	0.8	1.0	1.4	72.8
S24	72.8	98.4	0.4	0.5	0.8	1.1	74.0
S24	71.8	98.4	0.6	0.8	0.6	0.8	73.0
S24	72.4	98.9	0.6	0.8	0.2	0.3	73.2
S24	74.8	97.7	1.0	1.3	0.8	1.0	76.6
S24	75.8	99.5	0.4	0.5	0.0	0.0	76.2
S27	74.8	98.94	0.4	0.53	0.4	0.53	76.6
S27d	74.8	98.16	0.8	1.05	0.6	0.79	76.2
West Side							
L3*	64.2	95.2	1.8	2.7	1.4	2.1	67.4
L3*	66.8	97.6	1.0	1.5	0.6	0.9	68.4
B7*	73.8	98.1	0.8	1.1	0.6	0.8	75.2
B7*	66.0	98.8	0.4	0.6	0.4	0.6	66.8
B7*	62.8	96.6	1.4	2.2	0.8	1.2	65.0
T3*	43.4	98.2	0.2	0.4	0.6	1.4	44.2
T6a*	71.2	98.6	0.6	0.8	0.4	0.6	72.2
T6b*	71.2	97.0	1.0	1.4	1.2	1.6	73.4
T7c*	63.6	96.95	0.8	1.22	1.2	1.83	65.6
T8a*	71.6	98.3	0.4	0.6	0.8	1.1	72.8
T8c*	70.8	98.9	0.4	0.5	0.4	0.6	71.6
T8d*	66.4	99.4	0.2	0.3	0.2	0.3	66.8
Mean:	64.25		0.81		0.5		
St dev:	10.1		0.43		0.37		

The two figures in each column a, b and c refer to first, the proportion of the component as a percentage of the whole rock and, second the proportion of the component as a percentage of the sand-sized grains.

APPENDIX NO 5.3 Number of units and types of contacts in  
polycrystalline grains (Followed Basu, et al, 1975)

Samples number	No of quartz crystal unit in polycrystalline		Type of contact		
	2-3	>3	Straight	Straight- to-suture	Suture
W4	5	5	0	5	5
B6a	2	8	3	6	1
B6b	9	5	0	6	8
T15a	9	3	2	4	6
T15b	7	3	3	6	1
F3	11	6	3	6	8
F4	11	19	8	13	9
F5a	5	6	3	3	5
F5a	9	11	1	9	10
F5b	3	9	2	5	6
F5b	2	14	0	7	9
F5d	1	26	2	13	22
S3a	1	5	1	3	2
S3a	2	4	1	2	3
S3b	9	17	2	12	12
S8	7	11	3	5	10
S14	12	5	2	10	5
S17	10	8	5	6	7
S18	22	9	12	12	7
S21a	22	13	6	18	11
S21b	14	20	3	9	22
S21c	6	16	3	10	9
S21d	12	19	4	13	14
S24	12	22	1	14	19
S24	21	8	4	16	9
S24	12	10	6	7	9
S24	22	8	4	14	11
S24	10	30	5	19	16
S27	20	7	4	14	9
S27a	9	23	3	15	14
L3*	6	17	0	9	14
L3*	9	16	4	5	16
B7*	13	43	6	18	32
B7*	12	27	8	9	22
B7*	9	28	5	11	21
B7*	7	35	2	19	20
T3*	7	20	5	10	12
T6a*	19	12	7	11	13
T6b*	8	15	0	7	16
T7c*	12	12	2	9	13
T8a*	19	11	5	12	13
T8c*	26	23	15	24	11

Note \* = West side

APPENDIX NO 5.4 Details of quartz and other components of petrographic analysis.

KEY

MQ = Monocrystalline quartz  
 NU = Non-undulatory  
 U = Undulatory  
 Poly = Polycrystalline  
 CL = Clay  
 IO = Iron-oxide  
 C = Carbonate  
 TQ = Total quartz

Samples number	% of MQ	% of NU in MQ	% of U in MQ	% of U in TQ	% of Poly in TQ	% of CL + IO	% of C	Size in phi
W4	65.4	32.7	67.3	65.3	2.97	7.8	2.2	3.198
B6a	53.2	25.6	74.4	71.5	3.97	15.8	16.4	3.288
B6b	66.4	35.8	64.2	61.6	4.05	14.8	8.2	3.099
T15a	58.2	23.02	76.98	73.9	3.96	18.8	0.8	2.879
T15b	68.0	31.2	68.8	66.9	2.86	15.4	0.4	3.099
F3	60.8	23.4	76.6	70.3	52.6	11.0	0.8	2.656
F4	64.0	27.8	72.2	66.0	8.57	8.8	4.2	1.877
F5a	46.6	25.3	74.7	71.3	4.51	22.0	7.4	3.029
F5a	58.0	31.4	68.6	64.2	6.45	10.6	1.0	2.689
F5b	37.6	34.04	65.96	62.0	6.0	7.4	38.8	2.554
F5b	42.0	26.7	73.3	71.7	7.08	7.2	40.2	2.611
F5e	54.0	35.9	64.1	56.4	12.05	23.8	0.2	2.530
S3a	28.4	24.7	75.3	72.3	4.05	12.8	47.2	3.448
S3a	51.2	26.6	73.4	68.1	2.29	21.8	9.2	3.562
S3d	62.8	31.2	68.8	63.3	7.92	13.2	0.0	2.891
S8	47.83	28.2	71.8	67.5	5.9	14.33	30.83	2.933
S14	62.6	33.9	66.1	62.7	5.15	7.6	1.8	2.503
S17	60.8	23.4	76.6	72.4	5.59	14.2	0.0	2.476
S18	62.0	27.7	72.3	65.7	9.09	11.2	0.0	2.296
S21a	56.2	30.2	69.8	62.02	11.08	16.4	0.0	1.994
S21b	57.6	31.2	68.8	61.5	10.56	12.6	0.0	2.124
S21C	56.8	25.0	75.0	69.6	7.19	21.2	0.0	2.181
S21d	65.0	27.4	72.6	66.3	8.71	10.0	0.0	2.395
S24	66.0	35.4	64.6	58.5	9.34	4.8	0.0	2.244
S24	66.0	26.7	73.3	67.4	8.08	4.6	0.0	2.485
S24	68.0	29.1	70.9	66.6	6.08	3.2	0.0	2.295
S24	69.0	31.9	68.1	62.8	7.75	11.2	0.0	2.247
S24	67.8	32.7	67.3	60.2	10.55	4.8	0.0	2.166
S27	69.4	25.7	74.3	69.0	7.22	4.6	0.6	2.145
S27a	68.4	33.04	66.96	61.2	8.56	1.8	0.2	2.154
L3*	59.6	36.4	63.6	58.9	7.17	18.2	0.0	3.21
L3*	61.8	23.9	76.1	70.4	7.49	6.8	17.0	2.879
B7*	62.8	28.4	71.6	60.7	15.18	4.8	8.2	2.070
B7*	58.2	27.2	72.8	64.2	11.82	1.4	27.2	2.031
B7*	61.8	29.8	70.2	62.7	10.69	12.2	2.6	2.247
B7*	54.4	32.0	68.0	58.9	13.37	13.0	13.8	2.145
T3*	38.0	29.5	70.5	61.8	12.44	25.2	26.6	2.657
T6a*	65.0	29.2	70.8	64.6	8.71	5.0	7.0	2.599
T6b*	66.6	33.0	67.0	62.6	6.46	10.0	0.0	2.84
T7c*	58.8	30.6	69.4	64.2	7.55	18.8	1.0	2.927
T8a*	56.6	35.1	64.9	59.5	8.38	14.0	2.8	2.747
T8b*	65.2	31.6	68.4	63.0	7.91	6.2	16.0	2.759
T8d*	56.6	27.2	72.8	62.1	14.76	7.6	25.0	2.262

Note \* = West-side

Appendix 5.5 Separation of clay fraction from the whole rock

Unweathered parts of the samples (approximately 300 g) were chosen and any visible weathering and secondary effects were removed using the 6 inch diamond wheel. The material was crushed to chips (1-2 cm) and washed by distilled water, dried, then ground in a Teema Mill for one minute. Further disaggregation was obtained by placing the powder/water mixture in ultrasonic bath for 10 minutes. The slurry was then transferred to a water-filled glass test tube and shaken well to ensure thorough mixing. Samples were centrifuged for 40 seconds at a speed setting of 5, and the suspension transferred into other clean test tubes, again centrifuged for 40 seconds at a setting of 7. This time the suspension was removed and the settled fraction is the required clay fraction (2-6  $\mu\text{m}$ ) for XRD analysis.

Appendix 5.6 Instrumental condition of XRD for clay mineral determination

Source Cu K ( $\alpha$ ): normal focus: Ni filter

Chart speed: 1200 mm/h

Angular goniometer speed:  $1^{\circ}$ /min

Scan: 3-35  $^{\circ}$  2 $\theta$

Time constant: 2S: Z = 3

36 KV, 18mA

Glycolated and Heated specimens

The samples were treated with ethylene glycol for one hour, and heated up to 600  $^{\circ}$ C for one hour.

HCl treatment

Approximately 10 g of the powdered sample were mixed with 20 ml of HCl (18%), thoroughly mixed and heated up to 80  $^{\circ}$ C for 8 hours. The sample was then washed and transferred to a water filled 50 ml test tube, shaken well and left for 30 minutes. The uppermost sedimented layer was then mounted on a glass slide for XRD run.

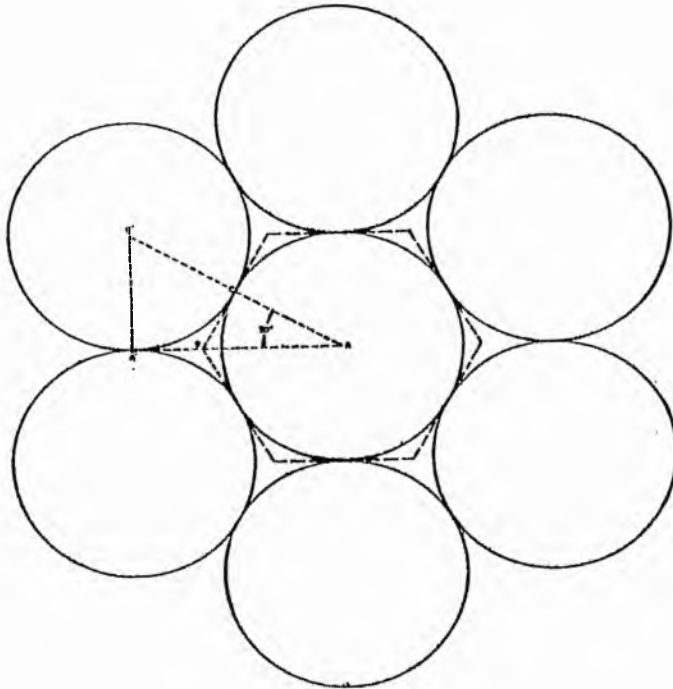
APPENDIX NO 6.1 Textural Parameters:-

Sample number	Mean M ( $\phi$ )	Inclusive St dev	Graphic WS	Inclusive Graphic Skewness SK	Graphic Kurtosis KG
W4	3.198 VF	0.366 WS		-0.078	0.881
B6a	3.288 VF	0.379 WS		0.033	0.951
B6b	3.099 VF	0.375 WS		-0.015	0.950
T15	2.879 F	0.421 WS		0.030	0.964
T15	3.099 VF	0.459 WS		0.022	0.921
F3	2.656 F	0.388 WS		0.130	1.247
F4	1.877 M	0.560 MWS		0.155	1.185
F5a	3.029 VF	0.413 WS		0.132	1.046
F5a	2.689 F	0.365 WS		0.224	1.180
F5b	2.554 F	0.410 WS		0.118	0.962
F5b	2.601 F	0.391 WS		-0.145	0.919
F5c	2.530 F	0.450 WS		0.097	0.974
S3a	3.448 VF	0.370 WS		-0.095	0.979
S3a	3.562 VF	0.326 VWS		-0.034	1.247
S3b	2.891 F	0.348 VWS		0.074	1.078
S8	2.933 F	0.456 WS		0.079	1.040
S14	2.503 F	0.349 VWS		-0.043	1.009
S17	2.476 F	0.404 WS		0.087	0.914
S18	2.296 F	0.390 WS		0.073	0.993
S21a	1.994 M	0.429 WS		0.145	1.039
S21b	2.124 F	0.324 VWS		0.164	1.014
S21c	2.181 F	0.442 WS		0.151	1.213
S21d	2.395 F	0.335 VWS		0.140	0.902
S24	2.244 F	0.496 WS		0.126	0.976
S24	2.085 F	0.512 MWS		0.048	1.055
S24	2.295 F	0.453 WS		0.208	0.998
S24	2.247 F	0.635 MWS		0.215	0.955
S24	2.166 F	0.484 WS		0.119	0.952
S27	2.145 F	0.470 WS		0.201	1.064
S27a	2.154 F	0.448 WS		0.087	1.096
L3	3.21 VF	0.357 WS		-0.032	0.944
L3	2.879 F	0.365 WS		0.068	1.146
B7	2.070 F	0.378 WS		0.309	1.248
B7	2.031 F	0.354 WS		0.073	1.221
B7	2.247 F	0.476 WS		0.238	0.917
B7	2.145 F	0.427 WS		0.224	0.986
T3	2.657 F	0.427 WS		-0.149	1.112
T6a	2.599 F	0.363 WS		0.061	1.110
T6b	2.84 F	0.376 WS		0.222	1.194
T7	2.927 F	0.377 WS		0.054	1.058
T8a	2.747 F	0.43 WS		0.009	1.161
T8b	2.759 F	0.436 WS		-0.058	1.054
T8d	2.262 F	0.476 WS		0.113	1.138

Note:-

- V F = Very Fine Sand
- F = Fine Sand
- M = Medium Sand
- V W S = Very Well-Sorted
- W S = Well-Sorted
- M W S = Moderately Well-Sorted

APPENDIX No 6.2



Spheres and associated pore space in orthorhombic packing, rotated 30°.

$$\text{Original porosity (\%)} = \frac{\text{Vol of hexagonal prism} - \text{Vol of Sphere}}{\text{Vol of hexagonal prism}} \times 100$$

$$\text{The volume of sphere} = \frac{4}{3} \pi r^3$$

$$\text{The volume of hexagonal prism} = \text{Area of the hexagon} \times 2r$$

$$\text{The hexagon area} = 12 \times \text{area of triangle (ABC)}$$

$$\text{area triangle} = \text{ABC} = \frac{\text{BC} \times \text{AC}}{2}$$

$$\text{AC} = r$$

$$\text{BC} = \text{AC} \tan 30$$

Calculation of original porosity, after Rittenhouse (1971)



APPENDIX No 6.3 Values Of Grain-To-Grain Contact

Sample number	Depth in meter from the top of Hosie Lst	Percent of the type contact				No of Contact			
		linear	Sutured	Tangential	Concovo-convex	linear	Sutured	Tangential	Concovo-convex
S27	1.70	28.96	2.76	44.14	24.14	42	4	64	35
S24	5.905	31.11	3.7	47.41	17.78	42	5	64	24
S24	6.505	33.3	5.8	44.17	16.67	40	7	53	20
S21C	9.835	35.54	4.13	47.11	13.22	43	5	57	16
S18	16.585	37.59	2.26	45.86	14.29	50	3	61	19
S8	28.600	39.5	4.7	44.2	11.6	17	2	19	5
S3a	62.500	35.71	10.71	26.79	26.79	20	6	15	15
F5b	79.040	41.46	4.88	29.27	24.39	17	2	12	10
F5a	83.460	43.67	4.43	29.75	22.15	69	7	47	35
F4	86.570	39.33	5.62	29.78	25.28	70	10	53	45
T15	108.550	42.55	6.38	28.37	22.70	60	9	40	32

APPENDIX NO 6.4 Variation Of Reservoir Qualities And Cementation:-

No of Samples	Porosity percent from Core-Samples	Permeability percent (Millidarcys)	Percent of Carbonate Cement (thin-section)
T15	22.05	171.04	0.4
F4	24.295	72.30	4.2
F5a	25.0	509.55	1.0
F5b	6.97	<0.5	40.2
S3a	8.58	<0.5	9.2
S8	4.62	<0.5	30.83
S18	27.605	924.9	0.0
S21C	21.985	878.95	0.0
S24	26.775	1245.05	0.0
S24	25.165	249.3	0.0
S27	29.33	393.8	0.2
T7	21.57	4.997	1.0

APPENDIX NO 6.5 Correlation between the Cumulative Percent Pore Space with ideal pore diameter in ( $\mu\text{m}$ ).

Data obtained from the curves.

Pore diameter in $\mu\text{m}$	Cumulative Percent Pore Space of Samples No																		
	T8d Group A			S3a			F5b			T7* Group B		S24		F5a Group C		S21 C		S27	
0.018	0.0		0.0		0.0		0.0		0.0		0.0		0.0		0.0		0.0		0.0
		=85.5		=88.0		=89.0		=41.0		=22.0		=15.0		=14.0					= 7.5
1.0	85.5		88.0		89.0		41.0		22.0		15.0		14.0		7.5				
		=11.7		=9.6		=9.7		=57.0		=73.05		=28.0		=16.0					=15.5
15.0	97.2		97.6		98.7		98.0		95.05		43.0		30.0		23.0				
		=2.1		=2.0		=1.2		=1.9		=4.85		=56.8		=69.6					=63.5
50.0	99.3		99.6		99.9		99.9		99.9		99.8		99.6		86.5				
		=0.7		=0.4		=0.1		=0.1		=0.1		=0.2		=0.4					=13.5
59.0	100.		100.		100.		100.		100.		100.		100.		100.				

APPENDIX NO 6.6 Comparison Between Microporosity Percentages And  
The Main Petrographic Variables.

	No Of Sample	% Of Microporosity	% Of Carbonate	% Of Clay	Mean in $\phi$	Median of pore size in $\mu\text{m}$	Sorting
A	T8	85.5	25.0	0.8	2.262	0.9	0.476
	S3a	88.0	9.2	21.6	3.562	0.8	0.326
	F5b	89.0	40.2	5.0	2.611	0.7	0.391
B	T7	41.0	1.0	13.2	2.927	3.2	0.377
	S24	22.0	0.0	2.6	2.295	6.3	0.453
C	F5a	15.0	0.0	9.4	2.689	19.3	0.365
	S21	14.0	0.0	19.8	2.181	24.7	0.442
	S27	7.5	0.2	0.8	2.154	29.8	0.448

APPENDIX NO 6.7 Summary of two highest percent microporosity samples contain.

No Of Samples	Percent of micro-porosity less than 1.0 Um diameter	Percent of micro-porosity less than 0.5 Um diameter	Percent of micro-porosity	Mercury injection break through	Percent of porosity	Percent of Permeability	Median of Pore size	Grain size in $\phi$	Percent of clay material	Percent of Carbonate Cement
F5b	89	66	89	1.8	6.97	>0.5	0.9	2.611	5.0	40.2
S3a	88	66	88	1.7	5.58	>0.5	0.85	3.562	21.6	9.2

APPENDIX NO 6.8 CLASSIFICATION OF MICROPOROSITY IN ST MONANCE SANDSTONES

Current classification schemes of microporosity have proved inadequate for use with the St Monance Sandstones. I have therefore, devised a comprehensive system to cope with the variety of styles found in these sandstones.

A principal element of the proposed classification is the characterisation of a given pore by such attributes as size, shape, genesis, and position or association relative to either particular constituents or overall fabric.

Thirteen basic types of microporosity are recognized. They are listed in the summary chart of Fig 6.1, and they are illustrated in Figs 6.2 to 6.18.

1 Spaces between grain surface and carbonate cement.

Where the contacts do not fit perfectly, there are three types of microporosity.

a - Smooth contact (Fig 6.2)

b - One irregular (mostly carbonate), while the other is smooth (Fig 6.3)

c - Zig-zag in shape of lamella pore (Fig 6.4).

2 Lamella pores along cleavage planes.

The dominant carbonate cement is calcite in these samples, and they have three sets of cleavage, which has formed planes of weakness along which microporosity has formed (Fig 6.5).

### Basic Microporosity Types

#### Due to carbonate cement

- 1 Spaces between grain and cement
  - a - Smooth space (SS)
  - b - One side smooth only (OSS)
  - c - Zig-zag spaces (ZZS)
- 2 Lamella along cleavage LC
- 3 Fracture and dissolution FD
- 4 Irregular cracks IC
- 5 Pitted P
- 6 Channel C

#### Due to other constituents

- 7 Lamella between bent mica and quartz overgrowth. MQ
- 8 Along mica cleavage MC
- 9 Lamella quartz overgrowth LQO
- 10 Feldspar alteration and Fracture FF
- 11 Network N
- 12 Within and between clay particles WCP
- 13 Internal spaces in polycrystalline quartz IP

Fig 6.1 Microporosity in St Monance Sandstones.

Fig 6.2 SEM photograph showing the smooth contact between quartz grain and carbonate cement, classification: Smooth space - primary microporosity. (SS Pr). Sandstone Unit (T8d) - West side. Scale bar equals 20  $\mu$ .

Fig 6.3 SEM photograph showing irregular (arrow) contact of carbonate cement with quartz grain. Classification: One side smooth-compound primary and secondary microporosity (Oss-Pr-Se). Sandstone Unit (F5b) - East side. Scale bar equals 20  $\mu$ .



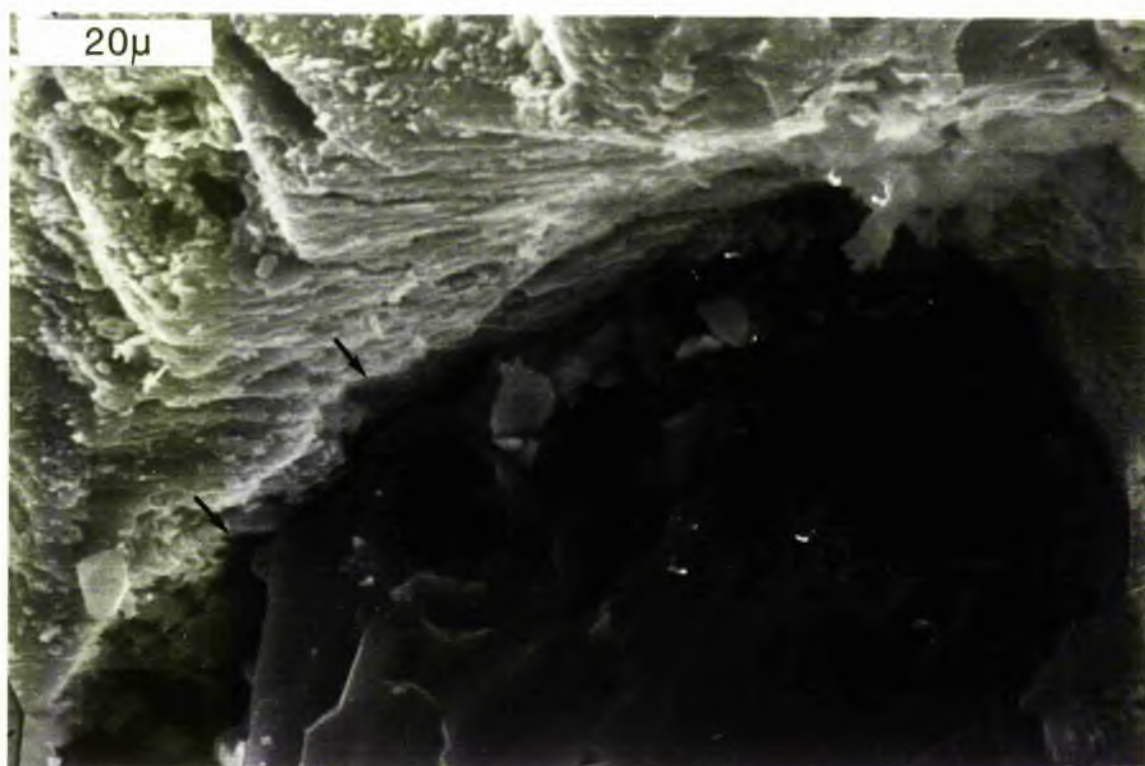
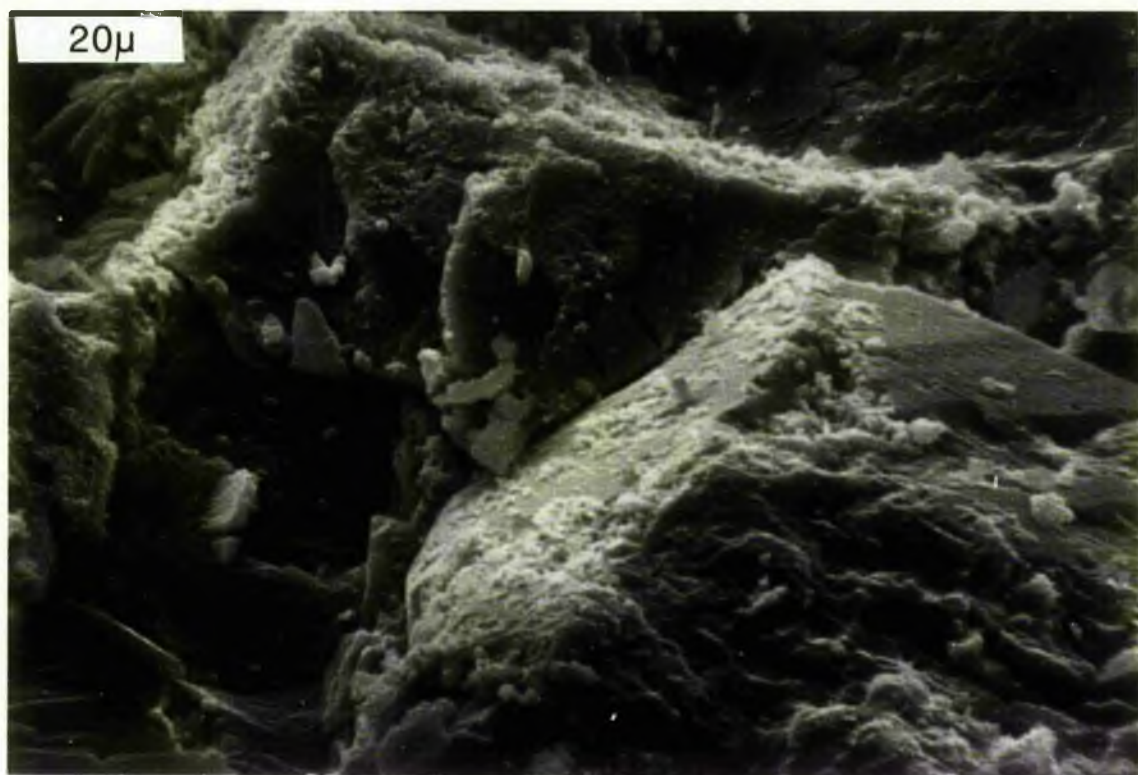
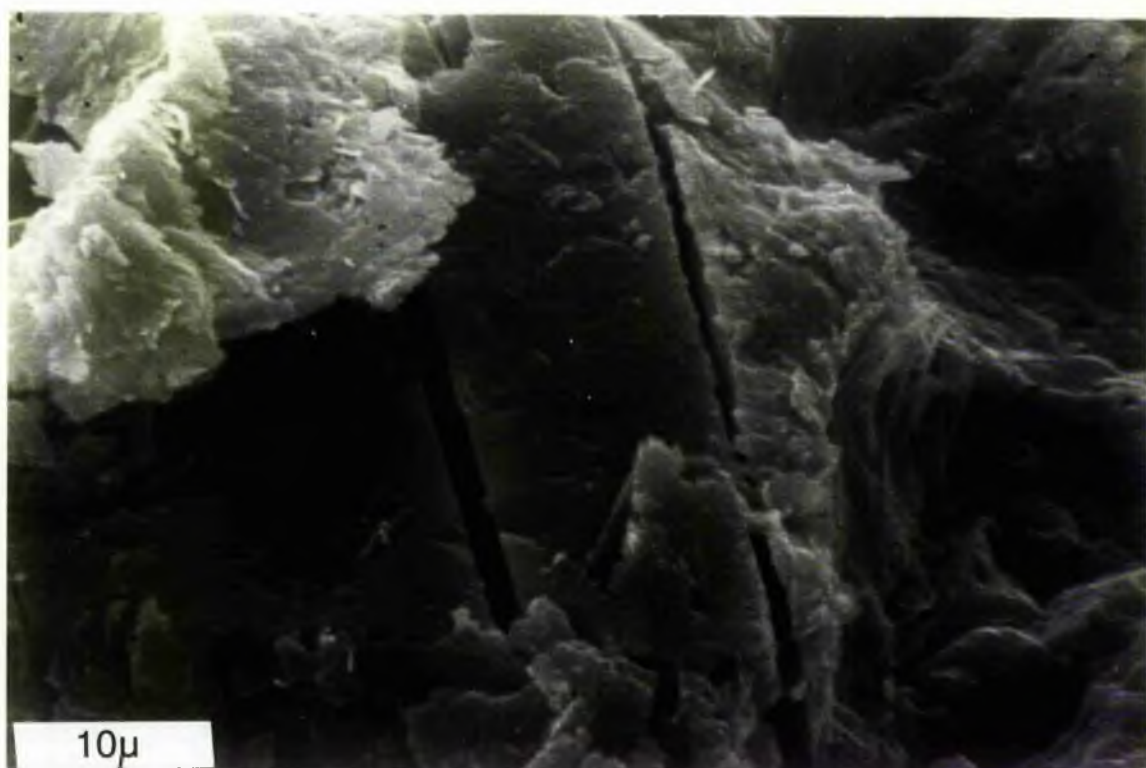
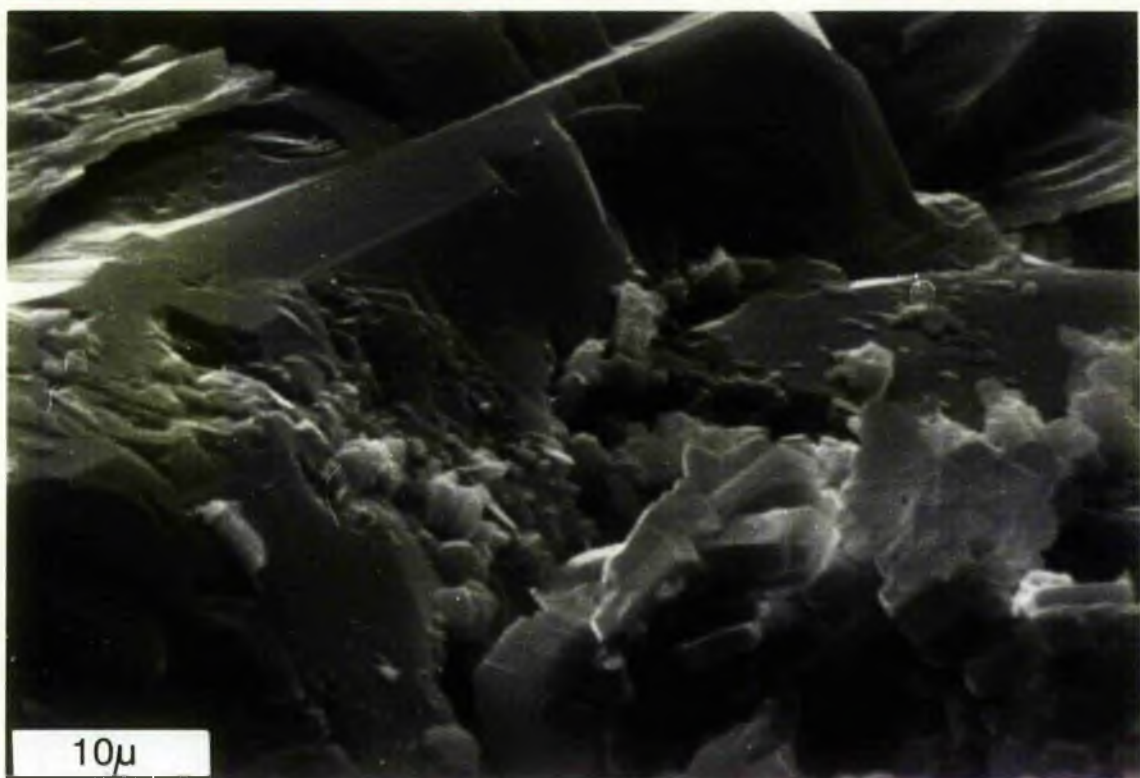


Fig 6.4 SEM photograph showing the irregular pore formed by replacement the edge of quartz by carbonate and then dissolution of some of the carbonate. Classification: Zig-zag spaces - Secondary microporosity (ZZ -Se). Sandstone Unit (F5b) - East side. Scale bar equals 10  $\mu$ .

Fig 6.5 SEM photograph showing lamella microporosity along cleavage plane of carbonate crystal. Classification: Lamella along cleavage - Primary formation (Lo-Pr). Sandstone Unit (F5b) - East side. Scale bar equals 10  $\mu$ .



### 3 Fracturing and dissolution.

Slight fracturing followed by some dissolution along the cleavage planes forming irregular more or less lamella micropores (Fig 6.6).

### 4 Irregular cracks.

Any mechanical deformation of calcite crystals, leads to the formation of three different directions of cracks through the crystals as microporosity (Fig 6.7).

### 5 Pitted micropores.

Pits formed when the detrital grains were corroded chemically (Figs 6.8, 6.9, 6.10). The pits may have been left unfilled by carbonate cement which subsequently dissolved leaving the micropores.

### 6 Channel micropores.

The intercalations between quartz grains and carbonate cement in forming micropores as channel in morphology. It contains two or more basic types of microporosity, which is composed of interconnected between intraparticles (such as cracks of calcite crystal ..... etc), and interparticles microporosity (as spaces between quartz grains and carbonate cement). Their connection leads to form channel, originated as compound (primary and secondary formed) (Fig 6.11).

Microporosity has formed with other types of material.

Fig 6.6 SEM photograph showing fracture of calcite crystal followed by dissolution, left side arrow indicates fracture, while right side arrows indicate some dissolution. Classification: Fracture and Dissolution - Secondary fracture (FD-Se). Sandstone Unit (F5b) - East Side. Scale bar equals 10  $\mu$ .

Fig 6.7 SEM photograph showing three different direction of cracks (arrow) through calcite crystal. Classification: Irregular cracks - Secondary formation (Ic-Se). Sandstone Unit (Fb5) - East side. Scale bar equals 10  $\mu$ .

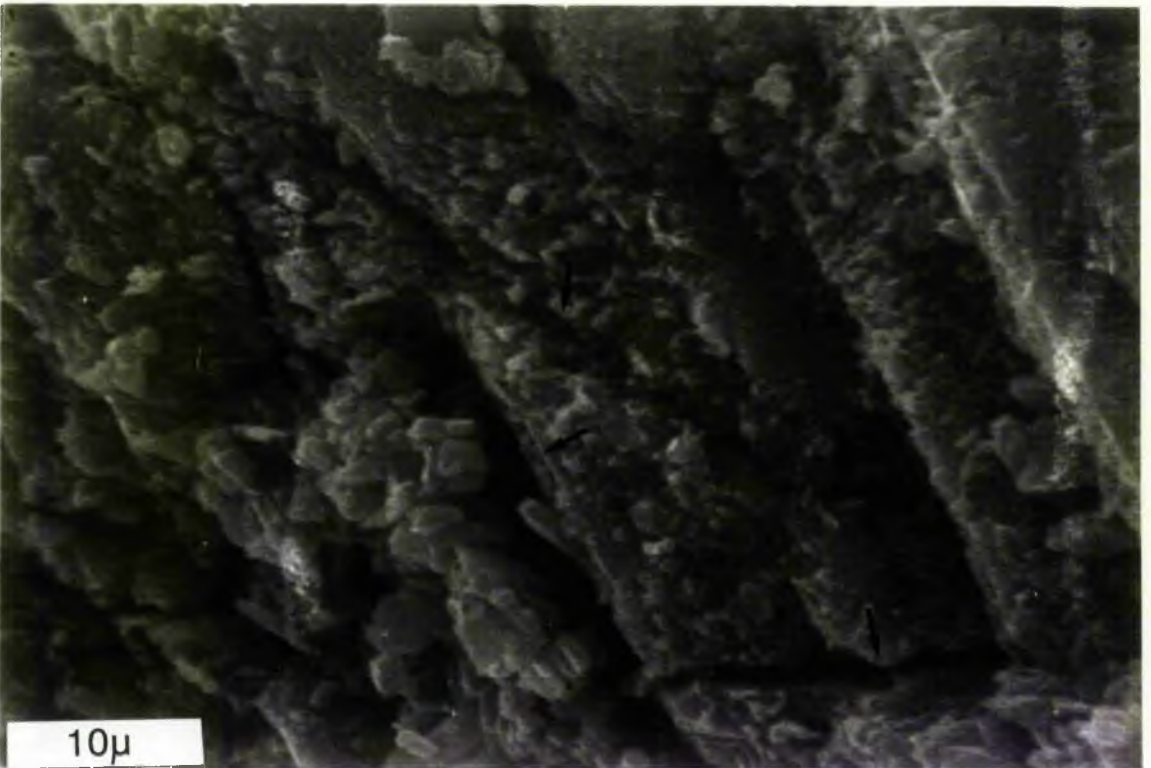
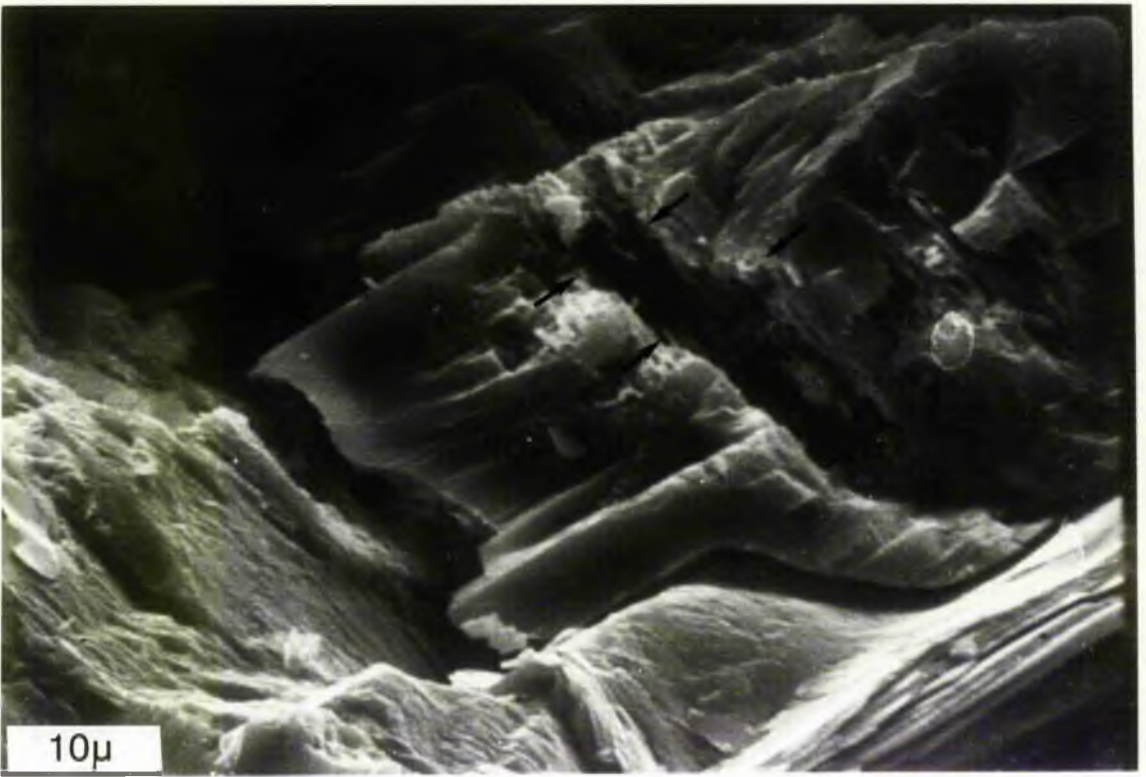


Fig 6.8 SEM photograph showing pitted or corroded detrital quartz grain by carbonate which was then dissolved to leave the micropores. Classification: Pitted micropores - Secondary formation (P-Se). Sandstone Unit (T7) - West side. Scale bar equals 10  $\mu$ .

Fig 6.9 SEM photograph showing corrosion of two quartz grains overgrowth, and formation of micropores while the contact between the two grains forms lamella micropore. ( $\rightarrow \leftarrow$ ). Quartz grain on the right side contains conchoidal fracture ( $\leftarrow$ ). Classification: Pitted micropore - Secondary formation (P-Se). Sandstone Unit (S24) - East Side. Scale bar equals 20  $\mu$ .

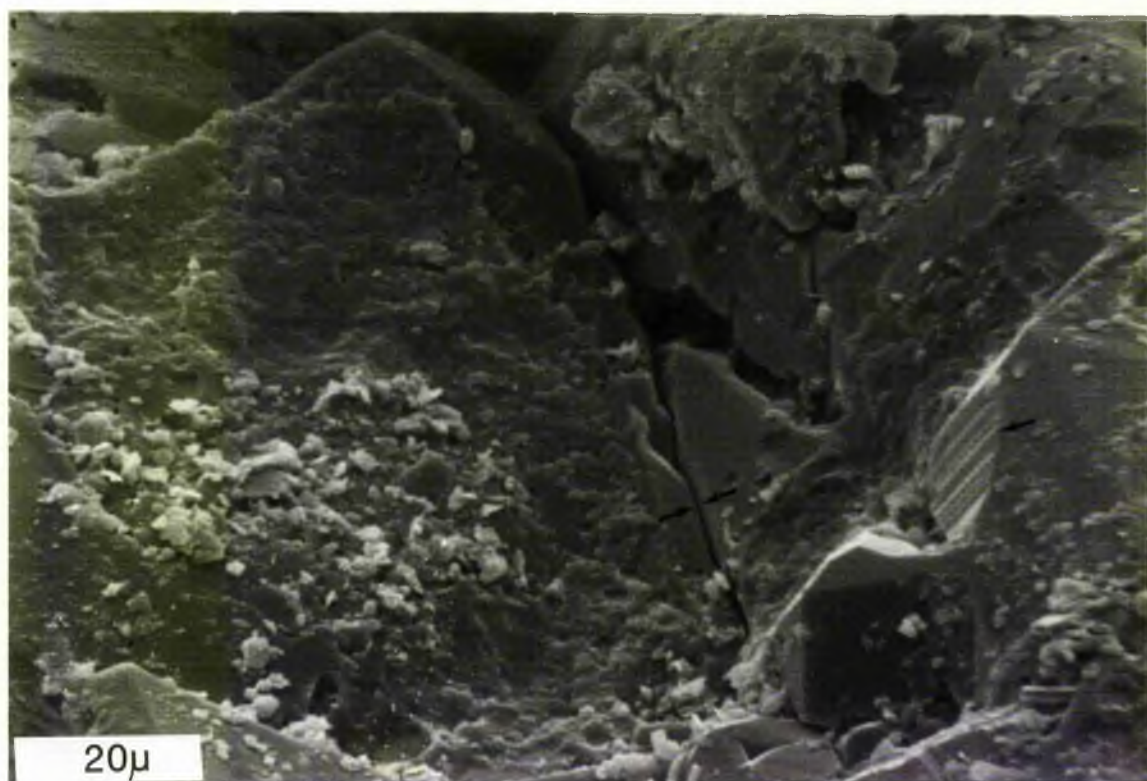
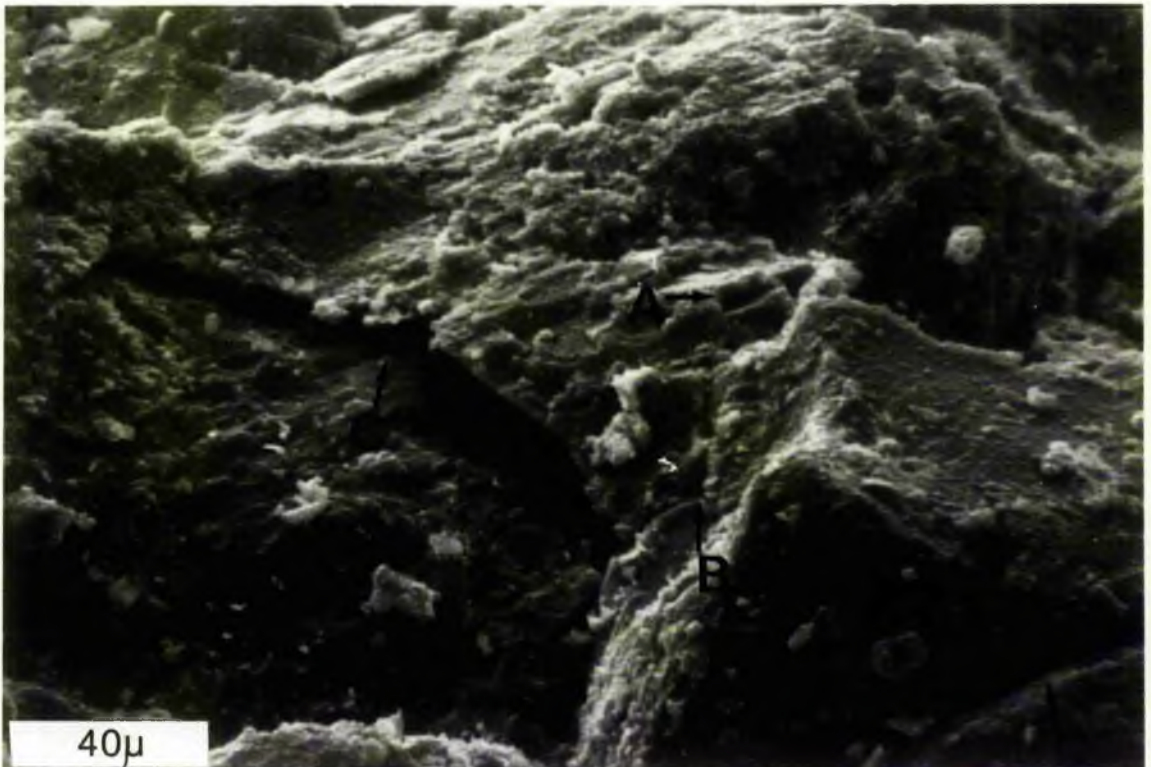
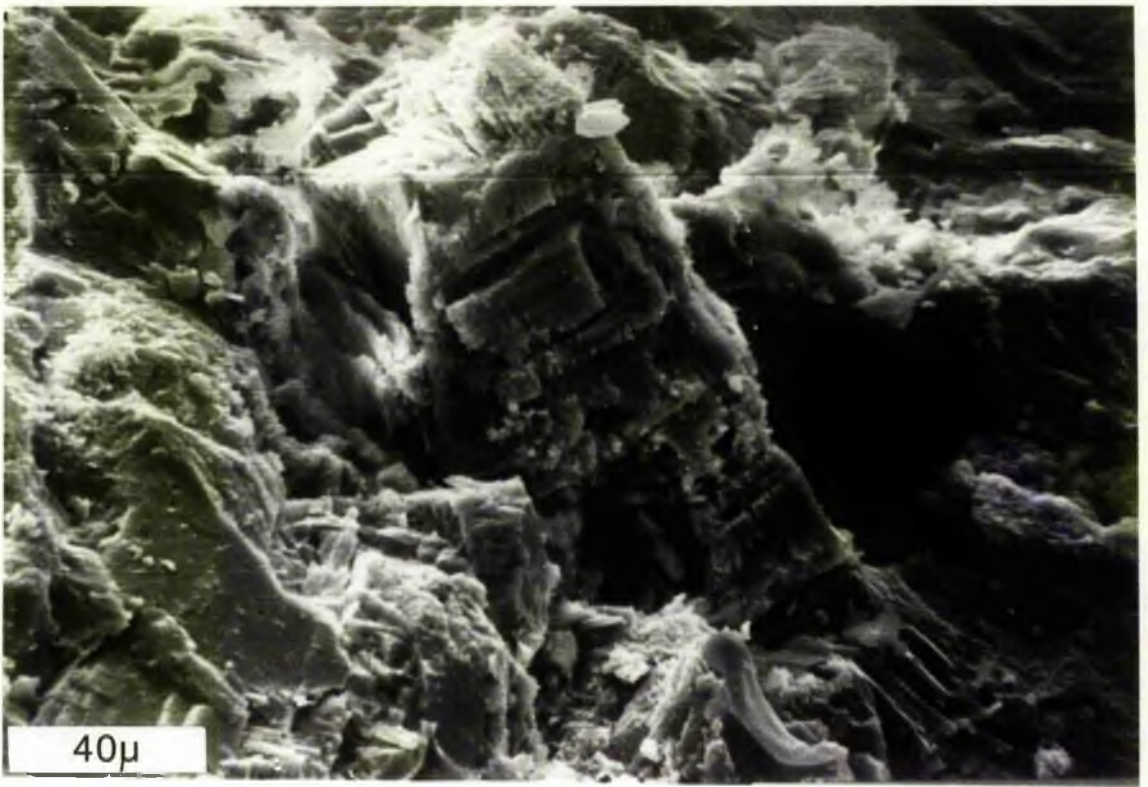




Fig 6.10 SEM photograph showing feldspar grain corroded to form micropores. Classification: Pitted micropores-Secondary formation (P-Se). Sandstone Unit (S3a') - East side. Scale bar equals 40  $\mu$ .

Fig 6.11 SEM photograph showing micropores formed by interconnection of more than two basic types. Pitted micropores as (arrow A), cracks in carbonate cement as (arrow B), and the micropores between the contacts between the quartz grains and carbonate cement as (arrow C). All of them are more or less connected together to form channel morphology. Classification: Channel micropore - Primary and Secondary formation (C-Pr-Se): Upper part of sandstone Unit (T8d) - West side. Scale bar equals 40  $\mu$ .



7 Lamella pores between mica and quartz overgrowth.

This micropore is primary. Originally the contact between the two types of constituent did not fit completely, left a lamella space (Fig 6.12).

8 Along mica cleavages.

Micropores develop along mica cleavage due to splitting and alteration along cleavages (Fig 6.13).

9 Lamella pores between quartz overgrowths.

If the silica cement does not completely fill the space between any two of quartz grains, a space is left as a micropore; (Fig 6.14).

10 Feldspar alteration and fracture.

Micropores develop by splitting along cleavage planes in feldspar or most often by alteration and dissolution along cleavage planes (Fig 6.15).

11 Network (Honeycomb) microporosity.

Sometimes the clay fills the pore with a honeycomb pattern (Fig 6.16), also shows a fine network of illite threads.

12 Microporosity within and between clay particles.

Kaolinite fills the pore and develop a lot of microporosity in between (Figs 6.17 A, B).

13 Internal spaces in polycrystalline quartz.

Fig 6.12 SEM photograph showing mica, fractured and slightly bent around quartz grain with micropore in between. Classification: Lamella between mica and quartz grain - Primary formation (MQ-Pe). Sandstone Unit (S3a') - East side. Scale bar equals 20  $\mu$ .

Fig 6.13 SEM photograph showing mica grain splitting (a) and alteration (b) along the cleavage lead to form micropore. Classification: Along mica cleavage - Secondary formation (MC-Se). Sandstone Unit (S24) - East side. Scale bar equals 10  $\mu$ .

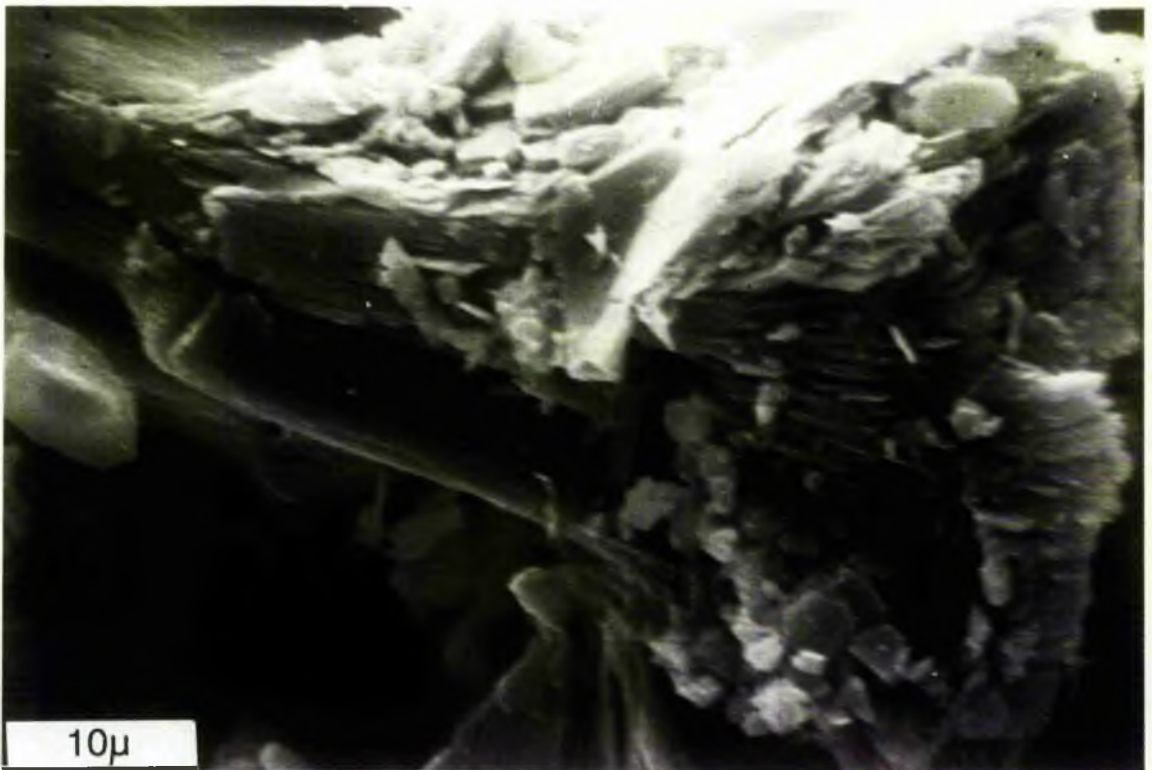
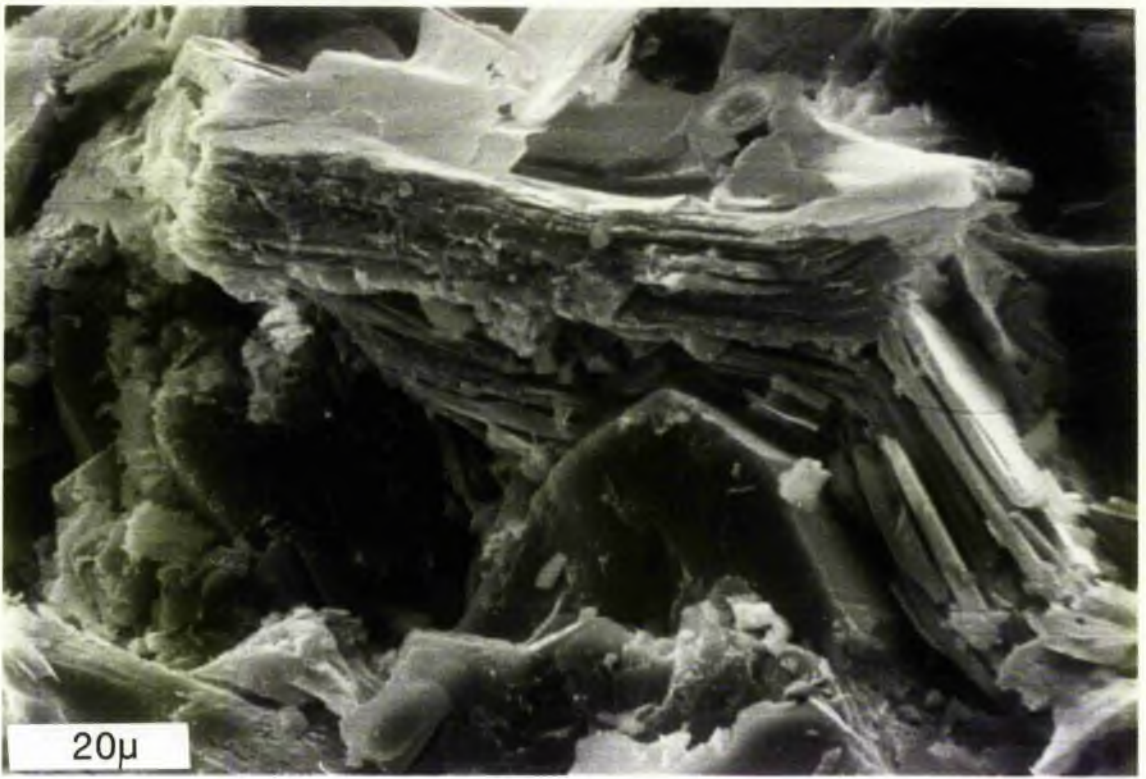


Fig 6.14 SEM photograph showing two quartz grains with overgrowth

contains lamella microporosity between them. Classification:

Lamella quartz overgrowth - Secondary formation (LQO-Se) Middle part of sandstone Unit (L3) - West side. Arrow = lamella micro-

porosity; Q = quartz grain with overgrowth. Scale bar equals 4  $\mu$ .

Fig 6.15 SEM photograph showing micropores formed along the cleavage

by splitting, alteration and pitting of feldspar grain. Classification:

Pitted grain - Secondary formation (PD-Se). Sandstone Unit

(S3a') - East side. Scale bar equals 20  $\mu$ .

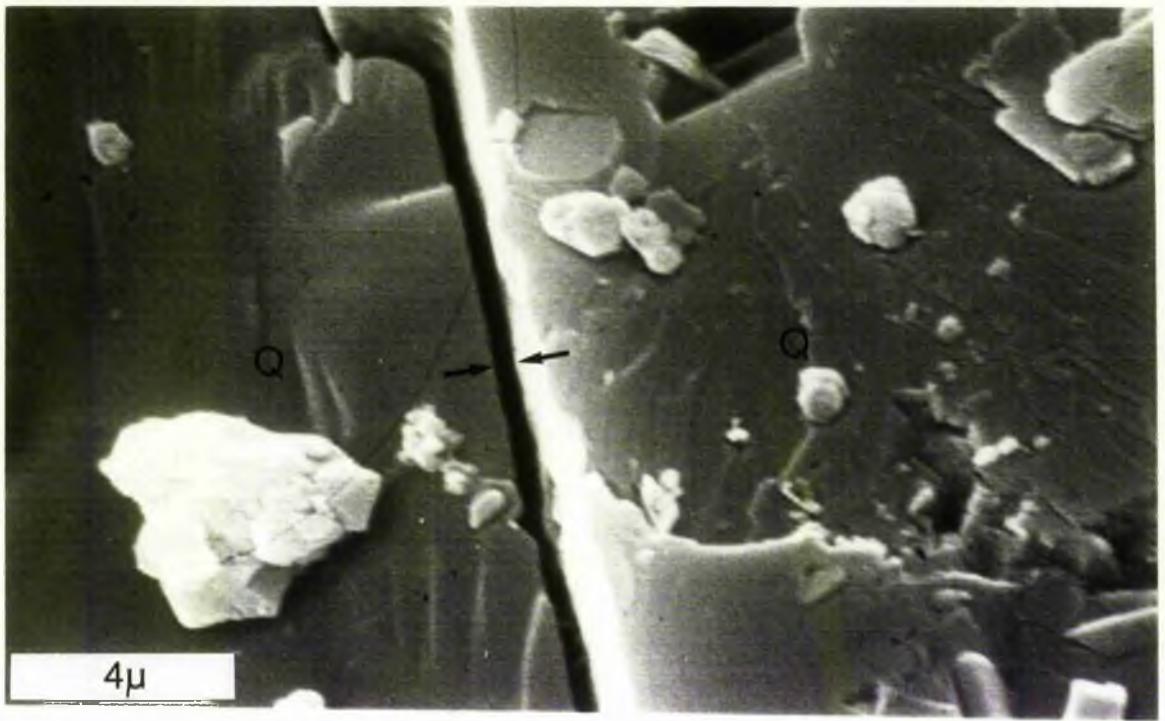


Fig 6.16 SEM photograph showing network pattern of micropore in  
between clay materials. Right side illite network. Classification:  
Network - Secondary formation (H-Se). Sandstone Unit (T8d) -  
West side. Scale bar equals 10  $\mu$ .



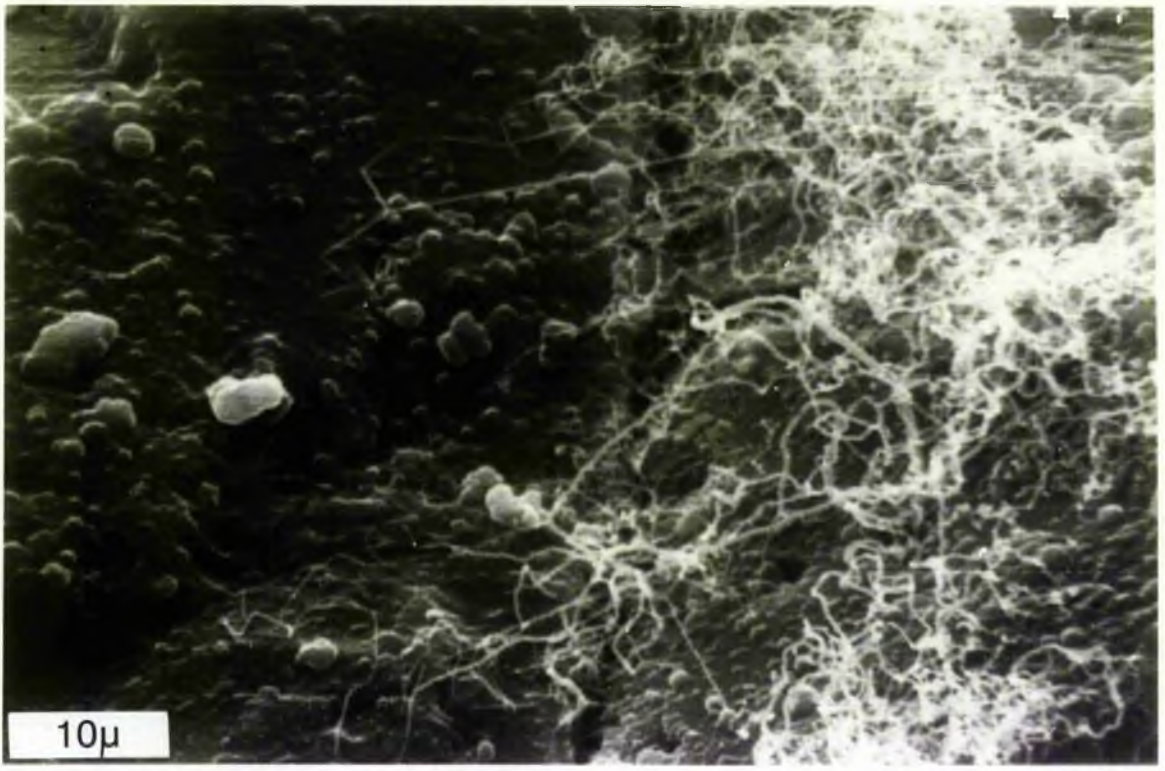
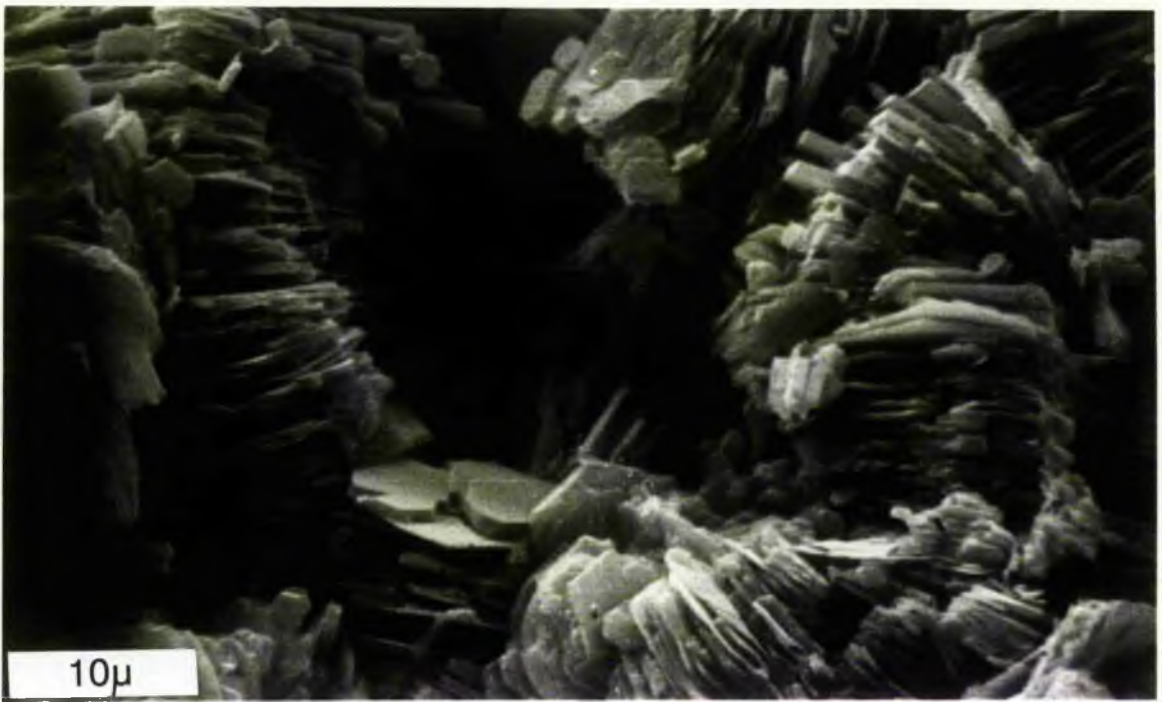


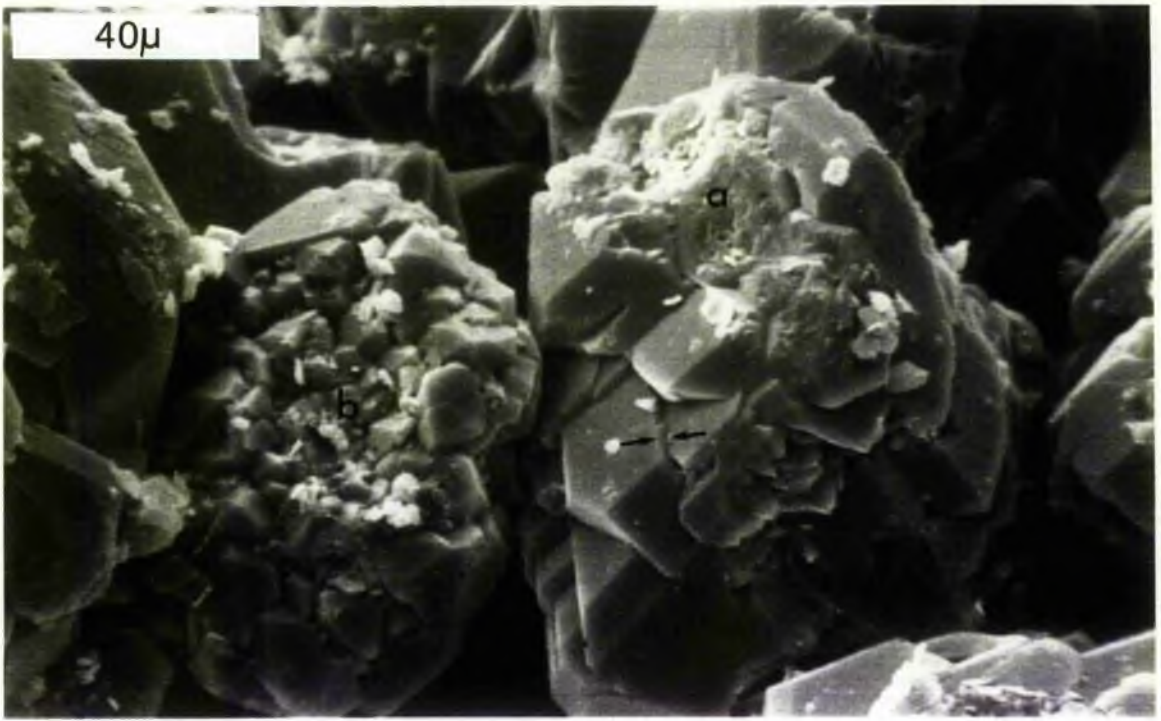
Fig 6.17A SEM photograph showing micropores between kaolinite particles partly filling a pore. Classification: Within and in between clay particles - Primary and Secondary formation (WCP-Pr-Se). Upper part of sandstone Unit (B7) - West side. Scale bar equals 10  $\mu$ .

Fig 6.17B SEM photograph showing vermicular authigenic kaolinite forming a crystal aggregate that make up a spiral shape formed by free growth in pores; micropores within and in between the particles. Classification: Within and in between clay particles - Primary and Secondary formation (WCP-Pr-Se). Sandstone Unit (T3) - West side. Scale bar equals 20  $\mu$ .

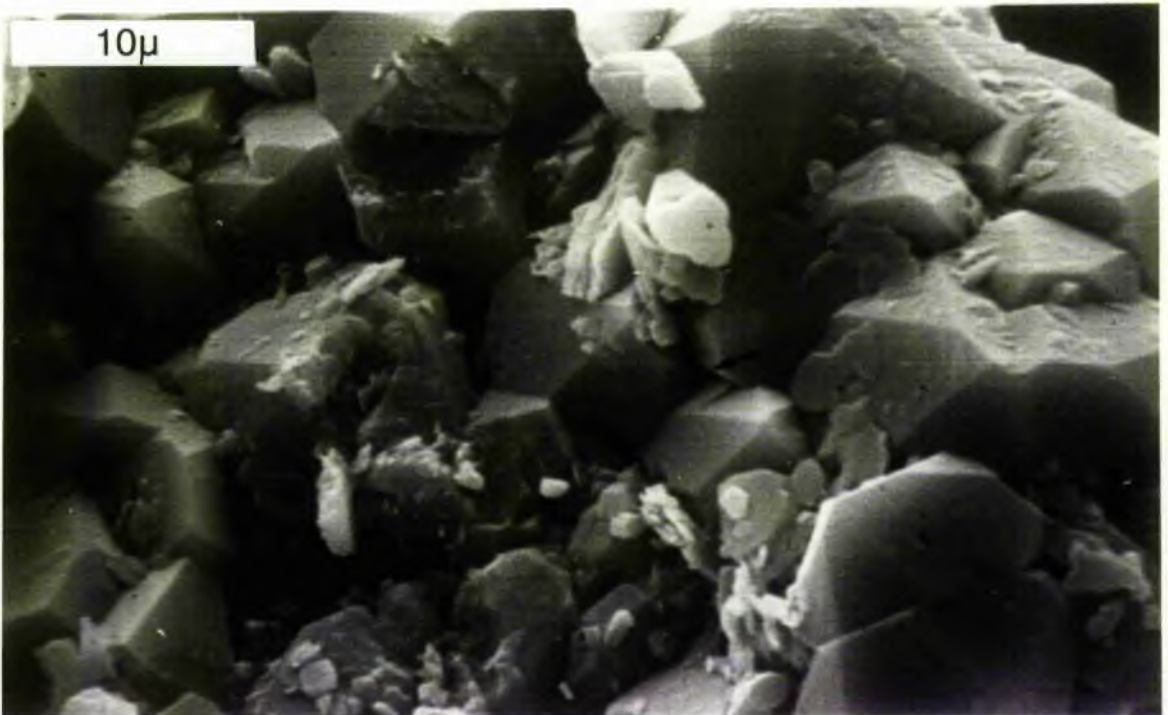


The grain contacts within the polycrystalline are more or less contain spaces in between as micropores (primary origin), and do not completely fit (Fig 6.18).

Fig 6.18 SEM photograph showing two polycrystalline grains, right grain in (a) and the left one in (b) both more or less corroded, in between the grain contacts a lot of spaces as micropores as in (A) and (B) as lamella ( $\rightarrow \leftarrow$ ) and sometimes triangular in shape ( $\leftarrow$ ). Classification: Internal spaces in polycrystalline quartz - Primary origin (IP-Pr). Sandstone Unit (T3) - West side. Scale bar equals 40  $\mu$ , 10 $\mu$  respectively.



--A--



--B--

APPENDIX NO 6.9 SECONDARY POROSITY - CLASSIFICATION

There are five principal classes of secondary porosity (Fig 6.19) occurring in these samples.

1 Porosity created by authigenic cement.

A large number of sandstones in this area show secondary porosity arising from the dissolution of carbonate cement. Pore size varies from microporosity to vuggy pores (Fig 6.20).

2 Porosity resulting from dissolution of authigenic replacive minerals.

The second commonest porosity type arises from the dissolution of soluble minerals, dominantly calcite, that previously replaced sedimentary constituents such as feldspar, and quartz grains. Porosity created by this type formed in three stages, filling, replacement and dissolution (Figs 6.21).

3 Porosity created by fracturing.

Porosity has arisen by fracturing in two ways. Some fractures have formed and remain open pores; others have been filled by cement and, later, this cement has been dissolved (Figs 6.22).

4 Porosity created by dissolution of sedimentary material.

In most cases, this type results from dissolution of shells or carbonate particles, such as dolomite, pore sizes (like vugs)

exceed the size of adjacent grains (Fig 6.23).

5 Shrinkage porosity.

This type plays a minor role in this area (Fig 6.24).  
Secondary pores resulting from shrinkage of feldspar grains.

In addition, of these five basic genetic types, there is another porosity type which might be a combination of more than one of genetic classes. Hybrid pores result from the complete dissolution or replacement of the margin of detrital grains by the same cement (Fig 6.25).



### DISSOLUTION OF AUTHIGENIC CEMENT



### DISSOLUTION OF AUTHIGENIC REPLACEMENT



### FRACTURING



### DISSOLUTION OF SEDIMENTARY MATERIAL



### SHRINKAGE



Fig 6.19. Genetic classes of secondary sandstone porosity (modified after Schmidt and McDonald 1979b).

Fig 6.20 Example of porosity after dissolution of secondary pore resulting from partial dissolution of intergranular cement. Sandstone Unit (B7) - West side. P = porosity; C = calcite; Q = quartz grains. Ordinary light, x 125.

Fig 6.21 Example of porosity created after replacement. Feldspar grain replaced by cement; secondary pore resulting from dissolution of the replacement materials. Sandstone Unit (S24). P = porosity; Q = quartz grains with silica overgrowth; F = feldspar. Ordinary light, x 250.

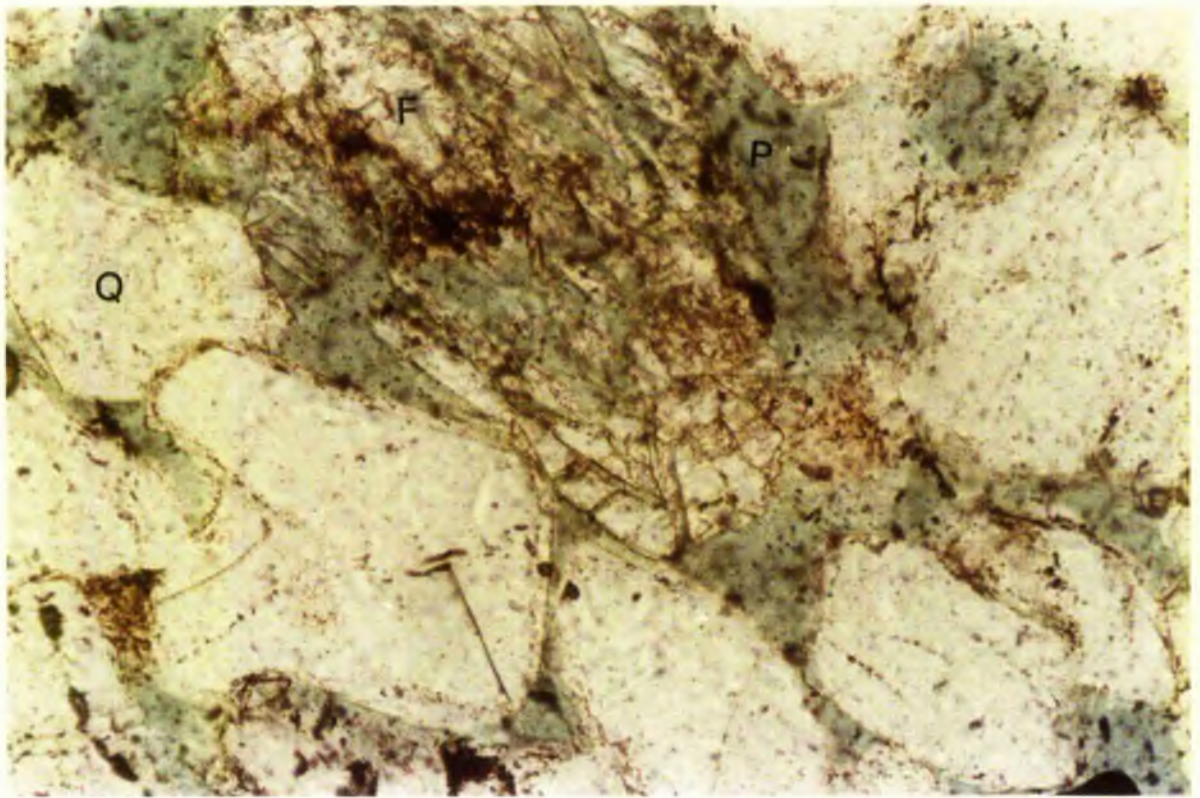
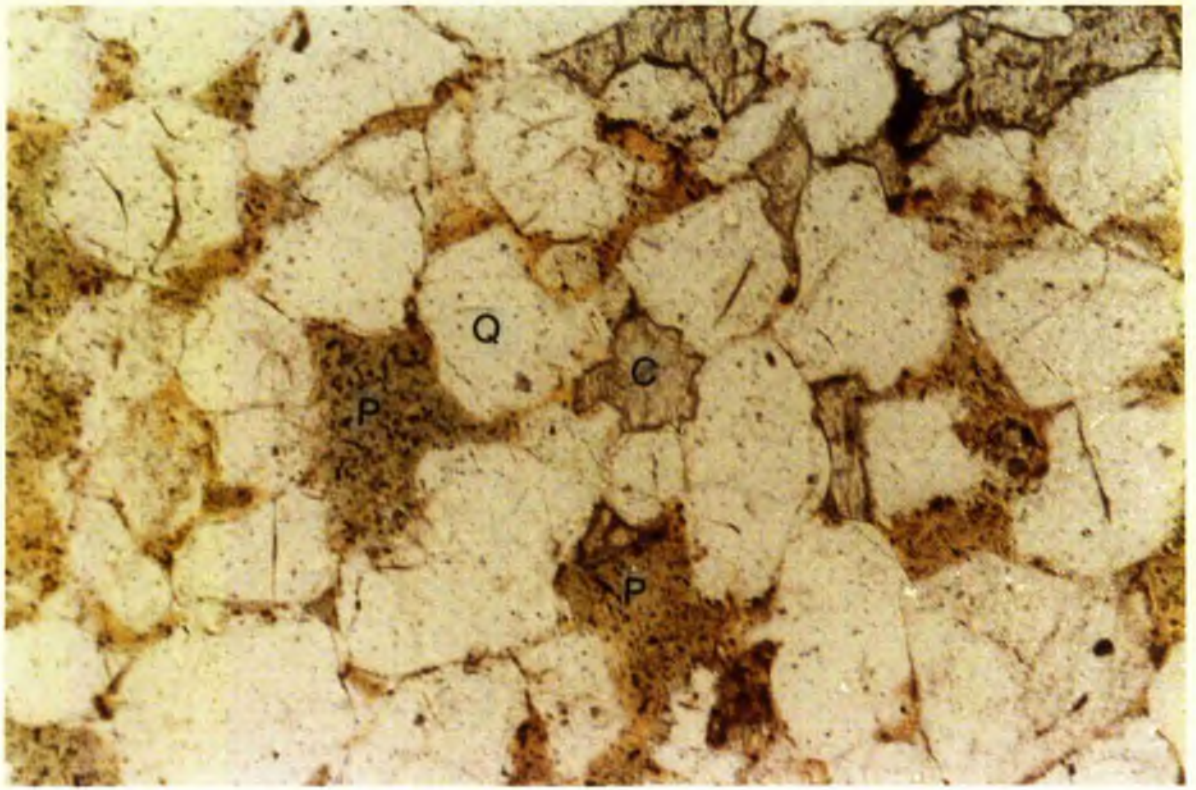


Fig 6.22 Photomicrograph showing secondary porosity resulting from fracture of feldspar grain. Carbonate cement filled the fracture, and replaced some parts followed by dissolution. Carbonate still remained around the grain and in fracture. Sandstone Unit (S24) - East side. P = porosity; F = feldspar; C = carbonate cement. Ordinary light, x 500.

Fig 6.23 Photomicrograph showing secondary porosity created by dissolution of sedimentary material as dolomite. Sandstone Unit (T6a') - West side. P = porosity; Q = quartz grains; D = dolomite(?). Ordinary light, x 125.

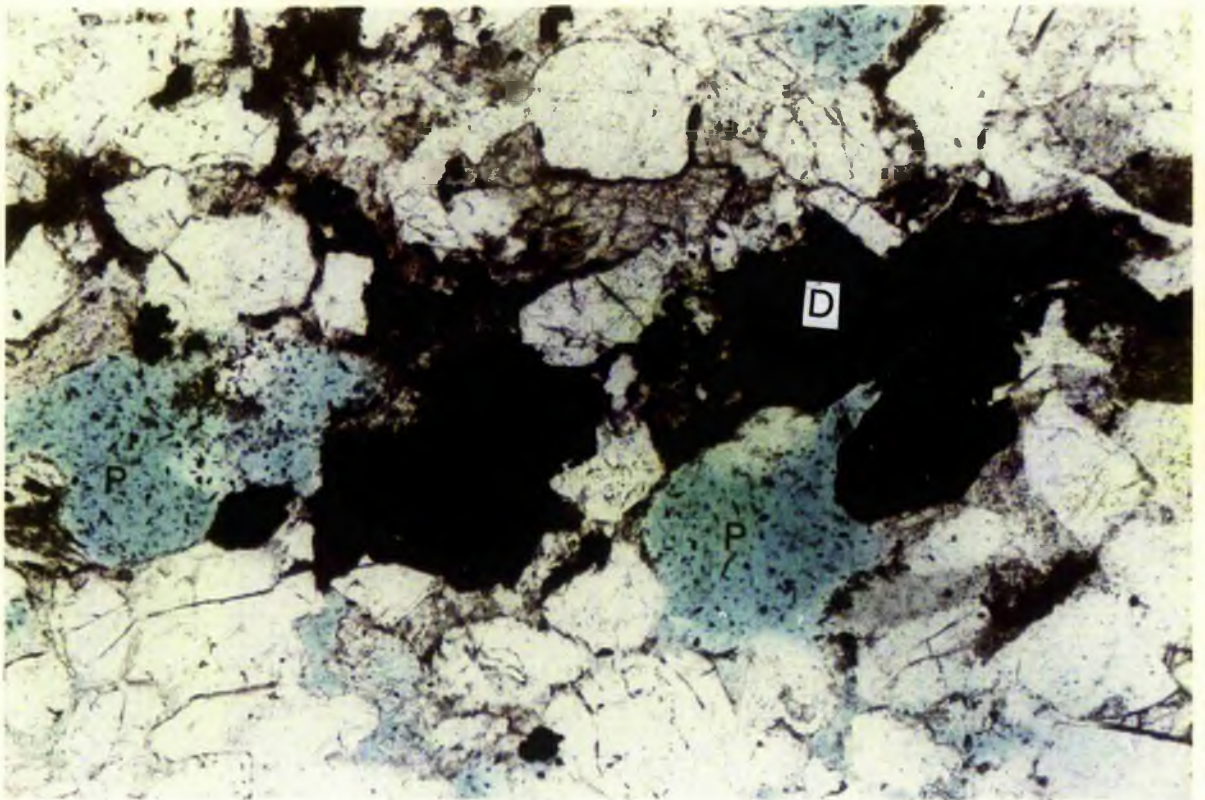
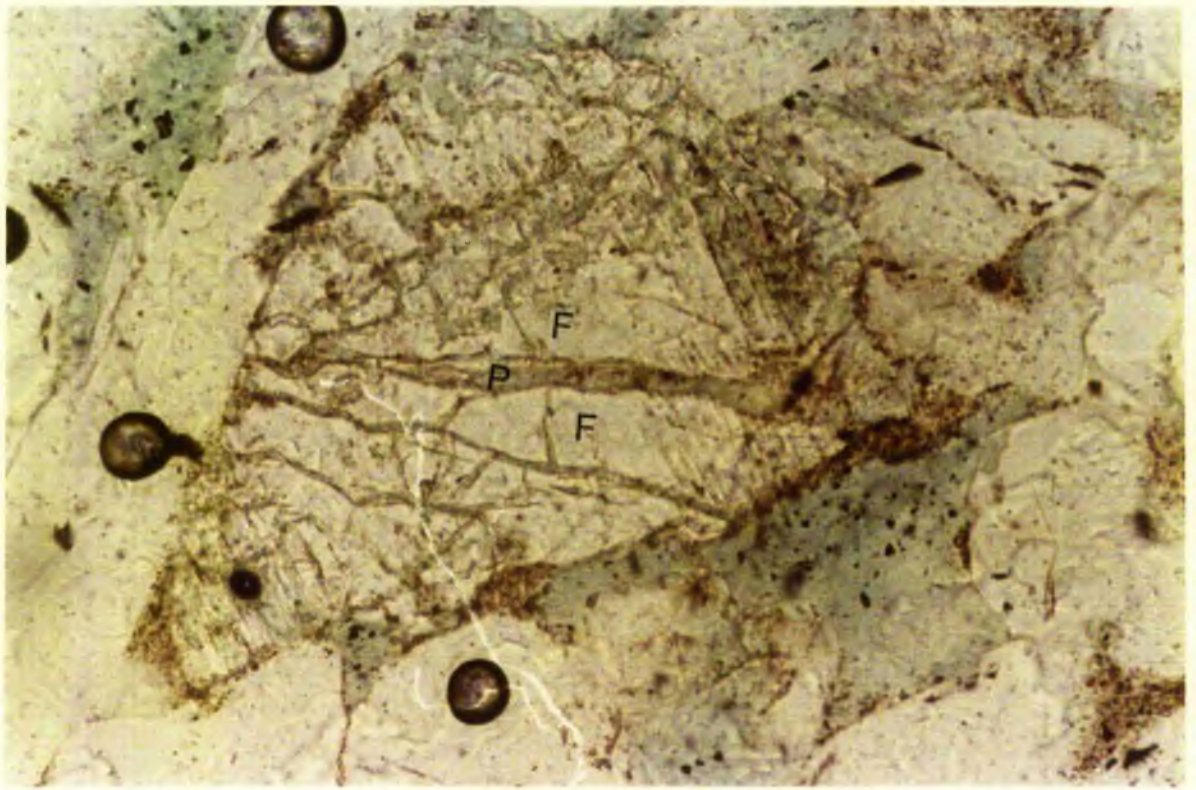
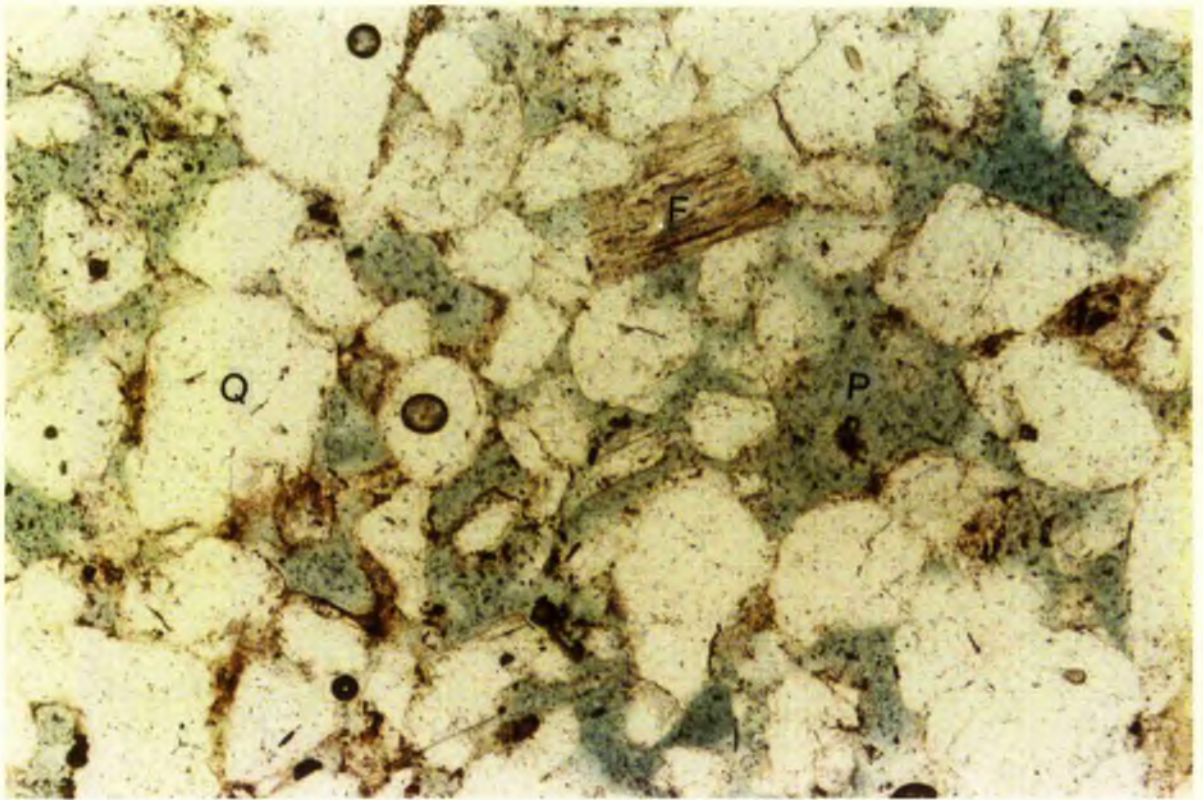
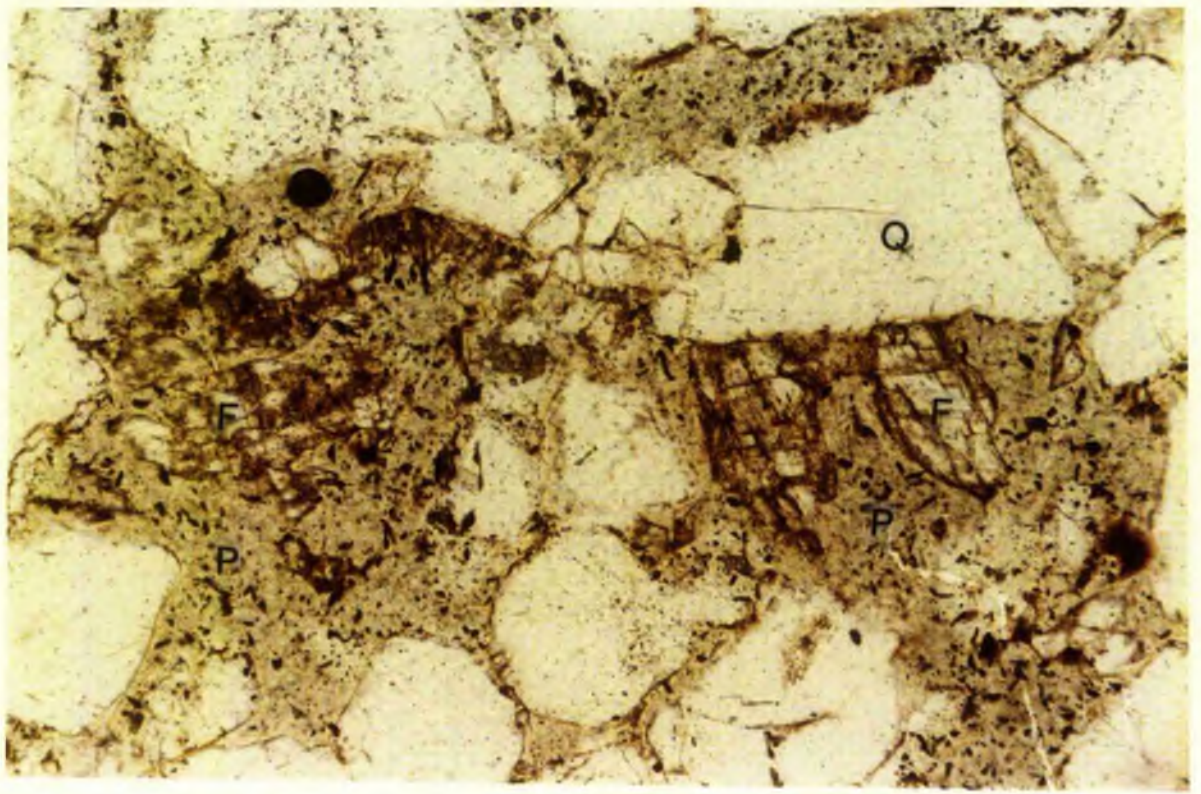


Fig 6.24 Example of porosity resulting from shrinkage. Secondary porosity created by shrinkage of feldspar grain. Sandstone Unit (S24) - East side. P = porosity; F = feldspar; Q = quartz grains. Ordinary light, x 125.

Fig 6.25 Example of hybrid porosity. Secondary porosity created by dissolution of intergranular cement and cement that replaced the margins of feldspar and quartz grains. Sandstone Unit (S27) - East side. P = porosity; F = feldspar; Q = quartz grain. Ordinary light, x 125.



APPENDIX No 6.10 TEXTURE OF SECONDARY POROSITY

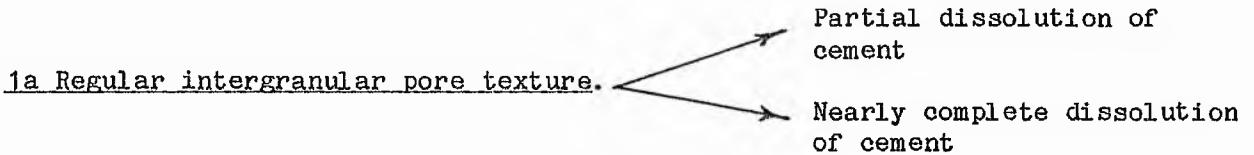
The texture of secondary porosity in this area (Fig 6.26) comprise the following:

- 1 Intergranular pore texture
- 2 Oversized pore texture
- 3 Sub-moldic pore texture
- 4 Intra-constituent pore texture
- 5 Fracture pore texture
- 6 Sub-isolated pore texture

(modified after Schmidt and McDonald 1979b)

1 Intergranular Pore Texture.

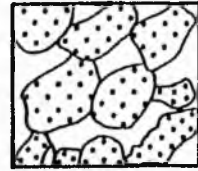
Often the intergranular pore texture recognized in this area are secondary, because of a variety of modification processes such as, cementation, replacement; and dissolution (partial or complete). It consists of three main subdivisions (Fig 6.27) of secondary intergranular pore texture as.



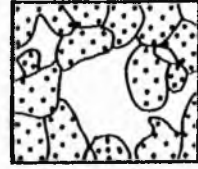
Secondary pores of regular intergranular texture result from partial or nearly completely dissolution of carbonate



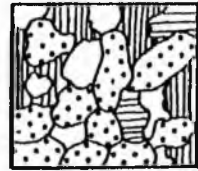
Inter-Granular Pores



Over-Sized Pores



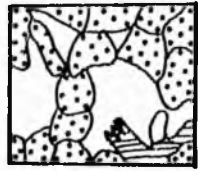
Intra-Constituent Pores



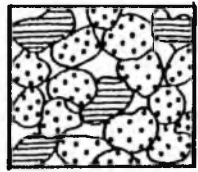
Sub-Moldic Pores



Fractured Grain



Sub-Isolated Pores



Porosity



Quartz  
grains



Feldspar  
grains



Carbonate  
cement

Fig 6.26 Types of secondary porosity texture (modified after Schmidt, and McDonald 1979).

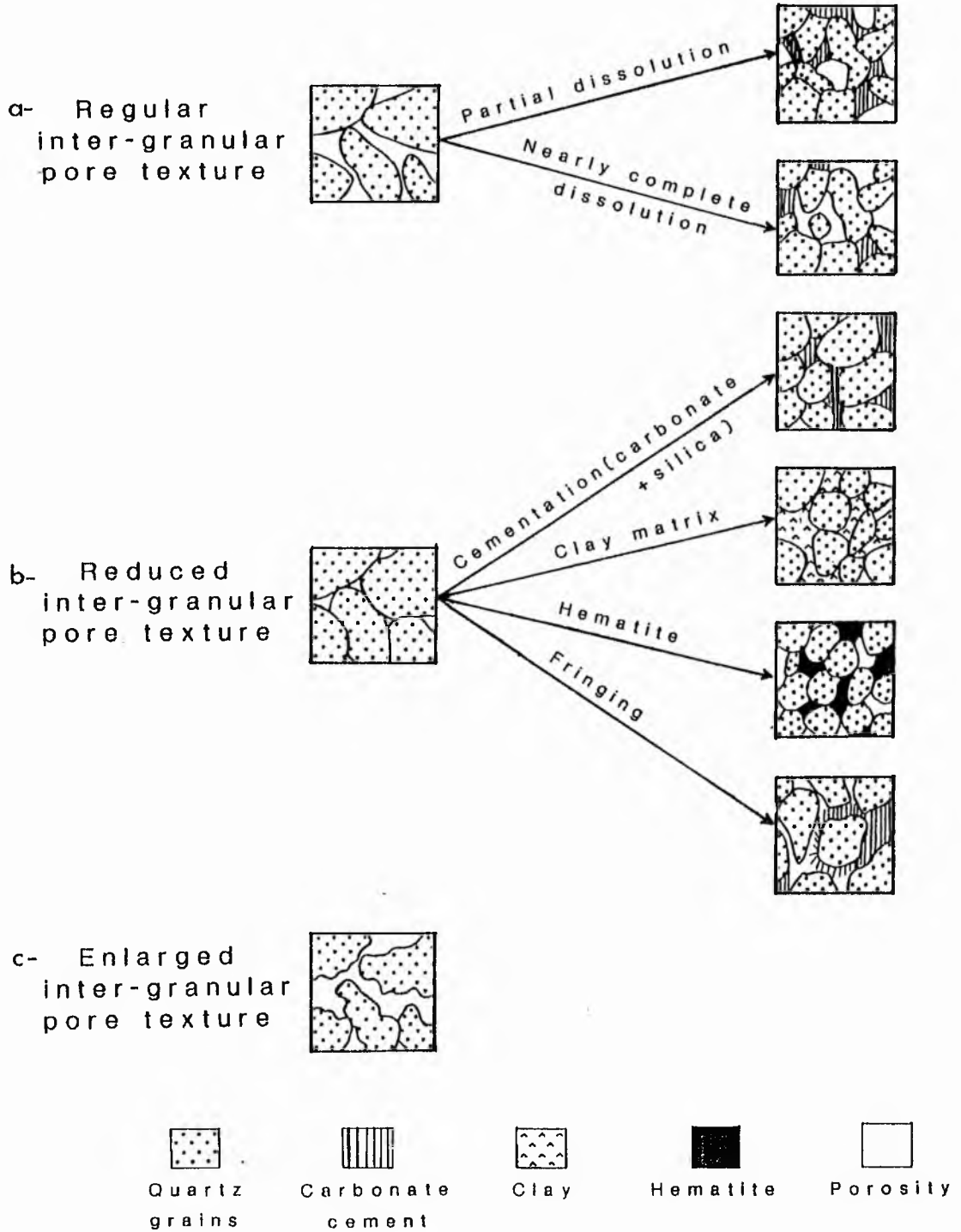
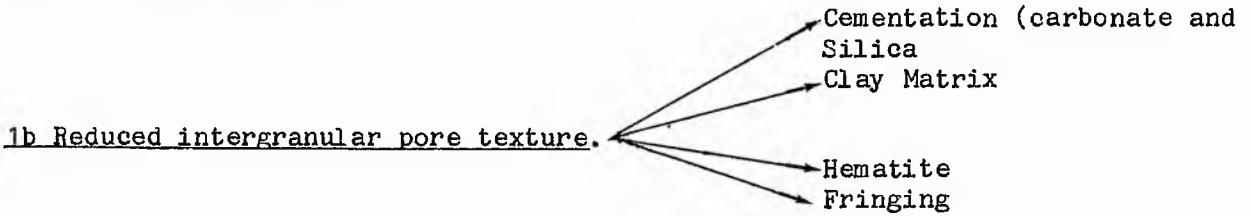


Fig 6.27 Intergranular texture of secondary porosity.

intergranular cement (Figs 6.28 - 6.29), but sometimes mixed with primary intergranular.



The reduction of intergranular pore texture (Figs 6.30 to 6.34), arises from cementation by quartz overgrowth and calcite, chemical compaction filling by clay matrix or hematite and fringing, or filling of intergranular spaces eg the filling of feldspar fractures by material. Schmidt and McDonald (1979b, p 213) pointed out that the secondary porosity appearing in the reduced intergranular texture commonly shows little or no modification after it formed. In my opinion, reduced intergranular pores could be altered to enlarged pore texture during further diagenesis, for example carbonate cement may enlarge in amount by replacing some quartz margins; the carbonate may then be dissolved.

1 Enlarged intergranular pore texture.

In most instances in this area, the enlargement of the intergranular spaces take place after the dissolution of carbonate cement replacement the margins of quartz and feldspar grains. Sometimes pores connect together forming a channel morphology (Figs 6.35, 6.36).

Fig 6.28 Example of regular intergranular pores resulting from partial dissolution of carbonate cement which filled the primary intergranular spaces. Sandstone Unit (T8d). West side. P = porosity; C = carbonate cement; Q = quartz grains. Ordinary light, x 125.

Fig 6.29 Example of regular intergranular pores resulting from nearly complete dissolution of intergranular cement. Sandstone Unit (B7) - West side (767F). P = porosity; C = carbonate spots; Q = quartz grains. Ordinary light, x 125.

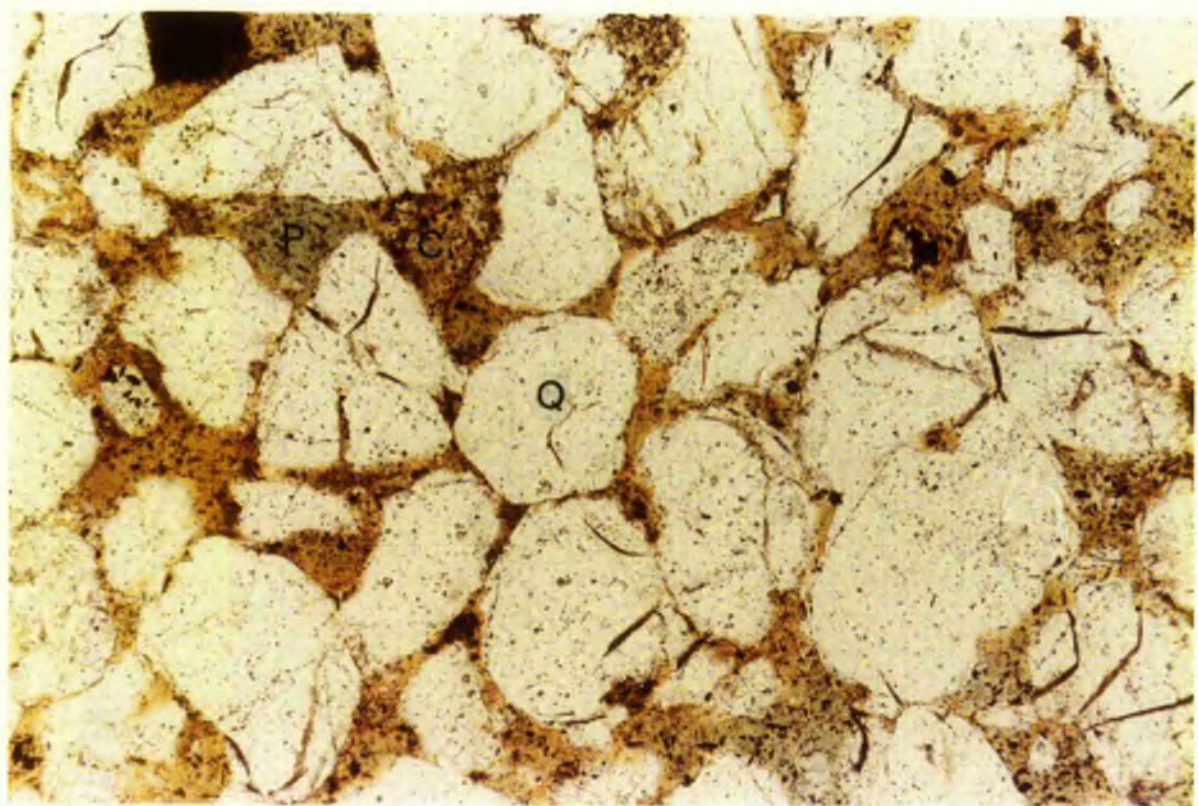
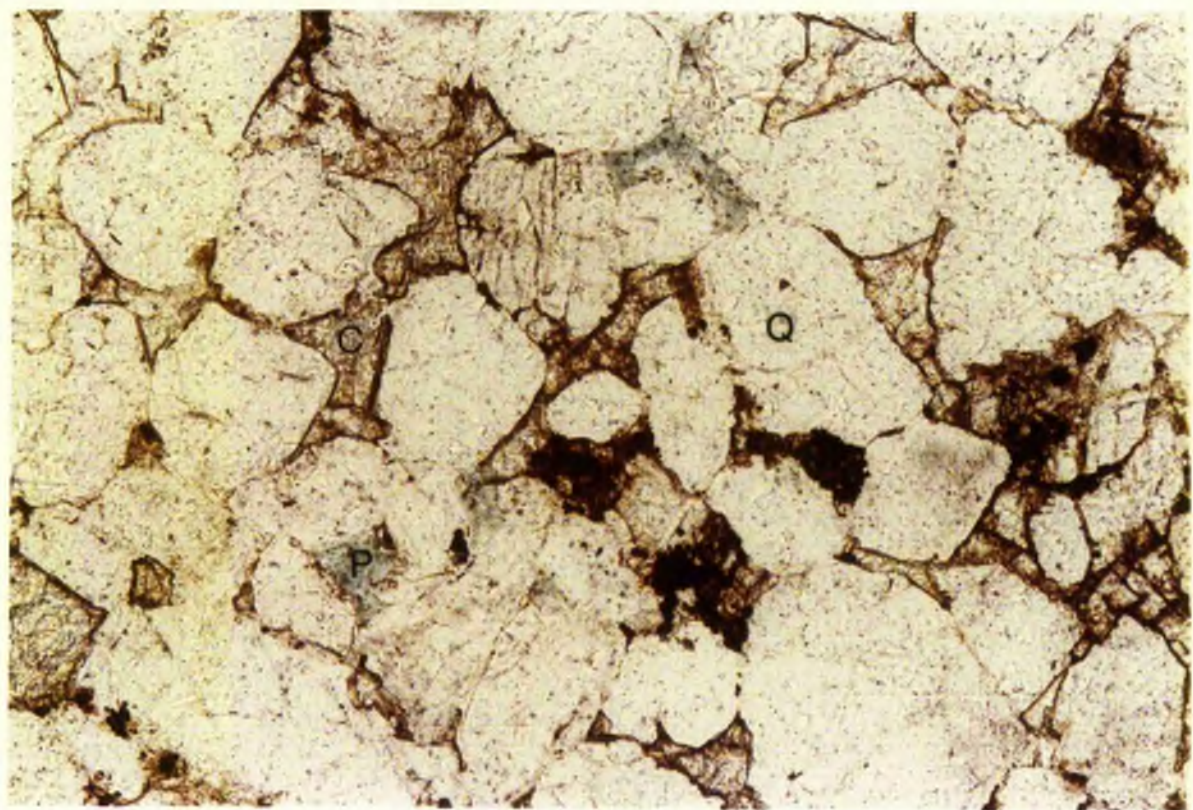


Fig 6.30 Example of intergranular pores which were reduced by carbonate cement nearly complete filling the spaces. Sandstone Unit (T8d) - West side. Q = quartz grains; C = carbonate cement. Ordinary light, x 125.

Fig 6.31 Photomicrograph showing silica cement around the original grains and reducing the intergranular pores. Sandstone Unit (T6a) - West side. Cross polars, x 500.

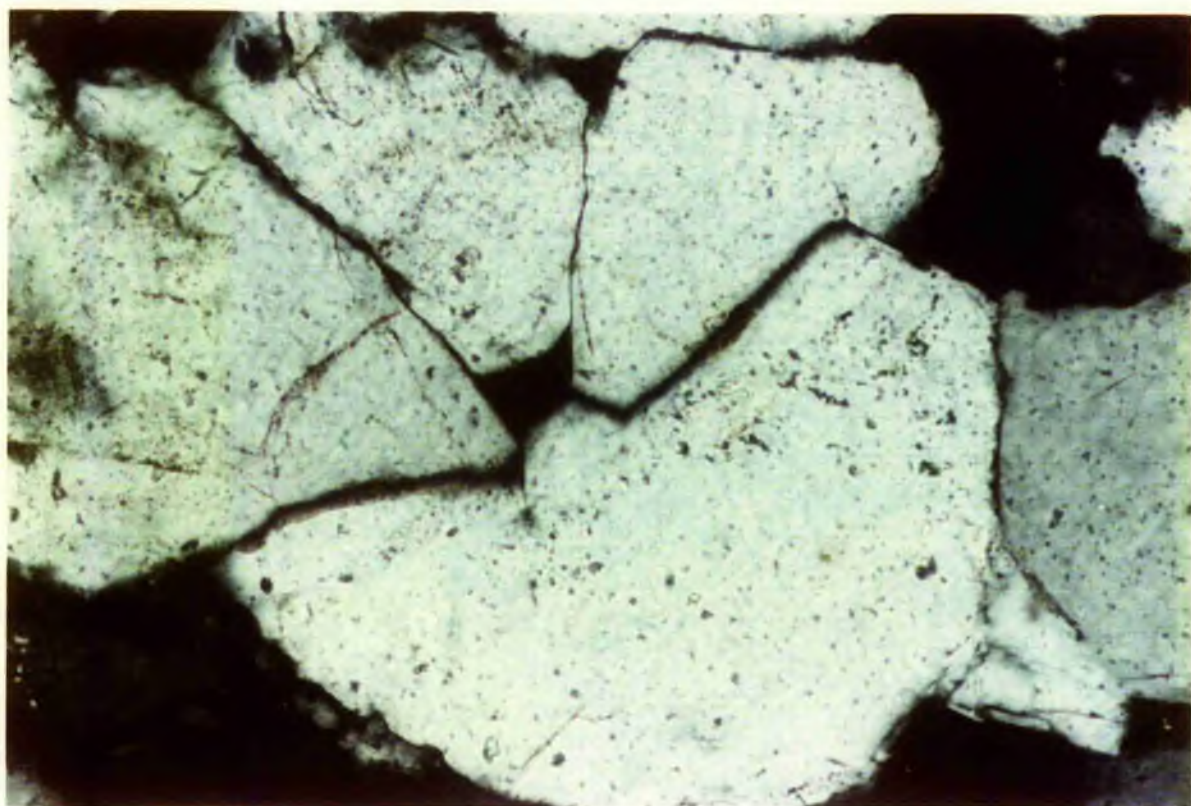
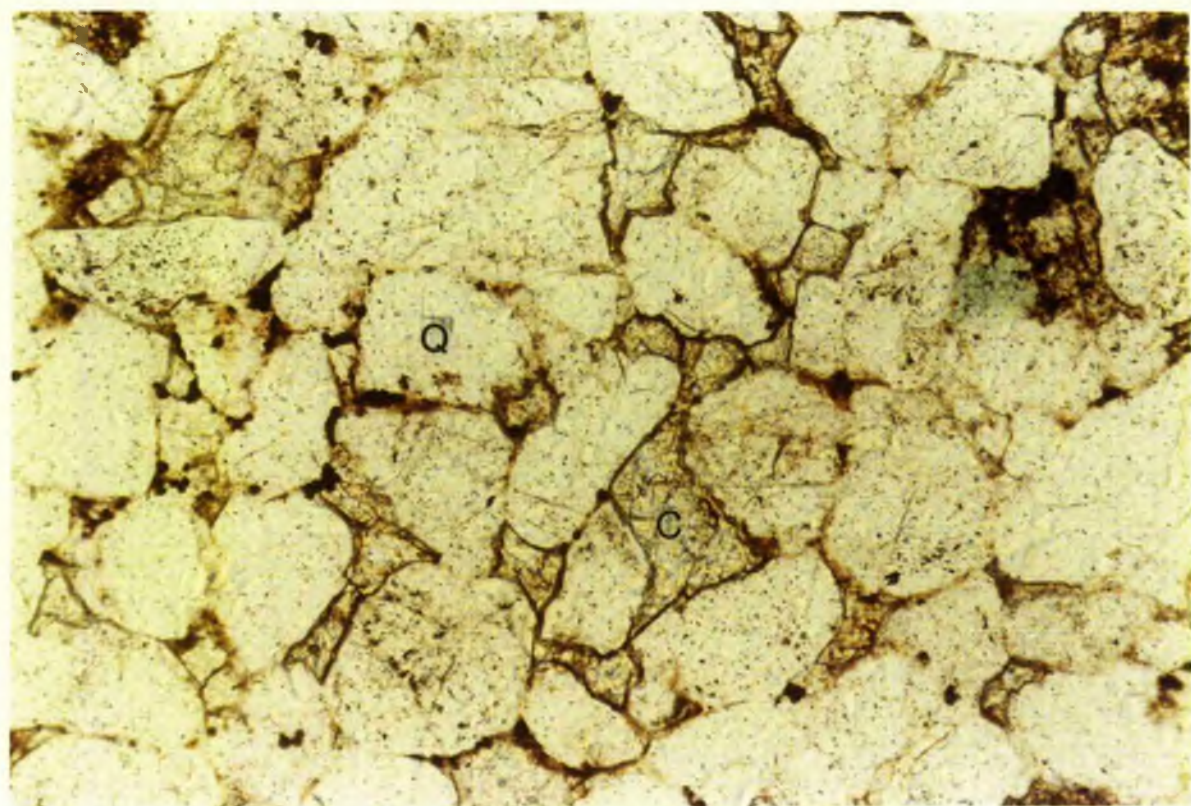


Fig 6.32 Photomicrograph of clay matrix filling the pores and reducing the intergranular pore spaces. Sandstone Unit (S21a) - East side.

CM = clay matrix; Q = quartz grains. Cross polars, x 125.

Fig 6.33 Photomicrograph of intergranular pores reduced by hematite filling the spaces in between the grains. Sandstone Unit (T7) - West

side. H = hematite; P = porosity; Q = quartz grains. Ordinary light, x 125.



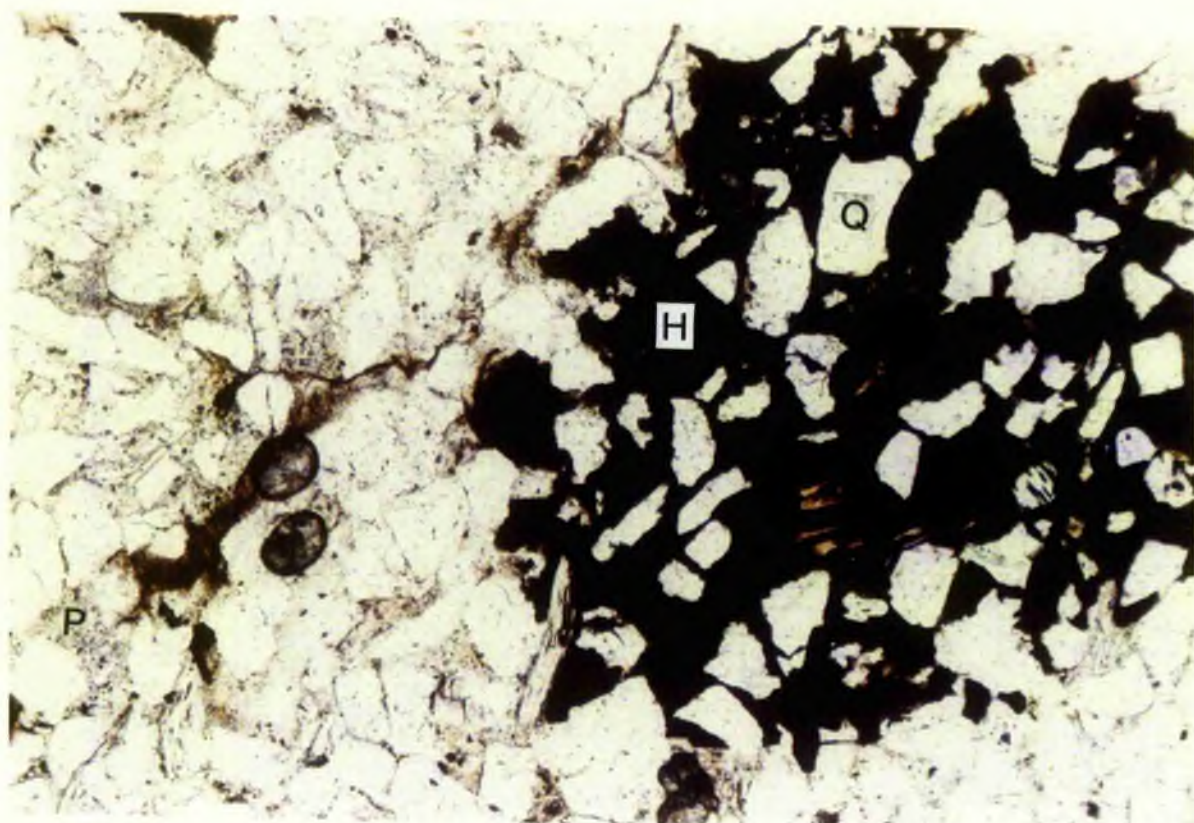
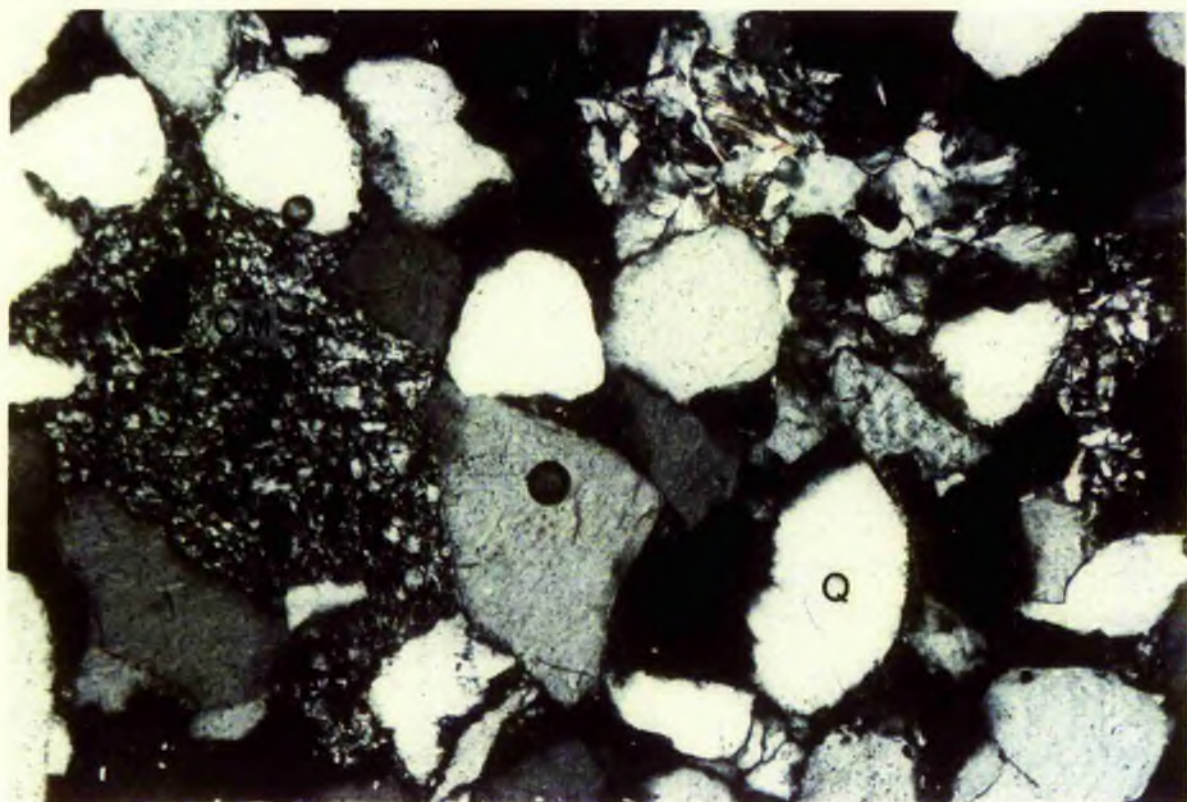


Fig 6.34 Photomicrograph of fringing cementation around quartz grain

(arrow) leads to reduction of the intergranular pore.

Middle part of sandstone Unit (B7) - West side. C = carbonate cement; Q = quartz grains. Crossed polars, x 250.

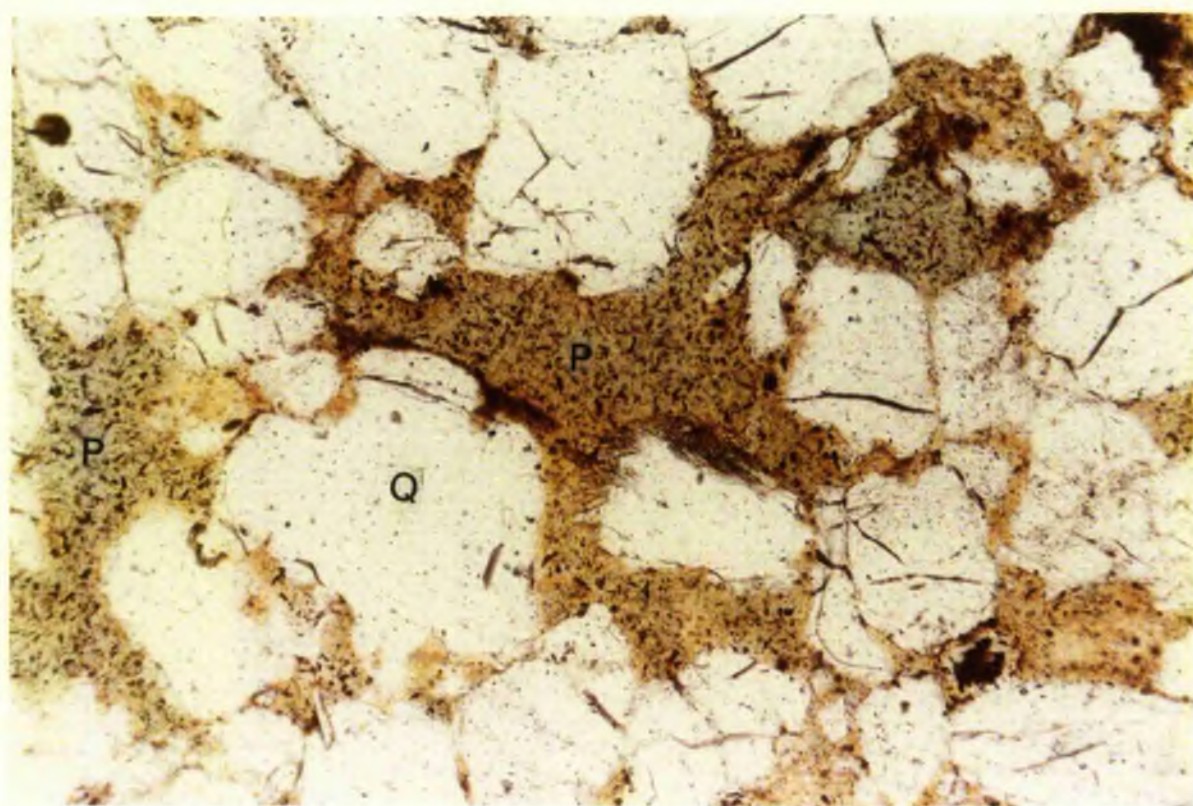
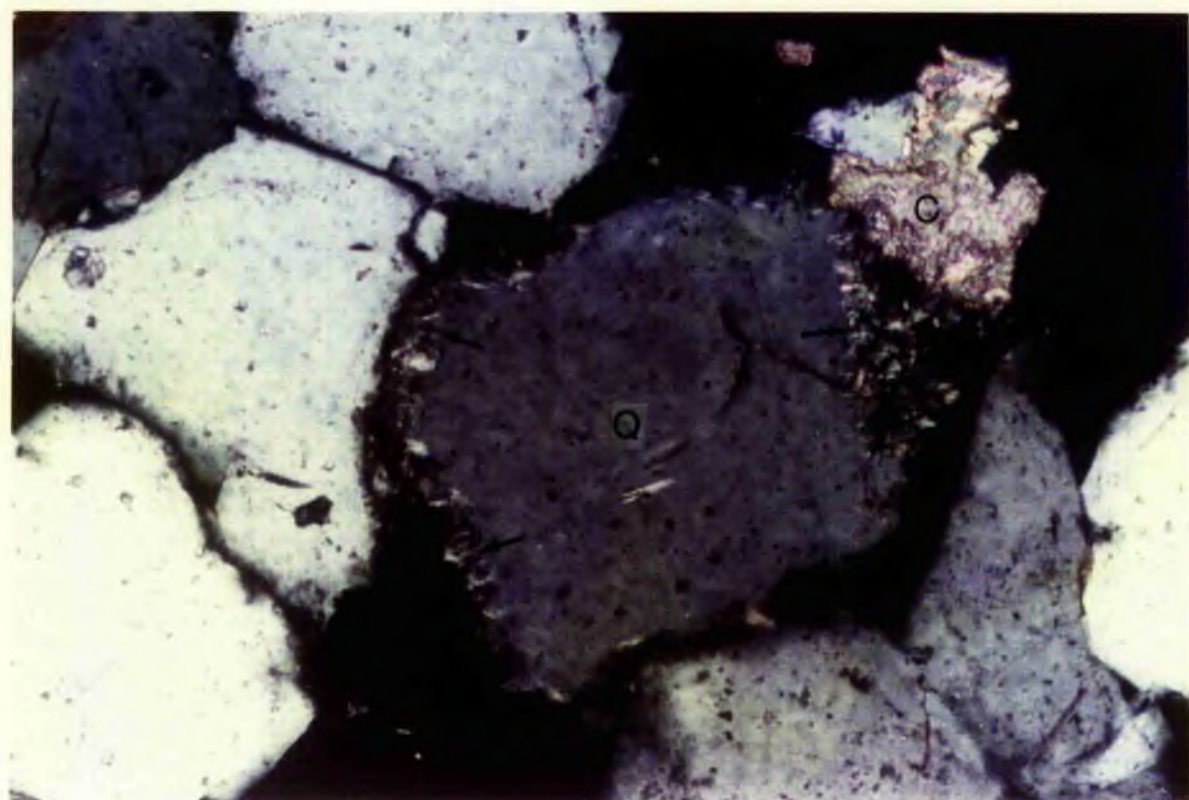
Fig 6.35 Photomicrograph of secondary pores of enlarged intergranular

texture resulting from complete dissolution of carbonate filling

and replacement of the margins of detrital grains forming a

channel. Middle part of sandstone Unit (B7) - West side.

P = porosity; Q = quartz grains. Ordinary light, x 125.



## 2 Oversized pore texture

This type with a significantly larger diameter than that of adjacent grains, is common and provides good evidence for secondary porosity. It results either from complete replacement of sedimentary grains such as rock fragments, feldspar, polycrystalline quartz, and then dissolution, in addition, of quartz grains; or from complete dissolution of carbonate cement. This pore type frequently occurs together with inhomogeneity of packing (Schmidt and McDonald 1979b) (Fig 6.37).

## 3 Moldic pore texture.

This was described as moldic pore texture (Schmidt and McDonald, 1979b), but I have modified it to clarify its meaning. Their description is as follows:-

- i Moldic pore texture welded by quartz grains (1979a, p 219)
- ii Moldic pores are always of secondary origin and formed by dissolution which is either partial or complete (1979a p 216).
- iii It forms where secondary porosity is created selectively at the expense of grains which are encased by other grains, matrix, cement, or replaced by other minerals.

My investigations suggest that complete welding of grains around the pore is unusual and unlikely. Micropores are generally seen between the quartz grains and such pores are presumably needed to carry solutions which cause dissolution and the formation of the moldic pores (Figs 6.38 - 6.39).

Fig 6.36 Photomicrograph of secondary pores of enlarged intergranular texture resulting from dissolution of cement filling and replacive cement. In places pores are connected and form channels. Sandstone Unit (S24). East side. P = porosity; C = carbonate cement; Q = quartz grains. Ordinary light, x 125.

Fig 6.37 Photomicrograph of secondary pores of oversized texture resulting from dissolution of carbonate cement and replacive cement. Sandstone Unit (S17) - East side. P = porosity; C = cement spots; Q = quartz grains. Ordinary light, x 125.

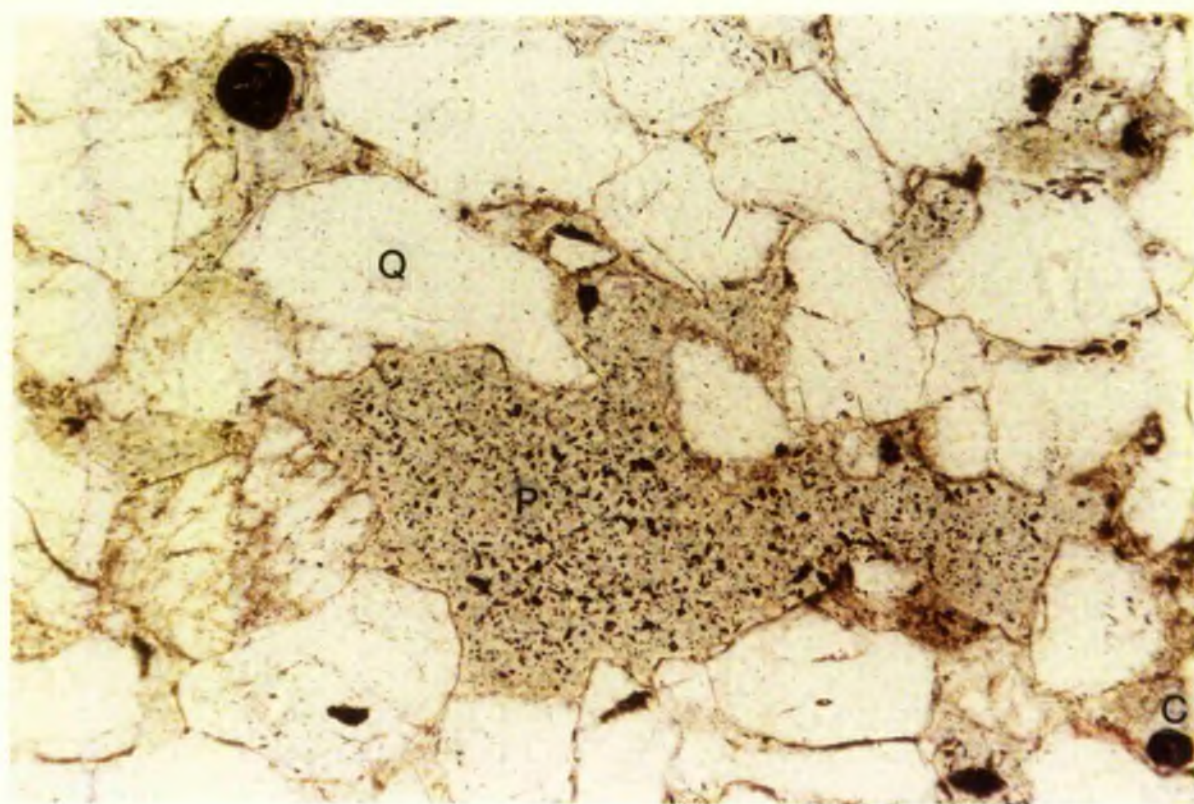
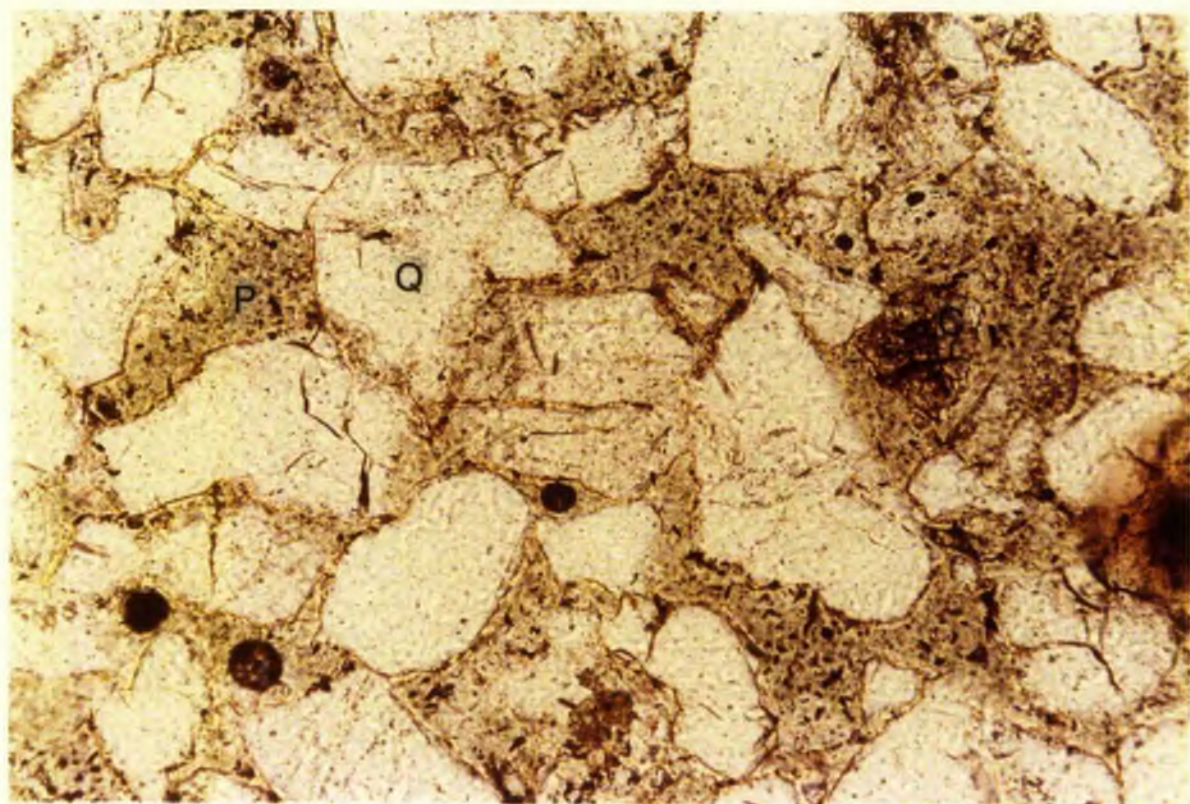
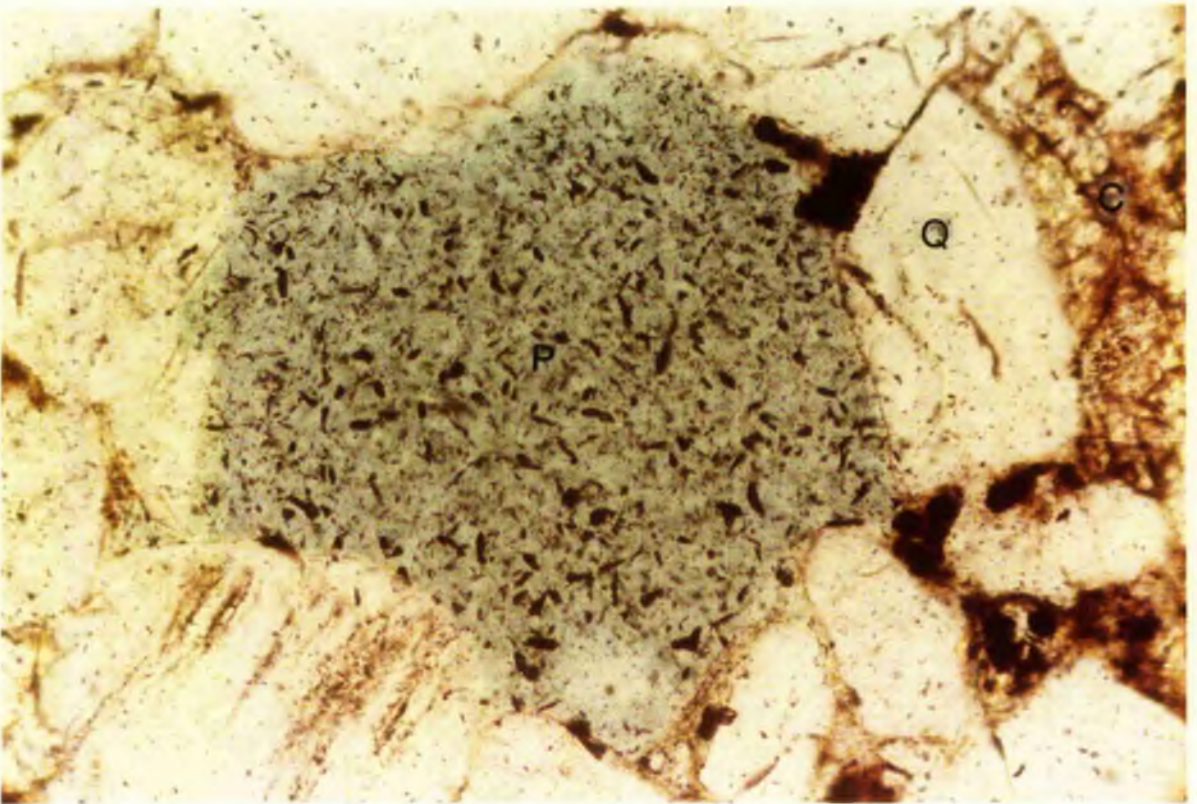
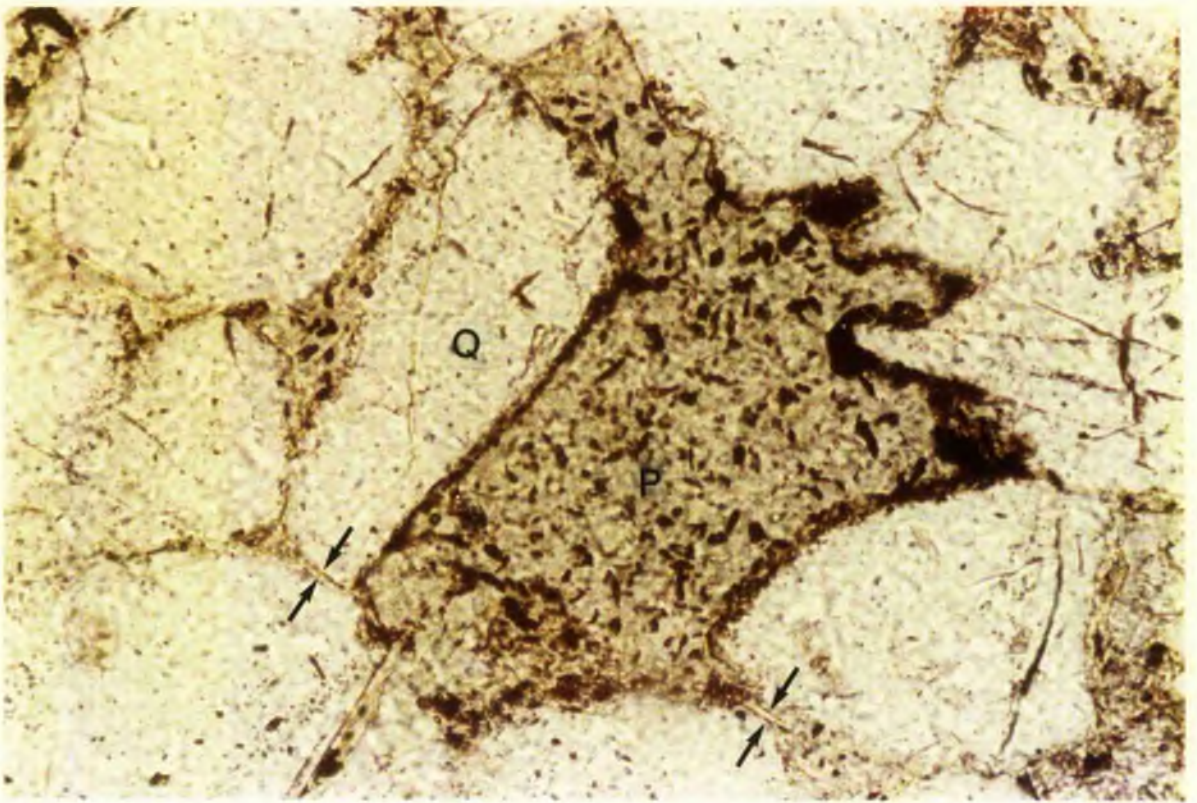


Fig 6.38 Photomicrograph of sub-moldic texture. Hand shape sub-moldic pore results from nearly complete dissolution of cement and cement which replaced the margin of quartz grains which surrounded the pore. Lamella pores (arrows) connected with the sub-moldic pore. Sandstone Unit (S17) - East side. Ordinary light, x 250.

Fig 6.39 Photomicrograph of secondary pore of sub-moldic texture result from nearly complete dissolution of calcite and surrounded by quartz grains. Sub-moldic pore interconnected with the secondary pores by micropores. Sandstone Unit (T8d) - West side. P = porosity; C = calcite; Q = quartz grains. Ordinary light, x 250.





#### 4 Intra-constituent pore texture

This type of texture includes all the pores within individual constituents. Pore size ranges from microporosity (less than 1  $\mu\text{m}$  in diameter) to nearly the same diameter of the individual constituents. Four main types of intra-constituent pore texture are recognized, in addition, to other subdivisions.

##### 4a Intragranular pore texture.

Two sub-division types of secondary intergranular pore texture are recognized:-

- i Internal shrinkage of muscovite grain forms pores in between and micropores within the grain (Fig 6.40).
- ii Internal selective dissolution of minerals that replaced part of the grain (eg dissolution of carbonate cement that incompletely replaced feldspar or quartz grains). (Figs 6.41, 6.42).

##### 4b Intra-matrix pore texture

Sometimes it is difficult to say definitely, whether this is primary or secondary porosity. This texture is fairly common especially between grains of the clay matrix (Fig 6.43).

##### 4c Intra-cement pore texture

The intra-cement pores are a mixture of secondary and primary origin, but the secondary pores are much more common than primary, even in small pores. Two types of intra-cement pores texture are recognized as large pore size (a) Internal incomplete

Fig 6.40 Photomicrograph of intragranular pore texture. Shrinkage of muscovite grain created pore in between (P), and micropores within the grain (arrows). Sandstone Unit (S24) - East side. P = porosity; Q = quartz grains. Crossed polars, x 250.

Fig 6.41 Photomicrograph of dissolution material gave rise to corroded margin of grain and intragranular pore in quartz grain. Sandstone Unit (S27) - East Side. P = porosity; Q = quartz grains. Ordinary light, x 250.

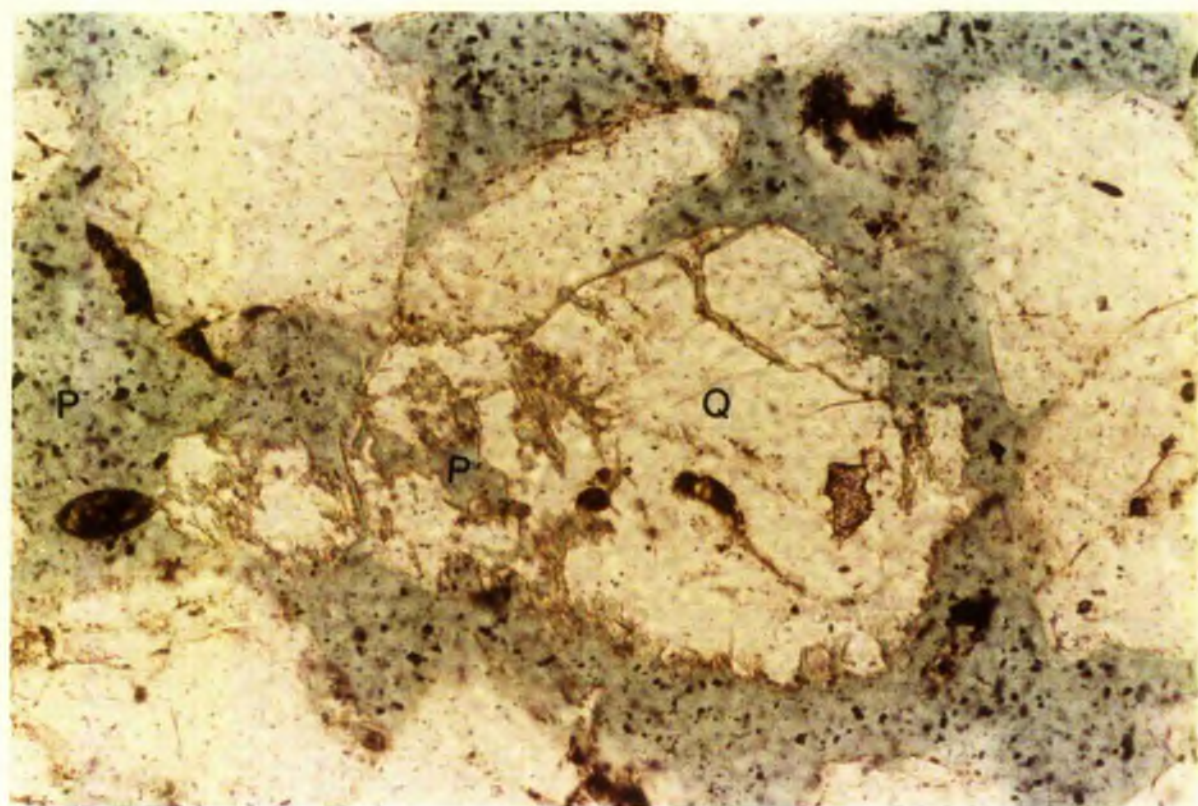
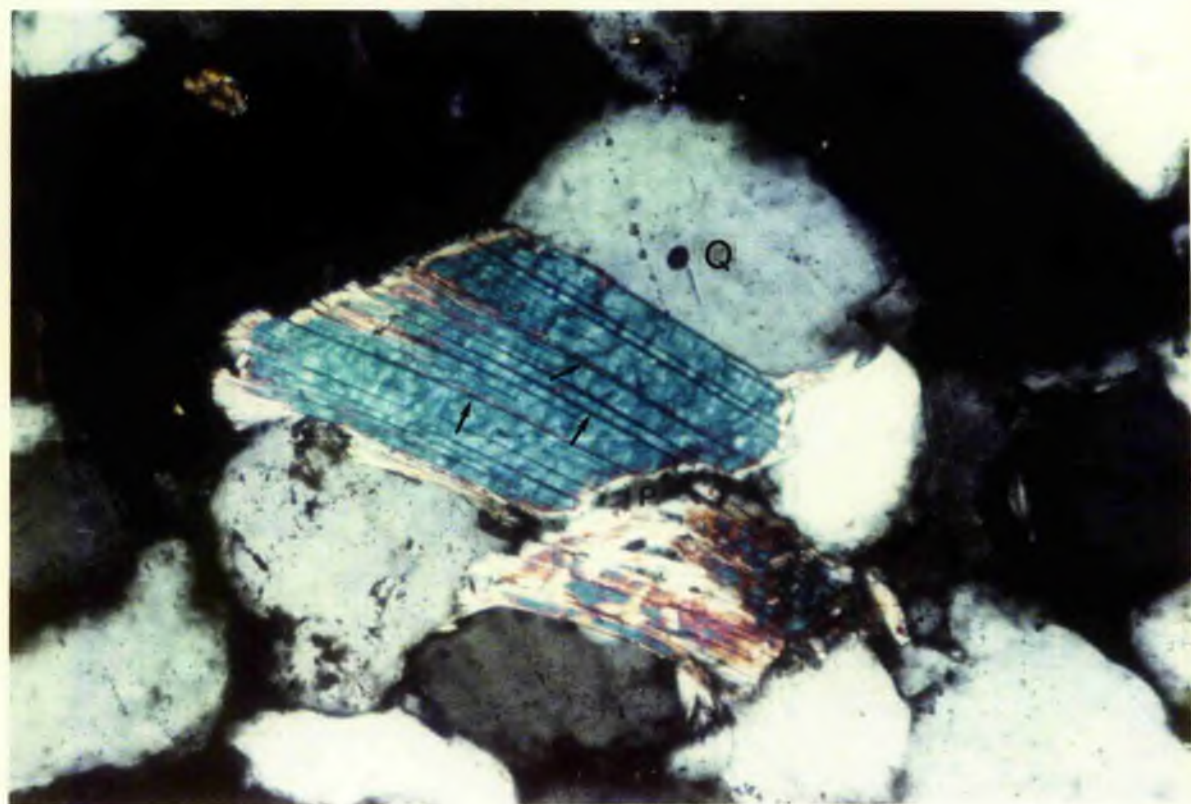
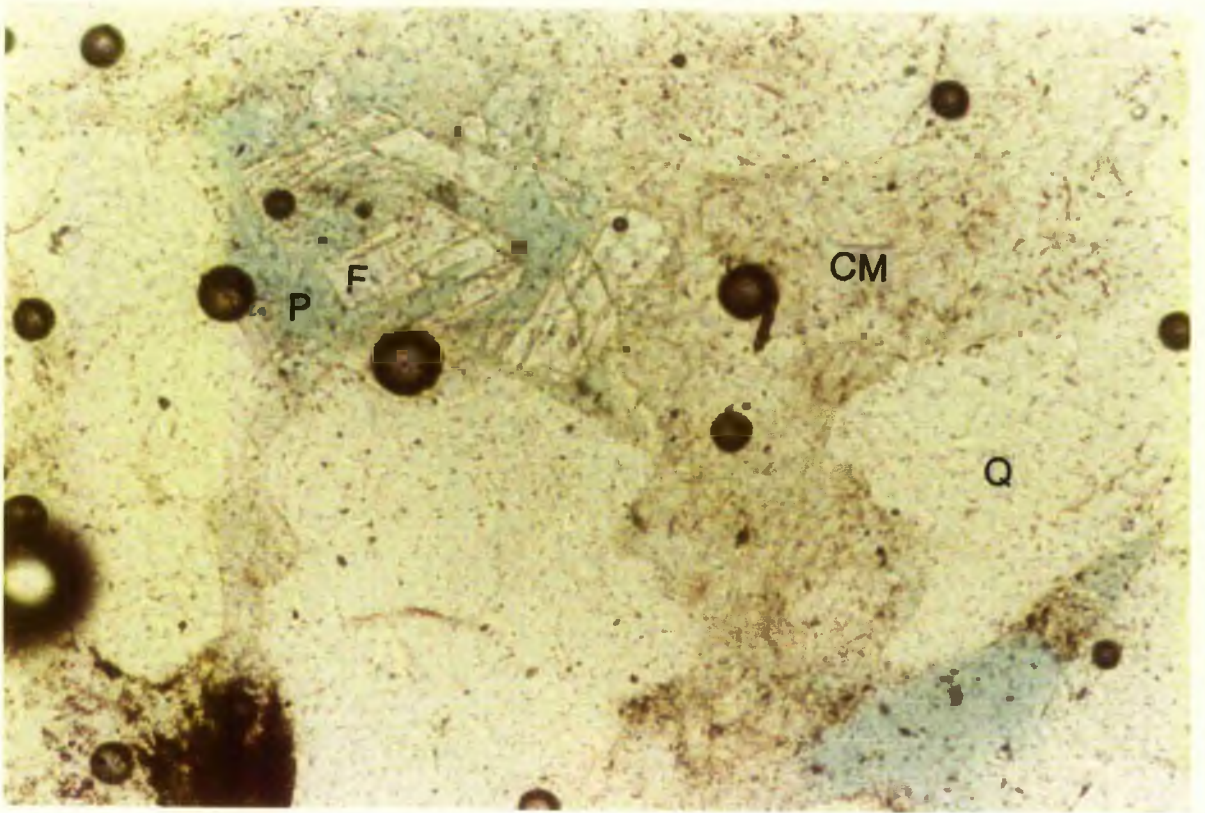
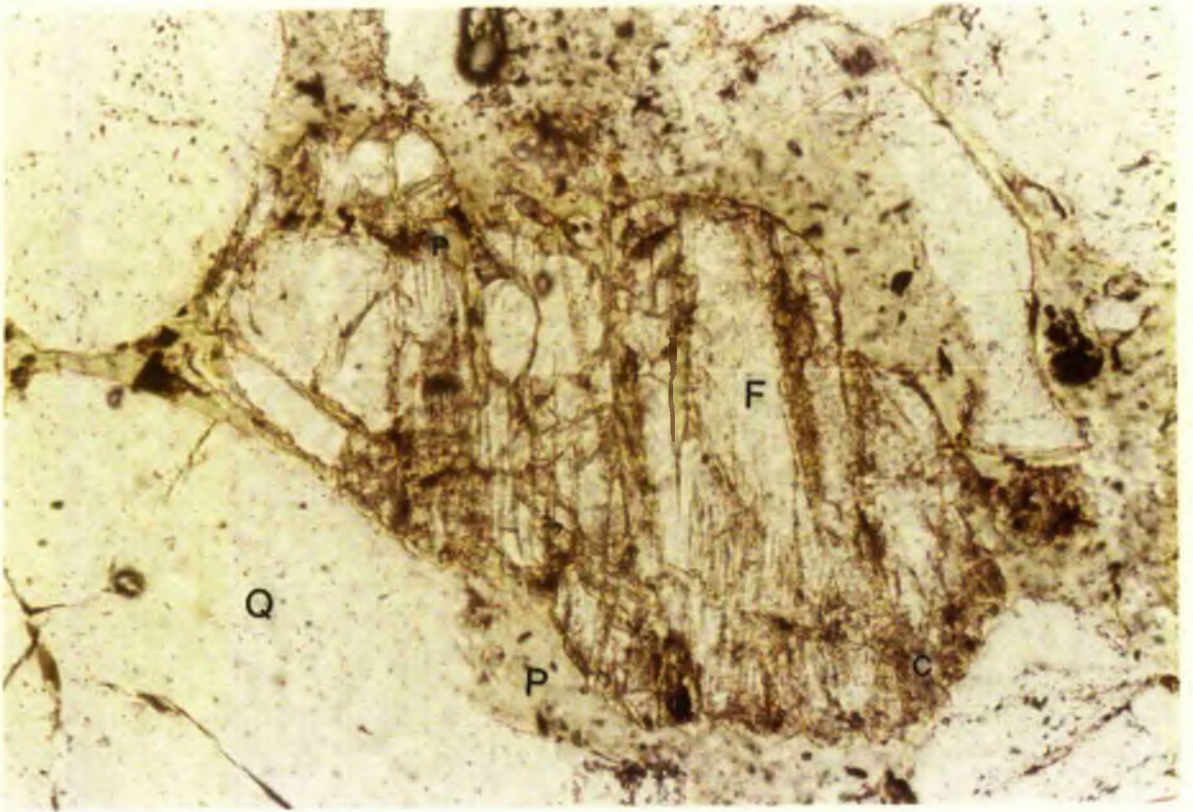


Fig 6.42 Photomicrograph of carbonate cement that incompletely replaced a feldspar grain and formed intragranular pores. Sandstone Unit (S24) - East side. P = porosity; F = feldspar grain; Q = quartz grains; C = carbonate cement. Ordinary light, x 250.

Fig 6.43 Photomicrograph of intra-matrix pore texture. Clay material incomplete filled the intergranular pores created intra-matrix pores, varies in size. Sandstone Unit (S21a) - East side. P = porosity; CM = clay matrix; Q = quartz grains. Ordinary light, x 250.



dissolution of cement (Fig 6.44) (b) Internal shrinkage of cement material (eg shrinkage of hematite cement created pores (fig 6.45). While four types of micro intra-cement pores texture are recognized:

- i Lamella pore along the cleavage.
- ii Fracture and dissolution.
- iii irregular cracks.
- iv pitted.

#### 4d Intra-replacement pore texture.

This is created either from the replacement of polycrystalline with micro-intergranular pores, or formed during replacement as for example the replacement of feldspar grain by porous kaolinite (Figs 6.46, 6.47). It is also created by internal dissolution of replacive minerals (Fig 6.48).

#### 5 Fracture pore texture.

Porosity may be created by fractures. Reopened fracture porosity commonly arises from the dissolution of cement. This porosity type is not very abundant in this area. Three types of fracture pore texture are recognized.

#### 5a Open rock fracture.

This type of pore includes more than a single constituent (Fig 6.49), has more than one subdivision (Schmidt and McDonald, 1979b, p 219). It is created after the fracture filling by cement and replacing of some of detrital grains, and then

Fig 6.44 Photomicrograph of intra-cement pore texture. Incomplete dissolution of carbonate cement (calcite) created intra-cement pores. Upper part of sandstone Unit (B7) - West side. P = Porosity; Arrow = corrosion of quartz grain; C = carbonate cement; O = opaque minerals; Q = quartz grains. Ordinary light, x 500.

Fig 6.45 Photomicrograph of intra-cement pore texture. Shrinkage of opaque minerals created intra-cement pores. Sandstone Unit (S21C) - East side. P = porosity; M = mica; F = feldspar; C = calcite spots; CM = clay matrix; Q = quartz grains. Ordinary light, x 125.

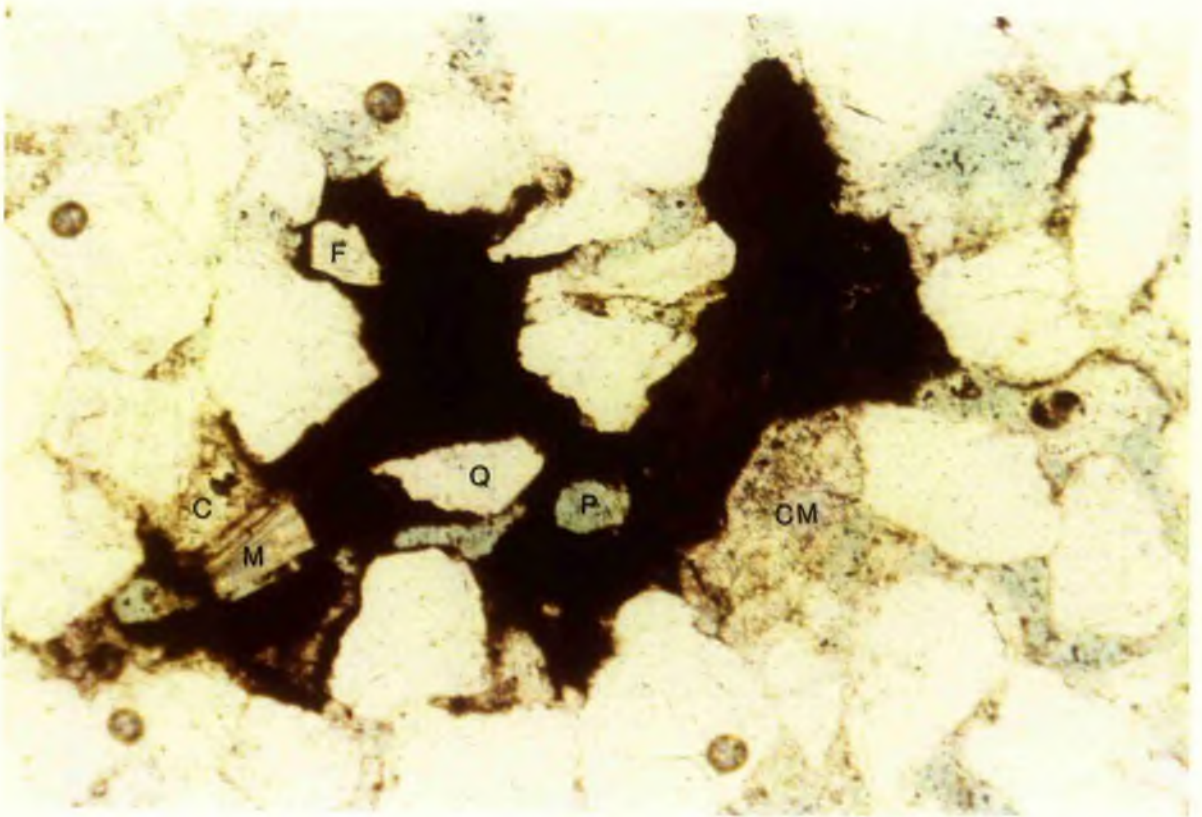
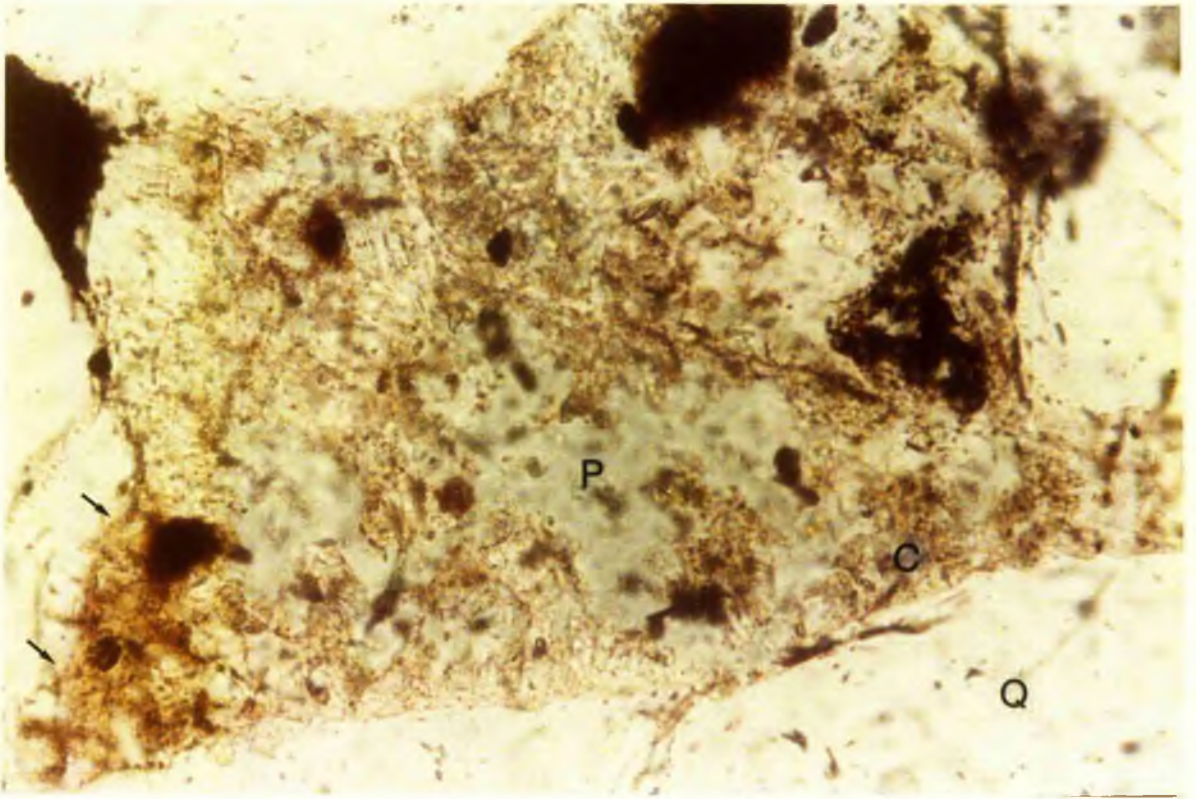




Fig 6.46 Photomicrograph of intra-replacement pore texture. Replacement of feldspar grain by clay matrix (kaolinite) created intra-replacement pores. Sandstone Unit (S21a) - East side.  
P = porosity; F = feldspar (plagioclase); CM = clay matrix;  
Q = quartz grains. Ordinary light, x 125.

Fig 6.47 Photomicrograph of intra-replacement pore texture. Three feldspar grains fractured and replaced by clay material formed intra-pore. Sandstone Unit (S21a) - East side.  
P = porosity; CL = clay matrix; F = feldspar; Q = quartz grains.  
Crossed polars, x 250.

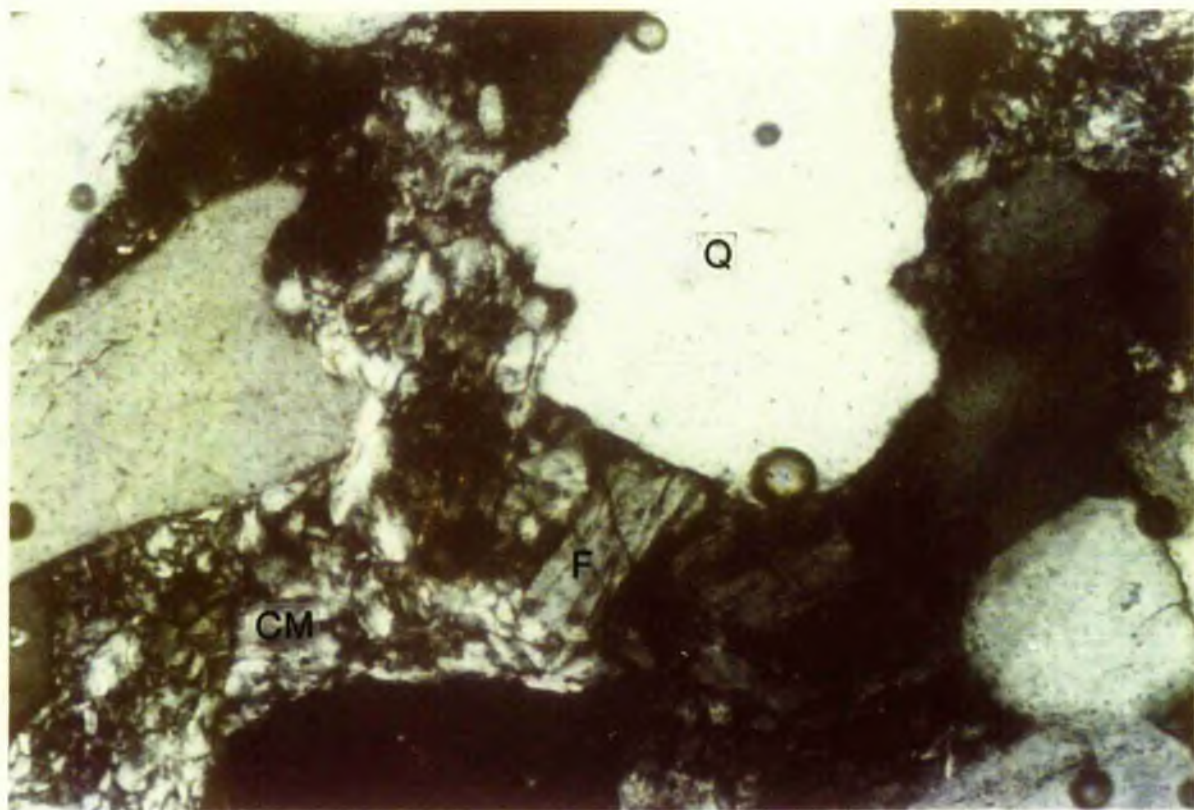
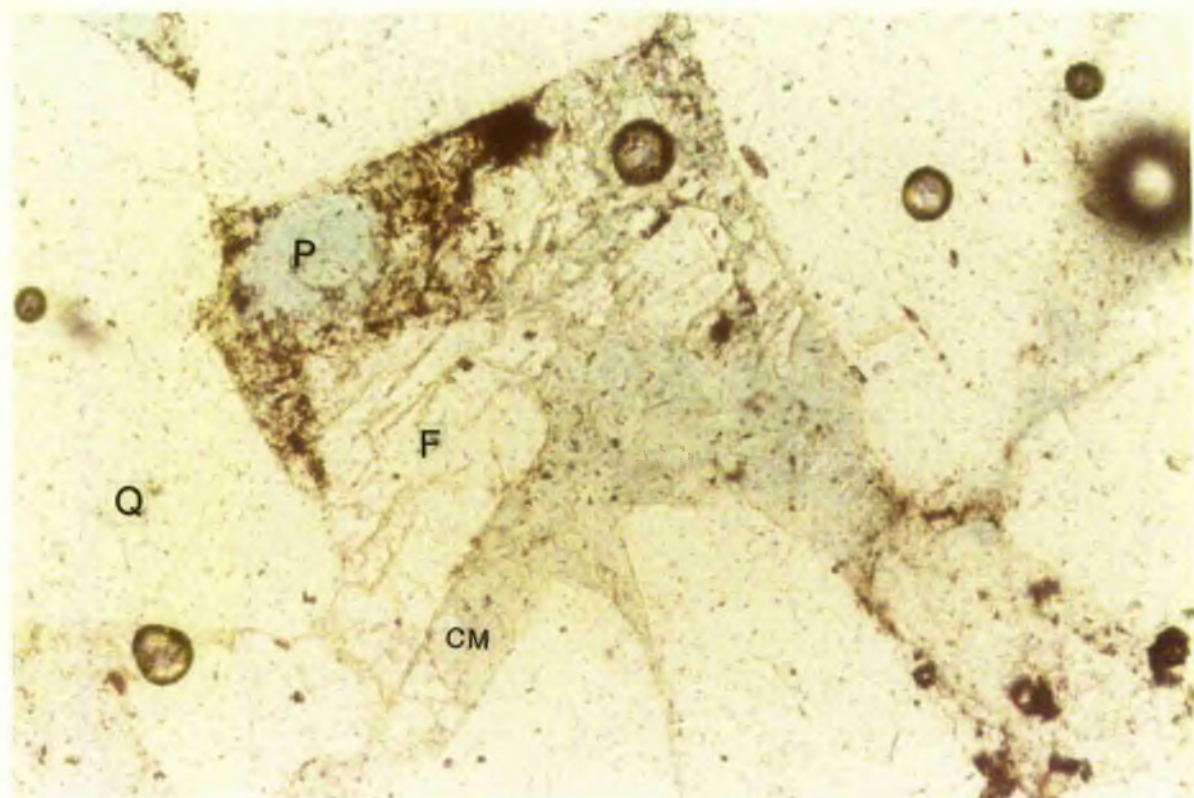
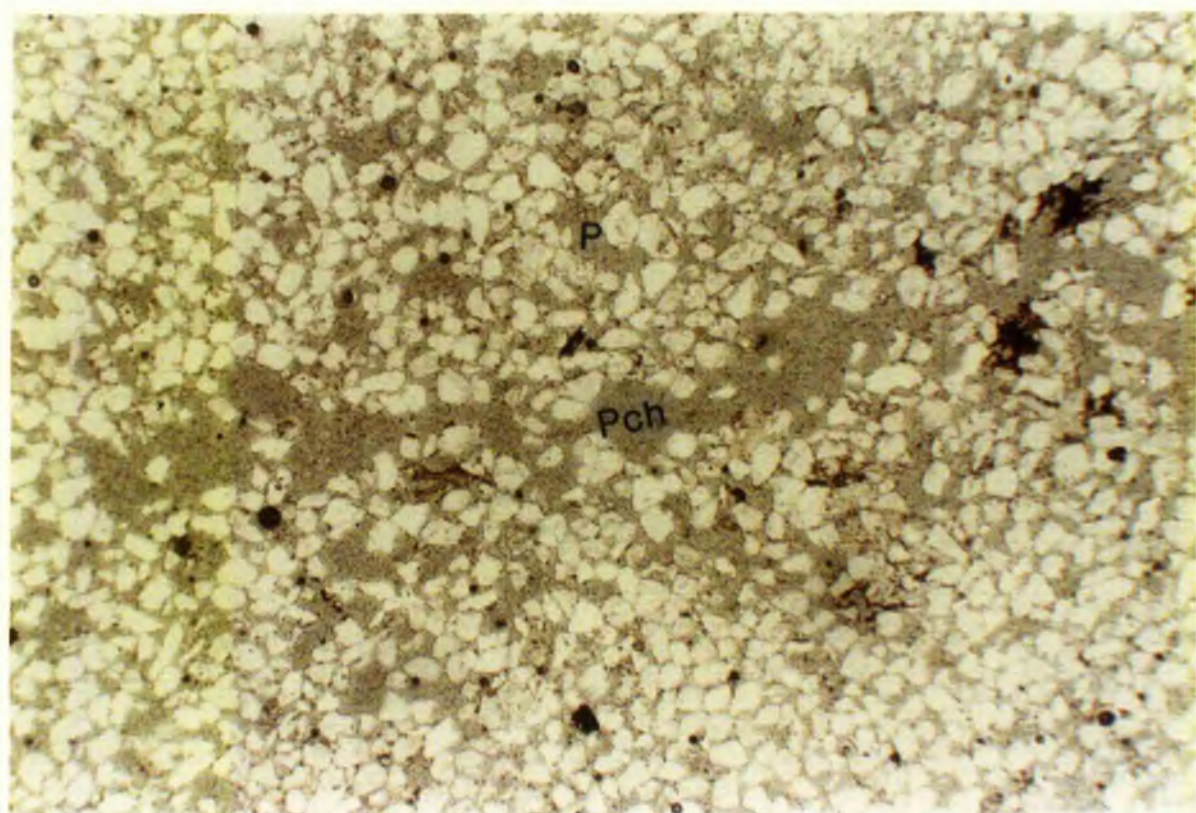
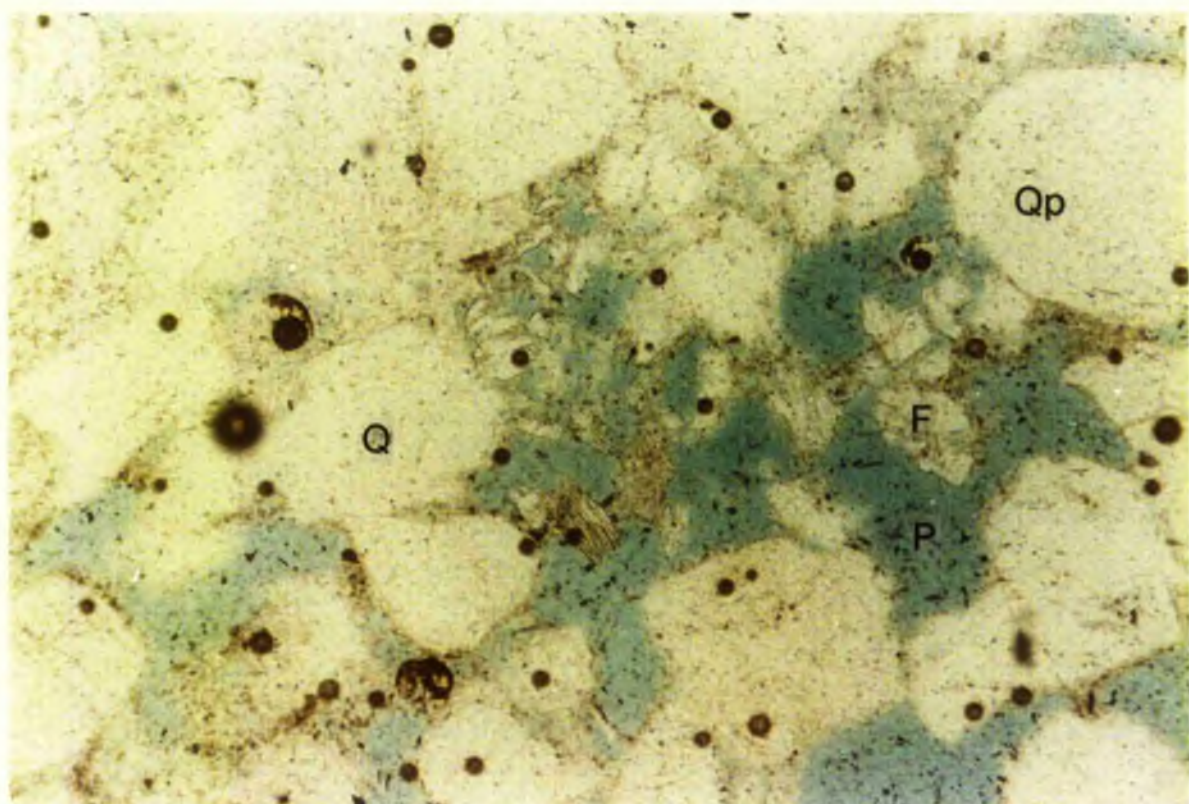


Fig 6.48 Photomicrograph of intra-replacement pore texture. Complete dissolution of replacive materials created intra-replacement pores and connected with intergranular pores. Sandstone Unit (S21a) - East side. P = porosity; F = feldspar grains; Qp = polycrystalline quartz; Q = quartz grains. Ordinary light, x 125.

Fig 6.49 Photomicrograph of open rock fracture. Dissolution of cement filling the fracture created large pore as a channel. Sandstone Unit (S14) - East side. P = porosity; Pch = channel porosity; Q = quartz grains. Ordinary light, x 25.



dissolution to form such large pores as channels.

5b Open grain fracture.

This is formed either through part of the grain, which may be a mixture (primary or secondary), or cutting completely through the grain when it is clearly of secondary origin. Most of the grain fractures recognized are not completely cutting through the grains, and some of them are branching in form. A secondary origin is suggested, because the fractures cut through the overgrowth they were filled by carbonate cement and some corrosion in the middle of the grain formed of void (Fig 6.50). This suggests that the void was not present before quartz overgrowth formed. The rare type which cuts the grain completely as in feldspar grain (Figs 6.51 A, B) is secondary and the pores were created by dissolution of the filling carbonate cement.

5c Open intergranular fracture.

Schmidt and McDonald (1979b) pointed out that this type occurs in intergranular matrix, in intergranular cement, and in intergranular replacive minerals. Two different types of open intergranular fractures are recognized in the Carbonate cement using the SEM as follows:-

- i Irregular fracture or dendritic fracture (Fig 6.52 A).
- ii Fracture followed by dissolution (Fig 6.52 B).

6 Sub-isolated pore texture.

The addition of this pore texture type to the system

erected by Schmidt and McDonald (1979) because the author suggests (following Pittman, 1979) that there are not completely isolated pores. This type may be intergranular (Fig 6.53 A), intra-cement (Fig 6.53 B) intra-matrix (Fig 6.53 C) or intra-granular (Figs 6.54 D, E).

Fig 6.50 Photomicrograph showing dendrite fracture and dissolution of carbonate cement corroded the middle of the quartz grain formed a void and it is connected with pores formed by fracture. Sandstone Unit (B7N) - West side. P = porosity; Q = quartz grains. Ordinary light, x 250.

Fig 6.51A Photomicrograph of open grain fraction. Feldspar grain (microcline) fractured and created pores. Sandstone Unit (S21C) - East side. P = porosity; F = feldspar microcline; QP = quartz polycrystalline; CM = clay material; Q = quartz grains. Ordinary light, x 250.

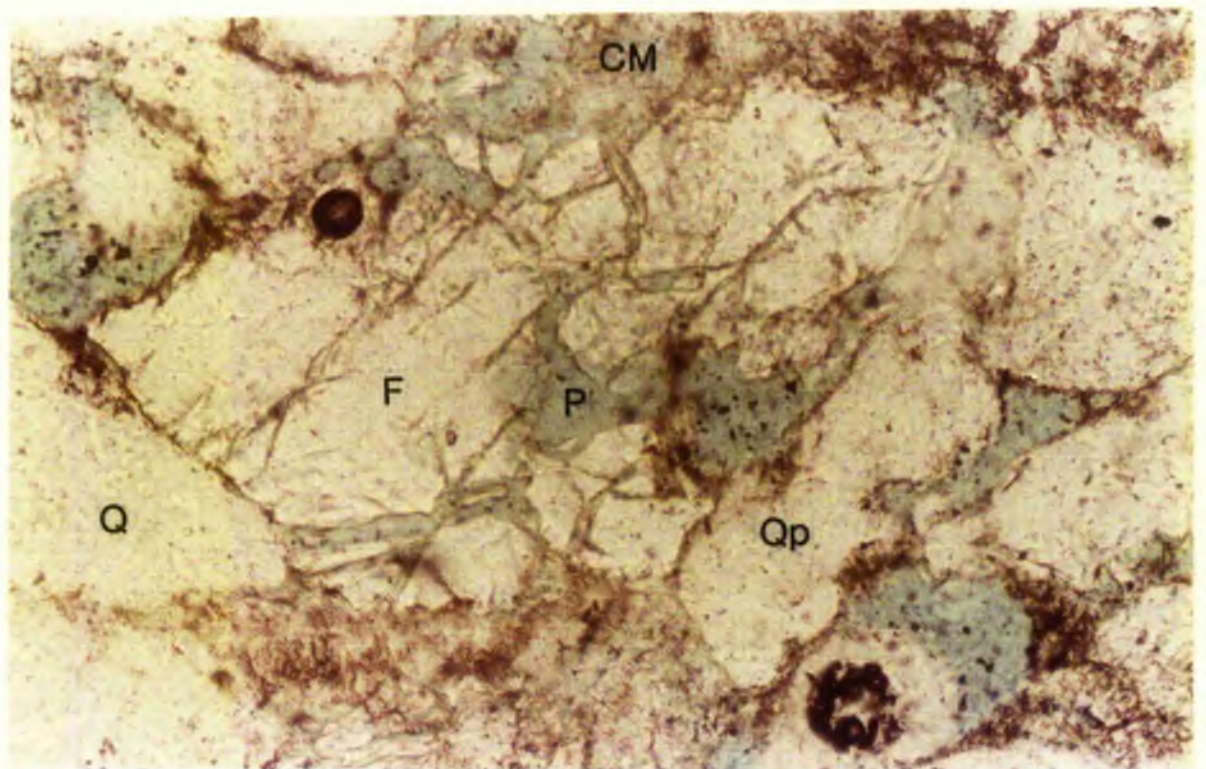
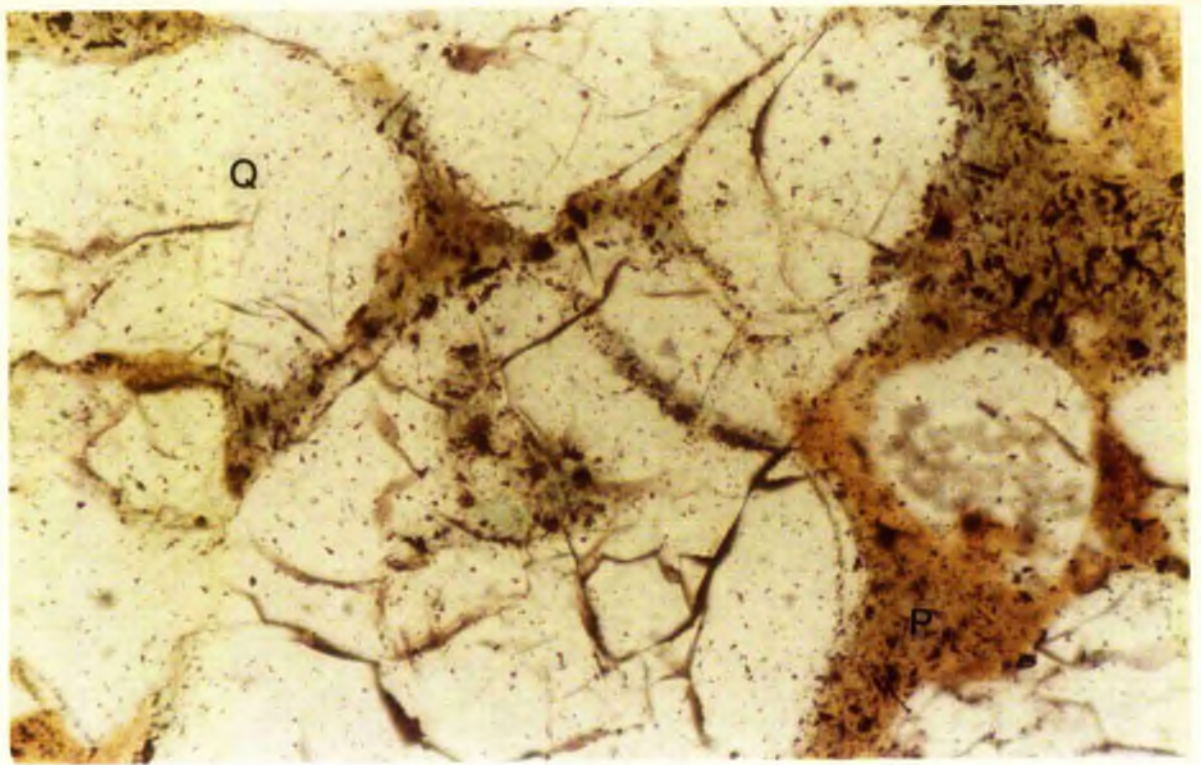




Fig 6.51B SEM photograph showing detrital feldspar grain fracture forming branching pore fracture (arrow). Sandstone Unit (S21a) - East side. Scale bar equals 20  $\mu$ .

Fig 6.52A SEM photograph of open intragranular fracture. Branching fractures (arrows) in different direction through the carbonate cement (calcite) created pores after the deformation. Sandstone Unit (F5b) - East side. Scale bar equals 20  $\mu$ .

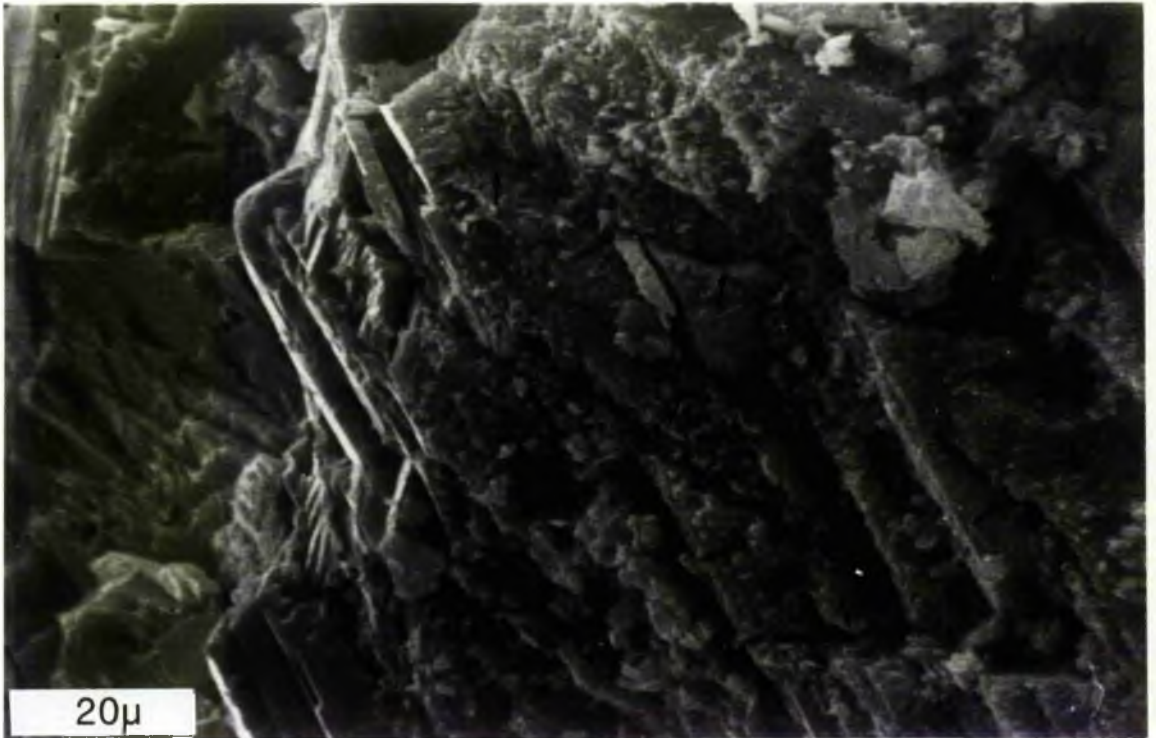
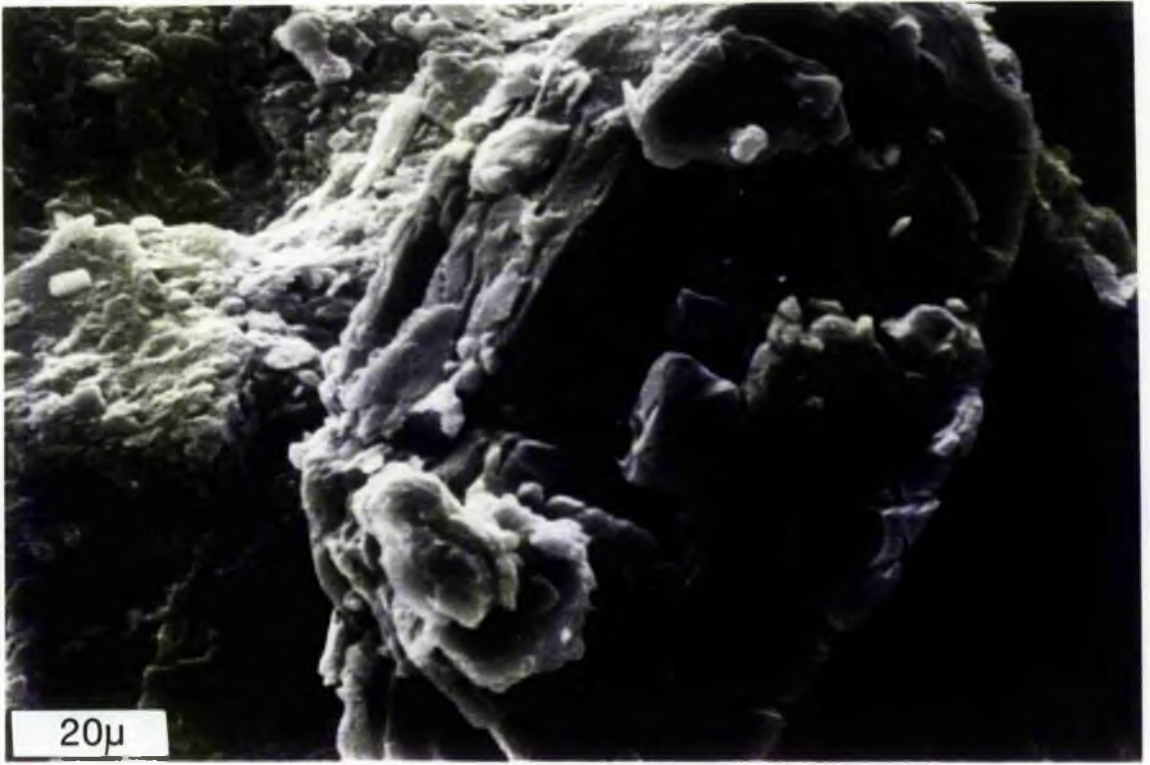


Fig 6.52B SEM photograph of open intragranular fracture pores created by the fracture of the carbonate crystal followed by dissolution, left side arrow indicates fracture, while right side arrow indicate as effected by dissolution. Sandstone Unit (F5b) - East side. Scale bar equals 20  $\mu$ .

Fig 6.53A SEM photograph of intergranular sub-isolated pore texture. Quartz grains overgrowth formed pores, which are now connected only by micropores. Sandstone Unit (S27) - East side. P = pores; Q = syntaxial quartz overgrowth. Scale bar equals 100  $\mu$ .

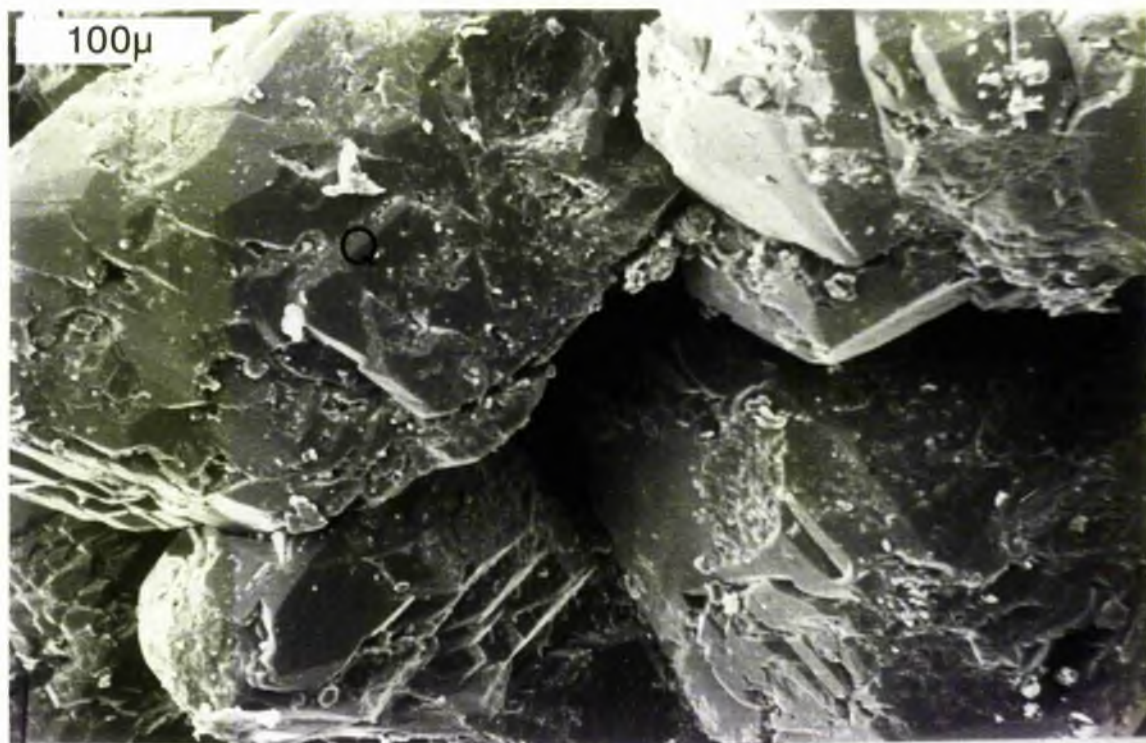
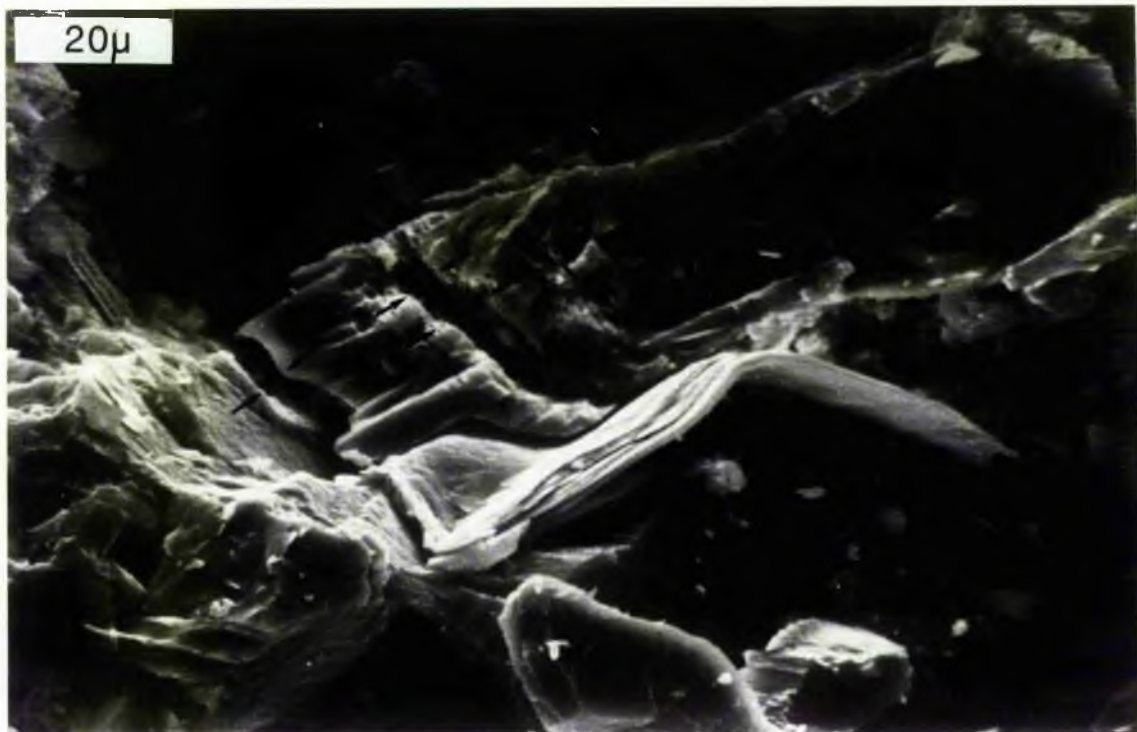


Fig 6.53B SEM photograph of intra-cement sub-isolated pore texture.

Corrosion of the carbonate cement created pores which are actually interconnected together. Middle part of sandstone Unit (L3) - West side. P = porosity; Q = quartz grain with conchoidal fracture; C = carbonate cement. Scale bar equals 20  $\mu$ .

Fig 6.53C SEM photograph of sub-isolated pores created from incomplete filling of the intergranular pore by clay matrix (kaolinite). Sandstone Unit (S21a) - East side. P = porosity; K = kaolinite; Q = quartz overgrowth. Scale bar equals 40  $\mu$ .

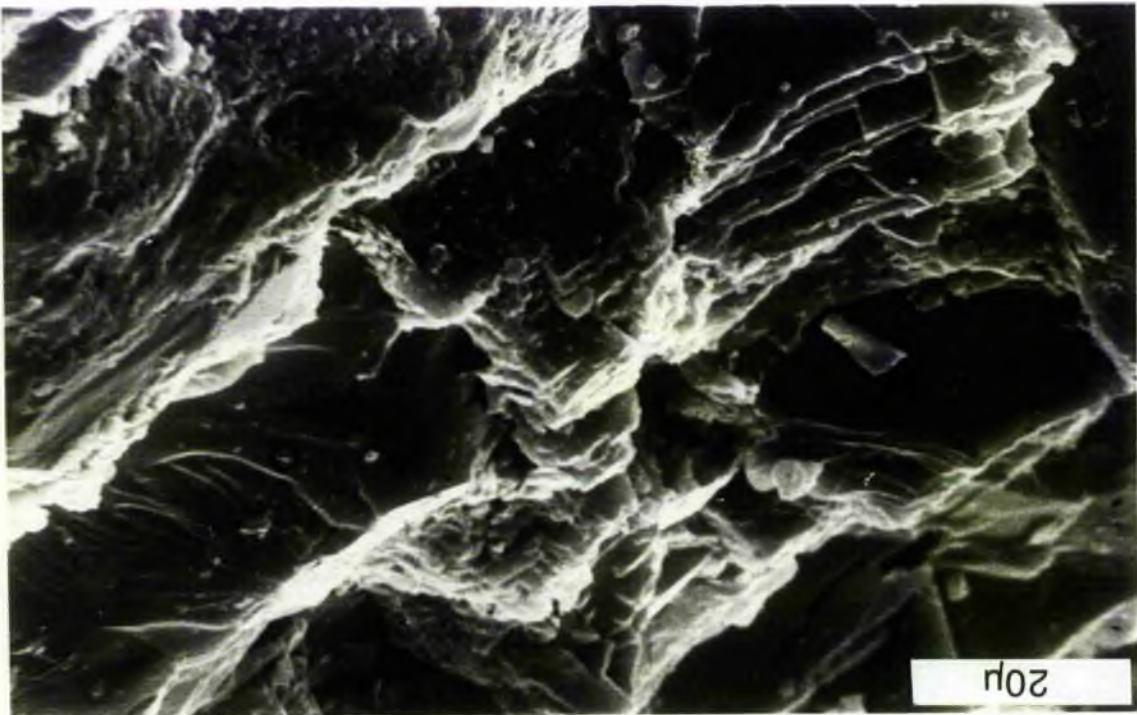
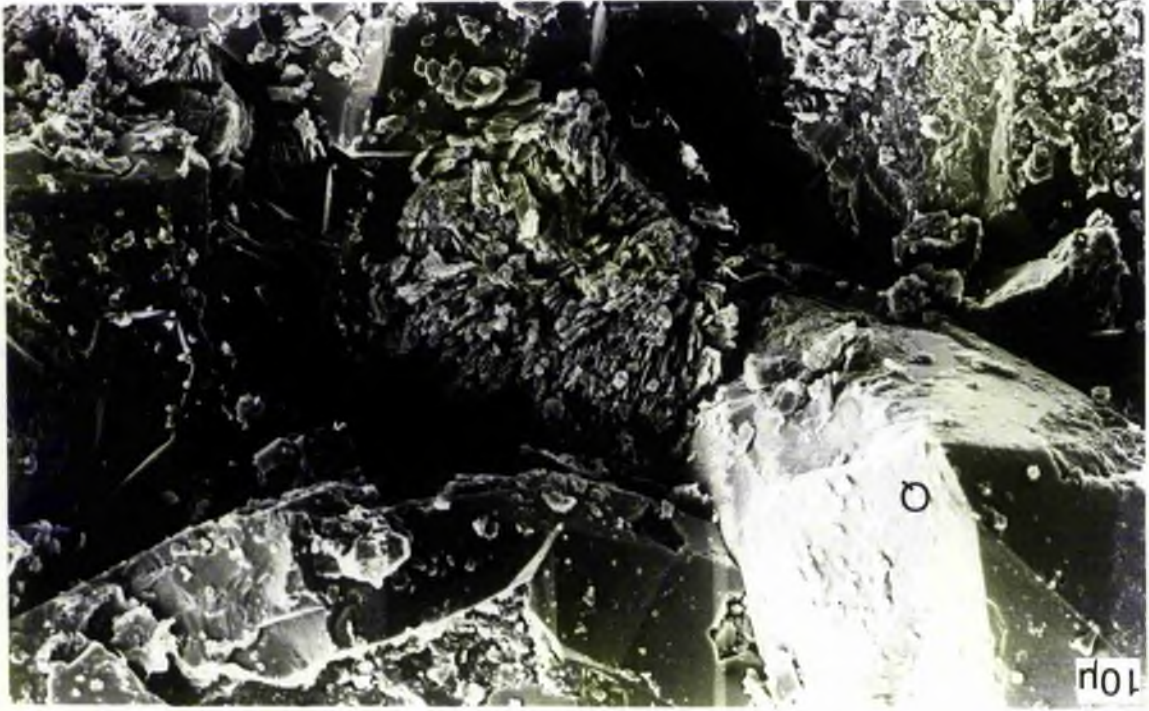


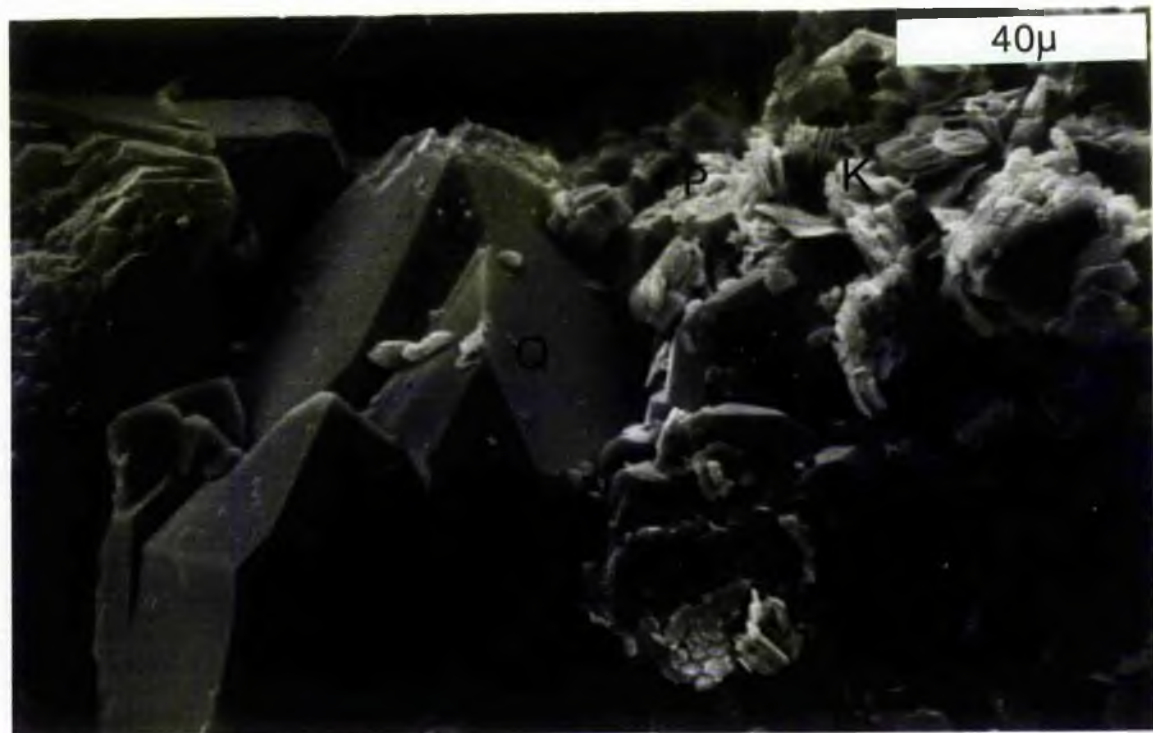
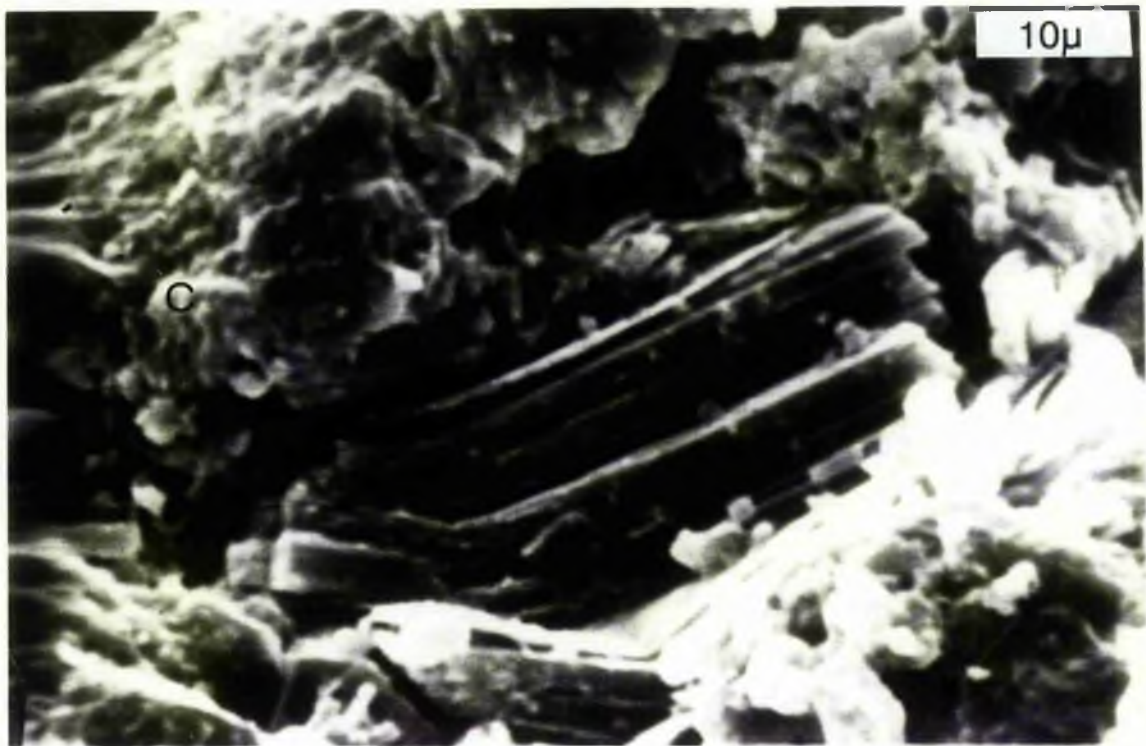
Fig 6.53D SEM photograph of intra-granular sub-isolated pore texture.

Feldspar grain effected by corrosion after splitting  
and creation of sub-isolated pore along the cleavage.

Sandstone Unit (F3) - East side. P = porosity; F = feldspar;  
C = carbonate cement. Scale bar equals 10  $\mu$ .

Fig 6.53E SEM photograph of intra-granular sub-isolated pore texture.

Cement material occupies the voids of polycrystalline quartz  
(right side), and created sub-isolated pores after dissolution,  
some of them were filled by clay materials. Middle part  
of sandstone Unit (B7) - West side. P = porosity; QP =  
polycrystalline quartz; Q = quartz overgrowth; K = kaolinite.  
Scale bar equals 40  $\mu$ .





Appendix No 7.1: Microprobe analyses of carbonate cement

SiO <sub>2</sub>	MgO%	FeO%	CaO%	MnO%		Type
0.097	9.9	12.04	29.6	0.0	middle	Ankerite
0.106	10.44	12.16	29.27	"		
1.23	9.31	14.59	26.27	"		
6.56	9.17	11.20	26.28	"	rim	
0.68	10.27	12.14	28.9	0.0	middle	Ankerite
0.57	9.93	12.36	28.6	"		
5.61	8.89	10.54	24.7	"	rim	
0.12	9.65	12.45	27.34	0.0	middle	Ankerite
0.19	9.90	11.39	28.83	"		
3.7	8.99	11.02	26.91	"	rim	
0.05	11.14	11.59	28.92	0.0	middle	Ankerite to
0.04	11.34	10.39	28.82	"		Ferroan dolomite
0.15	11.17	12.55	28.61	"		
0.29	12.55	11.58	25.92	"		
2.28	11.02	11.35	24.66	"	rim	
0.17	12.92	11.34	25.20	0.0	middle	Ferroan dolomite
1.15	13.11	9.56	24.4	"		
2.16	11.06	11.26	24.37	"	rim	
0.08	11.72	12.39	28.88	0.0	middle	Ankerite to
0.07	10.82	10.45	28.82	"		Ferroan dolomite
0.14	11.19	10.78	26.29	"	rim	
1.76	10.35	10.7	27.68	0.0	middle	Ferroan dolomite
2.91	9.33	8.8	23.33	"		
2.24	9.81	11.26	24.19	"	rim	

Appendix 7.2 Precision of electron microprobe data

Analysis was performed at the Grant Institute of Geology, University of Edinburgh, using the energy dispersive electron microprobe. Using the limited time available, carbonate, mica, clay and feldspar took precedent.

Subsequent analyses of further samples were made at the Geology Department, University of St Andrews on a Jeol 733 Superprobe under the direction of Dr W E Stephens and Donald Herd. The purpose of this was to investigate in greater detail variations found on the initial analyses.

Appendix 7.3 Precision of XRF analysis

X-ray fluorescence spectrometry (XRF) analysis was conducted on a PHILLIPS PW1212 automatic spectrometer linked to an APPLE IIe Computer in an on-line system. Software for the system and later data handling - CIPW normative mineralogy calculation and molar proportions of oxide was provided by Dr W E STEPHENS.

Major oxide analyses were - SiO<sub>2</sub>, Al<sub>2</sub>O<sub>3</sub>, TiO<sub>2</sub>, Fe<sub>2</sub>O<sub>3</sub>, MnO, CaO, Na<sub>2</sub>O, K<sub>2</sub>O - following the conditions of Norrish and Chappell (1977). Analyses were performed on fused beads of 0.5 g sample powder prepared after the method of Harvey et al. (1973) and adapted for use at St Andrews by R A Batchelor (Int Pub 1980). All beads were checked optically for quench crystals and re-fused if any found present.

Appendix 7.4 Wet chemical techniques

Major elements were determined by a scheme which utilises a combination of published techniques and formed the basis for wet chemical analysis at St Andrews. (Batchelor, 1980).

SiO<sub>2</sub> Determined spectrophotometrically as the reduced blue silicomolybdenic acid complex, after fusion of the sample (0.05 g) with NaOH in nickle crucibles.

Al<sub>2</sub>O<sub>3</sub>, Total Iron as Fe<sub>2</sub>O<sub>3</sub>, MnO, CaO, MgO Determined by AAS after fusion of 0.1 g sample with 0.7 g lithium metaborate, and dissolution in 2% V/V HNO<sub>3</sub>. Lanthanum chloride hexahydrate (10% La solution) was added to produce a 0.5% La concentration.

TiO<sub>2</sub> Determined spectrophotometrically as the yellow Ti-H<sub>2</sub>SO<sub>4</sub>-H<sub>2</sub>O<sub>2</sub> complex after dissolution of 0.5 g sample in HF/HClO<sub>4</sub>.

P<sub>2</sub>O<sub>5</sub> Determined spectrophotometrically as the reduced blue phospholybdenic acid complex after dissolution of 0.5 g sample in HF/HClO<sub>4</sub>.

Na<sub>2</sub>O, K<sub>2</sub>O Determined by AAS after dissolution of 0.5 g sample in HF/HClO<sub>4</sub>. Ammonia was used to precipitate trivalent cations prior to the determination of Na and K.

FeO Determined volumetrically (redox titration) with potassium dichromate after cold HF attack on 0.2 g sample in the presence of ammonium metavanadate.

H<sub>2</sub>O total Determined gravimetrically as a modified Penfield method.